From Dome to Disease: The Respiratory Toxicity of Volcanic Cristobalite

DAMBY, DAVID,ERNEST

From Dome to Disease

The Respiratory Toxicity of Volcanic Cristobalite

David Ernest Damby

A thesis submitted in partial fulfilment of the requirements for the degree of

Doctor of Philosophy

One Volume

Department of Earth Sciences

Durham University

2012

Abstract

Exposure to fine-grained volcanic ash can potentially cause acute and chronic respiratory disease. The toxicity of ash is likely to vary depending on the type and style of eruption; eruptions at dome-forming volcanoes, in particular, can produce ash containing substantial quantities of respirable crystalline silica, a recognised human carcinogen and causative agent of silicosis. Volcanic domes crystallise crystalline silica as cristobalite, which is metastable at dome-forming temperatures (ca. 850 °C), through deposition from silica-saturated vapours and through devitrification of volcanic glass.

Five dome-forming volcanoes are studied to constrain the hazard posed by volcanic cristobalite, including: Colima, Mexico; Merapi, Indonesia; Mount St. Helens, USA; Santiaguito, Guatemala; and Unzen, Japan. The evolution of the cristobalite hazard is investigated from crystallisation in volcanic settings to its potential effect on biological systems, through a series of petrological, physicochemical and toxicological studies.

We rationalise the presence of metastable cristobalite below its stability field in all domes studied by way of a textural investigation, and conclude that the incorporation of aluminium and sodium into the silica structure facilitates crystallisation. Since particle toxicology is dependent on composition and structure, the observation of cation substitutions is expanded in a geochemical and thermodynamic investigation of volcanic cristobalite to constrain its mineralogy. We find that incorporation of 1-4 wt. % aluminium leads to a poorly-ordered cristobalite structure. This investigation facilitates a mineralogical comparison of the cristobalite hazard among volcanic locations and provides the framework for assessing volcanic cristobalite toxicity. We investigate the ability of volcanic ash to elicit an *in vitro* pro-inflammatory response, focusing on silica-mediated experiments, and relate the influence of structure and composition to the potential physiological burden. We find that volcanic cristobalite can be mineralogically considered as a single entity among locations, and that cristobalite-bearing ash is less toxic than expected. Nonetheless, we recommend that eruptions be considered on a case-by-case basis to most effectively aid the risk mitigation work of disaster managers globally.

Declaration

I declare that this thesis, submitted for the degree of Doctor of Philosophy at Durham University, is my own work and not substantially the same as any which has been previously submitted at this or any other university. Where appropriate, I have clearly indicated the contributions of colleagues to fully acknowledge all collaborative work.

David Damby

Durham University

December 2012

Thank you to my supervisors:

Claire Horwell

Ken Donaldson

Ed Llewellin

This work was supported by the Christopher Moyes Memorial Foundation

http://www.moyesfoundation.org

The title of this work resembles a manuscript authored by Kathy Cashman and others: ‘From Dome to Dust: Shallow Crystallization and Fragmentation of Conduit Magma During the 2004–2006 Dome Extrusion of Mount St. Helens, Washington.’ Retrospectively, it is impossible to discern whether their title shaped the present; nevertheless, I gratefully acknowledge their creative phrasing.

Acknowledgements

Although not always apparent, I've spent the entirety of this non-linear attempt at scientific relevance being grateful; grateful for opportunities, for patience and goodwill, for friendship and advice. (Un)fortunately, the words in this thesis only reflect the scientific half of this pursuit; the life half is elsewhere recorded: in memories and scars, discarded airplane and train tickets, in the total number of brews (both coffee and beer) tallied, and in de-tagged pictures from dance floors. Acknowledgements for scientific contributions precede each chapter, but I'd also like to thank the people that I've shared my life with during this journey, to whom I will be forever grateful.

Family – thanks for putting up with me moving abroad and consequently missing some of the more mundane things in life: a first-born child, one in a streak of 25 consecutive summer holidays, etc. Thanks, Dad, for your unremitting enthusiasm about me becoming a volcanologist, irrespective of being unsure at first of what exactly the role entails. Thanks, too, for constantly asking if I'm almost finished and reminding me that it "seems to be taking a long time." Kathryn, Jon, Katie (and Sawyer), and Melissa, thanks for repeatedly questioning why I did this and asking when we'll live in the same country. Your phone calls kept me going. Mom, you traipse through my thoughts nearly every day, helping me to shape who I should be, how I should live, and which paths I should consider. I love you all.

Harriet – thanks for indulging me with your love of my country and of country music. You tore me away from the office when I most needed to be there, and I'll never wish it any other way. I couldn't be luckier.

Rob – thanks for maintaining your welcoming, exuberant nature whenever I'd randomly appear on the map. Your willingness to take me in eased the difficulties of life abroad during those calendar moments when family-time reigns, Easters and otherwise. It was always my hope to grow in step with you academically – something that I haven't managed, but something that I will continue to strive towards, nonetheless. Your infectious love of science and constant desire to philosophize keeps me constantly curious; whether we're sharing an office, a house, or we're cities apart, I often hear/read/see something and think… "Rob would love this." You were the first person that I met in Durham and the last person that I saw off. We'll have a conversation about the cyclicity of that some day – let's make that day soon.

Sabina – as a founding member of DUVs (a.k.a. 'Birds on Fire', the precursory volcanology group to DVG) and a stakeholder in my P.I. business, you are my partner in crime; when

they come for me, I'll deny it. Thanks for the cards, and chats, and cakes, and for not only entertaining my eccentric ideas, but supporting and encouraging them. We did this together, step-by-step. That said, we were rarely on the same step at the same time and were often unsure of whether we were going up or down… regardless, we always high-fived when we figuratively passed one another. Congratulations –well deserved.

Thanks, too, to the other Horwellites (to which this may be Claire's first hearing of the term): Jenn, for your well-heeded advice from day one, and extending an impeccable mix of friendship and professionalism whenever we crossed paths; Claire Nattrass, for putting up with the feigned know-it-all opinions of an older academic sibling and making my failed experiments seem worthwhile; and Sarah, for non-stop laughs and your contagious positive attitude.

Jon Davidson, Rich Brown, and Colin Macpherson – thank you for your open doors, free advice, and access to your wealth of knowledge. Thanks to the rest of the volcanology coffee group, as well, for making Wednesday lunches a bright spot in the week. Pete, don't ever forget a mug.

Please accept my blanket thanks to all of the post-grads who contributed to the life, culture and gossip of Durham Earth Sciences. In particular, thanks: BJ, for incessantly talking and your efforts to get me to go mid-week clubbing; Iona, for your ear and revelling in mutual freak-outs; Leo, for big plans and tunes… chooones!; Izzy, for your effortless capacity to rant in the face of life's injustices (Yum bread, for example); and Niamh, for tolerating my incessant gallivanting and re-introducing me to life. Thanks, too, to the undergrads for making me feel like I know something about geology.

Thanks to my Durham-based North-American contingent (and occasional housemates) – Jason and Mylène. One of you is a better role model than the other. Thanks for your shared enjoyment in absolutely devouring pulled pork.

Glovebox and Gordon: thanks for having a sofa, and for the banter. I'll be back.

Thank you Alison Rust, Rick Hoblitt, Dave Sherrod Matt Watson, Eliza Calder, Jess Ball, Jean-Christophe Komorowski, Susanna Jenkins and Peter Baxter for your willingness to welcome a stranger into your field studies. You were all beyond generous with your time, and those experiences and the knowledge learned are the foundation on which I hope to progress. Thanks to Gustavo, Paco, Alvaro and Julio for their brilliant support in Guatemala, and to Estu and Adrien for the same in Indonesia. The success of this project fully rests on their generosity.

Thank you Gordon Cressey, Jens Najorka, Bice Fubini, Maura Tomatis, and Leon Bowen for your tireless hospitality, tuition, and support with data analysis and beyond. I've done my best to file every bit of advice into a mental 'do not forget' folder. Fiona and Jen, thank you for your friendly welcome to life in Edinburgh and for gracefully enduring an endless string of "where is…?" Ben Williamson, thanks for your optimistic responses whenever things looked dire.

Thanks to Jon Boyson for unknowingly convincing me that research is the way forward. His asking of "what are you going to do for money?" the day that we met is as relevant now as it ever was. Thanks, too, to Alan Chant for suggesting a move England. Without that passing comment, this tome wouldn't exist. In a similar vein, thanks JR for showing me Edinburgh for the first time and implanting an indestructible need to return. Apologies for missing your first-born, too.

I'd also like to thank the Christopher Moyes Memorial Foundation and Jan Moyes for deciding that this project was worthwhile, providing a generous studentship, and for continually supporting applied research with tangible, community-orientated impacts.

Finally: Claire, Ed and Ken – your influence is rife throughout this thesis, but extends beyond the binding as well. Claire, I know that I caused many extended moments of stress, but thank you for your continued support and outwardly unwavering faith (whether deserved or not). Ed, thank you for re-igniting both my desire to quantify everything and my love for creative rhetoric. I'm in continuous awe of your endless supply of hyperbolic definitives. Ken, thank you for instilling in me the importance of understanding the history behind everything that we do, including me in your statements that started with 'us biologists,' and for proving that it is possible for a career in science to just 'be a hobby.' You have all helped shape this project and, more importantly, my way of thinking.

Contents

List of Figures

Chapter 5 – Structure and composition of volcanic cristobalite

Chapter 6 – Particle characterisation and *in vitro* toxicology of dome-collapse ash

List of Tables

Chapter 6 – Particle characterisation and *in vitro* toxicology of dome-collapse ash

1

Introduction

1.1 Project Rationale

Exposure to fine-grained volcanic ash can potentially cause acute and chronic respiratory disease. Multidisciplinary research into volcanic ash as a respiratory hazard came about in the wake of the 1980 eruption of Mount St. Helens, USA, where it transpired that the ash contained significant amounts of crystalline silica (Dollberg et al., 1986), a human carcinogen and causative agent of the scarring respiratory disease silicosis. 30 years on, it is known that exposure to ash can exacerbate existing conditions, triggering acute diseases such as asthma and bronchitis; however, clinical, epidemiological and toxicological studies have given inconclusive results regarding the ability of ash to cause chronic disease (Horwell and Baxter, 2006).

The focus of the current study is on dome-forming volcanoes, ash from which has been shown to contain up to 20 wt. % crystalline silica in the form of cristobalite (Horwell et al., submitted-a; Appendix 4). The active dome environment is thought to facilitate the crystallisation of cristobalite through devitrification and vapour phase deposition (Baxter et al., 1999; Horwell et al., post review; Appendix 4). Volcanic domes are inherently unstable, resulting in collapse and the generation of respirable, cristobalite-rich ash. The link between the inhalation of respirable silicas and respiratory diseases (e.g., silicosis) is widely recognised; therefore, prolonged exposure to respirable, cristobalite-rich ash raises concerns about the onset of chronic, injurious diseases similar to those seen in occupational settings, particularly coal mining, granite quarrying, and diatomaceous earth processing.

Extensive research has focused on the biological mechanisms of silica induced diseases; however, insufficient attention has been paid to the mineralogical properties that may influence biological reactivity. The effects of structure and composition on the physiological burden of volcanic cristobalite are ill-defined as the implications for toxicity have only been sufficiently studied at one location: Soufrière Hills volcano, Montserrat (Horwell et al., accepted; Appendix 4). It is therefore necessary to systematically characterise the mineralogical properties of crystalline silica from different volcanic settings to constrain the disease-causing potential of ash, and to elucidate the properties responsible for adverse biological responses.

This study focuses on a selection of volcanoes in developing nations in South Asia and Central America, where cultural influences and fertile volcanic soils provide incentives for populations to settle near potentially active volcanoes. Sustained population growth and continuing urbanisation in these areas could increase the consequences of future eruptions, stressing the capacity of local governments and international organisations to mitigate and

respond to emergencies. Nearly 10 % of the world's population lives within 100 km of a historically active volcano (Small and Naumann, 2001); therefore, recognising specific health hazards based on geological setting will significantly aid decisions made by disaster managers worldwide.

1.2 Project Background

This thesis stems from work initiated by my supervisor, Claire Horwell, along with Ben Williamson (University of Exeter) on the presence of cristobalite in volcanic domes. Their work, which commenced circa early 2005, aimed to characterise cristobalite in volcanic dome rock from Soufrière Hills volcano. It followed on from the landmark paper by Baxter et al. (1999), which raised concern about cristobalite in volcanic ash and traced the source to volcanic domes. Although originally aimed to be published prior to start of this PhD project, the work by Horwell and Williamson expanded, benefiting from substantial intellectual and experimental contributions that arose in tandem with this thesis, and was split into two publications: one addressing the petrological implications and one addressing the toxicological implications of cristobalite in dome rock and dome-derived volcanic ash. The two manuscripts are outlined below; however, we specifically request that the reader of this thesis become familiar with both manuscripts provided in Appendix 4.

The first manuscript by Horwell et al. (post review; Appendix 4) investigates the petrology of volcanic cristobalite and is pending resubmission at the time of writing. It texturally identifies the two modes of cristobalite crystallisation originally proposed by Baxter et al. (1999): devitrification and deposition from a vapour phase. Vapour-phase deposition requires a source of silica and, therefore, mechanisms of silica transport are discussed. The manuscript concludes that redistribution of silica within a volcanic system has implications for geochemical studies, due to enrichment of Si from the presence of non-magmatic cristobalite, and for dome stability, due to the competing factors of decreased permeability and cementation from cristobalite crystallisation in cracks and pore space.

The second manuscript by Horwell et al. (accepted; Appendix 4) specifically addresses the physicochemical properties of cristobalite in volcanic ash with implications for particle toxicology, and has just been accepted for publication in Particle and Fibre Toxicology. The manuscript does not contain any toxicity data but demonstrates that 1) volcanic cristobalite is closely associated with other mineral phases and, therefore, exposure will be to particles with heterogeneous surfaces; and 2) cristobalite deviates compositionally from pure SiO_2, containing up to 4 wt. % combined aluminium and sodium. Together, these two factors may

modify volcanic cristobalite toxicity, providing previously unconsidered particle-based insight into the well known variability in the toxicity of silica-bearing dusts.

This thesis conceptually and experimentally builds on the findings at Soufrière Hills, and sets the conclusions of the original studies in their global context through a systematic study of samples from a worldwide suite of dome-forming volcanoes.

1.3 Aims of Thesis

The current work has multiple aims which bridge scientific pursuit and hazard implications, and are as follows:

Regarding the presence of cristobalite in dome-forming volcanoes:

1) To understand the *formation* of cristobalite in volcanic dome rock by systematically characterising its presence in a suite of volcanoes worldwide.

2) To carry out a detailed *mineralogical analysis* of cristobalite in dome rock from multiple dome-forming volcanoes in order to constrain the hazard posed by silica-bearing volcanic ash that results from incorporation of dome material during an eruption.

Regarding the nature of dome-derived volcanic ash:

3) To adapt and develop novel physicochemical *methods* used to assess potentially toxic respirable silicas in dome collapse ash, which will be applicable to a range of ash types and other natural and industrial mineral dusts.

4) To evaluate the toxicologically relevant *physicochemical properties* of volcanic ash from dome-forming eruptions, and establish a foundation to contextualise toxicity results (the structural side of the structure-toxicity relationship).

5) To determine the *toxicity* of volcanic silica in well-characterised dome-eruption samples using *in vitro* experiments, and benchmark the findings against previous studies to expand the current understanding of the respiratory hazard posed by volcanic ash (the toxicity side of the structure-toxicity relationship).

Regarding the hazard of dome-forming volcanoes:

6) To assess the *crystalline silica hazard* posed, and link the knowledge of exposure to risk. This is done by constructing a comparative database for dome-related ash so that classical measures of the silica hazard can be linked to the origin and nature of the silica. This assessment improves the current understanding of volcanic hazards and will aid hazard management during a crisis by establishing the likely particulate hazard before an eruption.

1.4 Structure of Thesis

This thesis is presented as a series of individual studies that follow a linear, hazard-based narrative from 'dome to disease'; that is, it starts with determining the origin of cristobalite in volcanic material and finishes by defining the pathogenicity of cristobalite-bearing ash from dome-forming eruptions. Collectively, the study takes an in-depth look at the mineralogy of volcanic crystalline silica in order to understand what is challenging the body following exposure.

The remainder of this thesis is divided into six chapters:

Chapter 2 gives the necessary volcanological, medical, and social *background* to contextualise the study. This includes the presence of cristobalite in volcanic ash, physicochemical concerns regarding potentially toxic particulate matter, the biological stage for particle-lung interactions, and the community settings within which this study needs to be applied.

Chapter 3 is a comprehensive *methods* chapter that contains detailed information on all of the experiments carried out. Many techniques are repeatedly used throughout the thesis, and are therefore housed in one location for ease of reference. All of the research chapters refer back to the methods outlined in this chapter.

Chapter 4 details the presence of cristobalite in volcanic domes as a global study for the assessment of health hazard. It rests on the understanding that volcanic ash is fragmented rock; we can therefore use the bulk 'starting' material to characterise the hazard, which would otherwise be difficult to glean from isolated studies on ash. Extensive observations are used to identify and characterise cristobalite in dome rock, and are expanded to comment on the formation of cristobalite. This chapter, therefore, addresses the origin of cristobalite in ash (*aim 1*) and outlines the presence and abundance of cristobalite in volcanic dome rock. In doing so, it defines the crystalline silica hazard posed by dome-forming eruptions worldwide.

Chapter 5 examines the structure and chemistry of volcanic cristobalite in order to best constrain its physicochemical properties (*aim 2*). Crystalline silica in the workplace has been called a 'variable entity' (Donaldson and Borm, 1998), meaning its toxicity is dependent on a variety of ill-defined 'internal characteristics and external factors' (International Agency for Research on Cancer, 1997). Two approaches are taken in this chapter: physical and chemical. The lattice structure and crystallinity of volcanic cristobalite are investigated using the alpha-beta transition, and the composition is analysed to determine its chemical 'purity' (i.e., degree of elemental substitution). Analyses are performed on both dome rock and volcanic ash to assess whether changes in the hazard occur due to eruptive processes; for example, fragmentation, transport, or cooling of material. The composition and structure are collectively discussed to further define conditions of formation and to initiate a discussion on the physicochemical characteristics which can control the toxicity of natural mineral dusts.

Chapter 6 is an investigation into the pathophysiological response to being challenged by volcanic ash, and is presented in two parts. In Part I, particles are first physicochemically characterised with respect to the newfound understandings laid out in the previous chapters (*aims 3 and 4*), and are then subjected to a range of surface-reactivity tests. In Part II, the *in vitro* toxicity of volcanic ash is assessed through experiments that determine the likely response elicited by the body in response to exposure (*aim 5*). The mechanism of crystalline silica toxicity is unknown; therefore, particles could not simply be considered alongside a predefined disease pathogenesis. As occupational health concerns continue to move policy towards limiting exposure to toxic particulate, particle characterisation has become a useful platform for defining a potential hazard (*aim 5*). Accordingly, the physicochemical characterisation in Part I investigates the abundance of crystalline silica in ash samples (therefore, the burden for any given exposure) and particle morphology to further consider lung penetration and, ultimately, bioaccessibility. In Part II, *in vitro* assays are used to model the likely interactions of ash in the lung and, therefore, the likely biological response following exposure. Individual studies on distinct eruptions have previously been undertaken; however, this extensive, comparative study on volcanic ash will serve hazard management during future eruptions as all samples are benchmarked according to current knowledge.

Chapter 7 draws together all of the key findings of this research and discusses the results with respect to the main aims set out here. The discussion is both geologically and hazard focused (*aim 6*), and considers the implications beyond the bounds of the individual chapters.

Appendices

Appendix 1 contains a catalogue of SEM images. Appendix 1 is only available digitally. Please see hard copy for data CD or contact the author for a copy.

Appendix 2 contains raw data from analytical work. Appendix 2 is only available digitally. Please see hard copy for data CD or contact the author for a copy.

Appendix 3 contains health hazard assessments for ash from three volcanoes (Colima, Mexico; Eyjafjallajökull, Iceland; Pacaya, Guatemala) which were conducted during this study using concurrently employed techniques.

Appendix 4 contains the publications that have resulted from concurrent studies with this research, many of which have been incorporated into this thesis and are included here for reference. They are examples of the techniques that I have learned, helped develop and utilised during this study.

1.5 Approach and Limitations

It became apparent after the commencement of this project that a one-to-one comparison of ash and dome rock was not feasible. Ideally, ash samples and a selection of dome rock would be sourced from the same dome-collapse event; however, this was not possible since volcano observatories do not often carry out systematic sampling of this nature, and there were no dome-collapse eruptions during fieldwork while sampling dome rock. Therefore, the overriding limitation of the current study is in directly linking investigations on dome rock samples with ash samples. The second limitation follows on from the first, in that eruptive behaviour among the study locations was not directly comparable. For example, samples of ash from Santiaguito were entirely from ash-venting episodes, whereas ash samples from Merapi are almost exclusively explosive. This limitation propagates through comparisons with previous results for Soufrière Hills, where the majority of ash samples analysed were derived from cataclysmic dome collapses.

Considering the temporal differences in cristobalite abundance for dome rock, evident in samples from Soufrière Hills (approximately 1-11 wt. %; Horwell et al., post review; Appendix 4), as well as a heterogeneous spatial distribution of abundances, evidenced from fieldwork at Santiaguito, it is impossible to constrain the source of ash derived from non-cataclysmic events without detailed volcano monitoring. This is an inherent difficulty of carrying out field work at active volcanoes in developing countries, where the infrastructure

and financial support do not exist to collect and archive well-documented samples. Even at Mount St. Helens, for which an extensive archive of dome rock samples exists at the United States Geological Survey (USGS) Cascades Volcano Observatory, very few ash samples have been stored from events following the cataclysmic 18 May 1980 eruption.

The above limitations mean that unavoidable gaps exist in the scientific interpretation of the results. From a hazards perspective, however, the results are more representative of past and future exposure. They are also more representative of the generalisations that need to be made during hazard management, as up-to-date knowledge of the extent of cristobalite crystallisation in the dome would be unavailable. Additionally, if another case like the present Soufrière Hills eruption arises, where the origin of ash and dome rock samples are well documented, the methods and considerations now exist to corroborate these samples.

2

Background

2.1 Crystalline Silica

Silica (SiO_2) is a combination of two of the most abundant elements in nature, and can exist in a number of amorphous and crystalline forms (polymorphs). Quartz is the most common of these because it is stable at ambient pressure and temperatures; as a result, it is the most abundant mineral on Earth (Deer et al., 1996). Cristobalite and tridymite are high-temperature crystalline silica polymorphs most commonly found in volcanic environments (Figure 2.1). All of the silica polymorphs have structures consisting of SiO_4 tetrahedra that share all oxygen atoms with adjacent tetrahedra. Transitions can occur between polymorphs in a reconstructive manner, which requires physically breaking bonds to form new structural configurations. This transformation can be paramorphic, where the origin crystal shape is retained.

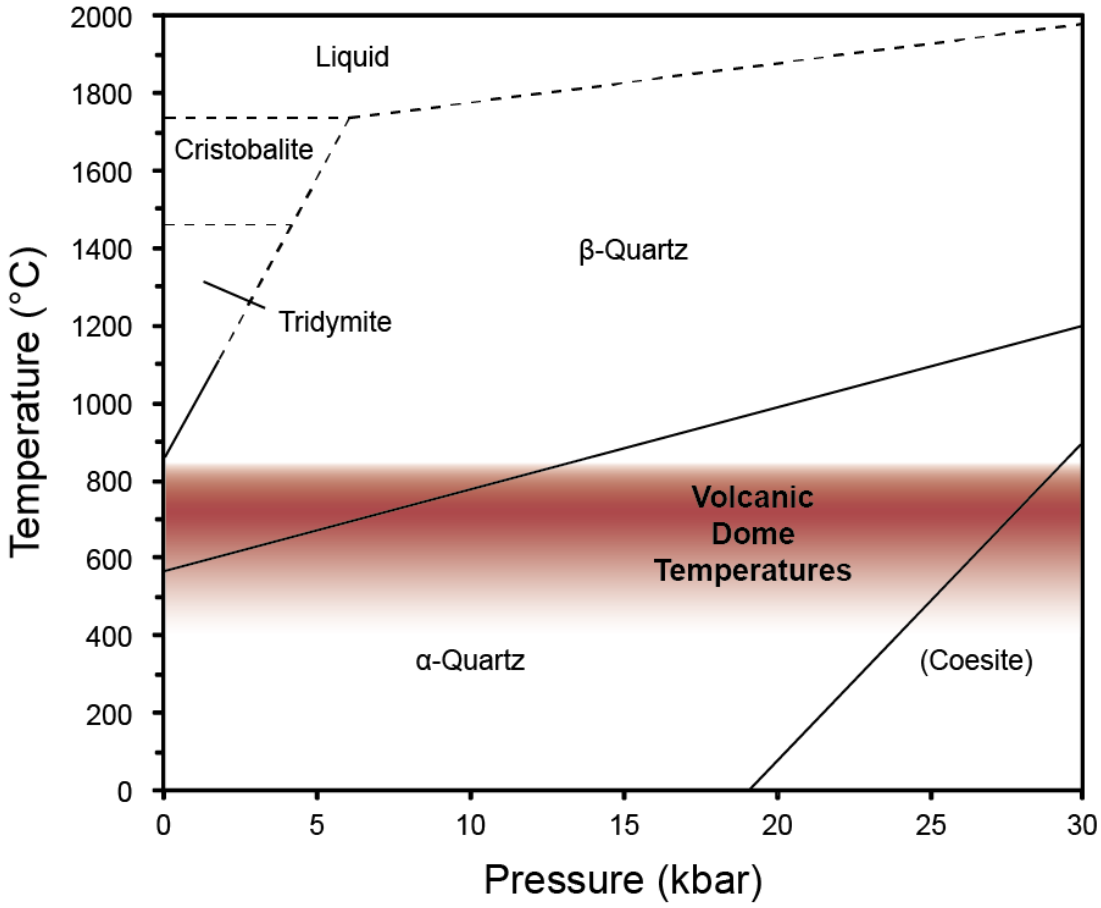

Figure 2.1: Low pressure polymorphs of crystalline silica. Average temperature range for active volcanic domes shown in red (temperature data from Barclay et al., 1998; Murphy et al., 2000). Diagram adapted from Introduction to Mineralogy (Nesse, 2000).

Each polymorph has two closely related, temperature-dependent crystallographic structures: low (alpha, α) and high (beta, β) forms. The transition between α and β forms is displacive, requiring only the rotation of atoms without bond breakage (Carpenter et al., 1998). Reconstructive transformation to the most stable polymorph (i.e., quartz) will not always occur, since it requires greater activation energy than displacive transitions. Therefore, α-β transformations preferentially occur in nature. Consequently, polymorphs can exist outside of their thermodynamic stability field (termed metastable).

Cristobalite and tridymite exist metastably at ambient conditions. Their persistence is likely facilitated by their relatively open crystal structures compared to the tightly packed quartz structure, which allow for the substitution of ions into the crystal lattice. For cristobalite and tridymite, Al^{3+} commonly substitutes for Si^{4+} in the lattice, and incorporation of Na^{+}, K^{+} and Ca^{2+} in the open lattice space acts to balance the charge deficit introduced by the substitution (Deer et al., 1996). The presence of these interstitial ions physically bolsters the structure, preventing the reconstructive transformation to the tighter quartz structure, and can inhibit displacive transitions altogether if present in sufficient amounts. As a result, the composition of quartz is normally very close to pure SiO_2, whereas cristobalite and tridymite tend to contain appreciable amounts of aluminium and alkali earth ions (Deer et al., 1996).

2.2 Occurrence and Formation of Crystalline Silica

Crystalline silica is ubiquitous in nature. Quartz is a common constituent of igneous, sedimentary and metamorphic rocks, and can be found in rocks, soils and other surface deposits. It can also form as a secondary mineral in hydrothermal veins and act as a cementing medium in sediments (Deer et al., 1996). Tridymite and cristobalite occur less frequently, and typically occur in felsic volcanic rock (especially obsidian) and deposits, where they are found lining cavities in the host rock (Bish and Aronson, 1993; Williamson et al., 2010; Yurtmen and Rowbotham, 1999). Cristobalite is often a late product of crystallisation, sometimes replacing tridymite.

The presence of tridymite and cristobalite outside of their stability fields does not necessarily imply that the conditions at the time of crystallisation were above their respective inversion temperatures (Rowe et al., 2012).

2.2.1 Volcanic Domes

Volcanic domes serve as a source for the mass crystallisation of cristobalite (Baxter et al., 1999; Horwell et al., post review), evidence for which stems from its presence in dome rock

samples at a number of volcanoes (e.g., Blundy and Cashman, 2001; Damby et al., 2012; Lavallee et al., 2012; Nakada and Motomura, 1999; Pallister et al., 2008; Scott et al., 2012; Williamson et al., 2010) as well as ash from a number of dome-forming eruptions (e.g., Baxter et al., 1999; Dollberg et al., 1984; Hillman et al., 2012; Horwell et al., 2010a). At the Soufrière Hills volcano on the British Island of Montserrat, Horwell et al. (post review; Appendix 4) have reported upwards of ~10 wt. % cristobalite in samples of dome rock.

Volcanic domes are massive mounds of viscous lava that have extruded slowly and piled up over the vent rather than moving away as a lava flow. They grow by a combination of endogenous (intrusive) and exogenous (extrusive) addition of magma, either as a continuous event or through a series of pulses which build a larger construct (Fink et al., 1990). They can also occur as cryptodomes, which are domes that form within an edifice and deform the surface topography without exposure at the surface. The 1980 Mount St. Helens cryptodome is a classic example, which is thought to have grown in the 2-3 months preceding the eruption (Pallister et al., 2008). Lavas with compositions ranging from basaltic andesite to rhyolite can form domes (Blake and Bruno, 2000). Most dome lavas have been depleted in volatiles; however, younger domes may contain enough pressurised gas to occasionally cause explosions during dome extrusion (Miller, 1989). The sides of most domes are very steep and are typically mantled with unstable debris and ejecta as a result of emplacement and on-going eruptive activity (Hoblitt et al., 1987).

Lava domes are inherently unstable (Calder et al., 2002), and dome collapse due to slope over-steepening and gravitational instability (Sparks et al., 2000), rainfall (Elsworth et al., 2004; Matthews et al., 2002), gas pressurisation (Elsworth and Voight, 2001; Voight and Elsworth, 2000) and hydrothermal weakening (Edmonds et al., 2003), along with periodic explosions, results in dome-collapse pyroclastic density currents (PDCs) containing particularly fine-grained co-PDC ash (Horwell, 2007).

2.3 Exposure to Crystalline Silica

Dusts containing crystalline silica can be produced through a variety of industrial processes, such as quarrying of granite and volcanic deposits, and can also be produced from a number of manufacturing industries (e.g., diatomaceous earth processing and ceramics manufacturing). Dusts rich in crystalline silica can also be produced naturally; for example, eruptions at dome-forming volcanoes (Baxter et al., 1999; Dollberg et al., 1986) or re-suspension of respirable sand grains in desert storms (Lyles et al., 2006).

Inhalation of natural mineral dusts containing crystalline silica are known to exacerbate pre-existing respiratory conditions and increase the prevalence of respiratory disease (e.g., Baxter et al., 1983; Horwell and Baxter, 2006). For example, an increase in asthmatic symptoms was reported in children up to 12 years old after exposure to volcanic ash on Montserrat (Forbes et al., 2003). Guidelines have been set to limit occupational exposure to crystalline silica, however very few non-occupational environments have been monitored for crystalline silica exposure (see Searl et al., 2002).

2.3.1 Respiratory Hazard of Volcanic Ash

Humans can be exposed to airborne volcanic particulate through primary and/or secondary exposure of re-suspended material in daily life as well as in the workplace, raising concern of acute and chronic exposure to many millions of people exposed worldwide. Of particular concern, prolonged exposure to cristobalite-bearing ash, even where silica concentrations are low, may contribute to the incidence of chronic mixed dust fibrosis in populations residing near persistently active volcanoes.

Horwell and Baxter (2006) reviewed more than 60 studies focusing on the respiratory hazard of volcanic ash, concluding that experimental, epidemiological and clinical studies on the toxicity of ash range from inert to highly reactive. Since their review, at least 18 further studies have been published on the direct effects of volcanic ash to human health; 12 were eruption-specific studies, 2 were clinical studies, and 4 addressed physicochemical mechanisms of exposure and toxicity. Of the eruption-specific studies, 4 were specific to the 2010 eruption of Eyjafjallajökull, and the others were on separate, individual eruptions (e.g., Damby et al., 2012 (Merapi); Le Blond et al., 2010 (Rabaul, Papua New Guinea)). The impacts of many individual volcanoes have been assessed over the years; however, three volcanoes stand out as having significantly progressed the nascent field of volcanic health hazards, and were also the focus of the review by Horwell and Baxter (2006): Mount St. Helens, Soufrière Hills, and Sakurajima (Japan). These cases, in particular, garnered comparatively more research than other eruptions due to the sponsorship of United States, British and Japanese scientists, respectively. Only Mount St. Helens and Soufrière Hills are addressed in the present study; a study on Sakurajima ash along with an extensive review of health studies near Sakurajima was recently published by Hillman et al. (2012).

2.3.1.1 Mount St. Helens

The 18 May 1980 eruption of Mount St. Helens, USA was the first to draw copious scientific research on the impacts of ashfall to communities and health. Although the volcano was well monitored and an eruption forecasted, no hazard plan existed to address the acute and chronic ash-related hazards (Buist et al., 1986a). Even still, the effects on health were

investigated promptly (e.g., Baxter et al., 1981), where laboratory studies indicated that the ash was not acutely toxic, but crystalline silica in the respirable fraction posed a potential chronic hazard to heavily exposed populations (Baxter et al., 1981; Green et al., 1981). The crystalline silica fraction was found to comprise approximately 7 wt. % of the <10 μm fraction, of which 4 wt. % was cristobalite (Dollberg et al., 1984). In the event, however, the eruption was short lived, and a follow-up clinical study did not find any adverse effects after 4 years (Buist et al., 1986b).

2.3.1.2 Soufrière Hills

The 1995 to present eruption of the Soufrière Hills volcano ignited international concern about the respiratory hazard posed by volcanic ash, as frequent ashfalls and re-suspension of deposits resulted in greater exposure than at Mount St. Helens. Unlike Mount St. Helens, where the ash hazard to surrounding populations was primarily due to the single 1980 eruption, Soufrière Hills' ash generation is a continuous hazard fed by on-going explosions and co-PDC (pyroclastic density current) ash resulting from dome growth and collapse. Elevated levels of cristobalite in the dome-collapse ash posed a chronic respiratory hazard, and were linked to crystallisation in the andesitic dome (Baxter et al., 1999).

Ash from Soufrière Hills was also found to not be acutely pathogenic (e.g., Cullen et al., 2002; Wilson et al., 2000), although its toxicity is perhaps comparable to coal dust. A time series simulation was conducted for the risk of long term exposure to respirable Soufrière Hills ash, concluding that the highest exposure (for gardeners, continuous over 20 years) corresponded with a 2-4 % risk of silicosis (Hincks et al., 2006).

2.4 The Fate of Inhaled Particles

The response elicited by a particle following exposure is governed by the interaction between the particle and the body. Particle-host interactions can be occur indirectly between a mineral surface and extracellular or intracellular fluids or they can occur directly between a mineral surface and the components of a cell membrane (Guthrie, 1997). Therefore, an anatomical outline of the respiratory system is needed to understand where particles deposit following inhalation as well as the consequences of deposition in different regions of the respiratory system.

2.4.1 The Respiratory System

The respiratory system facilitates the exchange of oxygen in the air for carbon dioxide waste in the blood. For gas exchange to occur, external air must be introduced to the interior of the

body, where air and blood can be brought into close proximity. As the lungs draw in air from the environment, any exogenous pathogens and particulates in the immediate vicinity of airflow will be inhaled. To combat this hazard, the body has evolved an effective defence system to trap, remove or kill any unwanted material.

2.4.1.1 Gross Anatomy

Air is drawn into the body through the nose and mouth and passes through the larynx and the trachea (Figure 2.2), which is structurally supported and held open by cartilage. The trachea branches (at the hilum) into two primary bronchi that serve the left and right lungs. This is the start of the bronchial tree, where penetration into the lungs can occur. The primary bronchi branch to form the secondary bronchi, which transmit air into the separate lobes of the lungs (the left lung has 2 lobes, and the right has 3). From this point, the bronchi branch to a tertiary level, and again successively through 26 orders, progressively narrowing to the terminal bronchioles, which are ~0.5 mm in diameter (Huether and McCance, 1996). The terminal bronchioles access the respiratory bronchioles, which mark the beginning of the respiratory zone (Ten Have-Opbroek, 1986). The respiratory bronchioles feed into the alveolar ducts and terminate in the alveoli.

2.4.1.2 The Alveolar Region

Alveoli are the terminal structure of the highly branched respiratory tract, and are the primary gas exchange units. They are botryoidal, hollow air sacs that are 75-300 μm in diameter (Huether and McCance, 1996), and account for more than 99 % of the internal surface area of the lungs (Dobbs et al., 2010).

Alveoli are comprised type I and type II alveolar epithelial cells. Type I alveolar epithelial cells provide the basic structure and surface of the alveolar region. They cover more than 90 % of the alveolar surface area due to their large shape and surface area, but account for less than 10 % of total number of lung cells (Crapo et al., 1982; Gardner, 2006). Their thin (50-100 nm) structure allows for efficient transfer of gases between the air and blood. Type II alveolar epithelial cells differ significantly in structure and function. They are more abundant than Type I cells, but occupy less surface space (Crapo et al., 1982). The primary role of type II cells is the secretion of pulmonary surfactants that lower the surface tension at the air-alveoli interface. Type II cells also play an important role in inflammation and can divide to replace damaged type I cells (Dobbs et al., 2010). They are employed for toxicology experiments in Chapter 6.

Pulmonary surfactants are a primary component of the lining fluid, a thin film (0.1-0.5 μm) covering the alveolar surface (Notter, 2000). Particles depositing into this region of the lung

'splash down' into the lung surfactant, which may cause aggregated particles to break up due to the tension-lowering compounds and might also coat particles with host proteins. Adsorption of proteins to particle surfaces facilitates engulfing by immune defence cells (phagocytosis), a major mechanism used to remove pathogens and small mineral particles (Pedraza et al., 2008).

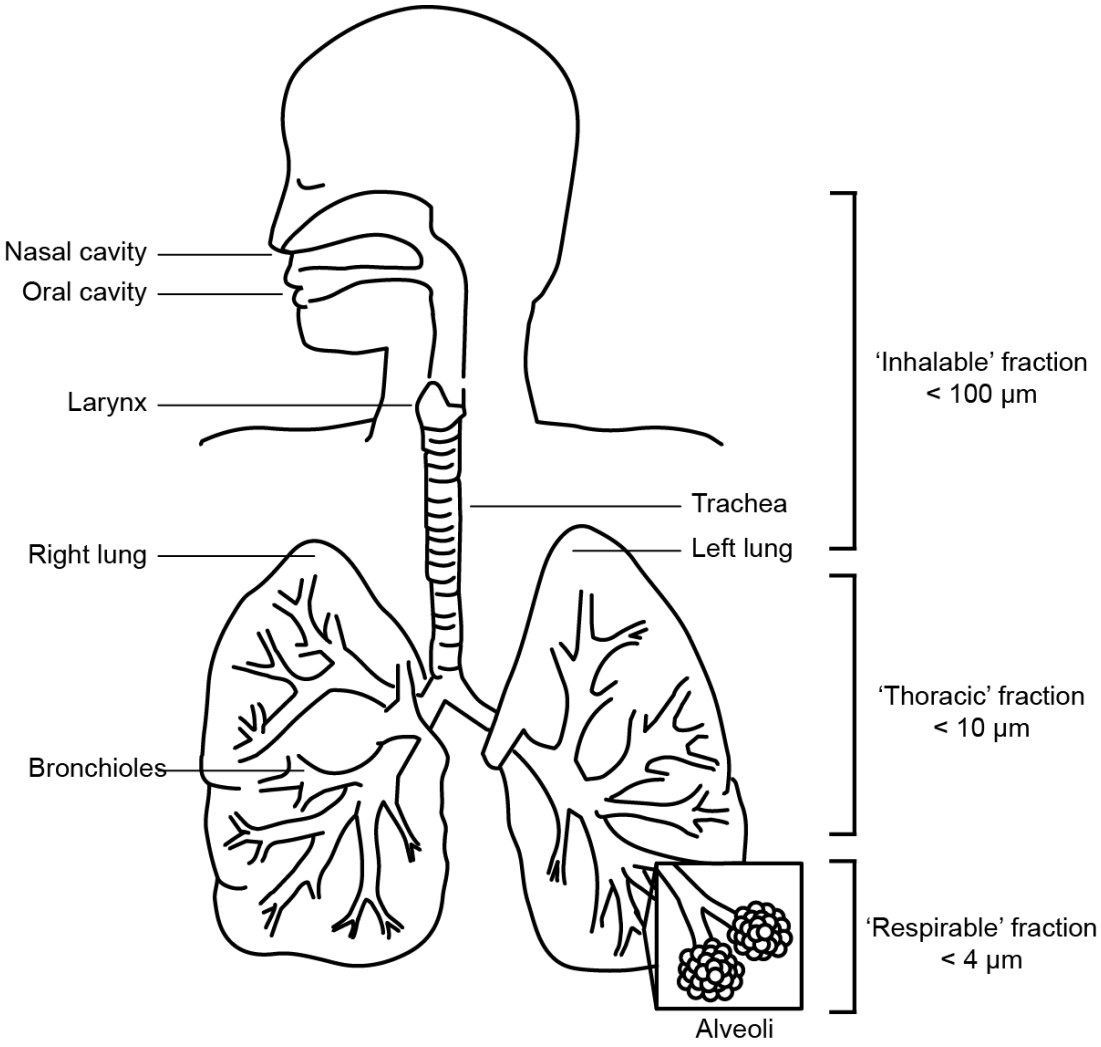

Figure 2.2: Gross anatomy of the respiratory system. Particle size fractions are from the Quality of Urban Air Review Group report (QUARG, 1996). Figure redrawn and adapted from a public domain image (http://contactscience.wikispaces.com/respiratory+system).

2.4.2 Particle-lung Interactions

The airway epithelium forms a continuous lining to the airspace, and is therefore often the site of first contact for physical environmental stimuli (Thompson et al., 1995). Due to the

necessary exposure, the respiratory system has a number of defences to deal with foreign material. These mechanisms help to reduce particle accumulation and minimise contact between the particles and the fixed cells of the airway epithelium.

2.4.2.1 Particle Deposition

Particles which enter the conducting airways are subjected to various modes of deposition. The location of deposition within the respiratory tract is dictated by both particle-specific characteristics (e.g., size, shape, and density) and host respiration (Schulz et al., 2005). The tidal volume, respiration rate, and respiratory tract dimensions can differ between species (e.g., rodents and humans) as well as within species due to age, growth and illness (Coleman et al., 2006; Janssens et al., 1999).

Inhaled material that can deposit in the alveoli is considered 'respirable'(Figure 2.2; Jones, 1993). Due to the elutriating effect of the progressively narrowing airways, the size fraction of 'respirable' particulates is considerably smaller than those which deposit in the upper respiratory tract; however, the respiratory system does not abide by strict size filtering. Different studies assign a different upper limit for the 'respirable' fraction, ranging from approximately 3–10 μm; however, assigning a maximum empirical size is complicated since the effective size in humans differs from rodents (Davis, 1993; Guthrie, 1997). The majority of deposition for ~10 μm particles occurs within the upper portion of the respiratory system (Gehr and Heyder, 2000). As particle size reduces to <4 μm, deposition in the pulmonary region increases. The largest level of particle deposition in the trachea-bronchial and alveolar regions occurs when particles are < 1 μm. When particle size reduces further (< 0.2 μm), particles are influenced by Brownian motion, which enhances the chance of deposition in all regions of the airway (Schulz et al., 2005).

Deposition of particles approximately > 0.5 μm is related to aerodynamic diameter (Schulz et al., 2005). Aerodynamic diameter is a simple means of categorising the sizes of particles having different shapes and densities with a single dimension. It is the diameter of a spherical particle having a density of 1 g cm^{-3} that has the same inertial properties as the particle of interest (i.e., terminal settling velocity). The mechanisms by which particles are subject to deposit under aerodynamic and gravitational forces are akin to the ways in which particles sediment in the Earth Sciences (Figure 2.3). They include impaction, sedimentation, diffusion, interception, and electrostatic deposition (in the case of charged particles). These processes lead to heterogeneous particle-size deposition through the conducting airway and lungs (see Gehr and Heyder, 2000).

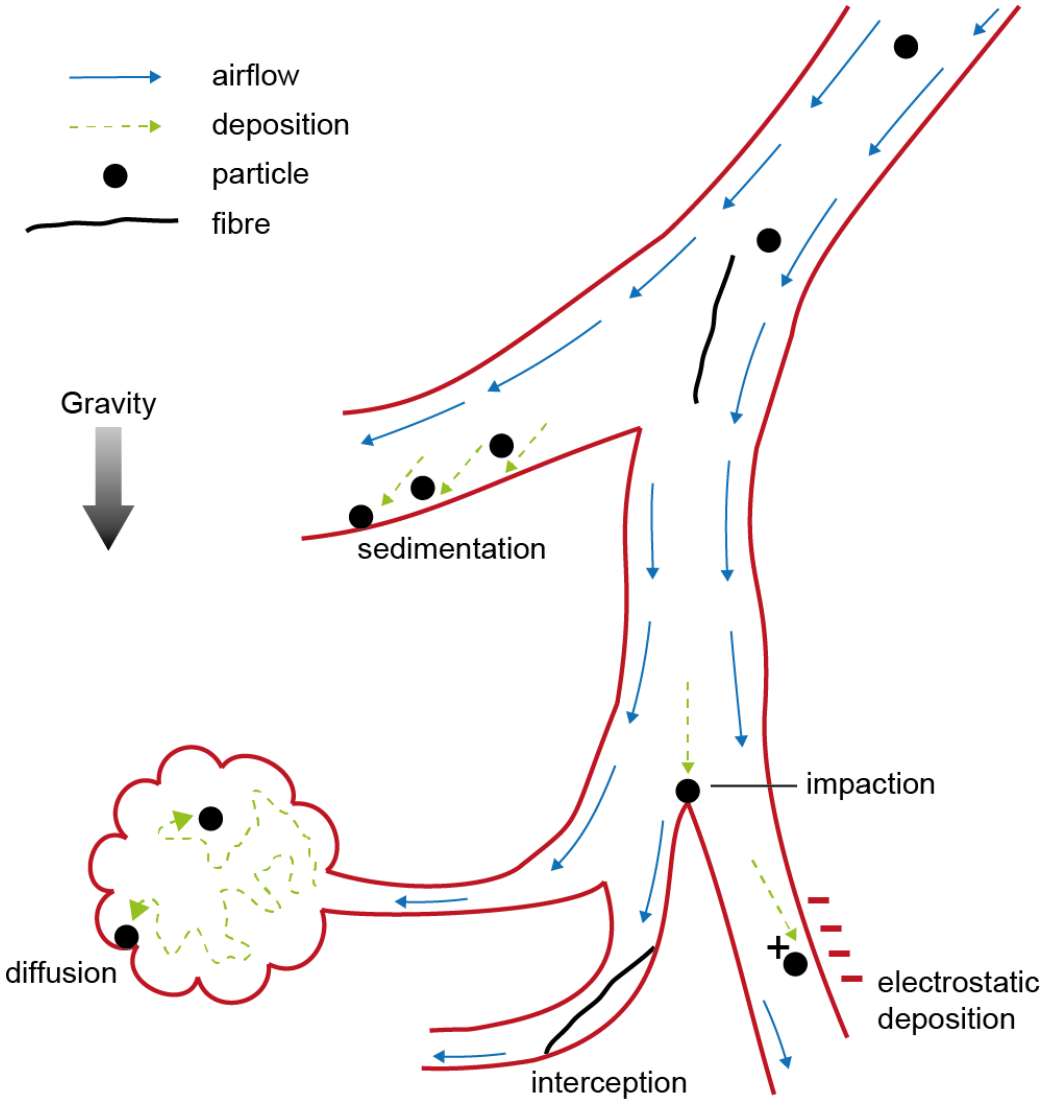

Figure 2.3: Mechanisms of particle deposition. Redrawn and adapted from Particle Interactions with the Respiratory Tract by Roger McClellan (in Gehr and Heyder, 2000).

Impaction occurs at bifurcation points, where the airflow deviates but a particle maintains its trajectory. Interception occurs when the edge of a particle or fibre catches the airway wall and deposits immediately, even if the centre of mass follows the airflow. Sedimentation occurs in the direction of movement when the airflow no longer supports a particle. Airflow is minimal in the respiratory zone, and larger and denser particles tend to sediment out. Particles that are approximately < 5 µm deposit according to a diffusion equivalent diameter, where Brownian motion enhances the chance of spontaneous deposition (Schulz et al., 2005).

2.4.2.2 Particle Clearance

The mechanism by which a particle is removed from the respiratory system (deemed *clearance*) is contingent on where the particle deposits. Deposition of a particle into the upper airways is into physiological fluids, which can be swallowed or expectorated. This is facilitated by the mucociliary escalator, which continuously shuffles trapped debris up and out of the ciliated airways (trachea to the bronchioles). The rate of clearance in the trachea is approximately 5 mm min^{-1}, with a decreasing rate down the bronchial tree (Foster, 1988), allowing for 60-80 % m/m of deposited material to be cleared after 24 hours (Asgharian et al., 2001; Forster et al., 2000).

In the non-ciliated alveolar region, clearance is mediated by a population of patrolling macrophages. Alveolar macrophages identify and engulf foreign material, and transport it out of the alveolar region (deemed *translocation*). Once internalised through the process of phagocytosis, the macrophage attempts to digest foreign material with acids and enzymes. Particles of ~20 µm and fibres with a length of ~15 µm can be successfully phagocytosed (Brandwood et al., 1992; Schinwald et al., 2012). Clearance in the alveolar region is much slower than in the larger airways as it relies on the arrival of a macrophage (which is mediated by signal molecules (*chemokines*) released by affected cells), phagocytosis and movement out of the lung. Some particles (e.g., quartz-bearing) are unable to be successfully cleared and result in the activation of an immune response (Donaldson and Borm, 1998; Peeters et al., 2013). Deposition in the alveolar region requires particle 'splash-down' in the lining fluid (as discussed in Section 2.4.1), which immediately bathes a particle and may give a particle its 'biological identity' in the form of a protein corona, dictating its interaction with cells (Lynch et al., 2007).

2.4.2.3 Particle Solubility

In addition to the physical mechanisms of particle clearance, particles can also be dissolved by lung chemistry. The *biopersistence* of a particle is defined as its ability to resist substantial structural modification *in vivo*. It describes the ability of a particle to endure the biological environment once it has been deposited, but specifically refers to the *in vitro* methods of establishing a particle's resistance to such environments. Dissolution can be a significant component of particle clearance mechanisms.

Different natural and man-made fibres have very different lung retention times, and those that are most durable have the highest fibrogenic and carcinogenic potential (de Meringo et al., 1994; Luoto et al., 1996; Muhle et al., 1994).

Particles may break down due to leaching of certain structural components by physiological fluids or due to the milieu of macrophage phagolysosomes (a purpose-built encasement for digestion of foreign material). The components in a heterogeneous dust may break-down at different rates, meaning the mineral burden in the lungs is not exactly representative of the dusts to which an individual is exposed (Churg, 1993; Guthrie, 1997). Crystalline silica, in particular, does not readily dissolve in lung-lining fluids. Different solubility rates for the mineral components in volcanic ash are discussed in detail in Chapter 6.

2.5 Factors Controlling Particle Toxicity

An underlying theme throughout this thesis is that pathogenesis originates at the particle-lung interface and, therefore, characterising the particle and/or source material will provide insight into the aetiology of disease. The physicochemical properties of inhaled minerals are an integral component of particle toxicity, and control dosimetry parameters such as deposition, clearance, retention, translocation and dissolution. Such properties also allow for the derivation of a link between biological reactivity and geological origin, enabling a reciprocal understanding whereby toxicity can be inferred from particle characteristics. These characteristics dictate the way a mineral interacts with its environment, and are largely borrowed from geosciences, where a range of mineral-fluid interactions have been studied. Those of greatest concern for health are: (1) composition and structure, (2) particle size and morphology, (3) surface properties and reactivity, (4) dissolution/biopersistence (discussed above) and (5) sample history and surface chemistry. Full characterisation of these components within mixed samples is therefore essential to elucidate mechanisms of toxicity and to interpret the contribution to toxicity from all phases in a heterogeneous sample.

One of the tenets of geology is that the properties of a mineral species can vary among samples (Guthrie, 1997). As a result, the provenance of a mineral has been shown to be an important factor in toxicity (e.g., quartz; Donaldson and Borm, 1998). Therefore, mineralogical approaches to toxicity can provide novel insights into the molecular processes that occur, and care must be taken to ensure that mineralogical properties are as adequately addressed as the physiological response.

2.5.1.1 Particle Size and Shape

Particle size and shape are universally considered important factors in pathogenesis. There are several mechanisms by which size and shape may influence toxicity and the fate of the particle in the lung (Section 2.4.2). Particle shape and size determine the surface area of a

particle and, importantly, the surface area per unit volume or mass of the sample. Small particles have larger surface areas per unit mass than large particles, which means that smaller particles have more reactive surface available on a per-mass basis. As such, a surface area dose metric has been established (e.g., Duffin et al., 2007; Monteiller et al., 2007) and, while still under debate, has emerged as a more defensible basis on which to compare results.

2.5.1.2 Surface reactivity

Ultimately, it is the surface of a particle that interacts with a biological fluid or a cell. Accordingly, particles of a similar size, shape, and bulk chemistry can have different pathogenic effects if the reactivity of the surface differs. Differences in the potency of particles can result from inherent surface reactivity, for example, quartz owes its malignant aptitude to the damaging effects of surface silanol groups on cellular membranes (Castranova, 2004; Fubini, 1998), and the propensity of siloxyl radicals on the surface of freshly-fractured quartz to generate reactive oxygen species (Vallyathan et al., 1988). Or, surface reactivity can result from the adsorption of xenobiotics onto the particle surface or from contamination by transition metals; for example, iron has been shown to increase oxidative stress within cells *in vitro* and *in vivo* via the generation of hydroxyl radicals ($^{\bullet}OH$) as a consequence of redox cycling and Fenton chemistry (see Equation 3.3) (Fubini et al., 1995b; Kamp and Weitzman, 1999).

For some materials, the structure at the surface can differ substantially from the structure exhibited by the bulk. These differences can be a simple distortional relaxation of surface atoms to a completely different material on the surface. Even chemically simple materials such as quartz can have surfaces that are structurally different than the bulk. Worden et al. (2012b), for example, showed quartz crystals could have a micro-quartz surface layer which is not syntaxial with the orientation of the host grain. For volcanic ash, Horwell et al. (accepted; Appendix 4) proposed that the crystalline silica may be occluded by an annealed amorphous layer, termed a 'Beilby' layer (Finch et al., 1934), as has been observed for quartz (Šolc, 1996; Talbot and Kempis, 1960; Worden et al., 2012a).

2.5.1.3 Sample History and Surface Modifications

The surface of a particle can be significantly altered by processes related to the sample's history. Indeed, intentional alteration ('functionalization') of particles for biomedical purposes has garnered much attention recently (Gupta and Gupta, 2005; Liu et al., 2012; Villanueva et al., 2009), and is known to affect the way in which a particle interacts *in vivo*. Consequently, the surface reactivity of a particle can be tempered by intentional surface modification; for example, coating quartz with aluminium lactate (Duffin et al., 2001).

With respect to natural minerals, grinding can produce freshly fractured surfaces with numerous reactive sites, e.g., unsatisfied bonds and steps or ledges, which are known to increase reactivity in both geological and biological environments (Vallyathan et al., 1995). Another broad example is the geological weathering of material, which can lead to surface oxidation (e.g., Fe^{2+} to Fe^{3+}) amongst a host of other surface-modification processes.

One way, in particular, in which a particle can interact with its surroundings, be it during transport in the plume or post-deposition in the case of volcanic ash, is through chemical sorption and exchange of an element or molecule (e.g., cation exchange). Ion exchange occurs when a sorbed species on the mineral exchanges with a similarly charged species in a fluid (Guthrie, 1997). Most minerals have a limited capacity for cation exchange because sorption occurs only at the surface; the capacity for cation exchange for such minerals is therefore related to surface area and ion diffusion. The complexation of ions or molecules with the surface has an important effect on a mineral's reactivity. Cation exchange could play an important role in cellular responses through a number of mechanisms, including cation buffering (e.g., Na-Ca) activity at the surface of a cell, and has been shown to affect the cytotoxicity, gene response, and apoptosis induced by cation-exchanged (Na, K, Ca, Fe^{3+}) asbestos (Timblin et al., 1998). Although no pursued, it may also be the reason why colleagues at the ELEGI-Colt Lab in Edinburgh have observed reduced and inconsistent haemolytic potentials in experiments using a phosphate buffered saline solution (PBS) compared to deionised H_2O. The kinetics of cation exchange in a complex biological fluid (e.g., lung lining fluid) are unknown.

2.6 Mechanisms of Ash Toxicity

The components of volcanic ash are derived, in the truest sense, from the chemistry of the Earth, and the morphologies of ash particles are shaped by the most energetic force of nature. Its mineral assemblage is source dependent, but can comprise any number of potentially toxic elements. For example, ash can contain the classically toxic crystalline silica (Baxter et al., 1999; Dollberg et al., 1986), including crystalline-silica nanofibres (Reich et al., 2009); a prominent morphology-of-interest in particle toxicology research. In addition to hazardous minerals, reactivity can be mediated by surface chemistry. For example, iron at the surface of particles has been implicated in the pathogenic response to particulate matter (Fubini et al., 1995b). Freshly erupted ash differs from other hazardous particles in that the surfaces are un-weathered (and therefore not oxidised) or leached. As such, freshly erupted ash can serve as a carrier of adsorbed species, including fluorides, sulphates, chlorides, and various heavy

metals. Similarly, there may be condensed acidic volatiles, polycyclic hydrocarbons, halogens and anthropogenic pollutants adsorbed to the surface (Horwell and Baxter, 2006). With the available chemistry and temperatures in an eruptive column, even the formation of polychlorinated dibenzodioxins (PCDDs) on solid surfaces could be envisaged, as has been seen on fly ash (Lu et al., 2007). Therefore, it is difficult, from a toxicity perspective, to constrain the components responsible for the potential toxicity of ash as well as the contribution of each.

The toxicity of a particle is unlikely to be based upon a single overriding attribute which dictates toxicity, and it will likely be a combination of a variety of factors that come into play at different times during a particle's journey from formation to exposure to internal effective dose to causation of a clinical disease (Boffetta, 1994). As noted, volcanic ash has the potential to cause harm through a variety of mechanisms. Two of the better established mineral-based pathways result from the presence of surface iron (Horwell et al., 2007; Horwell et al., 2003a), with the corresponding generation of reactive oxygen species (ROS), especially the hydroxyl radical ($^{\bullet}OH$), and from the presence of crystalline silica, for which the pathogenic mechanisms of silica-induced inflammation and fibrosis are not well understood.

2.6.1 Oxidation-Reduction Chemistry

The transfer of electrons between a mineral and fluid drives a number of geochemical processes. Similarly, several lines of evidence support the notion that electron transfer processes at the surface of minerals are important in pathogenesis .Electron transfer has been attributed to the increased biological activity and heighted formation of free radicals associated with freshly fractured quartz compared to aged quartz (Fubini et al., 1987; Vallyathan et al., 1991; Vallyathan et al., 1988). Further, Fubini et al. (1995b) reported that magnetite will break down hydrogen peroxide but hematite will not, suggesting ion (e.g., iron) coordination on the crystal face plays an important role in the formation of free radicals. Indeed, this has been confirmed for volcanic ash, and is considered in Chapter 6. In this way, minerals which provide a reaction surface to donate or accept electrons or protons can function in a similarly catalytic way to biological enzymes. At physiological temperatures, rates may be too low to effectively measure, but may be sufficiently high to provide a chronic source (or sink) of electrons for reduction (or oxidation) of fluid species to form free radicals.

The donor-acceptor characteristics of framework silicates are strongly influenced by the substitution of aluminium for silicon in the tetrahedral framework (Guthrie and Heaney, 1995). This substitution can be charge compensated in a number of ways, including the

association of a proton with the under-bonded oxygen atoms around the aluminium, or by the presence of Na^+ as was shown for volcanic cristobalite (e.g., Horwell et al., accepted). A number of different sites can exist on the surface of a mineral, and range from silanol groups (Si-O-OH) to the aluminium equivalent (Al-O-H) and protons associated with an aluminium exchange (e.g., Al-O(H)-Si). Surface sites (e.g., silanol groups) are thought to be responsible for silica toxicity because they function as hydrogen donors (Guthrie, 1997).

2.6.2 Crystalline Silica

The mechanism of silica-induced inflammation and fibrosis are still poorly understood (Mossman and Churg, 1998), although it is generally believed that no single characteristic is responsible for silica toxicity (Fubini, 1998). Exposure to crystalline silica results in the activation of both alveolar type II cells (Hefland et al., 2001; Hook and Viviano, 1996) and macrophages (Hamilton et al., 2008), amongst other cell types. Research into the mechanisms of silica-induced disease has focused on the physicochemical properties, particle retention and translocation, surface chemistry at silica-cell interfaces (e.g., Fubini et al., 1995a; Schins et al., 2002), and inflammatory response.

Historically, crystallinity has been considered a prerequisite for silica toxicity. Recent work, however, has shown completely amorphous vitreous silica to be cytotoxic and capable of generating free radicals, calling into question the role of crystallinity (Ghiazza et al., 2010).

Recently, global gene expression profiling was used to identify significantly affected gene expression following silica exposure in cultured type II epithelial cells and in the lungs of rats (Sellamuthu et al., 2011; Sellamuthu et al., 2012). The identified functions perturbed by silica exposure were involved in oxidative stress, inflammation, cancer, cellular proliferation and development, tissue remodelling and fibrosis; however, unresolved inflammation was the single most significant biological response to silica exposure. Further, excessive mucous production was identified as a potential novel mechanism for silica-induced pulmonary toxicity. Silica toxicity has also been linked to destabilisation of the phagosome, the vesicle formed around a particle engulfed by phagocytosis, following uptake (Hornung et al., 2008). This process can result in apoptotic cell death and concomitant release of the ingested particle, which is available to be engulfed by another macrophage, initiating a cycle of sustained inflammation (Huaux, 2007).

2.7 Diseases associated with crystalline silica inhalation

Crystalline silica is one of the most toxic minerals known. Exposure to respirable dust containing quartz, cristobalite, and tridymite has long been recognised as a significant health hazard, especially for prolonged exposure in occupational settings. Dust containing the crystalline silica polymorphs are known to result in silicosis, silico-tuberculosis, various pneumoconioses, and potentially lung cancer (International Agency for Research on Cancer, 1997).

2.7.1 Silicosis

Silicosis is an incurable, irreversible progressive pulmonary disease that results specifically from the inhalation of crystalline silica, and is marked by inflammation and scarring in the lungs. Although host factors (e.g., genetics, smoking, underlying disease) play a role in the development of silicosis, the primary determinants of disease onset and progression are the particle size, silica dose in the exposure, the duration of exposure, the inherent characteristics of the crystalline silica, and the matrix within which it is present (Donaldson and Borm, 1998; Hughes et al., 1982).

Silica exposure results in two distinct physiological disease states: acute and chronic (classic) silicosis (Banks, 2010). Acute silicosis is the result of overwhelming exposure to respirable crystalline silica over a short duration, and manifests within a relatively short period of time following exposure (a few months to years). Chronic silicosis results from a cumulative dose of silica from low levels of exposure over time, requiring upwards of 20 years before becoming debilitating (Banks, 2010). Chronic silicosis which develops more quickly (<10 years) is termed accelerated silicosis, but presents with the same clinical appearance. The lungs of average city dwellers without occupational particulate exposure contain approximately 500 x 10^6 exogenous mineral particles per gram of dry lung, whereas lungs of patients with silicosis may contain up to 16,000 x 10^6 exogenous mineral particles per gram of dry lung, which is up to 20 % of the dry weight in the most severe case (Green and Vallyathan, 1996; Smith and Wikoff, 1933). The latency period (the duration between exposure and the appearance of symptoms) associated with disease progression makes it common for silicosis to first become apparent many years after cessation of exposure, and is an impediment to current epidemiological studies on volcanic ash exposure and risk.

2.7.2 Silico-tuberculosis

Tuberculosis (and other opportunistic bacterial infections) is a common complication of silicosis that may occur during any stage in disease progression (Cowie, 1994). Cumulative silica exposure increases the lifelong risk for developing silico-tuberculosis, and the risk

persists even after silica exposures ceases (Hnizdo and Murray, 1998). Epidemiologically, silica exposure is associated with increased morbidity and mortality from tuberculosis, and individuals who suffer from silicosis have an increased risk of contracting tuberculosis (Chen et al.; Hnizdo and Murray, 1998; Nasrullah et al., 2011; teWaterNaude et al., 2006). The mechanism that accounts for the enhanced infection is ill-defined; however, experimentally, the potentiating effect of silica on infection generally implicates pulmonary macrophages (e.g., Allison and Hart, 1968; Ebina et al., 1960).

Tuberculosis is widespread in many developing countries, especially Indonesia, which is ranked number five in the world for pulmonary tuberculosis (World Health Organisation: Regional Office for South-East Asia, 2011).

2.7.3 Silica and Lung Cancer

The relationship between silica and lung cancer has not yet been resolved (McDonald, 1996; Pairon et al., 1991). A number of epidemiological and case-specific studies have shown that individuals with silicosis and workers in industries exposed to silica have higher mortality than control populations (Erren et al., 2009; Holland, 1990; Steenland et al., 2001); however, no clear dose-response relationship has been demonstrated in positive studies (Green and Vallyathan, 1996; Lacasse et al., 2009). Animal studies have shown a general increase in tumour development, which, combined with epidemiological studies, led the International Agency for Research on Cancer (IARC) to classify crystalline silica as a probable carcinogen in 1987, and reclassify it as a Group 1 carcinogen in 1997 (International Agency for Research on Cancer, 1997); i.e., there was sufficient evidence for carcinogenicity in animals and humans. The IARC working group noted that carcinogenicity in humans was not detected in all circumstances, and there is little evidence in animal models for a dose-response relationship (McDonald, 1996). In May 2009, IARC reaffirmed the carcinogenicity of “silica dust, crystalline in the form of quartz or cristobalite” as a Group 1 carcinogen, with the lung as the sole tumour site, and concluded that the only established mechanism was “impaired particle clearance leading to macrophage activation and persistent inflammation” (Borm et al., 2011; International Agency for Research on Cancer, 1997). A recent literature-based study by Borm et al. (2011) concluded that inflammation is the driving force for genotoxicity, and direct interaction of silica with target cells of crystalline silica would only result in genotoxicity at very high, possibly implausible, doses. More work is needed on the mechanism of silica carcinogenesis in silica-exposed populations.

2.8 Field Locations

The hazard posed by volcanic cristobalite is likely to vary depending on the type and style of eruptions (e.g., Horwell, 2007; Horwell et al., 2003a). However, before the commencement of this project, only one location had been studied in detail: Soufrière Hills volcano, Montserrat. This trans-disciplinary endeavour to systematically characterise the mineralogical and toxicological properties of crystalline silica in volcanic ash focuses particularly on dome-forming volcanoes, as dome-forming eruptions have the potential to generate substantial quantities of crystalline silica, which crystallises within the dome as the lava cools. An inherent feature of these domes is their instability, resulting in collapse of the dome and generation of ultra-fine (respirable) cristobalite rich ash and consequently a route of exposure.

As such, three renowned dome-forming volcanoes in developing countries were studied – Volcán de Colima, Mexico; Mount Merapi, Indonesia; and Santa María volcano (Santiaguito), Guatemala – and were compared with three other well-studied dome-forming volcanoes – Mount Unzen, Japan; Mount St. Helens, USA; and Soufrière Hills volcano, Montserrat (shown in Figure 2.4). Colima, Merapi and Santiaguito are all currently active, with Merapi erupting during this study in 2010 (see Damby et al., 2012; Appendix 4); therefore, the results of this study are both timely and urgent. Colima, Merapi, Santa Maria and Unzen have all been designated 'Decade Volcanoes' by the United Nations in 1991, a label which recognises their history of violent activity and location in densely populated areas. Much of the discussion in this thesis compares the results from the above locations with results from previous studies on Soufrière Hills, as it is the best-characterised volcano in terms of the respiratory hazard of crystalline silica (e.g. Horwell et al., 2003b; Horwell et al., accepted; Wilson et al., 2000).

2.8.1 Volcán de Colima, Mexico

Colima is an andesitic stratovolcano situated in the western end of the Trans-Mexican Volcanic Belt, and is one of the most active volcanoes in North America. Dome lava recently erupted at Colima contains 20-30 vol. % phenocrysts, with a porphyritic texture of plagioclase, orthopyroxene and clinopyroxene, minor hornblende, and Fe-Ti oxides (titanomagnetite) (Lavallee et al., 2012).

Historically, the behaviour of Colima has been characterised by 100 year cycles of dome growth and minor eruptions, culminating in a Plinian eruption which complete destroys the dome (Luhr and Carmichael, 1980). Colima's eruptive cycles of lava dome growth and explosions have been thoroughly monitored between 1998-2010 (Lavallee et al., 2012).

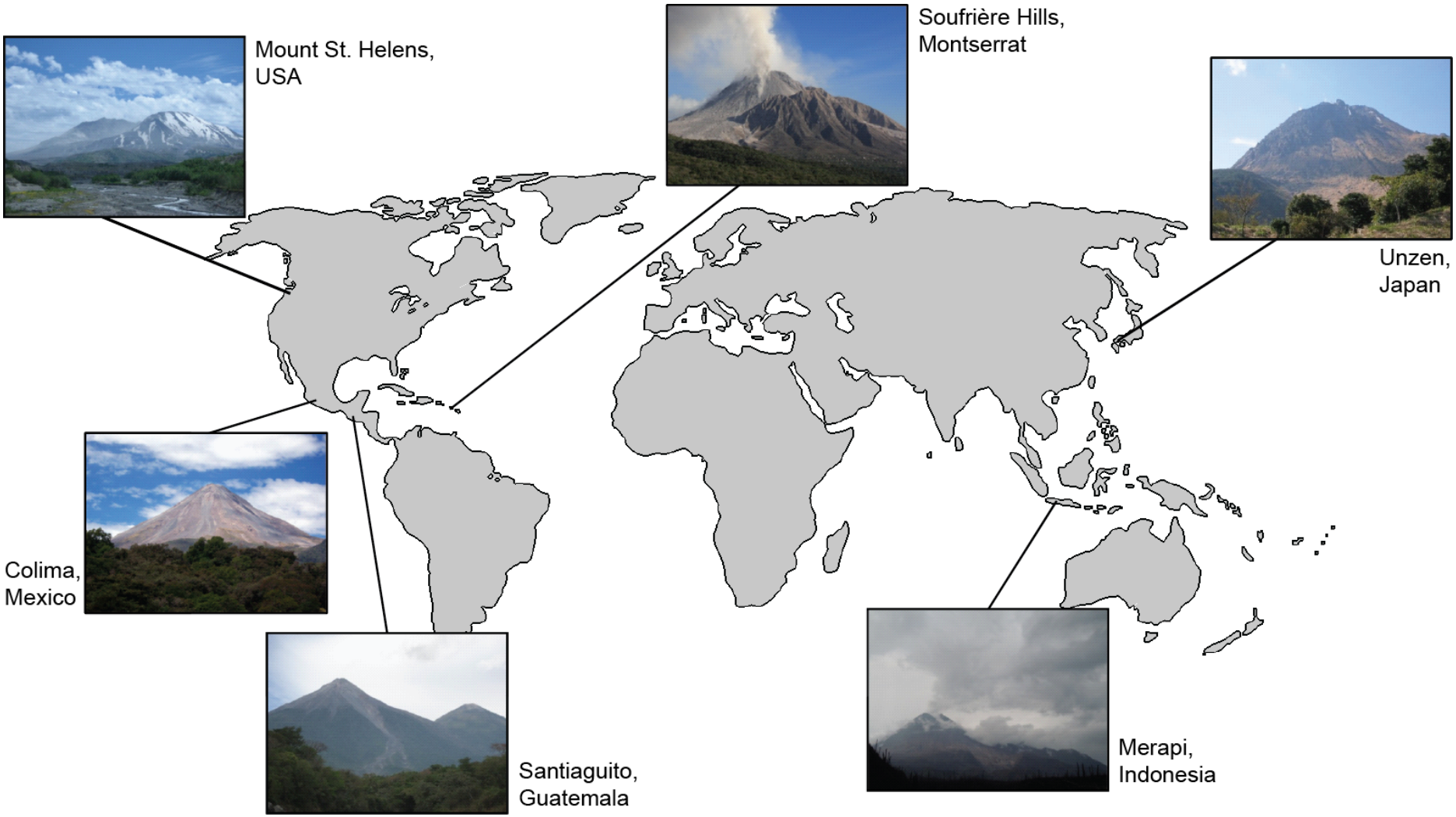

Figure 2.4: Global distribution of all volcanoes studied.

From 2003 to 2011, between two and six daily, sporadic explosions have occurred, producing varying amounts of ash. The previous two catastrophic endings were in 1818 and 1913, hinting Colima is potentially nearing the end of its current cycle (Luhr, 2002), posing a serious hazard to the ~300,000 people living within 40 km of the volcano as well as the city of Colima located ~30 km south.

2.8.2 Mount Merapi, Indonesia

Mount Merapi is a stratovolcano situated within the active volcanic front of the Sunda arc in Central Java, Indonesia. Recent volcanism at Merapi is generally characterised by growth of a viscous lava dome followed by collapse and resultant small-volume pyroclastic flows (Charbonnier and Gertisser, 2008). Effusive dome growth can last for several years, with frequent collapses, but is frequently interrupted by large, explosive eruptions (Camus et al., 2000; Gertisser and Keller, 2003; Newhall et al., 2000; Voight et al., 2000). Merapi erupts basaltic-andesite lavas, which are fairly typical of an intermediate arc volcano. The phenocryst assemblage (60 vol. %) is highly plagioclase-porphyritic, and also contains clinopyroxene (plus minor orthopyroxene), Fe-oxides and amphibole (Troll et al., 2012).

Merapi is located 25-30 km north of the metropolitan area of Yogyakarta, home to approximately 3.5 million people, and is one of the most historically deadly volcanoes in the world (Witham, 2005), with an estimated 1300 fatalities in the last 100 years. Its behaviour changed abruptly from late October to early November 2010, when it had its largest and most explosive eruption in more than a century (Surono et al., 2012). The eruption displaced a third of a million people and claimed nearly 400 lives. The eruptive history at Merapi suggests frequent VEI 4 eruptions have occurred in the past and are therefore likely to occur again (Camus et al., 2000; Gertisser and Keller, 2003). Gertisser and Keller (2003) suggest that Merapi is currently at the beginning of a phase of increased activity, which will pose formidable problems to disaster mitigation in the decades to come (Itoh et al., 2000; Thouret et al., 2000), especially considering that Java has among the highest population densities in the world (1000 people km^{-2}) (Troll et al., 2012).

2.8.3 Santa María volcano (Santiaguito), Guatemala

Santa María volcano is one of the most prominent of a chain of large stratovolcanoes that rises dramatically above the Western Highlands/Pacific coastal plain of Guatemala along the Central American Volcanic Arc. The massive (~1.2 km^3) dacitic lava-dome complex named Santiaguito lies within a crater formed during the VEI 6 eruption of Santa María in 1902 (Harris et al., 2003; Rose, 1972); the second largest eruption of the twentieth century (Williams and Self, 1983). The area covered by at least a trace of ash from the climactic eruption was calculated to be greater than 1.2 million km^2 (Williams and Self, 1983).

Compound exogenous and endogenous dome growth at Santiaguito has occurred episodically since 1922 from four westward-younging vents: El Brujo, El Monje, La Mitad, and Caliente (Figure 2.5) (Harris et al., 2003). Dome growth has been accompanied by almost continuous vulcanian explosions of steam, gas and ash (Yamamoto et al., 2008), with periodic lava extrusion, larger explosions, pyroclastic density currents, rock falls, and lahars. Lava flows have become increasingly dominant since the 1960s, with some extending over ~3 km from the vent (Rose, 1972). Santiaguito dome rocks are porphyritic andesites and dacites, with phenocrysts of plagioclase, pyroxenes, titanomagnetite, and amphibole, apatite, and pyrrhotite are common accessory minerals (Scott et al., 2012).

Figure 2.5: Santiaguito dome complex. Image reproduced from Ball et al. (2013).

Quetzaltenango (*Xela*), Guatemala's second largest city with a population of approximately 660,000 in the metro region is less than 10 km north. Quetzaltenango, along with other surrounding towns, e.g., Loma Linda, Palajunoj, and San Marcos, experience ash fall from the frequent (~0.5 h^{-1}), low-intensity strombolian eruptions explosions, which produce plumes to heights of up to 2 km above the dome (Holland et al., 2011; Sahetapy-Engel et al., 2008). The explosions, comprised mainly of steam and fine ash, originate from a ring-shaped pattern of fractures within the circumference of the dome (Bluth and Rose, 2004). The frequency of ashfall to the surrounding populations, and the volume of dome material, which has never undergone collapse and the stability of which is only currently being investigated

(Jessica Ball, University of Buffalo, personal communication), pose an on-going, and potentially catastrophic future, hazard.

2.8.4 Mount St. Helens, USA

Mount St. Helens is an active stratovolcano located in the Cascade Range of the Pacific Northwest region of the United States, and is part of the Cascade Volcanic Arc. The cataclysmic May 18, 1980 eruption of Mount St. Helens and resultant ashfall across populated areas of the north-western USA spurred the concern of volcanic ash as a respiratory hazard, leading to the publication of a dedicated issue of the American Journal of Public Health (March 1986) as well as numerous health-focused studies (reviewed by Horwell and Baxter 2006). The public health alarm and the discovery of cristobalite in the ash ignited research to determine the pathogenicity of crystalline silica-bearing ash (e.g. (Dollberg et al., 1986); however, toxicological, clinical and epidemiological studies gave inconclusive results as to whether the ash posed a chronic respiratory health hazard.

Largely episodic extrusion and endogenous growth between 1980 and 1986 produced a relatively symmetrical lava dome. By 1986, 17 episodes of dome growth had occurred (Mellors et al., 1988). The composite dome stood about 270 m above the 1980 crater floor and had a total volume of nearly 90 x 10^6 m^3 (Scott et al., 2008). Numerous lava spines protruded from the dome, existing for only a few weeks before collapsing. A few large rock falls spawned minor PDCs, however, none had sufficient volume to leave the crater (Mellors et al., 1988). The 1980-1986 dome rock varies in its degree of crystallinity; the most crystalline (~50 %) contains 30-35 % plagioclase, 5 % hypersthenes, 1-2 % hornblende, 1-2% Fe-Ti oxides, and <0.5 % clinopyroxene (Swanson et al., 1989).

Seismic unrest at Mount St. Helens again started in 2004, and evolved into a dome building eruption. The new dome grew as a series of spines within the existing 1980 crater, and reached a volume of 93 x 10^6 m^3 (Major et al., 2009). Revisiting samples from the 1980-1986 eruption serves to (1) provide the broadest foundation possible to contextualise the current study, (2) (re)define the respirable crystalline silica hazard posed by Mount St. Helens in light of up-to-date techniques, and (3) allow for a direct comparison between a well-studied eruption and the current suite of samples, including those from the renewed 2004-2008 eruption of Mount St. Helens.

2.8.5 Soufrière Hills volcano, Montserrat

The Soufrière Hills volcano, Montserrat is an active stratovolcano in the British West Indies on the northern part of the Lesser Antilles volcanic island arc. It is one of the most studied volcanoes in the world. It began its current eruption in July 1995, and growth of an andesitic

lava dome has continued intermittently since. There have been five phases of dome growth, interspersed with significant pauses, characterised by no dome extrusion but some vulcanian explosions, ash venting and dome collapses (Sparks and Young, 2002; Wadge et al., In review). The lava is a porphyritic andesite, containing phenocrysts of plagioclase, hornblende, orthopyroxene, titanomagnetite and oxides along with minor quartz (Murphy et al., 2000). Crystalline silica as cristobalite was identified in ash of the Soufrière Hills volcano (Baxter et al., 1999), reigniting concern about the adverse health effects of long-term human exposure.

The on-going eruption has been socially and economically disruptive for the island's inhabitants, with the complete evacuation and burial of the capital city, Plymouth, and the death of 19 people within the exclusion zone in June 1997. Major assets of Montserrat as an island nation were destroyed, including the port, rice mill and airport; and the original population of 10,500 was reduced to fewer than 3,500 at one point (Kokelaar, 2002). Mining of volcanic deposits is a large industry, resulting in dual-exposure (home and work) of volcanic particulate to the labour force (Sabina Michnowicz, personal communication, 2010). Albeit in the face of devastation, the eruption has provided opportunities to develop innovative monitoring and mitigation strategies.

2.8.6 Mount Unzen, Japan

Mount Unzen is a back-arc volcano enclosed in the Beppu-Shimabara graben, located on the Shimabara peninsula in Kyushu Island, Japan (Cordonnier et al., 2009). It is a group of overlapping stratovolcanoes most recently active from 1990-1995, when a large pyroclastic density current killed 43 people in 1991. An initial phreato-magmatic eruption was later followed by an explosion and the extrusion of a dacitic lava dome in 1991.

Many cycles of dome growth and collapse occurred over the 5 years, with activity transitioning between vulcanian and phreato-magmatic eruptions and dome extrusion, culminating in the generation of pyroclastic density currents (Nakada and Motomura, 1999). Dome growth was mainly exogenous when the dome was small and the effusion rate high, and endogenous when the dome became large and the effusion rate declined (Nakada et al., 1995). Ultimately, thirteen different domes were created, most destroyed by further dome growth, with 2.1×10^8 m^3 extruded in total. The final volume of the dome is about 0.1 km^3 (Nakada and Motomura, 1999). Unzen lava contains 20-30 % phenocrysts of plagioclase, hornblende, biotite, magnetite, and minor quartz in a rhyolitic glass, all of which show disequilibrium with the melt (Nakada and Motomura, 1999). As a result of sub-surface mixing and mingling, the erupted material is thought to differ strongly from the more mafic magma which ascended from depth (Cordonnier et al., 2009).

3

Methods

Acknowledgements

The number of field sites and abundance of laboratory techniques required for this thesis necessitates training and collaboration with a diverse group of individuals. Support for fieldwork and analytic work outlined in this chapter are recognised below.

Field Work

Fieldwork at Mount St. Helens, USA was carried out with Claire Horwell and Ed Llewellin alongside the expertise of Rick Hoblitt and Dave Sherrod, both at the Cascades Volcano Observatory (USGS Vancouver). Thanks to Carl Thornber and Cynthia Gardner (USGS Vancouver) for facilitating our visit. Fieldwork at Merapi, Indonesia was carried out alongside Peter Baxter (University of Cambridge, retired), Jean-Christophe Komorowski (Institut de Physique du Globe de Paris), Susanna Jenkins (University of Bristol) and Jochen Berger (Universität Hohenheim) with invaluable logistical support provided by Estu Mei and Adrien Picquout (both of the Université Panthéon Sorbonne Paris I). Fieldwork at Santiaguito was made possible by logistical and field support from Matt Watson (University of Bristol), Jessica Ball and Eliza Calder (both at the University of Buffalo).

Laboratory Work

Training and support for all of the SEM analyses carried out at Durham University were provided by Leon Bowen (Department of Physics). Training and support for Electron Microprobe analyses were provided Chris Hayward (University of Edinburgh). SEM Raman analyses were carried out with the help of Tim Batten (Renishaw plc, UK). Training and support for XRD analyses was provided by Gordon Cressey and Jens Najorka (Natural History Museum, London) and Gary Oswald (Department of Physics, Durham University). Training and support for toxicological analyses was provided by Fiona Murphy, Jenn Raftis and Wan-Seob Cho (all at the University of Edinburgh), and for surface reactivity analyses by Maura Tomatis and Bice Fubini (both at the Università degli Studi di Torino).

Separation of the respirable fraction was carried out in collaboration with Gordon Fern and Steve Hankin at the Institute of Occupational Medicine, Edinburgh. Isolation of cristobalite from volcanic ash using heavy liquids was carried out by Sarah Hillman and Ben Williamson with the author available for support. Isolated cristobalite by the Talvite method was provided by Claire Horwell and used for analyses during her PhD (2002).

3.1 Fieldwork and sample collection

Samples used in this study were collected during fieldwork campaigns and were also donated by colleagues and local scientists. Sample collection for each of the locations studied is discussed below. A complete list of dome rock samples analysed is provided at the start of Chapter 4, and a complete list of ash samples analysed is provided at the start of Chapter 6. Additional information on each location can be found in Chapter 2.

3.1.1 Colima, Mexico

Dome rock and ash samples from Colima volcano were donated by Nick Varley, Universidad de Colima, Mexico. 3 samples of dome rock were provided from activity between 2007 and 2010, and 2 ash samples were provided from activity between 2009 and 2010.

3.1.2 Merapi, Indonesia

Dome rock samples from the 2010 eruption of Merapi were collected during fieldwork in 2010. Samples from activity in 1996 and 1998 were provided by Bettina Scheu *(*Ludwig-Maximilians University, Munich, Germany). 16 dome rock samples were collected from the 2010 flow deposit, 6 samples were provided from the 1996 dome, and 3 samples were provided from the 1998 dome.

Ash samples from the 2010 eruption were sourced from colleagues near Merapi and additional samples were collected from deposits during fieldwork. 20 samples were collected in total and are detailed further in Damby et al. (2012; Appendix 4). 11 samples were provided by local contacts during the eruption and 9 further samples were collected in the field. 14 samples were explosive tephra fall, 5 samples were of detached surges from pyroclastic density currents, and 1 sample was from a lahar deposit. 1 additional sample from a dome collapse event in 1998 was included in the study from Claire Horwell's personal collection.

3.1.3 Mount St. Helens, USA

Rock samples were collected during fieldwork at Mount St. Helens (2009) and also sourced from the sample archives of the Cascades Volcano Observatory (CVO), Vancouver, Washington, USA. In total, 28 samples were collected. 11 dome rock samples from the 2004-2008 eruption and 8 dome rock samples from the 1980-1986 eruption were sourced from the CVO archive. 6 samples from the 1980 cryptodome were collected, 4 from the field and 2 from the archives. 3 other samples were collected from the field for comparison: 1 edifice sample was collected from the 1980 eruption, and 2 dyke samples were collected

from the Toutle River valley. Samples were sourced to represent the different domes and spines that grew during the periods of activity, and some were specifically sourced due to their use in previous studies (e.g., MSH.305, MSH.309, MSH.316 in Cashman et al., 2008) which had textural similarities to samples from Soufrière Hills (e.g., Horwell et al., post review; Appendix 4).

Ash samples were also sourced from the CVO archives. 5 ash samples were sourced from the 2004-2008 eruptive activity, which were a combination of dome collapse events and ash venting. 1 sample of fault gouge was sourced from CVO and was collected from the crater by CVO scientists during the 2004-2006 dome activity. Additionally, 1 ash sample from the 18 May 1980 eruption was incorporated from Claire Horwell's personal collection.

3.1.4 Santa María (Santiaguito), Guatemala

Dome rock samples from Santiaguito were collected *in situ* from the dome during fieldwork in 2010. 7 samples were collected in total: 4 samples were collected from the 'Brujo' dome, 2 samples were collected from the 'Mitad' dome, and 1 sample was collected from the 'Monje' dome. No samples were collected from the currently active 'Caliente' dome due to the frequency of eruptions.

Samples of ash were donated by Jeannie Scott, University of Oxford, some of which were originally sourced from the Santiaguito Volcano Observatory (OVSAN) and from Jonathan Stone, University of East Anglia. 5 samples from activity in 2005 and 4 samples from activity in 2009 were donated. Caliente is the likely source for all of the ash samples, and samples are either from ash venting or small pyroclastic density currents.

3.1.5 Soufrière Hills, Montserrat

No dome samples were used in this study as dome rock samples were characterised for Horwell et al. (post review; Appendix 4).

Three ash samples were sourced from Claire Horwell's personal collection. Two were samples that has been widely used by Horwell in characterisation studies (MBA5/6/99 and MBA7/12/03; Horwell, 2007; Horwell et al., 2007) and the other was MVO1498, a sample containing ~20 wt. % cristobalite and sourced from a complete dome collapse (see Horwell et al., submitted-a; Appendix 4 for complete sample information).

3.1.6 Unzen, Japan

Dome rock samples from Unzen were donated by Setsuya Nakada (Shimabara Earthquake and Volcano Observatory (SEVO) and Volcano Research Centre, Earthquake Research

Institute, University of Tokyo, Japan) and Yasuhiro Ishimine (RIKEN, Japan). 4 samples were provided from activity during 1992-1993.

Ash samples obtained from Unzen were erupted during 1990-1995, and are discussed further in Takahashi et al. (2007) and Shimizu et al. (2007). All samples were sourced or collected by Sarah Hillman and provided for the current study. Three samples (UNZ.01-UNZ.03) were provided by Professor S. Nakada from lofted ash from pyroclastic flows and were collected within 24 hours after dome collapse and before rainfall. Three further samples (UNZ.05, UNZ.06 and UNZ.08) were collected from ash deposits at Kita-Kamikoba, Shimabara city and Minami-Senbongi, and were collected from ash layers sitting between pyroclastic flows in the stratigraphic sequence. UNZ.05 was provided by S. Nakada and the other two (UNZ.06, UNZ.08) were collected by Sarah Hillman.

3.2 Sample preparation

Due to the breadth of techniques used for this study and restrictions of the analyses performed for different sample types, various sample preparations were necessarily required and are outlined below.

3.2.1 Dome rock samples

Dome rock samples were investigated as rock chippings, in thin section, and as powders.

Stubs of rock chippings were made to observe the 3-dimensional morphology of cristobalite within dome rock by scanning electron microscopy (SEM). SEM stubs were prepared by mounting a small fragment of rock (~0.5 cm diameter) onto an aluminium SEM stub using carbon paste. Samples were sputter coated with approximately 25 nm gold/palladium and silver dag was applied to dispel charging on the sample surface.

Polished thin sections (27 mm x 46 mm, ~30 μm thick) of dome rock were prepared in the Department of Earth Sciences, Durham University for comparisons of crystallinity and groundmass textures among samples, and for observation of sections through cristobalite particles. Resins used for impregnation of samples were SpeciFix-40 and CaldoFix-2 (Struers Limited), and rock slices were bound to slides with Type 301 epoxy (Logitech Limited). Sections were coated with 25 nm carbon and compared to a concurrently coated brass plate to ensure equivalent coating thicknesses between runs. Prior to coating, samples were ultrasonicated for 10 minutes in petroleum ether at room temperature.

Only small quantities of powdered samples were needed, and therefore samples were powdered by hand. Chippings of ~1 cm^3 were ground with an agate pestle and mortar.

3.2.2 Ash samples

All samples were dried at 80 °C for 24 hours after removal of a sample split, as heating can affect adsorbed species.

Ash stubs for imaging by SEM were prepared by sprinkling ash onto a polycarbonate disc without the use of a solvent. Discs were adhered to an aluminium stub with a carbon sticky pad and sputter coated to ~20 nm with gold/palladium.

Filter samples collected during the separation of a respirable fraction (Section 1.3.6) were mounted onto a 25 mm aluminium SEM stub and coated with a thin layer of gold in preparation for SEM.

3.2.3 Isolation of the Respirable Fraction

As chronic toxicity is instigated in the deep lung (see Chapter 2), separation and collection of the respirable ash fraction for use in representative toxicity assessments was essential. Samples for separation were selected based on the physicochemical results in Chapter 6 (part I), choosing the most potentially toxic sample from each of the volcanic locations studied. Sample mass was also a consideration as an estimated 5-10 g of material was required for separation, and most bulk sample masses were less than 20 g. Rationales for the individual samples chosen are outlined in Chapter 6: Toxicology.

An AERO PA100 particle aerosoliser (SAFENANO Section of the Institute of Occupational Medicine (IOM), Edinburgh) was used to generate particulate aerosols of an isolated respirable fraction, which were subsequently analysed by a variety of real-time instruments to quantify size distributions and morphologies (see Figure 3.1). This was the first time the AERO PA100 was used to isolate a particular size fraction; based on the findings of the study, the aerosoliser can be considered as a rudimentary particle classifier where the respirable fraction of bulk powder material with a broad particle size distribution can be successfully isolated and analysed.

3.2.3.1 Sample Aerosolisation

The aerosolisation chamber was loaded with approximately 5 g of bulk volcanic ash and the container screwed shut to seal. HEPA-filtered compressed air was driven through a nozzle at a typical flow rate of 5 L/min, creating high velocity jets which disturb and separate particles from the powder surface to form an aerosol. The concentration of the aerosol was altered by varying the distance between the nozzle and the powder.

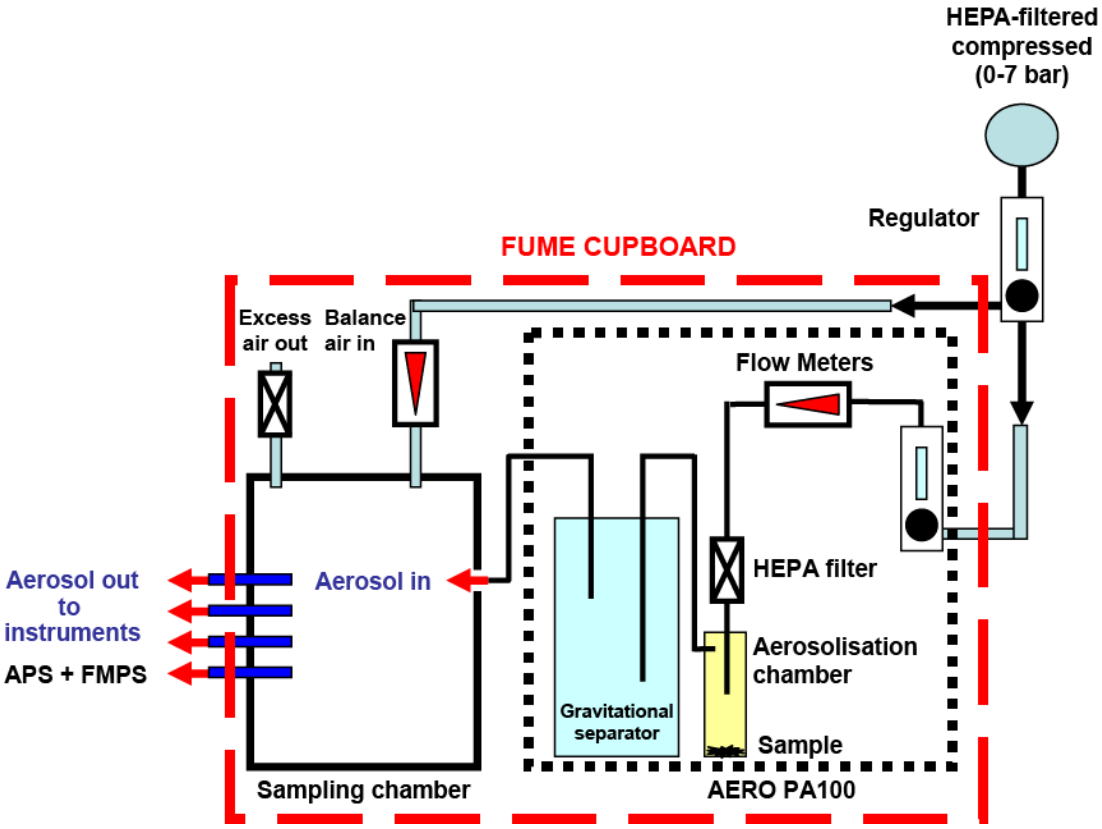

Figure 3.1: Schematic representation for the SAFENANO laboratory set up of the aerosolisation and detection equipment. Diagram adapted from SAFENANO internal report (SNP-014, project number 695-00204).

The aerosol was passed through a gravitational separator where large particle agglomerates were separated from the aerosol on the basis of particle diameter, density, and air flow. Particles exiting the aerosoliser do so in accordance with Stoke's Law (Equation 3.1), where only particles below a given aerodynamic diameter will exit the unit (for a given air flow and particle density), resulting in the generation of an aerosol comprised of particles below a desired aerodynamic size (i.e., particles within the respirable range).

After leaving the aerosoliser and gravitational separator, the aerosol enters the sampling chamber (approximately 30 L capacity) at a flow rate of 5 L min^{-1}. The balance air is adjusted in order to maintain a near-neutral (slightly positive) pressure in the sampling chamber, which ensures that the correct operating parameters of the equipment are achieved. Excess air is passed through a HEPA-filter and is vented into the fume cupboard.

The settling velocity (m s^{-1}) was taken as being equal to the air velocity calculated for a gravitational settling chamber with an inner diameter of 25 cm using a flow rate of 5 L min^{-1}. Maximum theoretical aerodynamic diameters for particles are presented in Table 3.1.

$$Particle\ Diameter = \sqrt{\frac{18\ x\ \mu_m\ x\ settling\ velocity}{G\ x\ (\rho_p - \rho_m)}} \qquad \textit{Equation 3.1}$$

Where: μ_m = viscosity of the medium (1.807×10^{-5} kg m^{-1} s^{-1} for air)

G = Gravity (9.807 m s^{-2})

ρ_p = density of the particles (in kg m^{-3}, from Table 3.1)

ρ_m = density of the medium (1.20478 kg m^{-3} for air)

Table 3.1: Maximum theoretical aerodynamic diameter calculated for particles in the IOM gravitational settling chamber from Equation 3.1 based on the likely range of particle densities for volcanic ash.

Particle Density (g/cm^3)	Air Flow (L/min)	Theoretical Maximum Particle Aerodynamic Diameter (μm)
1.0	5.0	7.51
1.4	5.0	6.35
1.8	5.0	5.60
2.2	5.0	5.06
2.8	5.0	4.49

A Fast Mobility Particle Sizer (FMPS) and Aerodynamic Particle Sizer (APS) were connected to the sampling chamber. Before aerosolisation begins, HEPA-filtered balance air is admitted and data recording started to obtain a background (observed to read close to zero particle count on both instruments). Upon aerosolisation, the real-time instruments employed (FMPS, APS) are used to identify the presence of particles in the sampling chamber. The FMPS measures particles from 5.6–560 nm based on electrical mobility, and the APS measures particles from 500–20000 nm by light scattering. By overlapping the two instrument readings at their detection boundaries, a total range of 5.6 nm–20 μm was analysed. The APS data highlight the particle size cut-off at ~8 μm, which is consistent with the maximum particle size approximations calculated for the aerosolisation conditions (Table 3.1); a nominal particle density of 1.0 g/m^3 results in a maximum theoretical particle size anticipated to exit the aerosoliser of 7.51 μm. Mass and surface area are not directly measured by the instruments, however, software in both instruments automatically translates particle number concentration into mass and surface area concentration based on a given particle density for particles that are uniform spheres. Data were recorded over a 15-30 minute period. Samples were recovered from the sampling chamber for use in toxicological experiments (Section 3.4).

A second aerosolisation experiment was run for each sample to capture a suitable mass of classified volcanic ash for SEM-EDS analysis. An open cowl sampling head was placed inside the sampling chamber and collected particles for approximately 10 minutes during the aerosolisation process when particle concentration was approximately 30000-40000 particles cm^{-3}. This sampling technique was developed by the IOM to yield a sample which has minimised particle impaction and agglomeration on the filter surface, and allows for adequate imaging of primary aerosol particles. Samples were collected on 25 mm/0.04 μm polycarbonate filters with a pump rate of 2 L min^{-1}. Particle size data obtained during the second run were consistent with the first run.

3.3 Analytical techniques

This section contains descriptions of methods followed for the main mineralogical and toxicological techniques used to characterise samples.

3.3.1 SEM based analyses

Scanning electron microscopy (SEM) was used in conjunction with numerous analytical techniques to determine the physicochemical characteristics of dome rock and ash samples. In an SEM, an electron beam is emitted from an electron gun and focused onto the sample.

The beam electrons interact with electrons in the sample and produce various signals that can be detected (Figure 3.2). These signals contain information about the topography and composition of the sample and include, amongst others: secondary electrons (SE), surface topography; backscattered electrons (BSE), atomic number and topography; X-rays, chemical composition at the surface; cathodoluminescence (CL), internal structures and chemistry. The spatial resolution of SEM depends on the source and instrument optics (both a field-emission gun (FEG) SEM and a tungsten filament SEM are used here) as well the interaction volume with the sample, but is generally < 5 nm in the current study.

3.3.1.1 Sample Characterisation: FEG-SEM

Imaging and analysis of all samples was carried out on a Hitachi SU-70 (FEG) SEM in the GJ Russell Microscopy Facility, Department of Physics, Durham University. Operating voltage and working distance for individual images varied depending on the mode of operation (see below) and are recorded on the image.

Images were recorded at various magnifications for a representative analysis of the distribution, size, and shape of particles sampled.

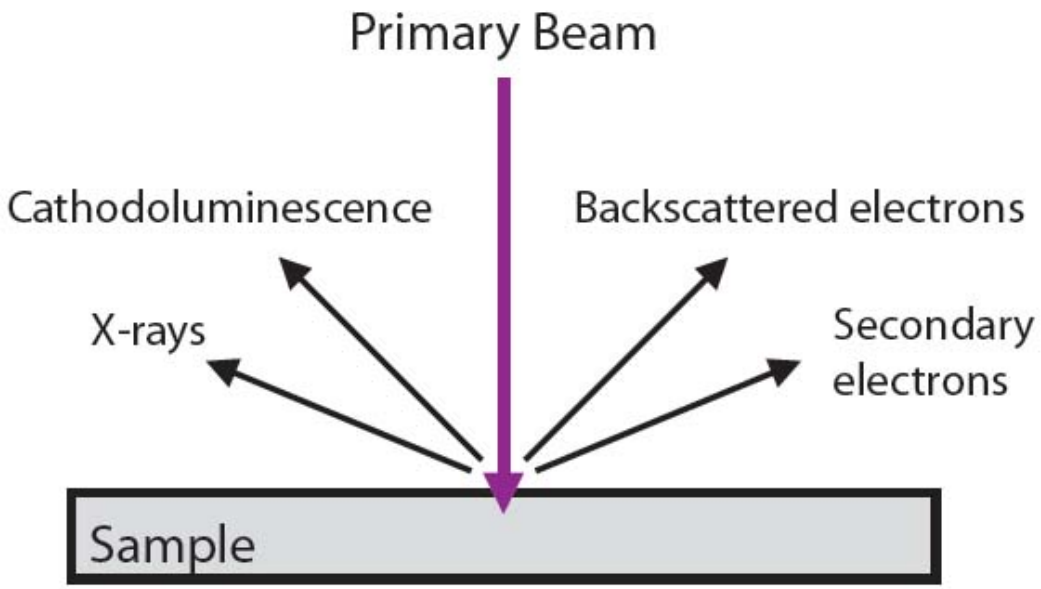

Figure 3.2: Schematic representation of the energies produced from incident electron beam interaction with solid matter in an SEM.

Secondary electron (SE) imaging was used to collect topographical and morphological data for dome rock stubs and ash samples. Dome rock stubs were principally used to image vapour-phase crystalline silica crystals *in situ* to identify morphological differences among samples. Ash samples were primarily imaged for the identification of fibrous particles, which would raise fibre-related respiratory concerns (see Chapter 2).

Backscatter electron (BSE) imaging was carried out on carbon-coated polished thin sections of samples. BSE imaging is ideal for obtaining high-resolution compositional images of a sample, allowing for quick discrimination among different phases. The interaction of an accelerated electron beam with a sample target produces a variety of elastic and inelastic collisions. The number of backscattered electrons reaching a BSE detector is proportional to the mean atomic number of a sample, with larger atoms (high atomic number) having a higher probability of producing an elastic collision. Therefore, brighter BSE intensity correlates with a greater atomic number and darker areas have a lower atomic number. Differences in mineral polymorphs (e.g., crystalline silica) are not distinguishable by BSE due to crystals having the same mean atomic number.

Energy dispersive X-ray spectroscopy (EDS) was used to semi-qualitatively determine elemental phases for locations of interest in sample thin sections and to produce lower magnification elemental maps. All measurements were performed with an Oxford Instruments EDX system (INCAx-act LN_2-free analytical Silicon Drift Detector) and interpreted using Oxford Instruments INCA software.

Wavelength dispersive X-ray spectroscopy (WDS) was used to quantitatively analyse elemental phases for locations of interest in sample thin sections and to quantitatively map single elements using combined EDS/WDS mapping. All measurements were performed with an Oxford Instruments WDS system (INCAWave 700 spectrometer) and interpreted using Oxford Instruments INCA software.

3.3.1.2 Elemental Analysis: Electron Microprobe

Electron probe micro analysis (EPMA) was used to quantify elemental substitutions in volcanic cristobalite. EPMA uses an incident electron beam to generate X-rays with energies and wavelengths specific to the elements present in the sample, allowing quantification of elements of interest. Analyses were carried out on a CAMECA SX100 SEM equipped with five vertical crystal WDS detectors and a PGT Spirit EDS analyser at the Grant Institute of Earth Science, University of Edinburgh.

Specific locations on carbon coated (25 nm) thin sections were quantitatively analysed for Na, Si, Mg, Al, K, Ca, Ti, Mn, and Fe. Measurements for Na and Si were analysed at 4 nA,

and the rest of the elements at 80 nA. Sodium was measured first to minimize the effects of sodium drift on the results. Instrument calibration was carried out by analysing the following reference materials of known compositions: Na on Jadeite-BL7, Si on Quartz, Mg and Al on Spinel-Bl-8, K on Orthoclase-BL7, Ca on Wollast-BL8, Ti on Rutile-BL8, Mn on PuMn-BL8, Fe on Fayalite. The crystals used for sample measurements were: Spectrometer 1 TAP (Si, Al), Sp2 LLIF (Mn, Fe), Sp3 LPET (K, Ca, Ti), Sp4 TAP (Al), Sp5 LTAP (Na, Mg). The large analysing crystals enabled higher analytical precision, lower detection limits, and faster analysis times. Spatial resolution of the set up conditions was approximately 1 μm and detection limits of <0.009 to <0.002 wt. % were obtained.

3.3.1.3 Structural Determination: Cathodoluminescence

Cathodoluminescence is the emission of light from a solid following excitation by an electron beam; and, when applied to geological samples, can provide information on provenance, growth fabrics, diagnostic textures, deformation and defects, and mineral zonation.

The structural composition of crystalline silica phases in dome rock as well as the identification of any internal structures that could elucidate crystal growth history was determined by CL. Cristobalite can be distinguished from the other crystalline silica polymorphs by its excitation wavelength – cristobalite is at 400 nm (blue), quartz is at 650 nm (red), and tridymite has peaks at 430 and 650 nm – as well as from groundmass feldspar (680-740 nm range) and glass (285, 460, 650). However, Al^{3+}, Mn^{2+} and $Fe^{2+/3+}$ defects within crystalline silica can lead to spectra that are broader and/or displaced from ideal as well as the presence of minor peaks which are difficult to de-convolve. Incorporation of elemental defects allows for discrimination of different generations of the same mineral, e.g., zoning in zircon and plagioclase. As is the case with quartz, cristobalite luminescence was determined here to degrade with time, making long-duration and multiple measurements of excited areas difficult.

Monochromatic imaging and serial-CL analyses were carried out at the Durham GJ Russell Microscopy Facility using a Gatan MonoCL cathodoluminescence system and Digiscan II image processing software (Gatan, Inc., Pleasanton, CA, USA) attached to the Hitachi SU70 FEG-SEM. True-colour images were constructed from three consecutive grey-level analyses using a red, green and blue series of colour filters.

3.3.1.4 Structural Determination: Raman Microscopy

Raman spectroscopy provides information about molecular vibrations that can be used for structural identification of minerals. The technique involves shining a monochromatic light

source (i.e., a laser) on a sample and detecting scattered light. A very small amount of the scattered light is shifted in energy due to interactions of the incident laser (electromagnetic waves) and the vibrational energy levels of the molecules in the sample. The frequency shift corresponding to the energy difference between the incident and scattered photon is termed the Raman shift. This shift provides information about vibrational, rotational, and other low frequency transitions in molecules, thus providing crystallographic and mechanic data for the sample of interest. Plotting the intensity of this shifted light (Raman shift) versus frequency results in a Raman spectrum. Different materials have different molecular and macroscopic vibrational modes, and therefore different characteristic Raman spectra.

Crystalline silica polymorphs were distinguished in uncoated polished thin sections using a Renishaw SEM-Raman Structural and Chemical Analyser, which couples Raman spectroscopy (Renishaw inVia Raman microscope, 785 nm laser) with SEM-EDS (JEOL JSM-6060 LV SEM with Oxford Instruments INCA energy dispersive X-ray analysis) at Renishaw plc, UK. This allowed for the identification of silica polymorphs for individual crystals. Reference spectra were obtained from the online Handbook of Minerals Raman Spectra (http://www.ens-lyon.fr/Raman/index.php), which uses reference spectra from Kingma and Hemley (1994).

3.3.2 X-ray Diffraction: Identification of crystalline silica phases in bulk material

When a sample is bombarded by an X-ray beam, the atoms of a material cause the beam to diffract according to Bragg's law (Equation 3.2), providing information on the structure of the material. Minerals are a regular array of atoms and therefore have a characteristic diffraction pattern, allowing identification of the constituents in a heterogeneous sample. X-ray diffraction (XRD) was used for structural identification of mineral phases, quantification of cristobalite in bulk samples, and determination of lattice parameters for cristobalite.

$$n\lambda = 2d\sin\theta \qquad \textit{Equation 3.2}$$

Where n is an integer, λ is the wavelength (1.54 Å for Cu $K\alpha_1$), d is the distance between lattice planes, and θ is the scattering angle.

Quantification of crystalline silica polymorphs in both powdered dome rock and ash samples was performed following the Internal Attenuation Standard (XRD-IAS) method of Le Blond et al. (2009). This method allows for the rapid quantification of phases of interest without full knowledge of a sample's bulk mineralogical composition through the introduction of a known quantity of an internal attenuation standard into the sample. Zinc oxide (ZnO) was

used as the IAS in all experiments. Dome rock and ash samples were ground in an agate pestle and mortar to a grain size of <20 μm. For the IAS method, ~30 wt. % pure phased powdered ZnO was added to approximately 0.25 g of sample and mixed thoroughly in a pestle and mortar. XRD patterns for the original volcanic sample, the mixed-phase IAS sample, the pure phase internal ZnO standard, and pure phase standard mineral components (cristobalite, quartz, tridymite, feldspar) were all collected. A feldspar standard is analysed to allow 'stripping' of the feldspar pattern from the bulk pattern to overcome peak overlaps between feldspar and cristobalite. Labradorite was chosen as a feldspar standard during technique development as the plagioclase closest in composition to that found in Soufrière Hills ash (An% 50-70; Le Blond et al., 2009; Murphy et al., 2000), and was regarded as appropriate for the samples in this study. Samples were loaded into a deep-well Al circular mount with a volume of 180 mm^3 and packed using the knife edge of a spatula to create a flat yet roughened surface (as described by Batchelder and Cressey, 1998). This reduced preferential orientation of minerals, resulting in randomly generated XRD patterns. No sieving was undertaken to ensure no fractionation occurred due to experimental preparation.

The majority of experiments were carried out using an Enraf-Nonius X-ray diffractometer with an INEL curved position sensitive detector (PSD) at the Natural History Museum, London, UK, which allows simultaneous detection over 120 °2θ. A germanium (111) single-crystal monochromator was used to select only Cu $K\alpha_1$ radiation. Tube operating conditions were at 45 kV and 45 mA. Horizontal and vertical slits were at 0.24 x 5.0 mm^2, respectively. The geometry of the beam reflection on the sample was maintained at 12 degrees to the incident beam (μ=5.0). NBS silicon powder and silver behenate were used as instrument 2θ calibration standards. Patterns were collected and 2θ linearization performed using DIFGRAB software. Pattern acquisition time for each sample was 10 minutes, with the sample spinning continuously.

Data were analysed following the method for single phase quantification outlined in Le Blond et al. (2009) using two different analysis programs. Nonius GUFI software was used to scale and fit sample curves to pure-phase standard curves. This permitted the subtraction of a standard, single-phase pattern from the multiphase volcanic sample until the residual pattern had near-zero counts remaining. LinkFit software version 1.0.4 (written by John S. Loring and licensed to The Natural History Museum, London) was used to calculate the proportion of IAS and to determine the mass attenuation coefficient of the sample through a least-squares fitting approach. All phase quantifications are presented with a < 3 wt. % error, the accepted error of the XRD-IAS-PSD method (Le Blond et al., 2009).

Further experiments were carried out on a Bruker AXS D8 ADVANCE with DAVINCI design in the Department of Chemistry, Durham University. The IAS technique was adapted to this non-static system for this thesis, a task which was not previously considered possible. The instrument was used in parallel beam mode, using a Göbel mirror, Ni filter and a 0.1 mm fixed slit. The geometry of the incident beam was fixed at 8 degrees relative to the sample. Patterns were collected for 20 minutes using a multi-sample exchange arm, significantly cutting down on active preparation time. Data were analysed as outlined above using DIFFRAC.EVA software.

Lattice disorder needs to be carefully considered when quantifying mineral phases by XRD. Alcala et al. (1996) show that cristobalite sintered at lower temperatures are less well ordered, with XRD patterns having a higher background and decreased sharpness and intensity of reflections. As such, when quantifying crystalline phases it is imperative to use a comparable standard. A less well ordered standard will always overestimate the amount of crystalline silica present, and for this reason we have isolated cristobalite from volcanic ash by two methods to be used for quantification. Additionally, there is a difference in diffraction intensity between α and β cristobalite, making identification of the correct phase imperative for quantification.

3.3.3 X-ray Fluorescence: Determination of Magmatic Composition

The major elemental oxide compositions of dome rock and ash samples were determined by X-ray Fluorescence (XRF). XRF measures the secondary X-rays emitted from a sample that has been bombarded by a primary radiation source. Each element has a characteristic fluorescence, and can therefore be distinguished and quantified in a sample. Sample compositions were used to define the magmatic composition of each sample on a total alkali versus silica (TAS) plot (Figures 4.16 and 6.5), allowing identification of changes in eruptive composition as well as providing insights into crystal fractionation.

Experiments were carried out at the Department of Geology, University of Leicester, UK using a PANalytical Axios Advanced PW4400 X-ray fluorescence spectrometer. Samples were ground to a powder and ignited at 1050 °C for 1 hour, and the difference between un-ignited and ignited powders was used to calculate the loss-on-ignition (LOI) value. Fused beads were produced by mixing the ignited rock powder (0.3000 g) with an anhydrous metaborate fluxing agent in a 1:5 ratio. The flux-sample mixture was heated for 45 minutes at 1050 °C and homogenised. Heating the sample ensures mineralogical effects (e.g., preferred orientation) will not affect the analysis. The molten mixture was cast on a Pt-Au crucible and the flat, lower surface used for analysis.

3.3.4 Particle Size Distribution: Bulk Sample

Characterisation of the particle size distribution (PSD) for a bulk ash sample is a critical step in evaluating its health hazard (see Chapter 2), and can further provide information into the style of eruption and post-eruption modifications. There is a strong correlation between the amount of sub-4 and sub-10 μm material observed for all ash types, which is stable for all eruption styles and at all distances from the source (Horwell, 2007).

Oven dried samples were sieved to <1 mm (0 Phi) to ensure that grains greater than 2 mm were not analysed. This is the cut-off for the classification of particles as 'ash', and is the maximum particle size for measurement by laser diffraction. The grain size distribution of volcanic ash were binned according to the health-relevant cut-offs outlined in Table 3.2 following analysis.

Table 3.2: Definition of size bins for health-pertinent grain size fractions. Particles with a <10 μm aerodynamic diameter are able to penetrate into the human lung (Quality of Urban Air Review Group, 1996). <63 μm is included as this is the practicable size cut-off for sieving.

Size (Bin)	Fraction	Potential Health Effects
< 1 μm	Ultra-fine	Can enter the alveolar region where chronic disease can occur with long-term exposure
< 2.5 μm	"	
< 4 μm	Respirable	
< 10 μm	Thoracic	Can pass the bronchus, where bronchitis, asthma, and other acute disease may be triggered in susceptible individuals
< 63 μm	Sievable	n/a
< 100 μm	Inhalable	Can enter the throat, causing rhinitis, laryngitis, and irritation

Measurements were carried out using a Malvern Mastersizer 2000 laser diffractometer with Hydro MU and ultrasonics at the Department of Geography, University of Cambridge, UK after Horwell (2007). This technique works by diffracting light off of the surface of a particle using the Mie model for light scattering, and calculates a volume % for different particle sizes. Interpretation according to Mie scattering accounts for both diffraction and diffusion of light around a particle in medium, and is appropriate for the particle size range measured here: 0.02-2000 μm. The model assumes particles are spherical, which can result in non-spherical particles being assigned an incorrect diameter (Eshel et al., 2004). Analysis of non-spherical particles (e.g., fibres), however, requires specialised instrumentation and was deemed unnecessary as all samples had similar morphologies by SEM imaging (see Chapter 6). Particles were measured using a standard operating procedure of 20 s measurement time, obscuration of 5-20 %, and pump speed of 2500 rpm. Data are reported as the average of three measurement cycles. Samples were measured with a refractive index of 1.63 and an absorption coefficient of 0.1, calculated as being suitable for the present range of ash samples by Horwell (2007). Data were re-binned according to health relevant size fractions (Table 3.2), and results were adjusted to account for the coarser 1-2mm fraction, which was sieved and weighed but excluded from the analyses.

3.3.5 Specific surface area: BET method

Surface area defines the total surface available for reactions to occur, and is therefore one of the dominant controls on particle toxicology (Duffin et al., 2002; see Chapter 2). The potential for toxicity is inversely proportional to decreasing particle size and proportional to increasing surface area (Donaldson and Tran, 2004; Oberdorster, 1996). As such, results discussing the surface reactivity of particles are normalised to surface area throughout this thesis.

The Brunauer-Emmett-Teller (BET) method of nitrogen adsorption (Brunauer et al., 1938) was used to measure the specific surface area (SSA) of ash samples. BET theory explains the multilayer, physical adsorption of gas molecules (e.g., nitrogen) on a solid surface, accounting for adsorption beyond a saturated, monolayer coverage, whereby the amount of gas adsorbed correlates to the surface area of a solid. This is experimentally determined by measuring the number of moles adsorbed as a function of equilibrium pressure.

Experiments were carried out in the Department of Chemistry, Durham University on a Micromeritics TriStar 3000 Surface Area and Porosimetry Analyser. Prior to analysis, all samples were degassed under N_2 at 110 °C for at least 2 hours in order to remove any previously adsorbed species. Sample weights were recorded, and nitrogen adsorption was measured in glass BET tubes insulated with a thermal jacket following cooling in a liquid

nitrogen bath. Data are presented as the average of three independent runs of different subsamples.

3.3.6 Mean Effective Diameter: Dynamic Light Scattering

The size distribution of respirable particles when suspended in solution, which may differ from that determined as an aerosol (by FMPS/APS) due to aggregation, was determined by dynamic light scattering (DLS). This was necessary as toxicological experiments were carried out in solution (see Section 3.4). The mean effective diameter and polydispersion, a measure of a sample size distribution compared to unity, of samples were measured in solutions used in Section 3.4.

DLS works on the scattering of a monochromatic light (i.e., a laser) by a particle in all directions (Rayleigh scattering) in suspension as detected at a 90° angle from the source. A spherical particle in Brownian motion causes a Doppler shift when the light hits it, changing the wavelength of the detected light. This change is related to the size of the particle, and is therefore possible to compute the equivalent sphere size of the particle.

Experiments were conducted in the ELEGI/Colt Research Laboratories, MRC/University of Edinburgh, UK on a DLS (Brookhaven Instruments Corporation, NY, USA) using red light (675 nm). Experiments were conducted for 10 minutes, where data were averaged once every minute. Samples were suspended in each of the solutions used (RPMI or DMEM; see Section 3.5.2 for more information), a standard vehicle control (sterile saline), and RPMI+FBS (foetal bovine serum) to consider the effects of *in vivo* protein adsorption on particle size. Experiments were done in triplicate per sample per solution, except for in RPMI+FBS which was only done for sample MER.arc (n=3).

3.4 Surface Reactivity

3.4.1 Electron Paramagnetic Resonance

Electron paramagnetic resonance (EPR) was used in association with the 'spin-trap' technique to detect acellular free radical generation from the surface of the particles (Fubini et al., 1995b); in this case, the hydroxyl radical ($HO^{\bullet}$) and carboxyl radical ($CO_2^{\bullet-}$). The experiment uses an EPR spectrometer to detect unpaired electrons present in free radicals via alterations in electromagnetic energy. Free radicals, however, are notoriously short lived (~0.001 s; Halliwell and Gutteridge, 2007) so an organic sensing compound (i.e., spin trap) was used to detect free-radical production. The compound 5,5'-dimethyl-1-pyrroline-N-oxide (DMPO) was used, which is modified by the presence of short-lived free radicals to

form a spin-adduct (DMPO/$R^{\bullet}$, where $R^{\bullet}$ is a general free radical which can be organic or inorganic), a persistent nitrogen based radical which creates a larger, longer-lived signal. The amplitude of this spectrum is directly proportional to the level of free radical activity in the sample and, therefore, radicals can be quantified if a reference standard is used. The spectral features (number of lines and hyperfine coupling constant) depend on the radical trapped. DMPO is widely used for hydroxyl radical detection, but is capable of also trapping carbon, nitrogen and sulphur centred radicals (Rosen et al., 1999; Taniguchi and Madden, 2000). The spin-adduct DMPO/$H^{\bullet}$ results in the characteristic 4 event EPR spectrum as shown in Figure 3.3a, with a nitrogen (αN) and proton hyperfine coupling constant (αH) of 14.9 Gauss. The spin-adduct DMPO/$CO_2^{\bullet-}$ exhibits an EPR spectrum with six lines (Figure 3.3b), with hyperfine values of αN 15.6 G and αH 19 G.

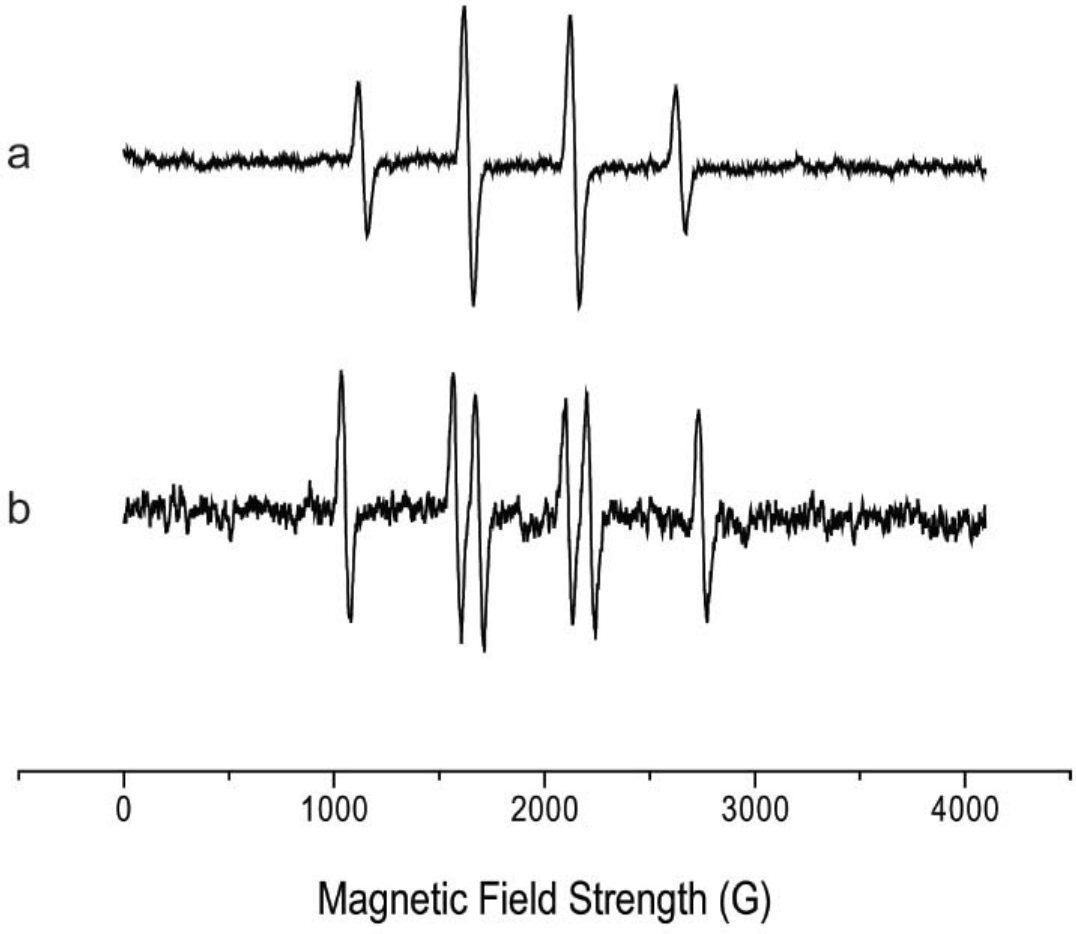

Figure 3.3: Characteristic EPR spectra of the (a) DMPO/$HO^{\bullet}$ adduct (Etna sample at 60 minutes) and (b) DMPO/$CO_2^{\bullet-}$ adduct (MER.04 first reduced by ascorbic acid) produced in suspensions of volcanic ash.

The generation of hydroxyl radicals ($HO^{\bullet}$) was measured in solution by replication of the iron-catalysed Fenton reaction (Equation 3.3) in the presence of H_2O_2 (see Chapter 2 for explanation of the reaction and the effects of hydroxyl radicals in the lungs). Experiments were performed by suspending 150 mg of ash in 500 µl phosphate buffered solution (0.5 M, Sigma-Aldrich) at pH 7.4 and adding 250 µl 0.17 M DMPO and 500 µl 0.2 M H_2O_2. Suspensions were incubated and stirred for 1 hour in darkened vials at room temperature.

Aliquots were removed at 10, 30, and 60 minutes, filtered through 0.2 µm cellulose acetate membrane filters and immediately transferred to 50 µl capillary tubes to be measured by EPR (Miniscope 100 ESR spectrometer, Magnettech GmbH, Germany) at the Università degli Studi di Torino, Italy. The number of free hydroxyl radicals produced was determined in arbitrary units against a Mn^{2+} standard based on the area under the curve for the third event of the four-event spectrum generated.

$$Fe^{2+} + H_2O_2 \rightarrow Fe^{3+} + OH^- + HO^{\bullet} \qquad \textit{Equation 3.3}$$

Generation of carboxyl radicals ($COO^{\bullet-}$) through homolytic cleavage of the C-H bond in the formate ion employed as a target molecule was performed in the same way: suspending 150 mg of ash in 500 µl 0.17 M DMPO and adding 500 µl 2 M sodium formate in TP 0.5 M. No quantification of carboxyl radicals was carried out.

The EPR spectra were recorded with the following instrumental conditions: receiver gain, 9 x 10^2; microwave power, 10 mW; microwave attenuation, 10 dB; modulation amplitude, 1000 mG; centre field, 3344; sweep length, 120 G; scan time, 80 seconds; number of scans, 2. Solutions without particles were measured in all experiments as blanks. Previously analysed ash samples (Etna, Cerro Negro, MBA5/6/99, Pinatubo) were run alongside samples of interest to compare results with previous experiments (Horwell et al., 2007; Horwell et al., 2003a). Data are reported as the average of 3 runs.

3.4.2 Iron Release: Mobilisation of iron at the solid/liquid interface

The identification of one hazardous component in a sample is insufficient to predict the toxicity of a particle, as the toxic moiety (e.g., di- and trivalent iron), must be bioavailable to elicit a biological response (Fubini et al., 1995b). Iron, itself, is capable of generating free radicals, however prolonged and catalytic generation of free radicals only occurs when iron is present on the surface of a mineral (Ghio et al., 1992). Surface properties (e.g., crystalline structure, surface area, coordination of the iron, and redox state) therefore regulate

phenomena relative to soluble iron, and mobilisation of iron from the surface does not parallel the mere iron content of the mineral (Fubini, 1994). Mobilisation rates measured under identical conditions enables accurate comparison of the behaviour of different solids, even when an equilibrium state is difficult to define due to iron mobility (Mollo et al., 1994).

Experiments were conducted to characterise the amount of removable Fe^{2+} and Fe^{3+} from the surfaces of ash following a method previously described (Horwell et al., 2007; Horwell et al., 2003a). The use of ferrozine, a bidentate N-donor chelator specific for Fe^{2+}, permits direct measurements of available ferrous iron. The introduction of ascorbic acid reduces Fe^{3+} to Fe^{2+}, which enables the measurement of total iron mobilised by first reducing all available ferric iron. Available Fe^{3+} was calculated by taking the difference between readings with ascorbate (total Fe) and without (Fe^{2+}). Chelation by ferrozine forms an intensely coloured complex which can be quantified spectrophotometrically by reading the absorption at 562 nm.

10 mg of ash were placed in tubes with either 5 ml ferrozine (1 M) and 5 ml ascorbate (6 mM) or 5 ml ferrozine and 5 ml distilled water, for a combined volume of 10 ml. The suspensions were incubated on a shaker at 37 °C and aliquots were taken every 24 hours for 9 days to determine iron release kinetics. Aliquots were centrifuged at 4000 rpm for 15 minutes and transferred into a cuvette and read in a Uvikon spectrophotometer. The instrument was blanked prior to each reading with a corresponding solution-only control sample incubated alongside the ash samples. The concentration was calculated by interpolation of a calibration curve using a molar extinction coefficient of 28.4, which was previously determined by calibration with an iron nitrate solution. Data are the average of 2 readings and expressed per unit surface area.

3.5 Toxicology

3.5.1 Haemolysis Assay: Potential for membrane rupture

The haemolysis assay is a basic *in-vitro* toxicity experiment to determine the potential of a particle to rupture a cellular membrane. Red blood cells lack a cell nucleus and most organelles, and therefore serve as a model cellular membrane for particle-induced lysis. It is employed here, and routinely elsewhere (e.g. Damby et al., 2012; Horwell et al., submitted-b; Appendix 4; Le Blond et al., 2010), for the rapid health assessment of volcanic ash, due to the high response persistently generated by crystalline silica. While, in general, crystalline silica is not the only mineral able to cause a positive haemolytic response, it is the only major phase in volcanic ash expected to be haemolytic.

3.5.1.1 Red blood cell (RBC) collection and preparation

40 ml of fresh, human venous blood was added to a 3.8 % w/v citrate solution to prevent coagulation. The blood was then mixed gently by inversion and centrifuged at 2000 rpm for 10 minutes. The supernatant was removed, leaving 85 % haematocrit (RBC volume fraction). Packed RBCs were added to buffer containing 0.428 g $NaHCO_3$ (30 mM), 0.386 g $NaHPO_4$ (16 mM), 3.360 g Dextrose/D-glucose (110 mM), 1.7 g mannitol (55 mM), diluted in 170 ml dH_2O. 13 ml of buffer were added for every 40 ml (original volume) of blood taken. RBCs were never stored for more than 3 weeks at 4 °C.

3.5.1.2 Haemolysis Assay

1 ml RBCs was washed x3 with saline by centrifugation at 4000 rpm for 5 minutes. 400 µl of packed RBCs were added to 7.6 ml saline (5 % by volume RBC in saline), which is enough for one 96-well plate.

Particles were weighed out, suspended in saline, and sonicated for 10 minutes. Different media/dispersants used to suspend particles may change the haemolytic potential of particles; saline was used as particles in PBS and 0.5 % BSA solutions have both shown a reduced haemolytic response. Dose response curves were obtained through serial dilutions of the top dose (generally 1 mg/ml).

150 µl of the particle suspension was added (in triplicate) to a 96-well flat bottom plate. Positive and negative controls were included: 150 µl of 0.1 % Triton-X100 and 150 µl of saline. To each well 75 µl of RBC suspension was added and mixed gently by pipetting.

After a 30 minute incubation at room temperature, shaking gently, the plates were centrifuged at 2500 rpm for 5 minutes. 75 µl was removed from each well and transferred to a clean 96 well plate. The absorbance of the plate was read at a wavelength of 550 nm, and the percentage haemolysis was calculated using the equation of a straight line (y=mx+b) as follows:

$$\%\ Haemolysis\ (x) = \frac{[optical\ density\ (y) - \ negative\ control\ optical\ density\ (b)]}{[(positive\ control\ optical\ density - negative\ control\ optical\ density)/100]\ (m)}$$

Equation 3.4

3.5.2 Cell Culture

Two cell types were used as models for investigations into the pulmonary toxicity of volcanic ash *in vitro*: macrophages (differentiated THP-1 cells), due to their contribution to particle clearance through phagocytosis, and type II epithelial cells (A549 cells), due to their

abundance and expected interaction with particles. See Chapter 2 for the pulmonary role of each cell type.

3.5.2.1 THP-1 Cell Line

The human monocytic THP-1 cell line was derived from the peripheral blood of a patient with acute monocytic leukaemia (Tsuchiya et al., 1980), and was cultured from laboratory stocks. These cells are used because they have been immortalised and can be kept in continuous culture. THP-1 cells are used as a widespread model for phagocytic cells, i.e., cells that actively take up particles.

THP-1 cells are large, round, single monocytes in culture. They were maintained in continuous suspension using RPMI 1640 medium (Roswell Park Memorial Institute medium) containing 10 % heat inactivated foetal calf serum (FCS; PAA Laboratories Ltd., UK) supplemented with 2 mM L-Glutamine. Penicillin (100 units ml^{-1}) and streptomycin (100 µg ml^{-1}) were added to inhibit bacterial contamination. The cells were maintained at 37 °C in a 5 % CO_2 environment, and used between passages 5-20 from stocks maintained under air-phase liquid nitrogen in freezing media. Cultures were maintained from 2-9 x 10^5 cells ml^{-1}.

Physiologically, the cell line behaves like monocytes and has the ability to differentiate into macrophage-like cells (phagocytic) by stimulation with phorbol esters, i.e., phorbol myristate acetate (PMA). Following stimulation with PMA, THP-1 cells express macrophage-like morphological characteristics such as increased size, granularity, decreased division, and also become adherent. Only differentiated THP-1 cells were used for experiments, and therefore all reference to THP-1 cells in the text will be in reference to differentiated THP-1 cells that behave like native monocyte-derived macrophages.

THP-1 cells were seeded at a density of 0.5 x 10^6 cells ml^{-1} in 12-well plates (RPMI containing 10 % FCS) and differentiated with 1 µl PMA per 10 ml media for 48 hours, then serum starved for 24 hours prior to particle exposure.

3.5.2.2 A549 Cell Line

The A549 cell line, a human adenocarcinomic derived alveolar basal epithelial cell, was used as an *in vitro* model of Type II pulmonary epithelial cells. The cell line was first initiated in 1972 by Giard et al. (1973) through removal and culturing of cancerous lung tissue in the explanted tumour of a 58 year old Caucasian male. These cells were further characterised by Foster et al. (1998).

In vivo, these cells are squamous (flat, scale-like) and contribute to the pulmonary barrier, being responsible for the diffusion of some substances (e.g., water and electrolytes) across the alveoli of the lungs. When cultured *in vitro*, cells grow as an adherent monolayer with Type II characteristic morphology. Cells were maintained in continuous culture in DMEM growth media (Dulbecco's Modified Eagle Medium) with 10 % FCS supplemented with 2 nM L-Gluatamine, penicillin and streptomycin as per the THP-1 media. The cells were maintained at 37 °C in a 5 % CO_2 environment, split at 70-80 % confluency, and used between passages 5-20 from stocks maintained under air-phase liquid nitrogen in freezing media. Cultures were maintained from 2-9 x 10^5 cells ml^{-1}.

To prepare A549 cells for toxicity assays, cells were trypsinized using a 0.25 % solution prior to re-suspension and seeding, and allowed to re-adhere overnight prior to particle treatment. All treatments were performed on 1 ml of cells at a density of 5 x 10^5 cells ml^{-1} in each well of a 12-well plate.

3.5.3 Cell Treatment

Cells were treated for 24 hours with four concentrations (doses) of volcanic ash and control particles: 5, 10, 25, and 50 mg ml^{-1} (see Chapter 6 for dose-response determination). Ground quartz (DQ12) was used as a positive control and titanium dioxide (TiO_2, rutile) was used as a negative control throughout toxicity experiments. Ash was suspended in the appropriate cell-line media without FCS, sonicated for 10 minutes to disaggregate the particles, and pipetted onto the cells to the final concentrations above.

DQ12 quartz (Robock, 1973) is a well-characterised standard quartz named for the region in which it was quarried: Dörentrup kaolinitic sand deposit, Germany, 'ground product No. 12.' The sample was isolated from a 60 mm sand fraction by centrifugation, producing a sample predominantly < 5 μm in diameter. It is composed of 87 % crystalline silica (α-quartz), 13 % amorphous silica and a small contamination of kaolinite, and has an average surface area from 7.5-10 m^2 g^{-1} (Clouter et al., 2001).

3.5.4 Cytotoxicity

Various assays were trialled to determine the cytotoxic effect of volcanic ash on cells propagated *in vitro*. These ranged from simple assays that measure the effect of exposure on cell membrane integrity and the effect on cell growth, to others that assess cell viability indirectly by assessing the ability of a cell to metabolise an introduced compound. After extensively trialling different assays, two were chosen to establish the cellular toxicity of ash on epithelial A549 cells and differentiated THP-1 macrophages: lactate-dehydrogenase

(LDH) release into cell media and metabolic conversion of alamarBlue reagent. The forgone assays are included below as an experimental record.

3.5.4.1 LDH Analysis

The level of cellular cytotoxicity/cytolysis was established using a lactate dehydrogenase (LDH) assay (Roche Diagnostics, Mannheim, Germany). The assay is based upon the release of the ubiquitous cytoplasmic enzyme LDH from damaged and dead cells into the surrounding culture media and its detection using the colorimetric assay described by Babson and Philips (1965). The assay is not restricted by target-cell type. The assay detects LDH via the reduction of NAD^+ (a molecule found in all cells) to $NADH/H^+$ by oxidation of lactate found in the test sample (reaction I of Figure 3.4). The addition of the catalyst diaphorase transfers two electrons from $NADH/H^+$ to the tetrazolium salt 2-p-iodophenyl-3-p-nitrophenyl-5-phenyl tetrazolium chloride (INT), reducing it to the red coloured compound formazan (reaction II of Figure 3.4). The total level of LDH activity in the supernatant directly correlates to the amount of formazan produced over time, and therefore to the level of dead and/or damaged cells. Formazan is water soluble and is read spectrophotometrically at wavelength 490 nm.

The experiment was carried out on both A549 cells and differentiated THP-1 cells. Cells were seeded in 12-well plates and treated with particles. After 24 hours exposure, the culture medium was transferred to 1.5 ml microcentrifuge tubes and spun at 12,000 x g for 10 minutes to remove any cell debris and remaining particulate. 35 µl of cell-free culture supernatant were transferred in triplicate to a 96 well plate, and diluted by adding 70 µl of PBS to each well. One hundred microlitres of the LDH test reagent (diaphorase/NAD+ mixed with iodotetrazolium chloride and sodium lactate at a ratio of 1:45) was added to each well. Following a 30 minute incubation period the absorbance of each well at 490 nm wavelength was determined using a Synergy HT microplate reader (BioTek Instruments, Inc. VT, USA). The level of LDH release was expressed as a percentage of the total LDH released (generated by total cell lysis using Triton X-100) as determined from Equation 3.5. The low control is vehicle treatment only (base line cell death), and high control is Triton X-100 treatment (total cell lysis). Data are expressed as the average of 3 experiments.

$$\%\ LDH\ Release = \frac{(Experimental\ Value - Low\ Control)}{(High\ Control - Low\ Control)} \times 100 \qquad \textit{Equation 3.5}$$

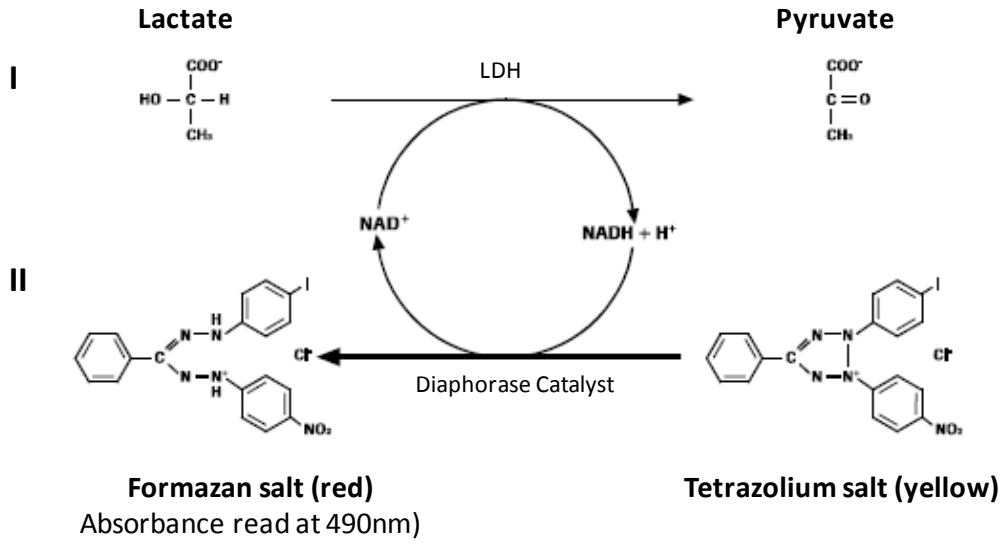

Figure 3.4: Catalysed formation of formazan salt in the detection of lactate dehydrogenase using the lactate dehydrogenase (LDH) assay. Process adapted from assay literature (Roche Applied Science, 2012, 3rd edition).

3.5.4.1 alamarBlue: Cellular metabolism

The level of cell viability following particle treatment was determined using the alamarBlue® cell proliferation assay. The assay is based on the maintenance of a reducing environment by metabolically active cells, which is measured through the reduction of resazurin (7-Hydroxy-3H-phenoxazin-3-one 10 oxide) to resorufin, a fluorescent and colorimetric indicator (Figure 3.5). Damaged and non-viable cells have lower innate metabolic activity and, therefore, generate a proportionally lower signal. The non-toxic nature of alamarBlue permits long-term exposure of cells.

The experiment was carried out on both A549 cells and differentiated THP-1 cells. Cells were seeded in 12-well plates and treated for 24 hours. Following treatment the supernatant was removed and the cells washed with PBS. Three-hundred microliters of PBS and 30 µl of alamarBlue (Invitrogen, Life Technologies, CA, USA) was added to each well. THP-1 cultures were incubated for 1 hour and A549 cultures for 30 minutes at 37 °C in 5 % CO_2. The solution was spun at 13.3 x g for 5 minutes, as the particles proved to interfere with the readings, and transferred to a 96 well plate. Resorufin was measured spectrophotometrically by absorbance at 570 nm using a Synergy HT microplate reader (BioTek Instruments, Inc. VT, USA). Cell viability was expressed as a percentage of base line cell viability (no particle

treatment) using Equation 3.6, with Triton X-100 used as complete cell death (low control). Data are expressed as the average of three runs.

$$\%\ Cell\ Viability = \frac{Experimental\ value - Low\ control}{Untreated - Low\ control} \times 100 \qquad \textit{Equation 3.6}$$

The limitation of the assay is that it needs to be performed under aseptic conditions because proliferating bacterial and fungal cells are able to reduce alamarBlue and may affect the results.

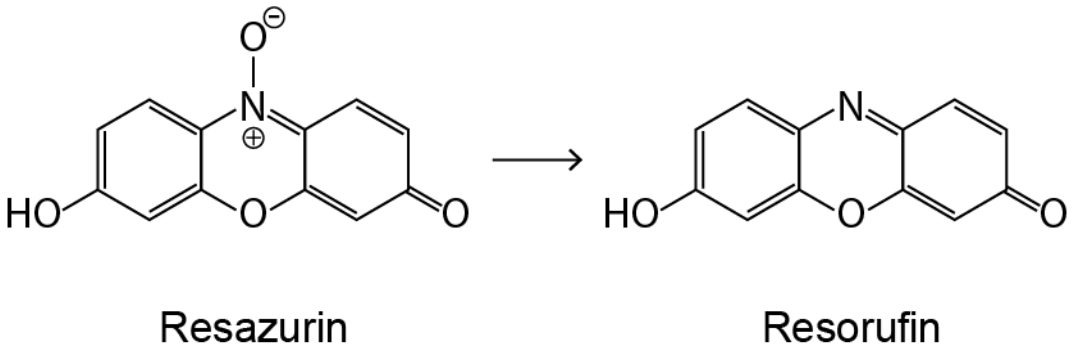

Figure 3.5: Reduction of resazurin sodium salt to the strongly fluorescent (blue) resorufin in the alamarBlue assay.

3.5.4.2 WST-1: Cell Proliferation

Determination of cellular viability by colorimetric assays is a widely used technique for testing cytoxicity, since cytotoxic agents inhibit metabolic activity and, therefore, the enzymatic reduction of coloured compounds. The colorimetric MTT (a tetrazolium dye) assay has been previously used for volcanic ash (e.g., Wilson et al., 2000), however, a water soluble tetrazolium salt (WST) was employed here. WST-1 is a cell proliferation agent which offers advantages over MTT, including a water-soluble cleavage product, greater stability, and a wider linear range for colour development and, therefore, effective signal. WST-1 is cleaved to formazan (a soluble coloured compound) by a bioreduction that occurs primarily at the surface (showing decreased toxicity to the cell-permeable MTT) and is dependent on the glycolytic NAD(P)H production of viable cells. The amount of formazan

dye formed therefore directly correlates to the number of metabolically active cells in the culture.

Although decreased viability was seen at 24 hours (n=4), DQ12 quartz was not as responsive as expected (Figure 3.6). Since crystalline silica is a primary concern in volcanic ash, the WST-1 assay was abandoned in favour of other cytotoxicity assays. Even still, MRA5/6/99 was the least reactive of all test particles.

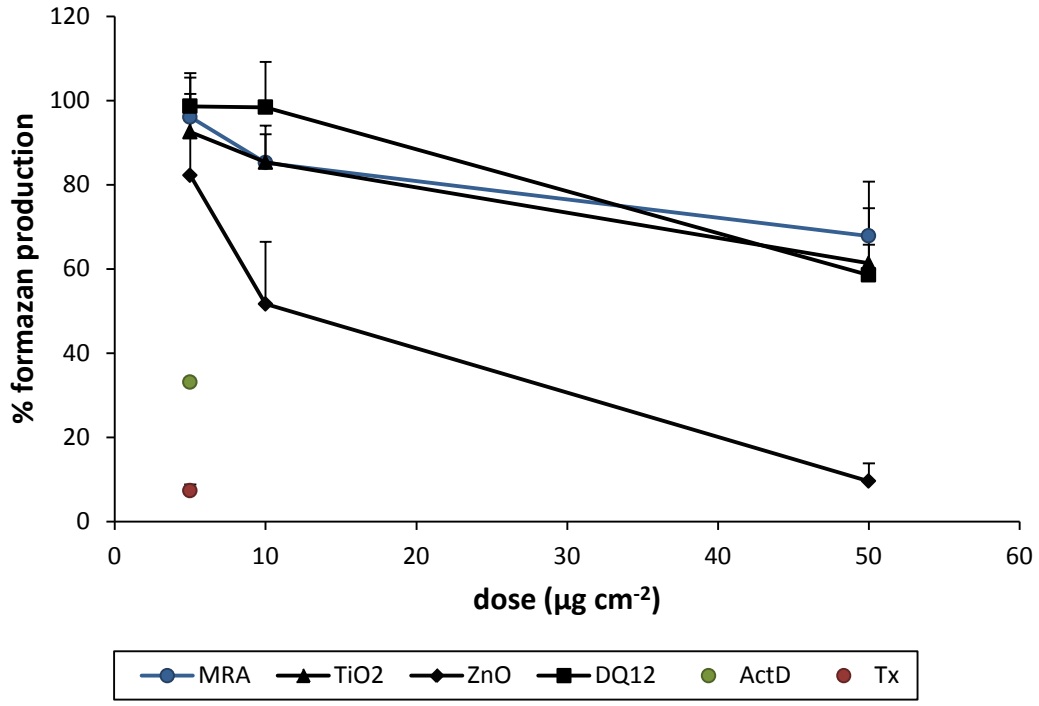

Figure 3.6: Wst-1 cell viability data for Soufrière Hills ash sample MRA5/6/99 plus positive (Quartz, DQ12; Zinc oxide, ZnO; Triton X, Tx; Actinomycin D, ActD) and negative (titanium dioxide, TiO_2) controls.

3.5.4.3 Calcein AM: Cell Viability

Calcein AM is a cell-permanent dye that can be used to determine cell viability. The non-fluorescent, hydrophobic acetomethoxy derivative of calcein (Calcein AM) can be easily transported through the cellular membrane of live, intact cells. Once inside, Calcein AM is converted to the hydrophobic, strongly green-fluorescent calcein after hydrolysis by intracellular esterases, which is well-retained in the cell cytoplasm. As dead cells lack active esterases, only live cells are stained, and the fluorescence (intensity read using a 490 nm excitation filter and a 520 nm emission filter) is proportional to the number of viable cells.

The assay proved to be inconsistent in repeat experiments when determining viability for ash-treated cells, and was also abandoned as a measure of cytotoxicity. Although the reason is not clear, it could be related to the leaching of metals from the ash. The calcein molecule chelates Ca^{2+}, Mg^{2+}, Zn^{2+}, and the fluorescence of calcein is quenched at physiological pH by Co^{2+}, Ni^{2+}, Cu^{2+} as well as Fe^{3+} and Mn^{2+} to a lesser extent.

3.5.4.4 Trypan blue exclusion: Cell Viability

The Trypan blue exclusion assay is a measure of a cell's ability to prevent the uptake of a dye, and is based on the principle that live cells possess intact membranes that exclude certain dyes whereas dead cells do not (Strober, 2001). A cell suspension is mixed with Trypan blue dye (which is not able to cross cell membranes) and visually examined on a glass slide to determine whether cells take up or exclude the dye: a viable cell will have a clear cytoplasm whereas a nonviable cell will have a blue cytoplasm. This task of counting individual cells can be automated by use of an automated cell counter; however, a proportion of ash particles were of the same size as cells being counted, distorting the results. Due to the inability of an automated counter to distinguish between particles and cells, this technique was manually time intensive and was abandoned in favour of other techniques.

3.5.5 Cytokine Production: Detection of immune response

Cytokines are a unique group of signalling molecules secreted by numerous cells that mediate immune function. They enable communication between cells via receptors expressed at the cell surface, and can act on the cells that secrete them, on nearby cells or on distant cells. Cytokines are not stored within cells, but are produced in response to a stimulus, such as encountering a particle. Once produced, cytokines interact with target cells and trigger a cascade of signals, ultimately altering a cell's behaviour and generating an immune response.

Table 3.3: Summary of cytokines measured. Cell types in italics are additional prominent cells which secrete the cytokines listed; however, they are neither used or discussed in the present study are included only for reference.

Cytokine/ Chemokine	Cell Source	Cell Target	Primary Effects
IL-1β	Macrophages, epithelial cells *monocytes, fibroblasts, astrocytes*)	T cells, B cells, endothelial cells, hypothalamus, liver	Co-stimulatory molecule; induction of chemotaxis; promotes activation (inflammation) and secretion of cytokines and other acute-phase proteins; pyrogenic
IL-6	Macrophages *T cells, fibroblasts*	T cells, B cells (liver)	Inflammatory and costimulatory action; induces proliferation and differentiation, acute phase reactants
IL-8	Macrophages, epithelial cells *platelets*	Neutrophils	Activation and chemotaxis

Two categories of cytokines were measured: interleukins and chemokines. Interleukins promote the differentiation and division of immune cells, and are particularly important in stimulating the immune response (e.g., inflammation). Chemokines are able to induce directed chemotaxis in nearby responsive cells, recruiting cells of the immune system to an area of insult. Cells that are attracted by chemokines migrate along a concentration gradient towards the source.

An overview of the cytokines analysed following exposure is provided in Table 3.3, and include:

> *IL-1β*: Interleukin-1β is a pleiotropic (affecting the activity of multiple cell types), pro-inflammatory cytokine expressed by many cells, including macrophages. Production of IL-1β occurs only in response to cellular stimulation, resulting in mediation of the innate immune response, including inflammation, cell proliferation,

differentiation, and apoptosis. In addition to its primary influence on T cells, IL-1β can induce proliferation in non-lymphoid cells.

IL-8 (CXCL8): Interleukin-8 is a chemokine produced by macrophages and other cell types including epithelial cells, and is an important mediator of the innate immune system response. Its primary function is as potent recruiter of neutrophils to the site of inflammation (chemotaxis). While neutrophils are the primary target cells, there is a relatively wide range of cells which respond to IL-8, suggesting IL-8 has crucial roles in various pathological conditions such as chronic inflammation and cancer. It is also known to possess tumorigenic and pro-angiogenic properties.

IL-6: Interleukin-6 is produced by macrophages, amongst other cells, and is one of the most important mediators of the acute phase immune response. It acts synergistically with IL-1β in many immune responses. Unlike IL-1β, IL-6 does not induce cytokine expression; its main effects, therefore, are to augment the responses of immune cells to other cytokines. It has an essential role in directing the transition from innate to acquired immunity. It is involved in haematopoiesis (i.e., the development of different blood cells from stem cells) and cancer progression.

Enzyme-linked immunosorbent assays (ELISAs) are used for the detection and quantification of cytokines in the supernatant by stepwise immobilization and conjugation of the molecule of interest (Figure 3.7). A detection reagent and enzymatic substrate are then used to produce a quantifiable signal. Cytokine production was measured using a cytokine specific ELISA DuoSet kit (R&D systems, Abingdon, UK) following the manufacturer's protocol. Ninety-six well flat-bottom microtitre plates (Corning, USA) were incubated overnight at RT with 100 µl of capture antibody raised against human cytokines. The plates were washed 3 times with 0.05 % Tween-20 in phosphate buffered saline (PBS; pH 7.2) and any non-specific binding sites were blocked using reagent diluent (1 % BSA in PBS; R&D systems, Abingdon, UK) for 1 hour at room temperature. Wells were washed following blocking and 100 µl of supernatant samples and standards were added in triplicate. Plates were incubated for 2 hours at room temperature, washed, and 100 µl of biotinylated detection antibodies added to each well followed by a further 2 hour incubation. Plates were washed following incubation and 100 µl of streptavidin conjugated to horseradish peroxidase (HRP) was added to each well for 20 minutes. The streptavidin-HRP bound any present biotin remaining in the well, which was associated to the secondary antibody and was bound to any detected cytokine present. After washing, the addition of 100 µl 3,3',5,5'-tetramethylbenzidine (TMB) substrate solution (Sigma-Aldrich, Poole, UK) leads to a catalytic reaction with any remaining HRP forming an intense blue colour. This development

reaction was stopped with 50 µl 2N H_2SO_4 (0.5 M), resulting in a yellow colour, and read at 450 nm. Sample cytokine concentrations were determined via extrapolation of a recombinant cytokine protein standard curve.

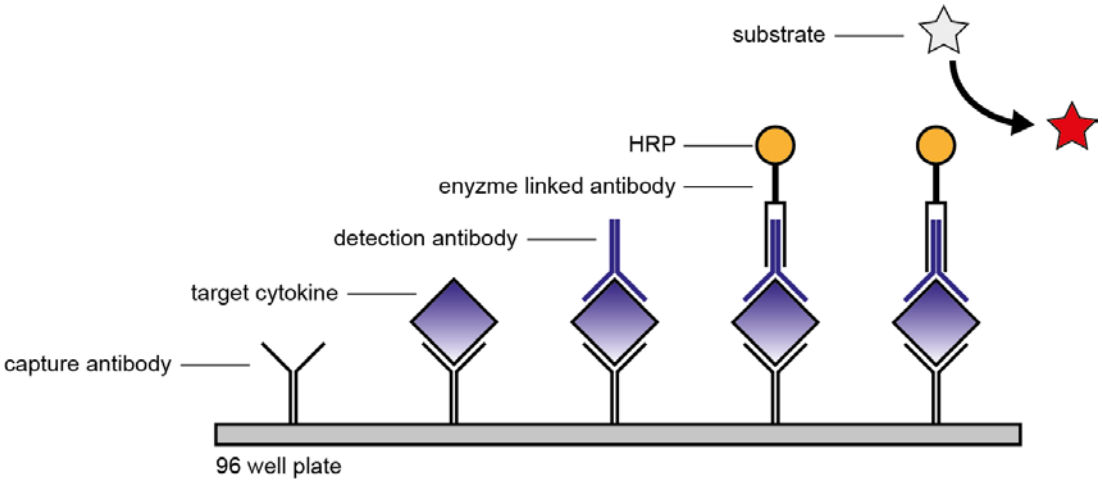

Figure 3.7: General schematic of an ELISA. A plate is coated with a cytokine-specific capture antibody. The sample is added to the plate and any target cytokine present will bind to the capture antibody. A suitable detection antibody is added to the plate and binds the target cytokine ('sandwich'). An enzyme (HRP) linked antibody is added which is specific to the detection antibody. A substrate is added to convert the enzyme (HRP) to a detectable signal.

3.5.6 Flow Cytometry: Intracellular staining

Flow cytometry is a technique for counting and individually examining microscopic particles (e.g., cells) as they flow in a fluid stream. It allows simultaneous, multi-parametric analysis of physical (size, granularity) and chemical characteristics, as well as emitted fluorescence, for thousands of cells per second. These characteristics are recorded as cells in a mono-disperse suspension are run single-file through a laser beam, which is quantifiably scattered. Incubating cells with exogenous fluorescent probes (fluorophores) enables the quantification of specific cellular structures indicative of cellular behaviour. Three fluorophores were used (see Table 3.4) and are further described below.

Table 3.4: Summary of the fluorophores (Annexin V, PI, MCB) used for flow cytometry.

Fluorophore	Laser	Measure
FITC-Annexin V	Green	Apoptosis
PI	Red	Necrosis
MCB	UV	Oxidative stress

FITC-Annexin V staining is used to quantitatively determine the percentage of cells within a population actively undergoing apoptosis. In apoptotic cells, the membrane phospholipid phosphatidylserine (PS) is translocated from the inner to the outer leaflet of the plasma membrane, exposing PS to the external cellular environment. Annexin V is a calcium-dependent protein with a high binding affinity for PS; therefore, when conjugated to a fluorochrome (e.g., FITC), it binds to exposed PS and serves as a cytometric probe for cells undergoing apoptosis. FITC-Annexin V staining precedes the loss of membrane integrity which accompanies the latest stages of cell death, and is typically used alongside a vital die (e.g., PI) to allow identification of early apoptotic cells.

Propidium iodide (PI) is a standard flow cytometric viability probe used to distinguish viable from non-viable cells. Viable cells with intact membranes exclude PI, whereas the membranes of dead and damaged cells are permeable to PI.

The following three staining combinations of FITC-Annexin V and PI can occur:

1. Cells that stain both FITC-Annexin V and PI negative are viable.
2. Cells that stain FITC-Annexin V positive and PI negative are undergoing apoptosis.
3. Cells that stain both FITC-Annexin V and PI positive are either in the late stages of apoptosis or are already necrotic (dead).

Glutathione (GSH) is the principal intracellular low-molecular-weight thiol (an organic compound with a sulfhydryl functional group) and plays a critical role in cellular defence against agents that impose oxidative stress. Monochlorobimane (MCB) added to cultures readily enters cells and forms a fluorescent GSH-MCB adduct that can be measured fluorometrically.

Supernatants from post-exposure THP-1 and A549 cell cultures were collected and spun at 1500 rpm for 3 minutes to recover un-adhered cells (cell-free supernatants were retained for other assays). Adhered cellular monolayers were washed with PBS (without Ca and Mg) x2

and washes were added to previously recovered cells. Cell monolayers were trypsinized (5 minutes, 37 °C, 5 % CO2), the trypsin neutralised with culture media, and recovered cells were added to previously collected cells. Cells collected cumulatively from the previous 3 recovery steps were washed x3 at 1500 rpm for 3 minutes, and re-suspended in Annexin buffer (Hank's Balanced Salt Solution (HBSS) with 2.5 mM $CaCl_2$, filter sterilised). Cells were stained with 5 µl FITC-Annexin V and 1 µl MCB per 195 µl cell suspension and incubated on ice for 10 minutes. Cells were spun at 1500 rpm for 3 min and re-suspended in 200 µl Annexin buffer. Propidium iodide (1 µl) was added immediately before flow analysis.

Unstained cells were run to determine the inherent fluorescence of both cell types. Unstained cells treated with ash were also run to determine any differences in size or granularity resulting from phagocytosis of particles. Untreated stained (i.e., negative vehicle control) cells were always run, as were a necrotic control (10 mM H_2O_2), an apoptotic control (amine beads at 50 µg ml^{-1}), and a GSH control (N-ethylmaleimide). Methods for utilizing Annexin V for flow cytometry on adherent cell types have been previously reported (van Engeland et al., 1996).

3.5.7 Cytostain: Cellular Imaging

Cells were imaged following exposure to volcanic ash to determine whether particles were being taken up by the cells. Macrophages are considered 'professional' phagocytes and readily ingest encountered material, whereas uptake by epithelial cells is mostly passive.

Cytospin preparations were made by placing ~ 40-60,000 cells into a cytology funnel with 300 µl of 0.1 % BSA/sterile saline solution. The funnel was clipped to a glass slide with a Shandon filter card (Thermo Scientific, UK) and centrifuged at 300 rpm for 3 minutes at room temperature using a Cytospin 4 cytocentrifuge (Thermo Scientific, UK). The slides were allowed to air dry then fixed in 100 % methanol and stained with eosin (Quick-Diff, Dade Behring, Inc.) followed by haematoxylin (REASTAIN Quick-Diff Blue). Slides were allowed to dry then submerged in xylene for 30-60 seconds. A drop of DPX mounting media (Sigma-Aldrich, Poole, UK) was added directly to the cell population and covered with a glass cover slip.

3.6 Biopersistence: In vitro assessment of durability

Biopersistence (the ability of a particle to resist dissolution *in vivo*) is a key parameter in particle toxicity, controlling the duration for which a particle remains in the respiratory tract due to mineral dissolution (see Section 2.4.2). *In vitro* biopersistence was determined by

digesting ash in two fluids likely encountered by a particle in the deep lung (Table 3.5): a synthetic lung fluid (SLF), which is a balanced electrolyte solution (Gamble's solution; Wolf et al., 2011) resembling the biological environment that a particle will rest in following lung deposition, and an artificial lysosomal fluid (ALF; Stebounova et al., 2010), which mimics the more acidic environment a particle will encounter inside of a phagolysosome following phagocytosis and is the most potentially degradative pH a particle should encounter following macrophage uptake.

Table 3.5: Chemical compositions of artificial preparations of biological fluids: Gamble's (SLF) and ALF solutions. Formaldehyde (37 % in formalin) was added to prevent microbial growth, and the pH adjusted by addition of HCl.

Artificial biological fluid	pH	Composition (per litre DI water)
Gamble's (synthetic lung fluid)	7.4	6.780 g NaCl, 1.770 g $NaHCO_3$, 0.029 g $CaCl_2$•$2H_2O$, 0.166 g Na_2HPO_4, 0.059 g Na_3-citrate•$2H_2O$, 0.535 g NH_4Cl, 0.630 g Na_2CO_3, 0.260 ml H_2SO_4, 0.450 glycine.
ALF (artificial lysosomal fluid)	5.5	3.210 g NaCl, 6.000 g NaOH, 20.800 g citric acid, 0.097 g $CaCl_2$, 0.179 g NaH_2PO_4•$7H_2O$, 0.039 g $NaSO_4$, 0.106 g $MgCl_2$•$6H_2O$, 0.059 g glycerin, 0.077 g sodium citrate dehydrate, 0.090 g sodium tartrate dehydrate, 0.085 g sodium lactate, 0.086 g sodium pyruvate, 1.000 mL formaldehyde.

Conventionally, biodurability is determined as a loss in mass following digestion or as a function of surface area against time. These metrics are appropriate for single phases investigated in toxicity studies; however, since volcanic ash is a heterogeneous mixture and as different components have different solubilities, biodurability was also assessed here by XRD. This allowed for the comparison of mineralogy prior to and following digestion. This method has the added benefit of quantifying crystalline silica enrichment or depletion as a proportion of the bulk. Secondary mineral determination by XRD of aqueous experiments is preferred to reaction path modelling based on saturation because it provides information regarding crystallinity (as well as polymorph and crystal size), which specifically informs the

physical and/or geochemical interactions with cells, and therefore the effect on disease processes. Surface area was not determined as there was no way to correlate it with individual mineral phases.

Bulk ash samples were used for the experiment as there was not a sufficient quantity of the respirable fraction to carry out repeat experiments; the samples chosen correspond with the subset of samples used for toxicology. No intermediate time points were investigated; therefore, results are presented as a total change rather than kinetically.

Two replicates of ash samples (approximately 0.375 g) were placed in 50 ml polypropylene Falcon tubes (BD Biosciences, CA, USA) with a liquid:solid ratio of 1:150 in either SLF or ALF (Table 3.5). Polypropylene tubes were cleaned overnight with 2N HCl shaking at 37 °C, then rinsed x5 with dd-H_2O. Sample-solution mixtures were sonicated (Fisherbrand ultrasonicating water bath, ultrasonic frequency: 40 kHz) for 20 minutes. All samples were then incubated and gently agitated at 37 °C for 3 weeks. Solutions were spun at 2500 x g for 20 minutes following the incubation period to remove all particles from solution. The supernatant was transferred to a cleaned (2 N HCl o/n, rinsed x5 dd-H_2O) 50 ml polypropylene tube and the ash was oven-dried for 24 hours at 37 °C. Dried samples were weighed to 0.001 mg, and per cent recoveries relative to recovery at 0 weeks were calculated.

XRD was carried out on the digested sample as previously outlined (Section 3.3), and phases present quantified. Following quantification, XRD traces for the digested samples were overlain with the traces for the bulk samples to identify any changes in peak patterns that may have arisen (i.e., dissolution and precipitation of new phase), and to qualitatively identify any changes in peak intensities that may be overshadowed by the accepted error in mineral quantification. These qualitative results were used to inform relative differences between samples.

3.7 Statistical Analysis

Statistical analysis was performed using GraphPad PRISM software (San Diego, CA). An unpaired Student's t-test or Welch's t-test were used for two sample comparisons. Multiple comparisons were analysed using one-way analysis of variance (ANOVA) with either Dunnett's post-test (for comparison to a single control) or Tukey's post-test (for multiple comparison of sample means) where appropriate. In all cases, tests were considered significant when $p<0.05$.

4

Volcanic cristobalite formation: A global study for the assessment of health hazard

Abstract

A petrographic investigation was carried out on 45 dome rock samples collected from 6 different volcanoes worldwide (Colima, Merapi, Mount St. Helens, Santiaguito, Soufrière Hills and Unzen) to constrain the nature and mode of formation of cristobalite in lava domes. SEM imaging combined with compositional (EDS, WDS, CL) and structural (CL, Raman spectroscopy) analyses provides insight into the origin and abundance of cristobalite in dome rock. Cristobalite can crystallise and persist metastably in all volcanic domes at temperatures below its thermodynamic stability field (>1470 °C). Comparison of cristobalite characteristics reveals evidence of crystallisation by both vapour-phase deposition and devitrification; however, dome rock samples display substantial heterogeneity in groundmass texture and degree of crystallisation. These differences result from 'sample maturation', where samples become progressively enriched in cristobalite through residence in the dome environment. Vapour phase crystals exist as two general morphologies, prismatic and platy forms, but display variable crystal habits due to dynamic conditions of formation within volcanic domes. Devitrification of glass in the dome rocks results in a mixture of mineral phases, including cristobalite, producing two distinct groundmass textures: 'feathery' and 'myrmekite-like'. No volcano-specific differences in cristobalite abundance were observed by semi-quantitative X-ray diffraction (XRD) or in cristobalite morphology observed in SEM. However, samples above approximately 60 wt. % whole-rock SiO_2 are able to crystallise substantially more cristobalite than samples below. Mechanisms of cristobalite nucleation and the causes of variations in crystal size and morphology are discussed and compared for the different volcanic centres, as well as the implications of this for the potential health hazard posed by ash derived from dome forming volcanoes. Heterogeneous cristobalite crystallisation increases uncertainty when attempting to define the eruptive and respiratory hazard before catastrophic dome failure.

Acknowledgements

Cathodoluminescence imaging was carried out by Leon Bowen of the G.J. Russell Microscopy Facility, Department of Physics, Durham University with the author present. X-ray fluorescence analyses on samples of dome rock were carried out by Nick Marsh at the University of Leicester. SEM-Raman microscopy was carried out at Renishaw plc (UK) with the assistance of Dr. Tim Batten.

Thanks to Ben Williamson (University of Exeter) for constructive feedback on a draft version of this chapter.

4.1 Introduction

Cristobalite is commonly found in volcanic dome rock, having been previously identified in samples from Colima, Mexico (Lavallee et al., 2012), Merapi, Indonesia (Damby et al., 2012; Appendix 4), Mount St. Helens, USA (Blundy and Cashman, 2001; Pallister et al., 2008), Santiaguito, Guatemala (Scott et al., 2012), Soufrière Hills, Montserrat (Horwell et al., post review; Appendix 4; Williamson et al., 2010), and Unzen, Japan (Nakada and Motomura, 1999). It is thought to crystallise in volcanic domes through two mechanisms; devitrification of groundmass glass and deposition from a silica-saturated vapour. These mechanisms were identified by Baxter et al. (1999), and have been recently characterised *in situ* at Soufrière Hills by Horwell et al. (post review; Appendix 4). The aim of the current study is twofold: 1) to compare the nature and mode of formation of cristobalite amongst the aforementioned volcanoes, contextualising the results of Horwell et al. (post review; Appendix 4) from Soufrière Hills for dome-forming volcanoes world-wide; and 2) to provide evidence for crystallisation by these two mechanisms, which, to date, has not been constrained.

Cristobalite is stable above 1470 °C (< 0.1 MPa; see Figure 2.1) and, therefore, crystallises and persists as a metastable phase in volcanic dome rock (<850 °C; Murphy et al., 2000). Cristobalite is usually the first of the crystalline silica phases to crystallise because it is the least thermodynamically stable polymorph (according to Ostwald's rule of stages, Nývlt, 1995) and has the lowest enthalpy of fusion of silica (Richet et al., 1982). Upon cooling through approximately 250 °C, cristobalite undergoes a phase transformation from the high temperature β- to the low temperature α-form (see Chapter 5 for further information on the transition). There is an approximately 5 % volume change (shrinkage) associated with this β-α transformation, causing the crystal to crack and consequently exhibit a characteristic 'fish-scale' texture (Carpenter et al., 1998).

Silica minerals found in vesicles of volcanic rocks are commonly interpreted as post-magmatic secondary phases since cristobalite can crystallise via gaseous transport and deposition from silica-saturated solutions (e.g., de Hoog et al., 2005). Vapours evolved from magmas and heated groundwater are generally acidic and have the ability to scavenge additional elements when percolating through a volcanic system, including Si, Al, and Na, amongst others (Shmulovich and Churakov, 1998; Symonds and Reed, 1993). Cooling of these fertile phases may result in the crystallisation of a variety of minerals (e.g., feldspar and cristobalite). As a result, cristobalite in pore spaces of volcanic rocks is frequently observed (Deer et al., 1996), and has been documented in dome rock (e.g., Williamson et al., 2010), ignimbrite deposits (e.g., Yurtmen and Rowbotham, 1999) and welded tuff (Bish and

Aronson, 1993). It is unknown, however, if cristobalite is ever a primary phase or whether it is entirely pneumatolytic, formed under the influence of vapours.

Transport of Si in the vapour phase and deposition as cristobalite has been investigated at temperatures and pressures relevant for the dome environment, and are reviewed by Horwell et al. (post review; Appendix 4). Briefly, thermodynamic modelling by Churakov et al. (2000) indicates that above 950 °C Si is transported as $SiO_{(g)}$ and $SiO_{2(g)}$. Between 900 and 950 °C, $SiOF_2$, SiF_4, SiO and SiO_2 all contribute to Si transport, and below 900 °C (temperatures appropriate for volcanic domes, e.g. Barclay et al., 1998; Murphy et al., 2000; Rutherford and Hill, 1993) SiF_4 prevails as the dominant Si-carrying species. Thermodynamic modelling by de Hoog et al. (2005) supports transport of Si in domes and fumarolic systems by $SiF_{4(g)}$ by the reaction:

$$SiO_{2(s)} + 4HF_{(g)} \leftrightarrow SiF_{4(g)} + 2H_2O_{(g)} \qquad \textit{Equation 4.1}$$

This reaction is strongly dependent on temperature, pressure, and HF fugacity (de Hoog et al., 2005), and therefore describes a mechanism for both deposition and corrosion of an SiO_2 source by HF. Geochemical modelling supports Si transport as $SiO_{(g)}$ at temperatures above 700 °C and 0.1 MPa (Korzhinsky et al., 1995). At temperatures below 750 °C (0.1 MPa), the main species for gaseous transport of Si is likely $SiCl_4$ (Shmulovich et al., 2006). Foustoukos and Seyfried (2007) add that Cl-bearing vapours contain significant concentrations (2.81 to 14.6 mmol kg^{-1}) of dissolved SiO_2 at temperatures between 365-430 °C (21.9-38.1 MPa). These studies suggest that Cl may be a dominant carrier of Si at lower temperatures and F at higher temperatures (as well as $SiO_{(g)}$ and $SiO_{2(g)}$). An HF/HCl gas ratio of 0.004 was reported at Soufrière Hills (Allen et al., 2000) and 0.005 at Mount St. Helens (calculated from data in Edmonds et al., 2008), suggesting Cl-bearing fluids could be responsible for the majority of Si transport in volcanic systems. Indeed, the solubility of fluorine in silicic melts is generally much higher than that of Cl and, therefore, it does not degas to the same extent (Carroll and Webster, 1994).

Devitrification is a post-magmatic process which refers to the crystallisation of volcanic glass, and results in the sub-solidus crystallisation of microlitres within a glassy mass. At Soufrière Hills volcano, groundmass silica phases occur in dome lavas but not pumice, indicating that crystalline silica can be produced by devitrification within the lava dome (Baxter et al., 1999). The factors controlling devitrification have not been outlined for volcanic dome rock; however, devitrification in ash-flow tuffs is dependent on the chemical

composition of the glass and crystallising mineral phases, cooling rate and temperature (Vaniman, 2006).

The confirmation of cristobalite in volcanic dome rock has often been marginalised, with it being assigned a general SiO_2 (quartz) status in the literature (e.g., Blundy and Cashman, 2001; Couch et al., 2003; and see Horwell et al., post review; Appendix 4). As a secondary mineral in volcanic settings, however, its presence has implications for dome permeability and bulk chemistry (Horwell et al., post review; Appendix 4). As we propose here, proper identification of crystalline silica as cristobalite can also provide valuable information on the history of a sample and, therefore, insight into the temporal and thermodynamic evolution of volcanic domes.

Horwell et al. (post review; Appendix 4) have identified five crystal habits for crystalline silica in volcanic dome rock at Soufriere Hills: quartz phenocrysts; prismatic vapour phase cristobalite; platy vapour phase cristobalite; devitrification cristobalite; and devitrification quartz. They propose that the silica-saturated vapours required for cristobalite deposition can result from local redistribution of silica within vesicles or through bulk transport of silica from other parts of the magmatic system. In both cases, silica transport is mediated by volcanic gases (e.g., SiF_4). Both mechanisms of silica redistribution likely occur within the dome, along with devitrification, resulting in cristobalite-bearing ash from eruptions involving dome material.

Exposure to cristobalite-bearing ash raises concerns about its chronic adverse effects on health. This chapter takes a multi-angle approach to identify and constrain the presence of cristobalite in dome rock from a suite of volcanic locations in order to define the origin and extent of the hazard. In doing so, a foundation is set to discuss the source of respirable volcanic silica as well as the predicted health hazard posed to exposed populations.

4.2 Materials and Methods

This chapter uses an assortment of compositional and structural scanning electron microscopy (SEM)-based techniques to characterise cristobalite in a suite of volcanic dome rock samples. These include: secondary electron (SE) imaging on rough chips of dome rock to constrain the *in situ* crystal habit of cristobalite observed in thin section; for polished thin sections of dome rock, backscattered electron (BSE) and cathodoluminescence (CL) imaging to constrain the presence and habit of cristobalite; energy dispersive X-ray elemental analysis (EDS) to qualitatively confirm the composition of silicas; wavelength dispersive X-ray spectroscopy (WDS) combined with (EDS) to produce quantitative chemical maps of cristobalite-rich areas in thin sections; and Raman spectroscopy combined with SEM to confirm micron-sized patches as cristobalite.

Other techniques employed are X-ray fluorescence (XRF) to determine the chemical composition of whole-rock samples, specifically the concentration of bulk SiO_2, and X-ray diffraction (XRD) to quantify the abundance of the crystalline silica polymorphs in bulk samples of dome rock.

A suite of dome rock samples from Colima, Merapi, Mount St. Helens, Santiagtuito, Soufrière Hills, and Unzen is used. From Colima, analyses were conducted on 3 dome rock samples from the current dome. From Mount St. Helens, 26 samples were analysed in total: 10 samples from the 2004-2008 domes, 8 from the 1980-1986 exogenous domes, and 6 from the 1980 cryptodome, a 1980 edifice sample, and a dyke sample, emplaced in the Toutle river valley during activity in 1980. From Santiaguito, 7 samples were analysed: 4 from the ‘Brujo’ dome, 2 from the ‘Mitad’ dome, 1 from the ‘Monje’ dome. From Merapi, 9 samples were analysed: 7 from the recent 2010 eruption, 1 from 1998, and 1 from 1996. From Unzen, 2 samples were analysed from activity during 1990 to 1995. A summary of the samples studied is provided in Table 4.1, and sample locations are discussed in detail in Chapter 2: Background. Sample collection, preparation and analytical techniques are discussed in detail in Chapter 3: Methods.

Table 4.1: Summary of eruption and collection information for the dome rock samples used in the present study.

Volcano	Sample	Origin	Date erupted	Date collected	Collected by
Colima, Mexico					
	COL.124	unknown	unknown	01-Nov-07	Nick Varley
	COL.165	unknown	unknown	09-Aug-09	Nick Varley
	COL.03.10	unknown	unknown	21-Mar-10	Nick Varley
Mount St. Helens, USA					
	MSH.304.2A1	Spine 3	18-Oct-04	04-Nov-04	CVO Archive
	MSH.304.2A9	Spine 3	18-Oct-04	04-Nov-04	CVO Archive
	MSH.304.2G	Spine 3	18-Oct-04	04-Nov-04	CVO Archive
	MSH.305.1A	Spine 3	20-Nov-04	03-Jan-05	CVO Archive
Dome rock	MSH.309.1A	Spine 4	13-Jan-05	22-Feb-05	CVO Archive
04-06	MSH.315.4	Spine 4	01-Apr-05	19-Apr-05	CVO Archive
	MSH.315.5	Spine 4	01-Apr-05	19-Apr-05	CVO Archive
	MSH.316.1	Spine 5	15-Apr-05	24-May-05	CVO Archive
	MSH.321	Spine 6	10-Aug-05	19-Aug-05	CVO Archive
	MSH.326.2	Spine 7	10-Jan-06	15-Feb-06	CVO Archive
	MSH.33	S Side of dome	18-Oct-80	22-Oct-80	CVO Archive
	MSH.67	W Side of dome	5/6-Feb-81	06-Feb-81	CVO Archive
	MSH.103	Federal building	Jun-81	09-Jun-81	CVO Archive
Dome rock	MSH.127	Talus	15-May-82	01-May-82	CVO Archive
80-86	MSH.131	W Side of talus	18-Aug-82	01-Aug-82	CVO Archive
	MSH.135	Talus from spine	Feb/Mar-83	05-Jun-05	CVO Archive
	MSH.156	Talus	17-Jun-84	17-Jun-84	CVO Archive
	MSH.201	N side of spine	May-85	07-Jun-05	CVO Archive
	MSH.166	cryptodome	18-May-80	01-Jul-83	CVO Archive
	MSH.192	cryptodome	18-May-80	01-Aug-85	CVO Archive
Cryptodome	MSH.BD.1	cryptodome	18-May-80	24-Jun-09	Damby/Horwell
(1980)	MSH.BD.2	cryptodome	18-May-80	24-Jun-09	Damby/Horwell
	MSH.BD.3	cryptodome	18-May-80	24-Jun-09	Damby/Horwell
	MSH.BD.4	cryptodome	18-May-80	24-Jun-09	Damby/Horwell
Edifice	MSH.ED.1	pre-1980 edifice	18-May-80	24-Jun-09	Damby/Horwell
Dyke	MSH.DY.1	Toutle River valley	1980	24-Jun-09	Damby/Horwell
Merapi, Indonesia					
1996	MRP.96.03	block and ash flow	1996	unknown	Bettina Scheu
1998	MRP.98.02	block and ash flow	1998	unknown	Bettina Scheu
	MER.10.01	PDC deposit	Oct/Nov-10	Dec-10	Damby
	MER.10.04	PDC deposit	Oct/Nov-10	Dec-10	Damby
2010	MER.10.06	PDC deposit	Oct/Nov-10	Dec-10	Damby
	MER.10.08	PDC deposit	Oct/Nov-10	Dec-10	Damby
	MER.10.09	PDC deposit	Oct/Nov-10	Dec-10	Damby
	MER.10.10	PDC deposit	Oct/Nov-10	Dec-10	Damby

MER.10.13	PDC deposit	Oct/Nov-10	Dec-10	Damby
Santiaguito, Guatemala				
SG.BR.F3	Brujo	1959-1963	20-Feb-10	Damby
SG.BR.SL7	Brujo shear lobe	1959-1963	20-Feb-10	Damby
SG.BR.P1	Brujo pancake	1959-1963	20-Feb-10	Eliza Calder
SG.BR.S1	Brujo spine	1959-1963	21-Feb-10	Damby
SG.MTD.1	Mitad spine	1939-1942	22-Feb-10	Damby
SG.MTD.2	Mitad spine	1939-1942	22-Feb-10	Damby
SG.MNJ.1	Monje spine	1949-1955	22-Feb-10	Damby
Unzen, Japan				
UNZ.92.01	PDC deposit	1990-1995	13-Aug-92	Setsaya Nakada
UNZ.Y1	unknown	1990-1995	1993	Yasuhiro Ishimine

4.3 Results

4.3.1 Nature of crystalline silica in dome rock

A combined compositional and structural approach was employed to classify three district crystalline silica habits in samples of dome rock. Both composition and structure were required as all polymorphs of crystalline silica are chemically indistinguishable and lattice configurations of the polymorphs are not unique to the SiO_2 system. The habits identified align with those observed by Horwell et al. (post review, Appendix 4) at Soufrière Hills; however, the categories have been amended here to account for various degrees of crystallinity not observed in Soufrière Hills dome rock. The occurrence of different morphologies identified in polished thin section and in rock chips is summarised in Table 4.2; the habits are defined as:

(1) Primary quartz phenocrysts. These are encountered in samples from all locations only occasionally; however, as all of the domes sampled are basaltic-andesite or more felsic (see Chapter 2: Background), magmatic quartz is expected (or as calc-silicate xenoliths at Merapi (Chadwick et al., 2007)) and is therefore not further discussed.

(2) Vapour-phase cristobalite. Crystals were interpreted as vapour phase when found to have grown into pore space (e.g., Figures 4.1 and 4.2), and where the base of the crystal (i.e., contact with the groundmass) follows the contour of the existing vesicle wall (e.g., Figure 4.3c and d). Crystals were also interpreted as vapour phase when present in a vug but unattached to the surrounding groundmass, seemingly protruding from a face either above or below the thin-section (Figure 4.4). All vapour phase crystalline silica appears to have grown directly from a glassy vesicle wall or sits amongst a druze of vapour-phase feldspars.

When observed *in situ* in pore space, vapour-phase cristobalite exists as a pseudo-spectrum of morphologies, ranging from euhedral, prismatic crystals (Figure 4.1) to hexagonal, platy crystals (Figure 4.2a and f), with a selection of botryoidal/reniform agglomerations (Figure 4.1c and e), stouter plates (Figure 4.2e), and ‘fans’ between (Figure 4.2d). This does not imply a continuum from platy to prismatic, where prismatic crystals are platy crystals that have undergone further growth, as no semi-formed prismatic crystals were observed. All of these morphologies were observed at a range of sizes (at least 3-70 μm; Table 4.2).

Table 4.2: Summary of observational investigations into the nature and formation cristobalite in volcanic dome rock. 'Habit and morphologies' registers the presence and crystal size of each; 'majority cristobalite' qualitatively denotes which habit was more abundant; 'devitrification progression' qualitatively registers the abundance of devitrification cristobalite in the groundmass; 'cristobalite textures' records the presence of each feature discussed in text in each sample; 'degree of order' qualitatively describes vapour phase crystals with respect to the ideal (denoted by ***) crystal shape; 'massive' registers the presence of cristobalite displaying a massive crystal habit: uniform masses (often botryoidal) showing no distinctive external crystal structure.

Volcano	Sample	Habit and Morphologies (μm; range and median)			*majority cristobalite*	*devitrification progression*	Cristobalite Textures				*degree of order*	*massive*
		devitrified	*prismatic*	*platy*			*fish scale*	*feathery*	*myrmekitic*	*veins*		
Colima, Mexico												
	COL.124	x	23-62 (44.3)	12.1-28 (18.9)	even	+ +	x	x	--	x	***	--
	COL.165	x	28-42 (35.3)	(52)	v.p.	+	x	--	--	x	***	--
	COL.03.10	x	34-105 (63.6)	--	v.p.	+	x	--	--	x	**	--
Mount St. Helens, USA												
	MSH.304.2A1	x	3.5-22.3 (12.9)	--	devit	+ + + +	x	x	--	x	*	--
	MSH.304.2A9	x	5.83-31.8 (15.5)	6.1-18.9 (9.9)	devit	+ + + +	x	x	--	x	**	--
	MSH.304.2G	x	15.6-21.3 (18.2)	--	devit	+ + + +	x	x	--	--	*	--
	MSH.305.1A	x	12.1-57.0 (27.8)	17.9-35.6 (27.2)	devit	+ + +	x	x	x	--	**	x
Dome rock 04-06	MSH.309.1A	x	--	16.9-57.4 (32.4)	devit	+ + + +	x	x	--	x	**	--
	MSH.315.4	x	17.5-52.6 (41.4)	25.2-71.1 (53.3)	even	+ + + +	x	x	x	x	*	--
	MSH.315.5	x	--	34.2-57.2 (44.5)	devit	+ + + +	x	x	x	x	**	--
	MSH.316.1	x	--	35.4-137.0 (64.3)	even	+ + + +	x	x	--	x	***	x
	MSH.321	x	--	22.9-136.0 (71.3)	even	+++	x	x	x	--	***	x
	MSH.326.2	x	7.4-18.3 (13.1)	--	devit	+ + + +	x	x	x	--	**	--
	MSH.127	n.d.	8.4-24.9 (18.4)	--	v.p.	n.d.	x	--	--	--	*	--
	MSH.201	x	8.7-14.5 (11.3)	12.3-30.2 (20.1)	devit	+ + +	x	x	--	--	**	--
	MSH.135	x	--	7.7-24.6 (12.8)	devit	+ + + +	x	x	--	--	**	--
Dome rock 80-86	MSH.131	n.d.	--	--	--	n.d.	--	--	--	--	--	--
	MSH.156	x	(15.1)	--	devit	+	x	x	x	--	--	--
	MSH.33	n.d.	--	3.2-6.9 (4.7)	v.p.	n.d.	--	--	--	--	***	--
	MSH.67	x	--	4.0-5.6 (4.8)	devit	+ +	x	x	--	--	**	--
	MSH.103	x	21.8-56.4 (35.6)	21.9-31.5 (26.6)	even	+ + +	x	x	x	x	**	--

	MSH.166	x	--	19.2-45.3 (31.9)	v.p.	+ + +	x	x	--	--	***	x
	MSH.192	x	unknown	--	devit	+ + +	x	x	--	x	*	x
Cryptodome (1980)	MSH.BD.1	x	28.3-84.5 (61.7)	9.8-42.1 (32.7)	even	+ + +	x	x	--	x	*	x
	MSH.BD.2	x	18.9-80.7 (46.6)	22.7-59.0 (42.5)	devit	+ + +	x	x	--	--	**	x
	MSH.BD.3	x	--	--	devit	+	x	x	--	--	--	x
	MSH.BD.4	x	--	--	devit	+	x	x	--	-=	--	x
	MSH.ED.1	x	6.2-15.8 (12.1)	3.4-14.2 (8.7)	devit	+ + + +	x	--	x	--	**	--
	MSH.DY.1	n.d.	--	--	--	--	--	--	--	--	--	--
Santiaguito, Guatemala												
	SG.BR.F3	n.d.	--	--	--	n.d.	--	--	--	--	--	--
	SG.BR.SL7	x	35.3-67.7 (52.8)	35.6-58.9 (49.2)	even	+ +	x	*x*	--	--	***	x
	SG.BR.P1	x	(47.6)	--	--	+	x	--	--	--	**	--
	SG.BR.S1	x	17.0-19.2 (21.2)	13.7-38.6 (26.9)	v.p.	+ + +	x	x	x	x	***	--
	SG.MTD.1	x	46.2-74.1 (62.32)	--	v.p.	+ +	x	--	x	--	***	--
	SG.MTD.2	x	28.5-108.4 (72.2)	39.8-76.8 (60.4)	devit	+ + +	x	x	--	x	**	x
	SG.MNJ.1	x	--	61.6-153.6 (102.8)	v.p.	+ + +	x	x	--	--	***	x
Unzen, Japan												
	UNZ.92.01	x	10.2-47.0 (26.3)	--	v.p.	+	x	--	x	x	**	--
	UNZ.Y1	x	12.3-62.5 (36.4)	--	v.p.	++	x	--	x	x	**	--
Merapi, Indonesia												
1996	MRP1996_03	x	8.7-20.5 (14.3)	--	devit	++	x	x	--	--	**	--
1998	MRP1998_03	x	17.3-21.4 (19.3)	--	even	+ +	x	x	--	--	**	--
	MER.10.01	n.d.	--	--	--	n.d.	--	--	--	--	--	--
	MER.10.04	n.d.	--	--	--	n.d.	--	--	--	--	--	--
	MER.10.06	n.d.	--	--	--	n.d.	--	--	--	--	--	--
2010	MER.10.08	x	18.4-32.5 (27.1)	--	devit	++	x	x	x	--	**	--
	MER.10.09	x	16.0.6-80.2 (63.9)	33.8-55.6 (40.1)	even	++	x	--	--	--	**	--
	MER.10.10	x	--	--	devit	+	x	--	--	--	--	--
	MER.10.13	x	21.1-30.9 (24.3)	--	v.p.	+	x	--	--	--	**	--

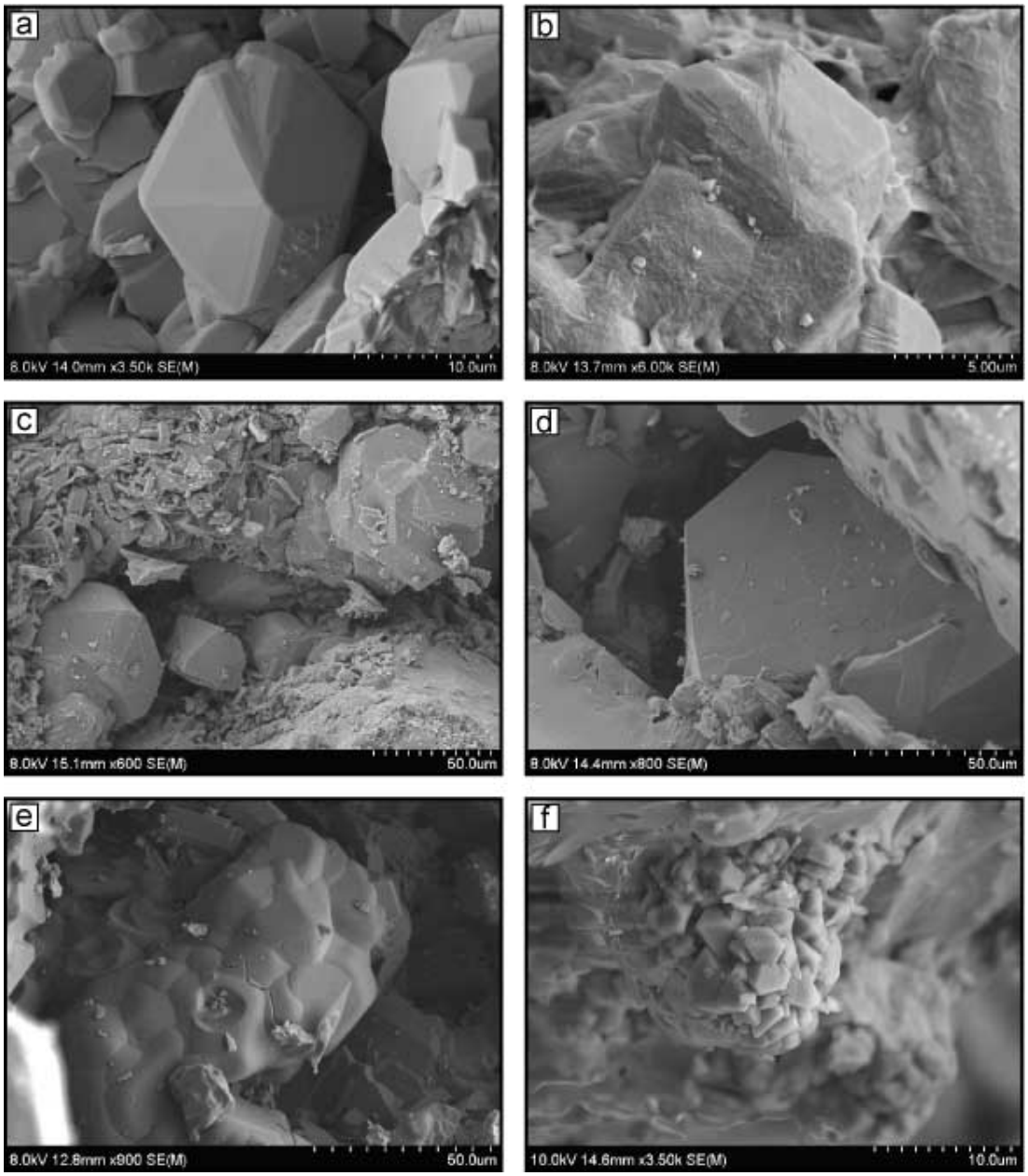

Figure 4.1: Selected scanning electron micrographs of prismatic vapour phase cristobalite protruding into pores space in rough chips of dome rock. a) well-formed euhedral crystal (MSH.304.2A9); b) hydrothermally altered, euhedral crystal (MSH.ED.1); c) large, euhedral crystals showing abundant twinning sitting within a crust of vapour phase feldspar crystals (SG.MTD.1); d) massive euhedral crystal (SG.BR.SL.7); e) botryoidal/ reniform agglomerate (SG.MTD.2); f) agglomerate of smaller cristobalite crystals (UNZ.92.01).

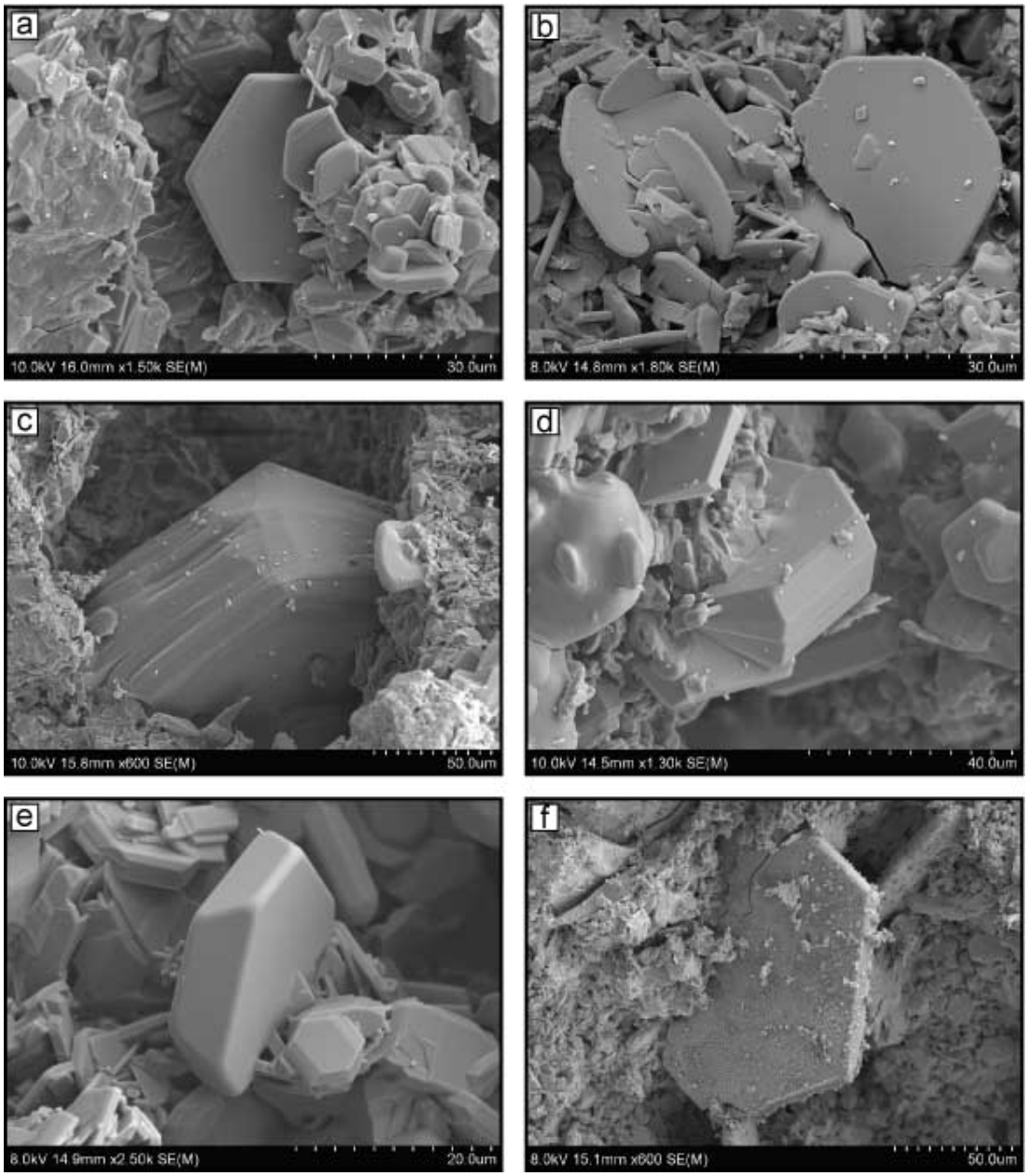

Figure 4.2: Selected scanning electron micrographs of platy vapour phase cristobalite in rough chips of dome rock. a) well-formed hexagonal crystal (MSH.166); b) less well formed, rounded and tabular crystals (MSH.309.1A); c) massive platy crystal (MSH.321); d) 'fan' like stack of twinned platy crystals (MSH.103); e) example of a stouter plate (MSH.BD.2); f) platy crystal with a layer of crust on the surface (MSH.316.1).

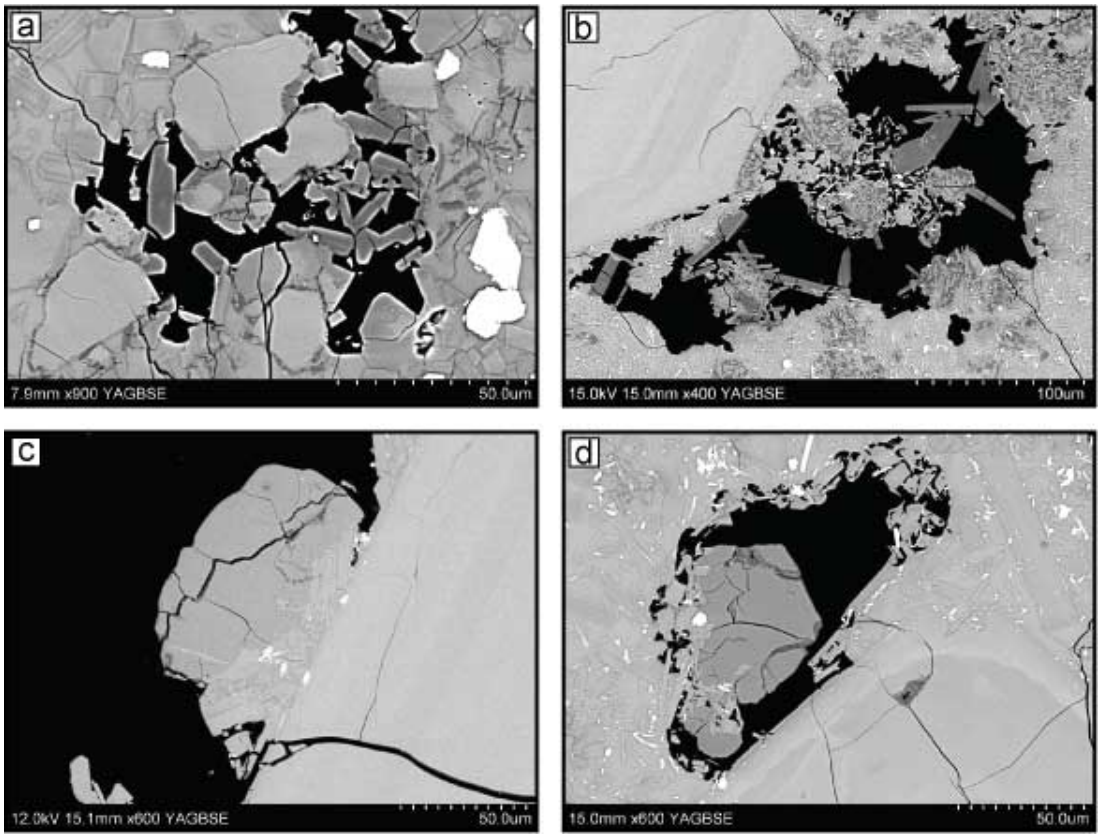

Figure 4.3: Backscattered electron (BSE) micrographs of vapour phase morphologies in thin section. Images show stout (a, COL.124) and well formed (b, MSH.166) platy cristobalite and prismatic (c, SG.MTD.2; d, SG.MTD.1) vapour phase cristobalite.

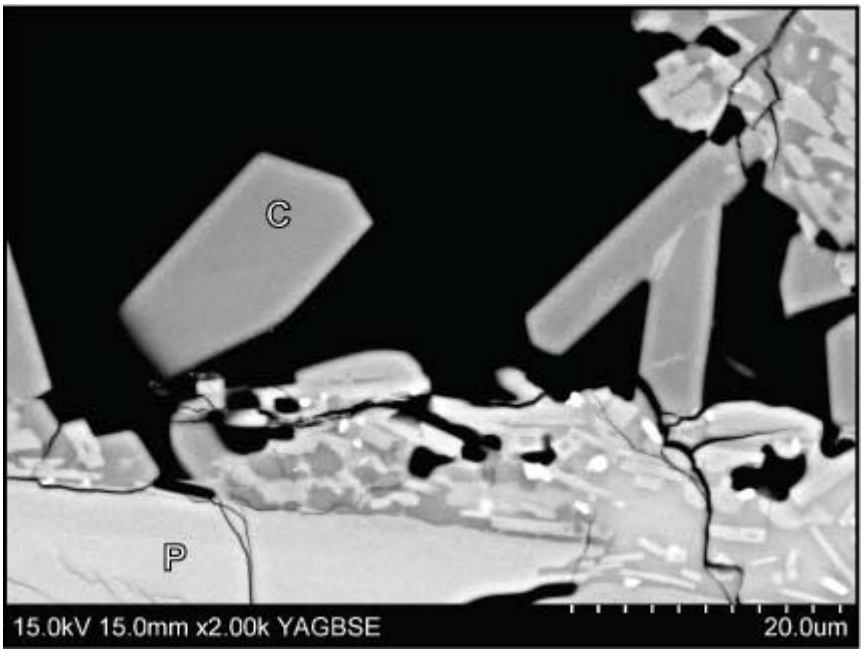

Figure 4.4: Backscatter electron micrograph of vapour phase cristobalite in pore space not attached to a vesicle wall. Labels in the image are 'C' for cristobalite and 'P' for a plagioclase phenocryst.

Two distinct classifications were assigned for the interpretation of crystal formation, either 'prismatic' or 'platy', as also classified by Horwell et al. (post review; Appendix 4). Vapour phase crystals in the prismatic-to-platy array were categorised through closer alignment with either morphology; that is, crystals with equal growth in three dimensions versus crystals with prominent growth in two dimensions (or acicular in thin section). The presence of 'prismatic' or 'platy' crystals observed in thin section was corroborated with *in situ* crystals in the pore spaces of rough chips (i.e., Figure 4.1 and Figure 4.2 with Figure 4.3).

Some samples contained only prismatic crystals and others contained only platy crystals, and the two morphologies often coexisted within a sample (14 samples of 41 samples in which vapour phase crystals were observed; see Table 4.2). Prismatic crystals were observed at all of the locations studied; however, platy crystals were not identified at Unzen. Overall, prismatic crystals had a greater frequency, occurring in 30 samples compared to 23 samples with platy crystals. When only one morphology was present in a sample, prismatic crystals were again more common; 16 samples compared to 9 samples with platy. All locations had prismatic-only samples, whereas only Mount St. Helens and Santiaguito had platy-only samples.

These two locations, however, had a greater number of characterised samples than other locations and, therefore, the occurrence of platy-only samples cannot be ruled out elsewhere. The distribution of morphologies is summarised in Table 4.2. The limited sample numbers for Colima and Unzen (n=3 and n=2, respectively) combined with the range in morphologies observed for intra-volcano samples being equivalent to that observed between samples precluded statistical analyses on the presence of different morphologies amongst volcanoes.

All varieties of prismatic to platy vapour phase crystals were confirmed as cristobalite by SEM-Raman spot analysis (Figure 4.5); and, if sufficiently large, could be visually identified as cristobalite by their 'fish-scale' texture (see Figure 3c and d, and most obvious in devitrification patches in Figure 4.6a). The 'fish-scale' texture was observed in samples from all volcanic centres, and is visible in both prismatic and platy crystals.

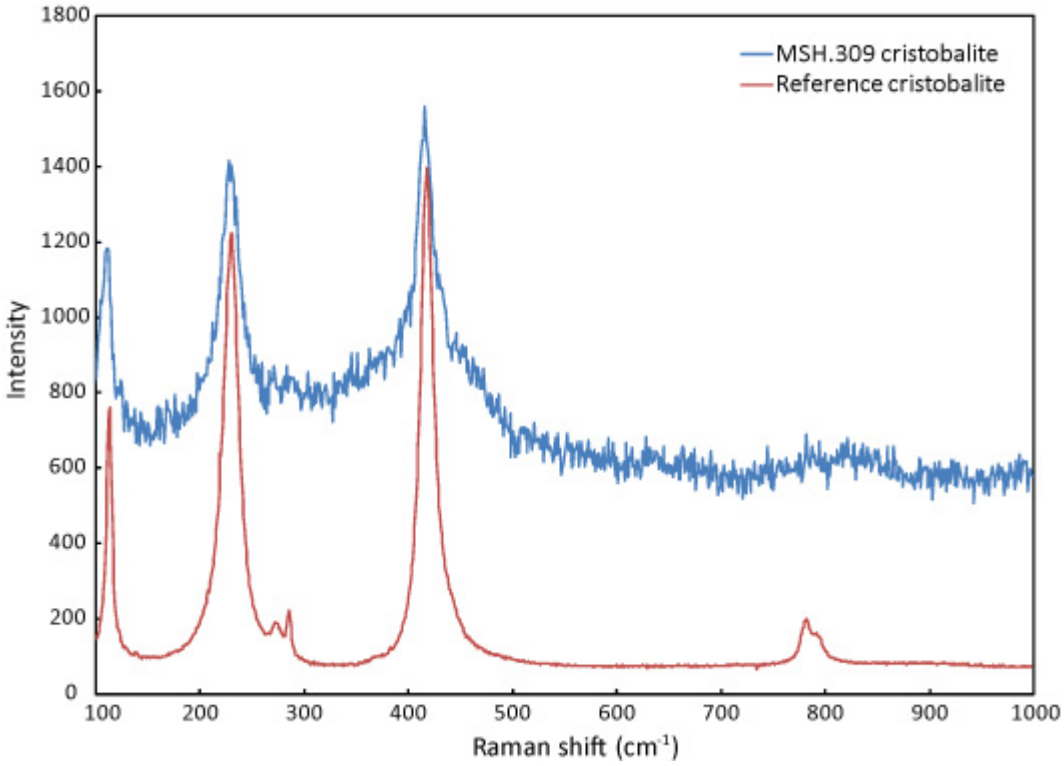

Figure 4.5: Representative Raman spectrum collected by SEM point analysis of cristobalite in MSH.309.1A. Reference spectrum taken from the Handbook of Minerals Raman Spectra (Laboratoire de Sciences de la Terre ENS-Lyon France, 2000-2012)

(3) *Devitrified groundmass cristobalite*. Well-defined patches of cristobalite were observed in the groundmass of 38 of 45 samples (Figure 4.6a and b). A 'feathery' texture, described by Horwell et al. (post review; Appendix 4), of poorly-formed crystallites was observed within the glassy groundmass of 29 of these 38 samples (Table 4.2; Figure 4.6c). A second, 'myrmekitic-like' texture was identified in 13 of the 38 samples (Figure 4.6d), and is texturally discussed in Section 4.3.2. For both textures, groundmass crystallites were too small to be directly identified by spot analysis, and were therefore confirmed as micro-cristobalite by a combination of BSE imaging, EDS/WDS elemental mapping and CL imaging. Figure 4.7 shows an area of partially devitrified glass, which contains plagioclase microlites and micron-sized crystallites with a BSE signal darker than glass, similar to that of the 'fish-scale' cristobalite ('C'; Figure 4.7a). The CL signal (Figure 4.7b) for this groundmass phase is similar to the 'fish scale' cristobalite. Compositionally (Figure 4.7c), it is predominantly Si (blue), and distinct from the Al-rich (red) plagioclase microlites and phenocrysts (Figure 4.7b and c). This devitrification texture, analogous to that identified by Horwell et al. (post review; Appendix 4, see their Figure 2), was further confirmed as cristobalite by SEM-Raman analysis on an area of partially devitrified glass.

These textures are interpreted to be products of devitrification due to their close association with the surrounding groundmass, with patches often enclosing glass and feldspar microlites (Figure 4.6b). The presence of microlites within these patches with a similar crystal distribution to microlites throughout the sample (e.g. Figure 4.6b and c) discounts the potential interpretation of pore-space infill. Further, patches do not impinge upon pre-existing vesicles, and no distinct contacts are ever observed which resemble a vesicle wall. The exception to this is the case when devitrification has progressed proximal to a vesicle, where the original bubble wall is still intact and the curvature is concave away from the cristobalite patch (e.g. right edge of Figure 4.6a). These patches of cristobalite are also frequently smaller than and shaped differently to the surrounding vesicle population, again discounting the interpretation of pore-space infill.

Some samples had areas which were almost completely devitrified, containing small patches of subhedral silica, which were confirmed as quartz using SEM-Raman spot analysis (Figure 4.8). Some of these patches were hexagonal in morphology. These patches are most prevalent in MSH.ED.1, where XRD further confirmed that the total crystalline silica content was about half cristobalite and half quartz (Table 4.3). Horwell et al. (post review; Appendix 4) refers to these patches as quartz microlites,

which will be adopted here. Samples with substantial devitrification quartz (MSH.ED.1 and MSH.321) show physical signs of alteration, with less groundmass glass and the degradation of crystal edges (Figure 4.8).

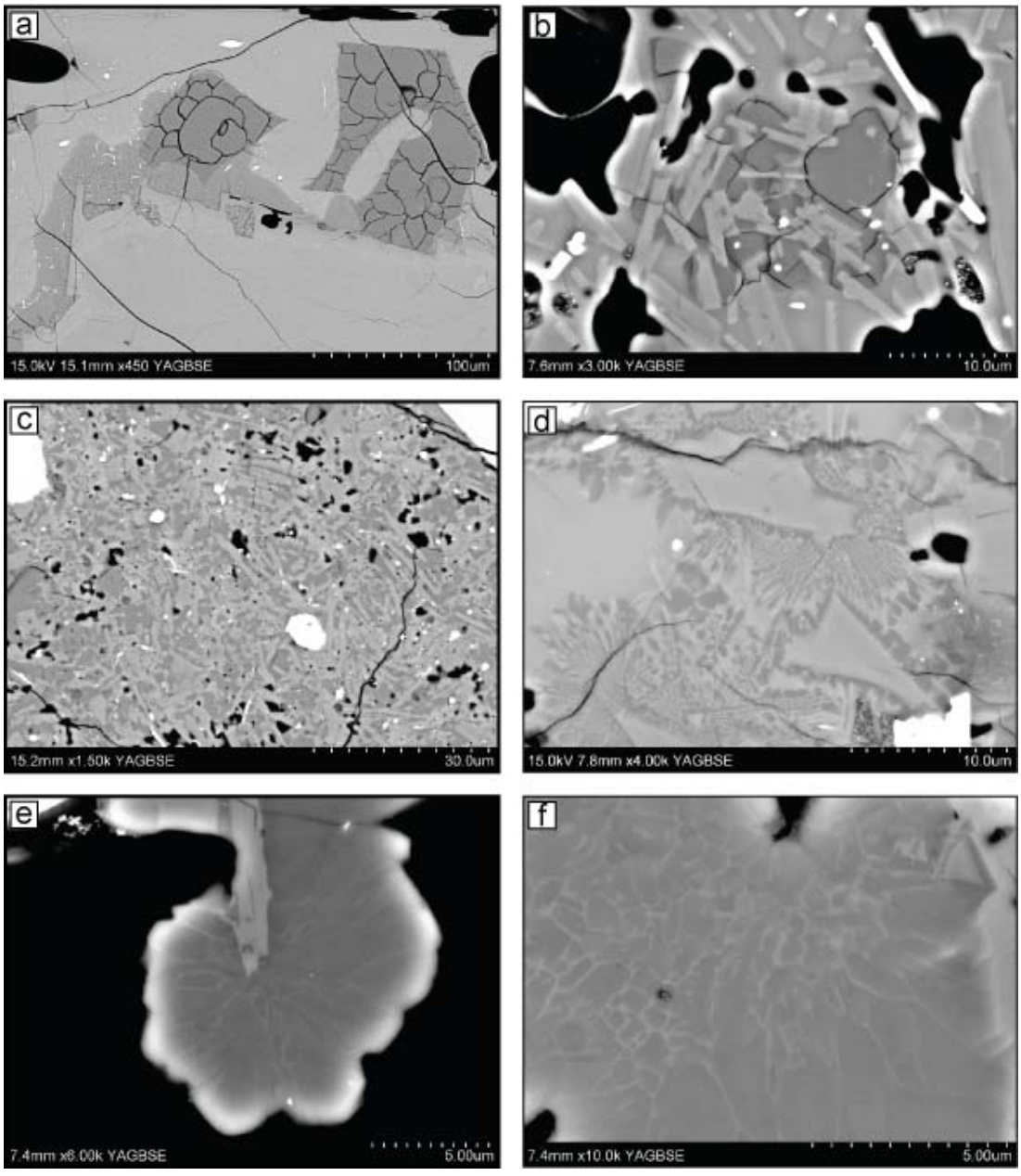

Figure 4.6: Devitrification cristobalite textures identified in thin section of dome rock and recorded in Table 4.2. a) and b) typical 'fish-scale' cracking (MSH.156; MSH.BD.2), c) 'feathery' groundmass texture (SG.BR.S1), d) 'myrmekitic-like' groundmass texture (MSH.103); e) and f) internal 'veins' (UNZ.92.01). Bright crystal edges in b), e) and f) are instrumental edge effects.

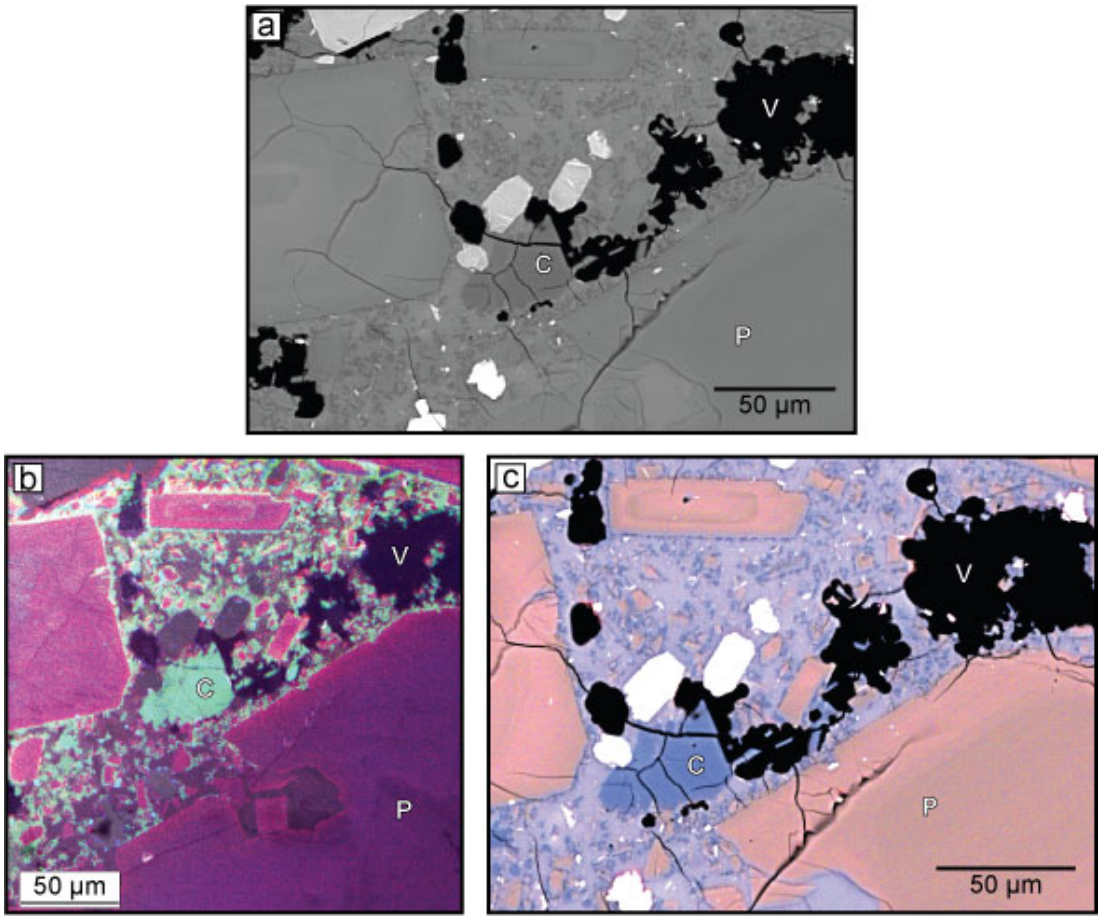

Figure 4.7: Identification of cristobalite through combined SEM-BSE (a), SEM-CL (b) and SEM-EDS/WDS (c) analysis. Images are of the same area in MSH.305.1A showing devitrification cristobalite (labelled 'C'; turquoise (b)/periwinkle(c)) and plagioclase phenocrysts and microlites (labelled 'P'; magenta (b)/salmon (c)). Vesicle is labelled 'V'.

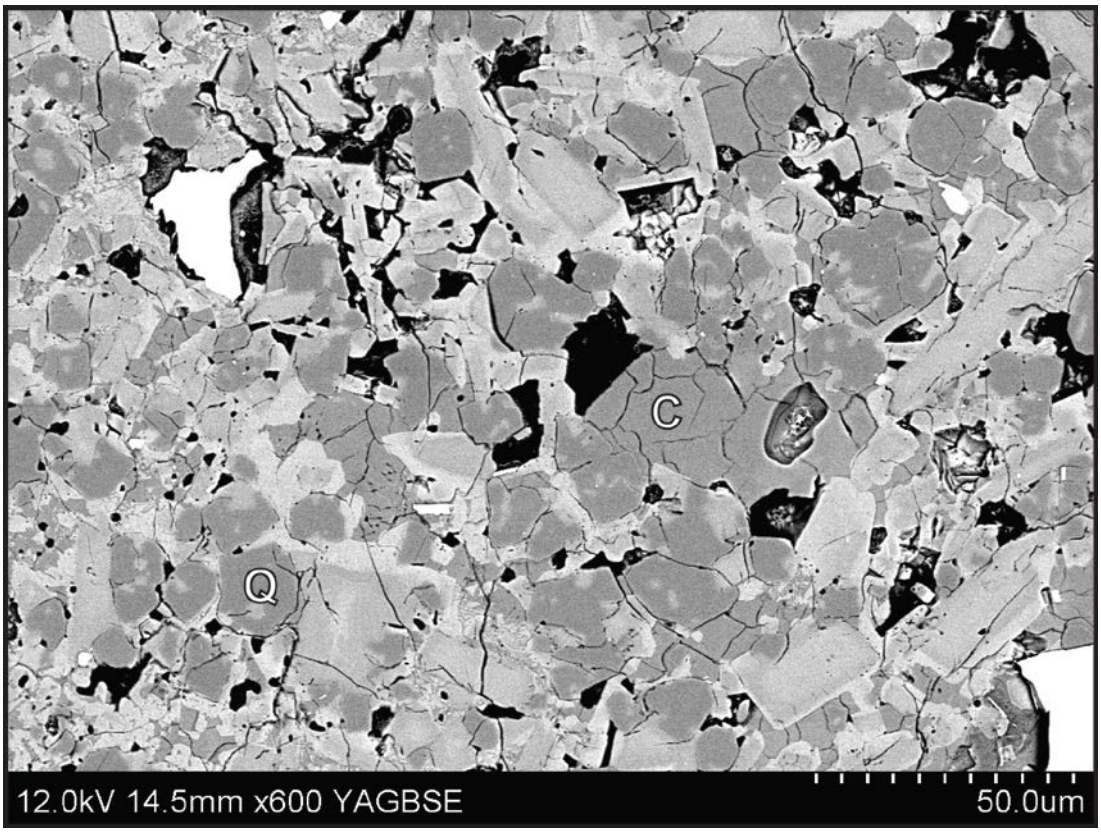

Figure 4.8: Backscatter electron micrograph of both cristobalite ‘C’ and quartz ‘Q’ as groundmass phases in sample MSH.ED.1.

Different samples underwent different degrees of devitrification, where different area percentages of the groundmass had crystallised. Samples were qualitatively ranked by progression of devitrification, with (+) equating to a sample where scarce patches were observed per section to (++++) indicating a sample that had undergone nearly complete devitrification. Samples where no devitrification was detected were marked ‘n.d.’ (none detected). The degree of devitrification undergone in each sample is summarised in Table 4.2, and the corresponding rankings are depicted in Figure 4.9.

Only two samples were found to have vapour-phase crystals with no sign of devitrification. These were both 1980-1986 Mount St. Helens samples (MSH.127 and MSH.33), and only contained 1-2 vapour phase crystals per section. Both samples were glassy and highly fractured, containing microlite fragments and resorbed phenocrysts.

Table 4.3: Abundance of crystalline silica polymorphs quantified by X-ray diffraction using the IAS technique of Le Blond et al. (2009). Data are as wt. %.

Volcano	Sample	Cristobalite wt.%	Quartz wt. %	Total Crystalline Silica wt. %
Colima	COL.124	4.8	0.0	4.8
	COL.165	3.2	0.0	3.2
	COL.03.10	3.7	0.0	3.7
Mt St. Helens	MSH.304.2A1	13.5	1.6	15.1
	MSH.304.2A9	--	--	--
	MSH.304.2G	--	--	--
	MSH.305.1A	13.8	0.9	14.7
Dome rock 04-06	MSH.309.1A	13.2	0.0	13.2
	MSH.315.4	13.7	4.1	17.8
	MSH.315.5	18.9	3.7	22.6
	MSH.316.1	14.9	1.4	16.3
	MSH.321	6.5	6.8	13.3
	MSH.326.2	17.1	2.2	19.3
	MSH.127	1.5	0.0	1.5
	MSH.201	15.8	1.0	16.7
	MSH.135	12.0	0.0	12.0
Dome rock 80-86	MSH.131	3.1	1.4	4.6
	MSH.156	0.0	0.0	0.0
	MSH.33	4.1	1.3	5.4
	MSH.67	7.5	1.3	8.8
	MSH.103			
	MSH.166	10.7	1.8	12.5
	MSH.192	11.7	0.0	11.7
Cryptodome (1980)	MSH.BD.1	13.8	0.0	13.8
	MSH.BD.2	13.6	0.0	13.6
	MSH.BD.3	6.9	0.9	7.7
	MSH.BD.4	3.4	2.2	5.6
	MSH.ED.1	11.8	12.5	24.2
	MSH.DY.1	0.0	3.9	3.9
Santiaguito	SG.BR.F3	4.4	0.0	4.4
	SG.BR.SL7	17.1	0.0	17.1
	SG.BR.P1	4.6	0.0	4.6
	SG.BR.S1	9.2	0.0	9.2
	SG.MTD.1	6.5	0.0	6.5
	SG.MTD.2	14.4	0.0	14.4
	SG.MNJ.1	24.1	0.0	24.1
Unzen	UNZ.92.01	3.2	0.0	3.2
	UNZ.Y1	11.7	0.0	11.7
Merapi	MER.10.01	4.5	0.0	4.5
	MER.10.04	0.0	0.0	0.0
	MER.10.06	3.6	0.0	0.0
2010	MER.10.08	4.4	0.0	4.4
	MER.10.09	5.1	0.0	5.1
	MER.10.10	4.8	0.0	4.8
	MER.10.13	3.9	0.0	3.9
1996	MRP.96.03	3.0	0.0	3.0
1998	MRP.98.03	5.4	0.0	5.4

4.3.2 Textural features of cristobalite and groundmass in volcanic dome rock

Four different types of textures were associated with the presence of cristobalite. These are defined as ‘fish-scale’, ‘feathery’, ‘myrmekite-like’ and ‘veins,’ and the occurrence of each is summarised in Table 4.2. As mentioned, cristobalite is easily distinguishable by its characteristic ‘fish-scale’ cracking (Figure 4.6a and b). It is a diagnostic feature of the β-α transition and was observed in all samples in thin section as well as occasionally on the surface of vapour phase crystals in rock chips (Figure 4.10), and indicates that cristobalite formed as the high temperature β-phase and currently exists as the metastable α-phase in the dome samples (see Chapter 5). Individual ‘scales’ were approximately 10-20 μm across. As discussed above, groundmass devitrification can manifest as two textures. The ‘feathery’ texture discussed by Horwell et al. (post review; Appendix 4) is partially defined by lath-shaped microlite growth (Figure 4.6c), whereas the ‘myrmekite-like’ microstructure is of cristobalite and ‘feldspathic’ glass (Figure 4.6d and Figure 4.11). The cristobalite in this second texture is compositionally similar to other cristobalite in the sample by combined WDS/EDS mapping; however, the glass is enriched in Al (and potentially other elements) relative to glass in non-devitrified areas. ‘Feathery’ and ‘myrmekite-like’ textures differ in the amount of residual glass and the abundance of feldspar microlites. Whereas the two devitrification types describe the general texture of the groundmass, the final texture, designated ‘veins’, is an internal texture within a cristobalite crystal (apparent in Figure 4.6e and f). ‘Veins’ occur in both devitrification and vapour phase crystals. In this case, nano-sized bands of heavier elements (potentially Ca and K, although barely visible by EDS spot analysis) exist within a cristobalite crystal, distinguished, however, by their lighter greyscale.

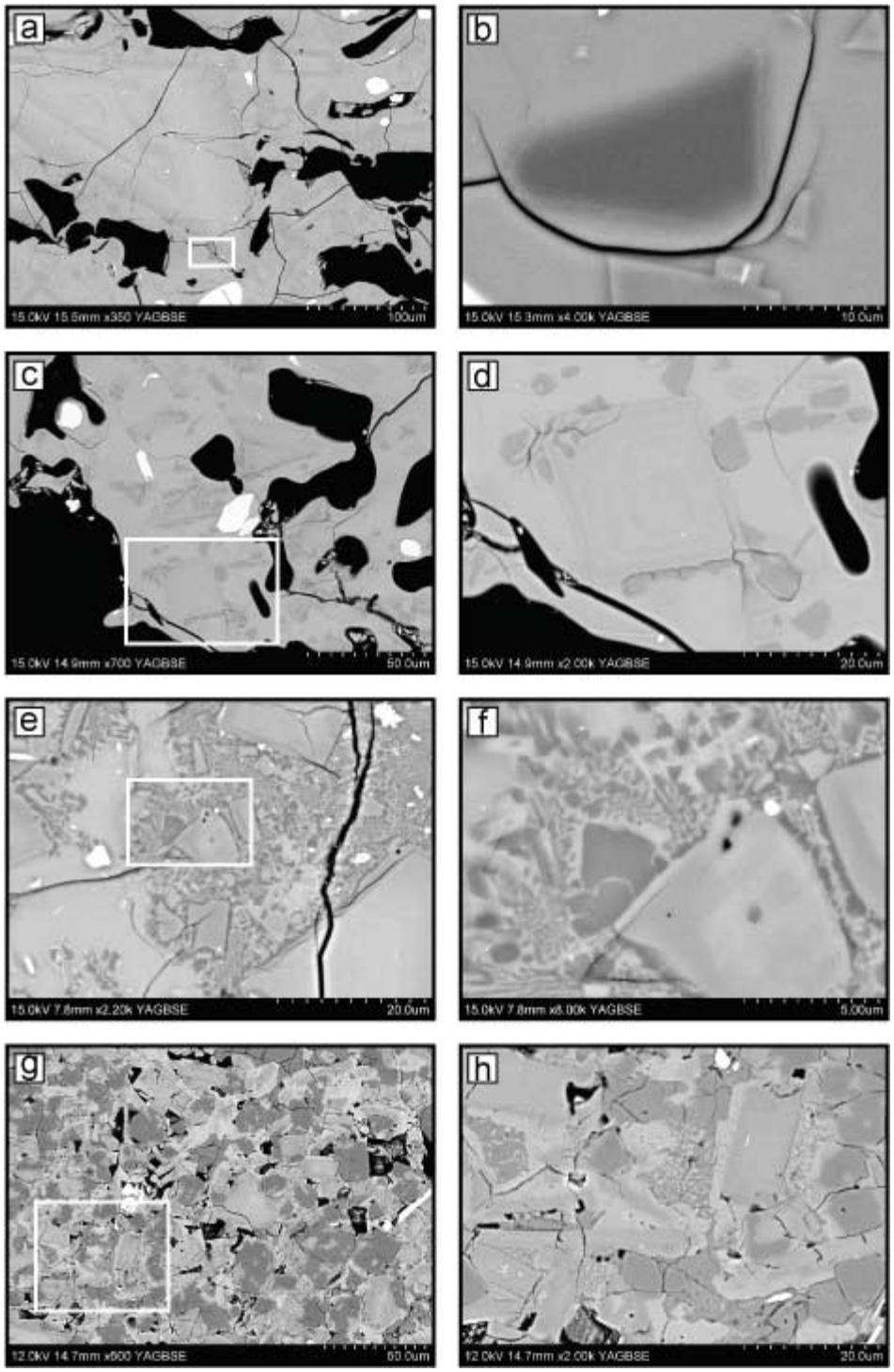

Figure 4.9: Backscatter micrographs showing the progression of devitrification at two magnifications. Images are qualitatively ranked as '+' (a and b; MSH.156), '+ +' (c and d; MSH.67), '+ + +' (e and f; MSH.103.3), and '+ + + +' (g and h; MSH.ED. 1).

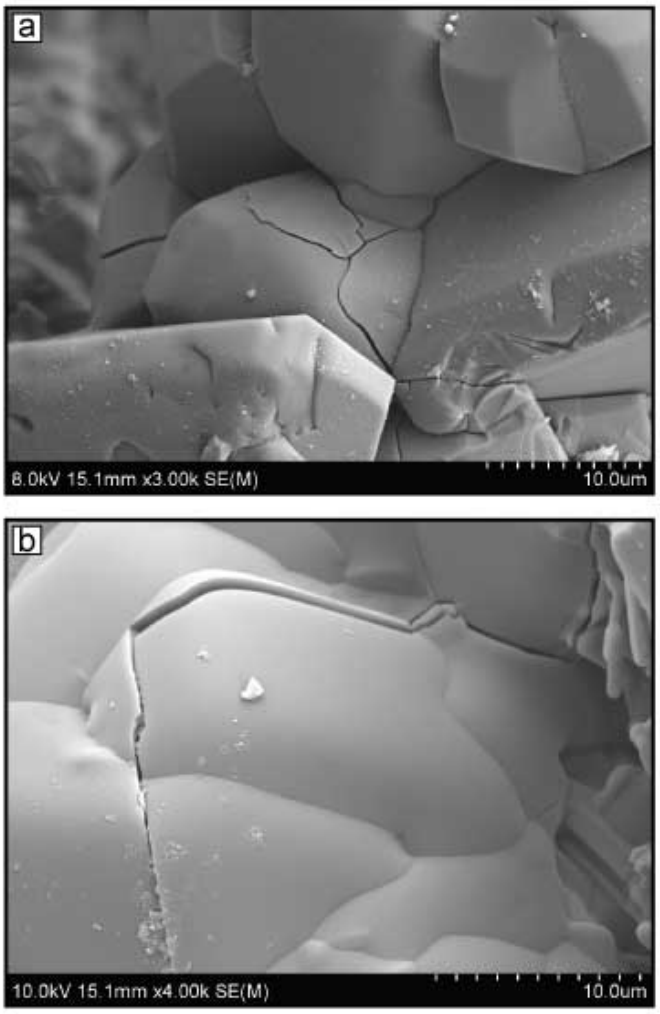

Figure 4.10: Scanning electron micrographs of characteristic 'fish-scale' cristobalite cracks manifesting on the surface of prismatic crystals (a, MSH.305.1A; b, MSH.103).

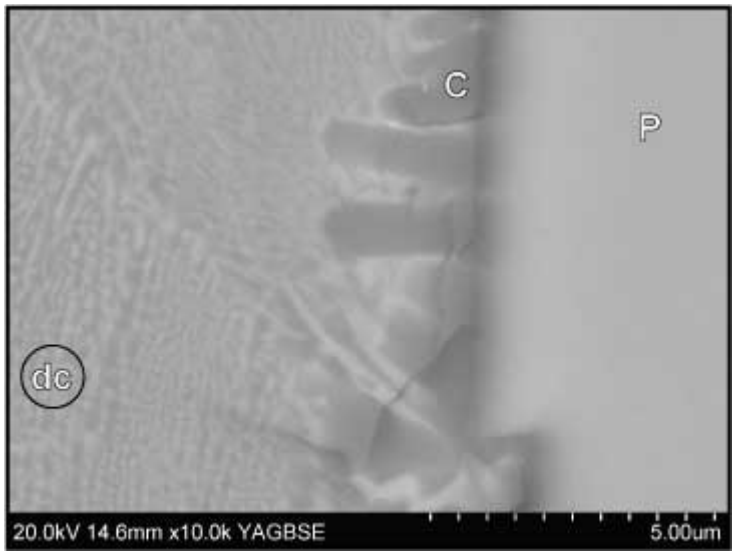

Figure 4.11: Backscatter electron micrograph showing the potential control of a plagioclase (P) crystal boundary on the nucleation of cristobalite (c), with 'myrmekitic' growth of devitrification cristobalite (dc).

Sub-micron sized 'vesicles' (possibly fluid inclusions) are often observed within devitrification cristobalite. These 'vesicles' are not ubiquitous in all crystals and, when present, show no consistent spatial relationship with the host crystal. Sub-micron 'vesicles' were also very occasionally observed (multiple instances in SH166, SH.315.4, SH.BD.2) in vapour phase crystals (Figure 4.12). These vesicles are aligned parallel to a crystal axis and are normally distributed with smaller, spherical, non-coalesced vesicles towards the crystal margins, and are not restricted to internal crystal growth faces.

Mount St. Helens cryptodome samples are texturally distinct from other dome samples from Mount St. Helens and elsewhere. These samples have a larger microlite population than other dome samples, and all of the microlites are of a uniform size distribution (quantified by Cashman, 1988). In these samples, microlites are often well aligned and orientated around groundmass features, e.g., vugs, phenocrysts, and cristobalite patches (Figure 4.13), showing evidence of flow alignment. The 1980 edifice sample was also texturally distinct from all dome samples, containing extensive devitrification to both cristobalite and quartz (Figure 4.8). This sample also contained voids among devitrification crystalline silica, phenocrysts and microlites rather than a glassy matrix as observed in dome samples. No cristobalite was observed in the dyke sample, although clays were ubiquitous in pore spaces.

In one sample from Santiaguito (SG.MTD.1), an internal 'rind' of feldspar in an SiO_2 matrix was identified within a vesicle (Figure 4.14). In each sample, it was present in multiple locations throughout the sample, although not present in all vesicles. The internal rind is always of a uniform thickness (25-50 μm depending on the vesicle), and is separated from the bulk sample groundmass by a thin cavity. The rind consists of plagioclase microlites similar in size and distribution to the surrounding groundmass, and the residual matrix is partially to completely comprised of crystalline silica. The matrix is likely cristobalite as no quartz was identified in these samples by bulk XRD (Figure 4.15; discussed below); we have found, empirically, that if crystalline silica is detectable by one technique (e.g., SEM or XRD) then it is always detectable by the other.

4.3.3 Abundance of crystalline silica

The abundance of crystalline silica as cristobalite, quartz and tridymite was determined for all dome samples by the XRD-PSD IAS method (Le Blond et al., 2009; see Chapter 3: Methods). Results are depicted as sample abundance per volcano (Figure 4.15), and raw data are in Table 4.3. Cristobalite content ranged from 0 to 25 wt. % (< 3 wt. % error). Ranges for individual volcanoes varied within these bounds: Colima, 3-5 wt. %; Mount St. Helens, 0-19 wt. %; Santiaguito, 3-25 wt. %; Merapi 0-12 wt. %; and Unzen, 3-5 wt. %. Data for Soufrière Hills is included from Horwell et al. (post review; Appendix 4) for comparison, which ranged from 1-11 wt. %.

Cristobalite was the main polymorph present for all volcanoes, with some quartz but no tridymite observed at any of the volcanoes. This is in direct contrast to previous investigations that identified tridymite in dome rock (e.g. Blundy and Cashman, 2001). Quartz was typically less than a few wt. % in samples when detected, except for samples MSH.ED.1 (edifice sample from Mount St. Helens) and MSH.321, that both had comparable abundances of cristobalite and quartz (11.78 vs. 12.47 wt. % and 6.54 vs. 6.76 wt. %, respectively). The crystalline silica content for these two samples corresponded with observations by SEM (see Figure 4.8), as both appear to have undergone extensive devitrification with the formation of quartz microlites. The presence of minor quartz in other samples is attributed to quartz phenocrysts.

Whole rock XRF data for samples of dome rock are presented in Table 4.4. Results define an overall range from basaltic trachyandesite to dacite (Figure 4.16), ranging from 53.80 (Merapi) to 64.71 wt. % SiO_2 (Mount St. Helens). XRF was not carried out for Unzen samples; however, samples are expected to fall within this range (e.g., Nakada and Motomura, 1999; Otsuka and Wayman, 1998).

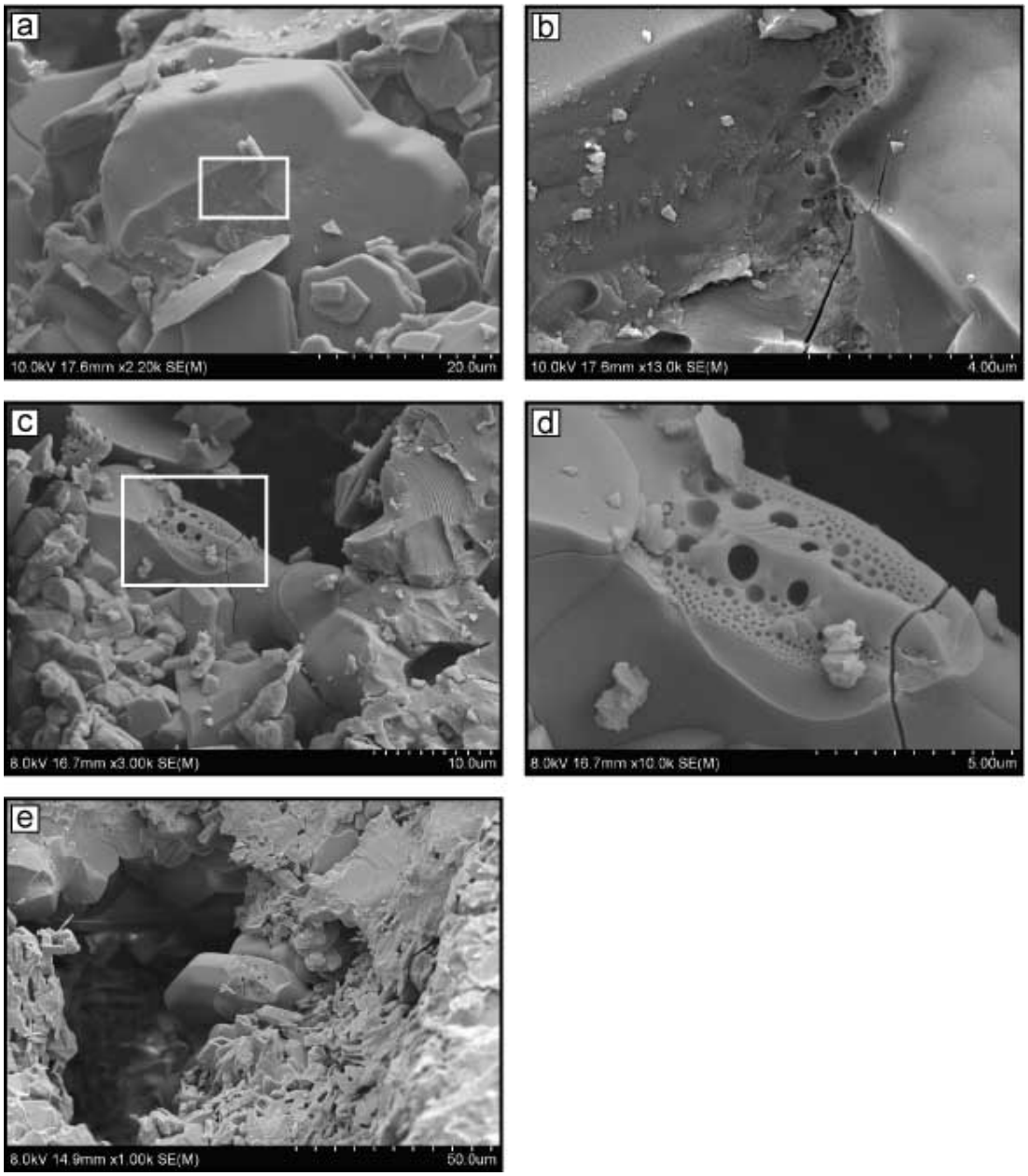

Figure 4.12: Scanning electron micrographs of vesicles within cristobalite crystals (a-b, MSH.166; c-d, MSH.315.4; e, MSH.BD.2).

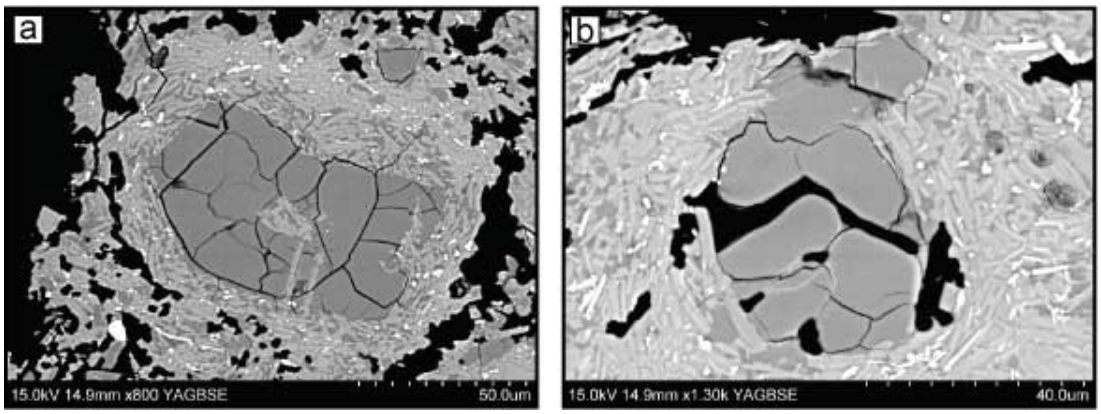

Figure 4.13: Backscatter electron micrographs of ductile deformation with groundmass plagioclase microlite alignment surrounding patches of cristobalite (MSH cryptodome sample MSH.192).

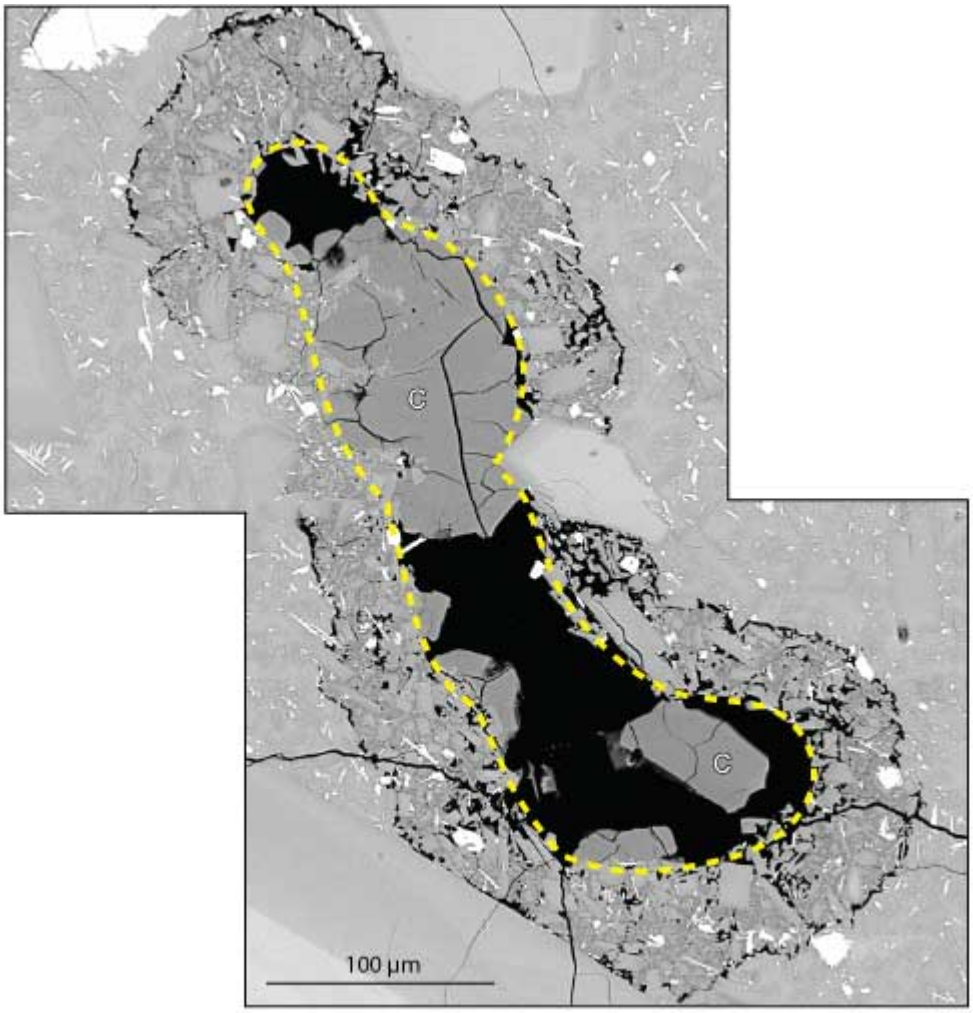

Figure 4.14: Backscatter electron micrograph of cristobalite 'rind' in a vesicle in cross section of sample SG.MTD.1. No analogous feature was identified in rock chippings.

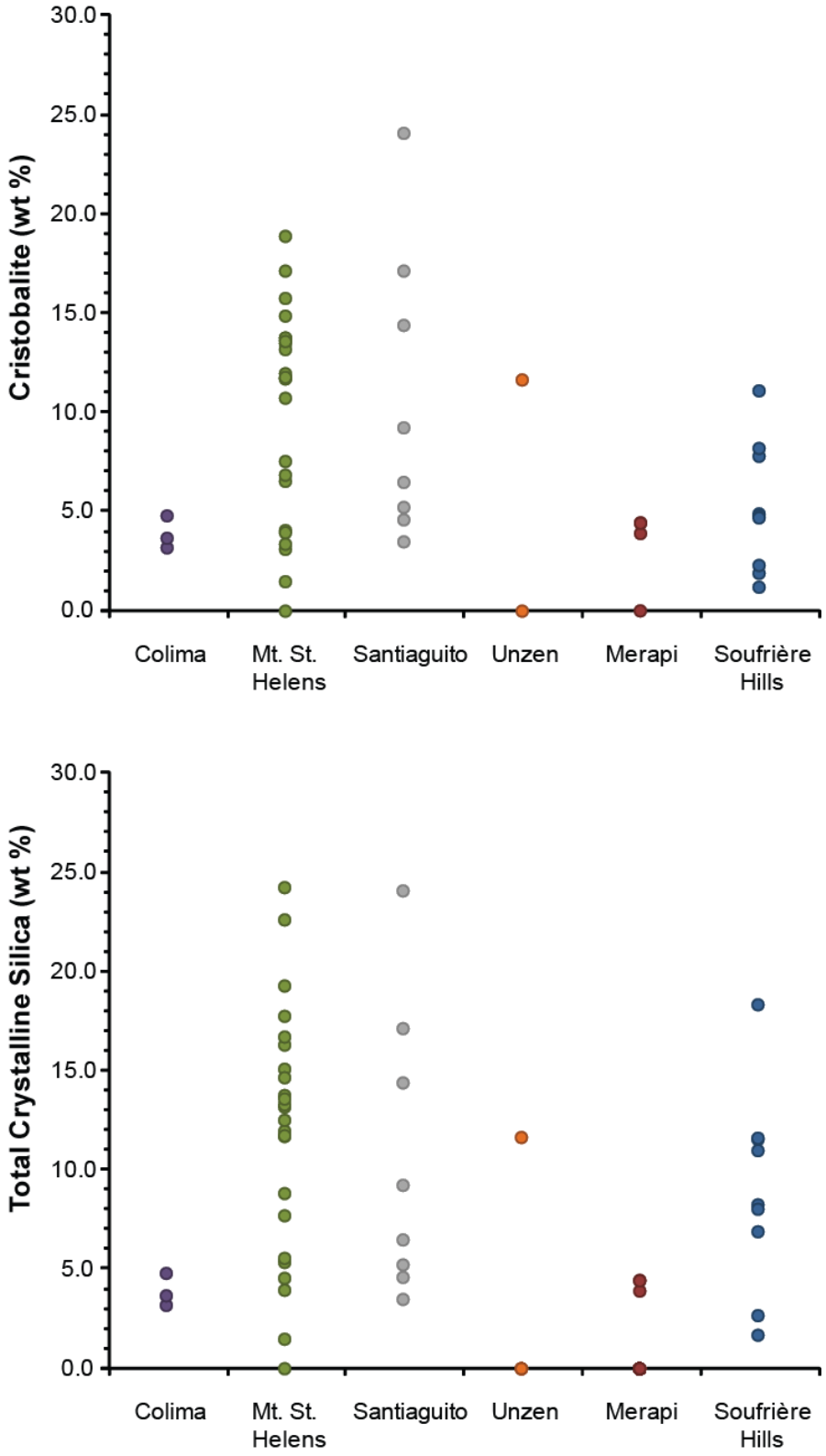

Figure 4.15: Abundance of cristobalite (a) and total crystalline silica (b) in dome rock samples determined for each volcano according the XRD-PSD IAS technique (Le Blond et al., 2009). Data have an error of < 3 wt. %. Data for Soufrière Hills are from Horwell et al. (post review; Appendix 4).

4.3.4 Size and distribution of crystalline silica

From BSE imaging, there are inter- and intra-sample differences in cristobalite crystal size. Sizes for vapour phase crystals are reported in Table 4.2; devitrification cristobalite is qualitatively reported as a degree of devitrification (Section 4.3.1) as distinguishing among individual crystals was not feasible. Measurements for vapour phase crystals were taken between opposite crystal faces where possible. If not possible, measurements were taken along an exposed crystal edge, adjacent edges, or between vertices, and an ideal crystal width (edge to edge) was calculated assuming a hexagonal structure. For all locations, prismatic crystals ranged from 3.5 to 108.4 μm (n=226) and platy from 3.2 to 153.6 μm (n=286); it is assumed that both ranges start from <1 μm but crystals less than those measured were not distinguishable amongst other vapour phase minerals. No statistically significant correlation was observed between crystal size and the range of morphologies (either prismatic or platy) categorised in Section 4.3.1 (Welch's t-test, $p>0.05$).

Dome samples from Mount St. Helens (especially the 1980 cryptodome) and samples from Santiaguito had distinctly larger crystals, denoted 'massive' in Table 4.2. These crystals are well-ordered when imaged in rock chippings, containing multiple twins, although do not always conform to a unique morphology. Their occurrence was easily identifiable and they are excluded from the crystal size distributions reported above. These crystals are obvious in thin section as well, where single crystals can measure up to 200 μm along the long axis, with 'fish scales' throughout (Figure 4.17).

No point of nucleation was systematically observable for devitrification cristobalite in thin section; this is expected for two dimensional textural investigations, since the three dimensional distribution of crystals is unknown. Often, however, growth appears to initiate in contact with plagioclase lamellae (as in Figure 4.11). Nucleation of prismatic and platy vapour phase crystals observed in rock chippings was generally associated with changes in surface contour (e.g., vesicle edges, exposed groundmass crystals, or other vapour phase minerals (Figure 4.18)). Radial crystal growth is often observed from the presumed point of nucleation for both prismatic and platy crystals (Figure 4.18b-e).

Table 4.4: Bulk chemical compositions of dome rock samples by XRF. Data are presented as wt. %.

Volcano	Sample	SiO_2	TiO_2	Al_2O_3	Fe_2O_3	MnO	MgO	CaO	Na_2O	K_2O	P_2O_5	SO_3	LOI	Total
Colima	COL.124	59.46	0.63	17.62	5.98	0.108	3.89	6.03	4.60	1.239	0.182	<0.002	0.74	100.47
	COL.165	60.06	0.62	18.06	5.90	0.105	3.69	6.04	4.63	1.227	0.188	<0.002	0.32	100.84
Mount St. Helens	MSH.304.2A1	64.11	0.66	17.28	4.57	0.07	1.87	4.82	4.80	1.32	0.13	0.01	0.27	99.90
	MSH.316.1	64.23	0.58	17.12	4.31	0.07	1.74	4.66	4.90	1.42	0.15	<0.002	0.25	99.44
2004-2006	MSH.326.2	62.68	0.66	16.82	4.54	0.07	1.85	4.55	4.69	1.29	0.11	<0.002	3.15	100.40
	MSH.309.1A	64.71	0.62	17.13	4.57	0.07	2.05	4.73	4.83	1.38	0.12	0.02	0.29	100.53
	MSH.127	62.67	0.72	17.32	5.39	0.09	2.37	5.20	4.78	1.30	0.15	<0.002	0.20	100.19
1980-1986	MSH.131	63.42	0.69	17.92	5.15	0.08	2.28	5.18	4.72	1.26	0.15	<0.002	0.22	101.08
	MSH.135	62.91	0.71	17.36	5.14	0.08	2.18	5.10	4.73	1.27	0.13	<0.002	0.40	100.01
	MSH.201	63.26	0.68	17.04	5.24	0.08	2.04	4.86	4.82	1.34	0.13	<0.002	0.37	99.87
	MSH.166	64.28	0.61	17.19	4.61	0.08	1.89	4.66	4.78	1.38	0.13	<0.002	0.35	99.95
Cryptodome	MSH.192	63.75	0.62	17.20	4.71	0.08	2.09	4.86	4.79	1.29	0.13	<0.002	0.44	99.95
	MSH.BD.1	64.20	0.62	17.49	4.56	0.07	1.94	4.86	4.85	1.29	0.13	<0.002	0.17	100.18
	MSH.BD.4	62.62	0.62	17.09	4.75	0.08	2.01	4.91	4.78	1.31	0.14	<0.002	0.48	98.80
Santiaguito	SG.BR.F3	62.87	0.47	17.58	5.01	0.153	1.79	4.72	4.85	1.627	0.238	0.003	0.46	99.78
	SG.BR.P1	61.90	0.48	16.89	4.86	0.142	1.73	4.43	4.83	1.625	0.187	<0.002	1.72	98.80
	SG.BR.SL7	63.20	0.46	17.51	4.78	0.141	1.61	4.64	4.88	1.606	0.224	<0.002	1.23	100.28
	SG.MTD.2	61.57	0.42	17.07	4.54	0.138	1.53	4.46	4.69	1.553	0.229	<0.002	4.19	100.39
	SG.MNJ.1	64.22	0.46	17.65	4.77	0.140	1.60	4.52	4.93	1.656	0.230	0.004	0.28	100.46
Merapi	MER.10.01	53.80	0.78	19.30	7.98	0.192	2.66	8.38	3.80	1.983	0.295	0.009	1.14	100.33
	MER.10.09	54.16	0.79	19.85	8.22	0.195	2.59	8.59	3.71	1.963	0.311	<0.002	-0.08	100.30
	MER.10.10	55.75	0.73	19.74	7.49	0.193	2.27	7.98	3.96	2.068	0.314	0.004	0.15	100.65
	MER.10.12	55.40	0.72	19.76	7.29	0.191	2.23	8.04	3.96	2.054	0.312	0.006	0.48	100.44
	MER.10.15	56.51	0.67	20.12	6.61	0.159	1.83	6.73	3.27	1.825	0.307	0.008	2.03	100.07

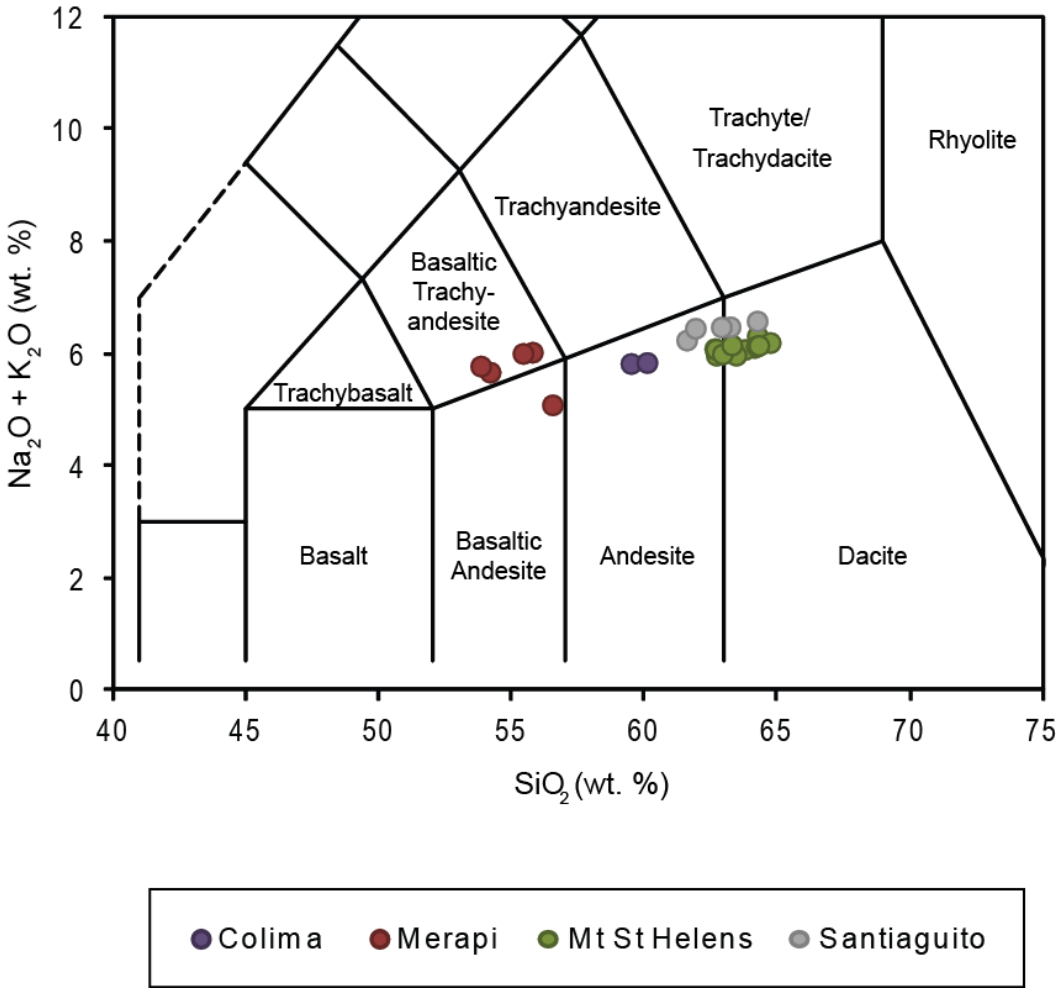

Figure 4.16: Total alkali-silica plot for the dome rock samples used in the current study from XRF data. Compositional boundaries are after Le Bas and Streckeisen (1991).

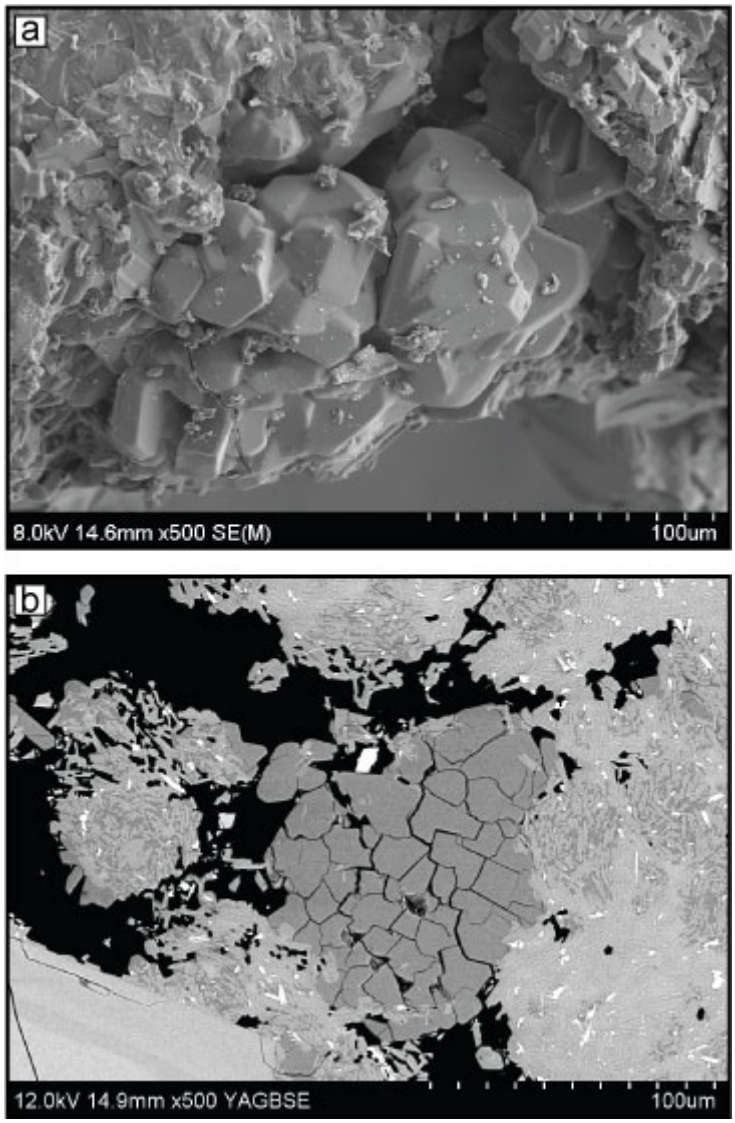

Figure 4.17: Backscatter electron micrographs of ‘massive’ cristobalite crystals from Santiaguito (a; SG.MTD.2) and Mount St. Helens (b; MSH.192).

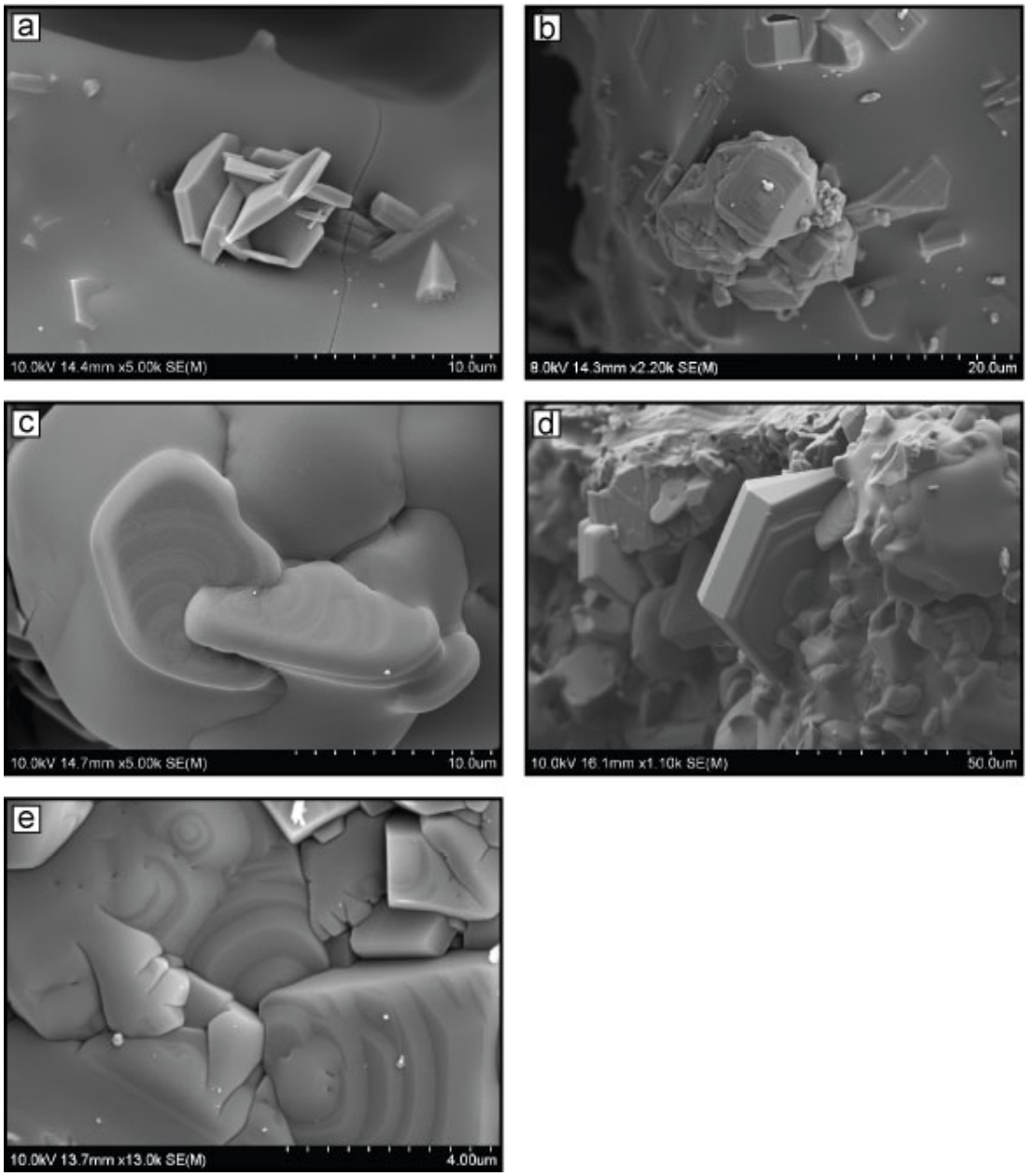

Figure 4.18: Scanning electron micrographs of the nucleation of platy (a) and euhedral (b) morphologies, and radial growth textures for platy (c, d) and euhedral (e) cristobalite.

4.4 Discussion

4.4.1 The presence of cristobalite in volcanic domes

The presence of cristobalite in dome rock samples from all locations studied suggests all volcanic domes are capable of crystallising cristobalite, and can be a source of respirable cristobalite-bearing ash. Evidence for the crystallisation of cristobalite in lava domes by both deposition from the vapour phase and devitrification of groundmass was found at all of the locations studied (Table 4.2); although, the contribution of each habit to the total abundance of cristobalite was sample dependent. Some samples were sourced from the same dome (e.g., at Santiaguito) or spine (e.g., at Mount St. Helens), highlighting the heterogeneity in crystallisation and deposition across a dome. This is likely due to the existence of pore networks and fractures which percolating vapours preferentially pass through as well as heterogeneity of temperatures; for example, between the dome surface and the core, or in areas of active extrusion. These differences in cristobalite content and resultant porosity increase uncertainty when attempting to define the eruptive and respiratory hazard before catastrophic failure.

4.4.1.1 Controls on vapour-phase deposition and morphologies

4.4.1.1.1 Effects of temperature and pressure

The well-ordered prismatic and platy crystals observed in dome rock samples from Soufrière Hills by Horwell et al. (post review; Appendix 4) appear to be two model end-members of variable crystal habits. The presence and morphological variability of both platy cristobalite, which is interpreted to be a pseudomorph after hexagonal tridymite (Horwell et al., post review; Appendix 4), and prismatic morphologies suggests variability in the pressure-temperature regime in the dome environment, since each polymorph occupies a different P-T stability field (Figure 2.1). The presence of platy cristobalite also implies a paramorphic transformation to cristobalite. Horwell et al. (post review; Appendix 4) have tentatively attributed the presence of the two different morphologies to a quantifiable difference in crystal impurities (see Chapter 5); however, the atomic structure of a crystal is also governed by P-T conditions, so we further propose that the type of polymorph crystallising depends on the combined effects of temperature, pressure and source composition (elemental abundance).

Temperatures in volcanic domes are estimated to be at or below approximately 850 °C (e.g., Barclay et al., 1998; Murphy et al., 2000). Cristobalite is stable at temperatures above 1470 °C, and must, therefore, crystallise and persist metastably at dome temperatures. Tridymite, however, is stable at temperatures above 870 °C, approximately dome temperature. Both

tridymite and cristobalite have been synthesised at temperatures below their stability field in the presence of a mineraliser, e.g., $Al_2(SO_4)_3$ and Na_2CO_3 (Chao and Lu, 2002a; Stevens et al., 1997). Al^{3+} can go into 4-fold coordination with oxygen and can therefore substitute for Si^{4+}. When such a substitution takes place, the charge imbalance is offset elsewhere in the silicate structure. This substitution in cristobalite can be stabilised by Na, Li, K, Ca and others (e.g.; Parise et al., 1994). Horwell et al. (2003b) identified trace amounts of aluminium and sodium in crystalline silica in Soufrière Hills ash, which has been confirmed for all current study locations (see Chapter 5). Therefore, we hypothesize that hexagonal tridymite may form initially when dome temperatures are near the tridymite stability field (i.e., at or above approximately 870 °C), whereas prismatic cristobalite will preferentially form below this temperature, facilitated by cation substitutions and according to Ostwald's rule of stages (Nývlt, 1995). This temperature dependence may account for the less frequent occurrence of hexagonal crystals in dome rock, since domes have an estimated upper temperature of approximately 880 °C (e.g., Soufrière Hills; Barclay et al., 1998). The effects of temperature on lattice substitutions, the degree of crystallinity, and the stability of cristobalite are discussed in detail in Chapter 5.

The depth of the dome rock will affect the pressure of crystallisation. Pressure is known to influence the silica crystal lattice, with the most extreme case being that of amorphous silica precipitation at >1 GPa (Hemley et al., 1988); therefore, depth of crystallisation may affect the crystal habit. Considering the case of dome formation at Mount St. Helens, the most extreme pressure difference in a static system would be that of the cryptodome versus an exogenous dome. For dome rock samples, we assume an average density of 2100 kg m^{-3} which is an approximation taken from the densities of the least and most dense cryptodome-derived pyroclasts from Mount St. Helens, ρ=1600 and 2300 kg m^{-3} (Hoblitt and Harmon, 1993). A depth of 500 m is taken as representative of the modelled depth for cryptodome formation (emplacement and pre-eruptive; Donnadieu and Merle, 2001). The pressure on a representative packet of dome material can be determined using:

$$P = \rho g h \qquad \textit{Equation 4.2}$$

where P is the magmastatic pressure, ρ is the density of the overlying rock mass, g is the acceleration due to gravity, and h is the depth below the surface of the volcano. From Equation 4.2, the crystallisation pressure for an average cryptodome sample was approximately 10.3 MPa, and the crystallisation pressure for an average exogenous dome sample approximately 2.1 MPa. Correspondingly, the pressure at the base of the Soufrière Hills dome is estimated around 7 MPa (Hicks et al., 2009). Woods et al. (2002) further show

that that pressure is > 1 MPa throughout the dome (with pressures near the centre of the dome of 5-10 MPa), except in a narrow boundary layer of 5-10 m near the surface where pressure decreases to atmospheric pressure (0.1 MPa). Although the calculation here is a first order approximation as it does not consider the effects of dynamic fluid pressure in a closed conduit system of interconnected pore networks, these pressures are well within the stability field for both tridymite and cristobalite (low pressure silica polymorphs), and orders of magnitude below that of pressure-induced precipitation of amorphous silica. Therefore, it is unlikely that pressure *directly* controls the preferential formation of either polymorph.

Pressure can also influence the abundance of substitutions in a crystal lattice (e.g, aluminium in hornblende; Schmidt, 1992). Both tridymite and cristobalite have very open structures which allow impurity ions to be incorporated, possibly influencing which of these structural modifications is adopted. So, while pressure probably does not control the structural arrangement directly, the degree of substitution and subsequent polymorph could be affected. The effects of pressure on lattice substitutions and morphology are further considered in Chapter 5.

4.4.1.1.2 Source of dissolved Si

Horwell et al. (post review; Appendix 4) propose two sources for dissolved Si: local redistribution and bulk transport. Local redistribution of silica occurs on a pore-size scale, where Si from the corrosion of amorphous SiO_2 or phenocrysts is re-deposited as crystalline silica. This would occur since the necessary silica-saturation level in a vapour is lower for cristobalite deposition than that required for deposition of amorphous silica (Renders et al., 1995). Bulk transport of silica describes the flow of Si-bearing gases from parts of the magmatic system where P-T conditions favour silica corrosion to parts of the dome where conditions favour mineralisation (see Equation 4.1). No textural evidence, however, has been previously provided for either process.

The embayment of vesicle walls in samples from Santiaguito and Mount St. Helens (Figure 4.14) are interpreted to be corrosional embayments, and the result of vapour flux. The ‘rind’ shows characteristic devitrification textures and, therefore, the inner edge is thought to be the original vesicle wall (demarcated in Figure 4.14). This is supported by the presence of vapour-phase cristobalite originating at this inner vesicle wall. The possibility of mineral deposition or precipitation forming the ‘rind’ is discounted since it is comprised of plagioclase microlites and oxides (in addition to crystalline SiO_2) with a similar distribution to the surrounding groundmass. Further, it is of a uniform thickness and mineral precipitation (e.g., of silica from water) would be expected to preferentially alter and precipitate silica on one surface. The possibility of a hydration halo, whereby a glassy rim has formed due to

rehydration of the melt, is discounted for similar reasons (although, some may be expected). The gap between the 'rind' and the pristine groundmass is interpreted as a 'path of least resistance', whereby fluid preferentially corrodes the more reactive glass than crystalline phases. The abundance of sub-micron vesicles throughout the 'rind' and their absence in the surrounding groundmass could further support the notion of interaction with corrosive fluids. If so, this may be the first textural evidence supporting the potential of volcanic gases to scavenge material from degassing pathways in a dome and contribute to local and/or bulk vaporous transport of Si. Considering the equilibrium equation of Equation 4.1, which outlines both precipitation and corrosion of SiO_2, higher pressures at depth would favour silica corrosion and lower pressures in the dome favour crystallisation. Contrary to this understanding, the Santiaguito sample was collected *in situ* from the surface of the dome. However, it is unknown whether this parcel of magma was held at depth before moving to shallower regions, thereby texturally preserving this process. Further examples are necessary to constrain the process recorded by this texture.

4.4.1.2 Controls on devitrification

No studies were found that address the mechanism producing devitrification cristobalite in volcanic domes; however, multiple studies from the ceramics industry investigate cristobalite crystallisation from amorphous SiO_2 under P-T conditions relevant to volcanic domes.

Direct crystallisation of cristobalite from glass is difficult and requires temperatures above 1000 °C (Sosman, 1965). However, studies on both natural rhyolitic and synthesised glass have shown that alkali-rich aqueous solutions increase devitrification rates (Bassett et al., 1972; Lofgren, 1971). In the presence of sodium and potassium salts, for example, α-cristobalite can form at 800 °C in as little as 2 hours (Bassett et al., 1972). Further, Na_2O, Na_2CO_3, K_2CO_3, and NaCl and KCl-bearing vapours can reduce the crystallisation temperature to 700 °C (Bassett et al., 1972; De Keyser and Cypres, 1961). Both studies are within the range of temperatures expected for volcanic domes.

The silica polymorph formed is dependent on the nature and size of cations incorporated within the structure, with Na^+ and K^+ leading to a less dense cristobalite structure (Bassett et al., 1972). Volcanic devitrification cristobalite in the current study, as well as that by Horwell et al. (accepted; Appendix 4), is known to contain up to 1.5 wt. % Na (see Chapter 5), potentially implicating alkali substitutions in reducing the crystallisation temperature in natural settings. It is likely that Na^+ preferentially substitutes compared to K^+ because of its smaller ionic radius (0.96 Å versus 1.3 Å), which facilitates the coupled, electrically-neutral substitution of Al^{3+} and Na^+ for Si^{4+} in the lattice (see Chapter 5). The structural substitution of Al^{3+} and Si^{4+} is common in rock forming minerals (Deer et al., 1996) and universally

occurs here due to the natural abundance of Al in volcanic glass. According to Pauling's rules on ionic coordination (Pauling, 1929), lower crystallisation temperatures will favour the larger elemental coordination number; that is, preferential substitution of Al for Si at lower temperatures.

The charge-balancing concentrations of Na^+ (and K^+, experimentally) preclude the formation of the tighter quartz lattice, which has a structural void of 1.4 Å, whereas cristobalite, at 1.7 Å, can spatially accommodate larger cations. These substitutions, combined with the low enthalpy of formation for cristobalite, results in the preferential devitrification of volcanic glass to cristobalite. We note that, in general, high temperature quartz has relatively greater levels of aluminium compared with low temperature quartz (e.g., Dennen et al., 1970; Perry, 1971; Scorrono, 1975); however, we hypothesize that this is directly related to increased lattice spacing at higher temperatures (Chapter 5), permitting the Si^{4+} substitution by Al^{3+} alongside interstitial trace cations (e.g., H and Li; Miyoshi et al., 2005).

The temperature required for rapid crystallisation (generally considered 2 hours experimentally) increases with increased cation size (e.g., $Na^+ < K^+$), which is also the order of increasing diffusion coefficients for the ions in glass (Bassett et al., 1972). Therefore, at the lower temperatures in volcanic domes than those used experimentally, the rate of devitrification (and corresponding cristobalite abundance in a sample) could be dependent on cation diffusion, with the greater diffusivity of Na^+ limiting the incorporation of K^+ and Ca^{2+} in volcanic cristobalite.

Rapid decompression can lead to a degree of undercooling which results in decompression-induced crystallisation. Hammer and Rutherford (2002) investigated the temporal evolution of feldspar crystallisation during isothermal decompression of equilibrated (780 °C, 220 MPa) dacitic Pinatubo pumice, and, in doing so, crystallised devitrification cristobalite (reproduced here as Figure 4.19, which has been adapted from their paper). Samples allowed to decompress to final pressures of 5-10 MPa (approximate dome pressures, as calculated above) contained particularly high levels of devitrification. Samples held at these pressures for 38 days were most effective at crystallising cristobalite, which although marked as quartz, show the indicative 'fish-scale' cracking and 'feathery' devitrification texture. According to the present ranking system for devitrification in samples, these samples would be assigned a progression rank of '+++' (e.g., Figure 4.9e and f). Williamson et al. (2010) estimated that cristobalite can form within hours to days, and these data lend credence to the rapidity with which cristobalite can form (i.e., < 38 days, and on the order of hours,. experimentally), as well as to the value of dome residence time and extrusion rate (discussed in Section 4.3.2) in crystallising devitrification cristobalite

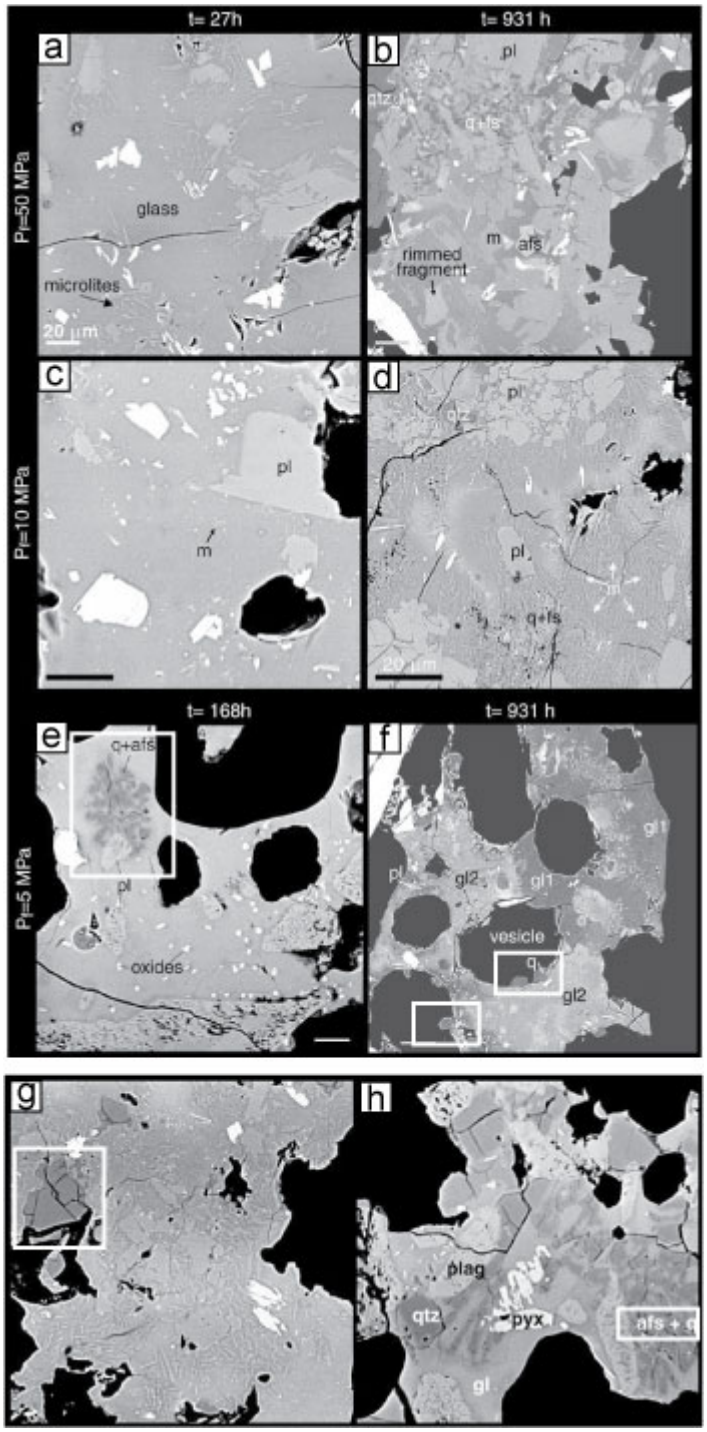

Figure 4.19: Backscatter electron micrographs of depressurisation-induced crystallisation adapted from Hammer et al. (2002; Figures 3 and 5 in their study). a)-f) pressure and duration dependent crystallisation of groundmass showing 'feathery' textures (b and d) identified as quartz, and 'fish-scale' cristobalite at P_{final} 10 MPa (g) and 5 MPa (h).

One sample in the experiments by Hammer and Rutherford (2002) also contains prismatic vapour phase cristobalite (Figure 4.19f). The sample used was pumice and assumed to have been cristobalite free; therefore, the vapour phase cristobalite is assumed to be an experimental product. Experiments were conducted in a closed system with no gas flux, thereby potentially supporting the local redistribution theory of Horwell et al. (post review; Appendix 4) discussed above. This would require Si exsolution, sourcing excess Si from plagioclase phenocrysts, glass, and the formation of microlites; the only other crystals present. A similar study on cristobalite-rich dome rock might reveal textural evidence of the effects of re-equilibrating cristobalite, which could be used to re-consider their experimental samples and confirm the observed cristobalite as experimental.

4.4.1.3 Cristobalite nucleation

The presence of both vapour phase and devitrification cristobalite in the majority of samples investigated here (Table 4.2) suggests these can be coeval crystallisation mechanisms. The existence of samples lacking one habit or the other in this study as well as that by Horwell et al. (post review; Appendix 4), however, suggests that they may be independent processes. Devitrification cristobalite has been observed in magmatic compositions (and therefore associated glass compositions) from trachybasaltic andesite to dacite in the present study. Likewise, vapour phase cristobalite has been observed from trachybasaltic andesite to dacite in the current study, and to rhyolite for Chaitén dome samples (from images in Lowenstern et al., 2012). Horwell et al. (post review; Appendix 4) suggest a potential role of devitrification cristobalite as a nucleation point for vapour phase deposition to lower the energy required, as discussed in Section 4.4.1. This idea is not discounted here since all samples which had vapour phase crystals also experienced devitrification, excluding SH 127. This sample, however, had less than 2 wt. % cristobalite and only one occurrence of vapour phase crystals observed in the rock chipping, providing insufficient evidence. Further, the presence of ‘nano-cristobalite’ in the glass (and therefore not identifiable by SEM) is possible as observed for devitrification pyroxenes and plagioclase by Sharp et al. (1996) in the Ben Lomond lava dome, Taupo Volcanic Centre, and for cristobalite in ash from the eruption at Chaitén volcano (Reich et al., 2009).

Devitrification has been experimentally shown to begin at the glass surface and continue progressively inward (Wyart, 1949), as well as to nucleate heterogeneously and grow internally within vitreous silica (Wagstaff, 1968); evidence of surface and internal nucleation was observed here for both ‘feathery’ and ‘myrmekitic-like’ textures. Internal growth within vitreous silica may help explain the presence of cristobalite nanofibres in ash from Chaitén volcano (Reich et al., 2009), which appear to be growing within an amorphous host grain by

TEM imaging. Reich et al. (2009) propose that cristobalite nanofibres may form by vapour phase reactions in the presence of fragments of glass and a reducing agent (e.g., carbon monoxide) in the explosive column (> 700 °C). The observations here offer the possibility of internal nucleation to their study, which argued that amorphous silica only provides a surface for nucleation.

Limited migration of a cation through amorphous silica (e.g., Na^+ and K^+) is sufficient to nucleate a new phase (Bassett et al., 1972). Migration of an adsorbed or integrated cation through the glass lattice ruptures Si—O—Si bridges, collapsing the structure and facilitating devitrification by lowering the crystallisation temperature (e.g., 400 °C; Mougey et al., 1958). Applicably, silica powder heated to just below its bulk crystallisation temperature in the presence of NaCl becomes an effective substrate for the formation of ice crystals from super-cooled vapour (Bassett et al., 1968). While this example considers opposite vapour conditions to those in volcanic domes, the nucleation potential of groundmass and glassy vesicle walls can be increased by the presence of foreign or integrated cations, potentially facilitating both devitrification and deposition at temperatures below those calculated for volcanic domes (e.g., ~850 °C at SHV; Barclay et al., 1998).

Often, growth of cristobalite appears to have nucleated on a plagioclase crystal (e.g., Figure 4.11), perhaps resulting in modulations parallel to the (202) plane. The agreement between the crystal lattice spacing of (010) plagioclase (d=0.404) and that of (101) cristobalite (d=0.406) is very good, making growth of the (101) cristobalite plane that of least energy at the interface. Charge balancing at the interfacial unit cell would be sufficiently accomplished by the abundance and diffusivity of Na^+ in the glass.

The ‘feathery’ texture, which has also been observed in volcanic tuffs (e.g., Vaniman, 2006, and is commonly described as 'plumose'), is interpreted to be mostly-complete patches of devitrification cristobalite between groundmass crystals (e.g., microlites). The ‘myrmekitic-like’ texture, however, is interpreted as an arrested reaction that was limited by diffusion, analogous to that seen in metamorphic growth (e.g., Peterman and Grove, 2010). Sub-solidus reaction textures like the ‘feathery’ and ‘myrmekitic-like’ therefore have the potential to provide records of temperature and pressure conditions. Although not pursued here, a reaction mechanism could be modelled for devitrification cristobalite using information on diffusion and identified cristobalite sizes and textures (see Table 4.2), similar to that which has been done for the formation of myrmekites (Yuguchi and Nishiyama, 2008).

Hydrothermal reconstruction is sensitive to temperature and water vapour content, where vitreous silica exposed to supercritical water vapour above 374 °C transforms to cristobalite (Wyart, 1949). Water vapour is the most abundant gas at degassing volcanoes, and could

therefore play a substantial role in the crystallisation chemistry of cristobalite. Water vapour works to decrease the activation energy of crystallisation by serving as a source of oxygen; the energy required for the intrinsic crystallisation from amorphous silica is 134 kcal mol^{-1}, whereas the energy required in the presence of water vapour is 77 kcal mol^{-1} (Wagstaff and Richards, 1966). Re-crystallisation is encouraged in the presence of oxygen at the crystal-glass interface, where it weakens the glass by breaking Si—O bonds (Wagstaff and Richards, 1966).

4.4.2 Cristobalite abundance and duration of formation

4.4.2.1 Influence of Dome Residence Time

A comparison of whole rock SiO_2 and crystalline SiO_2 shows that dome rocks of all magmatic compositions are able to crystallise cristobalite (Figure 4.20). The data, however, show that samples above an intermediate composition (e.g., ~59-60 wt. %) contain substantially more cristobalite than samples below. High viscosities (e.g., dacitic magmas at dome temperatures have viscosities around 10^7 Pa s, whereas andesites are nearer 10^4 Pa s (Spera, 2000)), and correspondingly slow extrusion rates, result in prolonged dome residence times (DRT; the duration for which a magma packet resides in a dome), where samples could be held at suitable crystallisation conditions for longer durations.

No constraints on vapour phase depositional kinetics are available; however, for devitrification cristobalite, crystallisation occurs by a continuous growth mechanism following linear growth kinetics (Wagstaff, 1969). Therefore, the abundance of devitrification cristobalite for a magma packet held at suitable crystallisation conditions could be partially constrained by time. This is supported by the decompression study of Hammer and Rutherford (2002), for which there was a greater abundance of groundmass cristobalite (labelled quartz; Figure 4.19) for longer duration experiments. Therefore, the abundance of devitrification cristobalite would be inversely proportional to the extrusion rate. Accordingly, in a concurrent study on ash samples from Soufrière Hills volcano, Horwell et al. (submitted-a; Appendix 4) found that ash sourced from slowly extruded domes is more abundant in cristobalite than ash from rapidly extruded domes, and show a correlation between DRT and cristobalite content for samples resulting from faster extrusion rates.

Analogously, a difference in viscosities could be sufficient to suppress the crystallisation of devitrification cristobalite; or, there may be a minimum viscosity for which cristobalite can crystallise (with further relevance for the plastic cryptodome samples). Supporting this,

Horwell et al. (post review; Appendix 4) note that the cristobalite content in Soufrière Hills dome rock is predominantly vapour phase in origin, whereas samples from Santiaguito and Mount St. Helens show extensive devitrification. Dome rock samples from a rhyolitic dome (e.g., Chaitén, Chile) as well as additional samples from the current, less-felsic sample suite (e.g., Unzen, Colima and Merapi) would substantially strengthen this viscosity-dependent interpretation.

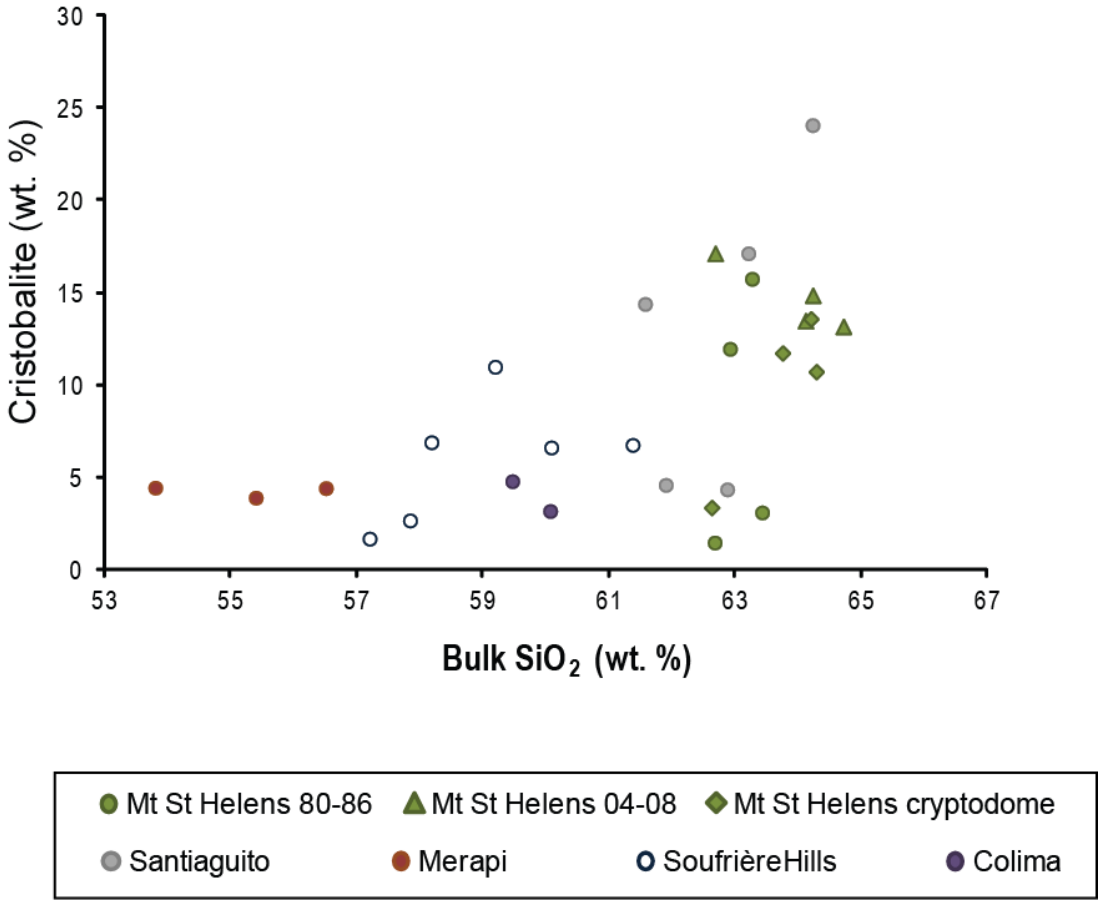

Figure 4.20: Comparison of cristobalite content determined by XRD with whole-rock SiO_2 content determined by XRF for all locations studied. Data for Soufrière Hills are included as an intermediate composition, and are taken from Horwell et al. (post review; Appendix 4).

A comparison of DRT with cristobalite abundance for the well-constrained sample suite from Mount St. Helens exhibits a visually asymptotic line for dome rock samples, with an average for asymptote-nearing samples of approximately 14 wt. % (Figure 4.21, dashed line). This correlation is somewhat tenuous as different sections throughout the relationship are comprised of data from different eruptive periods; however, the general shape of the curve may imply that cristobalite content increases with residence time until a critical value is reached. DRTs were estimated for the 2004-2006 samples by Pallister et al. (2008) using collection locations and known lineal rate of extrusion to track samples back to the vent. Residence times for the 1980-1986 samples were taken from the USGS sample record (unpublished). All cryptodome samples have been assigned a maximum DRT of 62 days, representative of the duration from March 17, 1980, the approximate date on which the first seismic activity was recorded (Endo et al., 1990), and May 18, 1980, the day of the eruption. Curiously, a possible recharge of the magmatic system by hotter magma at depth recorded in Spine 4 (2004-2008; Blundy et al., 2008) did little to influence the cristobalite abundance (samples SH.309.1A, SH.315.4, SH.315.5) relative to other samples. Two samples (circled) which do not conform to the paradigm are the plastic 1980 cryptodome samples. Extrusion rate may better correlate with cristobalite content than DRT (as determined for ash samples in Horwell et al., submitted-a; Appendix 4), since DRT does not directly reflect activity; however, data were not available for a sufficient number of samples.

Williamson et al. (2010) have suggested that cristobalite can form rapidly at the Soufrière Hills dome, perhaps between hours to days after a magma package is injected into the dome base. The best constraints on dome samples from Mount St. Helens, 1980-1986 suggest up to 8 wt. % can form in three days (MSH.67) and up 18 wt. % in less than three weeks (e.g., MSH.326.2 and MSH.315.5; Table 5). Dome collapse ash samples from Soufrière Hills confirm cristobalite abundances of 5 wt. % after just 1 day of growth and 15 wt. % after 1 month (Horwell et al., submitted-a; Appendix 4), indicating that even a short residence time can result in cristobalite-rich ash. We note that, for the case of ash, it is difficult to constrain the presence of cristobalite to a newly formed dome since the source may include older material, especially at Soufrière Hills which has been active since 1995 (and historically active for much longer). Similarly, Horwell et al. (2010a) found 16 wt. % cristobalite in ash after three months of dome growth at Chaitén volcano, Chile. Dome rock samples from Chaitén were not available for the present study to consider whether this rapid crystallisation was devitrification or vapour-phase driven (with additional implications for Figure 4.20); however the Soufrière Hills sample used by Williamson et al. (2010), MVO287, was found to have both devitrification and vapour phase cristobalite (Horwell et al., post review; Appendix 4).

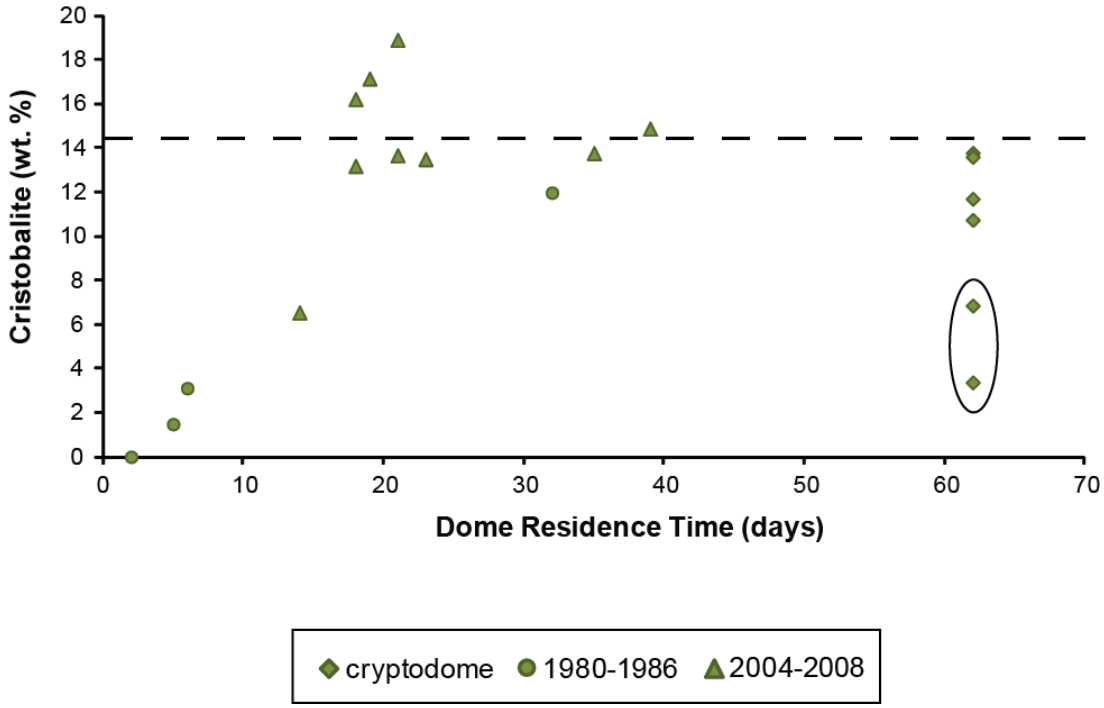

Figure 4.21: Comparison of cristobalite abundance with dome residence time (DRT) for dome rock samples from Mount St. Helens. The two data points circled are discussed further with respect to Figure 4.24. The dashed line is an average of all cristobalite values above 10 wt. %.

A sample from the Mount St. Helens cryptodome (MSH.BD.4) shows evidence of a final decompression event (Figure 4.22), recorded by frozen, burst melt inclusions in feldspar, analogous to those observed by Williamson et al. (2010). This is a sample of 'grey' dacite, which Hoblitt and Harmon (1993) suggest underwent a second vesiculation event during the 18 May 1980 lateral blast. This sample, along with MSH.BD.03 (another 'grey' dome rock sample), had substantially less cristobalite than texturally-identifiable 'black' cryptodome samples which did not undergo a secondary vesiculation event (3-6 wt. % versus 11-13 wt. %). It is possible that the grey dacite originated from a fresher batch of magma or was sufficiently ductile until the moment of depressurisation to limit sub-solidus cristobalite crystallisation. Both possibilities would limit the 'real' (fresher batch) or 'effective' (sufficiently ductile) dome residence time, and may account for the seemingly anomalous results of the two samples circled in Figure 4.21. This plasticity would also account for the flow alignment observed for microlites in cryptodome samples (Figure 4.13). Hoblitt and Harmon (1993) observed no difference in chemistry between 'grey' and 'black' samples, and Cashman (1988) identified no qualitative difference in microlite abundance or quantitative difference in crystal size distribution, concluding microlite nucleation was probably triggered

by a single intrusion of material. Cashman (1988) also suggests that microlite crystallisation occurred at depth rather than in the dome, which is supported here by incorporation of microlites within patches of devitrification cristobalite (e.g., Figure 4.6b). Therefore, based on these studies, material was likely too ductile to facilitate crystallisation.

In magmas, in general, prolonged cooling results in few, large crystals whereas rapid cooling results in many, smaller crystals. A similar distribution for size frequencies was qualitatively observed for cristobalite crystals in dome rock; however, insufficient data was available to compare mean crystal size to dome residence time and/or extrusion rate. The 'massive' crystals identified in samples from Mount St. Helens and Santiaguito lend credence to the notion of prolonged growth and warrant further research, considering the Brujo dome was active from 1959-1963, without experiencing a major dome collapse, and Mount St. Helens cryptodome samples were at ~900 °C (Cashman, 1992; Rutherford and Hill, 1993) for ~60 days (Pallister et al., 2008).

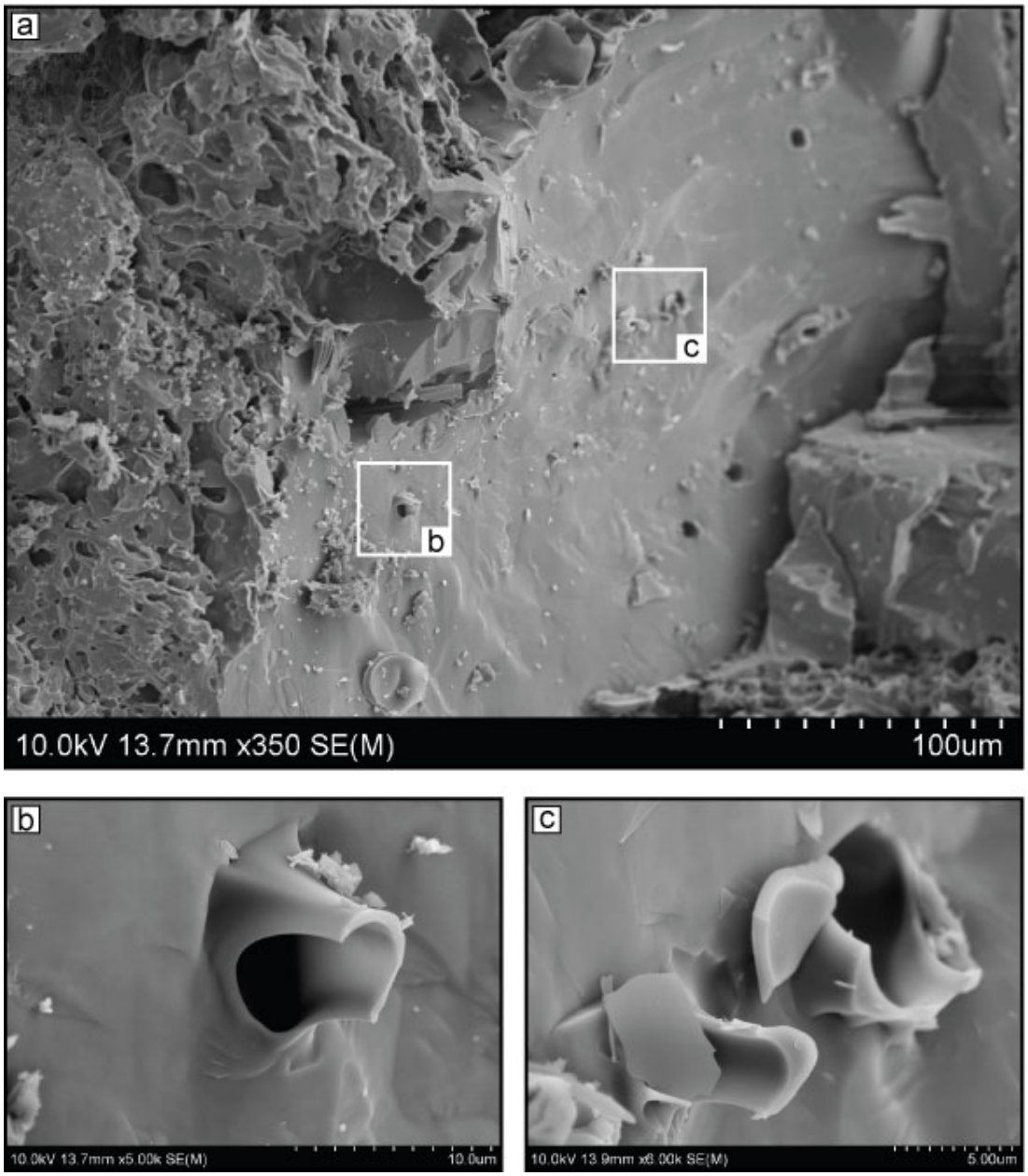

Figure 4.22: Scanning electron micrographs of ruptured plagioclase phenocryst melt inclusions (decompression features) in MSH.BD.4.

Table 4.5: Dome residence times for samples from Mount St. Helens.

Volcano	Sample	Origin	Dome Residence Time (days)
Mount St. Helens, USA			
Dome rock 04-06	MSH.304.2A1	Spine 3	23
	MSH.304.2A9	Spine 3	23
	MSH.304.2G	Spine 3	23
	MSH.305.1A	Spine 3	35
	MSH.309.1A	Spine 4	18
	MSH.315.4	Spine 4	21
	MSH.315.5	Spine 4	21
	MSH.316.1	Spine 5	39
	MSH.321	Spine 6	14
	MSH.326.2	Spine 7	19
Dome rock 80-86	MSH.33	S Side of dome	--
	MSH.67	W Side of dome	3
	MSH.103	Federal building	2
	MSH.127	Talus	5
	MSH.131	W Side of talus	6
	MSH.135	Talus from spine	328+
	MSH.156	Talus	--
	MSH.201	N side of spine	--
Cryptodome (1980)*	MSH.166	cryptodome	62
	MSH.192	cryptodome	62
	MSH.BD.1	cryptodome	62
	MSH.BD.2	cryptodome	62
	MSH.BD.3	cryptodome	62
	MSH.BD.4	cryptodome	62
Edifice	MSH.ED.1	Pre-1980 edifice	--
Dyke	MSH.DY.1	Toutle River valley	--

*All cryptodome samples are assigned a maximum possible duration of 62 days.

4.4.2.2 Enrichment of bulk SiO_2

Bulk transport of silica would be expected to increase the total abundance of silica for a packet of dome rock. Indeed, Horwell et al. (post review; Appendix 4) compared bulk SiO_2 concentrations in dome rock with those in pumiceous samples from Soufriere Hills and found dome rock to be enriched in SiO_2 compared to pumice by 2 wt. %. Any control on either whole-rock SiO_2 or crystalline SiO_2 by the other would be overshadowed by the range of starting compositions amongst volcanoes studied here (Figure 4.16); therefore, the individual case of Mount St. Helens, for which there is a well constrained sample history, is considered.

A comparison of whole-rock SiO_2 and crystalline SiO_2 for Mount St. Helens reveals no obvious correlation (Figure 20); although, no sample above 63.5 wt. % SiO_2 has less than 10 wt. % cristobalite. Accordingly, no correlation was observed between DRT and whole-rock SiO_2 (Figure 4.23). However, a correlation would assume that (1) bulk transport is entirely responsible as a source for dissolved Si, and (2) that vapour phase deposition is the overriding contributor to cristobalite content. The range in cristobalite abundances in the present study allows for a comparison of bulk SiO_2 concentrations between dome rock samples that experienced extensive cristobalite crystallisation and those which experienced less, assuming a cristobalite-free sample as the base material for crystallisation to occur.

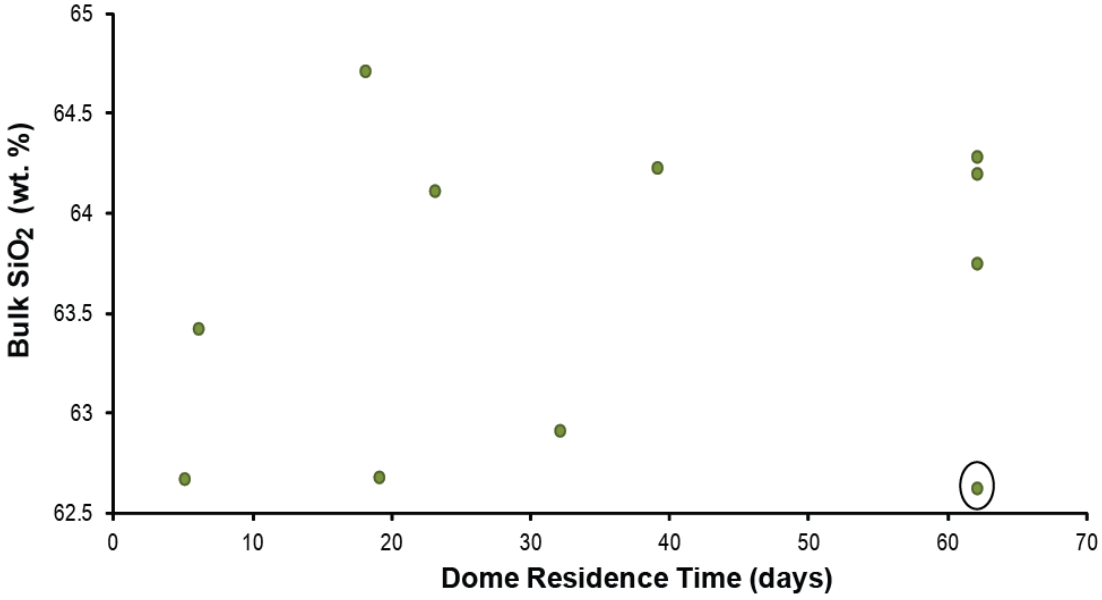

Figure 4.23: Comparison of bulk SiO_2 content with dome residence time for samples from all eruptive periods from Mount St. Helens.

Two theoretical end-member scenarios can be envisaged in a sample with abundant cristobalite, whereby a sample can either be rich in vapour phase cristobalite or rich in devitrification cristobalite (Figure 4.24). In the case of the former, a positive correlation would be expected since bulk transport is responsible for providing excess Si. In the case of the latter, however, where devitrification necessarily implies local redistribution, no change in bulk SiO_2 is expected. When applied to data from Mount St. Helens, all low-SiO_2 cristobalite samples (MSH.BD.4, MSH.127, and MSH.131) plot according to the 'little cristobalite' oval of Figure 4.24. Samples that plot in the 'devitrification dominant' oval (MSH.326.2, MSH.135, and MSH.201) contain entirely or mostly devitrification cristobalite (Table 4.2). Samples that plot as 'vapour phase dominant' (MSH.309.1A, MSH.304.2A1, MSH.316.1, MSH.BD.1, and SH.166) contain a substantial amount of vapour phase crystals (average crystal size of approximately 30-60 μm), but are a mixture of both devitrification and vapour phase cristobalite. Considering the overall distribution of samples in Figure 4.20, no samples contain high bulk SiO_2 and low cristobalite, further suggesting an influence of cristobalite enrichment on bulk composition. Indeed, Horwell et al. (submitted-a; Appendix 4) observed a 2 wt. % bulk SiO_2 increase in cristobalite-rich Soufrière Hills samples over a pumiceous control, and attributed the difference to vapour phase cristobalite and vaporous bulk transport of Si.

Horwell et al. (post review; Appendix 4) note that the addition of a substantial quantity of vapour-phase cristobalite would manifest as a modest increase in the total silica content of a sample. In the case of a cristobalite-free sample at Soufrière Hills, the addition of 10 wt. % cristobalite would increase the bulk SiO_2 content by only 4.3 wt. %, which is undetectable within the range of bulk SiO_2 contents measured. Considering the partitioned contributions of devitrification and deposition discussed above, however, this represents an extreme case. All of the samples in the present study with > 10 wt. % cristobalite contain more than half of the cristobalite present as a product of devitrification (Table 4.2), which involves local redistribution of silica. Therefore, a sample of 10 wt. % cristobalite would have an expected increase in bulk SiO_2 due to bulk transport of less than 2.2 wt. %, even less distinguishable within their observed range.

4.4.2.1 Maximum Cristobalite Abundance

Horwell et al. (submitted-a; Appendix 4) have proposed the idea of an upper limit for cristobalite content, which they determined to be approximately 20-25 wt. % for ash from Soufrière Hills. A maximum cristobalite capacity in dome rock is unknown, however, due to the competing effects of cementation and pressurisation on dome stability (Horwell et al., post review; Appendix 4), and spatio-temporal variability in crystallisation conditions. We

note, however, that an upper limit reported as a wt. % of the host rock is inevitable due to the presence pore space, phenocrysts and prior/concurrent crystallisation of microlites, since the available groundmass for devitrification cristobalite is limited. Therefore, each volcano or eruption may have a distinct upper limit.

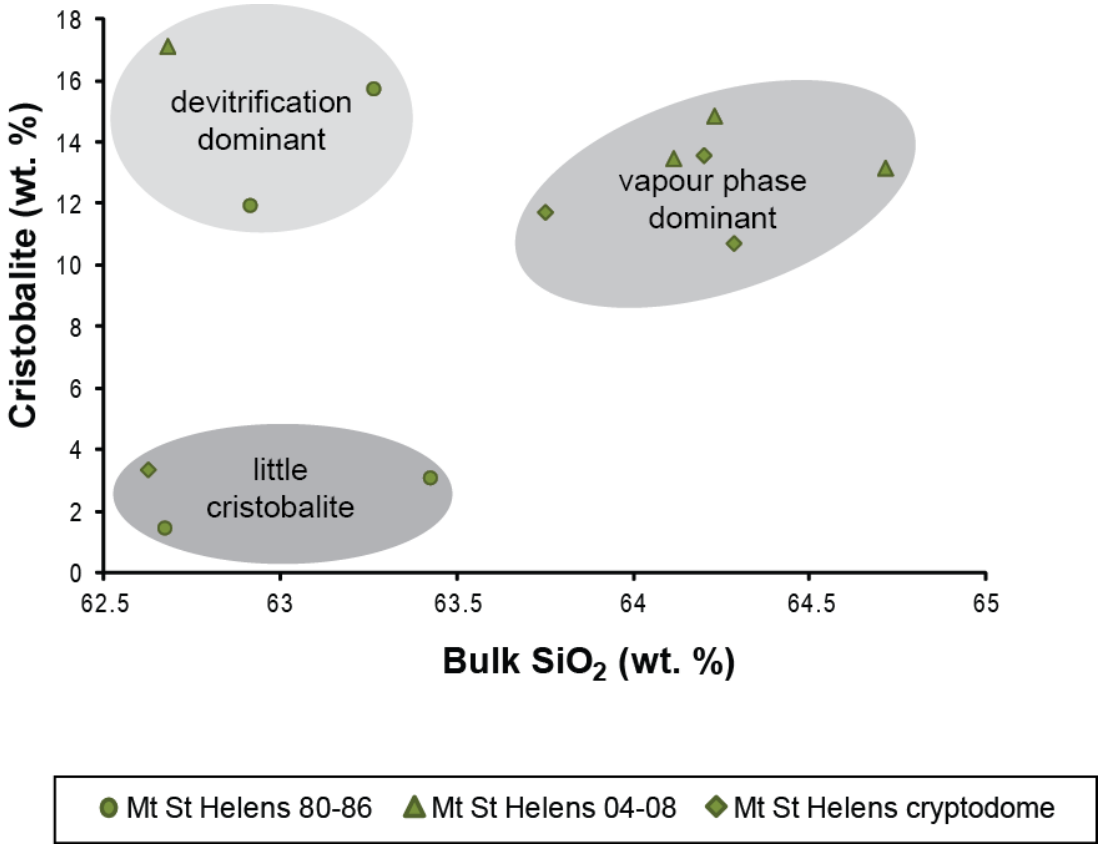

Figure 4.24: A theoretical model for the influence of cristobalite origin and abundance (by XRD) on whole-rock SiO_2 content (by XRF) showing expected envelopes for samples dominated by devitrification versus vapour phase cristobalite. Axes correspond to those for Mount St. Helens samples.

Soufrière Hills dome rock has a maximum concentration of approximately 10 wt. % (Horwell et al., post review; Appendix 4), roughly half of the abundance determined for Soufrière Hills ash (20-25 wt. %; Horwell et al., submitted-a; Appendix 4). This difference is likely due to preferential elutriation of cristobalite into finer ash fractions upon dome collapse (Horwell et al., 2003b). However, the relationship between abundance in dome rock and ash is not straightforward, as both dome rock and ash from Mount St. Helens contained

approximately 20 wt. % (Table 4.3, and see Table 6.7 for ash values). Similarly, dome rock and ash from, Colima, Santiaguito and Unzen all contained similar abundances of cristobalite (approximately 5, 20 and 10 wt. %, respectively); however, ash from Merapi contained roughly double that of dome rock (10 and 5 wt. %, respectively). The discrepancy likely arises due to the different energies involved in fragmentation and transport, and is considered further in Chapter 7.

4.5 Conclusion

This chapter systematically characterises the nature of cristobalite in samples of dome rock in order to elucidate its presence and formation in the dome environment. Samples from all volcanoes were found to contain cristobalite with some quartz but no tridymite observed at any of the volcanoes, in contrast to previous investigations (e.g. Blundy and Cashman, 2001). Abundance is sample dependent, making it difficult to determine bounds for individual locations. No samples were found to exceed ~20 wt. % cristobalite, providing evidence of an upper limit for abundance in dome rock.

Textural, compositional, and structural evidence was found to support crystallisation of cristobalite by both devitrification of groundmass glass and deposition from a silica-saturated vapour. This evidence suggests that cristobalite in dome rock is entirely pneumatolytic, resulting from the sustained temperature and vapour flux in a volcanic dome. Vapour phase cristobalite exists in both platy and prismatic morphologies; however, the euhedral varieties previously observed at Soufrière Hills (Horwell et al., post review; Appendix 4) appear to be well-ordered morphological end-members. Devitrification is proposed to progress as a function of duration at suitable crystallisation conditions; therefore, the abundance of cristobalite in dome samples may progressively increase with time. Devitrification cristobalite presents multiple textures; however, confirmation of the mechanisms by which they form would require petrological experimentation.

Based on the well-constrained samples collected from Mount St. Helens, cristobalite crystallisation can commence immediately upon a packet of magma entering the dome environment, and shows a loose correlation with time. A more effective comparison would perhaps be extrusion rate, as was seen by Horwell et al. (submitted-a; Appendix 4); however, those data are neither directly available nor are there enough data available in the literature to calculate it for a sufficient number of samples.

Textural observations help constrain the mechanisms by which cristobalite forms in volcanic environments, providing the first discussion of cristobalite crystallisation in a volcanic setting below its stability field. The increased short- and long-range lattice order due to heating (see Chapter 5) combined with cation diffusion can likely provide a site of nucleation. Overall, devitrification to form cristobalite, at temperatures determined for volcanic domes, is likely to be facilitated by the local abundance of Al within volcanic glass and the high diffusivity of Na. The role of cation substitutions on cristobalite crystallisation seems critical, and is therefore addressed in greater detail in Chapter 5.

The identification of cristobalite with similar habits in dome rocks from all volcanoes studied implies cristobalite may be a hazard at dome forming volcanoes worldwide, and further consideration of the effects of cristobalite-rich ash on respiratory health is warranted (see Chapter 6).

5

Structure and composition of volcanic cristobalite with implications for crystallisation and toxicity

Abstract

The fundamental toxicity of a particle is governed by intrinsic chemical and physical properties (Fubini and Otero Areán, 1999). Here, we assess the chemistry of volcanic crystalline silica according to its compositional purity (i.e., deviation from pure SiO_2), and the physical nature according to its structural perfection and thermal history. Both dome rock and ash samples are investigated to confirm that properties identified in rock samples are applicable to health studies, and that no alteration takes place during the eruption, transport, or deposition of ash. Electron microprobe analyses quantify the presence of aluminium and sodium in all samples of volcanic cristobalite, which is shown by XRD and differential scanning calorimetry to alter the crystal structure as well as thermodynamic properties. Cristobalite crystals are compositionally distinct from quartz, and contain up to 4 wt. % aluminium. They undergo the α-β transition at ~200 °C, near the low end of the accepted 170-270 °C range, implying a disordered crystal structure. Constraining this chemical and resultant structural modification expands the discussion on cristobalite crystallisation in a volcanic dome, which is introduced in Chapter 4. The presence of lattice substitutions leads to a more open crystal structure, likely permitting formation at temperatures below the cristobalite stability field. Devitrification is likely facilitated by temperature, hydration, local abundance of Al within glass and the high diffusivity of cations (e.g., Na). Exposure to volcanic cristobalite will always be to aluminium-containing, structurally modified α-cristobalite, and these chemical and physical modifications could partly account for the toxicity of volcanic ash being lower than expected (see Chapter 6).

Acknowledgements

Electron microprobe calibration was carried out by Chris Hayward at the University of Edinburgh with the author present. Thermal XRD was carried out by Jens Najorka (Natural History Museum, London) and by Gary Oswald (Dept. of Chemistry, Durham University) with the author present. The differential scanning calorimetry analysis was carried out in collaboration with Lian Hutchings, Department of Chemistry, Durham University.

Work on cross sections of ash from Sakurajima was carried out by the author with the assistance of Leon Bowen (Dept. of Physics, Durham University) on samples from Sarah Hillman. This work was independent of her MSc thesis, and was not included in the manuscript that resulted from her thesis (Hillman et al., 2012; Appendix 4).

Thanks to Professor Michael Carpenter (University of Cambridge), Dr. Gordon Cressey and Dr. Jens Najorka (Natural History Museum, London) for comments on a manuscript version of this chapter.

5.1 Introduction

Cristobalite forms in volcanic lava domes through vapour-phase mineralisation and devitrification and persists metastably at ambient conditions (see Chapter 4). It is found in preference to quartz in volcanic domes since its formation is kinetically favoured (Chapter 4; Brodie and Rutter, 2000), and because of the large activation energy required for the reconstructive phase transition from cristobalite to quartz. Cristobalite is stable at high-temperatures and low pressures (1470-1728 °C at 1 atm.) in its cubic, beta (β) form, and undergoes a spontaneous, displacive phase transition to tetragonal alpha (α) cristobalite between approximately 170 and 270 °C upon cooling (Frondel, 1962). A pilot study using X-ray diffraction (Claire Horwell, Personal Communication, 2010) observed β-cristobalite in volcanic ash; however, due to this transition, β-cristobalite should not be preserved in ambient conditions.

Ash from dome collapse eruptions has been found to contain up to 20 wt. % cristobalite (Horwell et al., submitted-a; Appendix 4, and see Chapter 6), which has led to concern for exposed populations as crystalline silica is a known human carcinogen and exposure can result in silicosis in industrial settings (Beckett, 2000). It has long since been understood that the toxicity of a particle is governed by intrinsic physicochemical characteristics (Fubini and Otero Areán, 1999; International Agency for Research on Cancer, 1997), and that the toxic potential of crystalline silica has been shown to vary by origin (Donaldson and Borm, 1998). Therefore, the control a source exerts on the mineralogy will consequently affect toxicity.

Crystal formation is governed by temperature, pressure and composition (see Chapter 4); therefore, the 'intrinsic factors' identified by the IARC (1997) (which, along with 'external factors', result in the 'variable' quartz hazard) are subject to the amalgamated influence of these three variables. These three controls, however, can be treated as analogous variables, with the outcome being structural and compositional modification of a crystal. This chapter aims to characterise the crystal structure and quantify the role of cation substitutions (which were postulated in Chapter 4 to facilitate cristobalite crystallisation at temperatures below its stability field). The crystal structure is discussed through the thermochemistry of the α-β phase transition, and crystal composition through electron microprobe analysis (EMPA). The presence of lattice substitutions has immediate implications for the formation of volcanic cristobalite (Chapter 4) as well as its toxicity (Chapter 6).

It has been suggested that variable crystallinity may be related to fibrogenicity (Altree-Williams and Sprogis, 1982), and sequential rankings based on a crystallinity index, scaled from 1-10 (Murata and Norman, 1976; Shoval et al., 1991), may be related to the specific

toxicity and fibrogenicity of quartz. Indeed, the importance of crystallinity to the toxicity of particles has been demonstrated for SiO_2 (Kaewamatawong et al., 2006). Additionally, association with, or contamination by, substances other than silica might activate or blunt quartz fibrogenicity and carcinogenicity (Donaldson and Borm, 1998; Fubini, 1998). In this way, the classic pro-inflammatory response elicited by crystalline silica may be modified by the addition of a range of compounds; in particular, treatment with aluminium (Al) salts lessens quartz toxicity (Begin et al., 1986; Duffin et al., 2001). Low levels of Al have been detected in volcanic cristobalite by SEM-EDS (Horwell et al., 2003b), and quantified at less than 3 wt. % at Soufrière Hills volcano (Horwell et al., accepted; Appendix 4). The presence of Al has been proposed as a potential passivating factor for volcanic cristobalite, supporting evidence from toxicity assessments (see Chapter 6) that show cristobalite-bearing ash to be more benign than expected.

Having extensively characterised the presence of cristobalite in samples from dome forming volcanoes in Chapter 4, this chapter approaches the question of variable toxicity from a mineralogical standpoint so that toxicity studies can be re-interpreted in light of the factors which control cristobalite formation. From the discussion of temperature and pressure on crystal formation in Chapter 4 (Section 4.3.5.1), it is believed that any pressure effect will be masked by temperature and composition; therefore, only the effects of temperature and composition are investigated here.

5.2 Materials and Methods

Cristobalite composition was investigated for dome rock samples from the locations outlined in Chapter 4, and are listed in Table 5.1: Colima (n=2), Merapi (n=5), Mount St. Helens (n=20), Santiaguito (n=4), and Unzen (n=2). The composition of volcanic cristobalite in thin sections of volcanic dome rock was quantified by electron microprobe analysis (EMPA) following qualitative identification as SiO_2 by energy dispersive X-ray spectroscopy (EDS). Crystals were analysed for Si, Al, Na, K, Fe, Ca, Ti, Mg, and Mn (see Chapter 3 for further details and conditions used for EMPA). Based on detection limits, data were only used when the sum of elements detected was 100 ± 0.8 wt. %. Therefore, there are fewer data points used than the total number of spot analyses, and the number of viable analyses is reported for each volcano.

Field emission scanning electron microscopy (FE-SEM) was used to confirm the presence of characteristic 'fish-scale' cracking in cristobalite in polished resin-mounted ash particles (as observed in dome rock thin sections in Chapter 4). Energy dispersive X-ray spectroscopy (EDS) was used to qualitatively confirm the presence of cation substitutions in these ash samples, which were not examined by EMPA.

The crystal structure of volcanic cristobalite was assessed by X-ray diffraction (XRD) for a subset of samples: bulk ash samples MBA5/6/99 and MBA12/7/03 from Soufrière Hills, the respirable sample MRA5/6/99 (which was separated from MBA5/6/99), isolates of crystalline silica from volcanic ash using the Talvitie method (from MBA5/6/99) and heavy liquid separation (from MBA12/07/03) (see Chapter 3 for separation techniques), and dome samples MVO1406 (from Soufrière Hills), SG.MNJ.01 and SG.MTD.02 (Santiaguito dome rock samples). Samples (of ash and dome rock) were run by XRD under ambient conditions as well as with thermal XRD from 30-300 °C (through the α-β transition) in order to consider its metastable structure and transition temperature compared to that of well-characterised cristobalite standards (Hemenway and D.K. Smith samples from the Natural History Museum, London). Patterns were collected isothermally every 5 °C to allow for a sequential, snap-shot visualisation of the changes in diffraction peak locations. Samples of volcanic ash were also heated to 300 °C and cooled at different rates (ambient cooling versus rapid quenching in liquid nitrogen) to investigate whether it is possible to modify the crystal structure by controlling the rate of cooling (e.g., preserve β-cristobalite).

The thermochemistry of the α-β cristobalite transition was investigated by differential scanning calorimetry (DSC) to constrain further its thermal history in sample MBA5/6/99. These results provide a more accurate transition-temperature range than thermal XRD as

data are unobstructed by other mineral phases present (as is the case by XRD due to an overlapping peak of feldspar and cristobalite). DSC also determines the enthalpy of transition, which provides insight into the energy required for formation of volcanic cristobalite. Experiments were carried out from 30-300 °C.

A comprehensive, comparative investigation of 13 ICDD (International Centre for Diffraction Database) library cristobalite patterns was conducted in order to define an observed range for the primary (101) α- and (111) β-cristobalite peaks. This allowed for confirmation of volcanic cristobalite in either the α- or β-phase, and allowed for direct comparison to database samples for parameters that were not directly determined here (e.g., lattice cell parameters). The numerous theoretical and empirical diffraction patterns in the database were compiled using STOE WinX^{POW}. The primary peak is used for identification of cristobalite in volcanic ash samples as less-intense secondary and tertiary peaks are often masked by the presence of other minerals. For consistency, the cristobalite isolates are also discussed with regards to their primary peaks.

Statistical analyses were carried out where appropriate, and considered significant at $p<0.05$. A Welch corrected unpaired t-test was used when comparing two groups of data after first checking distributions for normality using a Kolmogorov–Smirnov test. A one-way ANOVA with Tukey-Kramer multiple comparisons post-test was used when comparing more than two groups of data.

Sample preparation and analytical techniques are discussed in detail in Chapter 3: Methods.

Table 5.1: Summary of analyses performed on samples of dome rock and ash. Sample prefixes are: COL, Colima; MER and MRP, Merapi; MSH, Mount St. Helens; SG, Santiaguito, UNZ; Unzen; MBA/MRA, Soufrière Hills (Montserrat) bulk/respirable ash. SEM imaging was always accompanied by EDS analysis of cristobalite, and is the same as that carried out in Chapter 4 for dome rock samples. Sample information for dome rock is located in Table 4-1, ash samples in Table 6-1, and SAK22 in Hillman et al. (2012; Appendix 4).

Sample	SEM	EMPA	T-XRD	DSC
Dome Rock Samples				
COL.124	x	x		
COL.165	x	x		
MRP.96.03	x	x		
MRP.98.02	x	x		
MER.10.08	x	x		
MER.10.09	x	x		
MER.10.13	x	x		
MSH.67	x	x		
MSH.103	x	x		
MSH.131	x	x		
MSH.135	x	x		
MSH.156	x	x		
MSH.166	x	x		
MSH.192	x	x		
MSH.201	x	x		
MSH.304.2A1	x	x		
MSH.304.2A9	x	x		
MSH.304.2G	x	x		
MSH.305.1A	x	x		
MSH.309.1A	x	x		
MSH.315.4	x	x		
MSH.315.5	x	x		
MSH.316.1	x	x		
MSH.321	x	x		
MSH.326.2	x	x		
MSH.BD.1	x	x		
MSH.ED.1	x	x		
SG.BR.SL7	x	x		
SG.BR.P1	x	x		
SG.MTD.2	x	x	x	
SG.MNJ.1	x	x	x	
UNZ.92.01	x	x		
UNZ.Y1	x	x		

Ash Samples			
MBA5/6/99	x	x	x
MRA5/6/99		x	
MBA12/7/03	x	x	
SAK22	x		
Talvitie		x	
Heavy liquids	x	x	

5.3 Results

5.3.1 Composition of volcanic crystalline silica

The elemental composition of volcanic cristobalite determined by SEM-EDS and electron microprobe spot analysis confirmed that crystals from all locations studied were not pure SiO_2. Crystals contained between 94.5 and 99.0 wt. % SiO_2 (Figure 5.1). The diminished SiO_2 content was predominantly offset by the presence of aluminium (Figure 5.1) and sodium (Figure 5.2a), with a correlation between aluminium and sodium (Figure 5.2b). Al_2O_3 abundances ranged from 0.7-4.0 wt. %, and Na_2O abundances from 0.02-1.5 wt. %. No other element analysed was systematically present in the cristobalite.

Data points for different volcanoes have different ranges of Al (Figure 5.1). For example, Santiaguito (28 viable analyses of 69 total) samples are more Al-rich than the Merapi (27 viable analyses of 77 total) samples, and the MSH (209 viable analyses 540 total) samples span the full spectrum as was seen for SHV samples (Horwell et al., accepted; Appendix 4). However, there is no statistical difference in Al among volcanoes. As noted in Chapter 4, cristobalite was rare in Colima and Unzen samples and, combined with microprobe resolution, only one data point was collected for Colima (despite 10 analyses) and none for Unzen (despite 7 analyses). The discrepancy between the number of viable data points and the total number of spots analysed was often due to EMPA penetration through a vapour phase crystal.

Compositional differences observed between prismatic and platy cristobalite, vapour phase and devitrification cristobalite, and between cristobalite and devitrification quartz (defined in Chapter 4) are summarised in Table 2 (and see Figure 5.3). Prismatic cristobalite contained 0.8-3.1 wt. % Al_2O_3, whereas platy cristobalite contained 0.7-2.0 wt. % Al_2O_3 (Table 5.2; Figure 5.3). These populations are statistically distinct ($p<0.01$), with prismatic cristobalite containing more Al. Platy cristobalite is also compositionally distinct from devitrification cristobalite ($p<0.01$). Both vapour phase and devitrification cristobalite are statistically distinct from devitrification quartz ($p<0.001$). Devitrification quartz (see Chapter 4) had a greater abundance of SiO_2 than the cristobalite analysed (99.1-100.0 wt. %), containing 0.0-0.6 wt. % Al_2O_3 and 0.0-0.3 wt. % Na_2O.

The spatial distribution of cation substitutions within single crystals was determined to be heterogeneous through EMPA spot analysis and EMPA mapping (Figure 5.4). Absolute compositional variance within single crystals was not determined as, at this point in time, it provides no additional quantifiable information on formation or reactivity.

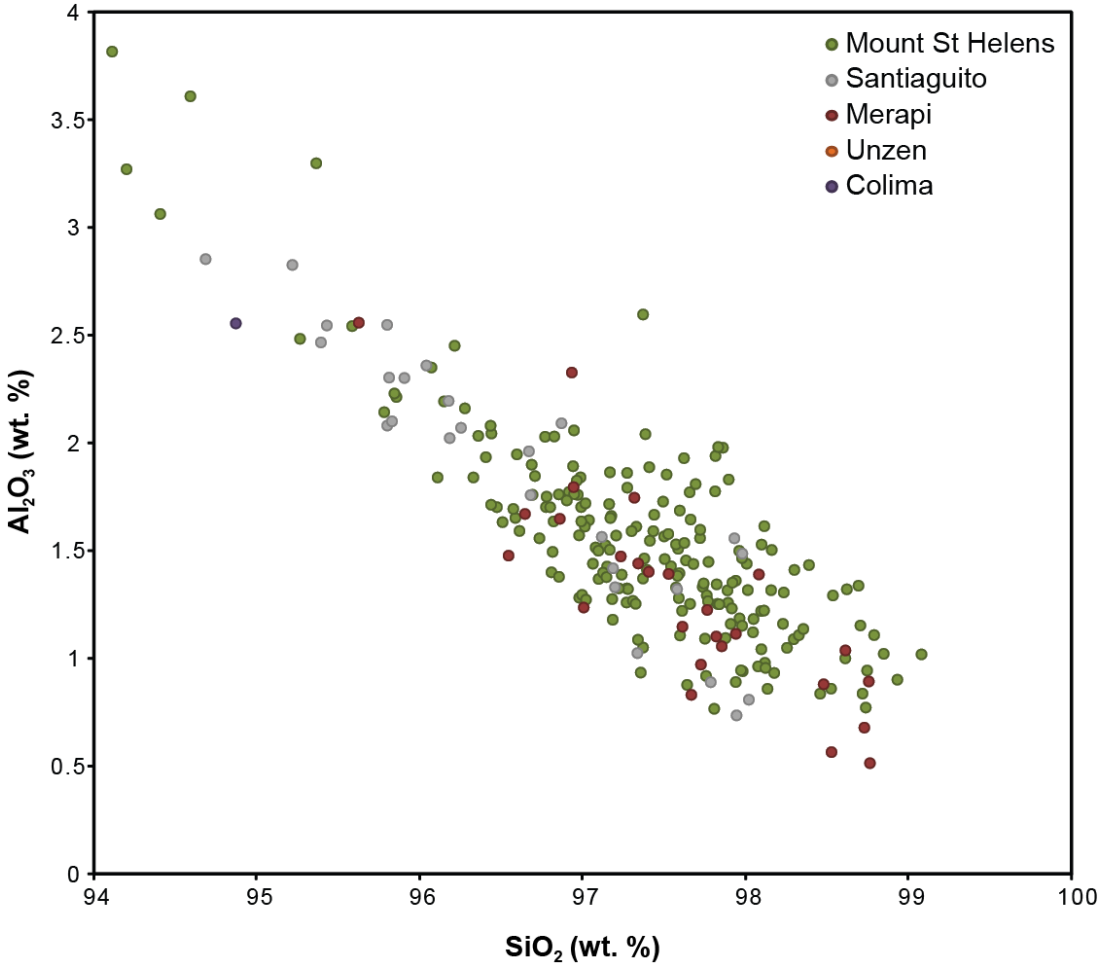

Figure 5.1: Range in chemical composition (SiO_2 and Al_2O_3) of volcanic cristobalite. Data are from EMPA spot analyses on samples from all locations considered in the present study

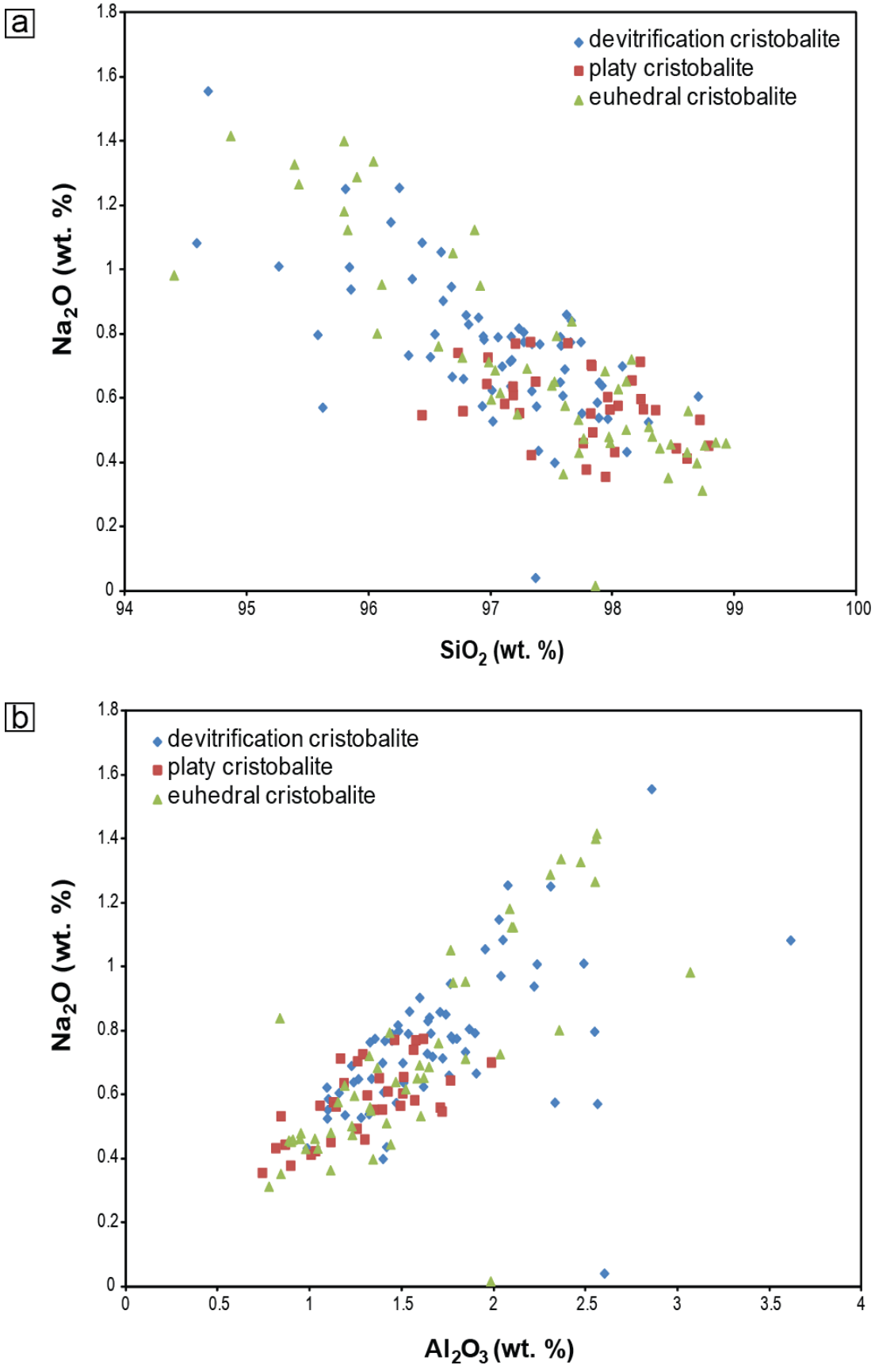

Figure 5.2: Correlation between the abundance of substituted elements Na_2O (a) and Al_2O_3 and Na_2O (b) in volcanic cristobalite as determined by EMPA.

Table 5.2: Compositional ranges for electron microprobe analyses in wt. % for the different crystalline silica habits identified in Chapter 4.

Crystal Habit	**SiO_2**	**Al_2O_3**	**Na_2O**
Prismatic	94.4 - 98.9	0.8 - 3.1	0.0 - 1.4
Platy	95.4 - 98.8	0.7 - 2.0	0.4 - 0.9
Devitrification cristobalite	94.6 - 98.7	1.0 - 3.6	0.0 - 1.6
Devitrification quartz	99.1 - 100.0	0.0 - 0.6	0.0 - 0.3

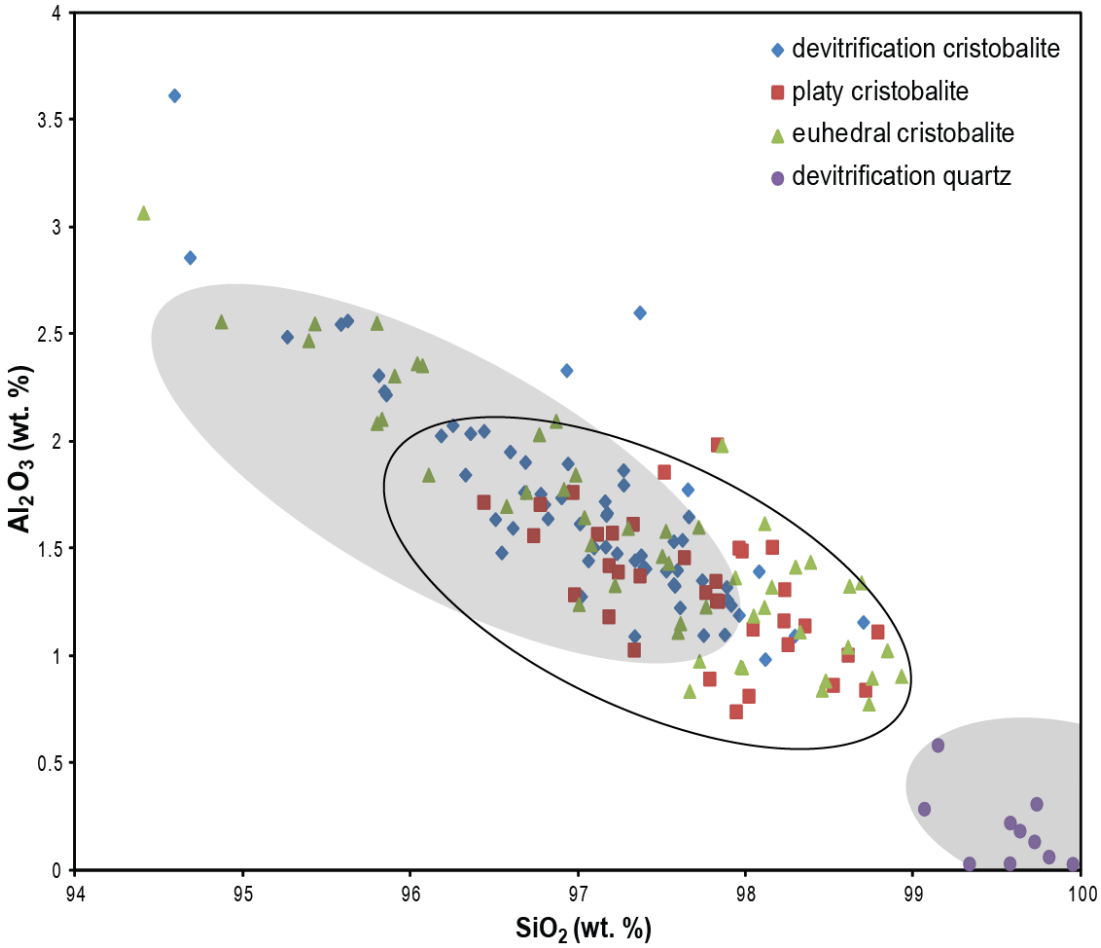

Figure 5.3: Variability in cristobalite composition according to crystal habit. Data are EMPA results on different cristobalite habits as defined in Chapter 4. Envelopes correspond to the ranges observed for platy (shaded) and prismatic (no fill) cristobalite and quartz by Horwell et al. (accepted; Appendix 4).

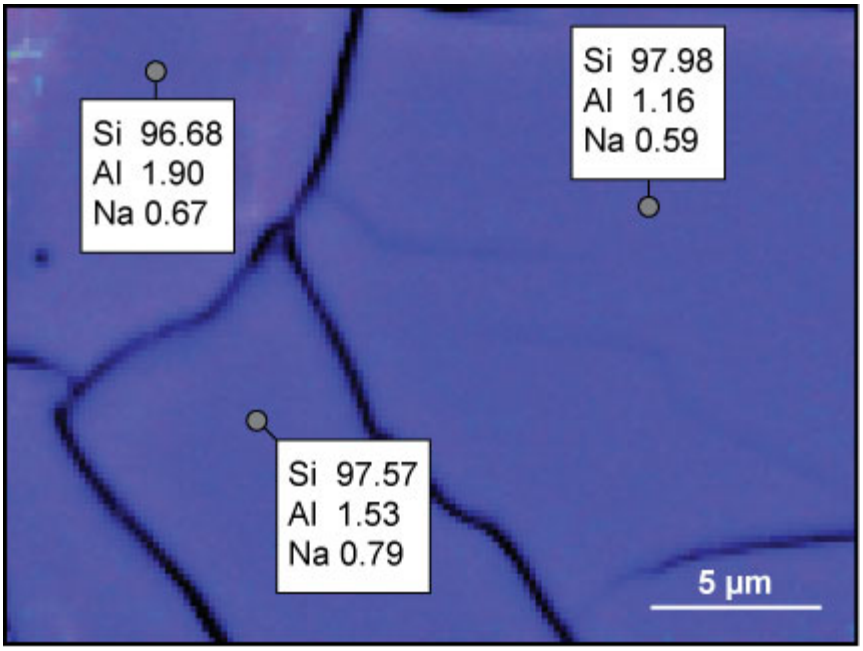

Figure 5.4: Compositional map (EMPA) of devitrification cristobalite in sample MSH.BD.1 showing a heterogeneous distribution of Si, Al and Na within a crystal. Dark lines are 'fish-scale' cracks.

5.3.2 Determination of lattice parameters using ICDD library patterns

A comprehensive comparison of ICDD library samples for cristobalite revealed two distinct ranges for α and β forms (Figure 5.5). The primary $(111)_\beta$ peak was between approximately d = 4.095–4.133 Å (21.5–21.7 °2θ) and the primary $(101)_\alpha$ peak was between approximately d = 3.952–4.077 Å (21.8–22.5 °2θ), where d is the spacing between adjacent lattice planes and is determined by the Bragg equation (Equation 3.2). The d-spacings observed in this study for all volcanic cristobalite ranged from 4.039–4.064 Å at ambient temperature (Table 5.1), including the Talvitie separate (d = 4.057 Å), which fit within the range for α-cristobalite.

5.3.3 Characterisation of the displacive transition

As was seen for dome rock samples in Chapter 4, the distinctive 'fish-scale' texture was also observed in cross sections through particles of volcanic ash (Figure 5.6). Occasionally, individual cristobalite particles did not display the 'fish-scale' textures; but, these were always < 8 μm diameter, and probably represent either a minimum crystal size for which the change in volume requires shattering, or sub-sections of individual crystals which fragmented along the pre-existing cracks during dome collapse.

Superimposed diffraction patterns of volcanic cristobalite at temperatures prior to, during, and following the α-β transition from continuous thermal XRD runs show a clear shift in the position of the primary cristobalite peak with increasing temperature (Figure 5.7). The shift in d-spacing between the α- and β- phases ($\Delta d_{\alpha\text{-}\beta}$) of cristobalite for all samples used in this study ranges from 0.038 – 0.057 Å. This definitive change in d-spacing follows a gradual migration of the $(101)_\alpha$ peak location from room temperature to a maximum prior to the transformation (see Table 3). This gradual shift is likely due to thermal expansion of the lattice (Δd_α of 0.006 - 0.014 Å). These phenomena apply to all samples investigated: ash-fall deposits, cooled dome rock, the separated fine fraction, and the cristobalite isolates. The observable transition supports the observations of fish-scale cracks by SEM and confirms that volcanic cristobalite exists in the α-form in samples at ambient temperature; however, trace amounts (<< 1 wt. %) of metastable β cristobalite would be undetectable by the techniques used here.

Differential scanning calorimetry showed two clear endothermic reactions during the first heating cycle, one at 130 °C and another at 202 °C (MBA5/6/99) (Figure 5.8). Only one exothermic reaction took place on cooling, near 180 °C, and only the higher temperature transition recurred when reheated, indicating the peak at 130 °C is a non-reversible event. As no other minerals identified in volcanic ash by XRD undergo a transition in this temperature range, the mirrored reactions at 202 °C and 180 °C are recording the transition from α to β

cristobalite on heating and the reverse on cooling. The temperatures at which the phase transitions occur on heating and cooling are not synchronised; however, the onset temperature of the transition during one cycle corresponds with the maximum transition temperature of the other cycle, i.e. the α to β transition on heating commences at the peak temperature of the cooling transition (176 °C onset vs. 182 °C cooling cycle maximum) and vice versa for the β to α transition (202 °C for both transition onset and heating cycle maximum) (Figure 5.8).

The transitions proceeded gradually and occurred over temperature ranges of 40 °C or more, taking place between 170–210 °C by thermal XRD and between 175–235 °C by DSC for MBA5/6/99. These ranges were independent of scanning rate, but showed a temperature hysteresis for repeat scans. The dome rock samples used for this study also underwent an inversion, albeit over a wider range and with an earlier onset (130-220 °C).

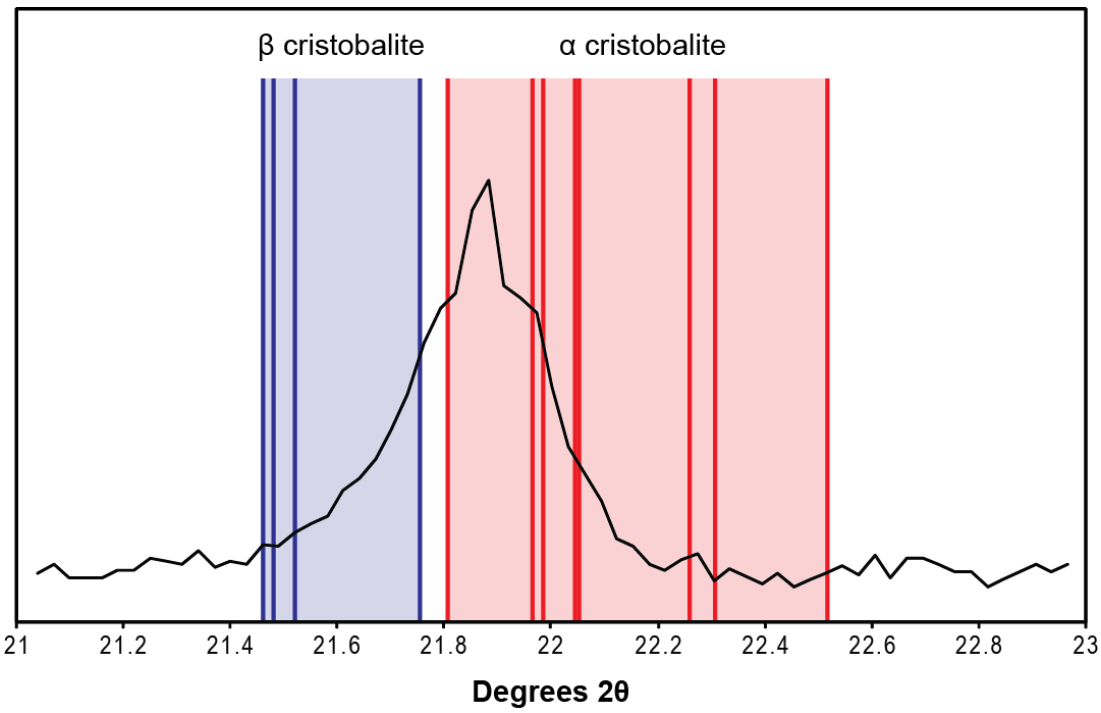

Figure 5.5: Range of primary $(101)_{\alpha}$ (red) and $(111)_{\beta}$ (blue) peak positions defined by the ICDD library samples. Solid lines record the peak positions for the different library samples. For α-cristobalite, library samples are: c39-1425, c76-941, c82-1235, c89-3434, c89-3606, c82-512, c82-1403, c82-1406, c82-1410. For β-cristobalite, library samples are: c76-934, c85-621, c89-3435, c89-3607. XRD curve shown is MBA5/6/99 (primary cristobalite peak) to demonstrate where volcanic cristobalite generally falls within these ranges.

Table 5.3: Summary of lattice parameters and thermodynamic data volcanic cristobalite in the samples investigated. ΔH measurement is approximate and is corrected based on quantifications of cristobalite in the sample (see Chapter 6).

Sample	d $(101)_{\alpha}$ (25 °C)	d $(111)_{\beta}$ (300 °C)	Δd_{α}	Δd transition	T_{tr} range (XRD)	T_{tr} range (DSC)	ΔH (J g^{-1})
MBA5/6/99	4.064	4.124	0.014	0.046	170 - 210	175 - 235	50
Talvitie	4.057						
SG MTD 2	4.053	4.097	0.006	0.038	130 - 210		
SG MNJ 1	4.039	4.103	0.007	0.057	130 - 220		

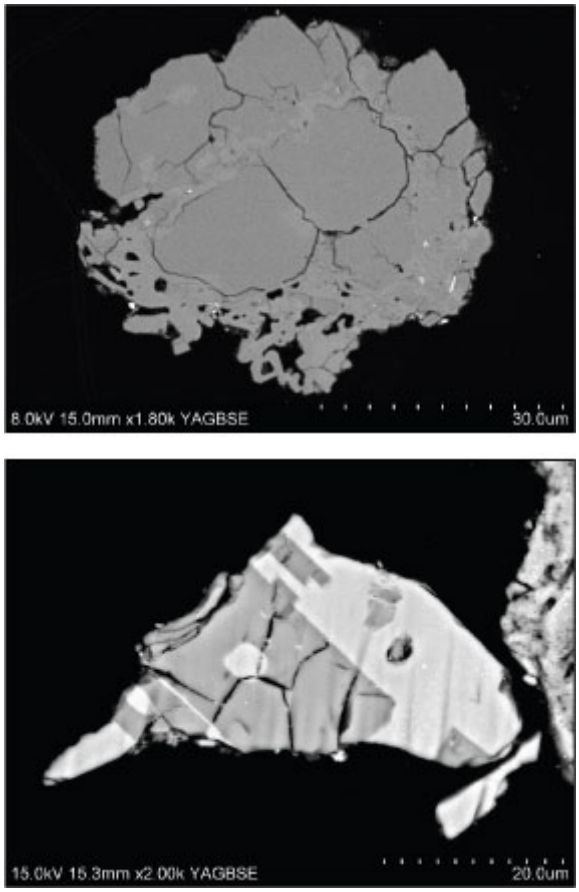

Figure 5.6: Backscatter electron micrograph of volcanic ash in cross section: Sample is the heavy liquids separate from Soufrière Hills sample MBA12/7/03. Cristobalite is identifiable by its characteristic 'fish-scale' cracking.

The transition observed by XRD was also independent of time. The effect of prolonged heating on the $(101)_\alpha$ d-spacing shift was determined by holding samples at various temperatures for different periods of time in the XRD. A 2 hour isothermal step upon heating through the transition range failed to progress the phase transition further; however, an additional increase in temperature following the isothermal step immediately resumed the inversion. When the temperature was held constant, the $(101)_\alpha$ reflection maintained the same d-spacing that was initially measured during the regular heating cycle.

Cooling rate had no control on the final crystal structure. No differences in the diffraction patterns were observed among the non-heat treated sample, the rapidly quenched sample, and the sample cooled under ambient conditions.

The enthalpy of transition increased for a consecutive structural rearrangement over two scans, from 9.00 J/g to 10.03 J/g for MBA5/6/99 (Figure 5.8).

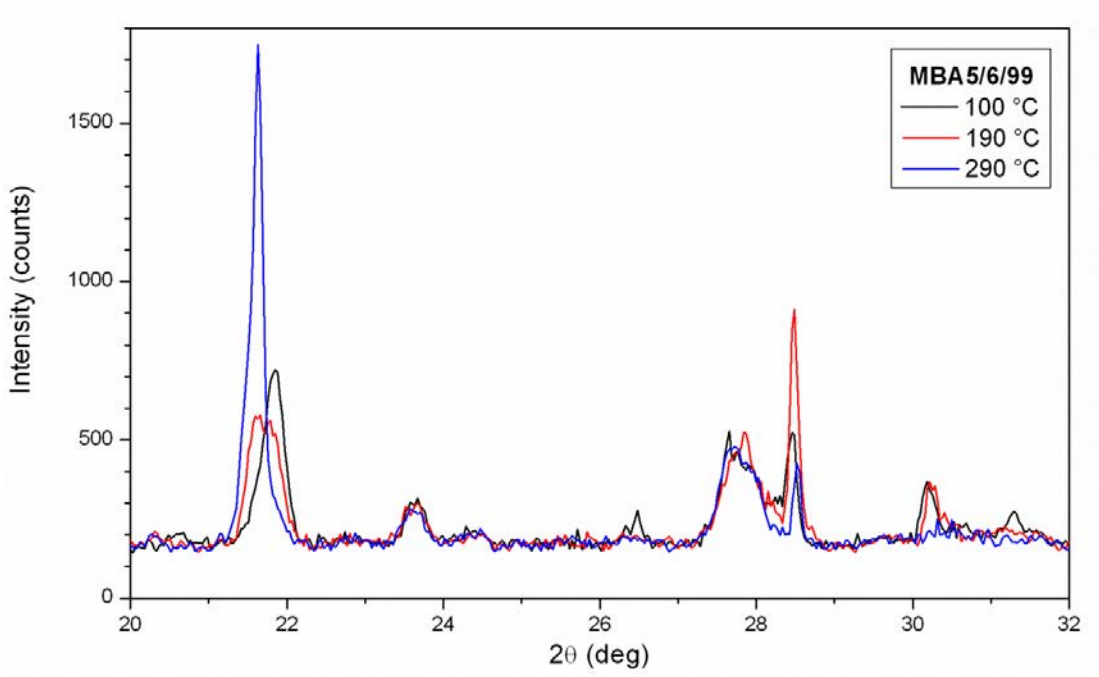

Figure 5.7: The α-β transition of cristobalite detected by thermal XRD. Figure shows overlain diffraction patterns of MBA5/6/99 at three distinct temperatures upon heating: before the transition (100 °C), during the transition (190 °C) and following the transition (290 °C). Patterns were collected for intervals of 1 minute per given temperature over the range. Patterns are displayed from 20 to 32 °2θ to enlarge the primary peak region.

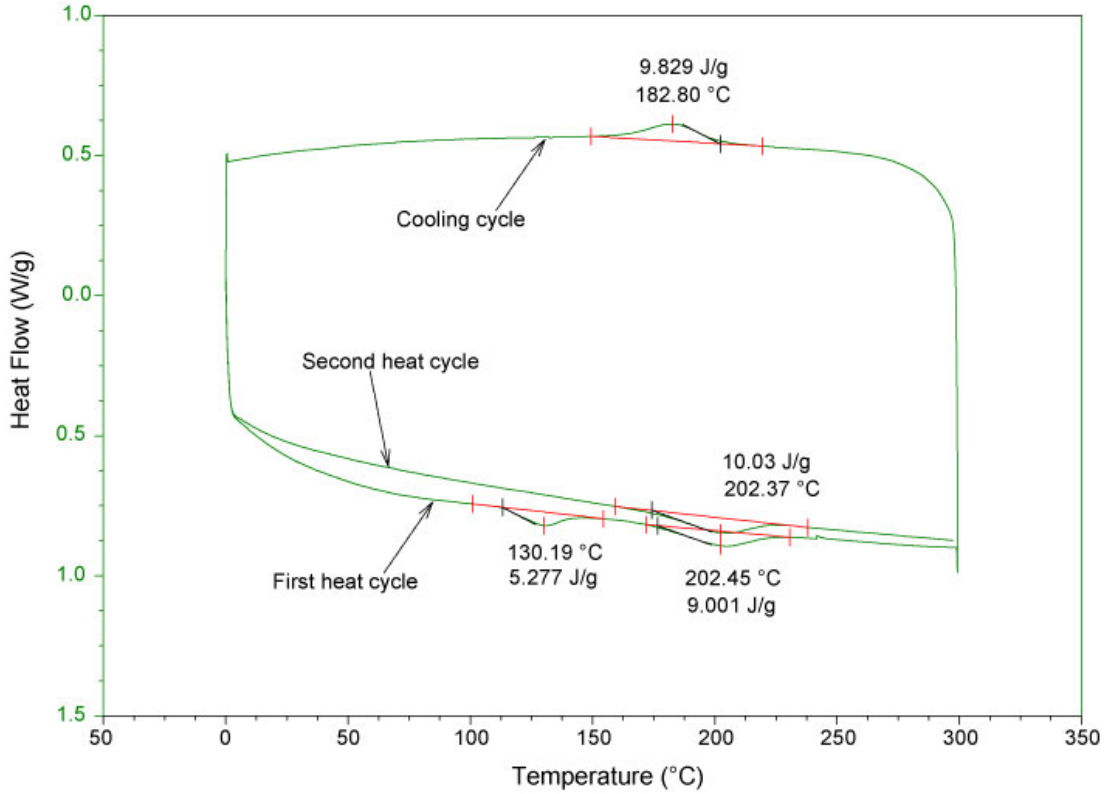

Figure 5.8: The α-β transition of cristobalite detected by DSC. Figure shows the heating curve for MBA5/6/99 with an initial heating cycle (bottom green line), a cooling cycle (upper green line), and a second heating cycle. Scanning rate is 10 °C/min.

5.4 Discussion

5.4.1 Composition of volcanic cristobalite

EMPA analyses on samples from all locations confirm the ubiquitous presence of Al and Na in cristobalite, which was also observed at Soufrière Hills volcano by Horwell et al. (accepted; Appendix 4). The data here confirm that these elements are found in all cristobalite habits (Horwell et al., accepted did not analyse devitrification cristobalite in their study), but are more or less absent in devitrification quartz. Although not determined directly here or in Horwell et al. (accepted; Appendix 4), it is believed that Al^{3+} substitutes for Si^{4+} within the silica tetrahedron, with Na^{+} present to balance the resultant charge deficit, as this is a common substitution in minerals, specifically in cristobalite (Deer et al., 1996). This is supported here stoichiometrically (assuming a simplified Si-Al-Na three phase system, and the maximum observed contents of 4.0 wt. % Al, and 94.5 wt. % Si, and 1.5 wt. % Na), where each mole of incorporated Al is equivalent to 0.99 moles of deficient Si. The fact that this substitution has been observed in all samples indicates that this is likely to be a world-wide phenomenon at dome forming volcanoes.

The substitution of aluminium for silica cannot be constrained by location, with Mount St. Helens, Santiaguito, and Merapi spanning the majority of the observed range (Table 5.2, Figure 5.1). Similarly, for domes with multiple samples from the same extrusive period (e.g., Mount St. Helens, see Table 1 in Chapter 4), differences cannot be attributed to the source spine or lobe.

The abundance of substitutions, however, can be constrained by crystal morphology. Platy and prismatic crystals show two distinct populations (Table 5.2, Figure 5.3), where prismatic crystals contain more Al than platy crystals at both Santiaguito and Mount St. Helens, the only two locations with sufficient data for both morphologies. This is in direct contrast to the results of Horwell et al. (accepted; Appendix 4), who found platy cristobalite to be enriched in Al compared to prismatic cristobalite at Soufrière Hills volcano (Figure 5.9). Since platy crystals are less frequently encountered than prismatic crystals in dome samples (Chapter 4), the discrepancy could result from compiling data from multiple samples from multiple locations. However, insufficient data were available to statistically corroborate the difference for individual samples which contain both morphologies (e.g., MSH.315.5 and MSH.321; see Chapter 4). Only one data point for platy cristobalite (of n=7) in Horwell et al. (accepted; Appendix 4) was above 2.0 wt. % Al_2O_3, the upper bound for platy cristobalite observed in the present study, and their upper limit for prismatic cristobalite was ~2.0 wt. % Al_2O_3, far lower than observed in the present study (approximately 4 wt. %). More than likely, their

dataset only represents a lower bracket of the substitution range (as Merapi does here, with all prismatic samples containing less than 1.5 wt. % Al_2O_3).

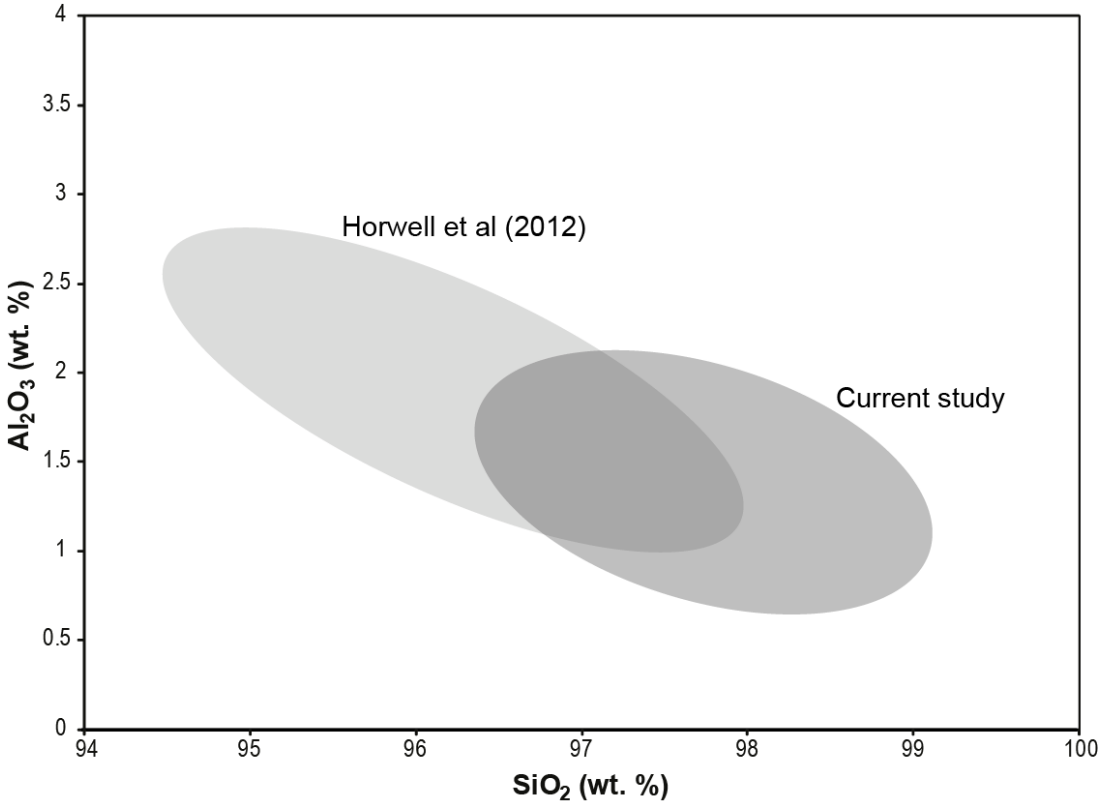

Figure 5.9: Elemental composition of platy cristobalite by EMPA in the present study compared to that reported by Horwell et al. (accepted; Appendix 4).

Platy cristobalite is thought to be a pseudomorph after tridymite (see Chapter 4). Both tridymite and cristobalite have voids large enough to house Na (and K or Ca, experimentally) amongst the Si tetrahedra (Buerger, 1954); however, when synthesizing crystalline silica, formation of tridymite is encouraged in the presence of higher levels of doping (e.g. Stevens et al., 1997). Some studies suggest that substitutions are required to stabilise tridymite entirely (Deer et al., 1996). The more open structure of tridymite (540.33 $Å^3$ versus 362.47 $Å^3$ for cristobalite) presumably eases substitution during formation, which should lead to a platy morphology with more abundant aluminium in dome settings. This interpretation is based on the notion that substitutions govern polymorph formation; however, in Chapter 4, we proposed that temperature may be a greater control on formation, as dome temperatures are at the thermal boundary between the tridymite stability field (867-1470 °C) and both polymorphs being metastable below 867 °C. We are currently synthesising cristobalite with

different Al-Na doping levels and at different temperatures to constrain the role of each factor on polymorph formation.

In the present study, patches of devitrification cristobalite always contain more than 1 wt. % Al; no devitrification data were reported in Horwell et al. (accepted; Appendix 4) for comparison. This likely results from the local abundance of Al in groundmass glass and is readily incorporated during crystallisation. Due to the lack of crystal shape, it is not possible to determine whether devitrification cristobalite is after tridymite, as might be implied by the study by Stevens et al. (1997) discussed above. 'Feathery' and 'myrmekitic-like' devitrification cristobalite were too intricate to be able to quantify substitutions through microprobe spot analysis so all analyses were carried out on larger devitrification cristobalite patches. A combined technique of low-current EDS and WDS mapping is currently being developed to quantify the aluminium content of these intricate textures, which likely contain the maximum abundance of substitutions due to the short-range diffusion required for these textures and mark an upper limit for incorporation of cations into volcanic cristobalite (or, conversely, a lower limit for the necessary diffusion of other elements for cristobalite to crystallise).

5.4.2 Structure and crystallinity of volcanic cristobalite

The interplanar d-spacings calculated for volcanic α-cristobalite (d_{101} = 4.039-4.064 Å) by XRD (Table 5.3) are generally larger than those reported for synthetic α-samples (e.g., d_{101} = 4.04 Å) (Chao and Lu, 2002a). Most likely, these result from structural cation substitutions observed by EMPA. Chao and Lu (2002a) have shown a displacement in the primary α-cristobalite peak proportional to the level of (Al_2O_3 + Na_2O)-co-doping during cristobalite synthesis. The lattice spacing in their experiments exhibits an increasing trend from lower doping levels to higher doping levels, from d_{101} = 4.040 Å at 2.91 mol. % Na_2O-Al_2O_3 to d_{101} = 4.058 Å at 4.65 mol. %. Doping levels used by Chao and Lu (2002b)were on the order of those seen for volcanic cristobalite (up to 2.4 mol. % Al_2O_3), and the observed monotonic trend suggests any amount of cation substitution can lead to structural discontinuities and a corresponding shift in lattice spacing (towards a lower degree 2θ in X-ray diffraction patterns).

The sharpness and intensity of an X-ray diffraction peak can generally be regarded as an indication of the degree of crystallinity and perfection of atomic arrangement within the structural framework of a mineral. Peak widths for volcanic cristobalite isolates are wider than the two cristobalite standards used, indicating a larger degree of disorder for the

volcanic crystals and variability in short-range interplanar spacings, which also likely results from incorporation of Al and Na into the crystal lattice. While a homogenous distribution of substituted cations would shift the 2θ diffraction position entirely, EMPA on single cristobalite crystals verifies a heterogeneous distribution of substitutions throughout a crystal (Figure 5.4). The resultant, non-uniform d-spacings lead to a broader XRD reflection, suggesting a poorly ordered lattice and further supporting the interpretation of structurally incorporated cations.

5.4.2.1 Characteristics of the α-β cristobalite transition

The nature of the α-β transition can provide information on the cristobalite structure. The transition-temperature range for MBA5/6/99 observed by XRD (170-210 °C) and DSC (onset at 175 °C, peak at 202 °C) are in close agreement, and likely only differ due to the different instruments and heating techniques. These temperature ranges are lower than generally reported for synthesized cristobalite samples cristobalite (e.g. 227-267 °C, Mosesman and Pitzer, 1941), which supports the hypothesis of a lower degree of crystallinity.

The breadth of the transition reflects the heterogeneity of cristobalite in the sample. Both DSC and thermal XRD data typically show a gradual transition interval with upper transition-boundary temperatures of approximately 270 °C (Stevens et al., 1997). The transition breadth observed for Soufrière Hills ash generally corresponds to that of synthetic samples, e.g., ~20-40 °C (Leadbetter and Wright, 1976; Mosesman and Pitzer, 1941); however, the transition interval observed for Santiaguito dome rock was much wider, ~80 °C. The increased transition breadth in the dome rock samples could result from a difference in grain size; cristobalite is preferentially enriched in the fine fraction (Horwell et al., 2003b) in ash samples which may not be replicated by grinding dome rock samples by hand for XRD. The difference could also represent a more heterogeneous distribution of lattice perfection for cristobalite from Santiaguito compared to Soufrière Hills as Santiaguito contained a greater abundance of cation substitutions. No systematic difference in d-spacings by XRD were noted to support this interpretation; however, Thompson and Wennemer (1979) report a sharp peak in heat capacity at 262 °C for a highly crystalline synthetic sample (prepared at 1500 °C for 20 hours), indicating that a narrow transition range may reflect a homogeneous cristobalite crystal population.

The cristobalite inversion involves an enthalpy of transition, which is indicated by the endo- and exothermic reactions on the thermal DSC curve (Figure 5.8): the peak at 200 °C on heating and 183 °C on cooling marks the phase transition. The difference between the transition temperatures upon heating and cooling is due to transition hysteresis, and is well

documented for cristobalite (Leadbetter and Smith, 1976; Schmahl, 1993). The susceptibility of cristobalite to hysteresis also eliminates concern over the difference in heat flow for the three recorded transitions. Further, there is no correlation between the α-β and β-α temperature ranges (Leadbetter and Smith, 1976). Hysteresis is associated with strain and surface free energy in the transforming crystals, which are dependent on the direction of thermal change. Stevens et al. (1997) showed marked hysteresis on heating and cooling for cristobalite, and this increased with firing temperature. The increase in inversion temperature and the extent of hysteresis with firing temperature are evidence of the production of better ordered cristobalite crystals at high temperatures (Stevens et al., 1997). Even the most crystalline samples obtained by Leadbetter and Smith (1976) still contained considerable strain due to disorder. As such, hysteresis is always expected to be present for cristobalite; however, the extent should be lower for less-ordered volcanic samples compared to better-ordered synthetic samples.

Based on the position and width of the $(101)_{\alpha}$ reflection before and after the transition, cristobalite reverts back to the original isomorph on cooling with little change in the structure. A similar occurrence was seen by Butler and Dyson (1997), whereby disordered cristobalite reverted to the same defect α-cristobalite structure following a transition to the β-phase. The most likely reason is that the foreign ions and vacancies that stabilise the disordered form cannot be spatially varied during the transition. This means that, in a volcanic dome, any continuous cooling and reheating should result in minimal change to the impurities observed here and by Horwell et al. (accepted; Appendix 4).

The athermal phenomenon, whereby the transition halts when held isothermally, has been observed for cristobalite (Leadbetter and Wright, 1976; Schmahl, 1993) as well as with quartz held isothermally for 20 hours, where no additional shift of the prominent $(101)_{\alpha}$ reflection occurred under isothermal conditions (Wahl et al., 1961). With an additional temperature increase, the d-spacing continues to increase in both cristobalite and quartz. Further, the finite width of the transition range is not simply a kinetic effect (Leadbetter and Wright, 1976). A transformation that does not proceed isothermally is analogous to martensitic transformations (i.e., diffusionless, displacive transformation in the solid state) in close-pack metals and alloys (Schmahl, 1993), which can result from the need of a crystal structure to accommodate the minimum energy state for a given temperature (Otsuka and Wayman, 1998). Since no redistribution of atoms occurs, time-dependent diffusional processes are absent, and the transformation is temperature, rather than time, dependent. This observation suggests self-pinning at the domain walls between the α- and β-phases, resulting in the thermal hysteresis and non-quenchable structural phase transition (Schmahl, 1993).

5.4.3 Crystallisation and the α-β transition

The enthalpy of fusion can potentially provide information on the energy required for crystallisation, which cannot be determined directly due to the presence of both vapour phase and devitrification cristobalite. The mixed-phase nature of volcanic ash makes it difficult to relate the heat of transition for the α-β inversion to that observed for pure-phase synthetic samples. However, in scaling up the enthalpy associated with the transition based on XRD quantification of cristobalite (i.e., MBA5/6/99 contains 15 wt. % cristobalite; Chapter 6), the heat flow for a 'pure-phase' sample of volcanic cristobalite would be approximately 2130 J mol^{-1}. This result is in agreement with values from previous studies on synthetic samples of 1300 J mol^{-1} and 2320 J mol^{-1} (Mosesman and Pitzer, 1941; Thompson and Wennemer, 1979, respectively). Butler and Dyson (1997) report that less energy is required to transform a disordered cristobalite sample with a larger unit-cell size compared to a better ordered sample, suggesting changes in structural defects affect the energy required.

5.4.3.1 Controls on the α-β transition temperature

The cristobalite transition temperature is highly dependent on crystallisation history and annealing conditions (Alcalá et al., 1996; Hill and Roy, 1958); and, therefore, may provide insight into the conditions of formation in a volcanic dome (as introduced in Chapter 4). In particular, the temperature and duration of formation (which exert a control on the structural order of the crystal lattice), cation substitutions and crystal grain size all affect the temperature and enthalpy of the cristobalite inversion (e.g., Leadbetter and Smith, 1976). Analogously, in the quartz system, the thermodynamics of the α-β transition in samples from different sources was shown to differ depending on the origin and size fraction of the sample (Wahl et al., 1961).

Lower crystallisation temperatures result in decreased inversion temperatures. Alcalá et al. (1996) observed a transition temperature of 250 °C by DSC for SiO_2 annealed at 1400 °C versus 230 °C when annealed at 1100 °C. The volcanic dome environment, which is typically between 500 to 850 °C (Barclay et al., 1998; Murphy et al., 2000), is more than 300 °C cooler than common sintering temperatures used to synthesize cristobalite (e.g., Alcalá et al. (1996) and Stevens et al. (1997) whose lowest crystallisation temperatures were 1100 °C). Initial magma temperatures at Soufrière Hills volcano were determined to be 820-840 °C, with an upper limit of ~880 °C (Barclay et al., 1998), so even an injection of fresh magma would be insufficient to result in the experimental sintering temperature in the dome. By assuming a crystallisation temperature less than 1000 °C and extrapolating the observed effects in synthetic samples annealed between 1000 and 1400 °C to cooler temperatures, the

lower inversion temperature seen for volcanic cristobalite could partially result from the crystallisation temperature in the dome.

Lower inversion temperatures are associated with longer firing times when a mineraliser (e.g. Na) is present during experimental crystallisation (e.g., Stevens et al., 1997). Therefore, duration of formation will also exert a control on the inversion temperature. The initiation of cristobalite crystallisation can occur within hours or days of a magma package entering the dome environment (Williamson et al., 2010), and crystals will be subjected to variable temperatures, pressures, and hydrothermal fluids throughout their growth and residence. Due to this dynamic environment, it is possible that volcanic cristobalite undergoes multiple phases of growth rather than a single crystallisation event, which could also affect the peak breadth observed by DSC (Stevens et al., 1997).

In addition to temperature and duration of formation, structural imperfections can affect the crystallisation temperature and resultant α-β inversion temperature. The non-silicon substitutions and interstitial impurities inferred from EMPA data along with conventional boundary and point defects will maintain a more open cristobalite lattice. By requiring a smaller Δd associated with thermal expansion prior to the transition to β-cristobalite, the α-β inversion can take place at a lower temperature.

The α-β inversion temperature is also dependent on crystal grain size. The broad peaks and prolonged transition observed by DSC and XRD could further result from polydisperse cristobalite crystal sizes in our samples, where individual crystallites transform at different temperatures. Leadbetter and Smith (1976) showed that individual crystallites have their own characteristic transition temperatures, giving a finite transformation range for a bulk sample. Similarly, the $(101)_{quartz}$ peak intensity changes which often accompany the α-β quartz inversion are a function of particle size (Wahl et al., 1961). Cristobalite grain size is dependent on duration of formation, where increased annealing times in synthetic samples lead to larger average grain sizes, and grain growth occurs heterogeneously (Lee and Lee, 2000). A critical grain size exists for which the thermally induced 'fish-scale' cracking can be observed, which Lee and Lee (2000) constrain to a grain size of 5 μm. This critical grain size is appropriate for volcanic samples, as a minimum crystal size of 8 μm is generally observed for 'fish-scale' cracking.

In general, large particles favour the spontaneous formation of low temperature (α) phases, whereas small particles stabilize the high temperature (β) phase (Lee and Lee, 2000). The volume change associated with the cristobalite phase transition is larger and more abrupt than in quartz, further emphasizing the possibility that surface tension effects could be more influential.

5.4.3.2 Coexistence of α and β phases

It is apparent from the continuous DSC endotherms and the gradual emergence of the $(111)_{\beta}$ peak and disappearance of the $(101)_{\alpha}$ peak during thermal XRD (Figure 5.7) that α- and β-forms coexist during the phase transition. Although the cristobalite transition is highly first-order and, therefore, discontinuous jumps in entropy corresponding with an instantaneous shift in the diffraction peaks are expected (Schmahl et al., 1992), a smooth decrease in the intensity of these modes is observed as the proportion of cristobalite existing in either α- or β-forms varies smoothly with temperature. Coexistence of α- and β-cristobalite is a widespread phenomenon of the transition in synthetic cristobalite (Leadbetter and Wright, 1976; Schmahl et al., 1992; Spearing et al., 1992; Swainson et al., 2003). It has relevance for toxicity only if coexistence persists metastably, since exposure may be to both α and β forms. However, it does have relevance for crystallisation, as a heterogeneous crystal structure may reflect the spatio-temporal conditions of crystallisation.

One form of coexistence is intergranular, whereby different grains of cristobalite have different transition temperatures (Krisement and Trömel, 1959a; Krisement and Trömel, 1959b). The different transition temperatures may be due to different residual stresses and defects in the grains requiring a different driving force for transition, which can renormalize the critical temperature for each grain (Swainson et al., 2003). This explains the variety of transition temperatures reported for cristobalite as a function of crystallisation temperature in the literature (e.g., Stevens et al., 1997). Further, a proportion of cristobalite grains can persist metastably in the β-phase, which results in a variety of observed transition temperatures even if all the grains have the same original potential and temperature of formation. This macro-scale distribution of transition temperatures leads to a wide coexistence range, and therefore a broad α-β transition interval (Swainson et al., 2003). The range of impurities observed between grains, from 0.30 – 2.38 mol. % Al (here and in Horwell et al., accepted; Appendix 4), and associated lattice faults, may also contribute to the existence of different transition temperatures amongst grains.

Another form of coexistence is intragranular, where distinct regions of α-phase potentially coexist with regions of β-phase within a single crystal (Swainson et al., 2003). In this instance, measurements reflect an average of the structural state of the whole sample as many grains. The transition time for a single grain was estimated to be less than 0.1 seconds from optical observations (Krisement and Trömel, 1959a; Krisement and Trömel, 1959b); therefore, the only evidence for coexistence within a single cristobalite grain is the retention of a trapped β-phase (e.g., Nord, 1994), and unlikely contributes to the broad (e.g., 130-200 °C) α-β transition intervals observed here.

5.4.4 Anomalous DSC peak

An additional endothermic reaction was seen by DSC in the initial heating cycle at 130 °C in addition to the established cristobalite α-β inversion at 202 °C (Figure 5.8). A mirrored reaction is expected for any reversible event; however, only one event took place on cooling, near 180 °C. The discontinuity observed is likely to be a dehydration reaction resulting from surface hydration or open porosity. Although the anomaly occurred above the expected transition temperature for dehydration, the temperature at which adsorbed water is lost may vary considerably depending on the amount present in the sample (Stevens et al., 1997). Thermal release of water from hydrothermal quartz has been observed from 80 °C–300 °C (Barker and Robinson, 1984), where decreased grain size enhances the amount of adsorbed water. It could also result from dehydration or crystallisation of a hydrous or semi-amorphous silica phase, the presence of which would have ramification for toxicity as the *in vivo* reactivity and biopersistence (see Chapter 2) will differ between cristobalite and other arrangements of silica.

It is also possible that the discontinuity observed during the first heating cycle reflects a tridymite inversion in portions of the cristobalite. Lambda transitions in tridymite are observed near 115 °C in synthetic tridymite-cristobalite mixed phases (Stevens et al., 1997; Thompson and Wennemer, 1979). However, as all tridymite phase transitions are reversible (Graetsch and Flörke, 1991), rather than a lambda transition observed in 'pure' tridymite it would require a discontinuous inversion, perhaps from tridymite to cristobalite, since no corresponding structural rearrangements are further seen on cooling or reheating. However, tridymite was not identified in any of the XRD patterns. Nevertheless, consideration of the integrated heat flow for the anomalous peak (5.277 J g^{-1}) conceivably suggests the transformation of SiO_2 initially existing as tridymite to cristobalite, with incorporation of its associated latent heat into the subsequent cristobalite inversion (9.001 J g^{-1} for the first heating cycle versus 10.03 J g^{-1} for the second). The transition enthalpy for the orthorhombic superstructure to monoclinic (OS-MC) tridymite transition was determined to be 4.0 meV (Cellai et al., 1994), which is the largest transition enthalpy associated with the sequence of phase transitions in tridymite. This energy is much smaller than the transition enthalpy for the α-β cristobalite transition in which there is just one phase transition associated with a comparatively large change in energy (13.0 meV) and volume (Pryde and Dove, 1998; Schmahl et al., 1992). Therefore, whilst the transition may represent a relatively large reduction in energy for the tridymite structure, it is comparatively small on the scale of phase transitions in similar crystalline silica structures.

The discontinuity is unlikely the result of volatile exsolution as it is well below the expected temperature. It is also unlikely to be recording the glass transition; the glass transition is

defined by DSC as a change in heat capacity as the polymer matrix goes from the glass state to the rubber state. This is a second order endothermic transition with no latent heat involved, so appears as a step transition by DSC rather than as a peak like those observed for phase transitions.

5.4.5 Identification and Classification

The observable phase transition by thermal XRD (Figure 5.7) and DSC (Figure 5.8) confirms the presence of α-cristobalite in all samples. Observation of characteristic 'fish-scale' cracking by SEM imaging of dome rock (see Chapter 4) and ash (Figure 5.6) further confirms that volcanic cristobalite underwent a spontaneous, displacive transition from the β to α phase. The indicative cracking has been observed by the author in dome rock from all volcanoes, e.g., Soufrière Hills (Horwell et al., post review; Appendix 4), Merapi (Damby et al., 2012; Appendix 4), Colima, Mount St. Helens, Unzen, and Santiaguito (see Chapter 4) and sectioned ash from Soufrière Hills and Sakurajima, implying volcanic cristobalite exists metastably in the α-form. Reich et al. (2009) identified β-cristobalite nanofibres in volcanic ash; however, these would constitute a sufficiently small proportion that their presence would not be detected by the bulk sample analyses used here.

5.4.5.1 Preservation of β-cristobalite

The charge-coupled substitutions in volcanic cristobalite are insufficient to suppress the β-α transition upon cooling of volcanic cristobalite as is possible with chemically stabilised cristobalite in the Na_2O-Al_2O_3-SiO_2 system (e.g., Chao and Lu, 2002b; Perrotta et al., 1989). An upper limit of ~2.40 mol. % Al (4.0 wt. % Al_2O_3) was observed in volcanic cristobalite (here and in Horwell et al., accepted; Appendix 4), whereas stabilisation of β-cristobalite in synthetic samples was only observed experimentally above 6.29 mol. % Al (Chao and Lu, 2002a). The β-α transition in the closely analogous quartz system can also be artificially suppressed by incorporation of other elements into the structure. Xu et al. (2001) found that high temperature β-quartz is preserved down to room temperature through the substitution of Li^+ and Al^{3+} for Si^{4+}. In this case, suppression is due to a reduction in the transition temperature from 573 °C to nearly -273 °C as the substitution of Li and Al increases from 0 to ~50 mol. % (Xu et al., 2001). The presence of foreign ions in the interstices and altered bond angles from Al coordination presumably inhibits the contraction of the structure during the transition.

Grain size also did not suppress the β-α transition for the bulk cristobalite fraction in this study. Phase transitions can become sensitive to grain size in nano-scale crystals due to the relationship between atomic positions and macroscopic strain (Pertsev and Salje, 2000), and likely accounts for the presence of β-cristobalite nanofibres identified in ash from Chaitén

(Reich et al., 2009). Rios et al. (2001) also show this effect for the β-α quartz transition, but complete suppression of the transition has not yet been observed. In quartz, the change from normal bulk properties to 'nano' properties, when the bulk properties become dominated by surface effects, occurs below ~50 nm (McKnight et al., 2008). This size fraction is minor within the bulk grain size distribution of volcanic ash (see Chapter 6).

5.4.5.2 Misidentification of volcanic cristobalite

Volcanic ash is a mixture of mineral phases and contains numerous overlapping diffraction peaks (e.g., plagioclase feldspar and cristobalite near 21 °2θ), which can hinder the identification and classification of phases present and make interpretation of full patterns difficult. Therefore, minerals are often identified by their primary reflections, using secondary and tertiary peaks (e.g., $(102)_\alpha$ and $(222)_\beta$ for cristobalite) as confirmation. In a pilot study, determination of α versus β polymorphs in volcanic ash based on primary peak matching with the ICDD database proved to be ambiguous.

We have found here, however, that the ambiguity may be attributed to 3 factors: 1) the increased lattice spacing of Al-bearing cristobalite, which broadens and shifts the $(101)_\alpha$ diffraction peak towards the $(111)_\beta$ peak; 2) the presence of an overlapping plagioclase peak, which may augment the position of the combined cristobalite-plagioclase peak; and 3) the range in the ICDD peak positions reported, with the primary peak often visually being a better fit with library patterns for β-cristobalite than α-cristobalite. Given the above findings and the results of the pilot study that identified β-cristobalite in MBA5/6/99, caution needs to be taken when indexing against library standards.

We have further observed that user-based differences in sample preparation results in slight, less than 1 °2θ shifts in the diffraction pattern. Combined with the three factors listed above, the primary cristobalite peak used for phase identification can vary across the full range defined by both α and β cristobalite patterns (21.5 – 22.5 °2θ).

Opal-C and opal-CT can also be mistakenly identified as cristobalite since the characteristic $(101)_\alpha$ XRD peak around 21 °2θ (4.00–4.10 Å) of these materials coincides. The confusion among opal-C, opal-CT, and cristobalite caused from the similarity of the XRD patterns can be resolved depending on their chemical and thermal behaviours. The crystallinity of cristobalite does not increase by heat treatment, whereas, because opaline silica is hydrated, the (101) reflection sharpens and shifts as a result of heating. No opal was observed in the samples run by thermal XRD in the present study; however, this should be kept in mind for the future as its presence would have an effect on mineral quantification as well as ash toxicity.

5.4.6 Implications for the toxicity of volcanic cristobalite

We were unable to preserve β-cristobalite in the ash even through rapid quenching. As such, exposure to volcanic cristobalite will always be to Al-bearing α-cristobalite. Therefore, α-cristobalite standards used to assess the toxicity of volcanic ash are appropriate from a polymorphic perspective, but perhaps not with regards to purity or crystallinity. The presence of aluminium, both chemically and structurally, is critical for assessing the hazard posed by volcanic cristobalite; however, as the mechanism of toxicity for crystalline silica is unknown, the extent to which these two factors could reduce toxicity is unclear.

Aluminium has been historically used to combat the progression of crystalline silica mediated disease (Leung et al., 2012; Rifat et al., 1990); however, the genuine clinical effect is spurious. In a clinical study designed to assess the effect of aluminium on established cases of pneumoconiosis, the improvement reported by participants was deemed to be primarily psychological (Kennedy, 1956). In the study, aluminium therapy failed to improve functional lung capacity of patients or affect disease progression. In laboratory studies, however, pre-treatment of quartz with aluminium is known to inhibit its otherwise relentlessly toxic effects (e.g. Begin et al. (1986) and Duffin et al. (2001)). In the study by Duffin et al. (2001), the production of cytokines from macrophages and epithelial cells (see Chapter 6) diminished significantly following aluminium lactate treatment of quartz.

Contrary to the notion of greater degrees of crystallinity resulting in greater toxicity (e.g., Altree-Williams and Sprogis, 1982), heat treatment of cristobalite (from ambient temperature to 800 or 1300 °C) decreases toxicity (Fubini et al., 1999). This could suggest that the low temperature of crystallisation for volcanic cristobalite does not act to impair toxicity. More than likely, however, heating of cristobalite samples in the experiments by Fubini et al. (1999) served to 'heal' the crystal surface, increasing structural perfection and, consequently, reducing the number of 'dangling bonds' (see Chapter 2) and silica radicals (e.g., $Si^{\bullet}$ and $Si\text{-}O^{\bullet}$) at the crystal surface. Also contrary to the idea of crystallinity being a prerequisite for silica toxicity, treatment of macrophages by vitreous silica results in remarkable cytotoxicity and oxidative stress, and is analogous to that induced by quartz (Ghiazza et al., 2010). Therefore, in the case of volcanic cristobalite, impurities may play a larger role in modulating the toxicity than the crystal structure.

5.5 Conclusions

The well known variability in the carcinogenicity of silica is put into context for volcanic cristobalite by showing that conditions of formation may directly influence the composition and structure of a particle. These mineralogical characteristics are implicated in the toxic response to silica, and could partially account for the reduced toxicity previously observed for volcanic ash in silica-mediated responses. Since quartz from different natural environments has been shown to be a variable hazard in industrial settings, constraining knowledge on the cristobalite hazard with the intent to make informed generalisations is imperative for hazard response during an eruptive episode. Exposure will always contain some degree of cation substitutions, and therefore the hazard of respirable volcanic cristobalite should be considered accordingly. The verification of α-cristobalite in volcanic ash means that toxicity studies which compare volcanic cristobalite to α-cristobalite standards (e.g., Low et al., 1990) are valid from a polymorphic perspective, although perhaps not from a structural or compositional perspective. Based on these results, as well as those by Horwell et al. (accepted; Appendix 4), the effects of impurities on toxicity are now being tested through systematic synthesis of cristobalite with various levels of aluminium.

The incorporation of aluminium and sodium substitutions may permit cristobalite to form at temperatures below its stability field and may also affect its thermodynamic behaviour. The ubiquity of the α-β transition and similar thermodynamics between samples implies that the conditions of cristobalite formation in volcanic domes are comparable for dome-forming environments worldwide. Volcanic cristobalite has a lower transition temperature than synthetic samples, suggesting a lesser ordered structure and a lower crystallisation temperature. It also undergoes the transition over a wider temperature interval than synthetic cristobalite. The cation substitutions are likely responsible for the structural disorder, but are insufficient to stabilise β-cristobalite at ambient temperatures and pressures as has been accomplished in synthetic samples with similar, albeit more, substitutions. They were, however, enough to confuse diffraction pattern indexing against library patterns, leading to an initial conclusion of metastable β-cristobalite in volcanic ash in a pilot study.

6

Particle characterisation and *in vitro* toxicology of dome collapse ash

Acknowledgments

XRF analyses were carried out by Nick Marsh at the University of Leicester, and grain size analyses were carried out by Chris Rolfe at the University of Cambridge. XRD analyses for Unzen samples UNZ.02 and UNZ.03 were carried out by Sarah Hillman.

Iron release, hydroxyl radical generation and carboxyl radical generation experiments were carried out under the supervision of Maura Tomatis and Bice Fubini at the Università degli Studi di Torino, Italy.

Experimental design for Part II was done in consultation with Fiona Murphy, now at the MRC Toxicology Unit, University of Leicester. Flow cytometry work was carried out under the instruction of Jenn Raftis at the University of Edinburgh. Solutions for the biodurability experiments were prepared with advice from Wan-Seob Cho, now at Dong-A University, Korea.

Separation of the fine fraction and corresponding grain size analyses were carried out in collaboration with Gordon Fern and Steve Hankin at the Institute of Occupational Medicine, Edinburgh.

6.1 Introduction

Volcanic ash can remain in the environment for years after an eruption, creating the potential long-term particulate exposure required for the development of chronic lung disease. Ash and volcanic deposits are also quarried for construction aggregate (Damby et al., 2012; Appendix 4) creating an occupational hazard. More than eighty studies have addressed the toxicology, epidemiology and clinical effects of volcanic ash (reviewed by Horwell and Baxter (2006), and addressed in Chapter 2), but the studies have given varied results. In particular, toxicological studies on volcanic ash vary in their outcomes from inert to highly reactive.

Reactions that occur at the particle-host interface are primarily controlled by the characteristics of the particle surface; as such, the pathogenicity of inhaled particles is governed by their physical and chemical surface manifestations (Fubini and Otero Areán, 1999; Guthrie, 1997). Accordingly, recent studies have clarified that different ash types pose varying health hazards depending on their mineralogical and geochemical properties. For example, ash from dome-forming eruptions can be particularly fine grained (Horwell, 2007) and rich in crystalline silica due to secondary mineralisation of cristobalite in the dome (see Chapter 4). Likewise, surface iron, particularly of more mafic ash, has been shown to participate in the production of reactive oxygen species (ROS), including the highly deleterious hydroxyl radical (Horwell et al., 2007; Horwell et al., 2003a) (see Chapter 2).

The three key elements of a toxicity screening strategy include physicochemical characterisation, *in vitro* assays (cellular and acellular), and *in vivo* studies (Oberdörster et al., 2005a). This chapter sets out to determine the toxicity of ash from dome-forming volcanoes by integrating the first two elements of the screening strategy, physicochemical properties and surface behaviour with the *in vitro* toxicological and inflammatory response, and is therefore presented in two parts. Part I focuses directly on the particle, and comprises extensive physicochemical characterisation of ash from six dome forming eruptions according to key factors implicated in the onset of disease mediated by natural mineral particles. Results are used to define the hazard and infer the potential toxic response that volcanic ash may induce in the lung. Part II then investigates the response elicited in a biological system by a subset of samples through an array of *in vitro* experiments. The results are used to marry the *in vitro* response with specific physicochemical parameters. Taken together, this combination of particle characterisation and *in vitro* toxicity can potentially clarify the varied results in previous studies, and simultaneously reduce the need for *in vivo* experiments.

6.2 Methods

Analyses were carried out on ash samples from Colima, Merapi, Mount St. Helens, Santiaguito and Unzen; sample collection information can be found in Chapter 3. Published results for Soufrière Hills ash are referenced throughout for comparative purposes as has been done throughout this thesis. A list of the samples analysed in Part I (particle characterisation) can be found in Table 6.1, and corresponding experiments for Part I are presented in Table 6.2. Some experiments in Part I were only carried out on a selection of samples due to an insufficient amount of material for the full complement of analyses or when experiments were time-intensive (e.g., 7 day iron release). For the latter, samples were selected based on the results of key tests carried out on all samples such as grain size distribution and crystalline silica content.

Experiments for Part I include: 1) bulk chemical composition by XRF to determine the chemical makeup of the sample, which provides information on mineral phases present and likely abundance of reactive metals; 2) particle size analysis by laser diffraction to determine the distribution and abundance of fine material in order to assess the potential for the material to deposit in different areas of the lung (Chapter 2); 3) particle morphology by SEM imaging to identify the general shape and presence of any high aspect ratio particles which could follow the structure-toxicity paradigm for fibrous particulate (Chapter 2), and to also consider particle aggregation; 4) particle surface area by nitrogen adsorption to constrain the available area for reactions to take place; 5) particle mineralogy by XRD to quantify the abundance of crystalline silica; 6) particle biodurability by digestion in synthetic biological fluids to assess how the heterogeneous nature of volcanic ash might change following deposition in the lung; 7) bio-available iron by species-specific chelation to determine the amount of reactive iron available at the particle surface (Chapter 2); and 8) free radical generation to constrain the ability of a particle to generate reactive oxygen species.

Haemolysis is also included in Part I, even though it uses red blood cells, since it is a direct reflection of a particle's ability to rupture a membrane and does not involve an elicited inflammatory response. Its sole purpose in this study is to assess the surface reactivity of the mixed-mineral ash rather than to understand the pathophysiology of the particles. Particle size distribution for the respirable fraction used in Part II (below) was analysed during the separation from the bulk and only a small amount of material is required for particle morphology analysis; therefore, grain size and morphology results for the respirable fraction are presented in Part I to complement those from bulk characterisation.

A subset of six samples was chosen for Part II to examine the affected biological response. Samples were chosen from each of the locations studied, and selected per location based on their potential toxicity as determined in Part I. An overview of the experiments carried out on the subset of samples is provided in Table 6.3. *In vitro* experiments were carried out on a respirable fraction isolated from the bulk ash to fully represent the interaction between particles and cells of the deep lung (see Chapter 2). Insufficient mass was recovered from the separation for complete particle characterisation, so experiments in Part I were conducted on the bulk sample (< 1 mm).

Experiments in Part II (affected *in vitro* response) are performed on pulmonary type II epithelial cells and macrophages (Chapter 2) and include: cytotoxicity determined through two complementary assays: LDH release and metabolism of the AlamarBlue reagent; investigation of a pro-inflammatory response as measured by the production of inflammatory markers; cell-particle interaction by imaging of stained cells; and determination of apoptosis, necrosis, and cellular stress measured by endogenous antioxidant production. The mean particle size for samples suspended in cell culture media (either DMEM or RPMI) was determined by dynamic light scattering (DLS) to consider differences in particle aggregation in air versus liquid since treatment of particles was performed in culture.

Additional information and experiment design are outlined in Chapter 3: Methods.

Table 6.1: Summary of eruption and collection information for volcanic ash samples.

	Sample ID	Ash type	Eruption date	Date collected	Distance to source
Colima, Mexico					
	COL.A09.09	unknown	unknown	08/08/2009	0.0
*	COL.A03.10	unknown	unknown	21/03/2010	unknown
Merapi, Indonesia					
	MER.A10.01	explosion	30/10/2010	30/10/2010	32.0
	MER.A10.02	explosion	26/10/2010	31/10/2010	5.5
	MER.A10.03	explosion	05/11/2010	05/11/2010	32.0
	MER.A10.04	explosion	31/10/2010	31/10/2010	28.0
	MER.A10.05	explosion	05/11/2010	13/11/2010	18.0
	MER.A10.06	explosion	05/11/2010	13/11/2010	16.0
	MER.A10.07	explosion	05/11/2010	13/11/2010	11.0
	MER.A10.08	explosion	05/11/2010	13/11/2010	15.0
	MER.A10.09	explosion	05/11/2010	13/11/2010	18.0
	MER.A10.11	explosion	unknown	09/11/2010	6.0
*	MER.A10.12	PDC surge	05/11/2010	30/11/2010	17.0
	MER.A10.13	PDC surge	05/11/2010	30/11/2010	17.0
	MER.A10.14	PDC surge	05/11/2010	30/11/2010	17.0
	MER.A10.15	PDC surge	05/11/2010	06/12/2010	17.0
	MER.A10.17	explosion	unknown	03/12/2010	4.5
	MER.A10.18	explosion	unknown	03/12/2010	8.0
	MER.A10.19	PDC surge	05/11/2010	08/12/2010	17.0
	MER.A10.20	explosion	unknown	04/12/2010	12.0
*	MER.arc	dome collapse	11-19 Jul 1998	09/08/1998	0.2
Mount St. Helens, USA					
	MSH.04.HSR	unknown	unknown	29/11/2004	< 1.0
	MSH.05.CT	dome collapse	19/04/2005	21/04/2005	< 1.0
*	MSH.05.DG	vent explosion	08/03/2005	10/03/2005	~6.5
	MSH.05.DZ	dome collapse	19/04/2005	19/04/2005	< 1.0
	MSH.05.PS	dome collapse	18/08/2005	19/08/2005	< 1.0
	MSH.309.G	fault gouge	--	13/01/2005	< 1.0
	MSH.arc	dome collapse	18/05/1980	18/05/1980	378.0
Santa Maria, Guatemala					
	SG.A09.04	vent explosion	unknown	24/03/2005	0.2
	SG.A09.07	PDC	unknown	02/06/2005	0.2
	SG.A09.08	vent explosion	unknown	03/04/2005	0.2
Soufrière Hills, Montserrat					
*	MBA5/6/99	dome collapse	05/06/1999	05/05/1999	4.0
	MVO1498	dome collapse	20/05/2006	23/05/2006	3.5
	MBA12/07/03	dome collapse	12/07/2003	12/07/2003	7.0

Unzen, Japan					
	UNZ.01	dome collapse	22/04/1992	23/04/1992	2.0
	UNZ.02	dome collapse	14/08/1992	14/08/1992	5.0
*	UNZ.03	dome collapse	03/04/1993	03/04/1993	5.0
	UNZ.05	dome collapse	1991-1992	unknown	unknown
	UNZ.06	dome collapse	23/06/1993	28/08/2009	unknown
	UNZ.08	dome collapse	23/06/1993	28.8.2009	unknown
Comparative Samples					
	Cerro Negro	unknown	30/11/1995	01/12/1995	20.0
	Etna	vent explosion	04/11/2002	04/11/2002	~12.0
	Pinatubo	unknown	04/07/1991	04/07/1991	31.5

*denotes samples used for separation of a respirable sample and analysis in Part II

Table 6.2: List of experiments undertaken on the bulk samples from each of the volcanic locations studied. SEM, scanning electron microscopy; XRD, X-ray diffraction; SSA, specific surface area measured by the BET method; XRF, X-ray fluorescence; GSD, grain size distribution; EPR, free radical production measured by electron paramagnetic resonance. Results for comparative samples can be found in Horwell et al. (2007).

Ash Sample	SEM (stub)	XRD	SSA	XRF	GSD	EPR	Iron Release	Haemolysis
Colima, Mexico								
COL.A09.09		x		x	x	x		
COL.A03.10	x	x	x	x	x	x	x	x
Merapi, Indonesia								
MER.A10.01		x		x	x			
MER.A10.02	x	x	x	x	x	x	x	x
MER.A10.03	x	x	x	x	x	x	x	x
MER.A10.04	x	x	x	x	x	x	x	x
MER.A10.05		x		x	x			
MER.A10.06		x		x	x			
MER.A10.07		x		x	x			
MER.A10.08		x		x	x			
MER.A10.09		x		x	x			
MER.A10.11		x		x	x			
MER.A10.12	x	x	x	x	x	x	x	x
MER.A10.13		x			x			
MER.A10.14		x			x			
MER.A10.15		x			x			
MER.A10.17		x			x			
MER.A10.18		x			x			
MER.A10.19		x			x			
MER.A10.20		x			x			
MER.arc	x	x	x	x	x	x	x	x
Mount St. Helens, USA								
MSH.04.HSR		x				x		
MSH.05.CT		x				x		
MSH.05.DG	x	x	x	x	x	x	x	x
MSH.05.DZ		x	x	x	x	x	x	
MSH.05.PS		x		x	x			
MSH.309.G		x				x		
MSH.arc		x	x	x	x	x	x	
Santiaguito, Guatemala								
SG.A09.04		x	x			x	x	
SG.A09.07		x						
SG.A09.08		x						
Soufrière Hills, Montserrat								
MBA5/6/99	x	x	x	x	x	x	x	x
MVO1498		x		x		x	x	
MBA12/7/03		x						

Unzen, Japan								
UNZ.01					x			
UNZ.02		x			x			
UNZ.03	x	x	x		x	x	x	x
UNZ.05					x			
UNZ.06					x			
UNZ.08					x			
Comparative Samples								
Cerro Negro		x	x	x	x	x	x	
Etna		x	x	x	x	x	x	
Pinatubo		x	x	x	x	x	x	

Table 6.3: List of the samples selected for Part II with an overview of the experiments carried out for the respirable fractions and their corresponding bulk samples. Haemolysis was carried out on both the bulk and the respirable fraction of samples. Data for TT1 results are from Damby et al. (2012; Appendix 4).

Sample	**Abbreviation**	**Particle Characterisation and Surface Reactivity**				**Cellular Response**				
		DLS	*SEM Resp*	*Biodur*	*Haem*	*Cytotox*	*TT1*	*A549*	*THP-1*	*GSH*
MSH.05.DG	MSH	x	x	x	x	x		x	x	x
MER.arc	MER	x	x	x	x	x	x	x	x	x
MER.A10.12	MER_PDC	x	x	x	x	x	x	x	x	x
COL.A03.10	COL	x	x	x	x	x		x	x	x
MRA5/6/99	SHV	x	x	x	x	x		x	x	x
UNZ.03	UNZ	x	x	x	x	x		x	x	x

6.3 Part I: Physicochemical characterisation and surface reactivity of bulk ash and respirable fractions

6.3.1 Introduction

Many rapid-response analyses on volcanic ash have been carried out in recent years in order to provide an early indication of the potential acute and chronic respiratory hazard to populations in need of urgent advice. To aid this process, a rapid-response protocol has been developed (Figure 1 in Damby et al., 2012; Appendix 4). It comprises a spectrum of analyses to characterise the physical properties of the ash, investigate the surface reactivity, and determine the likely physiological response through a set of *in vitro* assays. Rapid health assessments have been carried out according the evolving protocol since the 2007-2008 eruption of Rabaul volcano, Papua New Guinea (Le Blond et al., 2010), with investigations during crises at Kilauea, Hawaii (2008; Horwell et al., 2008), Chaitén, Chile (2008; Horwell et al., 2010a), Eyjafjallajökull and Grímsvötn volcanoes (2010 and 2011; Horwell et al., submitted-b; Appendix 4), Merapi, Indonesia (2010; Damby et al., 2012) and Puyehue Cordón Caulle, Chile (2011; unpublished). The methods have been further implemented in part or full for non-emergency studies on ash from Pacaya, Guatemala (2010, Appendix 3), Colima, Mexico (2012, Appendix 3), Sakurajima, Japan (Hillman et al., 2012; Appendix 4), Etna (unpublished) and Vesuvius, Italy (Horwell et al., 2010b). Studies like these are carried out to compensate for the limited number of long-term health studies on the pathogenicity of volcanic ash.

Results from health reports and toxicity studies for volcanic ash that do exist vary among different volcanoes (see Chapter 2). These differences likely arise from the different constituents in variably sourced ash, but also result from differences in experimental design. For example, haemolysis experiments in a study on Soufrière Hills ash commissioned by the UK Department for International Development (DfID) (Cullen et al., 2002) and those by Wilson et al. (2000) both used sheep erythrocytes for haemolysis and a top dose of 20-30 mg ml^{-1}, whereas studies by Le Blond et al. (2010) and Horwell et al. (submitted-b; Appendix 4) used fresh human erythrocytes and a top dose of 1 mg ml^{-1}. Consequently, haemolysis for ash from Soufrière Hills has ranged between non haemolytic and 45 % haemolytic (unpublished data and Wilson et al., 2000) in studies which cannot be directly compared. Within these studies, samples from the same volcano, and even eruptive phase, have elicited different responses (e.g., Horwell et al., submitted-b; Appendix 4; Wilson et al., 2000).

Particle characterisation in the present study according to the physicochemical parameters outlined in the protocol aims to overcome these disparities by concurrently considering samples from multiple volcanoes. It can therefore serve as a comparative study when considering inter-source differences in future studies. As such, samples from the current study were subjected to the majority of the rapid-response protocol and benchmarked against the same standard ash comparisons used for rapid-study experiments. Further, it provides a foundation to contextualise the toxicity results from Part II of this chapter according to the nature of the sample.

6.3.2 Results:

6.3.2.1 Physical properties of particles

6.3.2.1.1 Grain size analysis

Determination of the grain size distribution (GSD) for a bulk sample is carried out for two reasons. The first is to inform public health officials of the respiratory hazard during an eruption; if ash is too coarse to enter the lung then it poses little hazard (Chapter 2). The second reason is to further define the particle hazard itself: grain size can inversely correlate with pathogenicity for single-phase particulate (e.g., Driscoll and Maurer, 1991; Oberdörster et al., 2005b). For crystalline silica, a reduction in the particle size, and the associated increase in surface area, leads to a more robust response (Donaldson et al., 2001; Francis et al., 2009; Nolan et al., 1987), although somewhat contentious due to the variable toxicities observed for quartz (Donaldson and Borm, 1998; Warheit et al., 2007). Grain size distributions are reported up to 63 μm for comparative purposes with other studies as this is the minimum grain size for which sieving is practical (Horwell, 2007), but the discussion focuses specifically on the sub-10 μm fraction for respiratory health implications.

Grain size distribution data for the bulk ash samples investigated are presented in Figure 6.1 Samples ranged from 0-18 vol. % sub 4 μm (1-31 vol. % sub 10 μm), which falls within the previously defined bounds for explosive volcanic ash (0-12 vol. % sub 4 μm) and dome collapse material (7-18 vol. % sub 4 μm) (compiled from Hillman et al., 2012; Horwell, 2007; Horwell et al., submitted-b; Le Blond et al., 2010).

Separation of the respirable component for all samples yielded fractions ranging between approximately 0.08 μm and 7.0 μm with a sample mean of 1.51-2.23 μm (Figure 6.2). The distribution of sizes was similar for all samples, with similar relative particle concentrations for the size ranges. The full range is defined by two analytical techniques (Chapter 3): FMPS for particles from 5.6–560 nm and APS for measuring particles from 0.5–20 μm. By stitching together the results from both techniques, a bi-modal distribution arises (Figure 6.2); however, this is an artefact of the instrumentation and data presentation as a relative per cent. The upper tail of the FMPS data is likely the effect of instrument sensitivity at the margin of its detection limit as it occurs systematically for all samples and has been observed in other grain size determination techniques (Claire Horwell, personal communication, 2011). The APS data highlight the upper particle size cut-off at ~7 μm, which is consistent with the 7.51 μm maximum particle size approximation calculated for the aerosolisation conditions (Chapter 3, Methods 3.4.1). The gradual slope towards the upper cut-off is likely a physical artefact as the probability of re-suspension decreases towards the defined particles

size cut-off. The lower cut-off for all samples was around 0.08 μm; however, it is unknown whether the aerosolised particles aggregate and this value is therefore representative of a true minimum grain size. Imaging by SEM was used to substantiate the data, however investigation by TEM would be required for the investigation of nano-sized (< 100 nm) particles. As characterisation of the nano-fraction is outside of the aims of this study, further measurements were not pursued.

Cell cultures were treated with concentrations of ash in solution rather than aerosolised, and therefore dynamic light scattering (DLS) was used to determine the size and dispersion of particles in liquid. Particle treatment was performed in DMEM cell culture media for A549 cells and in RPMI media for THP-1 cells, and therefore results were determined in both types of media (Table 6.4). In RPMI, the mean effective diameter of particles was greater than in DMEM for all samples. Likewise, the mean effective diameter with foetal bovine serum was greater than that of DMEM. Re-suspension of samples in NaCl as a medium-free control yielded mean effective diameters less than those observed in cell culture media. The only apparent trend observed for polydispersity (a measure of the diversity in grain size, where values closer to unity equate to less diverse samples), is larger effective mean diameters are associated with a greater degree of polydispersion (~0.15 for 5.0 μm through to ~0.45 for 20 μm). Samples did not show multiple particle populations (e.g., bi- or tri-modal).

6.3.2.1.2 Specific surface area

Particle surface area ranged from 0.17 – 1.83 $m^2\ g^{-1}$ (Table 6.5), which corresponds with the lower end of the expected range for volcanic ash: 0.19-7.67 $m^2\ g^{-1}$, mean=1.91 $m^2\ g^{-1}$ (median=1.28 $m^2\ g^{-1}$, n=41) (compiled from Hillman et al., 2012; Horwell et al., 2007; Horwell et al., submitted-b; Appendix 4; Horwell et al., 2003b; Horwell et al., 2010b; Le Blond et al., 2010). Data reported are the average of n=3 since the samples are heterogeneous. An insufficient amount of material was recovered for specific surface area analysis on the respirable fraction; however, previous analyses on samples from Soufrière Hills returned surface area values from ~3.5-8 $m^2\ g^{-1}$ (Horwell et al., 2003a; Wilson et al., 2000).

6.3.2.1.3 Particle morphology

The shape of a particle is of primary concern because it directly influences particle deposition, particle surface area, as well as particle interaction with cells. Imaging of each sample by SEM reveals little difference in general morphology between the bulk sample and respirable fraction (Figure 6.3). Particles are poorly vesiculated, sub-angular and blocky with varying amounts of nano-scale particles adhering to the surfaces of larger particles. Only

scarce mineral fibres were observed in any of the samples by SEM (Figure 6.4), reducing the concern of high aspect ratio particulate for particles greater than ~1 μm.

Table 6.4: Grain size distributions for respirable samples by dynamic light scattering (DLS) experiments in different cell-culture media. Data are reported in μm and are the average of n=2.

Solution	Merapi	Merapi PDC	Colima	Mount St. Helens	Soufrière Hills	Unzen
Mean effective diameter						
RPMI	20.18	7.89	20.29	7.81	22.48	19.10
DMEM	5.14	3.56	10.53	5.73	8.89	9.55
DMEM + FBS	17.13	8.69	8.96	9.07	16.03	10.30
NaCl	4.56	2.33	5.02	3.11	5.03	5.73
Polydispersity						
RPMI	*0.488*	*0.204*	*0.472*	*0.207*	*0.498*	*0.460*
DMEM	*0.153*	*0.157*	*0.359*	*0.189*	*0.261*	*0.256*
DMEM + FBS	*0.422*	*0.273*	*0.253*	*0.276*	*0.398*	*0.317*
NaCl	*0.162*	*0.154*	*0.151*	*0.166*	*0.176*	*0.182*

Table 6.5: Specific surface areas (SSA) in m^2g^{-1}measured for samples by the BET method of nitrogen adsorption. Data are the average of n=3 reported with standard deviation (SD). Comparative ash samples are included here as data are normalised to surface area in the EPR and iron chelation experiments where standard ash samples are used for comparison with published data. Data for MER.arc, MSH.arc, MBA5/6/99, Etna, Cerro Negro, and Pinatubo are taken from Horwell et al. (2007) and were not reported with a SD.

Sample	SSA	SD
Colima		
COL.A03.10	0.69	0.03
Merapi		
MER.arc	1.83	--
MER.A10.02	0.99	0.02
MER.A10.03	0.51	0.01
MER.A10.04	0.78	0.01
MER.A10.12	1.03	0.04
Mount St. Helens		
MSH.05.DZ	0.17	0.02
MSH.05.DG	0.38	0.02
MSH.arc	1.62	--
Unzen		
UNZ.03	0.65	0.02
Soufrière Hills		
MBA5/6/99	1.34	--
Comparative Samples		
Cerro Negro	0.47	--
Etna	0.19	--
Pinatubo	0.89	--

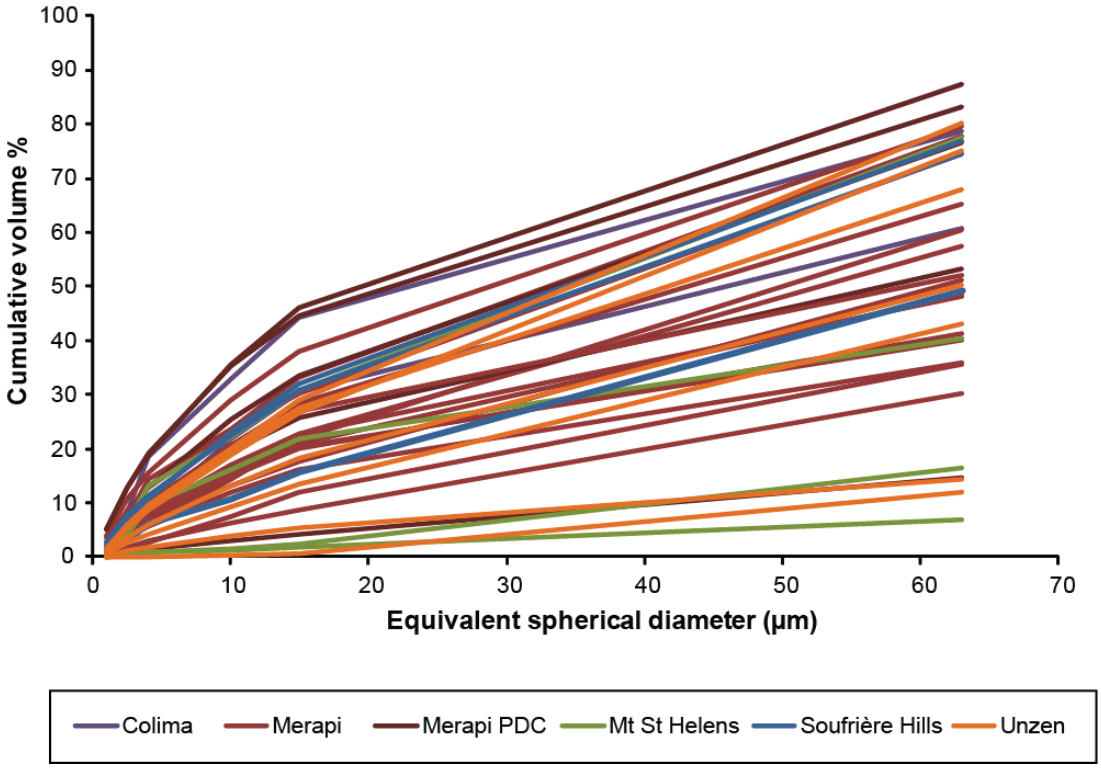

Figure 6.1: Grain size distribution of bulk ash samples determined by laser diffraction. Data for the ashfall and PDC samples from Merapi are from Damby et al. (2012; Appendix 4), and data for Soufrière Hills are from (Horwell, 2007).

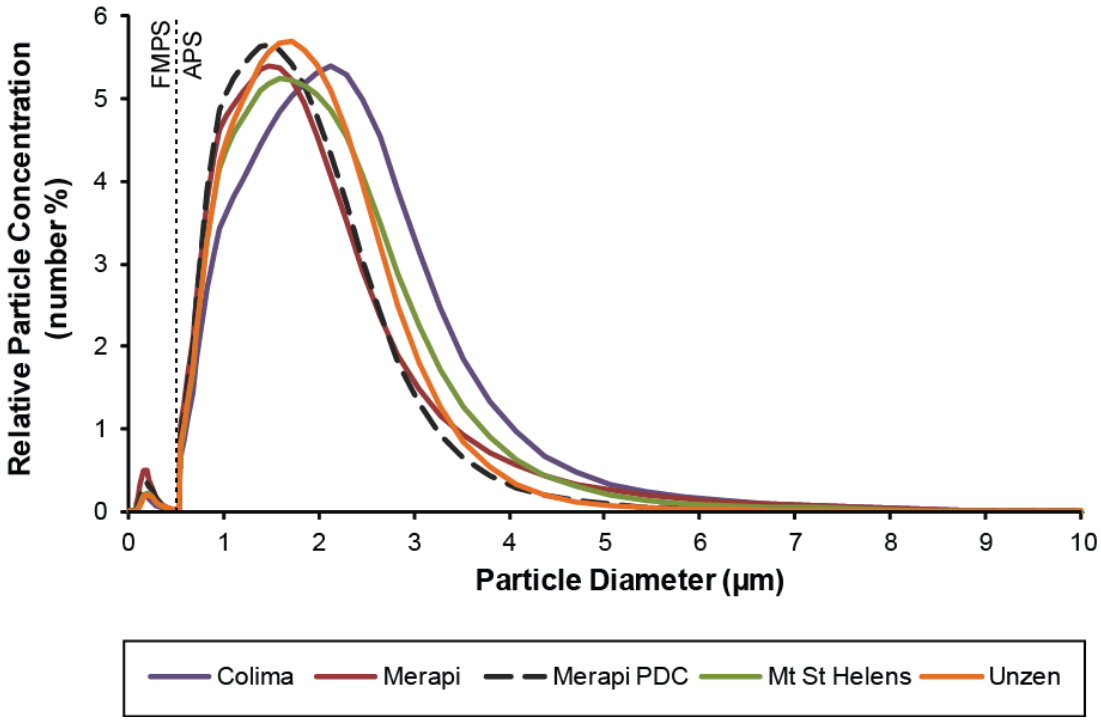

Figure 6.2: Grain size distribution for the respirable ash fractions used in toxicity studies. Data were collected during separation at the IOM; the respirable Soufrière Hills sample is from the collection of Claire Horwell and therefore does not have equivalent data (so is not plotted). Size data for particles smaller than 0.5 µm are collected by FMPS, and data above by APS.

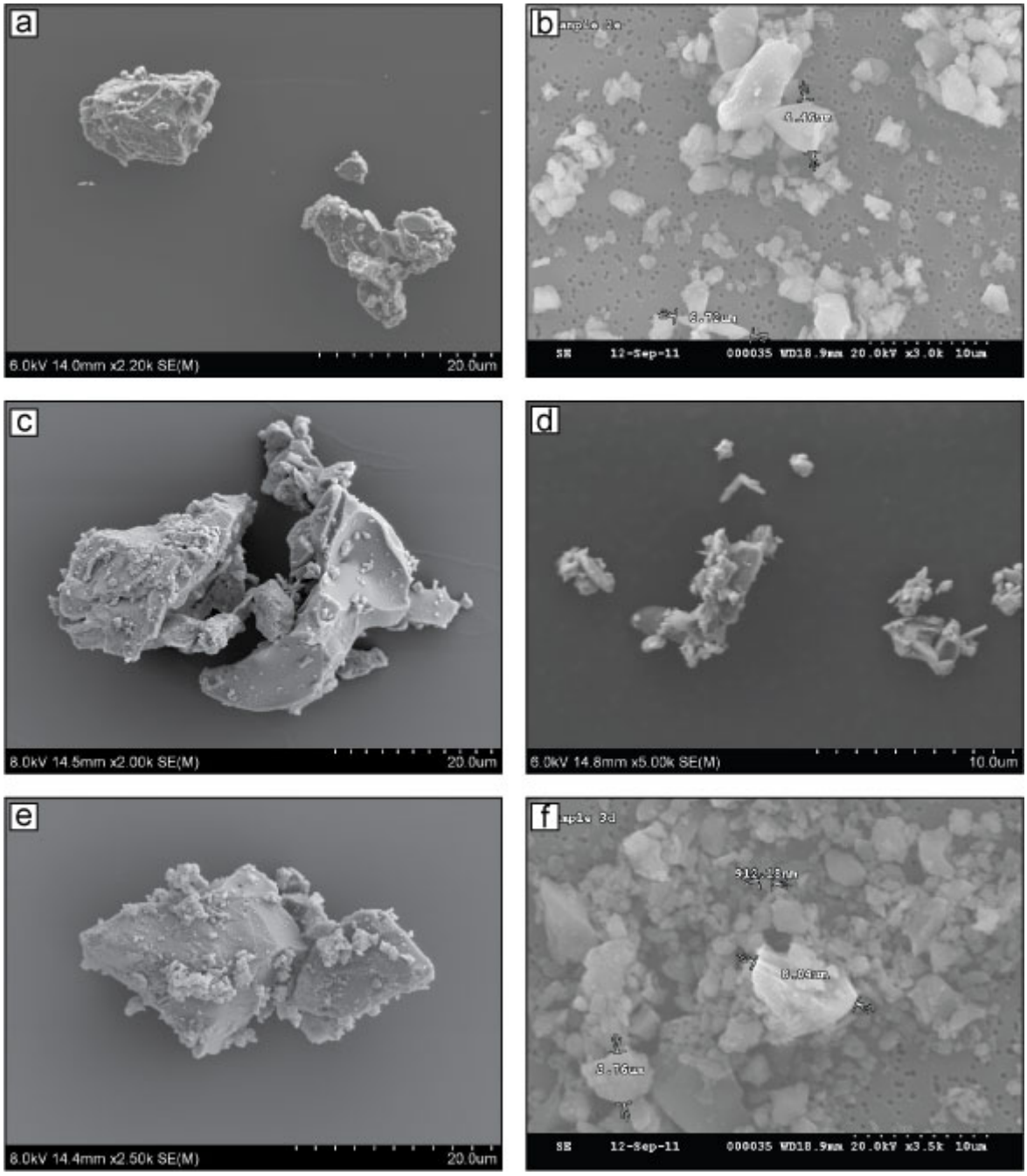

Figure 6.3a: Selected scanning electron micrographs of ash in bulk samples and corresponding respirable fractions. Scale bar and operating conditions are denoted on each image. Samples are COL.A03.10 bulk (a) and respirable (b), MER.arc bulk (c) and respirable (d), MER.PDC (10.12) bulk (e) and respirable (f).

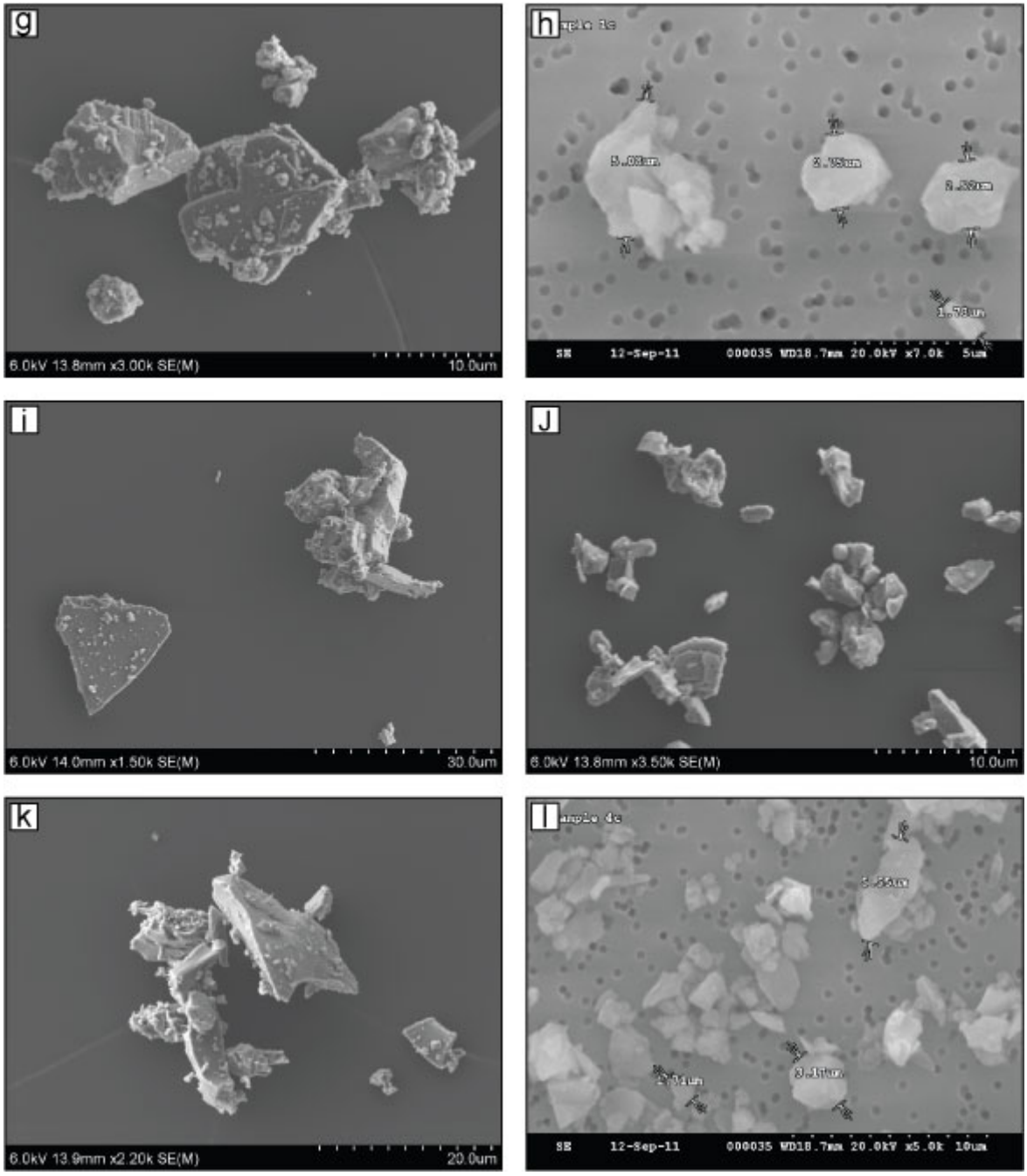

Figure 6.3b: Selected scanning electron micrographs of ash in bulk samples and corresponding respirable fractions. Scale bar and operating conditions are denoted on each image. Samples are MSH.05.DG3 bulk (g) and respirable (h), MBA5/6/99 bulk (i) and respirable (j), UNZ.03 bulk (k) and respirable (l).

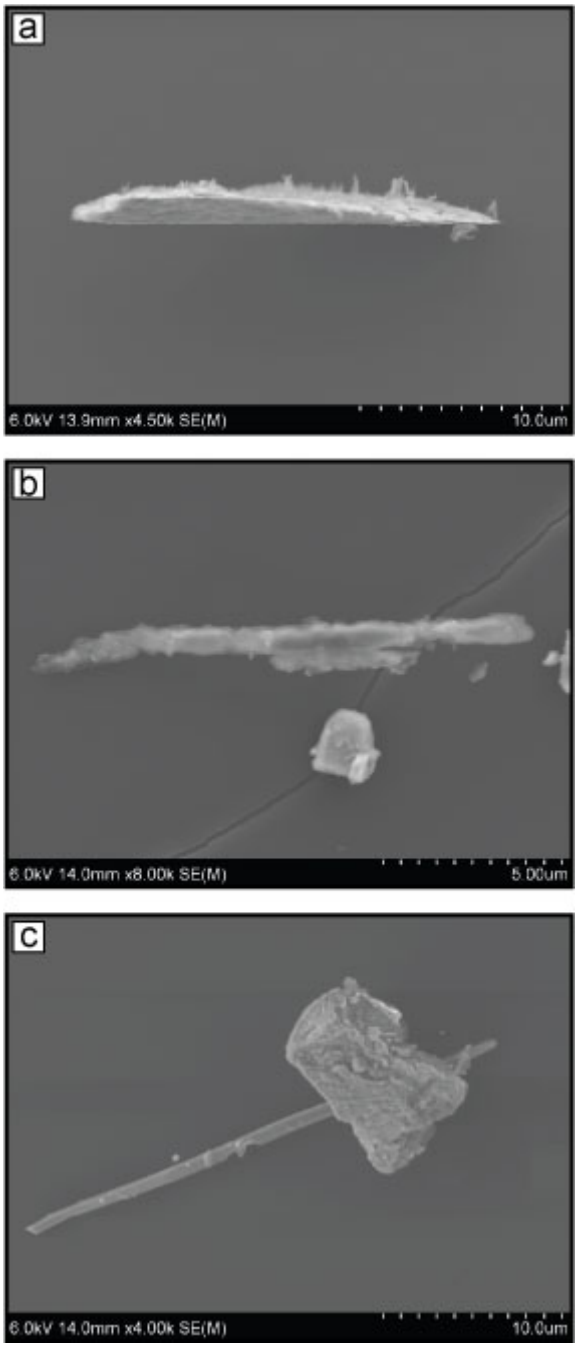

Figure 6.4: Scanning electron micrographs of fibre-like particles found in volcanic ash. Images are from COL.A03.10 (a) and MBA5/6/99 (b and c).

6.3.2.2 Particle Composition

The composition of a sample is of primary importance as it controls the post-depositional reactivity and duration for which a particle remains in the lung (termed *biodurability*). Particle composition was investigated in three ways: bulk chemistry, mineral assemblage, and biodurability.

6.3.2.2.1 Bulk Composition

The major elemental composition of bulk samples was determined by XRF. These data confirm the magmatic compositions of the samples, and provide insight into the toxicity-relevant chemistry of the samples; i.e., more mafic samples tend to release more iron from their surfaces and correspondingly generate more hydroxyl radicals (Horwell et al., 2007), whereas more felsic samples potentially have more crystalline silica (see Discussion).

XRF data for samples investigated are presented as a total alkali-silica (TAS) plot in Figure 6.5 and as raw data in Table 6.6. Results classify samples from Merapi as basaltic trachyandesitic to trachyandesitic, Colima as andesitic, Soufrière Hills as andesitic to dacitic, Santiaguito as dacitic, and Mount St. Helens as dacitic. It should be noted that the figure includes samples which may have undergone substantial fractionation in PDCs so the data may not entirely reflect whole rock compositions of the original lava. No XRF analyses were carried out on Unzen samples, and therefore representative data from Ossaka et al. (1994) are included purely for a TAS comparison. Specific samples used in Part II are noted in Figure 6.5.

6.3.2.2.2 Crystalline Silica

The presence of crystalline silica has been implicated in diseases resulting from industrial exposure to a variety of mixed dusts, including coal miners and granite workers (e.g., Vacek et al., 2010). The abundance of crystalline silica determined by the XRD-IAS technique as cristobalite and total crystalline silica (combined cristobalite and quartz) are shown in Figure 6.6. Cristobalite content and total crystalline silica both ranged from approximately 2 to 25 wt. %, with quartz being a minor phase in all but a few samples (Table 6.7).

Abundance is not constrained by volcanic centre ($p>0.05$, one-way ANOVA with Tukey's post test), as all location-specific sample suites with more than two samples span 8 wt. % or more: 14 wt. % at Santiaguito (3-17 wt. %); 15 wt. % at Mount St. Helens (4-19 wt. %); 8 wt. % at Merapi (2-10 wt. %); and 21 wt. % at Soufrière Hills (4-25 wt. %). No differences were determined between dome collapse, ash venting and explosive samples as could be done for Soufrière Hills samples (see Horwell et al., submitted-a; Appendix 4) since eruption style was predominantly constrained by volcano; e.g., all Santiaguito samples are ash venting whereas all Merapi samples, apart from MER.arc, are explosive (Table 6.1).

Table 6.6: Major element analyses by XRF for samples of ash. Data are in oxide weight %. Data for Unzen sample FG-9106b* are taken from Ossaka et al. (1994) for comparative purposes and are not used in this study.

Sample	SiO_2	TiO_2	Al_2O_3	Fe_2O_3	MnO	MgO	CaO	Na_2O	K_2O	P_2O_5	SO_3	LOI	Total
Colima, Mexico													
COL A03/10	59.12	0.62	16.52	5.91	0.11	3.76	6.27	4.21	1.19	0.17	--	1.38	99.26
COL A09/09	58.77	0.62	17.00	5.59	0.11	3.37	6.35	4.49	1.20	0.17	--	1.69	99.36
Mount St. Helens, USA													
MSH 05 DG 310-2	65.15	0.63	17.00	4.59	0.08	2.10	4.93	4.56	1.37	0.13	--	0.00	100.54
MSH 05 DZ-4-19	63.99	0.64	17.58	4.63	0.08	1.97	5.27	4.62	1.28	0.12	--	0.08	100.26
MSH 05 PS-8-19-1	64.66	0.68	17.05	4.88	0.08	1.95	4.90	4.56	1.34	0.12	--	0.10	100.32
MSH-CJH	65.07	0.62	16.36	4.33	0.08	1.58	4.60	4.51	1.50	0.15	--	1.11	99.91
Merapi, Indonesia													
MER 2010_01	55.52	0.71	18.02	7.73	0.18	1.81	6.69	3.92	2.67	0.28	0.44	1.07	99.04
MER 2010_02	57.42	0.51	19.13	5.25	0.15	1.51	6.52	4.11	2.84	0.28	0.12	1.38	99.24
MER 2010_03	54.69	0.74	19.29	7.76	0.19	2.25	8.12	3.73	2.16	0.30	0.05	0.28	99.55
MER 2010_04	56.48	0.65	18.17	6.64	0.17	1.75	6.61	4.02	2.84	0.29	0.42	1.16	99.20
MER 2010_05	52.98	0.79	18.59	8.41	0.21	2.89	9.11	3.64	2.10	0.30	0.03	0.10	99.15
MER 2010_06	53.58	0.83	18.64	8.61	0.21	2.91	8.87	3.51	1.97	0.29	0.00	0.20	99.62
MER 2010_07	51.90	1.02	17.41	10.72	0.26	3.77	9.47	3.31	1.80	0.31	<0.002	-0.02	99.95
MER 2010_08	54.37	0.75	19.29	7.86	0.20	2.67	8.52	3.75	2.19	0.27	0.01	0.11	99.98
MER 2010_09	54.75	0.73	19.04	7.53	0.19	2.48	8.32	3.71	2.23	0.27	0.23	0.31	99.78
MER 2010_10	53.45	0.82	18.93	8.72	0.21	2.89	8.98	3.52	2.03	0.28	<0.002	-0.17	99.67
MER 2010_11	53.77	0.79	19.15	8.35	0.20	2.56	8.75	3.60	2.08	0.28	0.10	0.04	99.67
MER 2010_12	55.91	0.57	19.88	5.89	0.16	1.81	7.70	3.91	2.38	0.28	0.05	0.54	99.09
MER-CJH	59.28	0.52	18.53	5.34	0.16	1.43	6.20	4.02	2.99	0.29	--	1.15	99.90
Unzen, Japan													
FG-9106b*	64.20	0.62	16.89	4.00	0.09	2.01	4.86	3.45	2.24	0.17	--	--	98.53

Soufrière Hills, Montserrat

MVO 1498	65.84	0.51	15.56	5.63	0.15	2.23	5.67	3.44	1.07	0.10	--	0.18	100.38
MBA5/6/99	63.92	0.52	15.60	6.18	0.15	2.34	5.85	3.78	0.87	0.15	--	0.42	99.79
MBA12/7/03	61.91	0.56	16.37	6.57	0.15	2.34	6.33	3.86	0.92	0.15	--	0.46	99.63

Table 6.7: Abundance of crystalline silica polymorphs by X-ray diffraction using the IAS method of Le Blond et al. (2009). Data are presented as weight %.

Sample	Cristobalite	Quartz	Total Crystalline Silica
Colima, Mexico			
COL.A09.09	5.57	0.54	6.11
COL.A03.10	5.32	0.62	5.94
Merapi, Indonesia			
MER.A10.01	1.93	0.00	1.93
MER.A10.02	3.18	0.00	3.18
MER.A10.03	2.72	0.00	2.72
MER.A10.04	5.96	0.00	5.96
MER.A10.05	3.44	0.00	3.44
MER.A10.06	4.30	1.25	5.55
MER.A10.07	5.54	0.00	5.54
MER.A10.08	4.44	0.00	4.44
MER.A10.09	4.60	0.00	4.60
MER.A10.11	6.01	0.00	6.01
MER.A10.12	8.81	0.00	8.81
MER.A10.13	3.17	0.00	3.17
MER.A10.14	4.48	0.00	4.48
MER.A10.15	7.87	0.00	7.87
MER.A10.16	3.20	0.74	3.95
MER.A10.17	9.52	0.00	9.52
MER.A10.18	4.21	0.66	4.87
MER.A10.19	3.43	0.00	3.43
MER.A10.20	10.33	0.00	10.33
MER.arc	3.84	0.00	3.84
Mount St. Helens, USA			
MSH.05.DZ	12.78	0.00	12.78
MSH.05.DG	18.75	4.05	22.80
MSH.05.PS	14.05	0.00	14.05
MSH.05.CT	14.05	0.00	14.05
MSH.04.HSR	9.49	4.92	14.41
MSH.309.G	16.21	0.00	16.21
MSH.arc	4.24	1.84	6.08
Santa Maria, Guatemala			
SG.A09.04	3.20	0.00	3.20
SG.A09.07	13.43	0.00	13.43
SG.A09.08	16.96	0.00	16.96
Soufrière Hills, Montserrat			
MBA5/6/99	15.23	1.20	16.43
MVO1498	31.87	0.00	31.87

MBA12/07/03	11.84	1.60	13.44
Unzen, Japan			
UNZ.02	7.95	*	7.95
UNZ.03	10.07	*	10.07

*Unzen data for quartz not available.

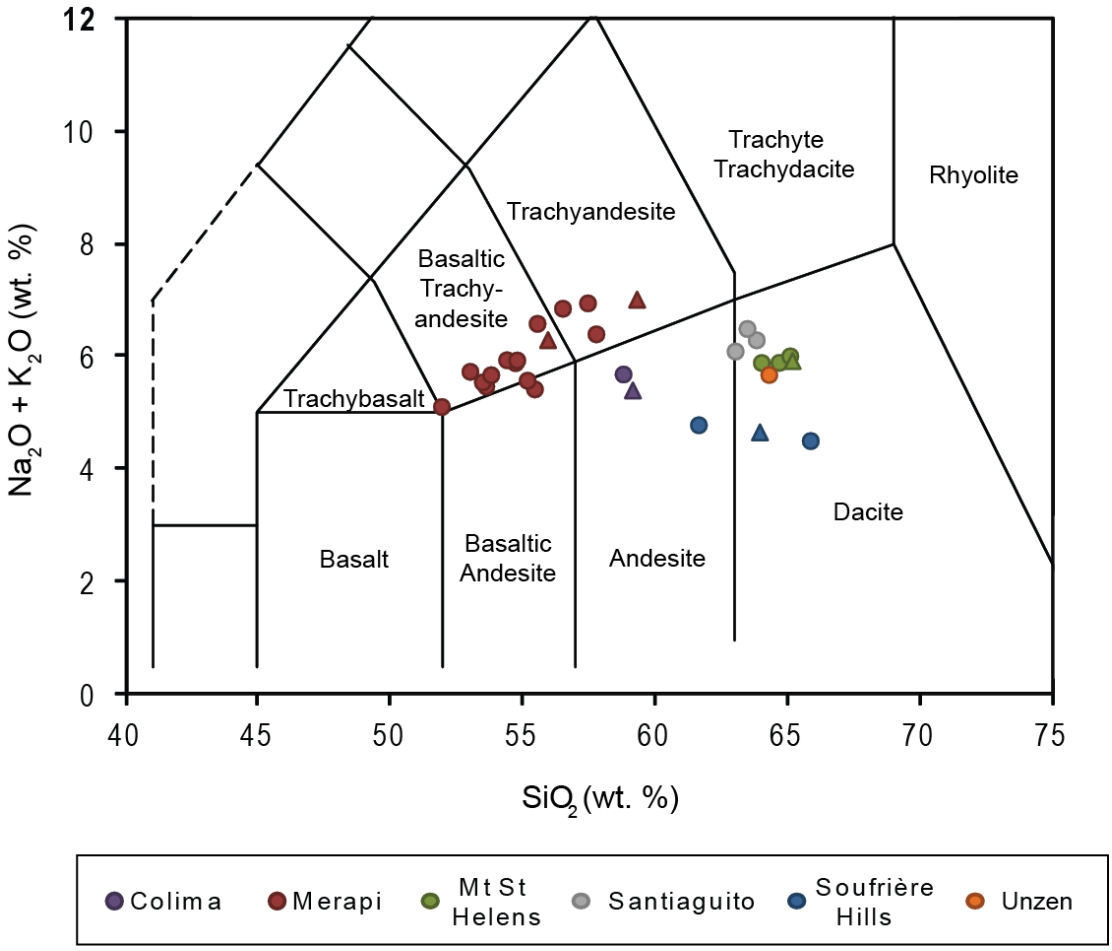

Figure 6.5: Total alkali silica (TAS) diagram for bulk ash samples used in this study. Samples marked with triangles are the bulk samples chosen for further analyses in Part II. Unzen data are from Ossaka et al. (1994) and do not correspond to a sample used in the current study, but are included as a reference for the Unzen TAS designation. Data for Soufrière Hills are from Horwell et al. (2007) as well as collected for this study. Compositional boundaries are after Le Bas and Streckeisen (1991).

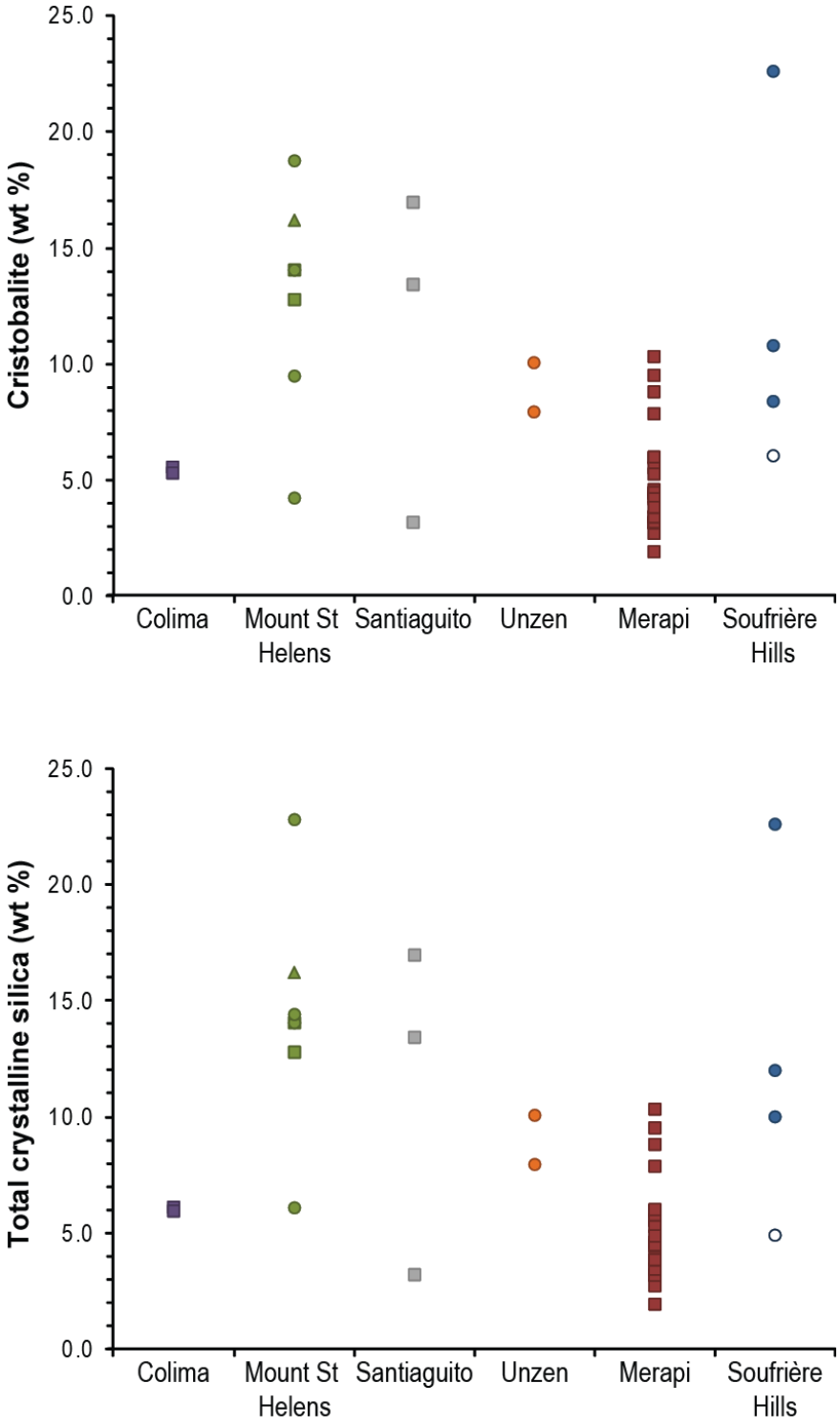

Figure 6.6: Abundance of cristobalite and total crystalline silica (cristobalite and quartz) determined for samples of volcanic ash by the XRD-IAS method of Le Blond et al. (2009). Dome collapse samples are circles, and explosive samples are squares. The triangle for Mount St. Helens is MSH.309.G, a gouge sample. All Soufrière Hills data are from Horwell et al. (submitted-a; Appendix 4). The open-circle Soufrière Hills sample (MVO22/10/09) is included to show the lower limit of the range observed for Soufrière Hills samples.

Sufficient mass of respirable material was not recovered for all samples to confidently quantify the amount of crystalline silica by XRD. Horwell et al. (2003b), however, showed by SEM analysis that crystalline silica in Soufrière Hills dome-collapse ash is enriched in the respirable fraction (< 4 μm), and is particularly concentrated in the very fine fraction (< 2 μm). This enrichment was further investigated in the present study using the XRD-IAS method for the respirable Soufrière Hills sample MRA5/6/99 (also used by Horwell et al. (2003b)), where equivalent abundances were found, 19.0 wt. % in the bulk versus 19.3 wt. % for the respirable fraction; indistinguishable within the 3 wt. % error of the technique. Due to the discrepancy, the cristobalite abundances reported for bulk samples (Table 6.7) are considered to be a minimum value for the respirable samples used here. We are currently working on a small-well technique to reproducibly quantify small amounts of material (< 30 mm^3).

6.3.2.2.3 Biodurability

Human respiratory and gastric systems are sites of deposition where many mineral phases are undersaturated with respect to biological fluids, and dissolution kinetics control the persistence of these minerals in biological environments. It is therefore generally agreed that the biodurability of particles (i.e., the resistance to dissolution in the lung; Chapter 2) is a major factor for the characterisation of potential health effects (Guthrie, 1997; Schwarzel et al., 2007).

Particle biodurability assays were conducted to investigate which primary minerals might dissolve in synthetic physiological fluids and the types of secondary minerals, if any, that are likely to precipitate in the lung following the inhalation of a mixed dust. This was determined through digestion of bulk ash in preparations of simulated lung fluid (modified Gamble's solution; SLF) and artificial lysosomal fluid (ALF) (Table 3.5). Bulk samples were used as insufficient mass was obtained from the separation experiments to use for biodurability as well as cellular toxicity assays.

Precipitation of secondary minerals in all samples was undetectable by XRD, and no major differences in the dissolution of the primary mineralogy (excluding glass) were observed among samples. All samples lost mass during digestion, with the Colima samples losing the most (8.05 wt. % in SLF; 14.07 wt. % in ALF) (Table 6.8), and all samples appear to be less biodurable in ALF (3.36 – 14.07 % of material lost) than SLF (1.95 - 8.05 % of material lost). This difference in effect on the original mineralogy between the two synthetic solutions is shown for sample MER.arc in Figure 6.7, where the plagioclase peak at 28 °2θ for the ALF digest is considerably reduced compared to the bulk and SLF digest. Crystalline silica is still present in all samples; however, the proportion relative to other phases is sample

dependent. The abundance was only quantified for two samples (MER.PDC and COL), where cristobalite enrichment occurred to a greater extent in ALF (a 35.4 and 21.4 % increase, respectively) than SLF (an 8.7 and 7.8 % increase, respectively). These data support the mass loss results observed between SLF and ALF (Table 6.8); however, the differences in the amount of cristobalite were not greater than the 3 wt. % error of the XRD-IAS technique.

Table 6.8: Differences in mineral phase proportions in bulk ash samples following digestion at 37 °C for 4 weeks in synthetic lung fluid (SLF; modified Gamble's solution; n=3) and artificial lysosomal fluid (ALF; n=1). Data are presented as a percentage loss in mass.

Sample	**% Dissolved**		**% Cristobalite**		**% Increase over bulk**	
	SLF	*ALF*	*SLF*	*ALF*	*SLF*	*ALF*
COL	4.4	8.0	5.7	6.5	21.4	7.8
MER	2.0	3.4				
MER.PDC	7.8	13.9	5.9	7.4	35.4	8.7
MSH	8.1	14.1				
UNZ	6.2	9.3				

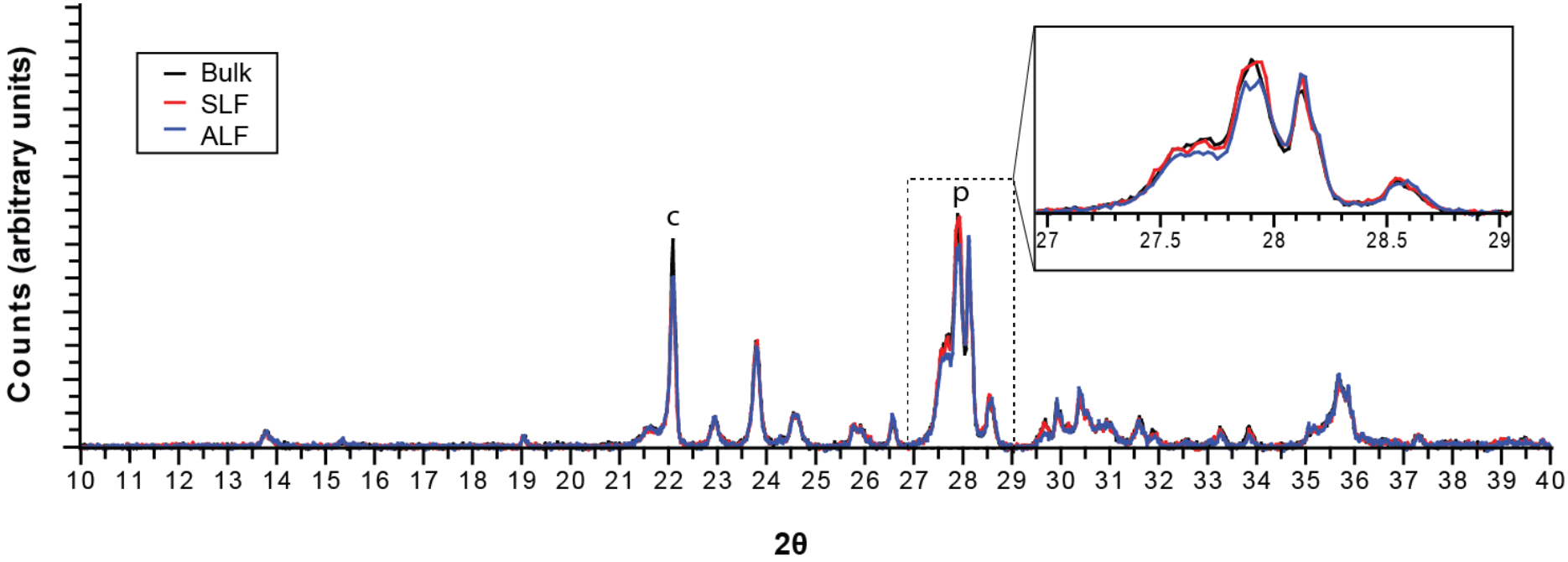

Figure 6.7: Biodurability of mineral phases in volcanic ash. Powder X-ray diffraction patterns from thin smears of digested (SLF and ALF) and untreated (bulk) mineral assemblages from batch experiments of sample MER.arc in simulated biological fluids. Inset is of the primary feldspar region. The primary cristobalite peak (c) and plagioclase feldspar peak (p) are labelled.

6.3.2.3 Particle surface reactivity

6.3.2.3.1 Bio-available iron

The presence of bio-available iron ions at the particle surface, which may partake in hydroxyl radical generation via the Fenton reaction (Chapter 2), was determined by incubating 15 ash samples (11 present study samples and 4 previously run samples for comparison) in an iron-specific chelating solution (Chapter 3). The amount of iron removed per unit surface area after 7 days of incubation is shown in Figure 6.8, and ranged from 2.5—30.7 μmol m^{-2} Fe^{2+}, 7.6—63.2 μmol m^{-2} Fe^{3+}, and 13.4—91.0 μmol m^{-2} total Fe. When considered against concurrently run 'comparative' samples, which have been used as standard samples in previously published studies (e.g., Hillman et al., 2012; Horwell et al., 2007; Le Blond et al., 2010), and include MBA5/6/99 also used in this study, these results are substantially lower than observed for basaltic samples from Cerro Negro and Etna (219.3 and 482.0 μmol m^{-2} total Fe). The four comparative samples all responded as previously observed under the same test conditions (Hillman et al., 2012; Horwell et al., 2007; Horwell et al., 2003a; Horwell et al., 2010b; Le Blond et al., 2010). The 2010 Merapi samples uniformly released the most Fe^{2+} as well as Fe^{3+}, which was expected as they are the most mafic in this study; however, no trend was observed for samples which released the least.

6.3.2.3.2 Free radical generation

Particle surface reactivity can be estimated by the ability of a particle to generate reactive oxygen species (Fubini et al., 1995b), which was measured here directly by means of the ESR/spin-trapping technique. Two types of radicals were measured; hydroxyl radicals ($^{\bullet}OH$) by Fenton activity and carboxyl radicals ($COO^{\bullet -}$) by cleavage of a C-H bond.

6.3.2.3.2.1 Hydroxyl radical generation

Horwell et al. (2007; 2003a) have shown that volcanic ash is capable of generating the hydroxyl radical via the iron-catalysed Fenton reaction. Eleven samples (Table 6.2) were tested alongside the four comparative samples used for the iron release experiment for their potential to generate $^{\bullet}OH$ radicals in aqueous suspension at 10, 30, and 60 minutes. Data were normalised per unit surface area (Figure 6.9). The two basaltic samples (Etna and Cerro Negro) generated more $^{\bullet}OH$ than the more silicic sample suite investigated, except for MSH.05.DZ which generated a commensurate amount as Cerro Negro. Except for MSH.05.DZ all samples presently investigated also generated fewer $^{\bullet}OH$ radicals than MBA5/6/99 (which is included in this study but is also used commonly as a comparative standard in this type of analysis; e.g., Damby et al. (2012; Appendix 4), Le Blond et al. (2009), and Hillman et al., (2012)), with UNZ.03 and COL.A03.10 generating equivalent numbers. Generation of $^{\bullet}OH$ did not correspond with the magmatic composition assigned in

Figure 6.5 for the other samples tested; e.g., the more mafic, iron-rich Merapi samples did not generate a greater number of radicals than the other samples.

For most samples, the production of $^{\bullet}OH$ increased with time, with a greater number of radicals measured at 60 minutes (and generally 30 minutes) compared to 10 minutes. This kinetic increase was not observed for samples that produced low levels of radicals in general (e.g., MSH.arc and MER.A10.12), and could partially result from error involved in quantifying very-low amplitude EPR signals.

6.3.2.3.2.2 Carboxyl radical generation

The second reaction used to investigate the iron-related activity is the cleavage of the C-H bond in the formate ion (HCO_2^-; Chapter 3). This is a model reaction that may occur with many molecules of interest, such as peptides, proteins, and lipids, and yields the formation of the carbon-centred radical $COO^{\bullet-}$. Data are qualitative as it was a preliminary experiment to assess the potential of homolytic C-H cleavage.

Of the three samples tested (MER.A10.03, MER.A10.04, and MER.A10.12) in a non-reducing environment, only MER.A10.03 generated carboxyl radicals at 60 minutes (Figure 6.10). In the presence of ascorbic acid, however, MER.A10.04 also generated carboxyl radicals from as early as 10 minutes.

6.3.2.3.3 Haemolysis

Haemolysis results are often expressed in terms of surface area since it is considered a better metric for inflammation than mass (Duffin et al., 2002; Oberdorster, 1996). However, an insufficient amount of respirable material was recovered to analyse the surface area by nitrogen adsorption. Further, the low surface area for bulk samples would require sufficient ash to overload the experimental setup if performed according to equivalent surface areas. Results are therefore reported per mass dose. Assays for bulk and respirable ash were run concurrently.

The haemolytic potential of the respirable fraction was compared to bulk ash (Figure 6.11) as an increased potential to cause erythrocyte lysis has been observed for equivalent doses of finer material (e.g., Francis et al., 2009); bulk haemolysis may therefore not be entirely representative of the hazard. Differences in haemolysis were observed between bulk and respirable samples from Colima and Merapi, where the respirable fraction showed a dose-dependent response. Results between the bulk and respirable fraction for all other samples (Merapi PDC, Mount St. Helens, Soufrière Hills, and Unzen) were not statistically distinct ($p>0.05$, Student's t-test). Haemolysis was carried out on the residual material following separation for the Merapi sample to consider the reactivity of the respirable and non-

respirable fractions relative to the bulk (Figure 6.12). Only the respirable fraction resulted in measurable haemolysis. Grinding of bulk ash to produce freshly fractured surfaces did not significantly increase the haemolytic potential of the samples ($p>0.05$).

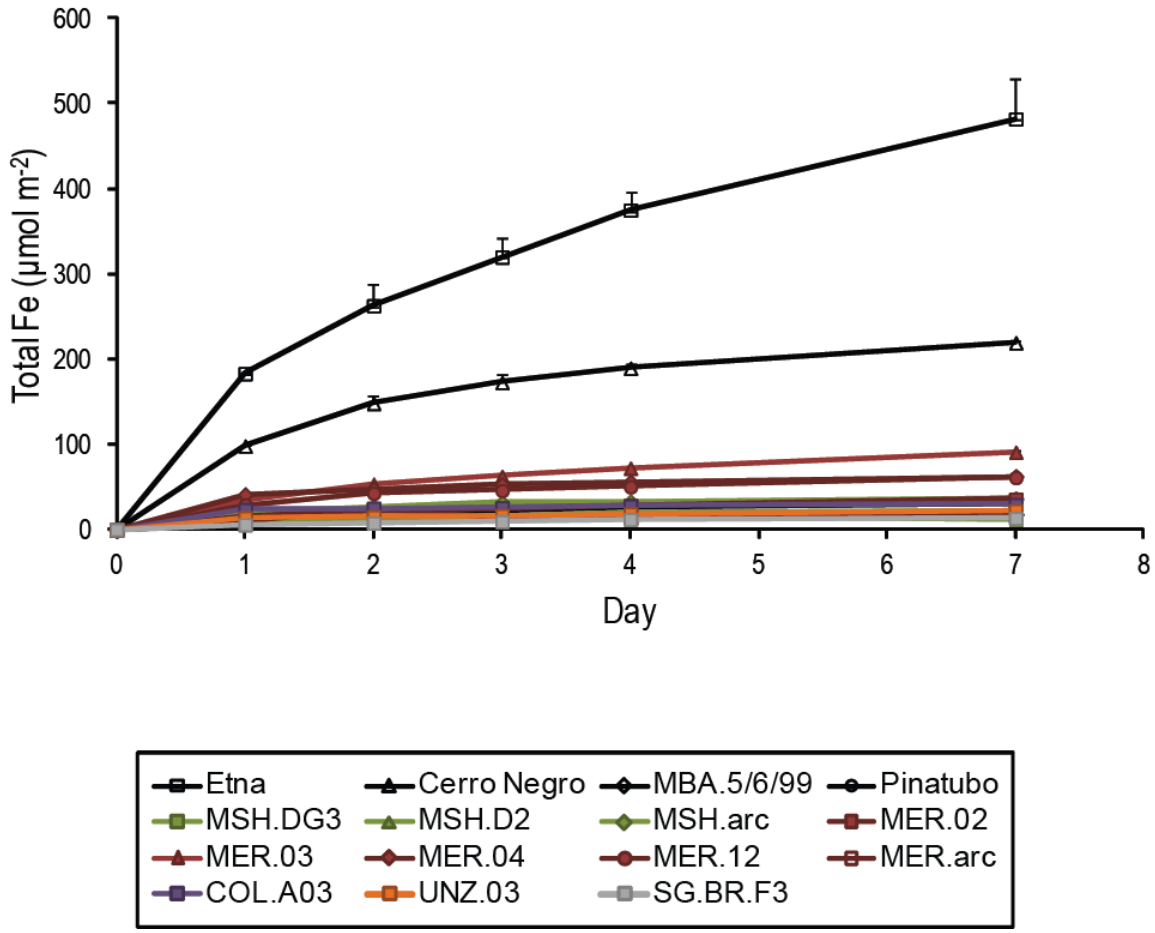

Figure 6.8: Total iron removed (ferrozine solution plus ascorbic acid as a reducing agent) from the surfaces of bulk ash samples over 7 days (n=2, error bars are 1 SD).

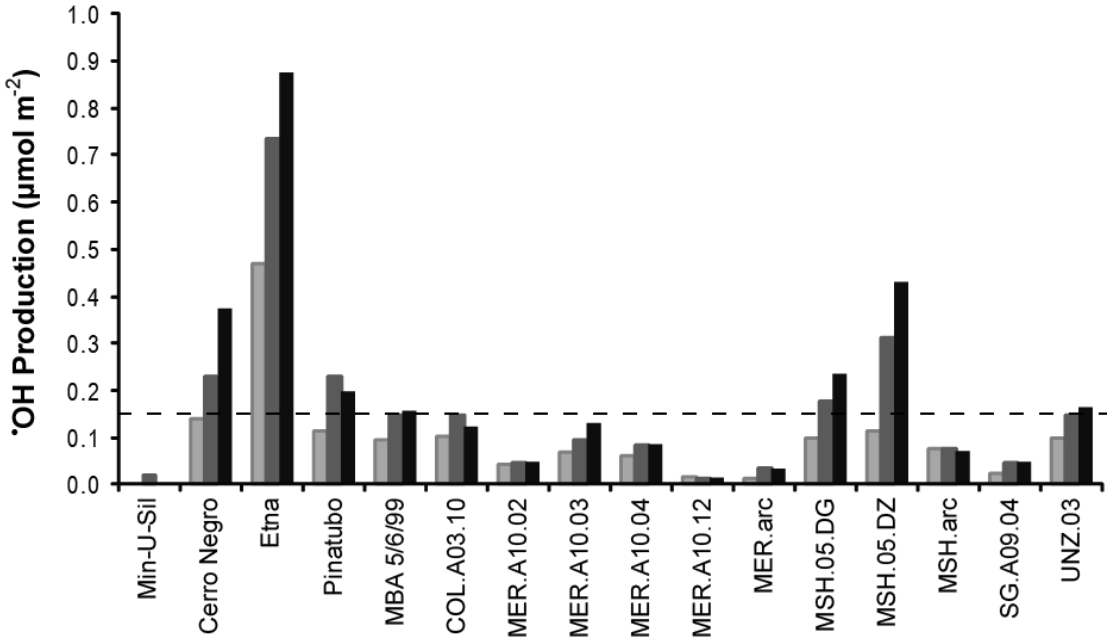

Figure 6.9: Hydroxyl radical (•OH) generation at 10, 30 and 60 minutes for bulk ash samples along with concurrently run ash comparisons. Data for Merapi samples (MER.A10.03 and MER.A10.12) are from Damby et al. (2012) but were analysed concurrent with all samples (n=3).

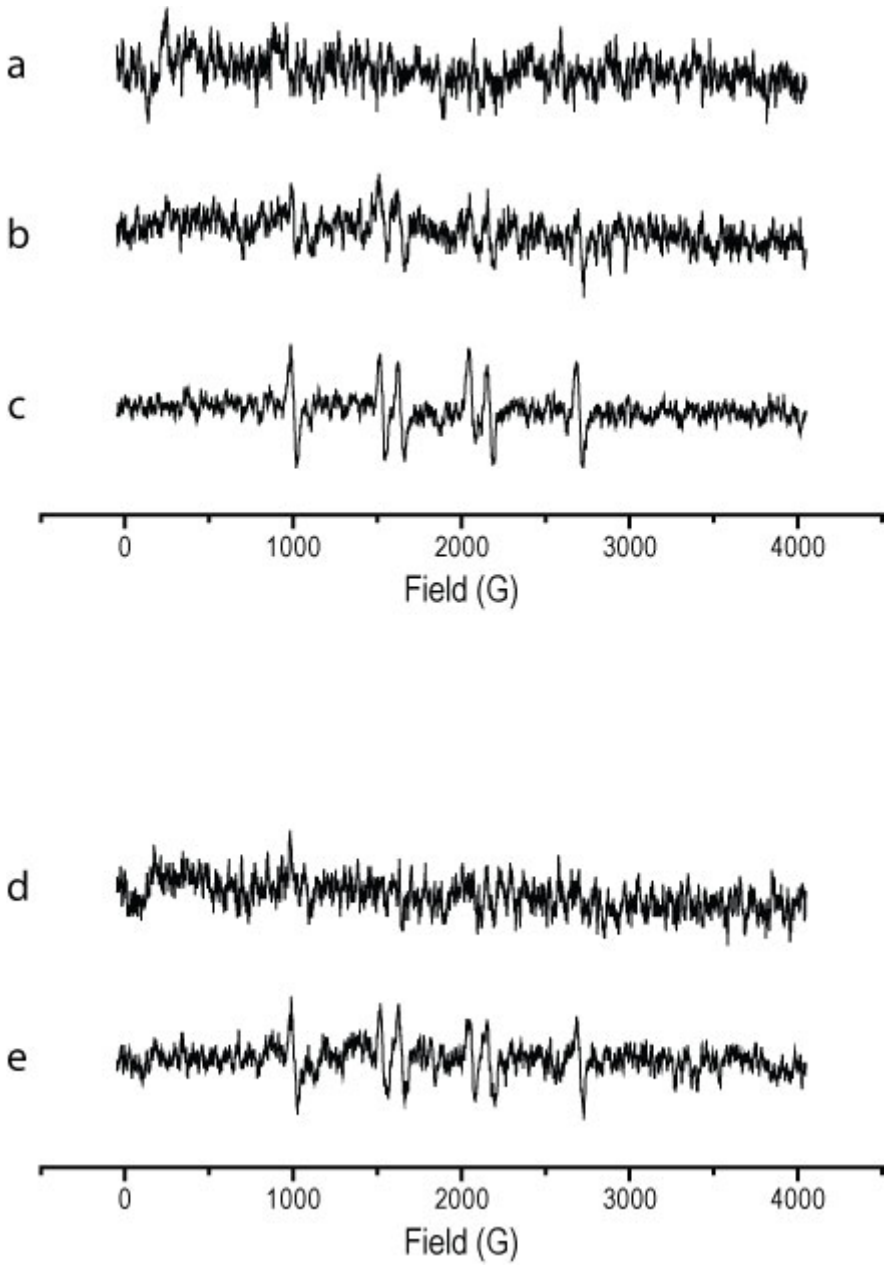

Figure 6.10: Carboxyl radical ($COO^{\bullet -}$) generation at 60 minutes for bulk samples (a) MER.12, (b) MER.04, and (c) MER.03. Carboxyl radical generation for (d) MER.04 at 10 minutes and (e) MER.04 at 10 minutes in the presence of ascorbic acid.

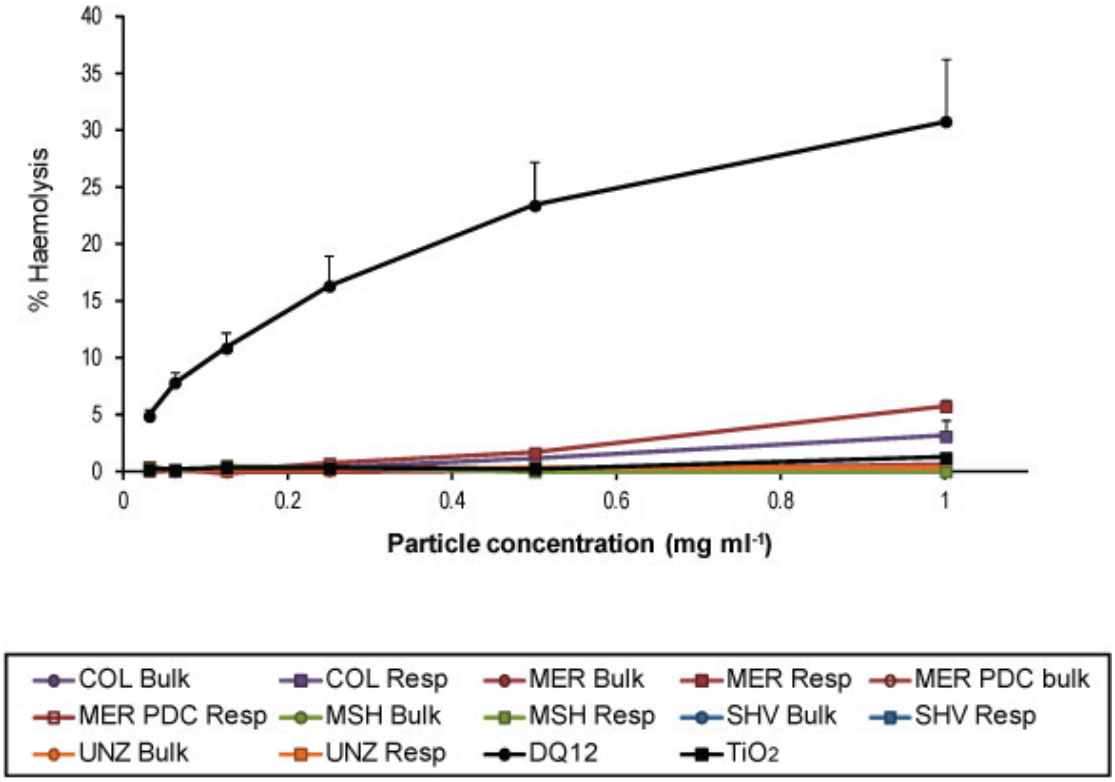

Figure 6.11: Dose-dependent haemolysis results for bulk ash compared to respirable fraction. DQ12 was used as a positive control and TiO_2 as a negative. Data are the average of n=3, reported with the standard error of the mean.

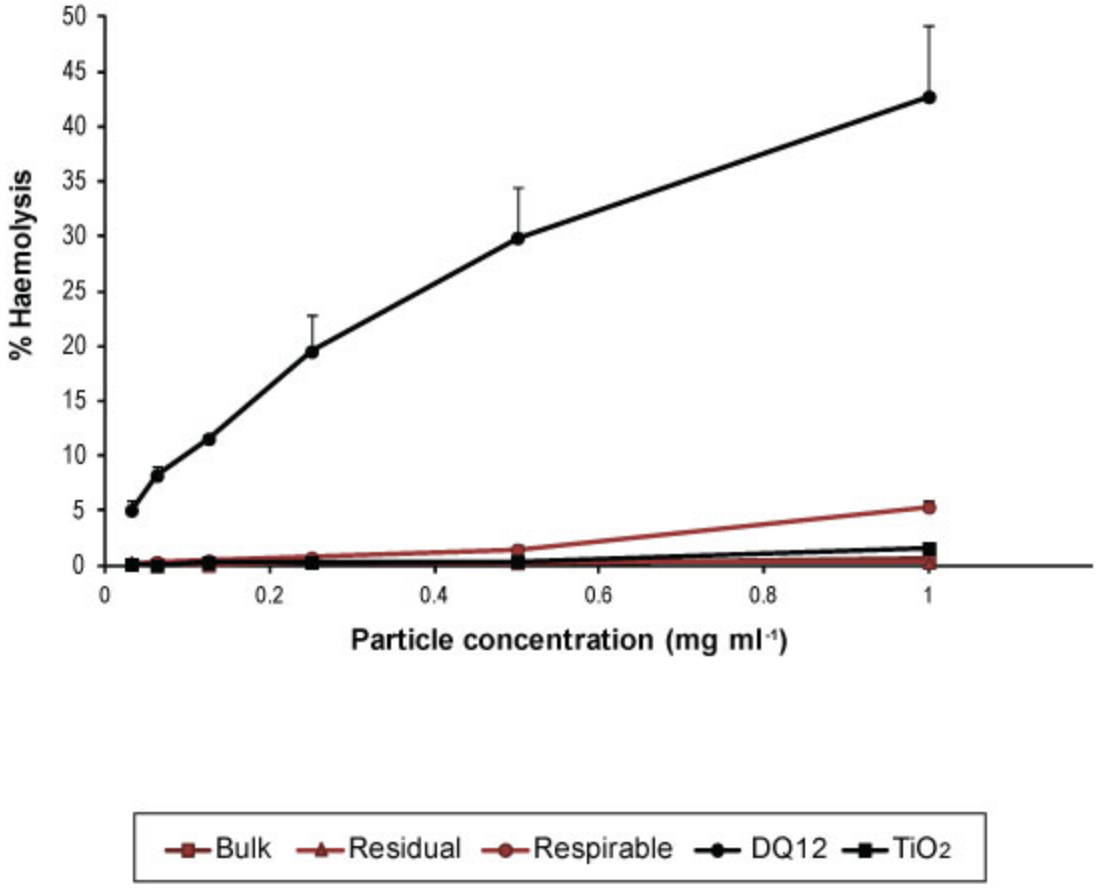

Figure 6.12: Comparison of the haemolytic potential for bulk sample MER.arc, the respirable fraction, and the residual material leftover following separation of the respirable fraction.

6.3.3 Discussion: Part I

6.3.3.1 Physical properties of bulk ash and separated respirable fractions

Grain size, surface area, and particle morphology directly affect the aerodynamic deposition of a particle in the lungs and the post-depositional interaction resulting from exposure (e.g., surface reactivity and mineral dissolution) and are, therefore, critical physicochemical controls on toxicity that need to be well constrained.

Ash from eruptions involving dome material, be it explosive (e.g., the 2010 eruption of Merapi) or dome-collapse (e.g., samples from Soufrière Hills) varies considerably in its grain size distribution, which makes forming generalisations difficult. The range of eruption energies and freshness of the fragmented material as well as plume dynamics and collection distance can all account for the observed natural variability. The breadth of observed grain sizes also emphasises the urgency with which GSD analyses need to be carried out when determining the respiratory hazard posed by an eruption.

No trends were interpreted within the observed range (0-18 vol. % sub 4 μm) for differences in eruption styles (i.e., explosive, full dome collapse, or ash venting) due to the deficiency of information concerning the eruptive origin of many samples. However, individual samples, e.g. COL.A09.09 (18.43 vol. % sub 4 μm), confirm previous observations by Horwell (Horwell, 2007) that incorporation of dome material can result in particularly fine-grained ash. Indeed, incorporation of dome material is thought to account for the particularly fine grained nature of MER.A10.02 (15.63 vol. % sub 4 μm) compared to other samples from the same eruption (0-12.76 vol. % sub 4 μm)(Damby et al., 2012; Appendix 4). Sample COL.A09.09 is the finest dome collapse sample analysed by more than 3 wt. % sub 4 μm and is comparable to the finer, lofted material of the Merapi PDC surge (MER.A10.13 and MER.A10.14), and similar to gouge material at Mount St. Helens. This perhaps indicates a contribution of abrasive fragmentation to the fineness of dome-collapse ash.

Deposition in the lung does not abide by strict size filtering; it depends on aerodynamic diameter (Chapter 2), which takes account of particle mass and drag (and therefore morphology). A general blocky morphology was similar for most particles examined, with rare exceptions. As seen with ash from other eruptions (e.g., Rabaul (Le Blond et al., 2010) and Eyjafjallajökull (Horwell et al., submitted-b; Appendix 4), although not dome forming), fibre-like particles can be observed in particular samples; however, they are non-asbestiform and occur infrequently (Figure 6.4). The imaging carried out here, however, does not discount the possibility of nanofibres, like the 20 nm wide cristobalite nanofibres identified in Chaitén ash by TEM (Reich et al., 2009), since they are beyond the resolution provided by

SEM. Nanofibres could be a common feature of volcanic ash given that Hillman et al. (2012) observed sparse nanofibres at Sakurajima by TEM, however, fibres in that study were not related to crystalline silica or other toxic minerals (e.g., asbestos). In both studies, fibres appear to comprise a minute fraction of the respirable material, suggesting a very low dose to the lung per exposure. Further, those imaged by Reich et al. (2009) in Chaitén ash appear to be hosted within amorphous material, resembling a growth texture rather than distinct fibres, and are hypothesised to have formed within the eruption plume rather than being a product of the dome. Although identified as nanofibres, the aerodynamics of the associated host grain may overshadow their immediate depositional hazard. Accordingly, their ability to impair phagocytosis and clearance (key elements of nanofibre toxicity; Donaldson et al., 2010) must be weighed against the dissolution of the surrounding host material and concomitant unveiling of the cristobalite nanofibres from within.

The range in surface area observed for the samples reinforces the expected order of magnitude for volcanic ash; although, similar to grain size and crystalline silica content, specific surface areas were not constrained by volcanic location. A rough correlation between surface area and grain size exists, where smaller particles have larger surface areas, assuming equivalent particle morphologies, particle size distribution in a heterogeneous mixture, surface porosity and surface roughness (Ono-Ogasawara and Kohyama, 1999). As such, the comparatively low surface areas observed could correspond with the coarse overall grain size distributions, where the majority of samples are below 10 vol. % sub 4μm. The surface area of volcanic ash is low compared to known toxic dusts; e.g., 10.1 m^2 g^{-1} for DQ12 quartz (Clouter et al., 2001), various forms of asbestos (1-50 m^2 g^{-1}) (Ono-Ogasawara and Kohyama, 1999) and nanoparticles (50-300 m^2 g^{-1}) (Monteiller et al., 2007; Oberdörster et al., 2005b).

6.3.3.2 Composition and crystalline silica content

Analysis of ash from the suite of field locations studied here confirms that each dome-forming volcano, from basaltic trachyandesitic to dacitic, is capable of producing cristobalite-bearing ash. Some samples contain elevated bulk SiO_2 content compared to dome rock samples from corresponding locations reported in Chapter 4. This results from fractionation of glass and lower density minerals into the finer fractions (Horwell et al., 2001; Horwell et al., 2003b) in an eruption or dome-collapse co-PDC plume. The subsequent elutriation and lofting of those fractions would result in SiO_2-enriched ash in comparison to the original magma or dome composition.

The abundance of cristobalite observed in ash is not constrained by location, with a range observed for each volcano (Figure 6.6). It is unknown whether similar eruption mechanics

among locations would result in better constrained, eruption-style dependent abundances, as was seen at Soufrière Hills, where dome-collapse ash was enriched relative to explosive ash (Horwell et al., submitted-a; Appendix 4). However, results from cristobalite in samples of dome rock (Chapter 4) suggest a wide range could still be observed; indeed, results from Mount St. Helens show that explosive samples (13-14 wt. %) sit within the range defined by dome collapse samples (4-19 wt. %). Horwell et al. (submitted-a; Appendix 4) have shown that even ash erupted during vulcanian explosions at Soufrière Hills can contain up to 7 wt. % cristobalite, confirming cristobalite as a hazard at dome-forming eruptions independent of eruption style.

The minimum amount of cristobalite can be assumed to be zero at dome forming volcanoes, although observed lower limits are ~2 wt. % (Table 6.7). A maximum cut-off is more difficult to define. Horwell et al. (submitted-a; Appendix 4) restrict the upper limit for cristobalite in ash from Soufrière Hills to 20-25 wt. % (n=20 for dome collapse and ash venting samples). No evidence exists from this study to suggest that concentrations in ash from other volcanic centres will surpass this upper limit. It may not, however, be a universal maximum, with other volcanoes having different limits restricted by magmatic and dome conditions; e.g., Chaitén volcano produced ash with concentrations below 19 wt. % (n=4 for samples erupted following dome growth; Horwell et al., 2010a), Sakurajima below 6 wt. % (n=12, from different eruptive phases; Hillman et al., 2012), and Rabaul below 3 wt. % (n=5, from the 2007-2008 eruptive period, where a small dome was observed but its contribution to the ash is unknown; Le Blond et al., 2010). These maximum values, however, are entirely dependent on the sample suite, evidenced here by a maximum of 19 wt. % at Mount St. Helens compared to the often-referenced 7 wt. % determined by an inter-laboratory study (Dollberg et al., 1986). Importantly, this upper limit needs to be interpreted in light of sample location, since cristobalite is preferentially fractionated into the finer fractions during fragmentation (Horwell et al., 2001; Horwell et al., 2003b), and eruption style; for example, the domes at Sakurajima are generally short lived (Hillman et al., 2012; Appendix 4) and only minor dome growth occurred at Rabaul (Smithsonian, 2012). Therefore, a better constrained sample suite would be required to statistically bolster these cristobalite-maximum observations.

Although abundance (or an upper limit) is not constrained by magma type, a comparison of whole rock SiO_2 (by XRF) with crystalline silica abundance reveals a positive correlation for ash from dome forming volcanoes (Figure 6.13). Cristobalite is a secondary mineral, and its abundance may not be a direct reflection of the lava in which it crystallised. As discussed in Chapter 4, Horwell et al. (post review; Appendix 4) found that dome rock from Soufrière Hills had up to 2 wt. % more bulk SiO_2 than pumice and postulated, therefore, that dome

rock had enriched SiO_2 following crystallisation of vapour phase cristobalite by bulk transport of Si in vapours; these results were supported for the locations studied here (Chapter 4). The results of the current study support the conclusions of Horwell et al. (post review; Appendix 4) and Chapter 4. In addition, however, this correlation for volcanic ash is likely strengthened by the fractionation of low density minerals such as crystalline silica and glass into the finer fractions, as discussed above.

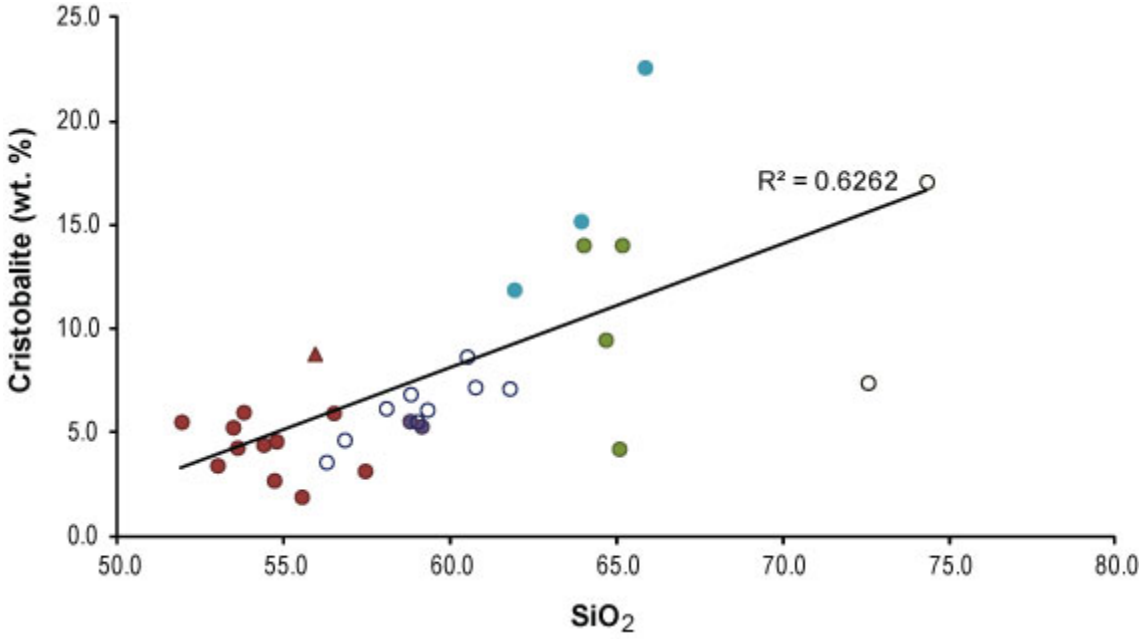

Figure 6.13: Comparison of cristobalite abundance determined by XRD with bulk elemental SiO_2 by XRF for bulk ash samples. Data for Chaitén samples are from Horwell et al. (2010a), Merapi data are from Damby et al. (2012; Appendix 4), Sakurajima are from Hillman et al. (2012; Appendix 4), and data for Soufrière Hills are from Horwell et al. (submitted-a; Appendix 4) as well as collected for this study. No samples from Unzen are included as no XRF data correspond to samples used for XRD. Red circles are Merapi, red triangle is Merapi PDC, empty purple circles are Sakurajima, filled purple circles are Colima, filled blue circles are Soufrière Hills, filled green circles are Mount St. Helens, and empty black circles are Chaitén.

Extrapolation of the trend line between bulk SiO_2 and crystalline SiO_2 in Figure 6.13 leads to an x-intercept at approximately 49 wt. % SiO_2. Taking this value as a hypothetical 'minimum' cristobalite threshold, ash at or below ~49 wt. % bulk SiO_2 should be devoid of cristobalite. This amount of bulk SiO_2 would categorise a sample as basaltic. The mechanisms differ for crystallisation of primary magmatic crystalline silica (i.e., quartz) and

secondary crystallisation of cristobalite in a volcanic dome; while quartz rarely forms in basaltic magma due to silica undersaturation, the expected lack of secondary cristobalite could suggest either localised or large-scale Si undersaturation in gas from basaltic volcanoes. More likely, as postulated in Chapter 4, there may be a viscosity control on the formation of cristobalite, whereby basaltic lavas are unable to provide the necessary conditions for a sufficient duration for devitrification and/or vapour phase deposition. Cristobalite has been documented in basaltic lavas as a secondary mineral deposited by hydrothermal fluids (e.g., Bargar et al., 1995); however, extrusive sub-aerial basaltic lava domes have not been observed and the possibility of analogous deposition in cinder cones has not yet been considered.

6.3.3.3 Dissolution of particles following lung deposition

Dissolution of minerals, thought to reflect the residence time of a mineral in the lungs (Davis, 1994), and formation of secondary minerals should be considered when addressing the respiratory health hazards of minerals as the mineral assemblage is unlikely to be static and fixed following deposition in the lungs.

X-ray diffraction analyses of the ash samples after four weeks of incubation in simulated lung fluid (SLF) and artificial lysosomal fluid (ALF) did not reveal any new minerals in the treated samples, suggesting any mineral precipitation in the lungs after exposure to heterogeneous volcanic dusts would require a longer duration than investigated here. Dissolution rates of single mineral phases in simulated lung fluid (pH 7.4) have been calculated by reaction-path modelling by Taunton et al. (2010). It was found that occupational exposure levels (1 m^2 g^{-1} surface area) of quartz (rate constant of 1.40×10^{-17} mol. cm^{-1} s^{-1}) (Jurinski and Rimstidt, 2001) and albite (rate constant of 1.00×10^{-16} mol. cm^{-1} s^{-1}) (Blum and Stillings, 1995) do not appreciably dissolve over a 50 year span, while anorthite dissolves in 5 years and 99 % of orthoclase dissolves in 12 years (rate constant of 1.00×10^{-14} mol. cm^{-1} s^{-1} for both feldspars (Blum and Stillings, 1995)). These durations are orders of magnitude longer than the current experiments, explaining the very limited change in the dominant silicate assemblage observed.

The increase in crystalline silica in the digest samples (by 20-25 %) is likely the effect of enrichment relative to other components rather than an absolute molar increase due to *in situ* precipitation. Crystalline and amorphous silica have been observed as products of chrysotile (Favero-Longo 2005) and talc (Jurinski and Rimstidt 2001) dissolution; however all forms of silica were undersaturated in the feldspar systems modelled by Taunton et al. (2010), where silica was preferentially incorporated by other phases (e.g., mesolite, celadonite, or talc) before silica supersaturation. Icopini et al. (2004) confirm that crystalline silica would not be

the first silica phase to precipitate under physiological conditions. However, complete conversion of volcanic glass to crystalline silica has been observed in less than 6 years in solution at ambient temperatures (Cuadros et al., 2012). The mechanism likely involved the rapid transformation of cation-depleted glass to quartz, which would result in both devitrification as well as deposition from solution. Minor alunite and calcite also formed, accounting for the other elements originally hosted in the glass. Crystalline silica precipitation *in vivo* on longer time scales than investigated in the present study would have obvious disease implications; however the transformation needs to be considered against particle residence time and, especially, the kinetics of glass dissolution in a fixed volume.

The aqueous composition of lung fluids is not well constrained for some of the critical ions associated with mineralisation, particularly those associated with organic complexation. Organic ligands generally increase dissolution rates for silicates (Cama and Ganor 2006, Golubey and Pokrovsky 2006, Welch and Ullman 2000, Blum and Stillings 1995), suggesting that the presence of organic acids in the body will likely increase the rate of mineral dissolution under physiologic conditions. Enzymatic effects on dissolution rates (positive or negative) need to also be considered to more fully describe the reactions governing mineral dissolution.

Dissolution of amorphous silica takes place over a much shorter timescale than crystalline silica, with rates of up to 0.05 mg cm^{-1} h^{-1} and solubilities of 2.5 mmol l^{-1} in biological media (pH 7, 37 °C) (Roelofs and Vogelsberger, 2004) compared to 0.45 mmol l^{-1} for cristobalite and 0.09 mmol l^{-1} for quartz (Iler, 1979). Roelof and Vogelsberger (2004) confirm that amorphous silica dissolution is more rapid than the reverse precipitation rate. Therefore, volcanic glass is likely to be undersaturated in extracellular and lysosomal fluid and readily dissolve, contributing Na, Al, Si, Mg, K, Ca, Ti, Fe, Mn, P, Cl, F, S and a host of other trace elements to the solutions already rich in physiological ions (Chapter 3: Methods). Acellular studies show that dissolution of amorphous silica is a function of time and pH, with a minimum solubility found around pH 4 (Vogelsberger et al., 1996), and a maximum similar to that of lysosomal fluid (pH 5.5 in this study; Chapter 3: Methods). X-ray diffraction analyses were performed in the present study as thin smears, which better detect differences in the mineral assemblage but provide little quantitative information. Therefore, as no new phases were present and little dissolution of other minerals was observed, the change in mass observed following digestion in SLF (2-8 %) and ALF (3-14 %) can be mostly attributed to glass dissolution.

The experiments performed here confirm that crystalline silica will persist preferentially to the rest of the assemblage. If volcanic cristobalite is coated by a different phase (as is

thought for crystalline silica in coal dust), has a heterogeneous surface (as observed by Horwell et al. (accepted; Appendix 4), where cristobalite particles frequently have adhered groundmass at the surfaces), or if there is an annealed glassy layer (as hypothesised by Horwell et al. (accepted; Appendix 4) for volcanic ash), residence in a biological system could sufficiently affect other phases present as to increase the crystalline silica surface-area burden experienced by the lungs. This effect would escalate during host defence, where increased dissolution occurs in the more acidic lysosomal environment.

6.3.3.4 Surface reactivity of ash

Surface and free-radical production have been closely linked to bioreactivity of dusts in the lung (Fubini, 1997; Fubini et al., 1995a). For volcanic ash, Horwell et al. (2007; 2003a) have shown this to be primarily mediated by iron, particularly iron rich silicate minerals, whereas cristobalite in the ash does not contribute much to $^{\bullet}OH$ production (Horwell et al., 2003a). The surface reactivity in the study by Horwell et al. (2003a) was measured on a sample of cristobalite isolated using the Talvitie method (see Chapter 3: Methods) and could, therefore, be misleading as strong acid treatment on crystalline silica has been shown to decrease reactivity (e.g., HF and quartz Fubini et al., 2001). Nonetheless, results here are not easily distinguishable from cristobalite abundances, with MSH.05.DG, MSH.05.DZ, and UNZ.03 all having > 10 wt. % cristobalite and generating the most $^{\bullet}OH$. The Min-U-Sil standard, however, only generated 0.02 μmol m^{-2} of $^{\bullet}OH$ (Horwell et al., 2007) and, therefore, the $^{\bullet}OH$ abundances produced by the three samples above (0.15-0.31 μmol m^{-2}) are likely unaffected by the contribution of crystalline silica.

Radical generation is often the result of complex interactions between active surface sites and target molecules, however, three different reaction kinetics were observed over the 60 minute incubation: an increase in signal intensity with time, a decrease in signal intensity with time, a consistent signal with time. For an increase in signal intensity, the active sites responsible for free radical generation are not easily accessible by the target molecule or have to first be activated (e.g., Fe^{3+} has to be reduced to Fe^{2+} before triggering the Fenton reaction as could happen *in vivo*). Therefore, the reaction starts slowly and the number of radicals released increases over time. A decrease in radicals with incubation time is typical of ions in solution, which are immediately available to react with the target molecule. For example, Fe^{2+} ions produce abundant $^{\bullet}OH$ in the presence of H_2O_2 via Fenton chemistry and are oxidised to Fe^{3+}. Fe^{3+} is poorly soluble at neutral pH and precipitates as $Fe(OH)_3$, which is not an effective producers of $^{\bullet}OH$ (Maura Tomatis, personal communication, 2012). For a constant release of radicals, the active sites are easily accessible and immediately react with the target molecule. As a consequence, an EPR signal is observed after a short incubation

period. The intensity does not change if the active sites act as a pure catalyst, where the number of radicals released depends on the concentration of the target molecule but not on the number of surface sites. These three kinetic observations can also be explained in more complex ways. For example, there could be both redox active ions able to generate ˙OH (increasing kinetics) and ions that may be released in solution (decreasing kinetics) on the ash surface. If the amounts of radicals released by the two mechanisms are similar then the result will be a relatively constant generation of radicals (constant kinetics). The source of ˙OH in volcanic ash is only loosely constrained (Horwell et al., 2003a), therefore assigning each sample a mechanism based on mineralogy would require further investigation. As the aim of this experiment was to constrain bulk sample reactivity and was not mechanistic, this was beyond the scope of the project.

Surface iron mobilised by endogenous chelators can contribute to free-radical production, causing oxidative stress in macrophages and DNA damage in epithelial cells (Fubini et al., 2001; Hardy and Aust, 1995). For volcanic ash analyses, it has become standard to compare the effects of iron release after 7 days with radical production at 30 minutes (e.g., Damby et al., 2012; Hillman et al., 2012; Appendix 4; Horwell et al., 2007; Le Blond et al., 2010). These are the optimal time frames based on stabilisation of iron release over time (see Figure 6.8) and the experimental time for ˙OH generation where the reaction is most likely at its peak (see discussion above). The amount of bio-available total iron removed from the surface of the samples analysed is as expected for the distribution of magma types, i.e., less than ~60 μmol m^{-2} for samples more silicic than a basalt (Horwell, unpublished data from 2004-2012), except for one sample from Merapi (MER.A10.03) which released 90 μmol m^{-2} total Fe. This sample generated a commensurate amount of ˙OH as other study samples; however, production was below the least-reactive comparative sample, MBA5/6/99, a dome-collapse ash sample from Soufrière Hills volcano, Montserrat. Indeed, only one sample (MSH.05.DZ) generated more radicals than Cerro Negro and Pinatubo samples at 30 minutes; however, it released the least amount of iron for all samples tested. Iron is only active when dispersed on a silicate matrix, with at least two or three coordination valencies unsatisfied (Fenoglio et al., 2001; Martra et al., 1999). Excess iron at the surface can reduce the reactivity and cellular response from a particle (Elias et al., 2002; Fubini et al., 2001) either by crowding-out potential reactive sites, changing the coordinative state of the iron, or forming groups of aggregated iron ions (Turci et al., 2011). Therefore, iron ions are expected to be isolated at the surface of this sample, resulting in the comparatively pronounced response.

Bulk iron by XRF corresponds loosely with iron release, allowing for general assumptions between magmatic composition and expected reactivity. For the comparative samples, the

basaltic Cerro Negro and Etna samples and dacitic Soufrière Hills sample (MBA5/6/99) show good correlation between available iron ions at the surface and Fenton activity (Figure 6.14). The Pinatubo sample from the 1991 eruption was dacitic, and is therefore expected to produce radicals in similar quantities to the samples analysed for this study. However, this sample has systematically generated unusually high numbers of radicals (e.g., up to 2.96 μmol m^{-2}) given its very low iron content (e.g., up to 33.86 μmol m^{-2} total Fe) (Damby et al., 2012; Hillman et al., 2012; Horwell et al., 2010b; Appendix 4; Le Blond et al., 2012), and highlights how radical generation seems unrelated to available iron content beneath a threshold of ~100 μmol m^{-2} total iron release at 7 days (Horwell, unpublished data). This has been observed in several recent studies (Damby et al., 2012; Horwell et al., submitted-b; Appendix 4) and is confirmed again here (e.g., MSH.05.DZ and COL.A03.10).

In general, there was preferential release of Fe^{3+} over Fe^{2+}. The comparatively lower production of $^{\bullet}OH$ for study samples than for 'standard' samples likely results from this preference, since removable divalent iron is required for $^{\bullet}OH$ generation (see Chapter 2). Similarly, all samples analysed by Horwell et al. (2007) had a greater abundance of Fe^{3+} than Fe^{2+} (Fe^{2+}/Fe^{3+} ratio of less than 1). The surface of the lung is both chelating (metal binding proteins) and reducing (GSH, ascorbate), therefore the balance between Fe^{2+} and Fe^{3+} is likely to be dynamic and complex *in vivo*.

Surface iron on ash exposed to the environment will have oxidised to Fe^{3+}, and it is therefore expected that only fresh ash will have dominant surface Fe^{2+}. Many of the samples used here were not collected fresh, and therefore oxidation of surface iron likely occurred. Although not performed for this study, grinding of volcanic ash samples has been previously shown to increase reactivity (Horwell et al., 2003a), and is likely attributed to the exposure of lattice Fe^{2+}. Mechanical fracture can break covalent bonds, providing fresh surfaces with highly reactive surface charges or 'dangling bonds' (Fubini, 1998) which, for crystalline silica, are not found on uncleaved surfaces (Vallyathan et al., 1995; Vallyathan et al., 1988).

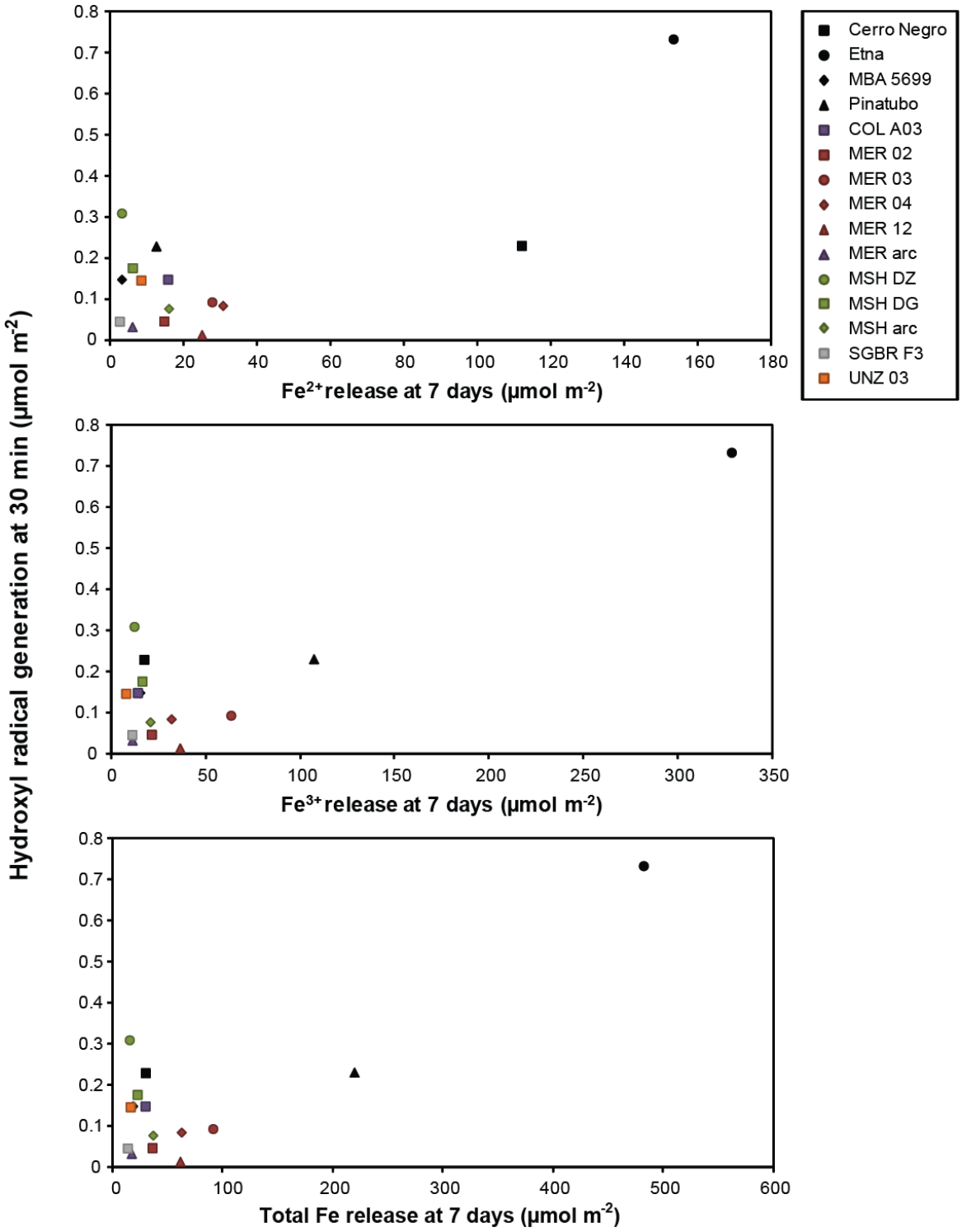

Figure 6.14: Hydroxyl radical generation at 30 minutes compared to removable Fe^{2+}, Fe^{3+} and total iron at 7 days for ash samples from Unzen, Mount St. Helens, Merapi, Colima and comparative ash samples. Data for samples from Merapi are from Damby et al. (2012; Appendix 4).

The ability of ash sample MER.03 to cleave the C-H bond in the carboxyl radical experiment is of strong biological interest as it is one of the most ubiquitous in a cellular system. The mechanism of formation for the carbon-centred radical is unclear, however, from experiments on asbestos it is thought that only Fe^{2+} iron is involved in the reactivity (Martra et al., 2003; Turci et al., 2011). Moreover, several particles are able to release carboxyl radicals only when a reducing agent is present (e.g., CuO). This suggests that only transition metal ions in low oxidation states are involved in the homolytic cleavage of the C-H bond. The low reactivity observed for the ash samples may be related to the amount of Fe^{3+}. As was observed with $^{\bullet}OH$ production, there is not always a clear correlation with the amount of iron. Radical release may be observed with even trace amounts of iron if it is present in an appropriate coordination state (Fubini et al., 1995b).

The involvement of Fe^{2+} in the generation of $COO^{\bullet-}$ for these samples is confirmed by activation of the MER.04 surface when ascorbic acid was present in the reaction medium. MER.04 was fully inactive, but a weak signal appeared after 10 minutes of incubation in the presence of ascorbic acid. This suggests that there are only a few ions involved in the reaction and that these ions have to be reduced before they can react. The potential of ash to directly interact with biological membranes should be considered for a larger suite of samples and in relation to iron coordination.

Haemolysis is a frequently used basic toxicity assay to quantify the ability of a particle to rupture a cellular membrane. The mechanism of haemolytic activity is still unclear, but the DQ12 quartz standard is particularly adept at membrane lysis. The assay is therefore used for volcanic ash as an indicator of quartz-like activity due to the abundance of crystalline silica. Haemolysis results did not differ from previous results for bulk volcanic ash (e.g., Hillman et al., 2012; Horwell et al., submitted-b; Appendix 4; Le Blond et al., 2010), with all samples causing < 5 % haemolysis at the top dose. The most haemolytic sample (MER.arc) at 1 mg ml^{-1} shows an equivalent haemolytic potential to DQ12 at 0.05 mg ml^{-1} (5 % haemolytic). Therefore, on a mass basis, sample MER.arc was approximately twenty times less haemolytic than quartz. Similarly, COL.A03.10 was about half as haemolytic as MER, and is therefore about forty times less haemolytic than quartz on a mass-base.

The separated respirable material has a greater total number of particles per mass dose as well as a greater corresponding surface area compared to the bulk ash. Haemolysis is thought to be surface area dependent, and therefore the difference between bulk and respirable treatment data could result from the difference in surface area. A universal increase in % haemolysis was not observed for all samples, suggesting the presumed increased in surface area for the respirable fraction is not the only factor contributing to the increased toxicity.

Even still, it should be considered in future experiments where surface area data for the respirable samples are available.

Grinding the ash failed to increase the level of haemolysis as has been previously observed for grinding quartz samples (e.g., Castranova, 1994). The assay is thought to be surface-area dependent, and Horwell et al. (2003a) observed little impact of grinding on surface area. Further, the percentage of crystalline silica for all samples is presumed to be less than 15 wt. % based on bulk sample contents (Table 6.7) and inferences regarding enrichment in the respirable fraction. Therefore, the minimal increase in surface area combined with the heterogeneous nature may account for the lack of increased activity. Abrading particles, however, may expose fresh surfaces, as discussed regarding the increased $^{\bullet}OH$ production observed by Horwell et al. (2003a). It has been shown that treatment of quartz with aluminium lactate significantly diminishes the haemolytic potential of quartz (Duffin et al., 2001); therefore, the distribution of aluminium in volcanic cristobalite (Chapter 5) may be sufficient to passivate any increased reactivity bestowed through grinding by simultaneous exposure of aluminium with the freshly fractured surface.

Other health-specific acellular tests not pursued here but that have been part of a rapid-response ash analysis (see Figure 1 in Damby et al. (2012); Appendix 4) for major eruptions are particle oxidative capacity and analysis of leachable elements. Oxidative capacity, as measured by the depletion of antioxidants in a synthetic respiratory tract lining fluid, was carried out for a selection of the Merapi samples (Damby et al., 2012; Appendix 4); however, results for those samples as well as others (e.g., Grímsvötn, Eyjafjallajökull) (Horwell et al., submitted-b; Appendix 4) have been uniformly negative, and therefore not pursued for additional samples here. Leachate analyses were also performed on a subset of the Merapi samples; however, quantifying leachable surface elements is more informative for public health issues when performed on freshly collected (i.e., not exposed to rain) samples. Further, results from previous eruptions (e.g., (Damby et al., 2012; Horwell et al., submitted-b; Le Blond et al., 2010)) have highlighted eruption and sample-specific results, thereby reducing the potential for drawing broad generalisations.

6.4 Part II: Potential Toxicity of Volcanic Ash samples

6.4.1 Introduction

Part II of this chapter comprises an entirely novel venture into determining the potential toxicity of volcanic ash. It serves to expand the existing knowledge of ash toxicity with the physicochemical foundation set out in Part I.

A subset of the samples used in Part I was selected to investigate the *in vitro* biological response elicited by dome collapse ash. Samples were chosen under the criteria that they represent a breadth of volcanic locations, and that each sample be the most likely toxic from each volcanic centre through combined consideration of physicochemical factors including crystalline silica content, iron release and free radical production. Samples are discussed according to sample location for ease, and are listed in Table 6.9. Further sample information can be found in Table 6.1.

Table 6.9: Sample abbreviations for the subset of samples used for further toxicology experiments in Part II.

Location	Abbreviation	Original sample name
Colima	COL	COL.A03.10
Merapi	MER	MER.arc
Merapi	MER.PDC	MER.A10.12
Mount St. Helens	MSH	MSH.05.DG
Soufrière Hills	SHV	MRA5/6/99
Unzen	UNZ	UNZ.03

The two samples from Merapi are differentiated by the designation ‘PDC’, which denotes the sample collected from a pyroclastic density current. A PDC sample was included to consider the effects of different mechanisms of fragmentation on the particle hazard for concurrently erupting material. The samples and corresponding experiments are listed in Table 6.3.

The biological effects of particle exposure assessed here are initiated in the deep lung, where cells are expected to encounter particles that are < 5-10 μm diameter. Therefore, the use of a

respirable ash fraction to assess cellular toxicity was essential. Methods used to separate, collect, and characterise the respirable fraction from the samples chosen are discussed in Chapter 3 (Methods 3.4.1.1), and results for grains size and morphology are discussed in Part I of this chapter. Insufficient quantities of Santiaguito ash were available to separate the fine fraction and, therefore, the potential toxicity of Santiaguito ash is limited to those assays discussed in Part I: haemolysis and hydroxyl radical generation.

6.4.2 Results: In vitro toxicity

6.4.2.1 Cell treatment with respirable panel

Investigations that assess the pulmonary toxicity of particulate matter *in vitro* often use a variety of models including macrophages, due to their role in particle clearance and host-response, and pulmonary epithelial cells, due to their abundance and expected interaction with particles. In accordance, the respirable ash panel was used to challenge macrophages (differentiated THP-1 cells) and lung epithelial cells (A549 cells). All experiments were performed on both cell types.

The dose-range and time point for particle treatments were determined by particle-induced cytotoxicity measured by LDH release (Figure 6.15) following exposure of cells to ash (SHV) compared to quartz (type DQ12, PC mid-size Dörentrup) and TiO_2 (rutile). The presence of crystalline silica is of primary concern in these analyses, and a treatment range of 1-100 μg cm^{-3} comprises an extensive dose-response curve for DQ12 quartz (positive control), from 10 % cytotoxic to a plateau near 60 % cytotoxic at 24 hours. DQ12 quartz is 87 wt. % α-quartz and 13 wt. % amorphous, with a mean grain size of 1.72 μm by number (3.01 μm by mass) (Creutzenberg et al., 2009). TiO_2 has been largely used in previous pulmonary toxicity studies as a negative control when assessing the pathogenicity of particulate matter, e.g., α-quartz (Johnston et al., 2009). However, depending on the characteristics of the TiO_2, it has been shown to have inflammogenic, oxidative, and genotoxic consequences if it is ultrafine in size; i.e., with a diameter less than about 100 nm and with a correspondingly high surface area per unit mass, which enhances particle retention and translocation (Johnston et al., 2009). Its use here in the pigment grade size (260-320 nm) for *in vitro* analyses is justified in light of numerous previous studies which show it to be much less toxic than quartz (e.g., Simon-Deckers et al., 2008).

At 24 hours, a small dose-dependent response to ash was observed for concentrations between 1-100 μg cm^3, and therefore 4 treatment doses from 2.5 – 50 μg cm^3 were chosen: 5, 10, 25 and 50 μg cm^3. A treatment duration of 24 hours was chosen as 48 hours failed to incite a more intense response to ash (Figure 6.15). This dose-range and time-point has been further substantiated for ash by use against type1-like alveolar epithelial cells (TT1 cells) for Merapi ash (Damby et al., 2012; Appendix 4).

6.4.2.2 Assessment of cytotoxicity

Various assays are used to determine the effect of insult on cells propagated *in vitro*. They range from simple assays that measure cell viability following exposure (e.g., membrane integrity and the effect of treatment on cell growth) to assays that indirectly measure

viability by metabolic reduction of various compounds by cells (see Chapter 3: Methods). The advantages of these assays are ease-of-use and the rapidity with which multiple dilutions or particles can be tested.

Ash-induced cytotoxicity was determined through two methods: metabolism of the AlamarBlue reagent and LDH release. The AlamarBlue assay determines cell viability via metabolic activity (i.e., 'how alive'), and LDH release measures a cell's structural ability to retain its intracellular components (i.e., 'how dead'). This two-fold approach, therefore, provides complementary information on the degree of treatment-induced cellular toxicity for each cell line. As discussed in the Methods chapter, other cytotoxicity assays were trialled to determine membrane integrity (e.g., Trypan blue exclusion) and viability (e.g., wst-1 and calcein AM assays), but this combination was the most consistently adoptable and cost-effective.

6.4.2.2.1 THP-1 cytotoxicity

All samples induced some degree of decreased viability in THP-1 cells after 24 hour treatment as measured by metabolism of the AlamarBlue reagent (Figure 6.16a). The response to ash, however, did not follow a typical dose-dependent decrease as exemplified by the DQ12 quartz curve. The decrease in viability is similar to that elicited by TiO_2 (consistent 85 % viability over the same dose range). A similar response was seen for LDH release (Figure 6.16b), where treatment resulted in statistically lower release than DQ12 and was marginally lower than TiO_2. Ash treatment did result in minimal dose-dependent increase.

6.4.2.2.2 A549 cytotoxicity

Cell viability results determined by the alamarBlue assay showed little effect of particle treatment on A549 cells (Figure 6.17a) compared to DQ12 and TiO_2. For the LDH release assay (Figure 6.17b), some ash samples (MER, COL, UNZ) released more LDH than TiO_2 but less than DQ12 in a dose-dependent manner. None of the differences were statistically significant.

6.4.2.3 Assessment of apoptosis and necrosis

Apoptosis and necrosis are two fundamental types of cell death, and, although both ultimately result in death of the affected cells, the two processes differ significantly. In apoptosis, affected cells actively manage a cascade of reactions that lead to death, and has therefore been referred to as cell suicide (e.g., Nanji and Hiller-Sturmhöfel, 1997). It is programmed into cells and is therefore the physiological way in which cells are removed, although some toxins can elicit apoptosis. Necrosis is typically seen with toxins, adverse

conditions, and extreme changes in the cell's environment. It is not programmed and therefore not physiological. Apoptosis preserves genetic material and protects functional cellular components, whereas necrosis is characterised by the collapse of internal homeostasis and loss of cell membrane integrity (Bonfoco et al., 1995). Cells undergoing either apoptosis or necrosis have different surface expressions, and the two types of cell death can, therefore, be quantitatively differentiated for one another (see Chapter 3: Methods).

Following particle treatment, differentiated THP-1 cells experienced a limited reduction in viability (Table 6.10). Necrosis and apoptosis were also determined for THP-1 cells but not included in Table 6.10 as they were roughly equivalent and the reduction in viability was negligible. A549 cells, however, experienced an approximately 20 % reduction in viability, which was largely attributed to apoptosis (Table 6.11). Cell viability was not correlated with particle dose, and data for ash treatments are equivalent to the decreased viability observed for treatment with DQ12 and TiO_2.

Table 6.10: Viability of differentiated THP-1 cells by flow cytometry following exposure to different doses of volcanic ash. Data are reported as a per cent of an untreated control and are the average of n=2. Results are reported as a per cent of unexposed cells, representative of 100 % viable.

Sample	**% Viable**			
(dose μg cm^{-3})	*5*	*10*	*25*	*50*
Colima	98.6	97.3	98.0	98.0
Merapi	97.0	97.7	98.0	98.0
Merapi PF	93.9	97.5	97.9	98.4
Mount St. Helens	94.0	95.2	98.0	97.8
Soufrière Hills	97.0	96.6	98.2	97.2
Unzen	97.1	95.7	97.0	98.2

Table 6.11: Viability of A549 cells by flow cytometry following exposure to different doses of volcanic ash. Data are reported as a per cent of an untreated control and are the average of n=2. Results are reported as a per cent of unexposed cells, representative of 100 % viable.

Sample *(dose μg cm^{-3})*	**% viable**	**% necrotic**	**% apoptotic**
Colima			
5	80.3	1.2	18.6
10	80.6	1.3	18.1
25	82.1	2.2	15.7
50	84.5	1.3	14.2
Merapi			
5	69.0	3.9	27.2
10	77.5	1.4	21.1
25	79.8	1.4	18.8
50	74.4	4.9	20.8
Merapi PF			
5	75.3	3.8	20.8
10	88.8	1.3	10.0
25	83.1	1.1	15.9
50	82.3	0.7	17.0
Mount St. Helens			
5			0.0
10	80.2	5.7	14.2
25	83.4	3.5	13.1
50	84.3	2.9	12.8
Soufrière Hills			
5	77.7	1.7	20.5
10	88.9	1.7	9.5
25	83.7	1.7	14.6
50	79.1	1.3	19.6
Unzen			
5	62.6	12.0	25.3
10	78.5	2.0	19.5
25	81.6	1.8	16.6
50	83.3	4.7	12.0
DQ12 *50*	76.5	7.0	16.5
TiO_2 *50*	78.5	0.8	20.7

Table 6.12: Intracellular reduction of glutathione (GSH) for THP-1 and A549 cells. Data are presented as a per cent reduction relative to an untreated control as well as absolute mean fluorescence intensity (MFI) following exposure to different particle doses. NEM (N-ethylmaleimide) is used as a positive control. Data are an average of n=2.

Sample	Dose ($\mu g\ cm^{-3}$)	THP-1		A549	
		%	MFI	%	MFI
Colima					
	5	1.1	642.7	1.4	724.1
	10	1.1	648.8	1.7	704.6
	25	1.3	622.1	4.4	650.4
	50	1.7	596.3	7.9	532.1
Merapi					
	5	1.0	651.1	4.6	713.5
	10	0.8	625.7	1.0	728.5
	25	1.2	630.2	2.2	668.0
	50	2.2	613.5	3.9	623.5
Merapi PF					
	5	0.3	681.4	5.2	674.7
	10	0.9	684.4	1.9	736.2
	25	0.6	621.7	2.3	671.8
	50	1.8	571.8	3.4	597.5
Mount St. Helens					
	5	0.7	665.1	4.7	638.3
	10	0.5	664.2	4.8	671.8
	25	0.9	619.9	4.2	623.1
	50	1.0	600.9	3.2	624.5
Soufrière Hills					
	5	0.8	674.3	3.3	726.6
	10	0.6	669.8	4.8	689.4
	25	0.7	650.2	3.5	666.7
	50	1.1	644.9	1.3	702.7
Unzen					
	5	0.6	641.0	1.1	774.9
	10	1.0	625.6	1.5	698.1
	25	0.9	619.3	2.8	641.2
	50	1.4	608.1	6.0	570.1
DQ12		--	--	5.2	717.3
TiO_2		--	--	2.1	725.2
NEM		99.8	118.2	6.3	426.1
UT/stained		3.4	568.6	1.5	731.2

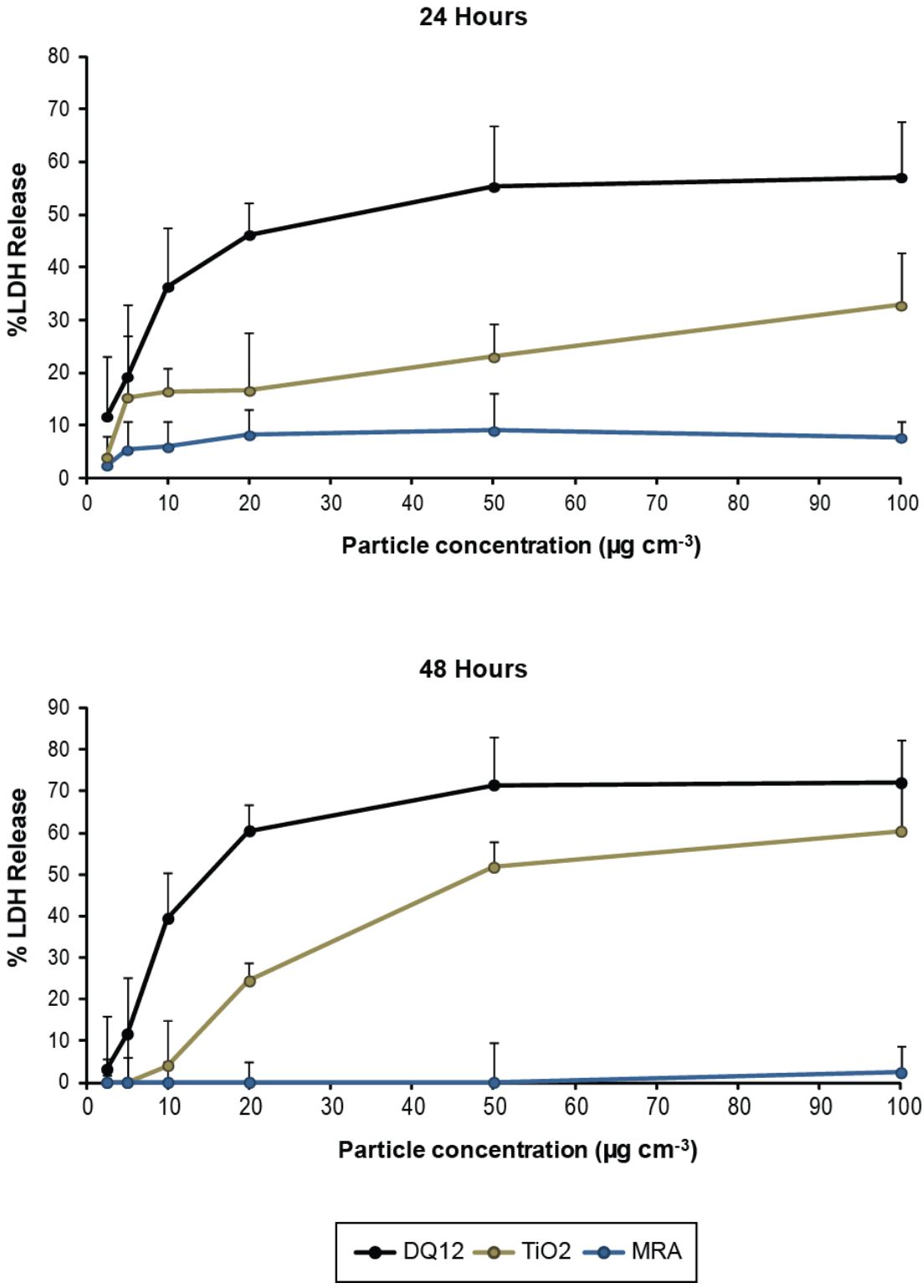

Figure 6.15: Dose and time-point determination for treatment with volcanic ash by LDH release. Six doses (2.5, 5.0, 10, 20, 50, 100 µg cm^{-3}) were tested to derive dose-response curves at two timepoints (24 and 48 hours).

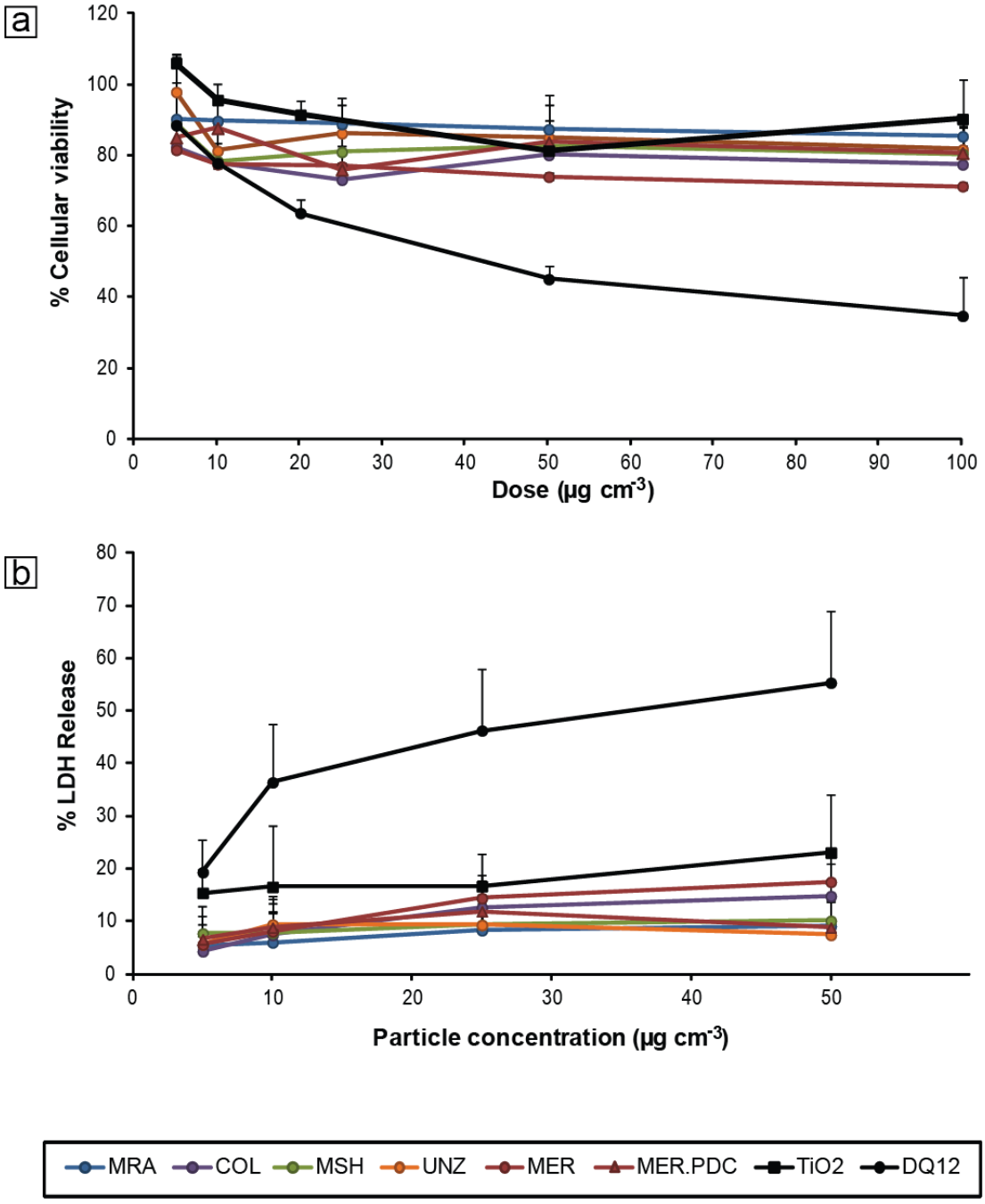

Figure 6.16: Cytotoxicity of THP-1 cells following exposure to respirable ash and controls measured by (a) metabolism of the alamarBlue reagent and (b) LDH release.

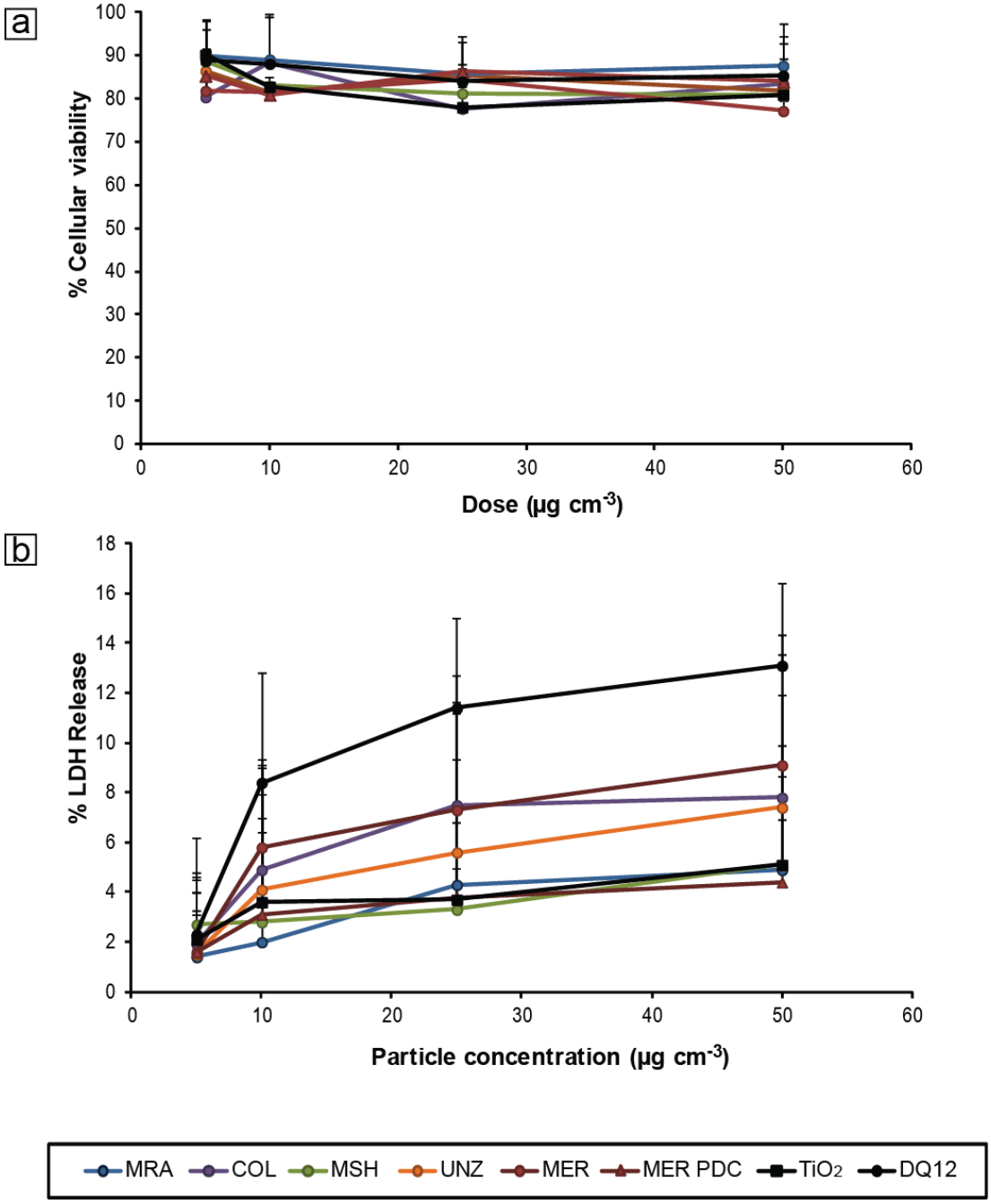

Figure 6.17: Cytotoxicity of A549 cells following exposure to respirable ash and controls measured by (a) metabolism of the alamarBlue reagent and (b) LDH release.

6.4.2.4 Intracellular oxidative stress

Oxidative stress due to environmental and cellular oxidants is an important component of inflammation and respiratory disease (Biswas and Rahman, 2009). Glutathione (GSH) is the most abundant small molecular weight intracellular antioxidant, and plays a crucial role in redox defence by protecting cells from oxidative damage through scavenging of free radicals and reducing oxidising species (Forman et al., 2009). Once oxidised to glutathione disulphide it is exported from the cell, and therefore intracellular oxidative stress was measured by the depletion of glutathione (GSH) using a fluorescent assay.

No reduction in GSH abundance resulting from ash treatment was seen in differentiated THP-1 cells compared to untreated cells (Table 6.12). However, an ash-induced effect was seen on A549 cells relative to the controls, where a decrease in the mean fluorescent intensity (MFI) was observed (Table 6.12); the extent of which was more pronounced for higher doses. In general, GSH was depleted in a dose-dependent manner, with samples from Unzen and Colima causing the most pronounced depletion relative to the controls. For most samples and doses, this effect was more prominent than that observed by quartz but substantially lower than that produced by N-ethylmaleimide (NEM), an effective oxidiser of GSH which rapidly removes it from the cell cytosol.

6.4.2.5 Pro-inflammatory response

The pro-inflammatory response elicited by the samples was analysed by measuring the production of IL-1β, IL-6 and IL-8 by ELISA. Data are reported as concentration of cytokine/chemokine per dose.

The response of A549 epithelial cells to insult was largely negative (Figure 6.18). Little to no response was seen for IL-1β or IL-6, especially compared to that induced by DQ12. Production of IL-8 was seen for all particles (ash and DQ12). However, the levels did not differ significantly from an untreated control ($p>0.05$, ANOVA with Dunnett's post-hoc test), suggesting minimal treatment-dependent production of IL-8 over a basal level for A549 cells.

The response of differentiated THP-1 cells was sample and cytokine dependent. The top two doses of SHV, MER and MER.PDC ash resulted in the production of IL-1β above the untreated control and were equivalent to the lowest dose of DQ12 (Figure 6.19), meaning it is about as active as DQ12. These three samples were run in parallel for each of n=3 (as were UNZ, COL, and MSH) and therefore the discrepancy seen between the less- and more-toxic groupings is repeatable and warrants further research. Treatment by all samples except for Merapi resulted in IL-6 production comparable to the untreated control (Figure 6.19). One

repeat experiment (of n=3) for Merapi resulted in similar levels as all other samples, resulting in the large error bars and perhaps emphasizing the heterogeneous mineralogy of the ash samples. Cells treated with both Unzen and Merapi ash produced significantly more IL-8 than untreated cells in a dose-dependent response (Figure 6.19). Levels for the top dose (50 μg ml^{-3}) were also greater than that induced by equivalent concentrations of DQ12. Although the Merapi ash induced significant production, results for the Merapi PDC sample were largely negative.

6.4.2.6 Cytostain: Particle-Cell images

Images of untreated (Figure 6.20a) and ash-treated (Figure 6.20b and c) differentiated THP-1 cells confirm that all particles were being internalised by cells, likely contained within cytoplasmic vacuoles or lysosomes. It is noteworthy, however, that particles can be internalised without having a detrimental effect on normal cell function.

Only differentiated THP-1 cells were imaged. A549 cells are an adhesive cell, permitting them to bind to surfaces and the extracellular matrix of other cells using cell adhesion molecules. While this is essential for maintaining multicellular structures (i.e., the lung epithelium), it led to cell clumping during preparation for staining despite the use of Trypsin and Accutase, a gentler alternative, to detach and dissociate cells. Although not imaged, laboratory observations confirmed the presence of particles within cells.

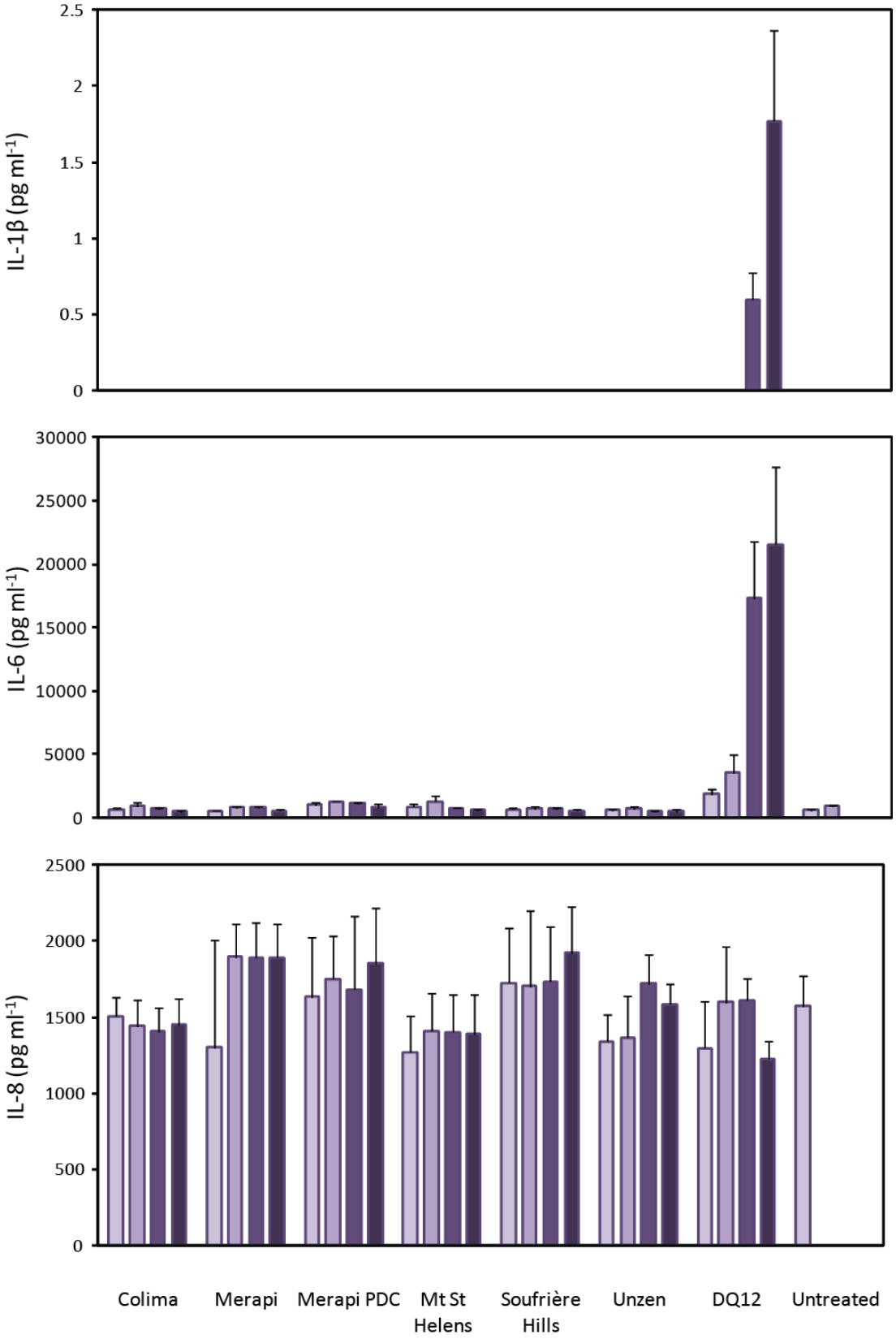

Figure 6.18: Production of proinflammatory markers IL-1β, IL-6 and IL-8 by A549 human type II epithelial cells at 24 hours post treatment with respirable volcanic ash. Data columns are treatment doses of 5, 10, 25 and 50 μg cm^{-3}.

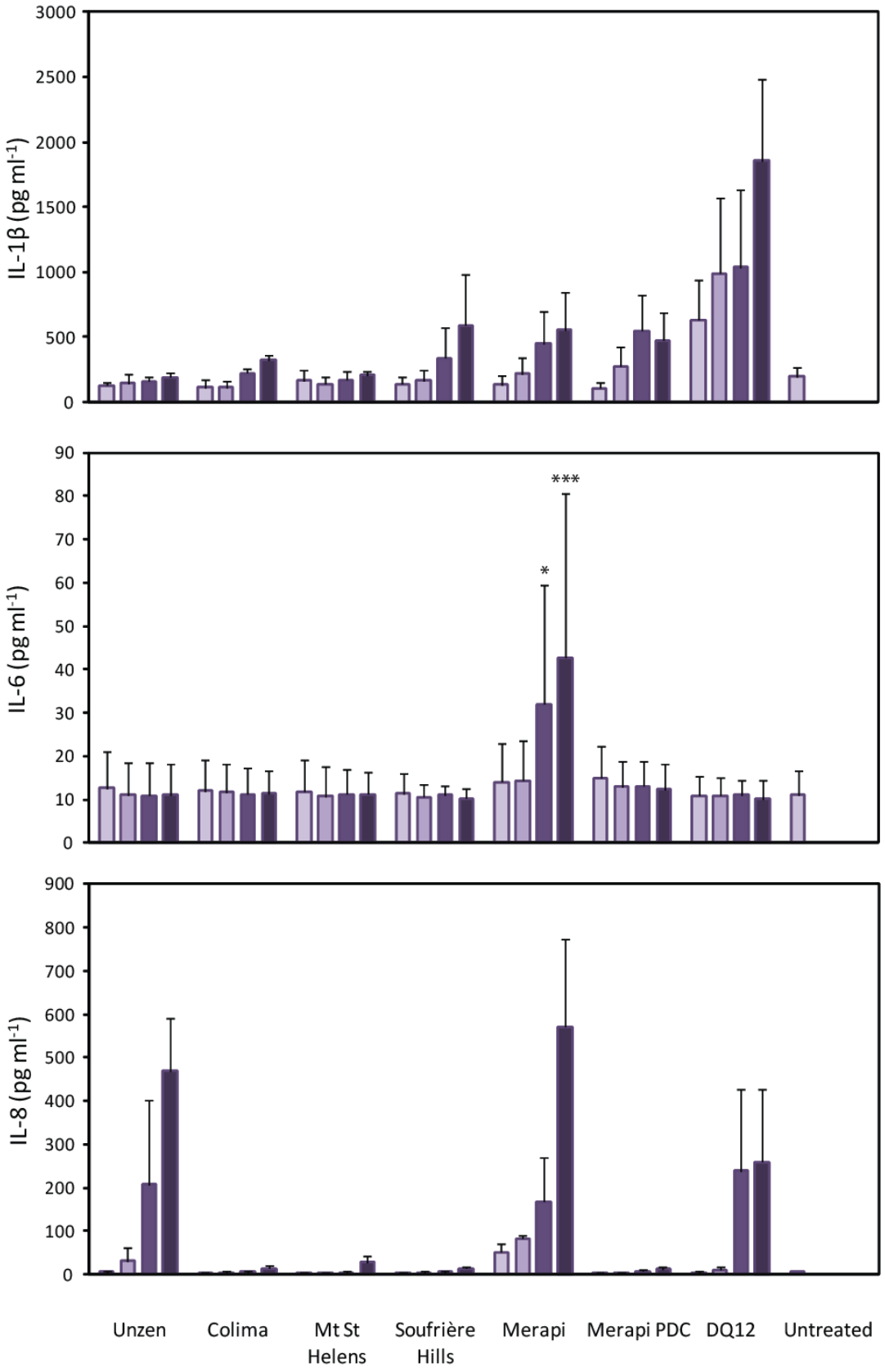

Figure 6.19: Production of proinflammatory markers IL-1β, IL-6 and IL-8 by differentiated THP-1 cells at 24 hours following treatment with volcanic ash. Data columns are treatment doses of 5, 10, 25 and 50 μg cm^{-3} *p<0.05, **p<0.01, ***p<0.001.

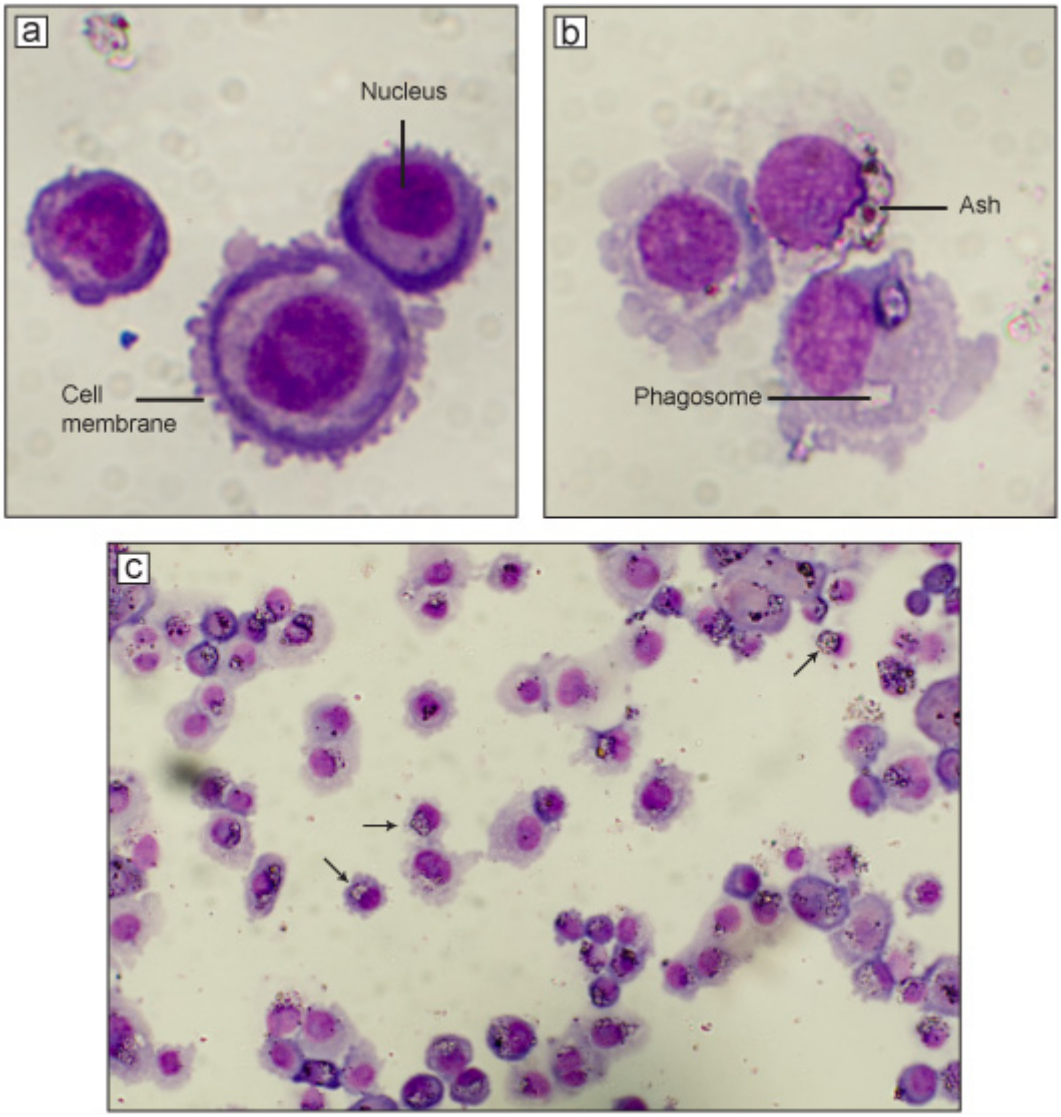

Figure 6.20: Light micrographs of the interaction of THP-1 cells with volcanic ash: a) untreated cells, b) cells treated with COL.A03.10, and c) low magnification view with most cells containing ash particles.

6.4.3 Discussion: Part II

Macrophages and alveolar lung epithelial cells are two of the main airway cell types likely to interact with inhaled particles. Macrophages are classically considered a crucial cell type in the initiation and progression of pulmonary inflammation due to their direct role in particle clearance, and evidence for the role of type II epithelial cells in pulmonary inflammation has been mounting (e.g., van Berlo et al., 2010). We therefore assessed the ash-induced insult and proinflammatory activation of these two cell types.

6.4.3.1 Alveolar epithelial type II cell toxicity

Overall, A549 lung epithelial cells experienced a moderate reduction in cell viability of up to 20 % (measured by LDH release and metabolism of the AlamarBlue reagent), which was more pronounced at lower doses. The decreased metabolic activity agrees with the results of Wilson et al. (2000) on A549 cells, where treatment with three samples of Soufrière Hills ash resulted in a similar decrease in metabolic activity to DQ12 quartz and TiO_2 measured by the MTT assay. The maximum effect was observed for particle treatments of 500 μg ml^{-1}, whereas the top dose by volume concentration used here was 170 μg ml^{-1}.

These data correspond with the reduction in viability measured by cell staining. Results for individual samples, however, did not always correspond among assays. For example, Colima was the most cytotoxic by LDH release and AlamarBlue metabolism, whereas it induced the least amount of apoptosis and necrosis at the lowest and highest doses. The propensity towards apoptosis rather than necrosis for all samples may explain the low haemolysis results in Part I, as membranolysis would constitute necrosis. Although, it is not a direct correlation since, for example, Unzen was strongly necrotic relative to the other samples but failed to display any haemolytic potential.

Cellular uptake of particles by A549 lung epithelial cells occurred for all samples tested. While some uptake through the cellular membrane would occur and be the equivalent of ‘non-professional phagocytosis’, transport through the membrane would have mostly been a passive process. As such, whole-sale particle exclusion versus particle ingestion is not responsible for any observed differences in toxicity. No attempt was made to quantify the comparative uptake between samples, so it is unknown whether differences in the percentage of cells with particles or the number of particles per cell account for observed variations between samples. Similarly, using the techniques here, it was not possible to determine if there was a preferential uptake of particular minerals relative to others as might be expected for particles with different surface polarities. Although particle treatment resulted in decreased viability, no pro-inflammatory response by A549 cells resulting from exposure was observed above an untreated control.

Exposure of A549 human epithelial lung cells to pure-phase crystalline and amorphous silica results in the release of IL-6 and IL-8, with amorphous silica being the most potent inducer of IL-6 and crystalline silica of IL-8 (Hefland et al., 2001). The amorphous component of volcanic ash failed to incite production of IL-6. Unexpectedly, the presence of a crystalline silica component in volcanic ash (and DQ12) did not result in an increase in IL-8 production above the untreated control (contrary to the results of Monteiller et al., 2007), especially considering crystalline silica quantities, where the sample from Mount St. Helens contained the most crystalline silica (approximately 15 wt. %) yet resulted in the least amount of IL-8 produced. Variability in the response of cultured cells to exposure is well known, however, and the response can vary over time (Ken Donaldson, personal communication).

Lung lining fluid contains high concentrations of antioxidants, which form a protective barrier for the lung from oxidative and other damage (Slade et al., 1993). Volcanic ash has been shown to have pronounced free radical activity (Part I of this chapter), and depletion of the antioxidant defence can result in oxidative stress to the underlying epithelial cells (Kelly et al., 1996). Depletion of the high concentrations of GSH (a primary antioxidant secreted by epithelial cells) in the lung lining fluid has been observed for various particles and fibres (Brown et al., 2000), however, studies on volcanic ash from Merapi (Figure 6.21, and discussed in Damby et al., 2013; Appendix 4), Eyjafjallajökull and Grímsvötn, Iceland (Horwell et al., submitted-b; Appendix 4) have shown no evidence of particle oxidative activity in composite respiratory tract lining fluid (including GSH) or ascorbate depletion assays. The extent of intracellular GSH reduction was, therefore, unexpected. A549 cells are known to have a higher level of GSH than primary epithelial cells (150 nmol mg^{-1} protein versus 60 nmol mg^{-1} protein) (Biswas and Rahman, 2009), and therefore the ability of cells *in vivo* to buffer these effects could be more pronounced.

6.4.3.2 Differentiated THP-1 cell (Macrophage) toxicity

As was seen with A549 cells by conventional light microscopy, all sample exposures resulted in internalisation of particles by THP-1 macrophages. Phagocytosis of particles resulted in minimal cytotoxicity; LDH release was lower than that induced by TiO_2 and decreased viability measured by apoptosis and necrosis was negligible. Metabolism of AlamarBlue was suppressed, however, responding only slightly to increases in dose, and was significantly less than quartz at all doses except the lowest two. These data suggest that clearance by macrophages should be effective with little insult to the cell.

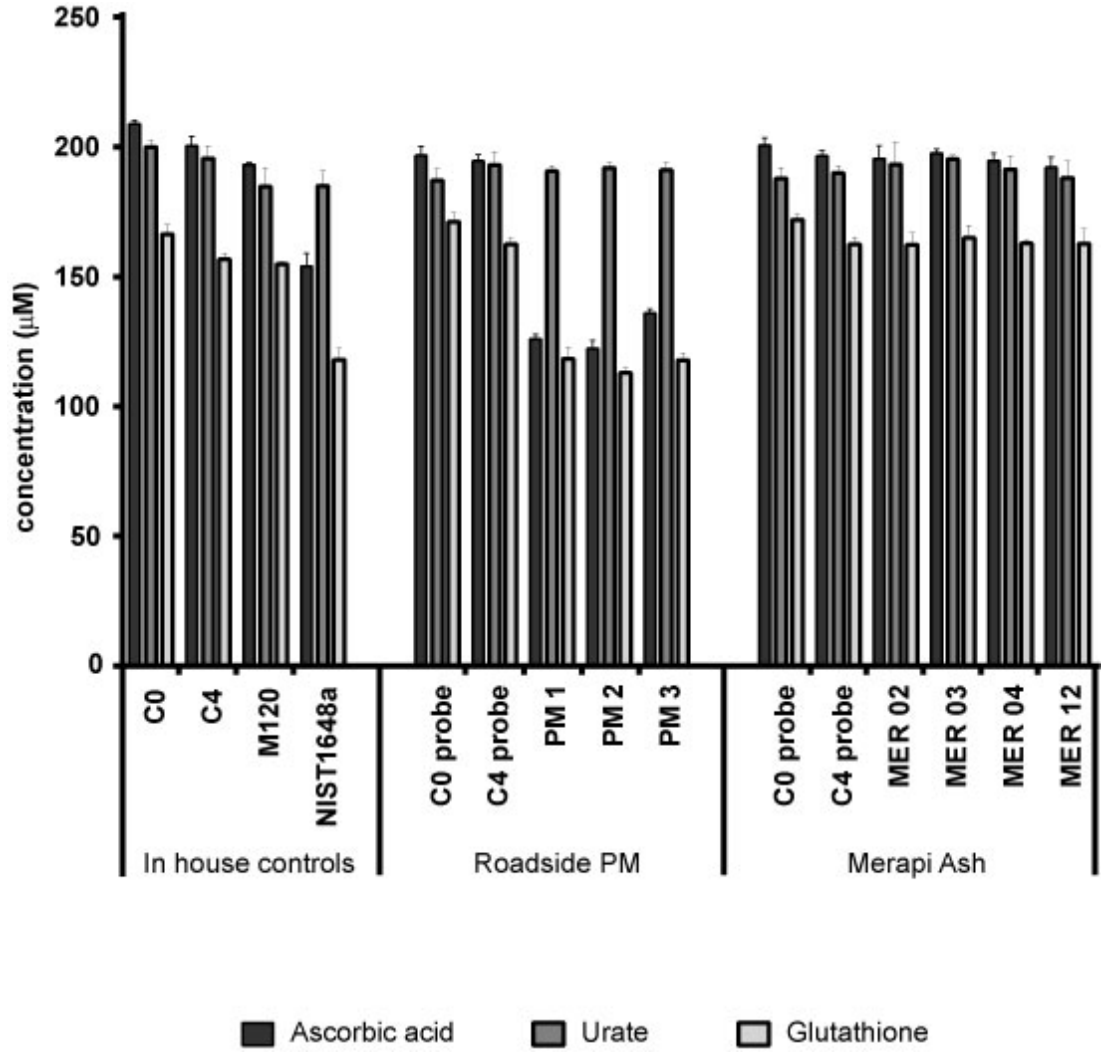

Figure 6.21: Depletion of the antioxidants ascorbic acid, urate, and GSH in artificial preparations by bulk samples of Merapi ash alongside in-house and roadside particulate matter controls.

Following ingestion, a dose-dependent production of IL-1β above the untreated control was observed for all samples, although not statistically significant for Unzen and Mount St. Helens. IL-1β is thought to be of great importance in the development of silicosis; accordingly, DQ12 treatment resulted in a significant increase in production. For ash samples it is not possible to assign the activity to crystalline silica abundance alone, as Mount St. Helens showed the smallest increase and has the most crystalline silica, whereas Merapi showed a pronounced increase and has the least crystalline silica. Iron uptake and accumulation in pulmonary macrophages has been shown to increase IL-1β production (O'Brien-Ladner et al., 2000); however, production was not correlated with cellular uptake of bioavailable iron or hydroxyl radical production at the particle surface. Therefore, if the

presence of crystalline silica is modulating the response, it must adhere to the 'variable entity' description of crystalline silica (Donaldson and Borm, 1998), where different samples elicit different responses depending on inherent characteristics of the silica particles and the effects of external factors, such as accompanying minerals. Although all samples have both inherent characteristics and external factors which may modify toxicity, such as the presence of structural Al and other phases adhering to the cristobalite particle surface (Horwell et al., accepted; Appendix 4), no clear differences were found amongst these factors in chapters 4, 5, and Part I of this chapter. The exception is the proportion and presence of other mineral phases in ash, which have not been characterised in detail here. The other major mineral constituents, e.g., feldspars, have no history of inducing inflammation *in vivo* (Bérubé et al., 2004; Housley et al., 2002), so have not been previously considered as toxic components, but they may well play a critical role in modulating the toxicity of crystalline silica.

A pronounced increase in IL-8 production was only observed for samples from Unzen and Merapi. IL-8 is a potent chemoattractant and activator of neutrophils, the transcription of which is dependent on Nuclear Factor-κB (NF-κB), a critical protein complex that regulates the immune response by direct interaction with DNA (DeForge et al., 1993). NF-κB becomes activated following quartz exposure, resulting in a coordinated inflammatory (Driscoll et al., 1995; Schins and Donaldson, 2000), and has been shown to play a role in discriminating between inflammogenic and non-inflammogenic quartz varieties (Duffin et al., 2001). However, NF-κB is an oxidative stress-responsive transcription factor that is involved in the pro-inflammatory effects of many pathogenic particles (Ahn and Aggarwal, 2005; Rahman and MacNee, 1998); therefore, again, crystalline silica cannot be independently implicated.

The release of IL-8 by THP-1 cells to UNZ and MER ash could result from a sub-10 μm biogenic fraction in the ash. Endotoxins (i.e., large molecules on bacterial membranes), in particular, have been shown to trigger the release of IL-8 in THP-1 cells (Tobias et al., 1993). However, IL-8 secretion by A549 cells, which has been demonstrated in response to endotoxin stimulation (Hansen et al., 1997; Palmberg et al., 1998) even though epithelial cells lack specific endotoxin receptors (Pugin et al., 1993), showed no significant difference for UNZ and MER above the other samples or the untreated sample. Even still, endotoxin is expected to be a stronger stimulus for macrophages since they have specific receptors. These two samples are the only two samples not collected specifically for this study; therefore, their handling and storage conditions are not well known. Endotoxin contamination is common, and further consideration of endotoxins in these samples is warranted.

Conversely to the response in A549 cells, differentiated THP-1 cells seem to have increased intracellular GSH levels. Macrophages are known to have lower levels of intracellular GSH than other cell types (10 nmol mg^{-1} protein compared to compared to 150 nmol mg^{-1} protein in A549 cells) (Biswas and Rahman, 2009), and perhaps increased production and/or release into the cytosol to cope with particle exposure. This would have the effect of increasing antioxidant defence in response to exposure.

6.4.3.3 Toxicity of volcanic ash

Exposure to volcanic ash showed little cytotoxicity to macrophages by the assays employed here, limiting concern over the consequences of persistent *in vivo* exposure due to concomitant release of ingested particles from cell death (see Chapter 2: Background). Therefore, little protracted interaction between the particles and epithelial cells is expected. Some interaction always occurs since the surface area of epithelial cells greatly exceeds the surface area of macrophages in any alveolus or terminal bronchiole, and so a particle first deposits on epithelial cells; however, prolonged interaction between particles and epithelial cells may never arise. Exogenous IL-1β has been shown to augment alveolar epithelial cell survival by reducing apoptosis (Coulter et al., 2002; Geiser et al., 2000), which can be provided by macrophages in co-culture (Herseth et al., 2008). I*n vivo*, this may facilitate epithelial survival during clearance of volcanic ash, but it may also allow cells with DNA damage that should have undergone apoptosis to persist and can be seen as a pro-carcinogenic effect.

These conclusions support the *in vitro* and lung instillation conclusions of Cullen et al. (2002) on Soufrière Hills ash, where samples had low toxicity, and also support the *in vivo* results by Housley et al (2002), where instillation of ash into rats had minimal bioreactivity. They also agree with early inhalation studies on Mount St. Helens ash, where there was no effect after six months of exposure (Raub et al., 1985). Most studies, however, conclude that ash is more toxic than a nuisance dust and TiO_2 (e.g., Cullen et al., 2002), and the results here do not suggest differently.

The cause of the pro-inflammatory response by macrophages to the Unzen and Merapi samples is unknown; however, if bacterially associated, the potential of resuspended volcanic ash to transport pathogens needs to be considered. Pathogens or soluble products on airborne mineral particles have been associated with a range of environmental impacts, including transport of *N. meningitidis*, a causative bacterium of meningitis, in Saharan dust palls (Molesworth et al., 2003), and bacteria in Middle Eastern desert dust (Lyles et al., 2006).

Inflammation is characterised by an acute phase and a chronic phase. Only the ability of a particle to incite an acute inflammatory response was assessed here. Early assessments of chronic toxicity on samples from Merapi (Damby et al., 2012; Appendix 4), Soufrière Hills (Horwell et al., submitted-b; Appendix 4), and the Icelandic volcanoes Eyjafjallajökull and Grímsvötn (Horwell et al., submitted-b) indicate prolonged production of inflammatory mediators IL-6, IL-8 and MCP-1 (which regulates the migration of immune cells to the site of inflammation) (Deshmane et al., 2009). This response is not mediated by crystalline silica, as the pro-inflammatory response of lung epithelial type I-like (TT1) cells to samples from Merapi and Soufrière Hills (including MBA5/6/99) resolved, whereas the response to the crystalline silica-free Iceland samples persisted, and increased in some cases.

6.5 Discussion and Conclusion

The aim of the present study was to consider the *in vitro* toxicity of cristobalite-bearing volcanic ash from a suite of dome forming volcanoes, where there may be a chronic risk of diseases such as silicosis, and relate the results to the physicochemical characteristics of the particles. The heterogeneous nature of volcanic ash, however, makes relating responses to particular components difficult, especially in the case of the observed minimal reactivity. As discussed in Chapter 1, analyses in this chapter had to rely on ash generated from a mixture of eruptions styles. All locations, however, are capable of crystallising cristobalite, which was present in ash samples and was the primary hazard under consideration.

Cumulatively, from Parts I and II, the two most toxic samples were from Colima and Merapi. These samples were marginally more reactive than the other samples for all of the indicators of toxicity, including the haemolysis assay, THP-1 model, the A549 model (for the Merapi sample) and noteworthy reactivity for the Colima sample in the production of hydroxyl radicals. While perhaps not applicable to all samples, Wilson et al. (2000) determined the haemolysis induced by samples from Soufrière Hills was independent of hydroxyl radical production. The Merapi and Colima samples in the present study were also the least biodurable of the samples tested, losing the greatest percentage of mass. These samples did not stand out in any of the physicochemical characterisations except that they had the least amount of cristobalite compared to the other samples tested *in vitro* in Part II (4-5 wt. % versus 9-19 wt. % for the other samples). The crystalline silica hazard, a primary focus of this study, was therefore not evident in indicators typically associated with silica toxicity, e.g., haemolytic potential and IL-6 release by lung epithelial cells. As such, much of the toxicity and surface reactivity stemmed from factors which could not be directly attributed to crystalline silica.

The Mount St. Helens sample was the least cytotoxic of the samples tested by all three methods. In the present study, however, it was also the oldest. Freshly fractured quartz surfaces are known to be more reactive than older or weathered surfaces (Fubini, 1998) and, therefore, age or storage may have acted to quell the reactivity. Nonetheless, the vast literature on the toxicity of Mount St. Helens ash could perhaps serve as a minimum response expected for eruptions at dome forming volcanoes. Importantly, however, maximum cristobalite contents previously reported in ash from Mount St. Helens were < 7 wt. % (Dollberg et al., 1986), whereas we have determined there to be more than double than in some samples used here.

Volcanic ash from eruptions involving dome material does not appear to be as toxic as would be expected for a cristobalite-bearing dust. This could plausibly result from two possibilities. The first, as has been detailed in preceding discussions, is based on the theory of 'variable toxicity' for crystalline silica. For volcanic ash, this could manifest in the four hypotheses proposed by Horwell et al. (accepted; Appendix 4), whereby surface occlusion or alteration from pure SiO_2 limits toxicity. The second, however, is simply that the crystalline silica burden per unit dose is not sufficiently high to illicit a response. In the case of haemolysis with the respirable fractions, for example, both Colima and Merapi resulted in minor haemolysis (3-5 % at the top dose) with approximately 5-10 wt. % cristobalite (bulk quantity). In the case of DQ12 quartz, 100 % crystalline silica results in 30 % haemolysis, whereas in a representative case of ash, 10 % crystalline silica results in 3 % haemolysis. The relationship would not be expected to scale linearly as dose response curves are generally parabolic or sigmoidal in shape. If this were the case, it is easy to envisage that 1 mg ml^{-1} marks the start of the exponential portion of a threshold dose-response curve, which could mimic that seen by DQ12 only offset by a difference in treatment concentration. Doses of higher concentrations, however, are entirely unrepresentative of a biologically effective dose.

More than likely, it is a combination of both 'intrinsic and external factors' and dosage that account for the suppressed toxicity of volcanic ash compared to control dusts. The mixed mineral matrix is generally attributed partial credit for suppressing the toxicity of heterogeneous dusts containing crystalline silica. It was observed for coal dust that a minimum threshold of 10-15 wt. % quartz was needed before an inflammatory response was observed (Le Bouffant et al., 1982). However, artificial mixtures of quartz and coal dust compared to natural quartz-bearing coal dust show a more pronounced reactivity (Stone et al., 2004), highlighting the importance of mineral provenance on the intrinsic factors affecting toxicity. Similar studies could be carried out on cristobalite-doped ash, although, as a heterogeneous dust, would need to be interpreted in light of the physicochemical properties address in Part I (e.g., surface area and grain size).

It is known that surface coatings can result in reduced toxicity (Le Bouffant et al., 1982); for example, DQ12 quartz showed reduced toxicity when treated with an extract from incubation of coal dust in water (Stone et al., 2004). These effects, however, depend entirely on the other minerals present in a mixed dust; especially clays, which are thought to have supplied aluminium which was responsible for the masking effect in both studies. No clays were observed in the present study in any of the samples examined by XRD nor was a clay coating observed on the surface of crystals in a study on volcanic cristobalite from Soufrière Hills (Horwell et al., accepted; Appendix 4), meaning the masking effect of crystalline silica

attributed to ‘external factors’ may be less than observed in the above studies. However, grinding of quartz with appropriate additives (e.g., kaolin, alumina) can reduce its biological activity (Fubini et al., 2004), which may occur during fragmentation in an eruption.

All locations studied here, aside from Colima (n=2), can contain ≥ 10 wt. % crystalline silica (within error). However, unlike the 10-15 wt. % quartz threshold in coal dust, which can cause silicosis at low exposures, volcanic ash samples with high crystalline silica contents were no more reactive *in vitro* than samples with lower crystalline silica contents. Study samples are from different sources; however, the observed threshold for coal dust was widely observed. It is possible that a toxicity threshold exists for the cristobalite content of ash, but it must be greater than approximately 20 wt. % based on the minimal reactivity observed for samples MBA5/6/99 (15 wt. % cristobalite) and MSH.05.DG (19 wt. % cristobalite). The practical implications of a higher threshold may be limited, however, as Horwell et al. (submitted-a; Appendix 4) have proposed an upper limit on cristobalite content for Soufrière Hills ash of 20-25 wt. %, and no samples from the volcanoes studied here contain a higher abundance.

In conclusion, ash samples from dome-forming eruptions are not as acutely bio-reactive as would be expected with up to 20 wt. % cristobalite, a known respiratory hazard. Results from the current study agree with previous studies on samples from the same locations, Soufrière Hills (e.g., Bérubé et al., 2004; Wilson et al., 2000), and Mount St. Helens (Dodson et al., 1982; Martin et al., 1984; and see Martin et al., 1986) so there is no reason to believe these results to be case specific. Comparison of the present *in vitro* results with those from previous studies (e.g., Cullen et al., 2002) suggests that ash toxicity may be comparable to that of coal mine dust, and is considerably less toxic than DQ12 quartz. These results are generally positive for hazard management considering acute high exposure to volcanic ash. Prolonged exposure may yet pose a hazard, as evidenced by the chronic *in vivo* toxicity experiments discussed; however, the role of crystalline silica is unclear. As discussed, the prolonged inflammatory effect in the type 1-like TT1 epithelial cell model (Damby et al., 2012; Horwell et al., submitted-b; Appendix 4) was not mediated by crystalline silica, which perhaps suggests a general potential for ash to exacerbate or induce inflammatory disorders as is attributed to PM pollution in urban air.

7

Concluding Remarks

7.1 Introduction

In 1997, the International Agency for Research on Cancer noted that the 'carcinogenicity [of crystalline silica] in humans was not detected in all industrial circumstances,' and that 'carcinogenicity may be dependent on inherent characteristics of the crystalline silica or on external factors affecting its biological activity' (International Agency for Research on Cancer, 1997). This vague statement prompted crystalline silica (specifically quartz) to be labelled a 'variable entity' by Donaldson and Borm (1998), whereby the hazard posed may vary dramatically depending on the origin of the silica or its contact with other chemicals and minerals. Therefore, constraining the physicochemical nature of a silica particle will lead to better understanding of the hazard posed. Accordingly, to address the toxicity of volcanic cristobalite, we set out to determine its provenance (Chapter 4), mineralogy (Chapter 5), and resulting toxicity (Chapter 6); that is, from 'dome to disease.'

7.2 Volcanic cristobalite

Cristobalite was found in samples of dome rock and ash from all of the locations studied, implying it is a world-wide hazard at dome forming volcanoes; and, the physicochemical and thermodynamic properties of cristobalite were comparable for all locations. From a hazards perspective, volcanic cristobalite can be constrained to a single entity within the variable-hazard spectrum posed by environmental and occupational crystalline silica.

The mineralogy of volcanic cristobalite, particularly the predominant substitution of Al^{3+} and Na^{+} for Si^{4+}, lies at the heart of this thesis. This substitution appears to enable the crystallisation of SiO_2 as cristobalite in a volcanic dome by both vapour phase deposition and devitrification, and appears to suppress (at least partially) the toxicity of cristobalite in volcanic ash. Therefore, this substitution mediates both the existence and suppression of the crystalline silica hazard in dome-derived ash.

Certain crystallisation conditions are required for cristobalite formation in the dome. The complex thermodynamics of the dome environment result in spatio-temporally heterogeneous crystallisation of cristobalite, which appears to be dependent on residence time and extrusion rate. Although this makes extrapolation of the hazard from dome rock to ash difficult, further work may reveal whether the thermal history of cristobalite can be used to derive information about conditions of formation. A somewhat analogous system has been tried with a 'quartz clock', however cristobalite is a secondary mineral grown above solidus and, therefore, the same crystal cargo defects in the system do not apply.

7.3 Crystalline silica hazard

The toxicity findings in this thesis, alongside the concurrent studies in Appendices 3 and 4, do not conclude whether or not volcanic ash is toxic. They do, however, reduce concern of the crystalline silica hazard. In Chapter 6, the respirable Unzen (UNZ.03) and Merapi (MER.arc) samples were determined to be the most cytotoxic, yet had only ~10 and 4 wt. % cristobalite, respectively, compared with up to 14 wt. % for the other samples. Similarly, respirable fractions from Merapi (MER.arc) and Colima (COL.A03.10) were the most haemolytic, yet contain the least amount of cristobalite of all samples. In the case of chronic studies, two samples from Soufrière Hills (one of which was used throughout this thesis, MBA5/6/99) failed to incite a lasting pro-inflammatory response, whereas a different sample from Soufrière Hills (MBA20/12/09) incited a pronounced response.

These interpretations assume comparable enrichment of cristobalite into the fine fraction, which was shown by Horwell et al. (2003b). This was precluded in the current study by available sample mass, but warrants confirmation in further studies. These interpretations also assume that different fragmentation mechanisms (i.e., ash venting, dome collapse, explosive, and pyroclastic density currents) result in similar fragmentation and exposure of the crystalline silica surface. When possible, only dome collapse samples were used for toxicity experiments (MSH.05.DG was not); however, the effects of fragmentation on the particle surface would be a valuable addition to the current study.

Horwell et al. (accepted; Appendix 4) noted that cristobalite particles in ash could have either a clean crystal surface or a heterogeneous surface comprised of cristobalite and closely associated mineral phases (see Figure 3 of their manuscript). Vapour phase crystals are expected to result in cleaner crystal faces compared to devitrification crystal which have more associated groundmass. As such, total cristobalite abundance may be less important than the distribution of cristobalite habits in the pre-collapse dome rock. Unzen and Colima dome rock samples tended to have more vapour phase cristobalite than devitrification cristobalite (Chapter 4) and, therefore, their more pronounced response in Chapter 6 may result from more available pure cristobalite surfaces. For Mount St. Helens and Merapi, a location-wide dominant habit is difficult to identify due to the variability that exists between samples. Soufrière Hills, however, was also predominately vapour phase cristobalite (Claire Horwell, personal communication, 2011) and did not elicit a pronounced response, implying crystal habit cannot solely account for the suppressed toxicity of volcanic silica. Mount St. Helens 2004-2008 samples, collectively, had the most devitrification cristobalite of all locations (although, not always the dominant habit). The associated groundmass phases may be responsible for the more pronounced surface reactivity via Fenton chemistry than

observed for other samples. Similarly, Merapi dome rock contained abundant Fe oxides in the groundmass, that, upon fragmentation, could be exposed in the surface and contribute to radical generation.

Volcanic cristobalite does not behave like standard quartz controls in the experiments conducted here, or in much of the literature); however, the chronic effects of volcanic cristobalite exposure are still unknown. According to results in the present study, this is likely controlled by clearance from the lung. Following phagocytosis, alveolar macrophages showed a limited reduction in viability. The rim of other minerals discussed above may be sufficient to allow macrophages to safely handle cristobalite particles before unveiling of the surface can occur. If, however, the cristobalite surface is digested in the lining fluid or within a lysosome following ingestion by a macrophage, then particles may pose a greater hazard than identified here. Consideration of the biopersistence of volcanic cristobalite has only recently commenced. It is entirely possible that the mineral surface will change with continuous phagocytosis and concomitant release of the particle, especially since acid etching, as could occur *in vivo*, has been shown to increase the toxicity of crystalline silica (Fubini et al., 1995a). Further, the synergistic effect of enzymes and the presence of proteins *in vivo* have not been considered in biodurability experiments to date. Therefore, a histological investigation of where particles reside following exposure and interaction with host defence cells would be informative.

Mineral chemistry (Chapter 5) may be an equally important ‘inherent factor’ in mediating the suppressed reactivity. Treatment of quartz with aluminium has been shown to reduce the toxicity of quartz (Duffin et al., 2001), and aluminium has been historically prescribed to sufferers of silicosis to slow progression of the disease, as there is no cure to date (Haldane, 1918; Kennedy, 1956; Leung et al., 2012; Rifat et al., 1990).

The suppression of quartz toxicity by aluminium (e.g., aluminium lactate) treatment is time dependent, where the observed reduction in toxicity is greater at 1 hour than 30 minutes of treatment, and greater at 3 hours than 1 hour of treatment (Wan Seob Cho, personal communication, 2011). Current investigations are underway to determine if treatment with aluminium provides a surface coating or corona, or if aluminium is incorporated into the crystal structure.

7.4 Response to volcanic eruptions

The ability to identify health concerns rapidly following volcanic eruptions has been an aim of the volcano hazards community since the 1980 eruption of Mount St. Helens (Buist et al., 1986a), and a protocol has been developed over the last decade to address these concerns. The existence of a single protocol allows for a direct comparison of hazards among eruptions, and has been most recently implemented at the 2010 eruption of Merapi (Figure 1 in Damby et al., 2012; Appendix 4). As Merapi was one of the locations considered in this study, implementation of this protocol alongside the characterisation and toxicology provided the opportunity to explore this protocol and suggest revisions accordingly. The protocol currently addresses many of the primary mechanisms of particle toxicology addressed throughout this thesis, namely: cell membrane rupture (haemolysis), free radical damage (hydroxyl radical generation), oxidative stress (depletion of antioxidants), and cell-based chronic inflammation (TT1 pro-inflammatory response). As is, the protocol is comprehensive in scope, and results from the present study do not encourage additions to current rapid-response protocol.

References

Ahn, K.S. and Aggarwal, B.B., 2005. Transcription factor NF-kappaB: a sensor for smoke and stress signals. Annals of the New York Academy of Science, 1056: 218-233.

Alcalá, M.D., Real, C. and Criado, J.M., 1996. A new "incipient-wetness" method for the synthesis of chemically stabilized β-cristobalite. Journal of the American Ceramic Society, 76(6): 1681-1684.

Allen, A.G., Baxter, P.J. and Ottley, C.J., 2000. Gas and particle emissions from Soufriere Hills volcano, Montserrat, West Indies: characterisation and health hazard assessment. Bulletin of Volcanology, 62: 8-19.

Allison, A.C. and Hart, D.A.P., 1968. Potentiation by silica of the growth of mycobacterium tuberculosis in macrophage cultures. The British Journal of Experimental Pathology, 49: 465-476.

Altree-Williams, S. and Sprogis, I., 1982. Quartz: Correlation between crystallinity index and fibrogenicity? The Annals of Occupational Hygiene, 25(4): 455-458.

American Journal of Public Health, March 1986.

Asgharian, B., Hofmann, W. and Miller, F.J., 2001. Mucociliary clearance of insoluble particles from the tracheobronchial airways of the human lung. Journal of Aerosol Science, 32(6): 817-832.

Babson, A.L. and Phillips, G.E., 1965. A rapid colorimetric assay for serum lactic dehyurogenase. Clinica Chimica Acta, 12(5): 210-215.

Ball, J.L., Calder, E.S., Hubbard, B.E. and Bernstein, M.L., 2013. An assessment of hydrothermal alteration in the Santiaguito lava dome complex, Guatemala: implications for dome collapse hazards. Bulletin of Volcanology, 75(676): 18.

Banks, D.E., 2010. The Health Effects of Silica and Coal Dust Exposures. In: M.I. Schwarz and T.E. King, Jr (Editors), Interstitial Lung Disease.

Barclay, J., Rutherford, M.J., Carroll, M.R., Murphy, M.D., Devine, J.D., Gardner, J. and Sparks, R.S.J., 1998. Experimental phase equilibria constraints on pre-eruptive storage conditions of the Soufrière Hills magma. Geophysical Research Letters, 25(18): 3437-3440.

Bargar, K.E., Keith, T.E.C. and Trusdell, F.A., 1995. Fluid-inclusion evidence for past temperature fluctuations in the Kilauea East Rift Zone geothermal area, Hawaii. Geothermics, 24(5-6): 639-659.

Barker, C. and Robinson, S.J., 1984. Thermal release of water from natural quartz. American Mineralogist, 69: 1078-1081.

Bassett, D.R., Boucher, E.A. and Zettlemoyer, A.C., 1968. Adsorption studies on hydrated and dehydrated silicas. Journal of Colloid and Interface Science, 27(4): 649-658.

Bassett, D.R., Boucher, E.A. and Zettlemoyer, A.C., 1972. The effect of alkali halides and silver nitrate on the crystallization of silica powders. Journal of Materials Science, 7: 1379-1382.

Batchelder, M. and Cressey, G., 1998. Rapid, accurate phase quantification of clay-bearing samples using a position-sensitive x-ray detector. Clays and Clay Minerals, 46(2): 183-194.

Baxter, P.J., Bonadonna, C., Dupree, R., Hards, V.L., Kohn, S.C., Murphy, M.D., Nichols, A., Nicholson, R.A., Norton, G., Searl, A., Sparks, R.S.J. and Vickers, B.P., 1999. Cristobalite in volcanic ash of the Soufriere Hills Volcano, Montserrat, British West Indies. Science, 283: 1142-1145.

Baxter, P.J., Ing, R., Falk, H., French, J., Stein, G.F., Bernstein, R.S., Merchant, J.A. and Allard, J., 1981. Mount St Helens Eruptions, May 18 to June 12, 1980: An Overview of the Acute Health Impact. The Journal of the American Medical Association, 256(22): 2585-2589.

Baxter, P.J., Ing, R., Falk, H. and Plikaytis, B., 1983. Mount St. Helens eruptions: the acute respiratory effects of volcanic ash in a North American community. Archives of Environmental Health, 38: 138-143.

Beckett, W., 2000. Occupational respiratory disease. N. Engl. J. Med., 342: 406-413.

Begin, R., Masse, S., Rola-Pleszcynski, M., Martel, M., Desmarais, Y., Geoffroy, M., LeBouffant, L., Daniel, J. and Martin, J., 1986. Aluminium lactate treatment alters the lung biological activity of quartz. Experimental Lung Research, 10: 385-399.

Bérubé, K.A., Jones, T.P., Housley, D.G. and Richards, R.J., 2004. The respiratory toxicity of airborne volcanic ash from the Soufriere Hills volcano, Montserrat. Mineralogical Magazine, 68(1): 47-60.

Bish, D.L. and Aronson, J.L., 1993. Paleogeothermal and paleohydrologic conditions in silicic tuff from Yucca Mountain, Nevada

Clays and Clay Minerals, 41(2): 148-161.

Biswas, S. and Rahman, I., 2009. Environmental toxicity, redox signaling and lung inflammation: the role of glutathione. Molecular Aspects of Medicine, 30(1-2): 60-76.

Blake, S. and Bruno, B.C., 2000. Modelling the emplacement of compound lava flows. Earth and Planetary Science Letters, 184: 181-197.

Blum, A.E. and Stillings, L.L., 1995. Feldspar dissolution kinetics. In: A.F. White and S.L. Brantley (Editors), Chemical Weathering Rates of Silicate Minerals. Reviews in Mineralogy, Mineralogical Society of America, Chantilly, Virginia, pp. 291–351.

Blundy, J. and Cashman, K.V., 2001. Ascent-driven crystallisation of dacite magmas at Mount St Helens, 1980-1986. Contributions to Mineralogy and Petrology, 140(631-650).

Blundy, J., Cashman, K.V. and Berlo, K., 2008. Evolving Magma Storage Conditions Beneath Mount St. Helens Inferred from Chemical Variations in Melt Inclusions from the 1980-1986 and Current (2004-2006) Eruptions. In: D.R. Sherrod, W.E. Scott and P.H. Stauffer (Editors), A volcano rekindled; the renewed eruption of Mount St. Helens, 2004-2006. U.S. Geological Survey Professional Paper, pp. 755-790.

Bluth, G.J.S. and Rose, W.I., 2004. Observations of eruptive activity at Santiaguito volcano, Guatemala. Journal of Volcanology and Geothermal Research, 136 297-302.

Boffetta, P., 1994. Biopersistence of respirable synthetic fibers and minerals: the point of view of the epidemiologist. Environmental Health Perspectives, 102(Suppl 5): 11-13.

Bonfoco, E., Krainc, D., Ankarcrona, M., Nicotera, P. and Lipton, S.A., 1995. Apoptosis and necrosis: Two distinct events induced, respectively, by mild and intense insults with N-methyl-D-aspartate or nitric oxide/superoxide in cortical cell cultures. Proceedings of the National Academy of Sciences, 92: 7162-7166.

Borm, P., Tran, L. and Donaldson, K., 2011. The carcinogenic action of crystalline silica: a review of the evidence supporting secondary inflammation-driven genotoxicity as a principal mechanism. Critical Reviews in Toxicology, 41(9): 756-770.

Brandwood, A., Noble, K.R. and Schindhelm, K., 1992. Phagocytosis of carbon particles by macrophages In vitro. Biomaterials, 13(9): 646-648.

Brodie, K.H. and Rutter, E.H., 2000. Rapid stress release caused by polymorphic transformation during the experimental deformation of quartz. Geophysical Research Letters, 27(19): 3089-3092.

Brown, D.M., Beswick, P.H., Bell, K.S. and Donaldson, K., 2000. Depletion of Gluathione and Ascorbate in Lung Lining Fluid by Respirable Fibres. The Annals of Occupational Hygiene, 44(2): 101-108.

Brunauer, S., Emmett, P.H. and Teller, E., 1938. Adsorption of gases in multimolecular layers. Journal of the American Chemical Society, 60: 309-319.

Buerger, M.J., 1954. The stuffed derivatives of the silica structures. American Mineralogist, 39: 600-614.

Buist, A.S., Martin, T.R., Shore, J.H., Butler, J. and Lybarger, J.A., 1986a. The development of a multidisciplinary plan for evaluation of the long-term health effects of the Mount St. Helens eruptions. American Journal of Public Health, 76(Suppl): 39–44.

Buist, A.S., Vollmer, W.M., Johnson, L.R., Bernstein, R.S. and McCamant, L.E., 1986b. A four-year prospective study of the respiratory effects of volcanic ash from Mt. St. Helens. American Review of Respiratory Disease, 133: 526–534.

Butler, M.A. and Dyson, D.J., 1997. The Quantification of Different Forms of Cristobalite in Devitrified Alumino-Silicate Ceramic Fibres. Journal of Applied Crystallography, 30: 467-475.

Calder, E.S., Luckett, R., Sparks, R.S.J. and Voight, B., 2002. Mechanisms of lava dome instability and generation of rockfalls and pyroclastic flows at Soufrière Hills Volcano, Montserrat. Geological Society, London.

Camus, G., Gourgaud, A., Mossand-Berthommier, P.-C. and Vincent, P.-M., 2000. Merapi (Central Java, Indonesia): An outline of the structural and magmatological evolution, with special emphasis to the major pyroclastic events. J. Volcanol Geotherm Res, 100: 139-163.

Carpenter, M.A., Salje, E.K.H. and Graeme-Barber A, 1998. Spontaneous strain as a determinant of thermodynamic properties for phase transition in minerals. Eur. J. Mineral., 10: 621-691.

Carroll, M.R. and Webster, J.D., 1994. Solubilities of sulfur, noble gases, nitrogen, chlorine and fluorine in magmas. Reviews in Mineralogy, 30: 231–280.

Cashman, K.V., 1988. Crystallization of Mount St. Helens 1980-1986 dacite: A quantitative textural approach. Bulletin of Volcanology, 50: 194-209.

Cashman, K.V., 1992. Groundmass crystallisation of Mount St Helens dacite, 1980-1986 - a tool for interpreting shallow magmatic processes. Contributions to Mineralogy and Petrology, 109: 431-499.

Cashman, K.V., Thornber, C.R. and Pallister, J.S., 2008. From Dome to Dust: Shallow Crystallisation and Fragmentation of Conduit Magma During the 2004-2006 Dome Extrusion of Mount St Helens, Washington. In: D.R. Sherrod, W.E. Scott and P.H. Stauffer (Editors), A volcano rekindled: The renewed eruption of Mount St. Helens, 2004-2006. U.S. Geological Survey Professional Paper 1750.

Castranova, V., 1994. Generation of oxygen radicals and mechanisms of injury prevention. Enivronmental Health Perspectives, 102(Suppl 10): 65-68.

Castranova, V., 2004. Signaling pathways controlling the production of inflammatory mediators in response to crystalline silica exposure: role of reactive oxygen/nitrogen species. Free Radical Biology & Medicine, 37(7): 916-925.

Cellai, D., Carpenter, M.A., Wruck, B. and Salje, E.K.H., 1994. Characterisation of high-temperature phase transitions in single crystals of Steinbach tridymite. American Mineralogist, 79: 606-614.

Chadwick, J.P., Troll, V.R., Ginibre, C., Morgan, D., Gertisser, R., Waight, T.E. and Davidson, J.P., 2007. Carbonate Assimilation at MerapiVolcano, Java, Indonesia: Insights from Crystal Isotope Stratigraphy. Journal of Petrology, 48(9): 1793-1812.

Chao, C.-H. and Lu, H.-Y., 2002a. Stress-induced β→α-cristobalite phase transformation in (Na2O + Al2O3)-codoped silica. Materials Science & Engineering, A328: 267-276.

Chao, C.-H. and Lu, H.-Y., 2002b. β-Cristobalite Stabilization in (Na2O + Al2O3)-Added Silica. Metallurgical and materials transactions, 33(8): 2703-2711.

Charbonnier, S.J. and Gertisser, R., 2008. Field observations and surface characteristics of pristine block-and-ash flow deposits from the 2006 eruption of Merapi Volcano, Java, Indonesia. Journal of Volcanology and Geothermal Research, 177: 971–982.

Chen, G.X., Burnett, C.A., Cameron, L.L., Alterman, T., Lalich, N.R., Tanaka, S. and Althouse, R.B., Tuberculosis Mortality and Silica Exposure: A Case—Control Study Based on a National Mortality Database for the Years 1983–1992. International Journal of Occupational and Environmental Health, 3(8): 163-170.

Churakov, S.V., Tkachenko, S.I., Korzhinskii, M.A., Bocharnikov, R.E. and Shmulovich, K.I., 2000. Evolution of Composition of High-Temperature Fumerolic Gases from

Kudryavy Volcano, Iturup, Kuril Islands: the Thermodynamic Modeling. Geochemistry International, 38(5): 436-451.

Churg, A., 1993. Asbestos lung burden and disease patterns in man. In: G. Guthrie, Jr and B. Mossman (Editors), Health Effects of Mineral Dusts. Mineralogical Society of America, Washington, pp. 409-426.

Clouter, A., Brown, D., Höhr, D., Borm, P. and Donaldson, K., 2001. Inflammatory Effects of Respirable Quartz Collected in Workplaces versus Standard DQ12 Quartz: Particle Surface Correlates. Toxicological Sciences, 63: 90-98.

Coleman, G.L., Barthold, S.W., Osbaldiston, G.W., Forster, S.J. and Jonas, A.M., 2006. Pathological Changes During Aging in Barrier-Reared Fischer 344 Male Rats. The Journal of Gerontology, 32(9): 258-278.

Cordonnier, B., Hess, K.-U., Lavallee, Y. and Dingwell, D.B., 2009. Rheological properties of dome lavas: Case study of Unzen volcano. Earth and Planetary Science Letters, 279(3-4): 263-272.

Couch, S., Sparks, R.S.J. and Carrol, M.R., 2003. The kinetics of degassing-induced crystallisation at Soufriere HIlls volcano, Montserrat. Journal of Petrology, 44(8): 1477-1502.

Coulter, K., Doseff, A., Sweeney, P., Wang, Y., Marsh, C.B., Wewers, M.D. and Knoell, D.L., 2002. Opposing effect by cytokines on Fas-mediated apoptosis in A549 lung epithelial cells. American Journal of Respiratory Cell and Molecular Biology, 26(58-66).

Cowie, R.L., 1994. The epidemiology of tuberculosis in gold miners with silicosis. American Journal of Respiratory and Critical Care Medicine, 150(5 Pt 1): 1460-1462.

Crapo, J.D., Barry, B.E., Gehr, P., Bachofen, M. and Weibel, E.R., 1982. Cell number and cell characteristics of the normal human lung. American Review of Respiratory Disease, 126(2): 332-337.

Creutzenberg, O., Ziemann, C., Hansen, T., Ernst, H., Jackson, P., Cartlidge, D. and Brown, R., 2009. In vivo study with quartz-containing ceramic dusts: Inflammatory effects of two factory samples in lungs after intratracheal instillation in a 28-day study with rats, Inhaled Particles X. Journal of Physics: ConferenceSeries 151, Manchester.

Cuadros, J., Afsin, B., Michalski, J.R. and Ardakani, M., 2012. Fast, microscale-controlled weathering of rhyolitic obsidian to quartz and alunite. Earth and Planetary Science Letters, 353-354: 156-162.

Cullen, R.T., Jones, A.D., Miller, B.G., Donaldson, K., Davis, J.M.G., Wilson, M. and Tran, C.L., 2002. Toxicity of volcanic ash from Montserrat. TM/02/01, Institute of Occupational Medicine, Edinburgh.

Damby, D.E., Horwell, C.J., Baxter, P.J., Delmelle, P., Donaldson, K., Dunster, C., Fubini, B., Murphy, F., Nattrass, C., Sweeney, S., Tetley, T.D. and Tomatis, M., 2012. The respiratory health hazard of tephra from the 2010 Centennial eruption of Merapi with implications for occupational mining of deposits. Journal of Volcanology and Geothermal Research.

Davis, J.M., 1994. The role of clearance and dissolution in determining the durability or biopersistence of mineral fibers. Environmental Health Perspectives, 102(Suppl 5): 113-117.

Davis, J.M.G., 1993. In vivo assays to evaluate the pathogenic effects of minerals in rodents. In: G.D. Guthrie, Jr and B.T. Mossman (Editors), Health Effects of Mineral Dusts. Mineralogical Society ofAmerica, Washington, pp. 471-487.

de Hoog, J.C.M., van Bergen, M.J. and Jacobs, M.H.G., 2005. Vapour-phase crystallisation of silica from SiF_4^- bearing volcanic gases. Annals of Geophysics, 48(4/5).

De Keyser, W.L. and Cypres, R., 1961. The action of mineralizers on the crystallization of colloidal silica. Silicates Industriels, 26(5): 237-243.

de Meringo, A., Morscheidt, C., Thelohan, S. and Tiesler, H., 1994. In Vitro assessment of biodurability: acellular systems. Environmental Health Perspectives, 102(Suppl. 5): 47-53.

Deer, W.A., Howie, R.A. and Zussman, J., 1996. An introduction to the rock forming minerals. Longman Scientific and Technical.

DeForge, L.E., Preston, A.M., Takeuchi, E. and al, e., 1993. Regulation of interleukin 8 gene expression by oxidant stress. Journal of Biological Chemistry, 268: 25568–25576.

Dennen, W.H., Blackburn, W.H. and Quesada, A., 1970. Aluminum in quartz as a geothermometer. Contributions to Mineralogy and Petrology, 27(4): 332-342.

Deshmane, S.L., Kremlev, S., Amini, S. and Sawaya, B.E., 2009. Monocyte Chemoattractant Protein-1 (MCP-1): An Overview. Journal of Interferon & Cytokine Research, 29(6): 313-326.

Dobbs, L.G., Johnson, M.D., Vanderbilt, J., Allen, L. and Gonzalez, R., 2010. The great big alveolar TI cell: evolving concepts and paradigms. Cellular Physiology and Biochemistry, 25(1): 55-62.

Dodson, R.F., Martin, R.R., O'Sullivan, M.F. and Hurst, G.A., 1982. In vitro response of human pulmonary macrophages with volcanic ash:a morphological study. Experimental and Molecular Pathology, 37: 406-412.

Dollberg, D.D., Bolyard, M.L. and Smith, D.L., 1986. Chapter 6: Evaluation of Physical Health Effects Due to Volcanic Hazards: Crystalline Silica in Mount St. Helens Volcanic Ash. American Journal of Public Health, 76(Suppl): 53-58.

Dollberg, D.D., Sweet, D.V., Bolyard, M., Carter, J.W., Stettler, L.E. and Geraci, C.L., 1984. Mount St. Helens volcanic ash: crystalline silica analysis. In: P.A. Russell (Editor), Fourth annual symposium on electron microscopy and X-ray applications to environmental and occupational health analysis. Ann Arbor Science, Ann Arbor.

Donaldson, K. and Borm, P.J.A., 1998. The Quartz Hazard: A Variable Entity. The Annals of Occupational Hygiene, 42(5): 287-294.

Donaldson, K., Murphy, F.A., Duffin, R. and Poland, C.A., 2010. Asbestos, carbon nanotubes and the pleural mesotheliomia review of the hypothesis regarding the role of long fibre retention in the parietal pleura, inflammation and mesothelioma. Particle and Fibre Toxicology, 7(5): 17.

Donaldson, K., Stone, V., Duffin, R., Clouter, A., Schins, R. and Borm, P., 2001. The quartz hazard: effects of surface and matrix on inflammogenic activity. J Environ Pathol Tox, 20: 109-118.

Donaldson, K. and Tran, C.L., 2004. An introduction to the short-term toxicology of respirable industrial fibres. Mutation research, 553(1-2): 5.

Donnadieu, F. and Merle, O., 2001. Geometrical contraints of the 1980 Mount St. Helens intrusion from analogue models. Geophysical Research Letters, 28(4): 639-642.

Driscoll, K.E., Howard, B.W., Hassenbein, D.G., Janssen, Y.M.W. and Mossman, B.T., 1995. Oxidative stress and silica-induced increases in nuclear NFKB binding activity in alveolar epithelial cells. American Journal of Respiratory and Critical Care Medicine, 151(A712).

Driscoll, K.E. and Maurer, J.K., 1991. Cytokine and Growth Factor Release by Alveolar Macrophages: Potential Biomarkers of Pulmonary Toxicity. Toxicologic Pathology, 19(4): 398-405.

Duffin, R., Gilmour, P.S., Schins, R.P.F., Clouter, A., Guy, K., Brown, D.M., MacNee, W., Borm, P., Donaldson, K. and Stone, V., 2001. Aluminium lactate treatment of DQ12 quartz inhibits its ability to cause inflammation, chemokine expression, and nulcear factor-κB activation. Toxicology and Applied Pharmacology, 176: 10-17.

Duffin, R., Tran, C.L., Clouter, A., Brown, D.M., MacNee, W., Stone, V. and Donaldson, K., 2002. The importance of surface area and specific reactivity in the acute pulmonary inflammatory response to particles. The Annals of Occupational Hygiene, 46(Supplement 1): 242-245.

Duffin, R., Tran, L., Brown, D., Stone, V. and Donaldson, K., 2007. Proinflammogenic effects of low-toxicity and metal nanoparticles in vivo and in vitro: highlighting the role of particle surface area and surface reactivity. Inhalation Toxicology, 19(10): 849-856.

Ebina, T., Takahashi, Y. and Hasuike, T., 1960. Effects of quartz powder on tubercle bacilli and phagocytes. American Review of Respiratory Disease, 82: 516-527.

Edmonds, M., McGee, K.A. and Doukas, M.P., 2008. Chlorine Degassing During the Lava Dome-Building Eruption of Mount St. Helens, 2004–2005. In: D.R. Sherrod, W.E. Scott and P.H. Stauffer (Editors), A Volcano Rekindled: The Renewed Eruption of Mount St. Helens, 2004–2006. U.S. Geological Survey Professional Paper 1750.

Edmonds, M., Oppenheimer, C., Pyle, D.M., Herd, R.A. and Thompson, G., 2003. SO2 emissions from Soufriere Hills Volcano and their relationship to conduit permeability, hydrothermal interaction and degassing regime. Journal of Volcanology and Geothermal Research, 124(1-2): 23-43.

Elias, Z., Poirot, O., Daniere, M.C., Terzetti, F., Binet, S., Tomatis, M. and Fubini, B., 2002. Surface reactivity, cytotoxicity, and transforming potency of iron-covered compared to untreated refractory ceramic fibers. Journal of Toxicology and Environmental Health, Part A, 65(23): 2007–2027.

Elsworth, D. and Voight, B., 2001. The mechanics of harmonic gas pressurization and failure of lava domes. Geophysical Journal International, 145: 187-198.

Elsworth, D., Voight, B., Thompson, G. and Young, S.R., 2004. Thermal-hydrologic mechanism for rainfall triggered collapse of lava domes. Geology, 32: 969-972.

Endo, E.T., Dzurisin, D. and Swanson, D.A., 1990. Geophysical and observational constraints for ascent rates of dacitic magma at Mount St Helens. In: M.P. Ryan (Editor), Magma transport and storage. John Wiley & Sons, New York, pp. 317-334.

Erren, T.C., Glende, C.B., Morfeld, P. and Piekarski, C., 2009. Is exposure to silica associated with lung cancer in the absence of silicosis? A meta-analytical approach to an important public health question. International Archives of Occupational and Environmental Health, 82(8): 997-1004.

Eshel, G., Levy, G.J., Mingelgrin, U. and Sinder, M.J., 2004. Critical evaluation of the use of laser diffraction for particle-size distribution analysis. Soil Science Society of America Journal, 68: 736-743.

Fenoglio, I., Prandi, L., Tomatis, M. and Fubini, B., 2001. Free radical generation in the toxicity of inhaled mineral particles: the role of iron speciation at the surface of asbestos and silica. Redox Rep, 6: 235–241.

Finch, G.I., Quarrell, A.G. and Roebuck, J.S., 1934. The Beilby Layer. Proceedings of the Royal Society A, 145: 676-681.

Fink, J.H., Malin, M.C. and Anderson, S.W., 1990. Intrusive and extrusive growth of the Mount St Helens lava dome. Nature, 348: 435-437.

Forbes, L., Jarvis, D., Potts, J. and Baxter, P., 2003. Volcanic ash and respiratory symptoms in children on the island of Montserrat, British West Indies. Occupational and Environmental Medicine, 60(3): 207-211.

Forman, H.J., Zhang, H. and Rinna, A., 2009. Glutathione: Overview of its protective roles, measurement, and biosynthesis. Molecular Aspects of Medicine, 30(1-2): 1-12.

Forster, W.M., Walters, D.M., Longphre, M., Macri, K. and Miller, L.M., 2000. Methodology for the measurement of mucociliary function in the mouse by scintigraphy. Journal of Applied Physiology, 90(3): 1111-1118.

Foster, K.A., Oster, C.G., Mayer, M.M., Avery, M.L. and Audus, K.L., 1998. Characterization of the A549 cell line as a type II pulmonary epithelial cell model for drug metabolism. Experimental Cell Research, 243(2): 359-366.

Foster, W.M., 1988. Is 24 Hour Lung Retention an Index of Alveolar Deposition. Journal of Aerosol Medicine, 1(1): 1-9.

Foustoukos, D.I. and Seyfried, W.E.J., 2007. Quartz solubility in the two-phase and critical region of the NaCl-KCl-H_2O system: Implications for submarine hydrothermal vent systems at 9°50'N East Pacific Rise. Geochimica Cosmochimica Acta, 71: 186-201.

Francis, S.M., Stephens, W.E. and Richardson, N.V., 2009. X-ray photoelectron and infrared spectroscopies of quartz samples of contrasting toxicity. Environmental Health, 9(Suppl 1): S4.

Frondel, C., 1962.

Fubini, B., 1994. Which surface functionalities are implied in dust toxicity? In: J.M.G. Davis and M.C. Jaurand (Editors), Cellular and Molecular Effects of Mineral and Synthetic Dusts and Fibers. NATO ASI Series. Springer-Verlag, pp. 347-358.

Fubini, B., 1997. Surface reactivity in the pathogenic response to particulates. Enivronmental Health Perspectives, 105: 1013-1020.

Fubini, B., 1998. Surface chemistry and quartz hazard. The Annals of Occupational Hygiene, 42: 521-530.

Fubini, B., Bolis, V., Cavenago, A. and Volante, M., 1995a. Physicochemical properties of crystalline silica dusts and their possible implication in various biological responses. Scandinavian Journal of Work, Environment & Health, 21(2): 9-14.

Fubini, B., Bolis, V. and Giamello, E., 1987. The surface chemistry of crushed quartz dust in relation to its pathogenicity. Inorganica Chimica Acta, 138: 193-197.

Fubini, B., Fenoglio, I., Ceschino, R., Ghiazza, M., Martra, G., Tomatis, M., Borm, P., Schins, R. and Bruch, J., 2004. Relationship between the state of the surface of four commercial quartz flours and their biological activity in vitro and in vivo. International Journal of Hygiene and Environmental Health, 207(2): 89-104.

Fubini, B., Fenoglio, I., Elias, Z. and Poirot, O., 2001. Variability of biological responses to silicas: effect of origin, crystallinity, and state of surface on generation of reactive oxygen species and morphological transformation of mammalian cells. Journal of Environmental Pathology, Toxicology and Oncology, 20: 95–108.

Fubini, B., Mollo, L. and Giamello, E., 1995b. Free radical generation at the solid/liquid interface in iron containing minerals. Free Radic Res, 23: 593-614.

Fubini, B. and Otero Areán, C., 1999. Chemical aspects of the toxicity of inhaled mineral dusts. Chemical Society Reviews, 28(6): 373-381.

Fubini, B., Zanetti, G., Altilia, S., Tiozzo, R., Lison, D. and Saffiotti, U., 1999. Relationship between surface properties and cellular responses to crystalline silica: studies with heat-treated cristobalite. Chemical Research in Toxicology, 12(8): 737-745.

Gardner, D.E., 2006. Toxicology of the Lung. Taylor & Francis Group, Boca Raton, FL.

Gehr, P. and Heyder, J., 2000. Particle-Lung Interactions. Mercel Dekker, Inc., New York, 802 pp.

Geiser, T., Jarreau, P.H., Atabai, K. and Matthay, M.A., 2000. Interleukin-1 beta augments in vitro alveolar epithelial repair. American Journal of Physiology-Lung Cellular and Molecular Physiology, 279(6): L1184-1190.

Gertisser, R. and Keller, J., 2003. Temporal variations in magma composition at Merapi Volcano (Central Java, Indonesia): magmatic cycles during the past 2000 years of explosive activity. J Volcanol Geotherm Res., 123: 1-23.

Ghiazza, M., Polimeni, M., Fenoglio, I., Gazzano, E., Ghigo, D. and Fubini, B., 2010. Does Vitreous Silica Contradict the Toxicity of the Crystalline Silica Paradigm. Chemical Research in Toxicology, 23: 620-629.

Ghio, A.J., Kennedy, T.P., Whorton, A.R., Crumbliss, A.L., Hatch, G.E. and Hoidal, J.R., 1992. Role of surface complexed iron in oxidant generation and lung inflammation induced by silicates. Lung Cellular and Molecular Physiology, 263(5): L511-L518.

Giard, D.J., Aaronson, S.A., Todaro, G.J., Arnstein, P., Kersey, J.H., Dosik, H. and Parks, W.P., 1973. In vitro cultivation of human tumors: establishment of cell lines derived from a series of solid tumors. Journal of the National Cancer Institute, 51(5): 1417-1423.

Graetsch, H. and Flörke, O.W., 1991. X-ray powder diffraction and phase relationship of tridymite modifications. Zeitschrift für Kristallographie, 195: 31-48.

Green, F.H.Y. and Vallyathan, V., 1996. Pathologica responses to inhaled silica. In: V. Castranova, V. Vallyathan and W.E. Wallace (Editors), Silica and Silica-Induced Lung Diseases. CRC Press.

Green, F.H.Y., Vallyathan, V., Mentnech, M.S., Tucker, J.H., Merchant, J.A., Kiessling, P., Antonius, J.A. and Parshley, P., 1981. Is volcanic ash a pneumoconiosis risk? Nature, 293: 216-217.

Gupta, A.K. and Gupta, M., 2005. Synthesis and surface engineering of iron oxide nanoparticles for biomedical applications. Biomaterials, 26(18): 3995-4021.

Guthrie, G.D., Jr., 1997. Mineral properties and their contributions to particle toxicity. Environmental Health Perspectives(105): 1003-1011.

Guthrie, G.D., Jr. and Heaney, P.J., 1995. Mineralogical characteristics of silica polymorphs in relation to their biological activities. Scandinavian Journal of Work, Environment & Health, 21(2): 5-8.

Haldane, J.S., 1918. Transactions of the Institute of Mining Engineers, London(55): 264.

Halliwell, B. and Gutteridge, J.M., 2007. Free radicals in biology and medicine. Oxford University Press.

Hamilton, R.F., Jr., Thakur, S.A. and Holian, A., 2008. Silica binding and toxicity in alveolar macrophages. Free Radical Biology & Medicine, 44(7): 1246-1258.

Hammer, J.E. and Rutherford, M.J., 2002. An experimental study of the kinetics of decompression-induced crystallization in silicic melt. Journal of Geophysical Research, 107(B1 2021).

Hansen, L.A., Poulson, O.M. and Nexc, B.A., 1997. Inflammatory potential of organic dust components and chemicals measured by IL-8 secretion from human epithelial cell line A549 in vitro. Annals of Agricultural and Environmental Medicine, 4: 27.

Hardy, J.A. and Aust, A.E., 1995. Iron in asbestos chemistry and carcinogenicity. Chemical Reviews, 95: 97–118.

Harris, A.J.L., Rose, W.I., Jr and Flynn, L.P., 2003. Temporal trends in lava dome extrusion at Santiaguito 1922-2000. Bulletin of Volcanology, 65: 77-89.

Hefland, R.B., Schwarzel, P.E., Johansen, B.V., Myran, T., Uthus, N. and Refsnes, M., 2001. Silica-induced cytokine release from A549 cells: importance of surface area versus size. Human & Experimental Toxicology, 20(1): 46-55.

Hemley, R.J., Jephcoat, A.P., Mao, H.K., Ming, L.C. and Manghnani, M.H., 1988. Pressure-induced amorphization of crystalline silica. Nature, 334: 52-54.

Herseth, J.I., Volden, V., Schwarze, P.E., Lag, M. and Refsnes, M., 2008. IL-1 beta differently involved in IL-8 and FGF-2 release in crystalline silica-treated lung cell co-cultures. Particle and Fibre Toxicology, 5(16): 18.

Hicks, P.D., Matthews, A.J. and Cooker, M.J., 2009. Thermal structure of a gas-permeable lava dome and timescale separation in its response to perturbation. Journal of Geophysical Research, 114: B07201.

Hill, V.G. and Roy, R., 1958. Silica Structure Studies: V, The Variable Inversion in Cristobalite. Journal of the American Ceramic Society, 41(12): 532-537.

Hillman, S.E., Horwell, C.J., Densmore, A.L., Damby, D.E., Fubini, B., Ishimine, Y. and Tomatis, M., 2012. Sakurajima volcano: a physico-chemical study of the health consequences of long-term exposure to volcanic ash. Bulletin of Volcanology, 74(4): 913-930.

Hincks, T.K., Aspinall, W.P., Baxter, A., Sparks, R.S.J. and Woo, G., 2006. Long term exposure to respirable volcanic ash on Montserrat: a time series simulation. Bull Volcanol, 68: 266-284.

Hnizdo, E. and Murray, J., 1998. Risk of pulmonary tuberculosis relative to silicosis and exposure to silica dust in South African gold miners. Occupational and Environmental Medicine, 55: 496-502.

Hoblitt, R.P. and Harmon, R.S., 1993. Bimodal density distribution of cryptodome dacite from the 1980 eruption of Mt St Helens, Washington. Bulletin of Volcanology, 55: 421-437.

Hoblitt, R.P., Miller, C.D. and Scott, W.E., 1987. Volcanic Hazards with Regard to Siting Nuclear-Power Plants in the Pacific Northwest.

Holland, L.M., 1990. Crystalline silica and lung cancer: a review of recent experimental evidence. Regulatory Toxicology and Pharmacology, 12: 224-237.

Holland, P.A.S., Watson, I.M., Phillips, J.C., Caricchi, L. and Dalton, M.P., 2011. Degassing processes during lava dome growth: Insights from Santiaguito lava dome, Guatemala. Journal of Volcanology and Geothermal Research, 202(1-2): 153-166.

Hook, G.E.R. and Viviano, C.J., 1996. Acute silicosis and the activation of alveolar type II cells. In: V. Castranova, V. Vallyathan and W.E. Wallace (Editors), Silica and Silica-Induced Lung Diseases. CRC Press.

Hornung, V., Bauernfeind, F., Halle, A., Samstad, E.O., Kono, H., Rock, K.L., Fitzgerald, K.A. and Latz, E., 2008. Silica crystals and aluminum salts activate the NALP3 inflammasome through phagosomal destabilization. Nature Immunology, 9: 847-856.

Horwell, C.J., 2007. Grain size analysis of volcanic ash for the rapid assessment of respiratory health hazard. J. Environ. Monitor., 9: 1107 - 1115.

Horwell, C.J. and Baxter, P.J., 2006. The respiratory health hazards of volcanic ash: a review for volcanic risk mitigation. Bulletin of Volcanology, 69: 1-24.

Horwell, C.J., Baxter, P.J., Cole, P.D., Damby, D.E., Hillman, S.E. and Christopher, T., submitted-a. Controls on variations in cristobalite abundance in ash generated by the Soufrière Hills volcano, Montserrat in the period 1997-2010. Geological Society of London Memoirs.

Horwell, C.J., Braña, L.P., Sparks, R.S.J., Murphy, M.D. and Hards, V.L., 2001. A geochemical investigation of fragmentation and physical fractionation in pyroclastic flows from the Soufrière Hills volcano, Montserrat. JVGR, 109: 247-262.

Horwell, C.J., Fenoglio, I. and Fubini, B., 2007. Iron-induced hydroxyl radical generation from basalitic volcanic ash. Earth Plan. Sci. Lett., 261: 662-669.

Horwell, C.J., Fenoglio, I., Ragnarsdottir, K.V., Sparks, R.S.J. and Fubini, B., 2003a. Surface reactivity of volcanic ash from the eruption of Soufriere Hills volcano, Montserrat, West Indies with implications for health hazard. Environ. Res., 93: 202-215.

Horwell, C.J., Hillman, S.E., Baxter, P.J., Damby, D.E., Calkins, J.A., Delmelle, P., Donaldson, K., Dunster, C., Fubini, B., Hoskuldsson, A., Kelly, F., Larsen, G., Le Blond, J.S., Livi, K.J.T., Mendis, B., Murphy, F., Thordarson, T. and Tomatis, M., submitted-b. Physicochemical and toxicological profiling of ash from the 2010 and 2011 eruptions of Eyjafjallajökull and Grímsvötn volcanoes, Iceland using a rapid respiratory hazard assessment protocol. Environmental Research.

Horwell, C.J., Le Blond, J.S., Michnowicz, S.A.K. and Cressey, G., 2010a. Cristobalite in a rhyolitic lava dome: Evolution of an ash hazard. Bulletin of Volcanology, 72: 249-253.

Horwell, C.J., Michnowicz, S.A.K. and Le Blond, J.S., 2008. Report on the mineralogical and geochemical characterisation of Hawai'i ash for the assessment of respiratory health hazard, International Volcanic Health Hazards Network (IVHHN).

Horwell, C.J., Sparks, R.S.J., Brewer, T.S., Llewellin, E.W. and Williamson, B.J., 2003b. The characterisation of respirable volcanic ash from the Soufriere Hills Volcano, Montserrat, with implications for health hazard. Bull Volcanol, 65: 346-362.

Horwell, C.J., Stannett, G.W., Andronico, D., Bertagnini, A., Fenoglio, I., Fubini, B., Le Blond, J.S. and Williamson, B.W., 2010b. A mineralogical health hazard assessment of Mt. Vesuvius volcanic ash. J. Volcanol Geotherm Res, 191: 222-232.

Horwell, C.J., Williamson, B.J., Le Blond, J.S., Donaldson, K., Damby, D.E. and Bowen, L., accepted. The structure of volcanic cristobalite in relation to its toxicity; relevance for the variable crystalline silica hazard. Particle and Fibre Toxicology.

Horwell, C.J., Williamson, B.J., Llewellin, E.W., Damby, D.E. and Le Blond, J.S., post review. The nature and formation of cristobalite at the Soufrière Hills volcano, Montserrat: implications for the petrology and stability of silicic lava domes. Bulletin of Volcanology.

Housley, D.G., Bérubé, K.A., Jones, T.P., Anderson, S., Pooley, F.D. and Richards, R.J., 2002. Pulmonary epithelial response in the rat lung to instilled Montserrat respirable dusts and their major mineral components. Occupational and Environmental Medicine, 59: 466-472.

Huaux, F., 2007. New Developments in the Understanding of Immunology in Silicosis. Current Opinion in Allergy and Clinical Immunology, 7: 168–173.

Huether, S.E. and McCance, K.L., 1996. Understanding Pathophysiology. Mosby, London.

Hughes, J.M., Jones, R.N., Gilson, J.C., Hammad, Y.Y., Samimi, B., Hendrick, D.J., Turner-Warwick, M., Doll, N.J. and Weill, H., 1982. Determinants of progression in sandblasters' silicosis. The Annals of Occupational Hygiene, 26(701-712).

Icopini, G.A., Brantley, S.L. and Heaney, P.J., 2004. Kinetics of silica oligomerization and nanocolloid formation as a function of pH and ionic strength at 25°C. Geochimica et Cosmochimica Acta, 69(2): 293-303.

Iler, R.K., 1979. The chemistry of silica: solubility, polymerization, colloid and surface properties, and biochemistry. John Wiley and Sons, New York.

International Agency for Research on Cancer, 1997. Silica, some silicates, coal dust and para-aramid fibrils (IARC monographs on the evaluation of carcinogenic risk of chemicals to humans), Lyon, France.

Itoh, H., Takahama, J., Takahashi, M. and Miyamoto, K., 2000. Hazard estimation of the possible pyroclastic flow disasters using numerical simulation related to the 1994 activity at Merapi volcano. Journal of Volcanology and Geothermal Research, 100: 503-516.

Janssens, J.P., Pache, J.C. and Nicod, L.P., 1999. Physiological changes in respiratory function associated with ageing. European Respiratory Journal, 13(1): 197-205.

Johnston, H.J., Hutchison, G.R., Christensen, F.M., Peters, S., Hankin, S. and Stone, V., 2009. Identification of the mechanisms that drive the toxicity of TiO2 particulates: the contribution of physicochemical characteristics. Particle and Fibre Toxicology, 6(33).

Jones, A.D., 1993. Respirable inductrial fibres:Deposition, clearance and dissolution in animal models. Annals Of Occupational Hygiene, 37(2): 211-226.

Jurinski, J.B. and Rimstidt, J.D., 2001. Biodurability of talc. American Mineralogist, 86: 392–399.

Kaewamatawong, T., Shimada, A., Okajima, M., Inoue, H., Morita, T., Inoue, K. and Takano, H., 2006. Acute and subacute pulmonary toxicity of low dose of ultrafine colloidal silica particles in mice after intratracheal instillation. Toxicologic Pathology, 34(7): 958-965.

Kamp, D.W. and Weitzman, S.A., 1999. The molecular basis of asbestos induced lung injury. Thorax, 54: 638-652.

Kennedy, M.C.S., 1956. Aluminium Powder Inhalations in the Treatment of Silicosis of Pottery Workers and Pneumoconiosis of Coal-Miners. British Journal of Industrial Medicine, 13(2): 85-101.

Kingma, K.J. and Hemley, R.J., 1994. Raman spectroscopic study of microcrystalline silica. American Mineralogist, 79: 269-273.

Kokelaar, B.P., 2002. Setting, chronology and consequences of the eruption of Soufriare Hills Volcano, Montserrat (1995-1999). The Geological Socieity, London, Memoirs.

Korzhinsky, M.A., Tkachenko, S.I., Shmulovich, K.I. and Steinberg, G.S., 1995. Native Al and Si formation. Nature, 375(6532): 544-544.

Krisement, O. and Trömel, G., 1959a. Die Umwandlung des Cristobalits. Z Naturforsch 14: 912–919.

Krisement, O. and Trömel, G., 1959b. Optische Beobachtung der Umwandlung von Cristobalitkristallen und statische Auswertung. Z Naturforsch, 14: 685–686.

Laboratoire de Sciences de la Terre ENS-Lyon France, 2000-2012. Handbook of Minerals Raman Spectra.

Lacasse, Y., Martin, S., Gagné, D. and Lakhal, L., 2009. Dose–response meta-analysis of silica and lung cancer. Cancer Causes & Control, 20(6): 925-933.

Lavallee, Y., Varley, N.R., Alatorre-Ibarguengoitia, M.A., Hess, K.-U., Kueppers, U., Mueller, S., Richard, D., Scheu, B., Spieler, O. and Dingwell, D.B., 2012. Magmatic architecture of dome-building eruptions at Volcan de Colima, Mexico. Bulletin of Volcanology, 74(1): 249-260.

Le Bas, M.J. and Streckeisen, A.L., 1991. The IUGS systematics of igneous rocks. J. Geol. Soc. Lond., 148: 825-833.

Le Blond, J., Horwell, C., Baxter, P., Michnowicz, S., Tomatis, M., Fubini, B., Delmelle, P., Dunster, C. and Patia, H., 2010. Mineralogical analyses and in vitro screening tests for the rapid evaluation of the health hazard of volcanic ash at Rabaul volcano, Papua New Guinea. Bull Volcanol, 72: 1077-1092.

Le Blond, J.S., Cressey, G., Horwell, C.J. and Williamson, B.J., 2009. A rapid method for quantifying single mineral phases in heterogeneous natural dust using X-ray diffraction. Powder Diffraction, 24: 17-23.

Le Blond, J.S., Tomatis, M., Horwell, C., Dunster, C., Murphy, F., Corazzari, I., Grendene, F., Turci, F., Gazzano, E., Ghigo, D., Williamson, B., Oppenheimer, C. and Fubini, B., 2012. The surface reactivity and implied toxicity of ash produced from sugarcane burning. Envrionmental Toxicology.

Le Bouffant, L., Daniel, H., Martin, J.C. and Bruyère, S., 1982. Effect of impurities and associated minerals on quartz toxicity. The Annals of Occupational Hygiene, 26(1-4): 625-634.

Leadbetter, A.J. and Smith, T.W., 1976. The α-β transition in the cristobalite phases of SiO2 and AIPO4 II. Calorimetric studies. Philosophical Magazine, 33(1): 113-119.

Leadbetter, A.J. and Wright, A.F., 1976. The α-β transition in the cristobalite phases of SiO2 and AlPO4 I. X-ray studies. Philosophical Magazine, 33(1): 105-112.

Lee, S.J. and Lee, C.H., 2000. Critical size effect for chemically doped β-cristobalite transformation. Materials Letters, 45: 175-179.

Leung, C.C., Tak Sun Yu, I. and Chen, W., 2012. Silicosis. The Lancet, 379(9830): 2008-2018.

Liu, J., Legros, S., Ma, G., Veinot, J.G., von der Kammer, F. and Hofmann, T., 2012. Influence of surface functionalization and particle size on the aggregation kinetics of engineered nanoparticles. Chemosphere, 8: 918-924.

Lofgren, G., 1971. Experimentally Produced Devitrification Textures in Natural Rhyolitic Glass. GSA Bulletin, 82(1): 111-124.

Low, R.B., Leslie, K.O., Hemenway, D.R., Absher, M., Adler, K.B., Giancola, M.S. and Vacek, P.M., 1990. Alveolar Type II Cell Response in Rats Exposed to Aerosols of Alpha-cristobalite. American Journal of Pathology, 136(4): 923-931.

Lowenstern, J.B., Bleick, H., Vazquez, J.A., Castro, J.M. and Larson, P.B., 2012. Degassing of Cl, F, Li, and Be during extrusion and crystallization of the rhyolite dome at Volcán Chaitén, Chile during 2008 and 2009. Bulletin of Volcanology.

Lu, S.-y., Yan, J.-h., Li, X.-d., Ni, M.-j., Cen, K.-f. and Dai, H.-f., 2007. Effects of inorganic chlorine source on dioxin formation using fly ash from a fluidized bed incinerator. Journal of Environmental Sciences, 19: 756-761.

Luhr, J.F., 2002. Petrology and geochemistry of the 1991 and 1998-1999 lava flows from Volcan de Colima, Mexico: implications for the end of the current eruptive cycle. Journal of Volcanology and Geothermal Research, 117(1-2): 169-194.

Luhr, J.F. and Carmichael, I.S.E., 1980. Colima volcanic complex, Mexico: part I. Post-caldera andesites from Volcan Colima. Contributions to Mineralogy and Petrology, 71(4): 343-372.

Luoto, K., Holopainen, M., Perander, M., Karppinen, K. and Savolainen, K.M., 1996. Cellular effects of particles--impact of dissolution on toxicity of man-made mineral fibers. Central European Journal of Public Health, 4(Suppl): 19-32.

Lyles, M.B., Fredrickson, H.L., Bednar, A.J., Fannin, H.B. and Sobecki, T.M., 2006. The chemical, biological, & physical characterization of dust particulates from the Middle East. Chinese Journal of Geochemistry, 25(S1): 2-3.

Lynch, I., Cedervall, T., Lundqvist, M., Cabaleiro-Lago, C., Linse, S. and Dawson, K.A., 2007. The nanoparticle-protein complex as a biological entity; a complex fluids and surface science challenge for the 21st century. Advances in Colloid and Interface Science, 134-135: 167-174.

Major, J.J., Dzurisin, D., Schilling, S.P. and Poland, M.P., 2009. Monitoring lava-dome growth during the 2004–2008 Mount St. Helens, Washington, eruption using oblique terrestrial photography. Earth and Planetary Science Letters, 286(1-2): 243-254.

Martin, T.R., Ayars, G., Butler, J. and Altman, L.C., 1984. The comparative toxicity of volcanic ash and quartz: effects on cells derived from the human lung. American Review of Respiratory Disease, 130: 778-782.

Martin, T.R., Wehner, A.P. and Butler, J., 1986. Evaluation of Physical Health Effects Due to Volcanic Hazards:The Use of Experimental Systems to Estimate the Pulmonary Toxicity of Volcanic Ash. American Journal of Public Health, 76(Supplement): 59-65.

Martra, G., Chiardola, E., Coluccia, S., Marchese, L., Tomatis, M. and Fubini, B., 1999. Reactive sites at the surface of crocidolite asbestos. Langmuir, 15: 5742–5752.

Martra, G., Tomatis, M., Fenoglio, I., Coluccia, S. and Fubini, B., 2003. Ascorbic Acid Modifies the Surface of Asbestos: Possible Implications in the Molecular Mechanisms of Toxicity. Chemical Research in Toxicology, 16: 328-335.

Matthews, A.J., Barclay, J., Carn, S., Thompson, G., Alexander, J., Herd, R. and Williams, C., 2002. Rainfall induced volcanic activity on Montserrat. Geophysical Research Letters, 29(13): 1644-1648.

McDonald, J.C., 1996. Silica and Lung Cancer. In: V. Castranova, V. Vallyathan and W.E. Wallace (Editors), Silica and Silica-Induced Lung Disease. CRC Press.

McKnight, R.E.A., Moxon, T., Buckley, A., Taylor, P.A., Darling, T.W. and Carpenter, M.A., 2008. Grain size dependence of elastic anomalies accompanying the alpha-beta transition in polycrystalline quartz. J. Phys.: Condens. Matter, 20: 075229.

Mellors, R.A., Waitt, R.B. and Swanson, D., 1988. Generation of pyroclastic flows and surges by hot-rock avalanches from the dome of Mount St. Helens volcano, USA. Bulletin of Volcanology, 50: 14-25.

Miller, C.D., 1989. Potential Hazards from Future Volcanic Eruptions in California.

Miyoshi, N., Yamaguchi, Y. and Makino, K., 2005. Successive zoning of Al and H in hydrothermal vein quartz. American Mineralogist, 90(2-3): 310-315.

Molesworth, A.M., Cuevas, L.E., Connor, S.J., Morse, A.P. and Thomson, M.C., 2003. Environmental Risk and Meningitis Epidemics in Africa. Emerging Infectious Diseases, 9(10): 1287-1293.

Mollo, L., Merlo, E., Giamello, E., Volante, M., Bolis, V. and Fubini, B., 1994. Effects of chelators on the surface properties of asbestos. In: J.M.G. Davis and M.C. Jaurand (Editors), Cellular and Molecular Effects of Minerals and Synthetic Dusts and Fibres. NATO ASI Series. Springer-Verlag, pp. 425-432.

Monteiller, C., Tran, L., MacNee, W., Faux, S., Jones, A., Miller, B. and Donaldson, K., 2007. The pro-inflammatory effects of low-toxicity low-solubility particles, nanoparticles and fine particles, on epithelial cells in vitro: the role of surface area Occupational and Environmental Medicine, 64(609-615).

Mosesman, M.A. and Pitzer, K.S., 1941. Thermodynamic properties of the crystalline forms of silica. Journal of the American Chemical Society, 63: 2348-2356.

Mossman, B.T. and Churg, A., 1998. Mechanisms in the pathogenesis of asbestosis and silicosis. American Journal of Respiratory and Critical Care Medicine(157): 1666–1680

Mougey, C., Francois-Rossetti, J. and Imelik, B., 1958. In: D.H. Everett and F.S. Stone (Editors), The Structure and Properties of Porous Materials. Butterworths, London, pp. 266-292.

Muhle, H., Bellmann, B. and Pott, F., 1994. Comparative investigations of the biodurability of mineral fibers in the rat lung. Enivronmental Health Perspectives, 102(Suppl 5): 163-168.

Murata, K.J. and Norman, M.B., II, 1976. An index of crystallinity for quartz. American Journal of Science, 276: 1120-1130.

Murphy, M.D., Sparks, R.S.J., Barclay, J., Carroll, M.R. and Brewer, T.S., 2000. Remobilisation of andesite magma by intrusion of mafic magma at the Soufriere Hills Volcano, Montserrat, West Indies. Journal of Petrology, 41: 21-42.

Nakada, S., Miyake, Y., Sato, H., Oshima, O. and Fujinawa, A., 1995. Endogenous growth of dacite dome at Unzen volcano (Japan), 1993–1994. Geology, 23: 57-160.

Nakada, S. and Motomura, Y., 1999. Petrology of the 1991-1995 eruption at Unzen: effusion pulsation and groundmass crystallization. Journal of Volcanology and Geothermal Research, 89(1-4): 173-196.

Nanji, A.A. and Hiller-Sturmhöfel, S., 1997. Apoptosis and Necrosis: Two types of cell death in alcoholic liver disease. Alcohol Health and Research World, 21(4): 325-330.

Nasrullah, M., Mazurek, J.M., Wood, J.M., Bang, K.M. and Kreiss, K., 2011. Silicosis Mortality with Respiratory Tuberculosis in the United States, 1968-2006. American Journal of Epidemiology, 174(7): 839-848.

Nesse, W.D., 2000. Introduction to Mineralogy. Oxford University Press.

Newhall, C.G., Bronto, S., Alloway, B., Banks, N.G., Bahar, I., del Marmol, M.A., Hadisantono, R.D., Holcomb, R.T., McGeehin, J., Miksic, J.N., Rubin, M., Sayudi, S.D., Sukhyar, R., Andreastuti, S., Tilling, R.I., Torley, R., Trimble, D. and Wirakusumah, A.D., 2000. 10,000 Years of explosive eruptions of Merapi Volcano, Central Java: archaeological and modern implications. J. Volcanol Geotherm Res, 100: 9-50.

Nolan, R.P., Langer, A.M., Eskenazi, R.A. and Herson, G.B., 1987. Membranolytic activities of quartz standards. Toxicology in Vitro, 1(4): 239-245.

Nord, G.L., Jr, 1994. Tranformation-induced twin boundaries in minerals. Phase Transitions, 48(1-3): 107-134.

Notter, R.H., 2000. Lung Surfactants: Basic Science and Clinical Applications. Marcel Dekker Incorporated, New York.

Nývlt, J., 1995. The Ostwald Rule of Stages. Crystal Research and Technology, 30(4): 443-449.

O'Brien-Ladner, A.R., Nelson, S.R., Murphy, W.J., Blumer, B.M. and Wesselius, L.J., 2000. Iron Is a Regulatory Component of Human IL-1b Production: Support for Regional Variability in the Lung. American Journal of Respiratory Cell and Molecular Biology, 23: 112-119.

Oberdorster, G., 1996. Significance of particle parameters in the evaluation of exposure-dose-response relationships of inhaled particles. Inhalation toxicology, 8: Suppl:73-89.

Oberdörster, G., Maynard, A., Donaldson, K., Castranova, V., Fitzpatrick, J., Ausman, K., Carter, J., Karn, B., Kreyling, W., Lai, D., Olin, S., Monteiro-Riviere, N., Warheit, D. and Yang, H., 2005a. Principles for characterizing the potential human health effects from exposure to nanomaterials: elements of a screening strategy. Particle and Fibre Toxicology, 2(8).

Oberdörster, G., Oberdörster, E. and Oberdörster, J., 2005b. Nanotoxicology: An Emerging Discipline Evolving from Studies of Ultrafine Particles. Enivronmental Health Perspectives, 113(7): 823-839.

Ono-Ogasawara, M. and Kohyama, N., 1999. Evaluation of Surface Roughness of Fibrous Minerals by Comparison of BET Surface Area and Calculated One. Ann Occup Hyg, 43(8): 505-511.

Ossaka, T., Kakegawa, K., Oi, T. and Mukaida, M., 1994. Major element analysis of selected rock and volcanic ash samples in the unzen area, Japan, by X-Ray Fluorescence Spectroscopy. Journal of Radioanalytical and Nuclear Chemistry, 183(2): 235-244.

Otsuka, K. and Wayman, C.M., 1998. Shape Memory Materials. Cambridge University Press.

Pairon, J.C., Brochard, P., Jaurand, M.C. and Bignon, J., 1991. Silica and lung cancer: a controversial issue. European Respiratory Journal, 4: 730-744.

Pallister, J.S., Thornber, C.R., Cashman, K.V., Clynne, M.A., Lowers, H.A., Mandeville, C.W., Brownfield, I.K. and Meeker, G.P., 2008. Petrology of the 2004-2006 Mount St. Helens lava dome - implications for magmatic plumbing and eruption triggering. In: D.R. Sherrod, W.E. Scott and P.H. Stauffer (Editors), A volcano rekindled: The renewed eruption of Mount St. Helens, 2004-2006. U.S. Geological Survey Professional Paper, pp. 647-702.

Palmberg, L., Larsson, B., Malmberg, P. and Larrson, K., 1998. Induction of IL-8 production in human alveolar macrophages and human bronchial epithelial cells in vitro by swine dust. Thorax, 53(260).

Parise, J.B., Yeganeh-Haeri, A., Weidner, D.J., Jorgensen, J.D. and Saltzberg, M.A., 1994. Pressure induced phase transition and pressure dependence of crystal structure in low and Ca/Al doped cristobalite. Journal of Applied Physics, 75(3): 1361-1367.

Pauling, L., 1929. The principles determining the structure of complex ionic crystals. Journal of the American Chemical Society, 5(1): 1010-1026.

Pedraza, C.E., Nikolcheva, L.G., Kaartinen, M.T., Barralet, J.E. and McKee, M.D., 2008. Osteopontin functions as an opsonin and facilitates phagocytosis by macrophages of hydroxyapatite-coated microspheres: Implications for bone wound healing. Bone, 43: 708-716.

Peeters, P.M., Perkins, T.N., Wouters, E.F.M., Mossman, B.T. and Reynaert, N.L., 2013. Silica induces NLRP3 inflammasome activation in human lung epithelial cells. Particle and Fibre Toxicology, 10(3).

Perrotta, A.J., Grubbs, D.K., Martin, E.S., Dando, N.R., McKinstry, H.A. and Huarg, C.-Y., 1989. Chemical Stabilization of β-Cristobalite. Journal of the American Ceramic Society, 72(3): 441-447.

Perry, E.C., Jr, 1971. Implications for geothermometry of aluminum substitution in quartz from Kings Mountain, North Carolina. Contributions to Mineralogy and Petrology, 30(2): 125-128.

Pertsev, N.A. and Salje, E.K.H., 2000. Thermodynamics of pseudoproper and improper ferroelastic inclusions and polycrystals: Effect of elastic clamping on phase transitions. Physical Review B, 61: 902-908.

Peterman, E.M. and Grove, M., 2010. Growth conditions of symplectic muscovite + quartz: Implications for quantifying retrograde metamorphism in exhumed magmatic arcs. Geology, 38(12): 1071-1074.

Pryde, A.K.A. and Dove, M.T., 1998. On the sequence of phase transitions in tridymite. Physics and Chemistry of Minerals, 26(2): 171-179.

Pugin, J., Schurer-Maly, C., Leturcq, D., Moriarty, A., Ulevitch, R.J. and Tobias, P.S., 1993. Lipopolysaccharide activation of human endothelial and epithelial cells is mediated by lipopolysaccharide-binding protein and soluble CD14. Proceedings of the National Academy of Sciences, 90: 2744.

Quality of Urban Air Review Group, 1996. Airborne particulate matter in the United Kingdom. Department of the Environment, London, UK.

QUARG, 1996. Airborne Particulate Matter in the United Kingdom (third report), Institute of Public and Environmental Health, University of Birmingham, Birmingham, UK.

Rahman, I. and MacNee, W., 1998. Role of transcription factors in inflammatory lung diseases. Thorax, 53: 601-612.

Raub, J.A., Hatch, G.E., Mercer, R.R., Grady, M. and Hu, P.C., 1985. Inhalation studies of Mt. St. Helens volcanic ash in animals. II. Lung function, biochemistry, and histology. Environmental Research, 37: 72-83.

Reich, M., Zúñiga, A., Amigo, Á., Vargas, G., Morata, D., Palacios, C., Parada, M.Á. and Garreaud, R.D., 2009. Formation of cristobalite nanofibers during explosive volcanic eruptions. Geology, 37: 435-438.

Renders, P.J.N., Gammons, C.H. and Barnes, H.L., 1995. Precipitation and dissolution rate constants for cristobalite from 150 to 300 °C. Geochimica Cosmochimica Acta, 59(1): 77-85.

Richet, P., Bottinga, Y., Denielou, L., Petitet, J.P. and Tequi, C., 1982. Thermodynamic properties of quartz, cristobalite and amorphous SiO2: drop calorimetry measurements between 1000 and 1800 K and a review from 0 to 2000 K. Geochima et Cosmochimica Acta, 46: 2639-2658.

Rifat, S.L., Eastwood, M.R., Crapper McLachlan, D.R. and Corey, P.N., 1990. Effect of exposure of miners to aluminium powder. The Lancet, 336: 1162-1165.

Rios, S., Salje, E.K.H. and Redfern, S.A.T., 2001. Nanoquartz vs. macroquartz: a study of the alpha <--> beta phase transition. European Physical Journal B, 20: 75-83.

Robock, K., 1973. Standard quartz DQ12 , < 5µM for experimental pneumoconiosis research projects in the federal republic of Germany. The Annals of Occupational Hygiene, 16: 63-66.

Roelofs, F. and Vogelsberger, W., 2004. Dissolution Kinetics of Synthetic Amorphous Silica in Biological-Like Media and Its Theoretical Description. The Journal of Physical Chemistry B, 108: 11308-11316.

Rose, W.I., Jr, 1972. Santiaguito Volcanic Dome, Guatemala. Geological Society of America Bulletin, 83(5): 1413–1434.

Rosen, G.M., Britigan, B., Halpern, H. and Pou, S., 1999. Free Radicals: Biology and Detection by Spin Trapping. Oxford University Press.

Rowe, M.C., Ellis, B.S. and Lindeberg, A., 2012. Quantifying crystallization and devitrification of rhyolites by means of X-ray diffraction and electron microprobe analysis. American Mineralogist, 97(10): 1685-1699.

Rutherford, M.J. and Hill, P.M., 1993. Magma Ascent Rates From Amphibole Breakdown: An Experimental Study Applied to the 1980-1986 Mount St. Helens Eruptions. Journal of Geophysical Research, 98(B11): 19,667-619,685.

Sahetapy-Engel, S.T., Harris, A.J.L. and Marchetti, E., 2008. Thermal, seismic and infrasound observations of persistent explosive activity and conduit dynamics at Santiaguito lava dome, Guatemala. Journal of Volcanology and Geothermal Research, 173: 1-14.

Schins, R.P.F. and Donaldson, K., 2000. Nuclear factor kappa-B activation by particles and fibers. Inhalation Toxicology, 12(10): 317-326.

Schins, R.P.F., Duffin, R., Höhr, D., Knaapen, A.M., Shi, T., Weishaupt, C., Stone, V., Donaldson, K. and Borm, P.J.A., 2002. Surface Modification of Quartz Inhibits Toxicity, Particle Uptake, and Oxidative DNA Damage in Human Lung Epithelial Cells. Chemical Research in Toxicology, 15: 1166-1173.

Schinwald, A., Chernova, T. and Donaldson, K., 2012. Use of silver nanowires to determine thresholds for fibre length-dependent pulmonary inflammation and inhibition of macrophage migration in vitro. Particle and Fibre Toxicology, 9(47).

Schmahl, W.W., 1993. Athermal transformation behaviour and thermal hysteresis at the SiO2 -alpha /beta - cristobalite phase transition. European Journal of Mineralogy, 5: 377-380.

Schmahl, W.W., Swainson, I.P., Dove, M.T. and Graeme-Barber, A., 1992. Landau free energy and order parameter behaviour of the α/β phase transition in cristobalite. Zeitschrift fur Kristallographie, 201(1-2): 125-145.

Schmidt, M.W., 1992. Amphibole composition in tonalite as a function of pressure: an experimental calibration of the Al-in-hornblende barometer. Contributions to Mineralogy and Petrology, 110(2-3): 304-310.

Schulz, H., Brand, P. and Heyder, J., 2005. Particle deposition in the repiratory tract. . In: P. Gehr and J. Heyder (Editors), Particle-Lung Interactions. Lung Biology in Health and Disease. Marcel Dekker, New York, pp. 229-290.

Schwarzel, P.E., Øvrevik, J., Hetland, R.B., Becher, R., Cassee, F.R., Låg, M., Løvik, M., Dybing, E. and Refsnes, M., 2007. Importance of size and composition of particles for effects on cells in vitro. Inhalation Toxicology, 19: 17-22.

Scorrono, D.M., 1975. A Test of Aluminum in Quartz as a Geothermometer. American Mineralogist, 60: 139-142.

Scott, J.A.J., Mather, T.A., Pyle, D.M., Rose, W.I. and Chigna, G., 2012. The magmatic plumbing system beneath Santiaguito Volcano, Guatemala. Journal of Volcanology and Geothermal Research, 237-238: 54-68.

Scott, W.E., Sherrod, D.R. and Gardner, C.A., 2008. Overview of the 200 to 2006, and Continuing, Eruption of Mount St. Helens, Washington. In: D.R. Sherrod, W.E. Scott and P.H. Stauffer (Editors), A Volcano Rekindled: The Renewed Eruption of Mount St. Helens, 2004-2006. U.S. Geological Survey Professional Paper.

Searl, A., Nicholl, A. and Baxter, P.J., 2002. Assessment of the exposure of islanders to ash from the Soufriere Hills volcano, Montserrat, West Indies. Occup Environ Med, 59: 523-531.

Sellamuthu, R., Umbright, C., Li, S., Kashon, M. and Joseph, P., 2011. Mechanisms of crystalline silica-induced pulmonary toxicity revealed by global gene expression profiling. Inhalation Toxicology, 14: 927-937.

Sellamuthu, R., Umbright, C., Roberts, J.R., Cumpston, A., McKinney, W., Chen, B.T., Frazer, D., Li, S., Kashonc, M. and Josepha, P., 2012. Molecular insights into the progression of crystalline silica-induced pulmonary toxicity in rats. Journal of Applied Toxicology.

Sharp, T.G., Stevenson, R.J. and Dingwell, D.B., 1996. Microlites and "nanolites" in rhyolitic glass: microstructural and chemcial characterization. Bulletin of Volcanology, 57: 631-640.

Shimizu, H., Matsushima, T., Nakada, S., Fujii, T., Hoshizumi, H., Takarada, S., Miyabuchi, Y., Ui, T., Miyake, Y., Sugimoto, T., Nagai, D., Hata, K., Sugimoto, S., Matsushita, E. and Yoshida, D., 2007. Unzen Eruption: Disaster and Recovery Field Guide.

Shmulovich, K.I. and Churakov, S.V., 1998. Natural fluid phases at high temperatures and low pressures. Journal of Geochemical Exploration, 62: 183-191.

Shmulovich, K.I., Yardley, B.W.D. and Graham, C.M., 2006. Solubility of quartz in crustal fluids: experiments and genearl equations for salt solutions and H_2O-CO_2 mixtures at 400-800 °C and 0.1-0.9 GPa. Geofluids, 6(2): 154-167.

Shoval, S., Ginott, Y. and Nathan, Y., 1991. A New Method for Measuring the Crystallinity Index of Quartz by Infrared Spectroscopy. Mineralogical Magazine, 55(381): 579-582.

Simon-Deckers, A., Gouget, B., Mayne-L'hermite, M., Herlin-Boime, N., Reynaud, C. and Carriere, M., 2008. In vitro investigation of oxide nanoparticle and carbon nanotube toxicity and intracellular accumulation in A549 human pneumocytes. Toxicology, 253: 137-146.

Slade, R., Crissman, K., Norwood, J. and Hatch, G., 1993. Comparison of antioxidant substances in bronchoalveolar lavage cells and fluid from humans, guinea pigs, and rats. Environmental Lung Research, 19: 469-484.

Small, C. and Naumann, T., 2001. The global distribution of human population and recent volcanism. Environmental Hazards, 3: 93-109.

Smith, C.S. and Wikoff, H.L., 1933. The silica content of lungs of a group of tunnel workers. American Journal of Public Health, 23: 1250-1254.

Smithsonian, 2012. Rabaul, USGS Weekly Volcanic Activity Reports. Global Volcanism Program.

Šolc, I., 1996. The optical determination of a surface layer on polished quartz plates. Czech Journal of Physics, 16: 525-528.

Sosman, R.B., 1965. The phases of silica. Rutgers University Press, New Brunswick, New Jersey.

Sparks, R.S.J., Murphy, M.D., Lejeune, A.M., Watts, R.B., Barclay, J. and Young, S.R., 2000. Control on the emplacement of the andesite lava dome of the Soufriere Hills Volcano by degassing-induced crystallization. Terra Nova, 12: 14-20.

Sparks, R.S.J. and Young, S.R., 2002. The eruption of Soufriere Hills Volcano, Montserrat (1995-1999): overview of scientific results. In: T.H. Druitt and B.P. Kokelaar (Editors), The Eruption of Soufriere Hills Volcano, Montserrat, from 1995 to 1999. The Geological Society, London, Memoirs.

Spearing, D.R., Farnan, I. and Stebbins, J.F., 1992. Dynamics of the α-β Phase Transitions in Quartz and Cristobalite as Observed by In-Situ High Temperature ^{29}Si and ^{17}O NMR. Physics and Chemistry of Minerals, 19: 307-321.

Spera, F.J., 2000. Physical Properties of Magma. In: H. Sigurdsson (Editor), Encyclopedia of Volcanoes. Academic Press, San Diego, CA, pp. 171-189.

Stebounova, L.V., Guio, E. and Grassian, V.H., 2010. Silver nanoparticles in simulated biological media: a study of aggregation, sedimentation, and dissolution. Journal of Nanoparticle Research.

Steenland, K., Mannetje, A., Boffetta, P., Stayner, L., Attfield, M., Chen, J., Dosemeci, M., DeKlerk, N., Hnizdo, E., Koskela, R. and Checkoway, H., 2001. Pooled exposure–response analyses and risk assessment for lung cancer in 10 cohorts of silica-exposed workers: an IARC multicentre study. Cancer Causes & Control, 12: 773-784.

Stevens, S.J., Hand, R.J. and Sharp, J.H., 1997. Temperature dependence of the cristobalite α-β inverstion. Journal of Thermal Analysis, 49: 1409-1415.

Stone, V., Jones, R., Rollo, K., Duffin, R., Donaldson, K. and Brown, D.M., 2004. Effect of coal mine dust and clay extracts on the biological activity of the quartz surface. Toxicology Letters, 149(1-3): 255-259.

Strober, W., 2001. Trypan Blue Exclusion Test of Cell Viability. Current Protocols in Immunology, 21: A.3B.1–A.3B.2.

Surono, Jousset, P., Pallister, J., Boichu, M., Fabrizia Buongiorno, M., Budisantoso, A., Costa, F., Andreastuti, S., Prata, F., Schneider, D., Clarisse, L., Humaida, H., Sumarti, S., Bignami, C., Griswold, J., Carn, S., Oppenheimer, C. and Lavigne, F., 2012. The 2010 explosive eruption of Java's Merapi volcano - a '100-year' event. Journal of Volcanology and Geothermal Research, 241-242: 121-135.

Swainson, I.P., Dove, M.T. and Palmer, D.C., 2003. Infrared and Raman spectroscopy studies of the α-β phase transition in cristobalite. Physics and Chemistry of Minerals, 30: 353-365.

Swanson, D.A., Cameron, K.A., Evarts, R.C., Pringle, P.T. and Vance, J.A., 1989. Cenozoic Volcanism in the Cascade Range and Columbia Plateau, Southern Washington and Northernmost Oregon. American Geophysical Union.

Symonds, R.B. and Reed, M.H., 1993. Calculation of multicomponent chemical equilibria in gas–solid–liquid system: calculation methods, thermochemical data, and application to tudies of high-temperature volcanic gases with examples from Mount St. Helens. American Journal of Science, 293: 758–864.

Takahashi, K., the Unzen-Fugendake Eruption Disaster Study Group, Department of Civil Engineering and Nagasaki University, 2007. Unzen-Fugendake Eruption Executive Summary 1990 - 1995. Unzen Restoration Project Office, Kyushu Regional Construction Bureau, Ministry of Land, Infrastructure and Transport: Nagasaki.

Talbot, J.H. and Kempis, E.B., 1960. Finely ground quartz: evidence against a `Disturbed' layer. Nature 188: 927-929.

Taniguchi, H. and Madden, K.P., 2000. DMPO-Alkyl radical spin trapping: an in situ radiolysis steady-state ESR study. Radiation Research, 153(4): 447-453.

Taunton, A.E., Gunter, M.E., Druschel, G.K. and Wood, S.A., 2010. Geochemistry in the lung: Reaction-path modeling and experimental examination of rock-forming minerals under physiologic conditions. American Mineralogist, 95(11-12): 1624-1635.

Ten Have-Opbroek, A.A., 1986. The structural composition of the pulmonary acinus in the mouse. A scanning electron microscopical and developmental-biological analysis. Anatomy and Embryology-Berlin, 174(1): 49-57.

teWaterNaude, J.M., Ehrlich, R.I., Churchyard, G.J., Pemba, L., Dekker, K., Vermeis, M., White, N.W., Thompson, M.L. and Myers, J.E., 2006. Tuberculosis and silica exposure in South African gold miners. Occup Environ Med, 63: 187-192.

Thompson, A.B., Robbins, R.A., Romberger, D.J., Sisson, J.H., Spurzem, J.R., Teschler, H. and Rennard, S.I., 1995. Immunological functions of the pulmonary epithelium. European Respiratory Journal, 8: 127-149.

Thompson, A.B. and Wennemer, M., 1979. Heat capacities and inversions in tridymite, cristobalite, and tridymite-cristobalite mixed phases. American Mineralogist, 64: 1018-1026.

Thouret, J.-C., Lavigne, F., Kelfoun, K. and Bronto, S., 2000. Toward a revised hazard assessment at Merapi volcano, Central Java. J. Volcanol. Geotherm. Res., 100: 479-502.

Timblin, C.R., Guthrie, G.D., Janssen, Y.W., Walsh, E.S., Vacek, P. and Mossman, B.T., 1998. Patterns of c-fos and c-jun proto-oncogene expression, apoptosis, and proliferation in rat pleural mesothelial cells exposed to erionite or asbestos fibers. Toxicology and Applied Pharmacology, 151(1): 88-97.

Tobias, P.S., Soldau, K., Kline, L. and al, e., 1993. Cross-linking of lipopolysaccharide (LPS) to CD14 on THP-1 cells mediated by LPS-binding protein. Journal of Immunology, 150: 3011.

Troll, V.R., Deegan, F.M., Jolis, E.M., Harris, C., Chadwick, J.P., Gertisser, R., Schwarzkopf, L.M., Borisova, A.Y., Bindeman, I.N., Sumarti, S. and Preece, K., 2012. Magmatic differentiation processes at Merapi volcano: inclusion petrology and oxygen isotopes. Journal of Volcanology and Geothermal Research.

Tsuchiya, S., Yamabe, M., Yamaguchi, Y., Kobayashi, Y., Konno, T. and Tada, K., 1980. Establishment and characterization of a human acute monocytic leukemia cell line (THP-1). International Journal of Cancer, 26: 171-176.

Turci, F., Tomatis, M., Lesci, I.G., Roveri, N. and Fubini, B., 2011. The Iron-Related Molecular Toxicity Mechanism of Synthetic Asbestos Nanofibres: A Model Study for High-Aspect-Ratio Nanoparticles. Chemistry A European Journal, 17: 350-358.

Vacek, P.M., Verma, D.K., Graham, W.G., Callas, P.W. and Gibbs, G.W., 2010. Mortality in Vermont granite workers and its association with silica exposure. Occupational and Environmental Medicine, 68(5): 312-318.

Vallyathan, V., Castranova, V., Pack, D., Leonard, S., Schumaker, J., Hubbs, A.F., Shoemaker, D.A., Ramsey, D.M., Pretty, J.R., McLaurin, J.L., Khan, A. and Teass, A., 1995. Freshly fractured quartz inhalation leads to enhanced lung injury and inflammation: Potential role of free radicals. American Journal of Respiratory Critical Care, 152: 1003-1009.

Vallyathan, V., Kang, J.H., Van Dyke, K., Dalal, N.S. and Castranova, V., 1991. Response of alveolar macrophages to in vitro exposure to freshly fractured versus aged silica dust: The ability of {rosil 28, an organosilane material, to coat silica and reduce its biological reactivity. Journal of Toxicology and Environmental Health, 33: 303-315.

Vallyathan, V., Shi, X., Dalal, N.S., Irr, W. and Castranova, V., 1988. Generation of free radicals from freshly fractured silica dust: Potential role in acute silica-induced lung injury. American Review of Respiratory Disease, 138: 1213-1219.

van Berlo, D., Knaapen, A.M., van Schooten, F.-J., Schins, R.P.F. and Albrecht, C., 2010. NF-kB dependent and independent mechanisms of quartz-induced proinflammatory activation of lung epithelial cells. Particle and Fibre Toxicology, 7(13): 20.

van Engeland, M., Ramaekers, F.C.S., Schutte, B. and Reutelingsperger, C.P.M., 1996. A novel assay to measure loss of plasma membrane asymmetry during apoptosis of adherant cells in culture. Cytometry, 24: 131–139.

Vaniman, D., 2006. Tuff Mineralogy. In: G. Heiken (Editor), Tuffs: Their Properties, Uses, Hydrology and Resources. The Geologicla Society of America, Boulder.

Villanueva, A., Cañete, M., Roca, A.G., Calero, M., Veintemillas-Verdaguer, S., Serna, C.J., del Puerto Morales, M. and Miranda, R., 2009. The influence of surface functionalization on the enhanced internalization of magnetic nanoparticles in cancer cells. Nanotechnology, 20.

Vogelsberger, W., Mittelbach, T. and Seidel, A., 1996. A contribution to the study of the solubility of oxidic solids in water: The disolution kinetics of silica gel and its interpretation. Berichte der Bunsengesellschaft für physikalische Chemie, 100(7): 1118-1127.

Voight, B., Constantine, E.K., Siswowidjoyo, S. and Torley, R., 2000. Historical eruptions of Merapi Volcano, Central Java, Indonesia, 1768-1998. Journal of Volcanology and Geothermal Research, 100: 69-138.

Voight, B. and Elsworth, D., 2000. Instability and collapse of hazardous gas-pressurized lava domes. Geophysical Research Letters, 27(1): 1-4.

Wadge, G., Voight, B., Sparks, R.S.J., Cole, P. and Loughlin, S.C., In review. An Overview of the Eruption of Soufrière Hills Volcano from 2000-2010. In: G. Wadge, R. Robertson and B. Voight (Editors), The Eruption of Soufriere Hills Volcano, Montserrat from 2000 to 2010. Memoir of the Geological Society of London.

Wagstaff, F.E., 1968. Crystallization Kinetics of Internally Nucleated Vitreous Silica. Journal of the American Ceramic Society, 51(8): 449-453.

Wagstaff, F.E., 1969. Crystallization and Melting Kinetics of Cristobalite. Journal of the American Ceramic Society, 52(12): 650-654.

Wagstaff, F.E. and Richards, K.J., 1966. Kinetics of Crystallization of Stoichiometric SiO2 Glass in H2O Atmospheres. Journal of the American Ceramic Society, 49(3): 118-121.

Wahl, F.M., Grim, R.E. and Graf, R.B., 1961. Phase transformations in silica as examined by continuous X-ray diffraction. The American Mineralogist, 46.

Warheit, D.B., Webb, T.R., Colvin, V.L., Reed, K.L. and Sayes, C.M., 2007. Pulmonary Bioassay Studies with Nanoscale and Fine-Quartz Particles in Rats: Toxicity is Not Dependent upon Particle Size but on Surface Characteristics. Toxicological Sciences, 95(1): 270-280.

Williams, S.N. and Self, S., 1983. The October 1902 plinian eruption of Santa María Volcano, Guatemala. Journal of Volcanology and Geothermal Research, 16(1-2): 33-56.

Williamson, B.J., Di Muro, A., Horwell, C.J., Spieler, O. and Llewellin, E.W., 2010. Injection of vesicular magma into an andesitic dome at the effusive-explosive transition. Earth Plan. Sci. Lett., 295(1-2): 83-90.

Wilson, M.R., Stone, V., Cullen, R.T., Searl, A., Maynard, R.L. and Donaldson, K., 2000. In vitro toxicology of respirable Montserrat volcanic ash. Environ. Med, 57: 727-733.

Witham, C.S., 2005. Volcanic disasters and incidents: a new database. Journal of Volcanology and Geothermal Research, 148: 191-233.

Wolf, R.E., Morman, S.A., Hageman, P.L., Hoefen, T.M. and Plumlee, G.S., 2011. Simulataneous speciation of arsenic, selenium, and chromium: species stability, sample preservation, and analysis of ash and soil leachates. Analytical and Bioanalytical Chemistry, 401: 2733-2745.

Woods, A.W., Sparks, R.S.J., Ritchie, L.J., Batey, J., Gladstone, C. and Bursik, M.I., 2002. The explosive decompression of a pressurized volcanic dome: the 26 December 1997 collapse and explosion of Soufriere Hills volcano. The Geological Society, London, Memoirs.

Worden, R.H., French, M.W. and Mariani, E., 2012a. Amorphous silica nanofi lms result in growth of misoriented microcrystalline quartz cement maintaining porosity in deeply buried sandstones. Geology 40 (2): 179-182.

Worden, R.H., French, M.W. and Mariani, E., 2012b. Amorphous silica nanofilms result in growth of misoriented microcrystalline quartz cement maintaining porosity in deeply buried sandstones Geology, 40(2): 179-182.

World Health Organisation: Regional Office for South-East Asia, 2011. Tuberculosis in the South-East Asia Region.

Wyart, J., 1949. Hydrothermal synthesis of minerals. Discussions of the Faraday Society, 5: 323-324.

Xu, H., Heaney, P.J. and Navrotsky, A., 2001. Thermal expansion and structural transformations of stuffed derivatives of quartz along the LiAlSiO4-SiO2 join: a variable-temperature powder synchotron XRD study. Phys. Chem. Min., 28: 302-312.

Yamamoto, H., Watson, I.M., Phillips, J.C. and Bluth, G.J., 2008. Rise dynamics and relative ash distribution in vulcanian eruption plumes at Santiaguito Volcano, Guatemala, revealed using an ultraviolet imaging camera. Geophysical Research Letters, 35: 5.

Yuguchi, T. and Nishiyama, T., 2008. The mechanism of myrmekite formation deduced from steady-diffusion modeling based on petrography: Case study of the Okueyama granitic body, Kyushu, Japan. Lithos, 106(3-4): 237-260.

Yurtmen, S. and Rowbotham, G., 1999. A scanning electron microscope study of post-depositional changes in the northeast Ni de ignimbrites, South Central Anatolia, Turkey. Mineralogical Magazine, 63(1): 131-141.

Appendix 3

Health Reports

Respiratory health hazard assessment of ash from the 2010 eruption of Eyjafjallajökull volcano, Iceland. A summary of initial findings from a multi-centre laboratory study

Co-ordinator: CJ Horwell, Director of the International Volcanic Health Hazard Network

Horwell, C.J.[1], Baxter, P.J.[2], Hillman, S.E.[1], Damby, D.E.[1], Delmelle, P.[3], Donaldson, K.[4], Dunster, C.[5], Calkins, J. A.[3], Fubini, B.[6], Hoskuldsson, A.[7], Kelly, F. J.[5], Larsen, G.[7], Le Blond, J. S.[8,9], Livi, K. J. T.[10], Mendis, B.[11], Murphy, F.[4], Sweeney, S.[12], Tetley, T.D.[12], Thordarson, T.[13], Tomatis, M.[6]

[1] Institute of Hazard, Risk and Resilience, Department of Earth Sciences, Durham University, Science Labs, South Road, Durham, DH1 3LE, UK.
Claire.horwell@durham.ac.uk Tel. ++ 44 (0)191 3342335

[2] Institute of Public Health, University of Cambridge, Cambridge, CB2 2SR, UK.

[3] Environment Department, University of York, Heslington, York, YO10 5DD, UK.

[4] The University of Edinburgh/MRC Centre for Inflammation Research, The Queen's Medical Research Institute, Edinburgh, EH16 4TJ, UK.

[5] MRC-HPA Centre for Environment and Health, King's College London, 150 Stamford Street, London, SE1 9NH, UK

[6] Dipartimento di Chimica I.F.M., Interdepartmental Center "G. Scansetti" for Studies on Asbestos and other Toxic Particulates, Università degli studi di Torino, Via P. Giuria 7, 10125, Torino, Italy.

[7] Institute of Earth Sciences, University of Iceland, 101 Reykjavík, Iceland.

[8] Department of Geography, University of Cambridge, Downing Place, Cambridge, CB2 3EN, UK.

[9] Department of Mineralogy, Natural History Museum, Cromwell Road, London, SW7 5BD, UK.

[10] The High-Resolution Analytical Electron Microbeam Facility of the Integrated Imaging Center, Departments of Earth and Planetary Sciences and Biology, Johns Hopkins University, Maryland 21218, USA.

[11] Department of Physics, Durham University, Science Labs, South Road, Durham, DH1 3LE, UK.

[12] National Heart & Lung Institute, Imperial College, Dovehouse Street, London, SW3 6LY, UK.

[13] Grant Institute, School of Geosciences, The King's Buildings, Edinburgh, EH9 3JW, UK.

Summary

- 14 samples were analysed from the ash fallout on Iceland from Eyjafjallajökull volcano. 12 samples were from ash erupted 15-19 April during the phreatomagmatic phase (when glacial meltwater interacted with the magma, 14-17 April) and the following 2 days. Two samples were from ash erupted 6-9 May in the drier phase (4-22 May).
- The samples range from basaltic trachy-andesite to trachy-andesite.
- The grain size pertinent to respiratory health of fine samples was variable: 2-13 vol. % < 4 μm and 4-26 vol. % < 10 μm. The finest samples were all erupted during the phreatomagmatic phase, but as we only obtained 2 samples from the drier phase they may not be representative.
- Very dark grey/black ash and lighter grey ash were both visible in the plume as it was being erupted. The darkest ash samples were, in general, coarser than the lighter ash samples, independent of the eruptive phase.
- The crystalline silica content in all ash samples was negligible (within the 1-3 wt. % error of the technique).
- Morphology showed mainly angular, glassy particles, typical of volcanic ash. Occasional fibre-like particles in one sample from the dry phase were either feldspar, glass, gypsum or a Fe/Mg silicate and were unlikely to be of health concern.
- Surface area varied substantially from 0.3-7.7 m^2g^{-1}, showing that some samples have high available surface for reactions in the lung.
- Leachate analysis showed low release of trace elements relevant to respiratory health, with the exception of one sample.
- *In vitro* screening tests for potential bio-reactivity of the ash particles showed low hydroxyl free radical generation in comparison to ash samples from other volcanoes (except for one sample with iron-related reactivity akin to basaltic ash); and low values for oxidative potential (ascorbic acid oxidative capacity). Measurement of haemolysis (quartz-like behaviour), cytotoxicity and inflammatory markers also revealed low activity.
- **Conclusion:** The ash fallout examined contains a substantial fraction of fine-grained material which could generate elevated levels of $PM_{2.5}$ and PM_{10} in the ambient air when re-suspended by dry, windy conditions, by traffic and by those working in the ash. Average outdoor air concentrations in the ashfall area can be expected to regularly exceed World Health Organisation (WHO) 24-hour guideline levels for particles in the ambient air until the ash is incorporated into the environment with repeated rainfall. The *in vitro* toxicity tests suggest that the potential for the ash to trigger acute pulmonary inflammation at ambient levels of exposure is low. Persistence of deposited ash in the soils and environment would not present a significant silicosis hazard, e.g. to outdoor workers, as crystalline silica content is negligible.

Introduction

The explosive eruption of Eyjafjallajökull volcano, Iceland during April - May 2010, produced plumes of ash which were blown, at times, across Europe, the Atlantic and northern Africa, causing severe air traffic disruption. Closure of parts of European air space for up to six days highlighted the widespread dispersal of ash, and countries were concerned about the potential impacts of ashfall on agriculture and the respiratory health hazard of the associated particulate air pollution. Here we present a brief summary of the initial results on a suite of tests using a protocol specifically developed for the assessment of the hazards to human health of ash from volcanic eruptions (Fig. 1). All samples were obtained on Iceland (Fig. 2). A full report will be published separately.

Health-pertinent volcanic ash characteristics

A detailed overview is given by Horwell & Baxter (2006)[1] along with a description of the mechanisms of pathogenicity in the lungs and a review of mineralogical, toxicological and

medical studies at previous volcanic eruptions up to 2006. The protocol used here (Fig. 1) has been developed in the light of this global experience[2].

The 2010 eruption of Eyjafjallajökull volcano

After an initial effusive eruption on the northeast flank, an explosive, phreatomagmatic eruption began beneath the central vent of Eyjafjallajökull volcano on 14 April 2010 as glacial meltwater from the icecap interacted with erupting magma. Fine ash and gases from Eyjafjallajökull were ejected up to 11 km into the atmosphere, with high intensity eruptive activity continuing until 18 April[3]. By 21 April, the eruption explosivity had decreased due to both a reduction in magma supply and reduced interaction with meltwater. Lava flows began on 21 April and activity continued with minor explosions. Between 4-6 May, explosive activity increased and effusive activity decreased again, resulting in increased tephra fallout. From 7-17 May, activity reduced but there was still considerable tephra fallout. On 18 May there was significant explosive activity with widespread ashfall across Iceland, but activity then decreased again and by 22 May the plume was ash-free[4]. Later, widespread drifting and remobilisation of ash deposits was reported in the vicinity of the volcano, indicating an ongoing respiratory hazard despite the cessation of ashfall.

Methods

- *Samples:* 14 samples were obtained, mainly from the phreatomagmatic stage (15-19 April), with 2 samples from the later, drier stage of the eruption (6-9 May)(Tab. 1, Fig. 2).
- *Bulk compositional analysis:* The major elemental composition of the ash was determined by X-ray fluorescence to categorise the magmatic composition of the bulk ash samples.
- *Grain-size analysis:* The grain-size distribution (0.02-2000 μm) was measured by laser diffraction to determine whether there was a significant proportion of 'respirable' (< 4 μm) and 'thoracic' (< 10 μm) material in the samples.
- *Crystalline silica quantification:* The quantities of cristobalite and quartz in the samples were determined using X-ray Diffraction with static position-sensitive detection[5].
- *Particle morphology and composition*: Images of the ash were obtained by Scanning Electron Microscopy and Transmission Electron Microscopy. The composition of fibre-like particles was determined from their elemental assemblage using energy dispersive spectroscopy and diffraction pattern indexing.
- *Sample appearance*: The colour of the samples was classified using the Munsell soil colour classification scheme (www.munsellstore.com).
- *Surface area*: The Brunauer Emmet Teller method with nitrogen adsorption was used to determine the specific surface area of the samples.
- *Leachate analysis*: The concentrations of water-soluble elements adsorbed on ash that may have potential relevance to ash toxicity were determined by shaking the ash in deionized water. The filtered solutions were acidified with HNO_3 and Cr, Fe, Ni, Cu, Zn, As and Cd were analysed by ICP-MS. The pH of the leachates was also measured.
- *Hydroxyl radical generation and iron release:* Electron paramagnetic resonance spectrometry was used to measure potentially deleterious hydroxyl radicals (HO•) released into solution from the samples through replication of the Fenton reaction[6]. UV-Visible spectrophotometry was used to estimate the amount of iron that could be released by chelators from the ash surface for participation in the Fenton reaction.
- *Particle oxidative capacity*: Ascorbate is an antioxidant found in the fluid lining the surface of the lungs, often referred to as the respiratory tract lining fluid (RTLF). Oxidising species on the surface of inhaled particles may cause changes in the natural balance of protective antioxidants found in RTLF, which may have an impact on cellular redox states, and hence may lead to airway irritation and oxidative stress. The depletion of antioxidants in the presence of ash particles might have significance for the health of asthma sufferers.

- *Haemolysis*: The propensity for the particles to display quartz-like toxic activity in the lung was examined by the Erythrocyte Lysis Assay.
- *Cytotoxicity and inflammation:* One sample (EYJ_10_13) was tested for its cytotoxicity against human lung epithelial type-1 cells as well as measuring induction of acute markers of inflammation: release of interleukin-6 (IL-6), interleukin-8 (IL-8) and monocyte chemotactic protein-1 (MCP-1).

Results

- *Bulk Composition:* The samples range from basaltic trachy-andesite to trachy-andesite (53 – 59 wt. % SiO_2). There was no obvious change in erupted composition with time.
- *Grain-size:* Respirable ash (< 4 μm diameter) varied from ~ 2-13 vol. %. Certain conditions during the phreatomagmatic stages produced significant quantities (> 10 vol. %) of respirable ash. This can be compared to phreatomagmatic ash from Vesuvius, Italy (≤ 17 vol. % < 4 μm material[7]). The two samples collected during the drier phase (1.96 and 5.09 vol. % < 4 μm material) are comparable to ash from other mildly-explosive eruptions (e.g. 5.9 vol. % for vulcanian explosions at the Soufrière Hills volcano, Montserrat[8]).
- *Crystalline silica content:* Total crystalline silica content (1.4-3.2 wt. %) was approximately within the 1-3 wt. % error for the technique. Tridymite was not identified. The samples were mostly amorphous, visible as a high background hump in the XRD patterns. It can be concluded with confidence that there is little to no crystalline silica in any of the samples analysed.
- *Particle morphology*: Morphology was typical of volcanic ash (blocky and angular). Some respirable, fibre-like particles were identified but were extremely rare and found only in sample EYJ_10_13.
- *Particle composition*: The fibre-like particles were either glass, feldspar, gypsum or a Mg/Fe rich mineral which could not be classified but was not related to asbestos minerals.
- *Surface area*: The BET specific surface area for the samples ranged between 0.29 – 7.67 $m^2\ g^{-1}$, with the higher values considered unusually high for volcanic ash.
- *Leachates*: Among the 8 elements measured, Fe was the most concentrated in the ash extracts (<1-26 mg kg^{-1}). Except for Zn in EYJ_10_13, the concentrations of all the other elements were less than 1 mg kg^{-1} and were low compared to ash from other volcanoes[9]. Some samples produced alkaline pH values (7.9-9.1) in the leachates, whilst others gave pH values < 6 with EYJ_10_13 being the most acidic (pH 4.4).
- *Hydroxyl radical generation*: The number of hydroxyl radicals released by all samples was very low (< 0.5 μmol m^{-2}) in comparison to a suite of standard ash samples analysed concurrently, with the exception of EYJ_10_13 which generated radicals and released iron on a scale akin to iron-rich basaltic samples. There was an excellent linear correlation (R^2 = 0.99) between iron release and HO• generation.
- *Haemolysis and oxidative capacity:* The propensity for haemolysis was low for all samples (< 5 %). No evidence of oxidative activity was observed for any samples. Positive and negative controls demonstrated expected results.
- *Cytotoxicity and inflammation:* EYJ_10_13 showed some cytotoxicity, being slightly higher than a sample from Soufrière Hills volcano, Montserrat. There was no change in release of IL-6, IL-8 or MCP-1 following exposure to either of these samples, indicating that the particles have little acute reactivity at physiologically-realistic exposure levels.

Discussion and health message

The ash fallout from Eyjafjallajökull volcano was variable in terms of grain size, most probably controlled by factors such as fragmentation mechanism and efficiency as well as location of fallout with respect to distance from the volcano and plume axis. According to Óskarsson (personal communication), the colour of the ash is related to oxidation of Fe in the glass during interaction with steam in the erupting plume. Darker samples were, in general,

coarser, although this was not always the case; furthermore no relationship was found between sample colour and surface iron availability (neither Fe^{2+} nor Fe^{3+}).

Other health-pertinent mineralogical characteristics, such as crystalline silica content and particle morphology, gave no specific cause for concern; bio-reactivity screening was also negative. One sample (EYJ_10_13) generated substantial hydroxyl radicals, was the most acidic, had the lowest surface area, contained fibre-like particles and leached more trace elements of relevance to ash toxicity in comparison to the low levels measured in all the other samples. This sample was erupted in the drier phase but otherwise has no distinguishable differences from the other samples except that it was collected dry, during the ashfall itself. It is possible that its pristine condition may have preserved leachable and reactive surface elements. However, the other samples are likely to be more representative of particulate in Iceland which is likely to be rapidly exposed to rainwater following deposition.

The substantial fraction of fine-grained material could generate elevated levels of airborne particulate matter < 2.5 μm and 10 μm in diameter ($PM_{2.5}$ and PM_{10}) when the deposits are re-suspended under dry, windy conditions or by outdoor human activity (outdoor workers in particular can be heavily exposed). As a result, average outdoor air concentrations can be expected to regularly exceed WHO 24-hour health guideline levels for particles after ashfalls until the ash is incorporated into the environment with repeated rainfall. Elevated ambient levels of respirable ash particles are known to exacerbate the symptoms of people with chronic respiratory conditions such as asthma and chronic bronchitis[1] who may need to adjust their medication and obtain medical advice if the dusty conditions persist. The results also indicate that the potential of the ash to cause long-term respiratory effects in healthy adults and children is low.

Measures to minimise individual exposure to fine ash are generally recommended after volcanic eruptions (e.g. wearing light weight, high efficiency masks outdoors, staying indoors during periods of raised re-suspension of ash and wetting down ash in school playgrounds and before remediation efforts), together with clean-up operations to remove ash from roofs and outside homes, along roads and other public places.

Further Information

All data (as tables and figures) are available upon request and will be published in an academic journal shortly. Further information on preparedness for ashfalls and the health hazards of volcanic ash can be found in the pamphlets available on the International Volcanic Health Hazard Network website (www.ivhhn.org) as well as a library of literature relating to the health hazards of volcanic emissions, including key references on the methods used in the protocol.

A separate study is being carried out on ash that fell over the UK and Europe. Please contact Claire Horwell for further information.

Fluoride analysis is not included in this study as it has been extensively studied by the Nordic Volcanological Center, Iceland (by Níels Óskarsson) and by Pierre Delmelle (York University, UK) and its relevance to respiratory health hazards is unclear.

Acknowledgements

This work was funded through a NERC Urgency Grant (NE/I007652/1). We particularly thank colleagues at the University of Iceland for collecting and providing samples (Gíslason, Sverrisdóttir). Thanks also to Susanna Jenkins (Cambridge Architectural Research) for sample collection and Evgenia Ilyinskaya (University of Cambridge) for providing an ash sample and for corresponding grain-size data[10]. Thanks to Sabina Michnowicz (Durham University) and Nick Marsh (Leicester University) for sample management and analyses, respectively. We are grateful to Níels Óskarsson for helpful discussions.

References

[1] Horwell, C.J. and Baxter, P.J., *Bulletin of Volcanology* **69**, 1 (2006).

[2] Le Blond, J.S., Horwell, C.J., Baxter, P.J. et al., *Bulletin of Volcanology* **DOI: 10.1007/s00445-010-0382-7** (2010).

[3] Icelandic Met Office, in *http://en.vedur.is/about-imo/news/2010* (2010).

[4] Institute of Earth Sciences, in *http://www.earthice.hi.is/page/ies_Eyjafjallajokull_eruption* (University of Iceland, 2010).

[5] Le Blond, J.S., Cressey, G., Horwell, C.J. et al., *Powder Diffraction* **24**, 17 (2009).

[6] Horwell, C.J., Fenoglio, I., and Fubini, B., *Earth Plan. Sci. Lett.* **261** (3-4), 662 (2007).

[7] Horwell, C.J., Stannett, G.W., Andronico, D. et al., *J Volcanol Geotherm Res* **191**, 222 (2010).

[8] Horwell, C.J., *J. Environ. Monitor.* **9** (10), 1107 (2007).

[9] Witham, C.S., Oppenheimer, C., and Horwell, C.J., *J Volcanol Geotherm Res* **141**, 299 (2005).

[10] Ilyinskaya, E., Tsanev, V.P., Martin, R.S. et al., *Geophys. Res. Lett.* (in review).

Figure 1. Protocol used for analysis of ash samples. Adapted from Le Blond et al. (2010[2]).

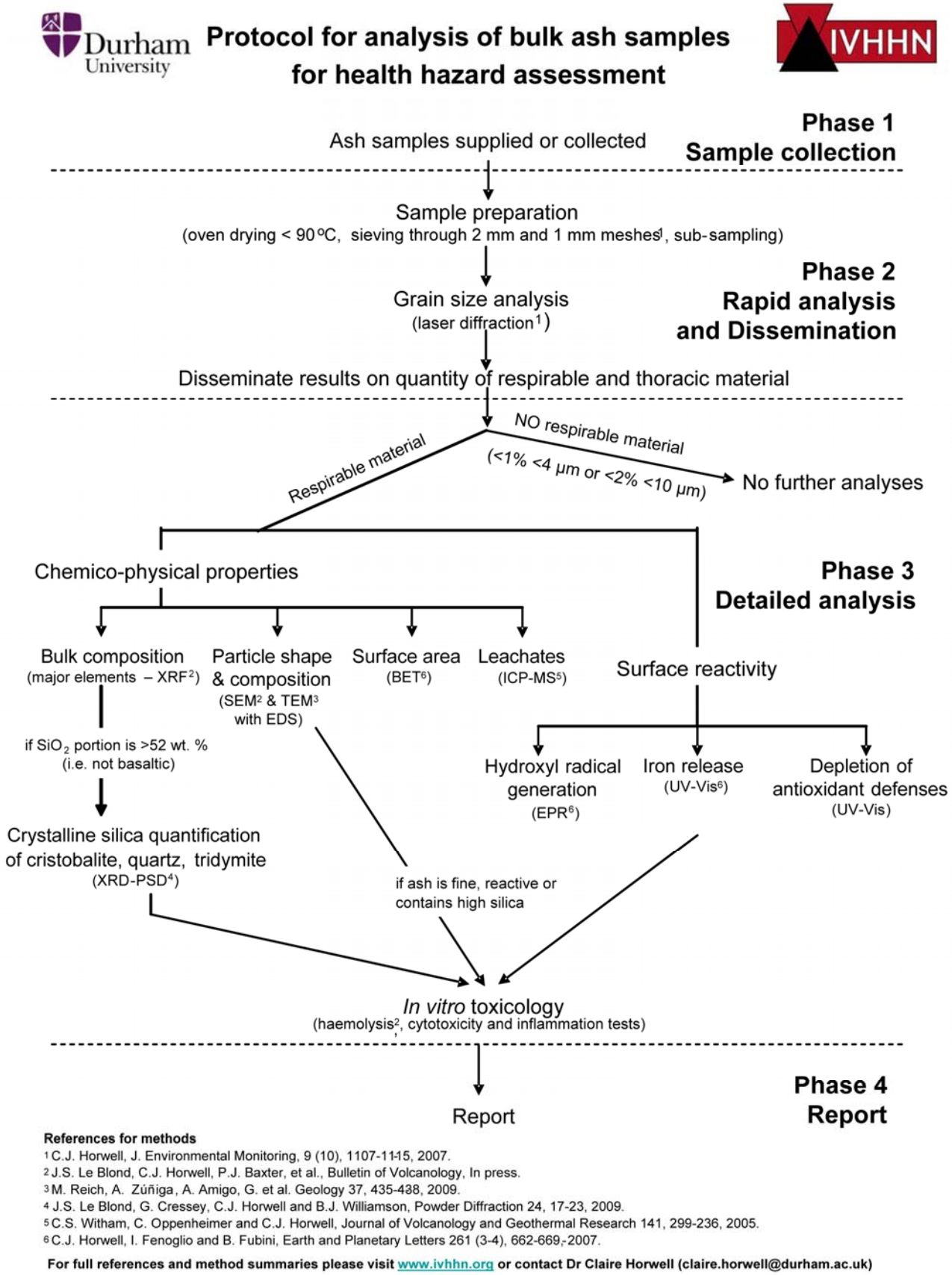

References for methods

1 C.J. Horwell, J. Environmental Monitoring, 9 (10), 1107-1115, 2007.
2 J.S. Le Blond, C.J. Horwell, P.J. Baxter, et al., Bulletin of Volcanology, In press.
3 M. Reich, A. Zúñiga, A. Amigo, G. et al. Geology 37, 435-438, 2009.
4 J.S. Le Blond, G. Cressey, C.J. Horwell and B.J. Williamson, Powder Diffraction 24, 17-23, 2009.
5 C.S. Witham, C. Oppenheimer and C.J. Horwell, Journal of Volcanology and Geothermal Research 141, 299-236, 2005.
6 C.J. Horwell, I. Fenoglio and B. Fubini, Earth and Planetary Letters 261 (3-4), 662-669, 2007.

For full references and method summaries please visit www.ivhhn.org or contact Dr Claire Horwell (claire.horwell@durham.ac.uk)

Figure 2. Map of sample collection locations in relation to Eyjafjallajökull and surrounding landmarks.

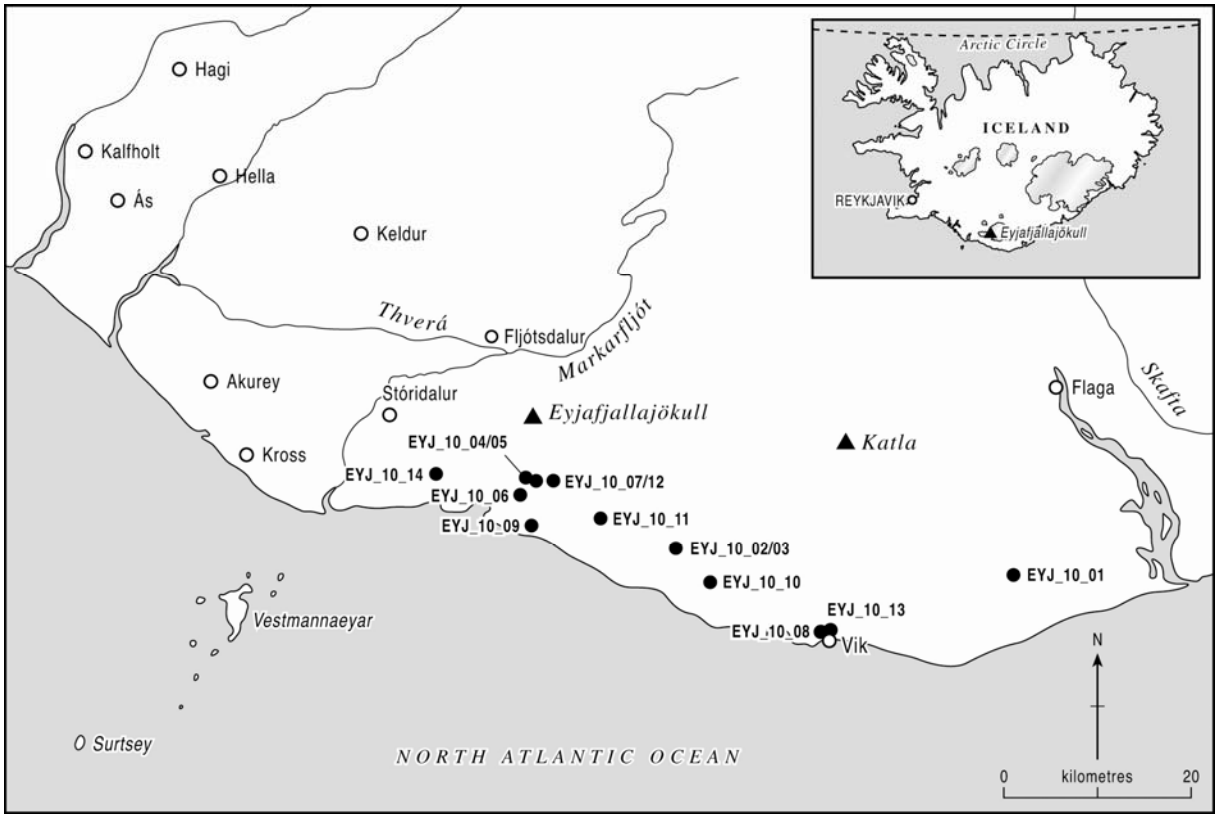

Table 1. Sample information

Sample I.D.	Original sample I.D.	Date erupted	Date collected	Location	GPS Co-ordinates	Distance from source (km)	Ash Colour (Munsell classfication)	Collected by	Collection information	State of sample
EYJ_10_01	15.04.10-2b	15.4.10	15.4.10	Myrdalssandur	N63°28.019' W18°35.939'	58	Dark/Very dark grey (5Y 3.5/1)	Gislason	All samples dried at 40 °C in Iceland. All samples in field for several hours up to 2 days before collection	Not known
EYJ_10_02	17.04.10-3	16-17.4.10	17.4.10	Solheimakot	N63°29.694' W019°19.727'	20	Dark/Very dark grey (5Y 3.5/1)	Larson & Höskuldsson		Dry
EYJ_10_03	18.04.10-4	17.4.10	18.4.10	Solheimakot	N63°29.694' W019°19.727'	20	Dark/Olive grey (5Y 4/1.5)	Larson & Höskuldsson		Damp
EYJ_10_04	18.04.10-18a	17.4.10	18.4.10	Thorvaldseyri power station	N63°33.643' W019°38.602'	8	Dark/Olive grey (5Y 4/1.5)	Larson & Höskuldsson		Wet
EYJ_10_05	18.04.10-18d	17.4.10	18.4.10	Thorvaldseyri power station	N63°33.643' W019°38.602'	8	Dark grey (5Y 4/1)	Larson & Höskuldsson		Wet
EYJ_10_06	20.04.10-1a	19.4.10	20.4.10	Thorvaldseyri	N63°32.757' W019°39.595'	9-10	Very dark grey (5Y 3/1)	Larson & Sverrisdóttir		Dry
EYJ_10_07	EYJ-A3	14-18.4.10	22.4.10	Seljavellir	N63°33.537' W19°37.322'	~6.5	Dark grey (5Y 4/1)	Delmelle		Fresh?
EYJ_10_08	EYJ-A15	14-18.4.10	24.4.10	Vik	N63°25.070' W18°59.501'	~37.5	Grey/Dark/ Olive grey (5Y 4.5/1.5)	Delmelle		Snowed on
EYJ_10_09	EYJ-A16	14-18.4.10	23.4.10	Onundarhorn farm	N63°31.440' W19°38.092'	~13	Very dark grey (5Y 3/1)	Delmelle		Fresh?
EYJ_10_10	EYJ-A17	14-18.4.10	22.4.10	Klifandi	N63°27.710' W19°13.877'	27	Dark grey (5Y 4/1)	Delmelle		Snowed on
EYJ_10_11	EYJ-A18	14-18.4.10	22.4.10	Hotel Skogar	N63°31.568' W19°29.607'	~14	Dark/ Dark olive grey (5Y 4/1.5)	Delmelle		Rained on
EYJ_10_12	5V #1	9.5.10	9.5.10	Seljavellir	N63°33.544' W19°37.327'	7.9	Very dark grey/Black (5Y 2.75/1)	Baxter & Jenkins		Damp
EYJ_10_13	VIK #1	6-7.5.10	7.5.10	Vik	N63°25.136' W19°0.568'	38.3	Dark grey (2.5Y 4/1)	Baxter & Jenkins		Fresh/ dry
EYJ_10_14	Holtsa 2.1	17.4.10	17.4.10	Bridge over Holtsa river on highway 1	N63°33.879' W19°50.593'	~5	Grey/Dark/ Olive grey (5Y 4.5/1.5)	Ilyinskaya		Fresh

Durham University
Department of Earth Sciences

David Damby
PhD Research Student
Christopher Moyes Fellow
d.e.damby@dur.ac.uk
Tel. +44 (0)191 334 1843

Institute of Hazard, Risk and Resilience
Department of Earth Sciences
Durham University
Science Labs., South Rd, Durham
DH1 3LE, UK
Fax. +44 (0)191 3342301

11 April 2012

Analysis of ash from Colima volcano for the assessment of health hazard

David E. Damby & Claire J. Horwell

Introduction

Two ash samples from Colima volcano were sent to Durham University by Nick Varley, University of Colima. We have carried out analyses to test for potential health hazard. Samples are as follows:

Sample ID	Date Collected
COL A09/09	08/08/2009
COL A03/10	21/03/2010

Table 1: Sample information

Methods

The following analyses were carried out:

1. Major element analysis (bulk composition) using X-ray Fluorescence.
2. Grain size distributions by laser diffraction[1] using a Malvern Mastersizer 2000 with Hydro Mu.
3. Imaging of particle morphology by Scanning Electron Microscopy.
4. Crystalline silica quantification (cristobalite and quartz) using X-ray Diffraction with static position-sensitive detection (XRD-sPSD)[2].
5. Particle surface area determined by the BET method of nitrogen adsorption.
6. Surface reactivity measured by hydroxyl radical generation and iron release.
7. Red blood cell lysis (haemolysis) as an indicator of potential toxicity.

Results

Bulk composition analyses confirmed that the ash samples are andesitic.

Sample	SiO_2	$Na_2O + K_2O$
COL A09/09	58.77	5.69
COL A03/10	59.12	5.40

Table 2: Total alkali silica results determined by XRF reported as oxide wt. %.

The grain size distribution between the two samples varied greatly (table 3), but both contained substantial quantities of respirable material. Dome collapse eruptions are expected to generate ash with 10-18 vol. % sub-4 µm material[1,3].

Bin	Fraction	COL A09/09	COL A03/10
< 1 µm	Ultra-fine	3.63	1.63
< 2.5 µm	"	8.29	5.20
< 4 µm	Respirable	18.43	8.15
< 10 µm	Thoracic	32.97	21.72
< 15 µm	Inhalable	44.36	30.38
< 63 µm	Sievable	78.54	60.81

Table 3: Quantity of material in health-pertinent size fractions in cumulative vol. %. < 63 µm is included as this is the reasonable cut-off size for sieving.

The ratio of the < 4:<10 µm fractions is usually ~ 1:2, as observed for COL A09/09[1]. The fact that this ratio is not seen for COL A03/10 indicates that this sample underwent some winnowing prior to collection.

Both samples contained approximately 5 wt. % crystalline silica as cristobalite (table 4). There was negligible quartz in the samples, however minor quantities were identified by XRD.

Sample	Cristobalite	Quartz
COL A09/09	5.57	0.54
COL A03/10	5.32	0.62

Table 4: Amount of crystalline silica in the samples. Results are reported with a ±3 wt. % error.

The general morphology of the ash was similar to previously-observed volcanic ash samples. Particles were sub-angular and blocky (figure 1), with no differences observed between the bulk and respirable fractions. No fibrous particles were observed.

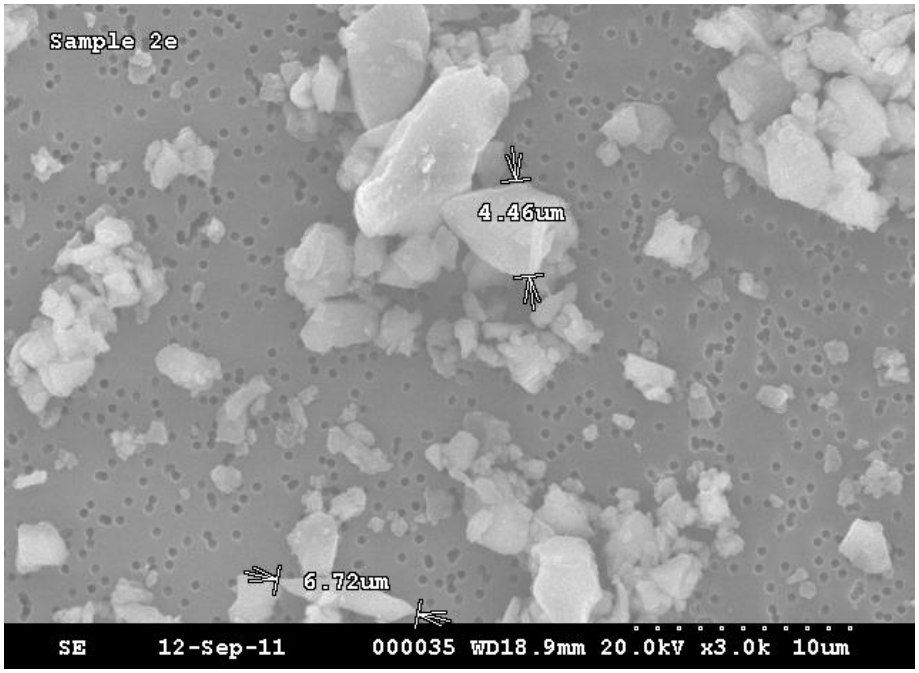

Figure 1. SEM image of the respirable fraction.

Particle surface reactivity was low when run alongside comparative ash samples (figure 2). The sample generated similar numbers of hydroxyl radicals to the andesitic Soufrière Hills sample (MBA 5/6/99), and fewer than the basaltic Etna sample. Poorly coordinated iron removed from the surface of the particles was also low (iron catalyses the generation of the hydroxyl free radical), as expected for an andesitic sample. Data are reported per unit surface area. The specific surface area for sample COL A03/10 was 0.7067 m^2 g^{-1}.

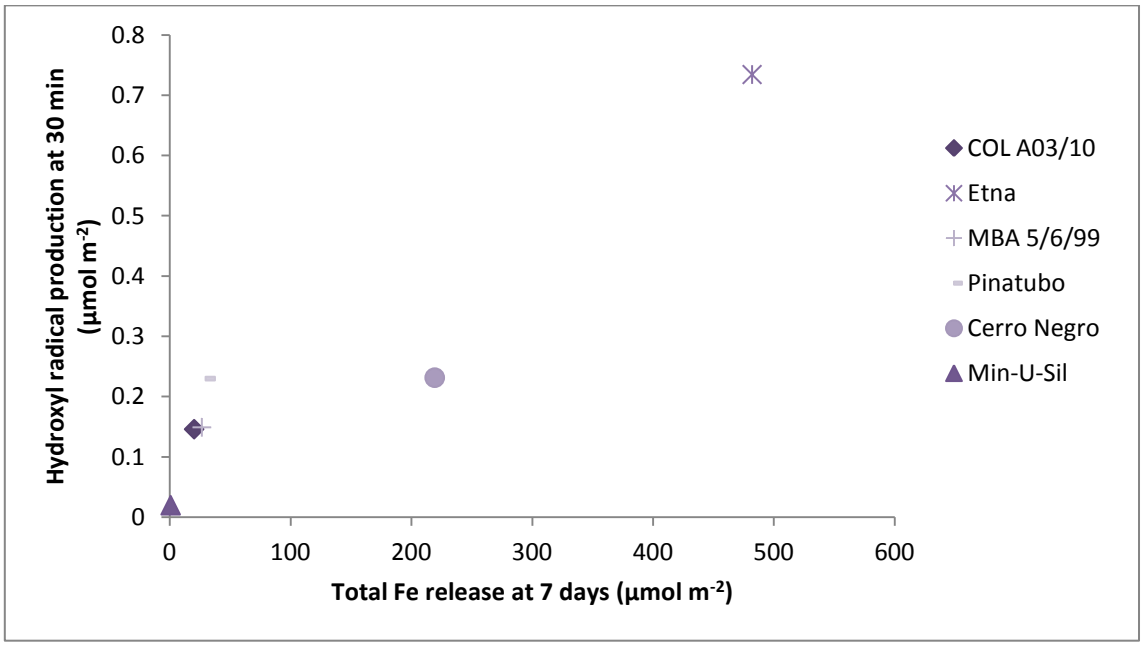

Figure 2: Hydroxyl radical generation after 30 minutes against total iron released at day 7 for COL A03/10 plus Min-U-Sil quartz standard and 4 regularly used comparative samples: Cerro Negro (1995), Etna (2002), Pinatubo (1991), Soufrière Hills (MBA 5/6/99). Min-U-Sil quartz values are those published in Horwell et al.(2007)[4]

Haemolysis (red blood cell membrane rupture) was performed on both the bulk ash sample COL A03/10 as well as a separated respirable fraction. The respirable fraction showed increased haemolytic potential compared to the bulk sample, and was only slightly elevated above the negative control TiO_2 (1.92 vs. 1.62 % haemolysis at the top dose). Relative to the positive quartz control used (DQ12), however, the respirable fraction was nearly 20 times less active at the top dose.

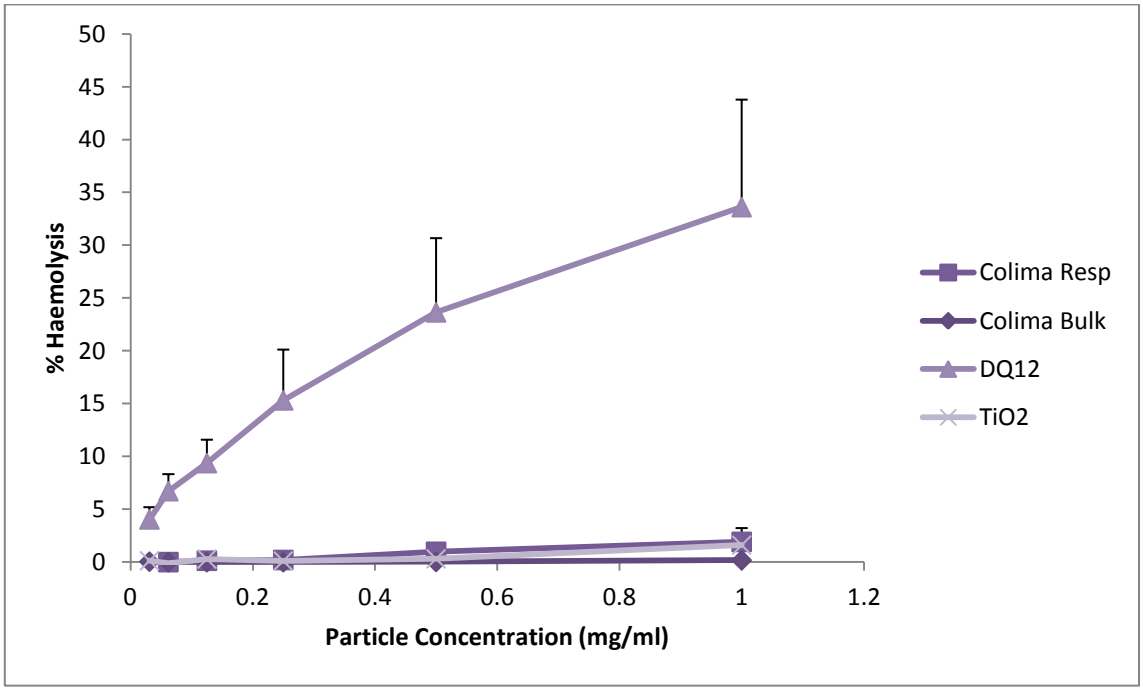

Figure 3: Haemolysis dose-response results for the bulk and respirable fraction of sample COL A03/10. Results are the mean of three runs and errors are reported as the standard error of the mean.

Discussion

The substantial respirable component of both samples warranted further characterisation of the physico-chemical properties and surface reactivity of the ash. The crystalline silica observed results from the presence of cristobalite in the dome rock, which was confirmed through identification in thin sections of dome material.

Particle reactivity experiments were carried out on COL A03/10, which was the sample for which we had more material. Reactivity in the lung determined by iron-catalysed free radical generation[5, 6] and the ability of particles to damage cellular membranes were both low when compared with other well-characterised ash samples and positive controls.

The obvious pinkish colour of the ash indicates either a readily oxidized iron phase or that the ash has been exposed to the environment. The iron component, however, was not easily mobilised in iron release experiments (figure 2), with both oxides being removed equally (10.73 µmol m^{-2} Fe^{2+} and 9.44 µmol m^{-2} Fe^{3+}). As such, we would expect little reactive iron to be available in the lung for hydroxyl radical generation.

From a health perspective, the ash is very fine and exposure could result in particle deposition in the lung. Although reactivity is low, we recommend limiting exposure as well as limiting re-suspension by wetting material prior to clean-up. We would further recommend a rapid analysis of fresh material following a more violent eruption of Colima (e.g., 2005) or dome collapse.

Acknowledgements

Many thanks to Nick Marsh (Department of Geology, University of Leicester) for carrying out XRF and to Chris Rolfe (Department of Geography, University of Cambridge) for carrying out grain size analyses.

Further information

Further information is available on all techniques upon request.

References

1. C. Horwell, *J. Environ. Monitor.*, 2007, **9**, 1107 - 1115.
2. J. S. Le Blond, G. Cressey, C. J. Horwell and B. J. Williamson, *Powder Diffraction*, 2009, **24**, 17-23.
3. C. Horwell, J. Le Blond, S. Michnowicz and G. Cressey, *Bulletin of Volcanology*, 2010, **72**, 249-253.
4. C. Horwell, I. Fenoglio and B. Fubini, *Earth Plan. Sci. Lett.*, 2007, **261**, 662-669.
5. C. Horwell, I. Fenoglio, K. V. Ragnarsdottir, R. Sparks and B. Fubini, *Environ. Res.*, 2003, **93**, 202-215.
6. B. Fubini, L. Mollo and E. Giamello, *Free Radic Res*, 1995, **23**, 593-614.

Durham University
Department of Earth Sciences

Dr Claire Horwell
RCUK Fellow
Director of IVHHN (www.ivhhn.org)
claire.horwell@durham.ac.uk
Tel. +44 (0)191 3342253

Institute of Hazard, Risk & Resilience
Department of Earth Sciences
Durham University
Science Labs., South Rd, Durham
DH1 3LE, UK
Fax. +44 (0)191 3342301

19 January 2011

Analysis of ash from Pacaya volcano for the assessment of health hazard

Claire J. Horwell & David E. Damby

Introduction

Two ash samples were sent to Durham by Bill Rose from the eruption of Pacaya Volcano on 27 May 2010. We have carried out basic analyses to test for potential health hazard. Sample information is as follows:

Sample #	Original ID	Time of eruption	Grid / location	Distance from Pacaya	Bearing	Info	Collector
PAC2010_01	VP 5/27/2010	8:10-8:40 pm	14°35'32.34"N 90°29'8.82"W	26.7 km	208 °	part of a 3mm thick layer, collected dry, unaffected by rain	Samuel Bonis
PAC2010_02	VP 5/27/2010 Coban		Coban 15°28' 14.80" N 90°22' 20.09" W;	122km	192 °	wet but not soaked	

Table 1. Sample information

Methods

The following analyses were carried out:

1. Grain size distributions by laser diffraction[1] using a Malvern Mastersizer 2000 with Hydro Mu.
2. Major element analysis (bulk composition) using X-ray Fluorescence.
3. Crystalline silica quantification (cristobalite and quartz) using X-ray Diffraction with static position-sensitive detection (XRD-sPSD)[2].

Results

Bulk composition analyses confirmed that the ash samples are basaltic (51.6 & 50.8 wt. % SiO_2; 3.9 & 4.8 wt. % $Na_2O + K_2O$).

Grain size analyses showed that there is no respirable or inhalable ash in either sample (Table 2). It is possible that some minor fines component had been lost from PAC2010_02 given that the < 63 µm fraction contained 7.89 vol. % material (which would give a predicted value of ~ 0.44 vol. % < 4 µm and ~ 1.9 vol.% < 10 µm material according to Horwell (2007[1])).

Bin	Fraction	PAC2010_01	PAC2010_02
< 1 µm	Ultra-fine	0.00	0.00
< 2.5 µm	"	0.00	0.00
< 4 µm	Respirable	0.00	0.00
< 10 µm	Thoracic	0.00	0.00
< 15 µm	Inhalable	0.00	0.00
< 63 µm	Sievable	0.00	7.89

Table 2. Quantity of material in health-pertinent size fractions in vol. %. < 63 µm is included as this is the reasonable cut-off size for sieving, after which the equations provided by Horwell (2007) can be applied to predict the health-pertinent fractions, where laser diffractometers are not available.

There was negligible crystalline silica in the samples, although PAC2010_02 has 3.41 wt. %, indicating that there are small quantities of cristobalite in the ash.

Sample #	Cristobalite Wt. %	Quartz Wt. %
PAC2010_01	0.00	0.79
PAC2010_02	3.41	0.00

Table 3. Amount of crystalline silica in the samples. 1-3 wt. % error.

Discussion

From a health perspective, this basaltic ash is not likely to cause significant respiratory issues. Neither sample contained any material that could penetrate into the respiratory system. In addition, as expected for a basaltic eruption, crystalline silica content was negligible. The small amount of cristobalite observed may have been sourced from altered edifice rock entrained into the eruption column. There is the possibility that the ash could be reactive in the lung due to iron-catalysed hydroxyl radical generation, as observed for ash from previous eruptions of Pacaya and other basaltic volcanoes[3]. However, as the ash is not inhalable, we did not carry out these experiments.

Acknowledgements

Many thanks to Nick Marsh (Department of Geology, University of Leicester) for carrying out XRF and to Chris Rolfe (Department of Geography, University of Cambridge) for carrying out grain size analyses.

Further information

Further information is available on all techniques upon request.

References

1 Horwell, C.J., Grain size analysis of volcanic ash for the rapid assessment of respiratory health hazard *J. Environ. Monitor.* **9** (10), 1107 (2007).

2 Le Blond, J.S., Cressey, G., Horwell, C.J. et al., A rapid method for quantifying single mineral phases in heterogeneous natural dust using X-ray diffraction *Powder Diffraction* **24**, 17 (2009).

3 Horwell, C.J., Fenoglio, I., and Fubini, B., Iron-induced hydroxyl radical generation from basaltic volcanic ash *Earth Plan. Sci. Lett.* **261** (3-4), 662 (2007).

Appendix 4

Publications

Bulletin of Volcanology, *accepted*

The nature and formation of cristobalite at the Soufrière Hills volcano, Montserrat: implications for the petrology and stability of silicic lava domes

C.J. Horwell, B.J. Williamson, E.W. Llewellin, D.E. Damby, J.S. Le Blond

Bull Volcanol (2013) 75:696
DOI 10.1007/s00445-013-0696-3

RESEARCH ARTICLE

The nature and formation of cristobalite at the Soufrière Hills volcano, Montserrat: implications for the petrology and stability of silicic lava domes

Claire J. Horwell · Ben J. Williamson · Edward W. Llewellin · David E. Damby · Jennifer S. Le Blond

Received: 12 May 2012 / Accepted: 31 January 2013 / Published online: 21 February 2013

Abstract Cristobalite is commonly found in the dome lava of silicic volcanoes but is not a primary magmatic phase; its presence indicates that the composition and micro-structure of dome lavas evolve during, and after, emplacement. Nine temporally and mineralogically diverse dome samples from the Soufrière Hills volcano (SHV), Montserrat, are analysed to provide the first detailed assessment of the nature and mode of cristobalite formation in a volcanic dome. The dome rocks contain up to 11 wt.% cristobalite, as defined by X-ray diffraction. Prismatic and platy forms of cristobalite, identified by scanning electron microscopy (SEM), are commonly found in pores and fractures, suggesting that they have precipitated from a vapour phase. Feathery crystallites and micro-crystals of cristobalite and quartz associated with volcanic glass, identified using SEM-Raman, are interpreted to have formed by varying amounts of devitrification. We discuss mechanisms of silica transport and cristobalite formation, and their implications for petrological interpretations and dome stability. We conclude: (1) that silica may be transported in the vapour phase locally, or from one part of the magmatic system to another; (2) that the potential for transport of silica into the dome should not be neglected in petrological and geochemical studies because the addition of non-magmatic phases may affect whole rock composition; and (3) that the extent of cristobalite mineralisation in the dome at SHV is sufficient to reduce porosity—hence, permeability—and may impact on the mechanical strength of the dome rock, thereby potentially affecting dome stability.

Keywords Cristobalite · Quartz · Soufrière Hills, Montserrat · Lava dome · Vapour-phase silica

Editorial responsibility: E.S. Calder

C. J. Horwell (✉) · D. E. Damby
Institute of Hazard, Risk and Resilience, Department of Earth Sciences, Durham University, Science Labs., South Road, Durham DH1 3LE, UK
e-mail: claire.horwell@durham.ac.uk

B. J. Williamson
Camborne School of Mines, College of Engineering, Mathematics and Physical Sciences, University of Exeter, Cornwall Campus, Penryn TR10 9EZ, UK

B. J. Williamson · J. S. Le Blond
Department of Earth Sciences, Natural History Museum, Cromwell Road, London SW7 5BD, UK

E. W. Llewellin
Department of Earth Sciences, Durham University, Science Labs., South Road, Durham DH1 3LE, UK

J. S. Le Blond
Brighton and Sussex Medical School, Falmer, Brighton, East Sussex BN1 9PX, UK

Introduction

The crystalline silica (SiO_2) polymorphs cristobalite, quartz and, to a lesser extent, tridymite are common components of lava domes at basaltic–andesitic to rhyolitic volcanoes, e.g. Soufrière Hills volcano (SHV), Montserrat (Baxter et al. 1999; Williamson et al. 2010), Unzen, Japan (Nakada and Motomura 1999), Mt. St. Helens (MSH), USA (Blundy and Cashman 2001; Pallister et al. 2008), Merapi, Indonesia (Damby et al. 2013) and Chaitén, Chile (Horwell et al. 2010). Quartz in dome rocks may be magmatic in origin or may have precipitated from hydrothermal fluids. Cristobalite and tridymite are mainly found in pores and fractures and are thus interpreted as vapour-phase

precipitates (Baxter et al. 1999; de Hoog et al. 2005). At SHV, cristobalite is also thought to form by devitrification, i.e. by solid-state crystallisation from amorphous volcanic glass (Baxter et al. 1999; Murphy et al. 2000); however, no direct evidence for this mode of formation has been presented. Cristobalite is also found as a hydrothermal product at some volcanoes (e.g. Mt. Augustine; Getahun et al. 1996) and in ignimbrite and tuff deposits (e.g. Stimac et al. 1996; Yurtmen and Rowbotham 1999) and is closely associated with K-feldspar within spherulites in devitrified obsidian domes and rhyolitic lavas (e.g. Swanson et al. 1989; Dadd 1992). The cristobalite stability field is between 1,470 and 1,713 °C at <1 GPa (Deer et al. 1996); hence, it exists as a metastable phase in dome-forming volcanic systems, where temperatures are typically ≤850 °C. Its persistence at ambient temperature and pressure is due to the considerable activation energy required for the reconstructive transformation of cristobalite to low-quartz (Deer et al. 1996).

Dome-collapse events of SHV produce volcanic ash rich in cristobalite (up to ~25 wt.%; Baxter et al. 1999; Horwell et al. 2003; Horwell et al. 2010; Baxter et al. Accepted; Horwell et al. 2013). The ash plumes produced by pyroclastic density currents (PDCs) resulting from these dome-collapse events (known as co-PDC ash fall) show notable cristobalite enrichment in the very-fine particle fraction (sub-2 μm; Horwell et al. 2003), probably as a result of size and density fractionation during fragmentation of dome rock within PDCs (Horwell et al. 2001). The presence of abundant sub-2 μm cristobalite particles in the ash may present a potential respiratory health risk to exposed populations (Horwell and Baxter 2006).

The aims of the current study are to determine the nature and mode of formation of cristobalite in the Soufrière Hills volcanic dome. We consider the nature of cristobalite formation through scanning electron microscopy (SEM) with Raman spectroscopy, energy dispersive X-ray spectrometry (EDS) and cathodoluminescence (CL) and by X-ray diffraction (XRD) and X-ray fluorescence (XRF). The work builds on that of Baxter et al. (1999) who showed, for the first time, that cristobalite forms in the Soufrière Hills dome lava and is sufficiently abundant in the resultant dome-collapse co-PDC ash fall to be a respiratory health hazard. Further to this, Baxter et al. (1999) suggest that the cristobalite is formed by vapour-phase crystallisation and devitrification, based on observations of groundmass silica phases as vesicle infills and fine-grained patches within interstitial glass. Here, we identify textural criteria by which these modes of formation can be inferred for individual cristobalite crystals in the dome rocks and ash. The use of SEM-Raman allows definitive confirmation of the silica polymorph of crystals and micro-patches of SiO_2 (identified by SEM-EDS). The results have implications for studies of dome stability in terms of assessing micro-structural evolution in response to vapour-phase mineralisation and promote consideration of the consequences of sub-solidus redistribution of silica for the interpretation of whole-rock geochemical data.

Active lava domes are inherently unstable, and partial or complete dome collapse poses a major hazard to local communities. This has motivated extensive research into the mechanisms of dome failure (Calder et al. 2002), with work focussing on collapse triggers, such as pressurisation of gas within the dome (Voight and Elsworth 2000; Elsworth and Voight 2001), heavy rainfall (Matthews et al. 2002; Elsworth et al. 2004), slope over-steepening (Sparks et al. 2000) and hydrothermal weakening of the dome (Edmonds et al. 2003). In this study, we propose a new hypothesis, based on our observations of the distribution of vapour-phase minerals: that vapour-phase mineralisation also plays an important role in dome stability via two opposing and thus competing processes: (1) The occlusion of pore space by vapour-phase precipitates could lead to a reduction in permeability, promoting gas pressurisation and subsequent destabilisation of the dome; (2) Mineralisation could cement and densify the dome, stabilising the edifice.

The presence of cristobalite that has precipitated from a vapour phase in dome rocks is evidence that silica is redistributed within the magmatic system. We propose two hypotheses for the transport mechanism: (1) Silica redistribution may occur locally (over the length-scale of individual vugs) as a result of leaching of volcanic glass and other phases adjacent to pore spaces, potentially mediated by HF and other acid solutions/vapours. In this scenario, which we refer to as 'local redistribution', the bulk SiO_2 content of dome rock is not affected. (2) Alternatively, or additionally, silica may be transported into the dome from magmatic gases below the dome or from sources outside the magmatic system, such as connate or meteoric waters incorporated via hydrothermal convection. In this scenario, which we refer to as 'bulk transport', the bulk SiO_2 content of dome rock is increased, implying that the whole-rock geochemical composition of a dome rock sample may not be the same as that of the magma from which it crystallised.

Cristobalite formation mechanisms

Rogers (1922) and Larsen et al. (1936) were the first to postulate that cristobalite can form in cavities in volcanic rocks as a consequence of the supply of silica by steam. This hypothesis has been supported by more recent work (described below), and there is now evidence that the transport of Si could be mediated by a number of different phases at temperatures and pressures appropriate for the conduit/dome system (the SHV dome is thought to be around 300 m thick (Watts et al. 2002), corresponding to a pressure of around 7 MPa (650–830 °C) at its base (Hicks et al. 2009 and references therein)):

Si- and F-bearing fluids

Churakov et al. (2000) identified ten silica-carrying gas species in volcanic systems. They found through thermodynamic modelling that, at >950 °C, Si in the gas phase is transported as SiO and SiO_2, with SiO being more prevalent at higher temperatures. Between 900 and 950 °C, $SiOF_2$, SiF_4, SiO and SiO_2 species play an equal role in Si transport. Below 900 °C, in the temperature range of the SHV dome, SiF_4 species prevail. Geochemical modelling also supports the theory that Si can be transported as SiO gas at temperatures >700 °C (0.1 MPa) (Korzhinsky et al. 1995). Formation of cristobalite from SiO is also suggested by Reich et al. (2009), who propose that amorphous glass may convert to SiO in the presence of a reducing agent (such as CO); however, they invoke this mechanism in an eruption column rather than in a lava dome. Thermodynamic modelling by de Hoog et al. (2005) confirmed that, upon degassing, magmatic SiF_4 gas will react with water to form vapour-phase silica in volcanic systems:

$$SiF_4(g) + 2H_2O(g) \leftrightarrow SiO_2(s) + 4HF(g). \quad (1)$$

The reaction equilibrium is strongly dependent on temperature, pressure and HF fugacity (White and Hochella 1992; de Hoog et al. 2005); hence, depending on ambient conditions, silica may be deposited (reaction moves to the right), or corroded by HF (reaction moves to the left).

Cl-bearing fluids

Foustoukos and Seyfried (2007) have conducted experiments on quartz solubility in Cl-bearing aqueous vapour fluids (at 365–430 °C, 21.9–38.1 MPa) and found that they can contain significant concentrations (from 2.81 to 14.6 mmol kg^{-1}) of dissolved SiO_2. Shmulovich et al. (2006) determined that the main species for the transport of Si at temperatures <750 °C (0.1 MPa) is likely to be $SiCl_4$ gas. The temperatures in these experiments are too low for deep dome conditions; however, elevated concentrations of HCl and HF gases have been measured at the crater's edge from the Soufrière Hills dome (533 and 22 ppbv, respectively; Allen et al. 2000). The HF/HCl gas ratio of 0.004 reported by Allen et al. (2000) suggests that $SiCl_4$ could be the dominant Si-bearing phase, with SiO and SiF_4 playing a subordinate role, if Cl-bearing fluids could support silica at higher temperatures.

Kinetic and thermodynamic constraints control the silica polymorph (or amorphous phase) that precipitates from a vapour. Renders et al. (1995) measured the rates of precipitation for cristobalite at 150–300 °C from $Si(OH)_4$ solution and found that cristobalite forms only where silica concentrations are above the cristobalite silica saturation limit but less than the amorphous silica saturation limit; crucially, they also found that there have to be cristobalite nuclei present. Jones and Segnit (1972) hypothesised that, if cristobalite nuclei are present in a hydrothermal environment, the epitaxial crystallisation of cristobalite requires less energy than re-arrangement of the cristobalite substrate to form quartz. These findings imply that, in the volcanic system, the formation of cristobalite by devitrification may be a necessary precursor to the formation of vapour-phase cristobalite, in order to provide the required nuclei.

Background to the Soufrière Hills volcano

Soufrière Hills, Montserrat, is an active, andesitic, dome-forming volcano in the Lesser Antilles Island Arc (see review in Druitt et al. 2002). The current eruption began in July 1995 with a series of phreatic explosions. This was followed by a period of dome growth from mid-November with the first major collapse occurring in April 1996. Since then, there have been intermittent cycles of effusive dome building and collapse, often closely followed by a period of Vulcanian explosive eruptions. To date, there have been five phases of dome growth, accompanied by significant pauses defined by residual activity (rockfalls, degassing and low levels of seismicity) (Wadge et al. 2013). At the time of writing (November 2012), SHV is still active; however, the last major dome collapse occurred in February 2010.

Sample selection

Nine samples of dome rock were acquired from the archives of the Montserrat Volcano Observatory (MVO) in June 2006. Sub-samples are currently held within the collections of the Natural History Museum, London. Sample numbers and a summary of sample properties are given in Table 1, along with information on eruption date and type and phase of dome growth.

The dome rocks were originally sampled from PDC (block-and-ash flow) deposits. The samples chosen spanned the current eruption (1995 onwards) and encompass a range of ages and densities of dome rock (vesicular to dense). They likely cover a range of sources, from shallow dome material to deeper dome/upper conduit, and dome residence times. Information on the sample history was obtained from the MVO sample database, but no information was available on the location, depth or residence time of each sample within the dome complex prior to collapse.

Where multiple samples from the same flow were available within the MVO archives, representative blocks were chosen with the help of MVO staff. It is noted, however, that the nine samples cannot be fully representative of the collapsed lobes of lava, given the heterogeneous nature of the dome and the PDCs.

Two samples were chosen which predate the current eruptive period (i.e. pre-1995). The oldest sample (MVO819) is

Table 1 Sample summary and crystalline silica features observed

Sample no.	Date of collapse/ eruption	Phase of dome growth[c]	Date of collection	Description	Information	Prismatic	Platy	Devit. cristob.	Devit. quartz
MVO819 BM.2007, P1(11)	174 k.a. BP		15/2/98	Dome lava; very dense, grey/brown	Ancient sample from old complex	✓ But rare	✓	✓	✓
MVO945 BM.2007,P1(12)	400 a. BP		?	Dome lava; dense, red/brown	Ancient sample from Castle Peak	✓	✗	✗	✓
MVO287 BM.2007,P1(2)	21/9/97	1	21/9/97	Juvenile block; vesicular; light grey	From dome collapse deposit	✓	✗	✓	✗
MVO288 BM.2007,P1(3)	21/9/97	1	21/9/97	Juvenile block; frothy, light grey	From dome collapse deposit	✓ but rare	✗	✗	✗
MVO617 BM.2007,P1(9)	21/9/97	1	16/5/98	Dome lava; Dense; green/ dark grey	From dome collapse deposit	✓	✗	✓	✗
MVO332 BM.2007,P1(8)	26/12/97	1	4/1/98	Dome lava; vesicular; pale grey	From 'Boxing Day' collapse deposit	✓	✗	✓	✗
MVO1236 BM.2007,P1(18b)	12/7/03	2	1/8/03– 15/11/03?	Dome lava; dense; pale grey	From dome collapse deposit (full collapse)	✓	✓	✓	✓
MVO1406 BM.2007,P1(24)	20/5/06	3	?	Dome lava; dense; pale grey	From dome collapse deposit	✓	✗	✓	✗
MontR1[a] BM.2007,P2(1)	20/5/06	3	22/6/06	Dome lava, dense, red	From dome collapse deposit	✓	✓	✗	✓
MVO244[b]	5/8/97	1	6/8/97	Large pumice block	Erupted during Vulcanian explosion	–	–	–	–
MVO289[b]	25/9/97	1	25/9/97	Juvenile pumice flow block	Erupted during Vulcanian explosion	–	–	–	–
MVO291[b]	29/9/97	1	29/9/97	Airfall pumice clast	Erupted during Vulcanian explosion	–	–	–	–
MVO374[b]	Sept/Oct 1997	1	23/12/97	Pumice	Erupted during Vulcanian explosion	–	–	–	–

[a] Collected by BW from deposit rather than archive

[b] Samples supplied by Prof. Steve Sparks, University of Bristol

[c] Dome growth phase defined by Wadge et al. 2013

from the ancient SHV, dated by Harford et al. (2002) using $^{40}Ar/^{39}Ar$, at 174±3 kaB.P. Sample MVO945 is from the seventeenth century eruption of the Castle Peak lava dome (part of the Soufrière Hills dome complex) (MVO, pers. comm.).

Three samples of rock were collected from the block-and-ash flow deposits resulting from the large dome-collapse (21 September 1997) which immediately preceded the onset of Vulcanian explosions. Sample MVO617 is a sample of dense dome rock; sample MVO287 is a moderately vesicular sample containing fractured phenocrysts and burst melt inclusions (described in detail in Williamson et al. (2010)); sample MVO288 is even more vesicular, showing pumiceous textures.

One sample (MontR1) was collected in June 2006 from the block-and-ash flow deposits from the 20 May 2006 dome collapse event. MVO1236 and MVO1406 are samples of dense dome rock collected from the block-and-ash flows generated by the collapses of 12 July 2003 and 20 May 2006, respectively. MVO332 is a sample of moderately vesicular dome rock collected following the lateral blast and collapse of the lava dome on 26 December 1997.

For comparative purposes, we also characterised pumice erupted during Vulcanian explosions at Soufrière Hills (August–October 1997, provided by Prof. R.S.J. Sparks, University of Bristol). These samples (MVO244, MVO289,

MVO291 and MVO374) provide an effective control because they should be unaffected by secondary mineralisation.

Methods

Imaging of vapour-phase minerals

Imaging was carried out at the Natural History Museum (NHM), London, on both rough chips of dome rock (~0.5 cm in diameter; Au (95 %)/Pd (5 %) coated) and as carbon-coated polished thin sections. High-resolution images were obtained using a Philips XL-30 field emission scanning electron microscope. Lower magnification back-scattered electron (BSE) images were obtained using a LEO 1455 Variable Pressure SEM with Oxford Instruments INCA energy dispersive X-ray analysis system (SEM-EDS). Colour (RGB) CL images, with complementary BSE images and EDS maps, were obtained using an EVO® LS 15 (20 kV, 10 nA) with a Gatan ChromaCL™ detector and DigiScan™ beam control system.

Mineralogical characterisation of vapour-phase minerals

To distinguish cristobalite from tridymite and quartz, uncoated polished sections were analysed using a Renishaw SEM-Raman Structural and Chemical Analyser which couples simultaneous Raman spectroscopy (inVia microscope, laser spot size 1.2 μm, 785 nm wavelength) with variable-pressure SEM-EDS (Jeol JSM-6060 LV SEM with Oxford Instruments INCA energy dispersive X-ray analysis) at Renishaw plc, UK. This allowed the imaging and identification of individual crystals of silica polymorphs. Reference spectra, used in the identification of silica polymorphs, were obtained from the online Handbook of Minerals Raman Spectra (http://www.ens-lyon.fr/LST/Raman/index.php, which uses reference spectra from Kingma and Hemley 1994).

Quantification of silica polymorph concentrations in dome rock

The proportions of the different silica polymorphs in the dome rock samples (cristobalite, quartz and tridymite) were determined by XRD using an Enraf-Nonius XRD (with Cu$K_{\alpha 1}$ radiation) with an INEL curved 120 °2θ position-sensitive detector (PSD) at the NHM, London. We followed the Internal Attenuation Standard (IAS, in this case using ZnO) method of Le Blond et al. (2009), which allows rapid quantification of single mineral phases in heterogeneous powders without prior knowledge of the mineral assemblage. The rocks were first powdered to approximately <20 μm using an agate pestle and mortar. Tube operating conditions were 45 kV and 45 mA, using horizontal and vertical slits set at 0.24×5.0 mm. NBS silicon and silver behenate were used as external 2θ calibration standards.

Whole-rock geochemical analysis of dome rocks

Dome rock and pumice samples were crushed and ground using an agate pestle and mortar. Major elements were determined on fused glass beads prepared using ignited powders mixed with 100 % Li tetraborate flux, with a sample to flux ratio of 1:30. The samples were analysed using a PANalytical Axios Advanced XRF spectrometer at the Department of Geology, University of Leicester, UK, to determine major-element oxides.

Results

Nature of crystalline silica phases in dome samples

Five different forms of crystalline silica were identified in the Soufrière Hills dome rock through imaging and analysis of dome-rock samples by SEM-EDS and SEM-Raman, which are detailed below:

Quartz phenocrysts These primary magmatic phenocrysts, between 300 and 1,000 μm max axis diameter, are often rounded and embayed (Fig. 1a). These are found in most samples but are not common, typically fewer than two or three phenocrysts in a standard polished section.

Prismatic cristobalite These crystals are between 20 and 50 μm max axis diameter. In polished section, the prismatic cristobalite (identified using SEM-Raman (Fig. 2a)) has characteristic 'fish-scale' cracks (Fig. 1b and c), which results from a 5 % decrease in volume from the displacive transition from ß to α cristobalite during cooling through ~240 °C (Carpenter et al. 1998). Prismatic cristobalite is observed in all samples of dome rock, including a few crystals in MVO288 (the pumiceous sample from the 21 Sept 1997 dome-collapse deposit). The prismatic cristobalite often appears to have either grown directly from the glassy vug wall (Figs. 1c and 3b–d) or sits on a crust of small (<5 μm diameter) plagioclase feldspar crystals (Fig. 3a, e and f) within the vesicle. In polished section, the fish-scale cristobalite is also seen as patches within the groundmass of dense dome rock (Fig. 1d).

The more vesicular samples allow direct observation into open cracks and pore spaces, which enabled the observation of cristobalite crystal morphology. The cristobalite crystals often appear to have cubic or tetragonal habit (Fig. 3a) and frequently display multiple twinning (Fig. 3b–f).

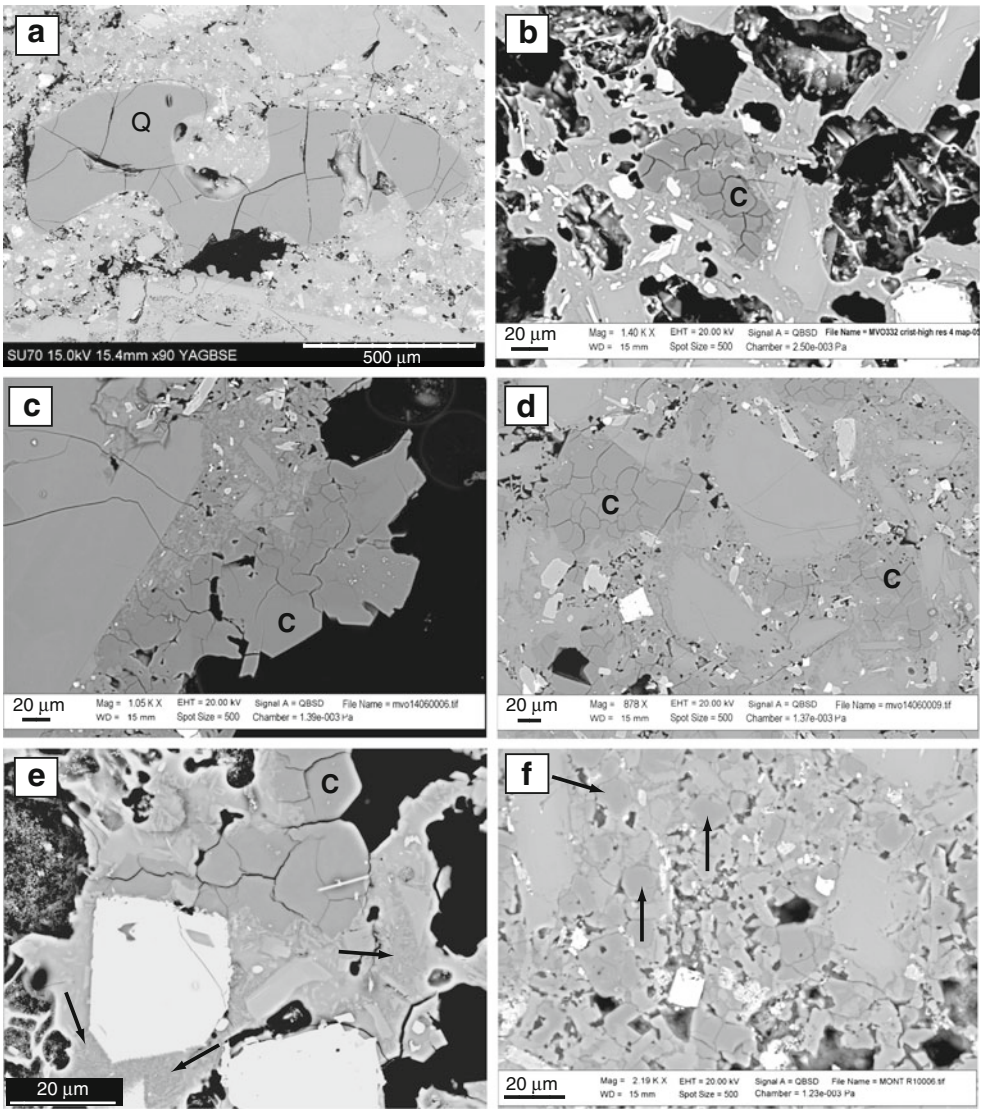

Fig. 1 Backscattered electron images showing dome rock morphology in thin section. **a** Quartz phenocryst (*Q*) in MVO617; **b** cristobalite crystal showing typical fish-scale cracking (*C*) in MVO332; **c** cristobalite crystals (*C*) protruding into open pore space in MVO1406. Note that the cristobalite and groundmass appear to merge; **d** cristobalite (*C*) apparently filling available void spaces in MVO1406; **e** 'Feathery' groundmass texture (indicated by *arrows*) in MVO287; **f** MontR1 groundmass appears completely devitrified with quartz (*dark grey*, indicated by *arrows*) and plagioclase feldspar (*lighter grey*) crystallites

Platy cristobalite The plates were confirmed as cristobalite (as opposed to tridymite) by SEM-Raman (Fig. 2b) and were observed growing into pore spaces in polished sections (where they appeared acicular, Fig. 4a and b) and in rough chips (Fig. 4c and d); the crystals appear to be hexagonal (Fig. 4 and d), although they could also be extremely flattened cubic or tetragonal forms (Fig. 4a and b). The crystals look very similar to those of hexagonal β-tridymite and may be paramorphs after this phase. The platy crystals were particularly common in MVO1236 (12 July 2003 collapse, dense dome lava), MontR1 (20 May 2006 collapse, dense dome lava) and MVO819 (177 ka B.P., dense dome lava).

Feathery crystalline silica in glass Within the glassy groundmass of most of the dome rock samples 'feathery' textures of poorly formed crystallites were observed (Fig. 1e). Individual patches are on a scale of <1–3 µm and are too small to be confidently identified by spot analysis with SEM-EDS, SEM-Raman or electron microprobe. Instead, the presence of micro-silicas in the volcanic glass was confirmed by carrying out a combination of BSE imaging, X-ray elemental mapping, CL imaging and SEM-Raman (of an area of partially devitrified glass) (Fig. 5a–d). Figure 5a shows an area of partially devitrified glass, labelled 'D', which contains plagioclase microlites and a phase with a BSE signal darker than the glass (labelled 'G') but similar to that of the cristobalite ('C'). The X-ray elemental map in Fig. 5b demonstrates that area 'D' is composed of plagioclase microlites (containing relatively abundant Al (green)) in a groundmass dominated by Si (blue) but with less K (red) than surrounding glassy areas. The dominance of blue indicates a Si-enriched area where glass is not the principal matrix phase. The CL signal is similar to that of the 'prismatic cristobalite' (type 2, Fig. 5c), although quartz can also show a similar colour (Boggs et al. 2002). Ultimately, the darker groundmass phase (by SEM-BSE) was confirmed as cristobalite using SEM-Raman, which gave a broad, curved background pattern, typical of amorphous glass, with peaks that match the

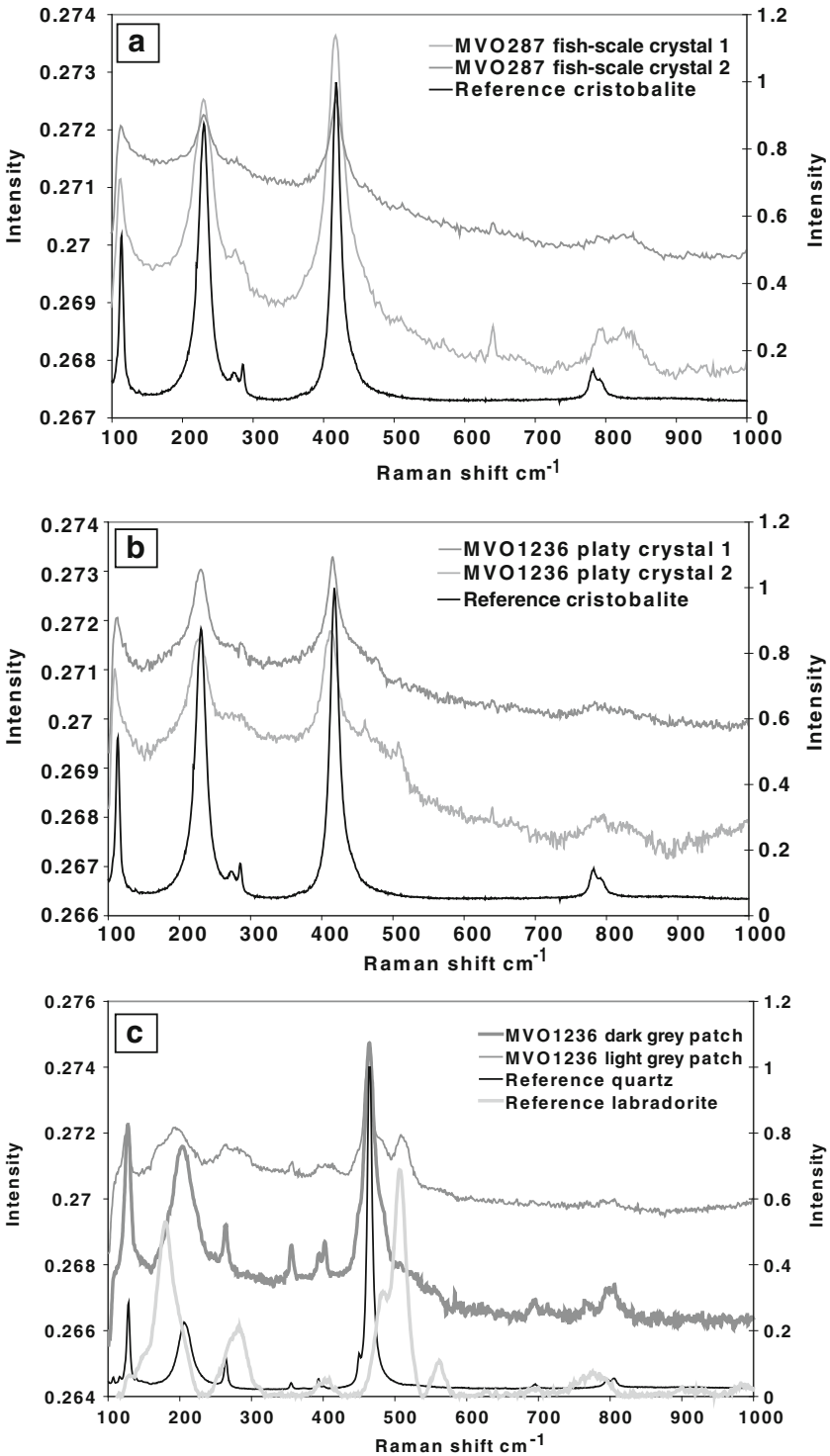

Fig. 2 Raman spectra. **a** Spectra for two fish-scale crystals in sample MVO287 with reference spectrum for cristobalite; **b** spectra for two platy crystals in sample MVO1236 with reference spectrum for cristobalite; **c** spectra for light-grey and dark-grey patches in the groundmass of MVO1236 with reference spectra for quartz and labradorite

reference patterns for both cristobalite and plagioclase (labradorite) (Fig. 5d). Quartz was not detected in these patches by SEM-Raman.

Quartz microlites Four of the samples (MontR1, MVO819, MVO945 and MVO1236) had areas which were glass-free, and the groundmass was composed entirely of microlites (<100 μm diameter) including ~10 μm diameter patches of subhedral silicas (indicated by arrows in Fig. 1f) confirmed to be quartz by SEM-Raman (Fig. 2c). These patches are found in MontR1, MVO945 and MVO1236 (note that cristobalite patches showing fish-scale cracking are still present in original pore spaces in these samples, Fig. 1f). In association with these forms are lighter grey, more lath-shaped

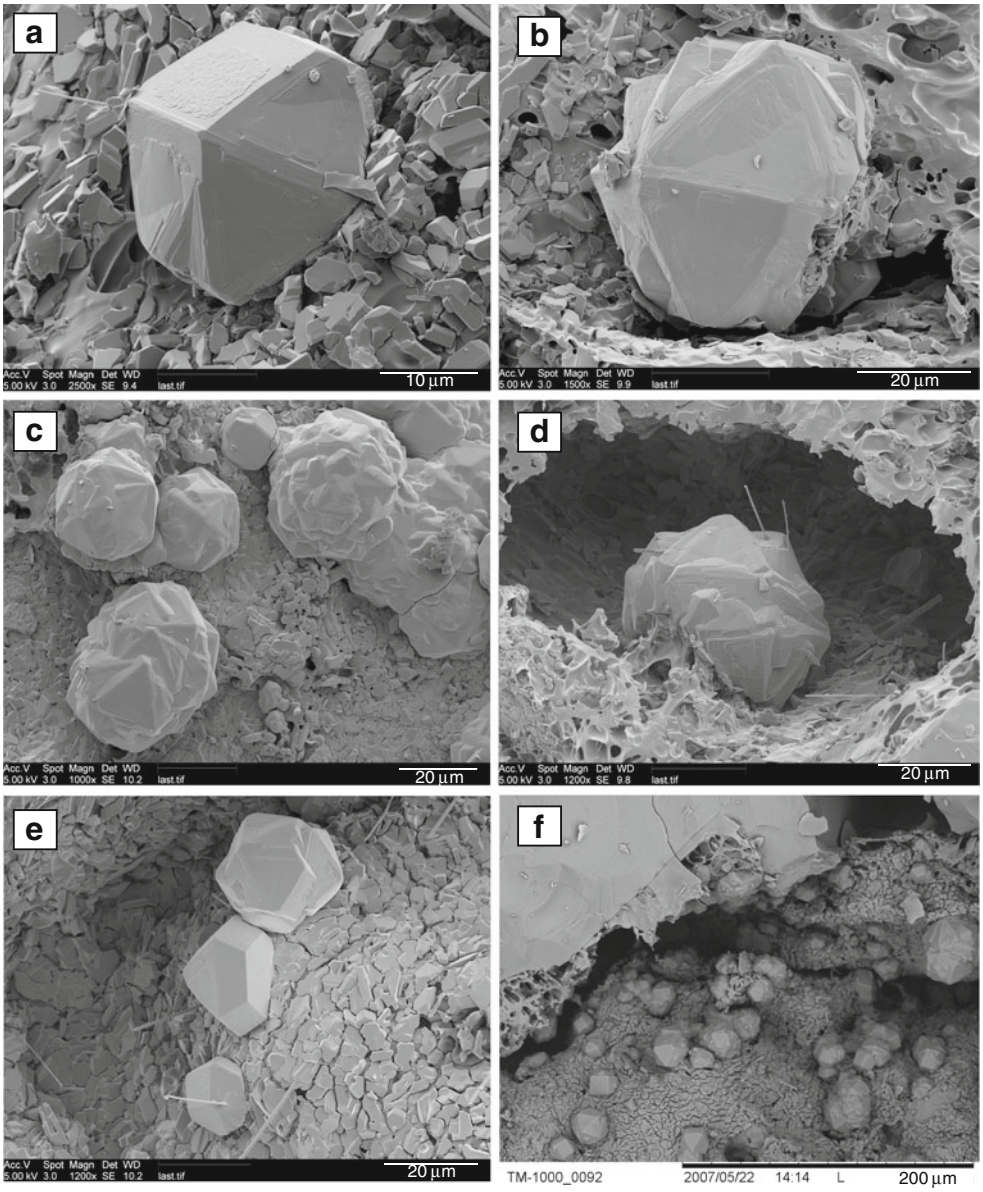

Fig. 3 SEM photomicrographs of prismatic cristobalite in rough chips of dome rock. **a**–**e** MVO287; **f** MVO819

plagioclase crystals which are often poorly formed (Fig. 1f). In addition, we noted that these samples also contained open spaces surrounding the microlites (e.g. Fig. 4b).

To put these observations into context, Table 2 summarises these crystalline forms along with others described in the literature at dome-forming volcanoes.

Other minerals

Other minerals were observed in the pore spaces including abundant plagioclase and occasional Mg-bearing phases (possibly periclase, brucite or magnesite) and TiO_2 (in MVO287, probably rutile), hornblende (in MVO1406 and MVO287) and halite (in MVO617). Sub-solidus crystallisation of plagioclase could not be identified from thin sections, but examination of rough chips by SEM clearly showed a crust of feldspar crystals lining some vugs (e.g. Fig. 3a, e and f).

Crystalline silica content of dome rocks

Cristobalite content of the dome rock samples ranges from 1.2 to 11.1 wt.%, determined using the XRD-PSD IAS method (Table 3) (with<3 % error; Le Blond et al. 2009). The lowest abundances are found in the more vesicular samples (e.g. MVO288 and MVO332). The samples with the most abundant cristobalite are dense dome rock, including the ancient sample MVO819 (174 k.a. B.P.). For most samples, quartz was not detected by XRD. However, MVO945 (400 a B.P., dense dome rock) and MVO1236 (12 July 2003, dense dome rock) both contain ~5 wt.% quartz, MontR1 (20 May 2006, dense dome rock) contains

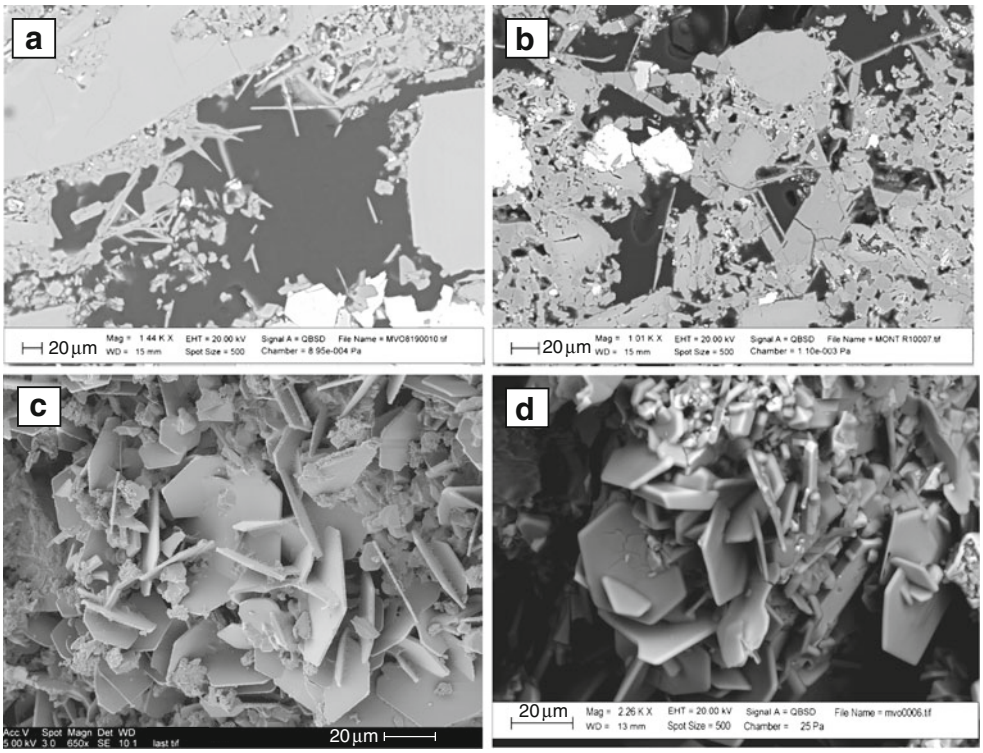

Fig. 4 Morphologies of prismatic cristobalite. **a**, **b** are backscattered electron images of MVO819 and MontR1, respectively. **c**, **d** are images of rough chips of dome rock samples MVO819 and MVO1236, respectively

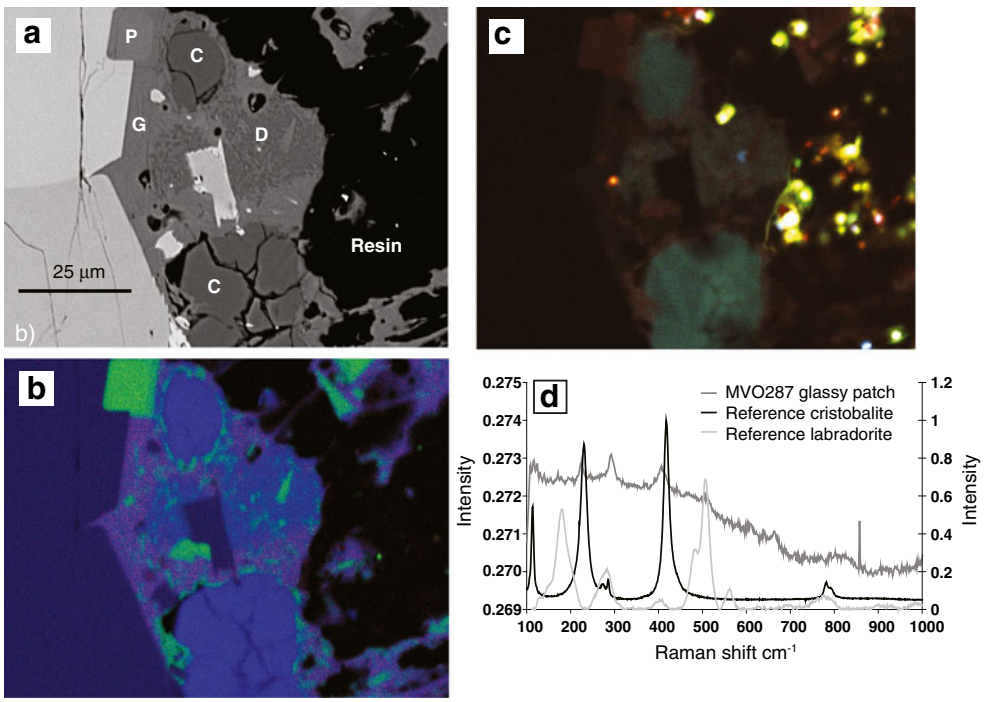

Fig. 5 **a** Backscattered electron image of sample MVO287 showing cristobalite (*C*) with fish-scale cracking and plagioclase (*P*) microlites in volcanic glass (*G*). '*D*' is a patch of devitrified glass; **b** X-ray elemental map of the same area as in (**a**) showing relative counts for Si in *blue*, Al in *green* and K in *red*, and mixtures of these colours where more than one element exists (each colour has a relative scale from black (zero counts) to the primary colour at maximum counts). Areas of volcanic glass are *purple* due to the presence of K (*red*) in addition to Si (*blue*) and Al (*green*); **c** SEM-cathodoluminescence image of the same area as in (**a**). The very *bright green/yellow areas* are artefacts from the sample preparation process; **d** Raman spectrum for a partially devitrified area of glass from MVO287 with library spectra for labradorite and cristobalite. Spike in glass spectrum at ~875 cm^{-1} is a cosmic ray artefact

Table 2 Summary of crystalline silica habits observed at dome-forming volcanoes

Silica polymorph	Morphology in thin section	Size	Interpretation	Magma type	Volcano	Key references
Quartz	Rounded and often embayed	Up to ~1 mm	Magmatic phenocryst	Andesitic–rhyolitic	Many	Murphy et al. 2000
Quartz	Subhedral, hexagonal	~10 μm	Devitrification product	Andesitic–dacitic	SHV, MSH	This study; Pallister et al. 2008
Cristobalite	Prismatic (3D), euhedral, fish-scale cracking, seen in vesicles	Up to~50 μm	Vapour-phase mineralisation	Andesitic–rhyolitic	SHV, MSH, Mt. Pelée, Inyo Domes	This study; Baxter et al. 1999; Pallister et al. 2008
Cristobalite	Platy (3D), hexagonal, acicular, fish-scale cracking, seen in vesicles	Up to ~30 μm	Vapour-phase mineralisation	Andesitic–dacitic	SHV, MSH	This study; Hoblitt and Harmon, 1993; Pallister et al. 2008 (identified as tridymite in both studies)
Cristobalite	Within groundmass with diffuse borders, fish-scale cracking	<50 μm	Devitrification product	Andesitic–dacitic	SHV	This study
Cristobalite	Feathery, inter-grown with feldspar and glass	<5 μm	Devitrification product	Andesitic–dacitic	SHV, MSH, Santiaguito	This study; Harford et al. 2003; Scott et al. 2013
Cristobalite	Lath, cutting across groundmass	Up to ~75 μm	Devitrification product?	Dacitic	MSH	Cashman et al. 2008
Cristobalite	Spherulitic, inter-grown with k-feldspar	Up to several millimetres	Devitrification product	Rhyolitic	Obsidian domes	Dadd 1992; Swanson et al. 1989
Cristobalite	Nano-fibre	<0.1 μm	Growth from vapour within eruption column	Rhyolitic	Chaitén	Reich et al. 2009
Tridymite	Arrow head with twin	Up to ~1 mm	Vapour-phase mineralisation?	Rhyolitic	Obsidian domes	Unpublished data
Tridymite	Acicular	<20 μm	Devitrification?	Dacitic	MSH	Cashman et al. 2008

Question marks in the Interpretation column indicate our interpretation of published images. Magma types are speculative. Morphologies describe thin section appearance, although 3D morphology given where observation of rock chips allowed imaging into pore spaces

Table 3 Quantification of silica phases by X-ray diffraction

Sample	Lava type	Cristobalite wt.%	Quartz wt.%	Total crystalline silica (wt.%)
MVO288	Highly vesicular	1.2	n.d.	1.2
MVO332	Vesicular	1.9	n.d.	1.9
MVO617	Dense	4.9	n.d.	4.9
MVO287	Vesicular	4.8	1.5	6.3
MVO945	Ancient, dense	2.3	4.8	7.1
MVO1406	Dense	7.8	n.d.	7.8
MVO819	Ancient, dense	8.2	n.d.	8.2
MVO1236	Dense	4.7	5.0	9.7
MontR1	Dense	11.1	2.7	13.8

All data have 1–3 wt.% error

n.d. not detected

2.7 wt.% quartz and MVO287 (21 Sept. 1997 vesicular sample) contains 1.5 wt. % quartz. These quartz quantities match the observations of devitrification-derived quartz for MVO945, MVO1236 and MontR1 (type 5, above), and we believe that MVO287 contained unusually high levels of magmatic quartz phenocrysts (observable in SEM) as there was no evidence of extensive devitrification in this sample. Tridymite was not identified in any sample.

Dome whole-rock major element compositions

XRF data are presented in Table 4 for dome rock samples (from this study and those in Devine et al. 1998; Murphy et al. 2000; Zellmer et al. 2003) and for pumice samples (analysed for this study as well as samples from Murphy et al. 2000; Zellmer et al. 2003).

The dome rock samples show a narrow range (~4 wt.%) of SiO_2 values, with the pumice data sitting amongst the dome rock data. We note that the two vesicular samples MVO288 (57.2 wt.% SiO_2) and MVO287 (61.4 wt.% SiO_2) bracket the SiO_2 range. Both samples are assumed to be from the same magma injection event (Williamson et al. 2010), but MVO287 contains some cristobalite (5.1 wt.%) and quartz (4.1 wt.%) whereas MVO288 contains rather less (1.1 wt.% cristobalite and no detectable quartz). No correlation was found between whole-rock SiO_2 content and cristobalite content (variation diagram not shown) for our dome rock samples.

Discussion

The origin of cristobalite in the Soufrière Hills domes

Two mechanisms have been proposed to explain the origin of cristobalite as a metastable mineral in lava domes:

Table 4 Whole-rock analyses by XRF for Soufrière Hills dome rocks and pumices (oxide wt.%)

Sample	Type	SiO_2	TiO_2	Al_2O_3	Fe_2O_3	MnO	MgO	CaO	Na_2O	K_2O	P_2O_5	LOI	Total
MVO288	Dome	57.20	0.69	18.41	8.27	0.18	3.15	8.41	3.20	0.63	0.14	0.18	100.45
MVO332	Dome	57.84	0.73	17.32	8.81	0.23	3.53	7.94	3.11	0.69	0.15	0.10	100.45
MVO617	Dome	58.18	0.68	18.04	7.91	0.18	3.05	8.07	3.19	0.71	0.13	0.36	100.48
MVO819	Dome	58.19	0.59	17.07	6.43	0.15	3.23	7.37	3.85	0.72	0.10	1.67	99.37
MontR1	Dome	58.63	0.69	17.19	8.24	0.20	3.40	7.83	3.17	0.75	0.14	0.10	100.35
MVO1406	Dome	59.19	0.65	17.84	7.41	0.18	3.26	8.07	3.18	0.73	0.12	-0.18	100.46
MVO945	Dome	59.42	0.67	16.95	7.87	0.20	3.03	7.42	3.23	0.76	0.14	0.69	100.38
MVO1236	Dome	60.08	0.61	18.42	6.73	0.16	2.96	7.74	3.40	0.78	0.12	0.39	101.39
MVO287	Dome	61.37	0.54	17.87	6.05	0.16	2.54	7.43	3.43	0.82	0.12	0.36	100.69
MVO289	Pumice	57.78	0.61	18.16	7.50	0.18	2.85	7.90	3.51	0.78	0.14	0.09	99.51
MVO244	Pumice	58.68	0.60	17.92	7.29	0.18	2.75	7.59	3.56	0.82	0.14	0.14	99.68
MVO291	Pumice	59.28	0.57	17.94	6.93	0.17	2.58	7.46	3.62	0.86	0.14	0.23	99.78
MVO374	Pumice	59.55	0.58	18.02	7.13	0.18	2.58	7.39	3.58	0.82	0.14	0.14	100.13
MVO1151 [c]	Dome	58.13	0.63	18.02	7.67	0.18	3.04	7.61	3.77	0.80	0.15	-0.14	100.00
MVO332 [a]	Dome	58.15	0.63	18.10	7.53	0.18	3.06	7.50	2.69	0.72	0.15	-0.13	99.57
MVO40 [c]	Dome	58.73	0.63	17.76	7.52	0.18	2.89	7.51	3.85	0.79	0.15	-	100.00
MVO201 [a]	Dome	59.08	0.62	18.09	7.30	0.18	2.89	7.56	3.45	0.75	0.15	-0.09	99.97
MVO34 [a]	Dome	59.13	0·63	18.29	7·50	0·19	2.91	7.57	3.58	0.77	0.15	-0.21	100.51
MVO231 [a]	Dome	59.15	0.63	18.01	7.35	0.18	3.05	7.64	3.66	0.72	0.14	-0.17	100.36
MVO104 [c]	Dome	59.33	0.64	17.75	7.28	0.17	2.96	7.61	3.39	0.73	0.14	-	100.00
MONT140 [b]	Dome	59.46	0.66	17.90	6.89	0.23	2.77	7.53	3.64	0.81	0.15	-	99.82
MONT128 [b]	Dome	59.72	0.58	18.26	6.61	0.13	2.80	7.43	3.33	0.92	0.14	-	99.92
MONT153 [b]	Dome	60.11	0.67	17.53	7.10	0.18	2.89	7.44	3.49	0.78	0.11	-	100.32
MVO47 [a]	Dome	60.12	0.65	17.29	7.42	0.18	2.97	7.39	3.35	0.77	0.14	-0.06	100.24
MVO1174 [c]	Dome	60.25	0.58	17.25	7.15	0.17	2.57	7.12	3.77	0.98	0.15	-0.05	100.00
MVO665L [c]	Dome	60.28	0.57	16.80	7.25	0.18	2.85	7.18	3.87	0.87	0.15	-	100.00
MVO1078 [c]	Dome	62.03	0.54	17.19	6.33	0.16	2.35	6.49	3.74	1.03	0.14	-	100.00
MVO237 [a]	Pumice	59.62	0.60	17.83	6.71	0.17	2.78	6.94	3.42	0.80	0.14	0.59	99.60
MVO244 [c]	Pumice	59.75	0.60	17.54	7.08	0.18	2.94	7.33	3.66	0.78	0.14	-	100.00

See Table 1 for sample descriptions of samples in top part of table, which were analysed for this study. The lower half of the table displays data taken from the literature (Devine et al. 1998; Murphy et al. 2000; Zellmer et al. 2003). Highlighted cells (in grey) show dome rock SiO_2 data greater than the pumice data

[a] Data from Murphy et al. 2000

[b] Data from Devine et al. 1998. For these samples, Fe is calculated as FeO, not Fe_2O_3

[c] Data from Zellmer et al. 2003. Only samples clearly identifiable as dome rock/pumice from the MVO sample database were used

vapour-phase transport and deposition, and devitrification of groundmass glass (e.g. Baxter et al. 1999). Through careful observations of crystalline silica textures in Soufrière Hills dome rock, this study affirms that both were likely emplacement mechanisms in Soufrière Hills dome lava.

Vapour-phase mineralisation

Prismatic cristobalite was found throughout the dome rock samples analysed in this study, from occasional crystals within vesicles in pumiceous samples to filling most pore spaces in dense dome rock. The prismatic cristobalite appears to be a ubiquitous feature of the Soufrière Hills dome lava.

The morphology of cristobalite varies from well-formed single, prismatic crystals, to forms with multiple, interlocking twins and, in some cases, platy, hexagonal crystals. The causes of these morphological variations are unclear, possibly relating to differences in vapour fluxes and composition, and fluctuations in temperature and pressure. Horwell et al. (2012) have shown that prismatic and platy cristobalite at SHV contain structural substitutions of aluminium and sodium (up to 3 wt.% Al_2O_3 and 1 wt.% Na_2O) with platy cristobalite containing significantly more substituted cations than prismatic cristobalite so morphology may be influenced by structural variations.

Prismatic cristobalite crystals are often observed growing into open pore spaces and fractures within the dome rock (Fig. 1c) leading us to interpret that these crystals have precipitated from vapour-phase fluids passing through the permeable dome. We also observe this form of cristobalite as patches in dense dome rock and conclude that, in instances where the boundaries of the crystal can be clearly identified, cristobalite has been deposited from a vapour

phase and has almost completely filled the available pore space (Fig. 1d). In some circumstances, it is difficult to determine a clear boundary between the cristobalite patches and the groundmass (Fig. 1c and e); in this case, the cristobalite may be the product of extensive devitrification, or of vapour-phase deposition on devitrification cristobalite. We also interpret the platy crystals as being vapour-phase precipitates.

Devitrification

We interpret the areas of 'feathery' groundmass containing micro-crystals of cristobalite to be formed by devitrification of the SHV glass (e.g. Fig. 1e) and the glass-free, quartz/cristobalite/feldspar microlite-rich areas as being patches of total devitrification. Little work has been done on devitrification of andesitic/dacitic dome rocks. However, Blundy and Cashman (2001), Cashman (1992), Harford et al. (2003) and Couch et al. (2003a) all recognised two types of glass at MSH and SHV: a 'true' glass and a glass with "very finely crystalline intergrowths of feldspar and quartz" (Couch et al. 2003a), which we believe to be devitrification patches similar (MSH) or identical (SHV) to those observed in this study (through comparison of their images with our textural observations). Production of spherulites by devitrification of rhyolitic obsidian is common (e.g. Swanson et al. 1989), but we did not observe spherulites in the andesitic SHV lavas, and, unlike in spherulites, the devitrification phases observed here were not in the form of axiolitic, radiative or acicular intergrowths. We have also clarified that the crystalline silica phase in devitrification glass at SHV is cristobalite unless complete devitrification occurs in which case thermodynamic factors may allow conversion of metastable cristobalite to quartz.

Harford et al. (2003) show that patches of devitrified glass at SHV are chemically distinct from true glass: K_2O (4–6 wt.% in true glass) is depleted in the devitrified glass (0.5 wt.%); Na_2O is slightly enriched (3.9 wt.% compared with 2.4–3.3 wt.% for true glass); and devitrified glass does not contain chlorine. The depletion of K and the absence of Cl indicates that volatiles are lost during devitrification; we conclude that these volatiles are likely transported to surface fumaroles in passing vapours, as we do not observe any K or Cl-bearing minerals (except rare halite in one sample) as vapour-phase precipitates within the dome. As far as we can tell, no studies have been carried out on active, magmatic-water-dominated fumaroles on Montserrat—those studied by Boudon et al. (1998) were venting fluids of mainly sea-water origin—and therefore, the precipitation of K-bearing phases cannot be assessed.

All samples containing vapour-phase cristobalite also showed devitrification textures, except the pumiceous sample MVO288 which only had trace amounts of vapour-phase cristobalite (by SEM). This supports the theory of Jones and Segnit (1972) which implies that vapour-phase cristobalite precipitation requires the pre-existence of devitrification cristobalite for nucleation (see "Cristobalite formation mechanisms"). It is possible that MVO288 contained devitrification cristobalite nuclei beyond the resolution of the SEM.

Scott et al. (2013) and Horwell et al. (2013) propose that the extent of devitrification in dome rock is related to the rate of lava extrusion, with slow extrusion promoting greater devitrification as the lava is held at suitable pressure/temperature conditions for longer.

Local redistribution versus bulk transport

The collection of XRD and XRF data for cristobalite and SiO_2 contents in the various Soufrière Hills dome rocks has allowed us to investigate the mechanisms of silica transport for vapour-phase mineralisation. Understanding the mechanisms and rate of formation of cristobalite is important because it affects the distribution and abundance of silica within the conduit/dome system. The formation of vapour-phase cristobalite in dome rock requires the transport of silica, via local redistribution (over the length-scale of individual crystals and vugs), via bulk transport from one part of the magmatic/hydrothermal system to another or, perhaps, via both routes.

Local redistribution of silica may result when reactive species, such as Cl and F, are trapped in closed vugs, where they may corrode amorphous glass and precipitate crystalline silica (e.g. via the reaction in Eq. 1). In experiments by Hammer and Rutherford (2002), vapour-phase cristobalite was grown (fish-scale prismatic crystals observed within vesicles, labelled as quartz) during decompression of Pinatubo dacitic pumice, providing evidence that, in experimental settings at least, cristobalite can form without an external vapour source (i.e. local redistribution).

Bulk transport may result from the flow of silica-bearing gases from parts of the magmatic system where pressure, temperature and speciation favour silica corrosion, to parts of the system where conditions favour mineralisation. If we consider the pressure and temperature dependence of the equilibrium of Eq. 1, we can infer from de Hoog et al. (2005) that higher pressures in the conduit favour silica corrosion and lower pressures in the dome favour mineralisation.

Bulk transport of silica would be expected to lead to changes in the bulk (whole rock) SiO_2 content of dome rock over time, whilst local redistribution would not (we note that, since devitrification involves redistribution of silica over very short distances only, it will not, on its own, cause a change in the bulk SiO_2 content of a packet of dome rock). In order to assess whether bulk transport has affected SiO_2 content in SHV dome rock, we compared the whole-rock compositions of samples of dome rock (from this study and Devine et al. 1998; Murphy et al. 2000; Zellmer et al. 2003) and explosive pumice (from this study and Murphy et al. 2000; Zellmer et al. 2003). Whilst pumice compositions should reflect the original

magmatic assemblage, since cristobalite does not form during the magmatic phase, the composition of dome rock samples may have been altered by the addition of SiO_2. The data (Table 4) demonstrate that the SiO_2 content of SHV dome rock samples fall in the range 57.2–62.0 wt.%, and pumice samples fall in the range 57.8–59.8 wt.%; the seven samples with the highest SiO_2 content are all dome rocks (highlighted in Table 4). Whilst this is not conclusive, it suggests that some dome rock samples have been enriched in SiO_2, relative to magmatic compositions, consistent with the hypothesis of bulk transport. For our samples, however, we also compared cristobalite content with bulk SiO_2 content, to see if samples with high cristobalite also had enriched SiO_2, but found no relationship between the two.

To aid with the interpretation of these results, it is useful to consider two contrasting scenarios. (1) If we assume that there is no bulk transport of silica, then the measured SiO_2 content of the samples must reflect the initial composition of the parent magma. In this scenario, the observed variation in SiO_2 content would indicate that the composition of the parent magma varied over a 5 wt.% interval over time and space (between ~57 and 62 wt.%), which is not uncommon in intermediate lavas and may also be the product of local heterogeneity in crystal assemblages. (2) If, instead, we assume that the composition of the parent magma is fixed, then any variations in measured SiO_2 content should reflect the bulk transport of SiO_2. To illustrate this effect, consider the vapour-phase mineralisation of a 100 g sample of dome rock sample MVO288 (vesicular sample containing only trace amounts of cristobalite). This sample has an initial SiO_2 content of 57 wt.% (Table 4; i.e. 57 g of the sample is SiO_2); if bulk transport of SiO_2 adds 10 wt.% cristobalite to the sample, the mass of the sample is now 111 g (of which 11.1 g is cristobalite). If the cristobalite is 98 wt.% SiO_2 (consistent with the range observed by Horwell et al. 2012), this mineralisation adds 10.9 g of SiO_2 to the sample so that 67.9 g of the 111 g sample is now SiO_2. The bulk SiO_2 content of the mineralised sample is, therefore, 61.1 wt.%; i.e. addition of 10 wt.% cristobalite increases the bulk SiO_2 content by only 4.1 wt.%. In general, the change in wt.% SiO_2 (ΔSiO_2) due to the addition of wt.% of a mineral W_{min} is given by:

$$(\Delta SiO_2) = \frac{W_{min}(X_{min} - X_0)}{100} \quad (2)$$

where X_{min} is the SiO_2 content of the added mineral in weight percent and X_0 is the initial SiO_2 content of the sample in weight percent. From this equation, we can see that the modest variation in bulk SiO_2 content that we measure in our samples (5 wt.%) is consistent with the addition of up to 12 wt.% vapour-phase cristobalite through bulk transport. Note that the addition of vapour-phase plagioclase has a much smaller impact on bulk SiO_2 content because X_{min} (~53 wt.% for labradorite; Deer et al. 1996) is very similar to X_0.

The compositional data alone do not allow us to determine conclusively whether the observed variation in silica content results from bulk transport of SiO_2, from variation in SiO_2 composition of the parent magma, or some combination of the two. However, we note that our textural observation that cristobalite almost completely in-fills relict porosity in some samples (e.g. MVO1406; dense dome lava from 20 May 2006 collapse) favours the bulk transport of SiO_2. The bulk transport of even modest amounts of SiO_2, therefore, could have important consequences for the interpretation of petrological and geochemical studies, and for porosity/permeability relationships which will affect the evolution of the stability of the dome; these consequences are considered in sections "Implications for petrological and geochemical studies" and "Implications for the evolution of lava dome stability" below.

Timescale of cristobalite formation and evolution

From studies of a single pyroclast from Montserrat (MVO287), believed to represent magma injected into the dome during the switch from effusive to explosive activity, cristobalite crystallisation appears to have occurred while the magma was still plastic (Williamson et al. 2010), probably within hours or days of the magma entering the upper conduit or dome environment. The short residence time of this material in the dome indicates that cristobalite crystallisation can be extremely rapid as the sample has 4.8 wt.% cristobalite and has both vapour phase and devitrification textures. This conclusion is supported by Horwell et al. (2010), who found 16 wt.% cristobalite in ash from the August 2008 collapse of the Chaitén (Chile) lava dome, just 3 months after the onset of dome growth (N.B. quantities of cristobalite are likely to be somewhat concentrated in co-ignimbrite ashfall compared with dome rock (Horwell et al. 2001)). Sample MVO288 was collected from the same deposit as MVO287 and is believed to have been part of the same magma injection event but was perhaps located slightly deeper in the dome at the time of collapse (Williamson et al. 2010). MVO288 contains just a few vapour-phase cristobalite crystals and no devitrification textures (see "Discussion," above). The difference in residence time in the dome of these two samples may be as little as a few hours.

Ostwald's rule of stages states that the first phase to crystallise from a melt is often the thermodynamically unstable polymorph, which then re-crystallises to form the thermodynamically stable phases (Nývlt 1995). This appears to be the case with cristobalite in volcanic domes, but the kinetics also seem such that re-crystallisation to quartz does not occur except during extensive devitrification. Analysis of our oldest sample (MVO819) indicates that, even over timescales of hundreds of thousands of

years, vapour-phase cristobalite does not transform to quartz, perhaps because there is insufficient energy for the reconstructive transformation (involving bond breakage) (Deer et al. 1996).

Duffy (1993) calculates that the conversion time for cristobalite to quartz at 35 °C (and at atmospheric pressure) is less than 10^5 years; however, experimental studies by Ernst and Calvert (1969) determined conversion times of tens of millions of years. This reconstructive transformation will hence be very slow, or will not occur if there is insufficient energy to break and re-form the bonds in the silica structure. The presence of quartz in totally devitrified samples (such as MVO1236) indicates that, in some environments, cristobalite formed by devitrification of glass can undergo reconstructive transformations to quartz very rapidly (collected from a total dome collapse on 12 July 2003, this sample was derived from dome material <24 months old; Horwell et al. 2013). We infer this from textures which indicate that the sub-hedral quartz was once part of a larger fish-scale crystal (Fig. 1f), although there is evidence in the experimental literature of quartz forming directly by devitrification (Lofgren 1971). The transformation could be initiated by heating and throughput of volatiles related to the new injection of magma into the dome. Alternatively, re-crystallisation might be caused by the circulation of hydrothermal fluids.

Further implications

Mineralisation of the dome through bulk transport of SiO_2-bearing vapours has important implications for the evolution of the physical properties of the dome, and for the interpretation of geochemical and petrological investigations of dome rock. Whilst our XRF data do not conclusively demonstrate that bulk transport has occurred at SHV, the textural evidence is sufficiently compelling to warrant consideration of its consequences. In particular, we observe that vapour-phase cristobalite (and subordinate vapour-phase plagioclase) partially fills pore space in all dome samples; furthermore, in some dense dome rock samples (notably MVO1406), pore space is almost completely occluded by vapour-phase mineralisation, indicating that the samples have undergone dramatic textural changes.

Implications for petrological and geochemical studies

The bulk transport of silica, in the vapour phase, from one part of the conduit/dome system to another may progressively change the composition and mineralogy of the dome rock. Consequently, samples of dome rock may not be strictly representative of the initial magma from which they are derived, as assessed in "Local redistribution versus bulk transport". If this is not taken into consideration in the petrological and geochemical analysis of dome rocks, it could lead to incorrect interpretations and poorly posed experimental studies.

Cristobalite has previously been identified in thin sections of dome rock from several volcanoes, including Mt. Pelée, Martinique (Martel et al. 2000) and MSH (e.g. Pallister et al. 2008 Fig. 10b and c). However, we believe that it has also been misidentified or misnamed in the literature as quartz (perhaps as a generic name for crystalline, or crypto-crystalline silica) at SHV (e.g. Couch et al. 2003b) and as quartz or tridymite at MSH (e.g. Hoblitt and Harmon 1993; Blundy and Cashman 2001; Pallister et al. 2008), based on SEM images showing the signature fish-scale cracking in those articles. Images of SHV samples MVO1217 and MVO34 (Fig. 16, Couch et al. 2003b) show them to be rich in vapour-phase, fish-scale cristobalite (labelled as 'quartz'). It has also been misidentified as quartz in experimental crystallisation studies (e.g. Hammer and Rutherford 2002; Couch et al. 2003a; Couch et al. 2003b) where fish-scale cristobalite has grown in preference to quartz.

Misidentification of vapour-phase cristobalite as primary quartz is important in experimental studies because whole-rock compositions are commonly used for partial or total phase equilibrium studies to determine pre-eruptive parameters such as P, T, fH_2O and fO_2 in magmatic systems. These fundamental parameters underpin a variety of further activities, for example, petrological monitoring of active volcanoes, determining magmatic timescales, depths of magma storage, pre-eruptive volatile composition of the magma and the composition of magmatic gases (Pichavant et al. 2007). Consequently, it is critical that they are constrained as accurately as possible. Experiments are typically conducted using material thought to have the same composition as the magma of interest, based on the whole rock composition of lava.

Pichavant et al. (2007) recognised that, sometimes, experiments are unable to reproduce phenocryst assemblages, indicating a compositional mismatch between the experimental material and the reactive magma (e.g. Holtz et al. 2005). We propose that such a mismatch could result if lava samples are affected by bulk transport. For example, Barclay et al. (1998) used a crushed and melted Soufrière Hills dome sample (MVO34, erupted in Feb. 1996, the same sample as used by Couch et al. 2003b, see above) for melting and crystallisation experiments to constrain the pressure, temperature and $X(H_2O)$ of the magma storage conditions prior to ascent and eruption. As described above, it appears from Fig. 16 in Couch et al. (2003b) that this sample contains vapour-phase cristobalite. It is possible that elevated levels of SiO_2 in the sample could have affected the accuracy of experiments and calculations; this could be

particularly important for the quartz stability field, which was determined to be quite narrow (<840 °C with a PH_2O of 115–130 MPa). If cristobalite in these examples is the product of bulk transport of silica from elsewhere in the magmatic system, then it represents excess silica above the magmatic composition.

Couch et al. (2003a) used the groundmass composition of MVO34 as the starting composition for crystallisation experiments to demonstrate late-stage microlite growth as a result of degassing during magma ascent. They determined the phase equilibria using the Qz-Ab-Or ternary system (after Blundy and Cashman 2001). In their Qz-Ab-Or ternary diagram, Couch et al. (2003a) found that the normative compositions of several experimental glasses (with a crystalline silica phase present) did not plot at the expected cotectic pressures. It is possible that this is because of excess silica present in the system but could also be explained by cristobalite forming metastably at lower PH_2O than expected for quartz (samples which should have plotted at 100, 50 and 25 MPa all plotted at ≤25 MPa).

It is difficult to confirm the influence of cristobalite without investigating the original samples, but the results of this study are sufficient to highlight the need for workers to select samples for experimental studies carefully to ensure that their data are not affected by the presence of secondary mineralisation.

Implications for the evolution of lava dome stability

Sample MVO1406 represents recent dense dome rock that has undergone almost complete porosity occlusion by vapour-phase mineralisation (Fig. 1d). Porosity occlusion must result in large-scale reorganisation of the gas-flow pathways through the dome, perhaps favouring flow along cracks, as permeable networks of vesicles become occluded (Fig. 6). The deposition of vapour-phase minerals within a lava dome will, therefore, affect its porosity and permeability, with important implications for dome stability. We propose two competing processes: (1) the occlusion of pore networks by vapour-phase minerals will decrease dome permeability, causing gas pressure to increase, promoting dome failure; (2) the precipitation of minerals in pore-spaces and cracks in dome rock will increase its mechanical strength making it less likely to collapse. We propose that (in addition to the other processes described in the "Introduction") dome stability is influenced by the competition between these two effects and that the evolution of dome stability over time may be influenced by progressive mineralisation (Fig. 6).

Permeability

The permeability k of dome rock depends strongly on its interconnected porosity ϕ (equivalently, its vesicularity).

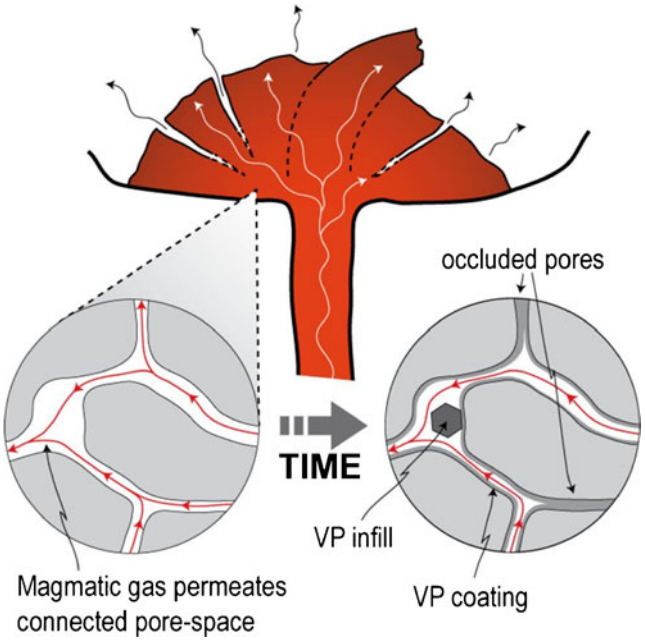

Fig. 6 Section through a dome. Over time, vapour-phase minerals precipitate from permeating gases, occluding pores and densifying rock

Mueller et al. (2005) present an empirical relationship for $k(\phi)$, based on laboratory measurements of the permeability of dome rock samples from Unzen (Japan), Merapi (Indonesia) and Shiveluch (Russia):

$$k = 10^{-17} \times \phi^{3.4}. \quad (3)$$

They find that this relationship, which is based on the Kozeny–Carman equation, is appropriate for dome rocks with porosity ϕ<0.3, where gas flows along tortuous pathways. We can use this relationship to explore the impact of vapour-phase mineralisation on the permeability of dome rock, using sample MVO287 as an example.

MVO287 has a porosity $\phi \approx 0.2$ (Williamson et al. 2010) and contains approximately 5 wt.% cristobalite. If we consider one extreme, that all of the cristobalite present in the sample was deposited from the vapour phase, into pore space, then we can calculate the original porosity of the sample before vapour-phase mineralisation:

$$\phi_0 = \frac{\phi+\alpha}{1+\alpha}, \quad where \quad \alpha = \frac{W_c}{(100-W_c)} \frac{\rho_A}{\rho_c} \quad (4)$$

where W_c is the wt.% cristobalite in the sample, ρ_A is the density of vesicle-free andesite and ρ_c is the density of cristobalite. Using ρ_A=2,600 kgm^{-3} (McBirney 1993), ρ_c=2,330 kgm^{-3} (Deer et al. 1996), and the values for ϕ and W_c given above, we find that ϕ_0=0.24, i.e. that the deposition of vapour-phase cristobalite has caused the porosity to decrease from 0.24 to 0.20. From Eq. 3, this corresponds to a decrease in permeability of a factor of 2 (from 5.2×10^{-13} to 2.7×10^{-13}m^2).

The calculation above, whilst illustrative, rather than definitive, does indicate that occlusion of porosity by vapour-phase mineralisation has had an important effect on the permeability of sample MVO287, and it should be noted that this sample was unusually vesicular for dome rock. More generally, the impact of mineralisation on permeability will be more pronounced for samples with a lower initial porosity, and with a greater degree of mineralisation. For example, if 10 wt.% vapour-phase cristobalite is deposited within the connected porosity of a sample with an initial porosity of ϕ_0=0.2, the final porosity is ϕ=0.1, and the permeability drops by a factor of 10, from 2.6×10^{-13} to 2.7×10^{-14} m^2. In some samples, such as MVO1406, where vapour-phase mineralisation appears to have completely filled all pore space, both the porosity and permeability will be negligible.

Rock strength

The strength of dome rock as a function of porosity has been investigated in uniaxial/triaxial compression experiments (Kennedy et al. 2009; Smith et al. 2011), in fracture toughness experiments (Scheu et al. 2008) and in decompression–fragmentation experiments (Spieler et al. 2004; Scheu et al. 2008). In all cases, the strength of dome rock is found to increase strongly as porosity decreases. None of these studies explicitly considers whether secondary mineralisation plays a role in decreasing rock porosity and increasing rock strength; however, it is known, from our own unpublished work and that of Pallister et al. (2008), that vapour-phase cristobalite is present in Mt. St. Helens 2004–2008 dome rock (used in the studies of Kennedy et al. 2009 and Smith et al. 2011) and in Unzen 1990–1995 dome rock (used in the study of Scheu et al. 2008).

Furthermore, a consideration of the microstructural controls on the failure of porous rocks suggests that progressive vapour-phase mineralisation would tend to increase rock strength. Paterson and Wong (2005) identify two different failure mechanisms for porous rocks depending on whether the solid matrix surrounding the pores is strong and coherent ('strongly cohesive'), or contains many planes of weakness ('weakly cohesive'). In strongly cohesive rocks, the pores act to localise stress, leading to micro-cracking of the pore walls; in this case, we propose that vapour-phase mineralisation will act to reinforce the pore walls and inhibit microcrack formation, hence strengthening the rock. In weakly cohesive rocks containing many pre-existing fractures, we propose that mineralisation will act to seal these fractures, again, strengthening the rock. The relationship between microstructure and rock mechanics is complex, and further work is needed to test this hypothesis; however, it seems intuitive that replacing gas-filled void spaces in a rock with crystalline material should have a significant impact on its rock mechanical properties and, hence, on the response of the dome to stress.

The calculations and experimental results discussed above indicate that occlusion of porosity by vapour-phase mineralisation—even through the addition of just 5–10 wt. % cristobalite—must substantially decrease permeability and may substantially impact the mechanical strength of dome rock. These two processes are likely to have opposing effects on dome stability: Permeability reduction will promote the development of gas overpressure within the dome, encouraging failure (Voight and Elsworth 2000); whilst an increase in mechanical strength of the rock would stabilise the dome. Dedicated work is needed to determine how these two processes interact to determine the evolution of stability of lava domes undergoing vapour-phase mineralisation.

Conclusions

Detailed observations and analysis have confirmed that cristobalite is formed both by vapour-phase mineralisation and by devitrification of volcanic glass and is ubiquitous within the Soufrière Hills dome rock. The vapour-phase cristobalite exists as prismatic and platy crystals within pore spaces whereas the devitrification cristobalite exists as feathery crystallites in the groundmass. In some dense dome rock, cristobalite almost completely fills porosity, occluding pore spaces. In some samples, glass devitrification is complete, resulting in a 'matrix' of quartz, cristobalite and feldspar with minor glass.

The rate and degree of cristobalite mineralisation is unlikely to be constant, varying with time, with position within the dome and with other factors such as magmatic activity and fluid availability. Investigation of the effects of pressure, temperature and dome residence time were not possible within the current investigation due to samples being sourced from PDC deposits rather than collected in situ from lobes. A recent analysis of SHV volcanic ash showed no correlation between dome residence time and cristobalite content except when lava extrusion rates were exceptionally high, where a positive correlation was observed (Horwell et al. 2013).

The origin of the silica that produces the vapour-phase cristobalite has important implications for the interpretation of the effects of mineralisation on whole rock compositions of domes, and on dome stability. Although we cannot categorically distinguish between bulk transport and local redistribution of silica, it is clear that a modest input of silica into the dome system can result in changes in whole rock geochemistry of several wt.% SiO_2. This has implications for the use of cristobalite-bearing samples in experimental phase-equilibrium petrological studies. The occlusion of porosity in dome rock may also have implications for dome-collapse hazard at silicic volcanoes; the addition of

just 5–10 wt.% cristobalite will impact the permeability and rock mechanical behaviour of dome rock, potentially influencing dome strength and gas pressurisation.

The observations in this study indicate that new experimental studies on the high-temperature kinetics of cristobalite formation in closed and open systems, thermodynamic modelling of cristobalite precipitation in lava domes and rock strength measurements are required to underpin more accurate assessment of the stability of lava domes.

Acknowledgements The work of CJH was supported by a Natural Environment Research Council (NERC) Postdoctoral Research Fellowship (Grant No. NE/C518081/2). JSL acknowledges a NERC CASE Studentship (NER/S/A/2006/14107) whilst at the University of Cambridge, UK. DED acknowledges a Moyes Foundation studentship. We are grateful to Sue Loughlin and Thomas Christopher from the British Geological Survey and Montserrat Volcano Observatory for access to MVO collections and guidance in the field, and to Prof. Steve Sparks (University of Bristol, UK) for providing the pumice samples. We would also like to particularly thank MVO staff for their help sourcing samples from their archives. We thank Alan Brooker of Renishaw plc for invaluable help with SEM-Raman analyses. Thanks also to NHM staff: Gordon Cressey, for advice on XRD, and Dave Smith for sample curation. Many thanks to Madeleine Humphreys (Oxford University, UK) and Yan Lavallée (University of Liverpool, UK) for useful comments on the draft manuscript and to Eliza Calder (University of Buffalo, USA) and Jenni Barclay (University of East Anglia, UK) for their helpful reviews.

References

Allen AG, Baxter PJ, Ottley CJ (2000) Gas and particle emissions from Soufriere Hills volcano, Montserrat, West Indies: characterization and health hazard assessment. Bull Volcanol 62:8–19

Barclay J, Rutherford MJ, Carroll MR, Murphy MD, Devine JD, Gardner J, Sparks RSJ (1998) Experimental phase equilibria constraints on pre-eruptive storage conditions of the Soufriere Hills magma. Geophys Res Lett 25(18):3437–3440

Baxter PJ, Bonadonna C, Dupree R, Hards VL, Kohn SC, Murphy MD, Nichols A, Nicholson RA, Norton G, Searl A, Sparks RSJ, Vickers BP (1999) Cristobalite in volcanic ash of the Soufriere Hills Volcano, Montserrat, British West Indies. Science 283:1142–1145

Baxter PJ, Searl A, Cowie HA, Jarvis D, Horwell CJ (Accepted) Evaluating the respiratory health risks of volcanic ash at the eruption of the Soufrière Hills Volcano, Montserrat, 1995–2010. In: Wadge G, Robertson R, Voight B (eds) The eruption of Soufriere Hills volcano, Montserrat from 2000 to 2010. Geol Soc Lon Mem

Blundy J, Cashman K (2001) Ascent-driven crystallisation of dacite magmas at Mount St Helens, 1980–1986. Contrib Mineral Petrol 140:631–650

Boggs SJ, Kwon Y-I, Goles GG, Rusk BG, Krinsley D, Seyedolali A (2002) Is quartz cathodoluminescence color a reliable provenance tool? A quantitative examination. J Sediment Res 72:408–415

Boudon G, Villemant B, Komorowski J-C, Ildefonse P, Semet MP (1998) The hydrothermal system at Soufriere Hills Volcano, Montserrat (West Indies): characterisation and role in the ongoing eruption. Geophys Res Lett 25:3693–3696

Calder ES, Luckett R, Sparks RSJ, Voight B (2002) Mechanisms of lava dome instability and generation of rockfalls and pyroclastic flows at Soufrière Hills Volcano, Montserrat. In: Druitt TH, Kokelaar BP (eds) The eruption of Soufrière Hills volcano, Montserrat, from 1995 to 1999. Geol Soc Lon Mem 21:173–190

Carpenter MA, Salje EKH, Graeme-Barber A (1998) Spontaneous strain as a determinant of thermodynamic properties for phase transitions in minerals. Eur J Mineral 10:621–691

Cashman KV (1992) Groundmass crystallization of Mount St Helens dacite, 1980–1986—a tool for interpreting shallow magmatic processes. Contrib Mineral Petrol 109:431–499

Cashman KV, Thornber CR, Pallister JS (2008) From dome to dust: shallow crystallization and fragmentation of conduit magma during the 2004–2006 dome extrusion of Mount St. Helens, Washington. In: Sherrod DR, Scott WE, Stauffer PH (eds) A volcano rekindled: The renewed eruption of Mount St. Helens, 2004–2006. U.S. Geological Survey Professional Paper, pp 387–413

Churakov SV, Tkachenko SI, Korzhinskii MA, Bocharnikov RE, Shmulovich KI (2000) Evolution of composition of high-temperature fumarolic gases from Kudryavy Volcano, Iturup, Kuril Islands: the thermodynamic modeling. Geochem Int 38 (5):436–451

Couch S, Harford CL, Sparks RSJ, Carroll MR (2003a) Experimental constraints on the conditions of formation of highly calcic plagioclase microlites at the Soufriere Hills volcano, Montserrat. J Petrol 44(8):1455–1475

Couch S, Sparks RSJ, Carroll MR (2003b) The kinetics of degassing-induced crystallization at Soufriere Hills volcano, Montserrat. J Petrol 44(8):1477–1502

Dadd KA (1992) Structures within large volume rhyolite lava flows of the Devonian Comerong Volcanics, southeastern Australia, and the Pleistocene Ngongotaha lava dome, New Zealand. J Volcanol Geotherm Res 54(1–2):33–51

Damby DE, Horwell CJ, Baxter PJ, Delmelle P, Donaldson K, Dunster C, Fubini B, Murphy F, Nattrass C, Sweeney S, Tetley T, Tomatis M (2013) The respiratory health hazard of tephra from the 2010 Centennial eruption of Merapi with implications for occupational mining of deposits. J Volcanol Geotherm Res. doi:10.1016/j.jvolgeores.2012.09.001

de Hoog JCM, van Bergen MJ, Jacobs MHG (2005) Vapour-phase crystallisation of silica from SiF_4-bearing volcanic gases. Ann Geophys 48(4/5):775–785

Deer WA, Howie RA, Zussman J (1996) An introduction to the rock forming minerals. Longman Scientific and Technical, New York, p 696

Devine JD, Murphy MD, Rutherford MJ, Barclay J, Sparks RSJ, Carroll MR, Young SR, Gardner JE (1998) Petrologic evidence for pre-eruptive pressure-temperature conditions, and recent reheating, of andesitic magma erupting at the Soufriere Hills Volcano, Montserrat, WI. Geophys Res Lett 25:3669–3672

Druitt TH, Young SR, Baptie BJ, Bonadonna C, Calder ES, Clarke AB, Cole PD, Harford CL, Herd RA, Luckett R, Ryan G, Voight B (2002) Episodes of cyclic vulcanian explosive activity with fountain collapse at Soufrière Hills Volcano, Montserrat. In: Druitt TH, Kokelaar, B P, (ed) The eruption of Soufrière Hills volcano, Montserrat, from 1995 to 1999. Geol Soc Lon Mem 21:281–306

Duffy CJ (1993) Kinetics of silica-phase transitions. In: Los Alamos National Lab., NM (United States), Report number LA-12564-MS, p 22

Edmonds M, Oppenheimer C, Pyle DM, Herd RA, Thompson G (2003) SO_2 emissions from Soufriere Hills volcano and their relationship to conduit permeability, hydrothermal interaction and degassing regime. J Volcanol Geotherm Res 124(1–2):23–43

Elsworth D, Voight B (2001) The mechanics of harmonic gas pressurization and failure of lava domes. Geophys J Int 145:187–198

Elsworth D, Voight B, Thompson G, Young SR (2004) Thermal-hydrologic mechanism for rainfall-triggered collapse of lava domes. Geology 32:969–972

Ernst WG, Calvert SE (1969) An experimental study of the recrystallization of porcelanite and its bearing on the origin of some bedded cherts. Am J Sci 267-A:114–133

Foustoukos DI, Seyfried WEJ (2007) Quartz solubility in the two-phase and critical region of the NaCl–KCl–H_2O system: implications for submarine hydrothermal vent systems at 9°50'N East Pacific Rise. Geochim Cosmochim Acta 71:186–201

Getahun A, Reed MH, Symonds R (1996) Mount St. Augustine volcano fumarole wall rock alteration: mineralogy, zoning, composition and numerical models of its formation process. J Volcanol Geotherm Res 71(2–4):73–107

Hammer J, Rutherford M (2002) An experimental study of the kinetics of decompression-induced crystallization in silicic melt. J Geophys Res 107(B1):2021

Harford CL, Pringle MS, Sparks RSJ, Young SR (2002) The volcanic evolution of Montserrat using $^{40}Ar/^{39}Ar$ geochronology. In: Druitt TH, Kokelaar BP (eds) The eruption of Soufrière Hills Volcano, Montserrat, from 1995 to 1999. Geol Soc Lon Mem 21:93–113

Harford CL, Sparks RSJ, Fallick AE (2003) Degassing at the Soufriere HIlls volcano, Montserrat, recorded in matrix glass compositions. J Petrol 44(8):1503–1523

Hicks PD, Matthews AJ, Cooker MJ (2009) Thermal structure of a gas-permeable lava dome and timescale separation in its response to perturbation. J Geophys Res 114:B07201

Hoblitt RP, Harmon RS (1993) Bimodal density distribution of cryptodome dacite from the 1980 eruption of Mount St. Helens, Washington. Bull Volcanol 55:421–437

Holtz F, Sato H, Lewis J, Behrens H, Nakada S (2005) Experimental petrology of the 1991–1995 Unzen dacite, Japan. Part I: phase relations, phase compositions and pre-eruptive conditions. J Petrol 46:319–337

Horwell CJ, Baxter PJ (2006) The respiratory health hazards of volcanic ash: a review for volcanic risk mitigation. Bull Volcanol 69 (1):1–24

Horwell CJ, Braña LP, Sparks RSJ, Murphy MD, Hards VL (2001) A geochemical investigation of fragmentation and physical fractionation in pyroclastic flows from the Soufriere Hills volcano, Montserrat. J Volcanol Geotherm Res 109(4):247–262

Horwell CJ, Hillman SE, Cole PD, Loughlin SC, Llewellin EW, Damby DE, Christopher T (2013) Controls on variations in cristobalite abundance in ash generated by the Soufrière Hills volcano, Montserrat in the period 1997–2010. In: Wadge G, Robertson R, Voight B (eds) The eruption of Soufriere Hills volcano, Montserrat from 2000 to 2010. Geol Soc Lon Mem (in press)

Horwell CJ, Le Blond JS, Michnowicz SAK, Cressey G (2010) Cristobalite in a rhyolitic lava dome: evolution of ash hazard. Bull Volcanol 72:249–253

Horwell CJ, Sparks RSJ, Brewer TS, Llewellin EW, Williamson BJ (2003) The characterisation of respirable volcanic ash from the Soufriere Hills Volcano, Montserrat, with implications for health hazard. Bull Volcanol 65:346–362

Horwell CJ, Williamson BJ, Le Blond JS, Donaldson K, Damby DE, Bowen L (2012) The structure of volcanic cristobalite in relation to its toxicity; relevance for the variable crystalline silica hazard. Part Fibre Toxicol 9:44

Jones JB, Segnit ER (1972) Genesis of cristobalite and tridymite at low temperatures. J Geol Soc Aust 18(4):419–422

Kennedy LA, Russell JK, Nelles E (2009) Origins of Mount St. Helens cataclasites: experimental insights. Am Mineral 94:995–1004

Kingma KJ, Hemley RJ (1994) Raman spectroscopic study of microcrystalline silica. Am Mineral 79:269–273

Korzhinsky MA, Tkachenko SI, Shmulovich KI, Steinberg GS (1995) Native Al and Si formation. Nature 375(6532):544–544

Larsen ES, Irving J, Gonyer FA, Larsen ES (1936) Petrologic results of a study of the minerals from the Tertiary volcanic rocks of the San Juan region, Colorado. Part 2. Silica minerals. Am Mineral 21 (11):679–700

Le Blond JS, Cressey G, Horwell CJ, Williamson BJ (2009) A rapid method for quantifying single mineral phases in heterogeneous natural dust using X-ray diffraction. Powder Diffract 24:17–23

Lofgren G (1971) Experimentally produced devitrification textures in natural rhyolite glass. Geol Soc Am Bull 82:111–124

Martel C, Bourdier J-L, Pichavant M, Traineau H (2000) Textures, water content and degassing of silicic andesites from recent plinian and dome-forming eruptions at Mount Pelee volcano (Martinique, Lesser Antilles arc). J Volcanol Geotherm Res 96 (3–4):191–206

Matthews AJ, Barclay J, Carn S, Thompson G, Alexander J, Herd R, Williams C (2002) Rainfall-induced volcanic activity on Montserrat. Geophys Res Lett 29(13):1644

McBirney AR (1993) Igneous petrology. Jones & Bartlett, Boston

Mueller S, Melnik O, Spieler O, Scheu B, Dingwell DB (2005) Permeability and degassing of dome lavas undergoing rapid decompression: an experimental determination. Bull Volcanol 67:526–538

Murphy MD, Sparks RSJ, Barclay J, Carroll MR, Brewer TS (2000) Remobilization of andesite magma by intrusion of mafic magma at the Soufriere Hills volcano, Montserrat, West Indies. J Petrol 41 (1):21–42

Nakada S, Motomura Y (1999) Petrology of the 1991–1995 eruption at Unzen: effusion pulsation and groundmass crystallization. J Volcanol Geotherm Res 89(1–4):173–196

Nývlt J (1995) The Ostwald rule of stages. Cryst Res Technol 30 (4):443–449

Pallister JS, Thornber CR, Cashman KV, Clynne MA, Lowers HA, Mandeville CW, Brownfield IK, Meeker GP (2008) Petrology of the 2004–2006 Mount St. Helens lava dome—implications for magmatic plumbing and eruption triggering. In: Sherrod DR, Scott WE, Stauffer PH (eds) A volcano rekindled: the renewed eruption of Mount St. Helens, 2004–2006. U. S. Geological Survey Professional Paper, pp 647–702

Paterson MS, Wong T (2005) Experimental rock deformation—the brittle field. Springer-Verlag, Berlin, p 351

Pichavant M, Costa F, Burgisser A, Scaillet B, Martel C, Poussineau S (2007) Equilibration scales in silicic to intermediate magmas—implications for experimental studies. J Petrol 48(10):1955–1972

Reich M, Zúñiga A, Amigo A, Vargas G, Morata D, Palacios C, Parada MA, Garreaud RD (2009) Formation of cristobalite nanofibers during explosive volcanic eruptions. Geology 37(5):435–438

Renders PJN, Gammons CH, Barnes HL (1995) Precipitation and dissolution rate constants for cristobalite from 150 to 300 °C. Geochim Cosmochim Acta 59(1):77–85

Rogers AF (1922) A new occurrence of cristobalite in California. J Geol 30:211–216

Scheu B, Kueppers U, Mueller S, Spieler O, Dingwell DB (2008) Experimental volcanology on eruptive products of Unzen volcano. J Volcanol Geotherm Res 175(1–2):110–119

Scott JAJ, Pyle DM, Mather TA, Rose WI (2013) Geochemistry and evolution of the Santiaguito volcanic dome complex, Guatemala. J Volcanol Geotherm Res 252:92–107

Shmulovich KI, Yardley BWD, Graham CM (2006) Solubility of quartz in crustal fluids: experiments and general equations for salt solutions and H_2O–CO_2 mixtures at 400–800 °C and 0.1–0.9 GPa. Geofluids 6(2):154–167

Smith R, Sammonds PR, Tuffen H, Meredith PG (2011) Evolution of the mechanics of the 2004–2008 Mt St. Helens

lava dome with time and temperature. Earth Planet Sci Lett 307 (1–2):191–200

Sparks RSJ, Murphy MD, Lejeune AM, Watts RB, Barclay J, Young SR (2000) Control on the emplacement of the andesite lava dome of the Soufriere Hills Volcano by degassing-induced crystallization. Terra Nova 12:14–20

Spieler O, Kennedy B, Kueppers U, Dingwell DB, Scheu B, Taddeucci J (2004) The fragmentation threshold of pyroclastic rocks. Earth Planet Sci Lett 226(1–2):139–148

Stimac J, Hickmott D, Abel R, Larocque ACL, Broxton D, Gardner J, Chipera S, Wolff J, Gauerke E (1996) Redistribution of Pb and other volatile trace metals during eruption, devitrification, and vapor-phase crystallization of the Bandelier Tuff, New Mexico. J Volcanol Geotherm Res 73:245–266

Swanson SE, Naney MT, Westrich HR, Eichelberger JC (1989) Crystallization history of Obsidian Dome, Inyo Domes, California. Bull Volcanol 51:161–176

Voight B, Elsworth D (2000) Instability and collapse of hazardous gas-pressurized lava domes. Geophys Res Lett 27(1):1–4

Wadge G, Voight B, Sparks RSJ, Cole P, Loughlin SC, Robertson R (2013) An overview of the eruption of Soufrière Hills volcano from 2000–2010. In: Wadge G, Robertson R, Voight B (eds) The eruption of Soufriere Hills volcano, Montserrat from 2000 to 2010. Geol Soc Lon Mem (in press)

Watts RB, Herd RA, Sparks RSJ, Young SR (2002) Growth patterns and emplacement of the andesitic lava dome at Soufrière Hills Volcano, Montserrat. In: Druitt TH, Kokelaar BP (eds) The eruption of Soufrière Hills volcano, Montserrat, from 1995 to 1999. Geol Soc Lon Mem 21:115–152

White AF, Hochella MF (1992) Surface chemistry associated with the cooling and subaerial weathering of recent basalt flows. Geochim Cosmochimi Acta 56:3711–3721

Williamson BJ, Di Muro A, Horwell CJ, Spieler O, Llewellin EW (2010) Injection of vesicular magma into an andesitic dome at the effusive–explosive transition. Earth Planet Sci Lett 295:83–90

Yurtmen S, Rowbotham G (1999) A scanning electron microscope study of post-depositional changes in the northeast Nigde ignimbrites, South Central Anatolia, Turkey. Min Mag 63(1):131–141

Zellmer GF, Hawkesworth CJ, Sparks RSJ, Thomas LE, Harford CL, Brewer TS, Loughlin SC (2003) Geochemical evolution of the Soufrière Hills volcano, Montserrat, Lesser Antilles Volcanic Arc. J Petrol 44(8):1349–1374

Particle and Fibre Toxicology (2012) 9:44

The structure of volcanic cristobalite in relation to its toxicity; relevance for the variable crystalline silica hazard

C.J. Horwell, B.J. Williamson, K. Donaldson, J.S. Le Blond, D.E. Damby, L. Bowen

PARTICLE AND FIBRE TOXICOLOGY

RESEARCH Open Access

The structure of volcanic cristobalite in relation to its toxicity; relevance for the variable crystalline silica hazard

Claire J Horwell[1*], Benedict J Williamson[2,3], Ken Donaldson[4], Jennifer S Le Blond[3,5], David E Damby[1] and Leon Bowen[6]

Abstract

Background: Respirable crystalline silica (RCS) continues to pose a risk to human health worldwide. Its variable toxicity depends on inherent characteristics and external factors which influence surface chemistry. Significant population exposure to RCS occurs during volcanic eruptions, where ashfall may cover hundreds of square km and exposure may last years. Occupational exposure also occurs through mining of volcanic deposits. The primary source of RCS from volcanoes is through collapse and fragmentation of lava domes within which cristobalite is mass produced. After 30 years of research, it is still not clear if volcanic ash is a chronic respiratory health hazard. Toxicological assays have shown that cristobalite-rich ash is less toxic than expected. We investigate the reasons for this by determining the physicochemical/structural characteristics which may modify the pathogenicity of volcanic RCS. Four theories are considered: 1) the reactivity of particle surfaces is reduced due to co-substitutions of Al and Na for Si in the cristobalite structure; 2) particles consist of aggregates of cristobalite and other phases, restricting the surface area of cristobalite available for reactions in the lung; 3) the cristobalite surface is occluded by an annealed rim; 4) dissolution of other volcanic particles affects the surfaces of RCS in the lung.

Methods: The composition of volcanic cristobalite crystals was quantified by electron microprobe and differences in composition assessed by Welch's two sample *t*-test. Sections of dome-rock and ash particles were imaged by scanning and transmission electron microscopy, and elemental compositions of rims determined by energy dispersive X-ray spectroscopy.

Results: Volcanic cristobalite contains up to 4 wt. % combined Al_2O_3 and Na_2O. Most cristobalite-bearing ash particles contain adhered materials such as feldspar and glass. No annealed rims were observed.

Conclusions: The composition of volcanic cristobalite particles gives insight into previously-unconsidered inherent characteristics of silica mineralogy which may affect toxicity. The structural features identified may also influence the hazard of other environmentally and occupationally produced silica dusts. Current exposure regulations do not take into account the characteristics that might render the silica surface less harmful. Further research would facilitate refinement of the existing simple, mass-based silica standard by taking into account composition, allowing higher standards to be set in industries where the silica surface is modified.

Keywords: Cristobalite, Volcano, Respiratory health, Crystalline silica, Volcanic ash, Soufrière Hills, Quartz, Variable hazards, Regulations

* Correspondence: claire.horwell@durham.ac.uk
[1]Institute of Hazard, Risk & Resilience, Department of Earth Sciences, Durham University, Science Labs., South Road, Durham DH1 3LE, UK
Full list of author information is available at the end of the article

Background

Exposure to respirable crystalline silica (RCS) has been known for centuries to be detrimental to health, and is linked to respiratory diseases such as silicosis, lung cancer and tuberculosis. However, when classifying crystalline silica as a Group 1 carcinogen, the IARC Working Group recognised that silica dusts are variably hazardous and that their carcinogenicity may depend on inherent characteristics of the silica, and/or external factors which affect the particle surface and biological activity [1]. The UK Health & Safety Executive assessed the potential of RCS to cause silicosis and concluded that all forms of RCS dusts of occupational relevance have this potential but that, again, the fibrogenicity will be influenced by the physicochemical characteristics of the dust [2].

Crystalline silica occurs as five main polymorphs with quartz, cristobalite and tridymite being more reactive and cytotoxic than coesite and stishovite [2]. Quartz is the most common mineral in the continental crust and is the most commonly-encountered polymorph. Occupational exposure to the other polymorphs is more unusual but cristobalite exposure occurs in the ceramics industry through conversion of quartz in industrial furnaces [3], and through crystallization from amorphous diatomaceous earth during calcination [4]. *In vitro* experiments have suggested that cristobalite and quartz are comparably cytotoxic, inflammogenic and fibrogenic [5-8].

In this paper, we investigate the structural side of the 'structure-toxicity relationship' for RCS generated during volcanic eruptions. Volcanoes are a major source of natural silica and 9% of the world's population lives within 100 km of a historically active volcano [9]. The discovery of substantial quantities of RCS in volcanic ash from both the 1980 eruption of Mt St Helens, USA and the eruption of Soufrière Hills volcano (SHV), Montserrat, West Indies (1995 onwards), resulted in widespread concern regarding exposure to volcanic ash over prolonged durations [10,11]. As volcanoes can mass-produce RCS, in close association with other minerals during eruptions, this presents a unique opportunity to characterise mineralogical factors which could influence respiratory toxicity.

Formation of cristobalite in volcanic environments

The mass formation of crystalline silica in volcanic environments usually follows lava dome eruptions where viscous, silicic magma is extruded from the volcano at ~800°C, forming a dome of rock in the crater. Magmatic vapours circulate through the dome depositing crystalline silica, as cristobalite, in cracks and pore spaces [10,12]. Horwell et al. [12] observed two forms of vapour-phase cristobalite in the pore spaces of SHV dome rock: prismatic crystals and platy, hexagonal crystals. Both display a distinctive 'fish-scale' cracked texture when observed in thin section (Figure 1). Volcanic glass in the lava may also devitrify, again forming cristobalite, or quartz if devitrification is influenced by hydrothermal fluids [10,12]. Cristobalite may also form in the volcanic edifice by deposition and alteration from circulating hydrothermal fluids. Lava domes are inherently unstable and frequently collapse, fragmenting the rock and forming pyroclastic density currents (PDCs, also known as pyroclastic flows), which move rapidly down the volcanic flanks. A 'co-PDC' ash plume lofts from the PDC, which is enriched in fine particulate and, in particular, RCS [13] and may travel hundreds of kilometres, depositing ash of which ~20-40% is composed of the 'thoracic' fraction (< 10 μm) and ~10-20% is 'respirable' (< 4 μm) [14]. At SHV, cristobalite comprises up to 23 wt. % of the bulk ash [15]. Quartz may be present in ash from intermediate to felsic (high SiO_2) volcanoes as crystals which grow in the ascending magma

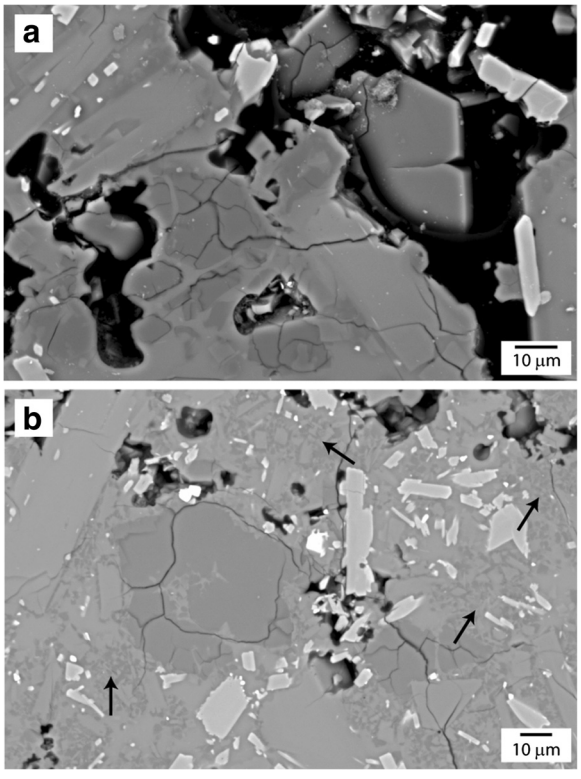

Figure 1 Backscattered electron (BSE) images showing cristobalite textures in thin section. a) Cristobalite crystal showing typical 'fish-scale' cracking in MVO1236. The boundary between the fish-scale cristobalite and surrounding groundmass is unclear. One platy crystal is protruding from a pore to the right, centre of the image; **b**) 'Feathery' groundmass texture (indicated by arrows) in MVO617, composed of cristobalite, glass and plagioclase feldspar (Horwell et al. [12]) with associated fish-scale cristobalite which, in this case, is probably a product of extensive devitrification and also has a diffuse boundary.

(phenocrysts) on its journey from the magma chamber to the surface. A summary table of the different habits of crystalline silica found at dome-forming volcanoes is found in [12].

Fragmentation of the lava produces freshly-fractured mineral surfaces, a factor which is known to increase the surface reactivity and pathogenicity of quartz [16-20] but the effects of which are less well characterised for cristobalite. Horwell et al. [21] showed that the surface reactivity of SHV volcanic ash is substantially reduced in aged, weathered samples, in comparison to fresh ash, and is enhanced in ground samples.

Dome-forming eruptions are often long-lived (e.g. SHV has been erupting since 1995) so it is imperative that the respiratory hazard of volcanic cristobalite is characterised. Although cristobalite has comparable toxicity to quartz, far fewer epidemiological and clinical studies have been carried out on industrial cristobalite exposure to support the laboratory conclusions, mainly because of the limited workplace exposures specific to cristobalite (e.g., pottery and refractory brick workers are usually co-exposed to quartz and cristobalite [1]). The diatomaceous earth industry, however, produces cristobalite from amorphous silica during calcination of diatomite, rather than a conversion from quartz to cristobalite as is the case with ceramics. We have found 24 epidemiological and clinical studies on diatomaceous earth workers in the literature; most have found a dose-response association between cristobalite exposure and lung cancer mortality, non-malignant respiratory diseases (NMRD) mortality and silicosis e.g. [22-25].

At both SHV and Mt St Helens, *in vivo* (inhalation and instillation) and *in vitro* toxicological studies were carried out to determine the likely outcomes of inhaling cristobalite-laden ash reviewed by [26,27]. Differing study designs made comparisons challenging; however, in general, the ash was not found to cause the rapid *in vivo* or *in vitro* response expected of a crystalline silica-rich dust e.g. [28,29]. Of the 19 studies on Mt St Helens ash (9 *in vitro*; 6 instillation and 4 inhalation studies), the exceptions were inhalation studies where very high doses of ash (50-100 mg m^{-3}) were administered over long durations (up to 24 months), causing fibrosis and lesions [30,31]. For SHV, it was concluded that the ash may pose a similar health risk to mixed coal mine dust [28]. This conclusion was based on *in vivo* studies carried out over relatively short time periods < 49 weeks e.g. [32], and one must be cautious in interpretation of these data as there is a mean latency period for chronic silicosis of around three decades, depending on exposure [33]. A risk assessment of the long-term, cumulative exposure to cristobalite at SHV concluded that, assuming continuing volcanic activity, the risk of silicosis for gardeners (highest occupational exposure) after 20 years of continuous exposure is 2 – 4% [34], based partly on the toxicology data. Overall, evidence suggests that the ash represents a relatively low hazard. Given the quantities of RCS in the ash, we sought to determine the structural factors that could be masking the toxicity of volcanic cristobalite.

The variability of the RCS hazard in workplaces is still a key issue, especially as regulations take a 'one size fits all' approach to crystalline silica [35]. Studies on the RCS hazard, such as the current structural work on volcanic ash, will add to the growing weight of evidence that inherent characteristics and external factors can be measured, which may provide an opportunity to refine RCS exposure limits to take such factors into account.

Potential factors affecting toxicity

The pro-inflammatory effects of quartz may be modified by addition of a range of substances that prevent the surface from producing the classic quartz inflammatory response [36,37]. In particular, treatment with Al salts, such as Al lactate, has been shown to lower quartz toxicity [38-40]. A feature of the SHV cristobalite (SiO_2) is the presence of low levels of aluminium (Al) and sodium (Na) as indicated from SEM energy dispersive X-ray spectroscopy (SEM-EDS) of individual cristobalite ash particles (see minor peaks for Al and Na in addition to the Si and O peaks in the crystalline silica EDS spectrum in Horwell et al. [41] Figure 2). Therefore, the presence of Al and Na in close association with RCS in volcanic ash could be important in passivating cristobalite. We propose four theories for the involvement of these elements in modulating the cristobalite hazard in SHV ash:

1. **Crystal composition.** The reactivity of particle surfaces could be reduced due to co-substitutions of Al and Na for Si in the cristobalite structure as the crystals form. Cristobalite has an open lattice structure which readily permits substitution of Si^{4+} by Al^{3+} with charge balancing by other cations such as Na^{+} or K^{+} [42].
2. **Heterogeneous surface.** During dome collapse, fragmentation of dome lava is unlikely to result in the production of fresh cristobalite crystal surfaces. Cristobalite ash particles may have fragments of other volcanic phases (plagioclase, glass, salts and other vapour-phase precipitates) inter-grown or adhered to their surfaces which will decrease the surface area of cristobalite available for reactions in the lung. Both feldspar and glass are Al-rich. The grain boundary between large (> 10 μm) 'fish-scale' cristobalite patches and vitreous groundmass is often diffuse, with cristobalite appearing to penetrate and merge with the groundmass [12]. In addition, sub-micron-scale 'feathery' cristobalite crystallites, along

with plagioclase feldspar, form as devitrification patches within groundmass glass [12].

3. **Annealed surface.** The surface of cristobalite particles could be occluded by an annealed glass layer (known as a Beilby layer [43]). Alternatively (or, in addition), during formation, if crystallization begins above the solidus when pores are still plastic (e.g. [44]) or during fragmentation, cristobalite particles may become coated in a nano-scale layer of amorphous volcanic glass.
4. **Silicate dissolution.** The mixture of cristobalite and other silicate and glass particles, in a heterogeneous dust, may affect the hazard. Proximity of cristobalite to soluble phases such as glass, following lung deposition and phagocytosis, could affect the RCS surface.

Theories 1-3 address 'inherent characteristics' of the RCS particles whereas theory 4 addresses 'external factors' which may influence the hazard in the lung. In this study we use mineralogical techniques to address theories 1 to 3. To address theories 1 and 2 we investigated 9 samples of SHV dome rock, mainly collected from the Montserrat Volcano Observatory (MVO) archives (see Table 1). Samples are described in detail in Horwell et al. [12]. To address theories 2 and 3 we analysed SHV dome-collapse ash samples, also detailed in Table 1.

Results

The extensive collection of well characterised dome rock and ash from the long-lived SHV eruption [12], held at MVO, provides the best archive of material to examine the theories for variable toxicity offered above.

Elemental composition of cristobalite

From electron microprobe analyses of cristobalite crystals in dome rock, we found that both prismatic and platy cristobalite forms were not pure SiO_2, containing up to ~ 3 wt. % Al_2O_3 (Figure 2 and Table 2). The prismatic cristobalite contained 0.7 - 2.1 wt. % Al_2O_3 and the platy cristobalite from 1.3 to 2.7 wt. % Al_2O_3. Comparison of these datasets by Welch's *t*-test yielded a *p*-value of 0.0292, indicating that the null hypothesis – that there is no difference in the data – can be rejected at the 5% level, hence the amount of Al_2O_3 in the platy and prismatic cristobalite forms is significantly different. The devitrification quartz (in samples MontR1, MVO1236 and MVO945), had Al_2O_3 values of 0.1 to 0.6 wt. %, and two quartz phenocrysts contained minimal Al_2O_3.

Sodium was also detectable in cristobalite, at levels up to 1.1 wt. % Na_2O. The prismatic crystals contained 0 – 1.1 wt. % Na_2O compared with 0.7 – 1.1 wt. % Na_2O in the platy crystals. These data are also significantly different at the 5% level (p=0.0301). The platy cristobalite, in general, also contained slightly elevated levels of other major element oxides (e.g. K_2O, Fe_2O_3, CaO and TiO_2).

Table 1 Sample summary with information on crystalline silica features observed by Horwell et al. [12]

Sample No.	Date of collapse/ eruption	Date of collection	Description	Eruption Information	Crystalline silica type			
					Prismatic	Platy	Devit. cristob.	Devit. quartz.
Dome rock:								
MVO819	174 k.a. BP	15/2/98	Dome lava; very dense, grey/brown	Ancient sample from old complex	✓ but rare	✓	✓	✓
MVO945	400 a BP	?	Dome lava; Dense, red/brown	Ancient simple from Castle Peak	✓	×	×	✓
MVO287	21/9/97	21/9/97	Juvenile block; vesicular; light grey	From dome collapse deposit	✓	×	✓	×
MVO288	21/9/97	21/9/97	Juvenile block; frothy, light grey	From dome collapse deposit	✓ but rare	×	×	×
MVO617	21/9/97	16/5/98	Dome lava; Dense; Green/dark grey	From dome collapse deposit	✓	×	✓	×
MVO332	26/12/97	4/1/98	Dome lava; Vesicular; pale grey	From 'Boxing Day' collapse deposit	✓	×	×	×
MVO1236	12/7/03	1/8/03 – 15/11/03?	Dome lava; Dense; pale grey	From dome collapse deposit (full collapse)	✓	✓	✓	✓
MVO1406	20/5/06	?	Dome lava; dense; pale grey	From dome collapse deposit	✓	×	✓	×
MontR1*	20/5/06	22/6/06	Dome lava, dense, altered, red	From dome collapse deposit	✓	✓	×	✓
Ash:								
MRA5/6/99	05/6/99	05/6/99	Co-PDC ash	Respirable (< 4 μm) fraction				
MBA12/7/03	12/7/03	12/7/03	Co-PDC ash	Bulk ash from which cristobalite separated				

'Prismatic' = euhedral cristobalite; 'Platy' = platelets of cristobalite; 'Devit. cristob.' = cristobalite during glass devitrification; 'Devit. quartz' = quartz formed (probably through phase transition from cristobalite) when the glass is totally devitrified.
*Collected by BW from deposit rather than archive.
MVO sample numbers assigned by the Montserrat Volcano Observatory.

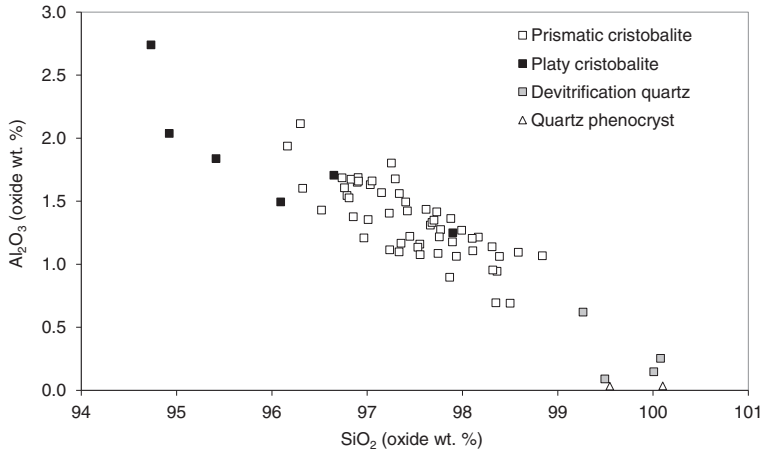

Figure 2 Al_2O_3 vs. SiO_2 (wt. %) for prismatic and platy cristobalite, and devitrified and magmatic quartz. Data derived from electron microprobe analyses of individual crystals for all dome-rock samples. No data for devitrification cristobalite as 'feathery' crystals were too small for the resolution of the microprobe.

Cristobalite and associated phases

Observations of sectioned dome rock by Scanning Electron Microscopy (SEM) confirmed that cristobalite is intimately inter-grown with surrounding mineral phases and glass (Figure 1a). Additionally, devitrification crystallites of cristobalite are sub-micron sized, and are closely associated with glass and feldspar (composition confirmed by Horwell et al. [12]) (Figure 1b). It was also observed that, whilst whole cristobalite crystals in the dome rock are usually 20-50 μm diameter (i.e. within the 'inhalable' sub-100 μm fraction, but larger than the 'thoracic' (sub-10 μm) or 'respirable' (sub-4 μm) fractions), 'fish-scale' cracking divides the cristobalite into roughly sub-10 μm segments (as can be seen in Figure 1a and b).

Observation of sectioned and polished cristobalite ash particles by SEM showed that: a) some particles are solely composed of cristobalite (Figure 3a); b) some particles are a mixture of cristobalite plus feldspar, glass or other volcanic minerals, either from break up of vapour-phase crystals and associated groundmass (Figure 3b) or devitrification patches (Figure 3c); c) some particles have a cristobalite core but also have patches of other minerals or glass adhered to their surface (Figure 3d). All 'rims' appeared to be patches of groundmass which had remained attached to the cristobalite during fragmentation. No cristobalite crystals appeared to be coated with volcanic glass (i.e. melt adhering to crystal surfaces within plastic vesicles prior to solidus).

Analysis, by both TEM-EDS and SEM-EDS, did not reveal obvious changes in cristobalite composition within nano- or micro-transects from crystal rim towards crystal core (Figure 4) with no observable higher concentration (or deficit) of Al and other elements at the grain

Table 2 Representative electron probe results for cristobalite and quartz phases

	Prismatic cristobalite			Platy cristobalite			Devitrification quartz			Quartz phenocryst
	MVO617	MontR1	MVO1406	MVO819	MVO819	MVO1236	MontR1	MontR1	MVO945	MVO287
Na_2O	1.14	0.30	0.41	0.98	0.70	0.96	0.14	n.d.	n.d.	n.d.
Al_2O_3	1.94	1.42	0.96	2.74	1.50	1.71	0.62	0.09	0.25	n.d.
SiO_2	96.16	97.42	98.32	94.73	96.10	96.65	99.27	99.49	100.08	100.10
MgO	n.d.	0.02	n.d.	0.04	0.12	n.d.	0.02	n.d.	n.d.	n.d.
K_2O	0.01	0.03	0.23	0.60	0.26	n.d.	0.03	0.13	n.d.	0.01
CaO	0.08	0.29	0.02	0.12	0.08	0.06	0.47	0.22	0.05	n.d.
TiO_2	0.23	0.09	0.17	0.17	0.17	0.15	0.11	0.08	0.08	0.03
MnO	n.d.	n.d.	n.d.	n.d.	n.d.	n.d.	n.d.	n.d.	n.d.	n.d.
FeO	0.20	0.20	0.09	0.34	0.37	0.19	0.16	0.29	0.15	n.d.
Total	99.79	99.77	100.19	99.75	99.27	99.75	100.81	100.12	100.64	100.21

Data are in oxide wt. %. n.d. = not detected.

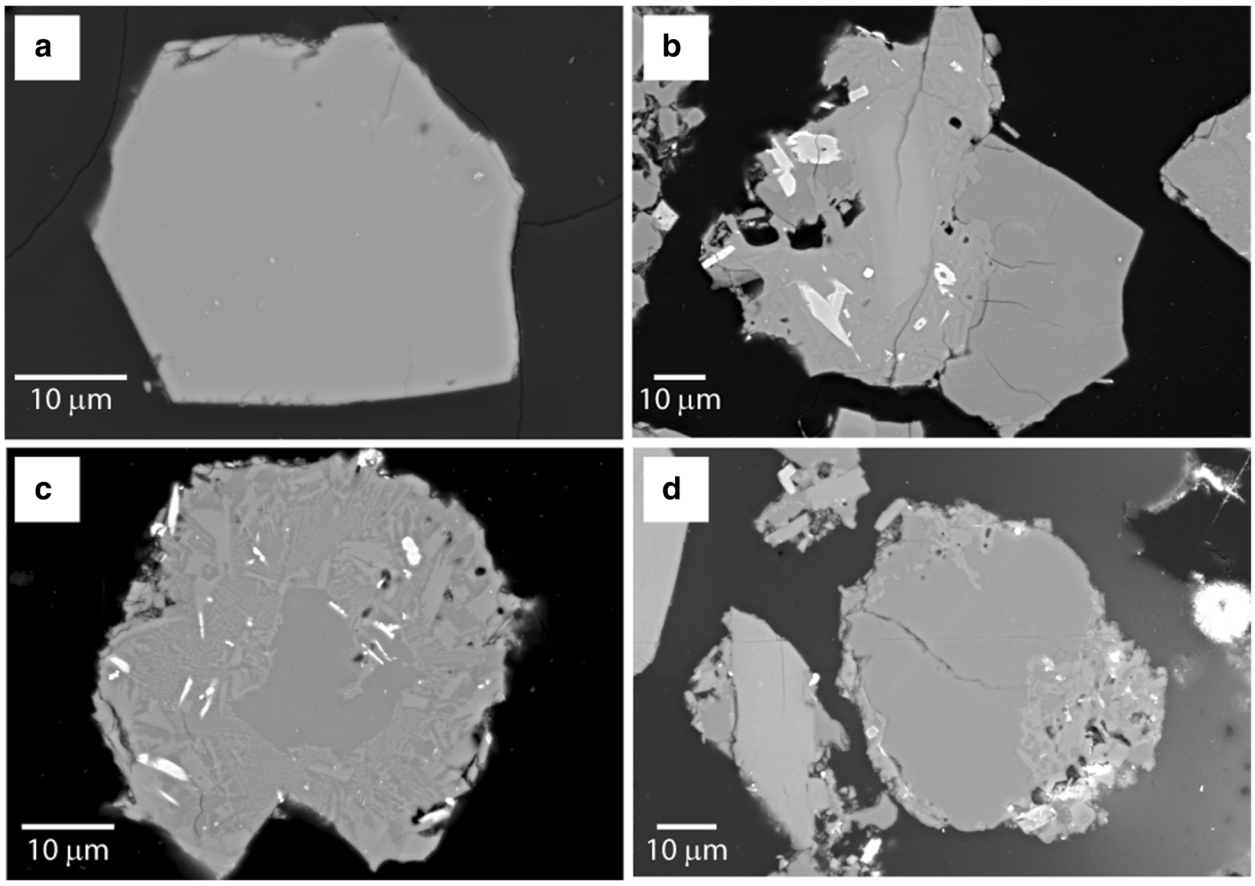

Figure 3 BSE images of resin mounted and polished cristobalite particles separated from volcanic ash sample MBA12/7/03. a) A particle composed solely of cristobalite; **b**) A particle composed of a cristobalite crystal still attached to the groundmass patch from which it nucleated; **c**) A particle of 'feathery' devitrified groundmass with a totally-devitrified cristobalite patch in the centre; **d**) A particle of cristobalite with a 'rim' of glassy groundmass.

margin. For the TEM-EDS transect, the observed decrease in SiO_2 towards the rim is attributed to reduced crystal depth towards the edge of the crystal. The minor increase in Al, Fe, Cl and K at the rim correspond exactly to the increase in Pt and are probably associated with an increase in background noise due to the thickness of the Pt strip. We were unable to observe changes in crystallinity by TEM (i.e. a nano-scale amorphous coating resulting either from annealing of the crystal surface or an artefact of the FIB thinning process) towards the samples' rims. The quartz Beilby layer has been determined to be between 0.03 and 0.8 μm [45,46] thick.

Discussion

Factors affecting cristobalite toxicity in Soufrière Hills ash

Electron microprobe analyses of *in situ* vapour-phase cristobalite crystals in dome rock confirmed that the Soufrière Hills cristobalite is not pure SiO_2 (theory 1). The fact that Al has been shown to be the dominant substituted cation in cristobalite is critical for understanding its toxic potential.

The toxicological effects of cristobalite surface modification have not been previously studied, but it is known that the structure of cristobalite allows substitutions of Al for Si [42]. The mechanism by which Al interacts with quartz is not well understood though (it does not have the open lattice structure of cristobalite or tridymite); however, in acidic conditions, Al is thought to insert into the quartz crystal lattice [37] at discrete points where defects enable this bonding to occur [47]. Duffin et al. [39] treated laboratory standard DQ12 quartz surfaces with Al lactate which had the effect of inhibiting the production of cytokines from macrophages and epithelial cells. The release of reactive oxygen species, capable of causing mutations in the cells of the lung, a likely mechanism for the development of cancer [48], would also be affected if the silica surface were affected by Al. Analogously, the presence of Al in the cristobalite structure and, therefore, at discrete points at its surface,

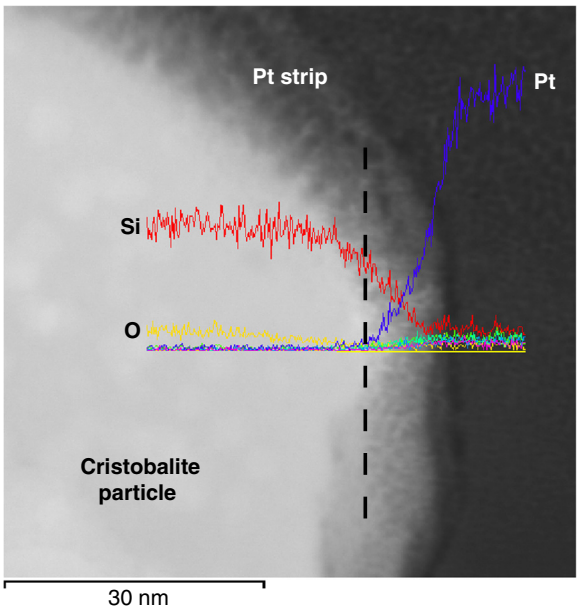

Figure 4 FEG-TEM image of thinned edge of a cristobalite crystal from volcanic ash sample MRA5/6/99. The platinum (Pt) strip shows as dark grey on the right hand side of the image with the mottled area being attributed to crystal thinning or background scattering from the Pt strip. The dashed black line represents the approximate boundary between the crystal and the strip. Superimposed on the image are the EDS results from a 50 nm transect from rim towards the core of the crystal. Pt = dark blue; Si = red; Al = green; K = pink; Fe = turquoise; Cl = light blue; O = yellow.

could have similar effects. To test the toxicity side of this structure-toxicity relationship, we are now synthesising cristobalite in the laboratory with controlled levels of Al and Na. The resulting powders will be exposed to alveolar macrophages and cytotoxic, metabolic and pro-inflammatory effects measured to test our theory that structural substitutions in cristobalite affect toxic response.

These structure substitutions may also control crystal morphology. The platy cristobalite contains significantly more Al and Na than prismatic crystals and, hence, at this level of substitution in the crystal structure, prismatic crystal formation may be inhibited. This leads to the possibility that differing cristobalite morphologies may also be variably pathogenic, depending on their Al content (i.e. platy crystals would be less toxic). However, Horwell et al. [12] did not observe solely platy crystals in these dome rock samples – they were always seen in association with prismatic and devitrification cristobalite (Table 1) - so it is unlikely that exposure would ever be restricted to the less-toxic variety.

A second mechanism for generation of cristobalite particles with heterogeneous surfaces is through dome-collapse fragmentation processes, generating particles which are mixed phases of cristobalite and other minerals (theory 2). Our results show this to be the case, as particles (in cross-section) are rarely observed to be solely comprised of cristobalite. These mixed-phase particles likely derive from: 1) vapour-phase crystals which were attached to (and will have nucleated from) groundmass or phenocrysts adjacent to the pore spaces, so we may expect that at least one surface of the vapour-phase cristobalite may have a 'rim' composed of other materials; or 2) break up of devitrified patches of glass where we would expect to see particles composed of feathery crystallites of cristobalite, plagioclase and a glassy matrix. These associated phases give an additional explanation as to why Horwell et al. [41] found that crystalline silica ash particles contain minor amounts of other elements (by SEM-EDS). It is also likely that many whole particles identified as plagioclase or glass by SEM-EDS e.g. by [41] would contain a crystalline silica component.

We did not observe evidence for any cristobalite surfaces being occluded by a thin coating of volcanic glass, clay, or an annealed amorphous layer (theory 3). In studies assessing the toxicity of coal dust, low-rank coals have been observed to contain crystalline silica coated with clays [49]. The clays, and associated soluble extracts, in the coal mine dust are thought to inhibit the cellular reactivity of quartz [50]. Fresh volcanic ash does not contain clay; however, old ash deposits, which may be quarried for volcanic aggregate, may well contain clays derived from chemical weathering of feldspar. Therefore, studies assessing the toxicity of crystalline silica-rich volcanic-derived quarry dust should assess whether silica occlusion is occurring.

When considering health, we can now say that, for the Soufrière Hills ash, there are two inherent factors which may act to reduce the toxicity of cristobalite: 1) the cristobalite is not pure SiO_2 (theory 1); 2) heterogeneous RCS surfaces will be produced by fragmentation of devitrified areas and will consist of vapour-phase cristobalite and adhered fragments of groundmass (theory 2). All of these processes involve the introduction of Al to the RCS surface.

This evidence of surface modification and heterogeneity provides an explanation as to why the predicted toxicity is not observed in reality e.g. [28,29] and also why SHV ash does not generate silica surface radicals (e.g., Si• and Si–O•) [21]. However, there is also evidence here for the formation of reactive RCS volcanic particulate; the cracked, 'fish-scale' cristobalite provides weakened planes for the generation of inhalable sub-particles (< 15 μm diameter) of cristobalite on fragmentation and it appears that these surfaces remain exposed (i.e. no glass coating). The exposed crack intersections and twin planes at the surface of a crystal can be highly reactive [18] and may

host transition metal ions, giving a possible source area for hydroxyl radical activity (HO•) [21]. In addition, in areas of extensive devitrification, cristobalite can recrystallize to quartz, which may form up to 5 wt. % of dome rock in altered samples [12]. The toxicity of quartz particles may be different to cristobalite and, therefore, a variably-altered volcanic dome may produce ash with a range of toxicities.

Considering external factors, the heterogeneity of volcanic ash, with the inevitable close association of cristobalite and Al-rich mineral particles (such as feldspar) in the lung could also contribute to impairment of RCS toxicity (theory 4). Diffusion of elements from dissolving/leaching particles to the RCS surface is a possibility on the lung surface but this is likely to be greatly increased within the acidic lysosomal environment following phagocytosis by macrophages, where several particles may be stored in close proximity. In industry, quartz is also extracted with other minerals (e.g. clays), for example, during quarrying and industrial processing of sedimentary rock. For coal-mine dust, it is believed that, where quartz levels are below 10 wt. %, the total mass dust exposure is the best correlate with coal workers' pneumoconiosis (CWP) [51,52]. However, above 10 wt. %, silicosis and rapid progression of CWP may occur [53]. The lack of silica reactivity at low concentrations cannot only be due to occlusion of RCS surfaces by clays, as discussed above. When DQ12 quartz is pre-incubated with an extract of coal-mine dust, haemolysis drops from 90% in non-incubated DQ12 quartz to virtually zero in incubated samples, demonstrating that there is an external control, such as diffusion of ions to the quartz surface [50].

Determining if volcanic cristobalite toxicity is affected by external factors such as accompanying minerals is challenging as volcanic cristobalite cannot be isolated from the other minerals without affecting the surfaces of the particles (for example through heavy liquid separation or boiling the ash in phosphoric acid). Additionally, several minerals in volcanic ash are iron rich (e.g. amphiboles, pyroxenes and oxides) and Horwell et al. [21,54] have shown that deleterious, iron-catalysed hydroxyl radicals can be generated by these minerals in Soufrière Hills ash, providing a possible separate mechanism for toxicity.

The variable hazard of RCS

Since IARC classified crystalline silica as a carcinogen, with the proviso that hazard was likely to vary depending on the characteristics of the dust [1], many authors have attempted to quantify the variability of the silica hazard. Studies have shown how cellular responses related to inflammation and fibrosis vary amongst different polymorphs and dust sources, and even amongst samples from the same source e.g. [48,55]. Donaldson and Borm [56] have clarified that the surface reactivity of quartz is key, and that the ability of particles to induce oxidative stress could be modified by substances which affect its surface, including those derived from accompanying minerals. Therefore, toxicity could vary dramatically depending on the origin of the silica. Other authors have suggested that transient piezoelectric charges on freshly-fractured surfaces or the hydrophilicity of the surface may play a role in reactivity [57,58].

In this study, we have investigated the mineralogical features which may modulate RCS toxicity. In the case of volcanic ash, we have shown evidence that the toxicity of RCS is likely affected by 'inherent characteristics' of the silica and hypothesized that 'external factors' may also act to hinder the reactivity of RCS. However, Fubini [37], postulated that the inherent characteristics and external factors may be active at different stages in disease development, or be involved in different disease pathways. There is also evidence that different disease mechanisms (e.g. inflammation and DNA damage) involve different properties of the silica particle [59,60].

In occupational settings, RCS surfaces may be exposed and activated by grinding or milling [20,61,62], modified by the environment in which they are ground [18] and altered by heating (e.g., for fly ash and biogenic silicas) [63,64]. These processes will variably alter their size, morphology, crystallinity, surface charges, hydrophilicity and external contaminants. However, the present investigation shows that the original mineralogy of the silica and its host material may also significantly influence its toxicity. Characterisation of these parameters can therefore shed light on the variable toxicity of respirable crystalline silica.

Conclusions

This study has shown that the surface properties and, therefore, toxicity of volcanic cristobalite particles are at least partly controlled by their geological origin. The results provide a compelling explanation for the anomalous toxicology data for cristobalite-rich volcanic ash and also highlight that inherent characteristics of industrial silica should be further studied. If RCS could be classified by its surface chemical composition and structure in relation to the factors that modify its hazard, then the single silica Occupational Exposure Limit (or Threshold Limit Value) currently adhered to across all industries could be modified to more closely represent the actual hazard of a particular RCS exposure.

Methods

Theory 1 (crystal composition) was addressed by electron microprobe (Cameca SX100 wavelength dispersive electron probe microanalyser (with PeakSight software)

at the University of Cambridge, UK. See Additional file 1 for detailed methods) to determine the composition of vapour-phase 'prismatic' (n = 55) and 'platy' (n = 8) cristobalite crystals, devitrification quartz (n = 4) and magmatic quartz crystals (for comparison) (n = 2). Only data with totals of 100 ± 0.8% were used in the study, as is common practice for anhydrous rock studies. Dome rock was used to provide large, flat, polished areas of crystals for analysis, which are harder to obtain from ash particles. The statistical difference in the compositions of prismatic and platy cristobalite crystals was determined using Welch's two-sample t-test.

To address theories 2 (heterogeneous surface) and 3 (annealed surface), we adopted two strategies: 1) imaging minerals in thin sections of dome rock to determine the association of cristobalite with other local minerals; 2) imaging individual cristobalite ash particles in cross section to distinguish a cristobalite 'core' and a potentially nano-scale 'rim' of other minerals or glass.

Imaging of dome rock was carried out on carbon coated (30 nm) thin sections in BSE mode, and combined with elemental analysis on a LEO 1455VP SEM with Oxford Instruments INCA Energy Dispersive (EDS) X-ray analysis system at the Natural History Museum, London (working distance = 14-15 mm, accelerating voltage = 20 kV).

Several methods were developed for thin sectioning individual volcanic cristobalite crystals and two were implemented here. See Additional file 1 for full details.

1) Individual cristobalite crystals were thinned by focussed ion beam in a dual beam FIB-SEM (FEI Helios Nanolab at Durham University) to make them electron transparent [65]. The rim (protected from the FIB by a platinum strip deposited by gas injection) was then analysed by TEM-EDS (JEOL 2100F FEG-TEM with Oxford INCAx-sight Si(Li) EDS software at 200 kV) over several 50 nm transects from the rim into the crystal. However, this time-intensive technique was not suitable for mass analysis of cristobalite crystals so just two cristobalite crystals were analyzed.

2) Cristobalite crystals were separated from ash sample MBA12/7/03 using heavy liquids and mounted in a resin block. The polished blocks were carbon coated (~30 nm) and analysed in the Hitachi SU-70 FEG-SEM at Durham University. High-resolution SEM allowed examination of hundreds of sections through cristobalite crystals with ~5 nm resolution. The Oxford Instruments EDS system (INCAx-act LN2-free analytical Silicon Drift Detector) allowed verification of particle elemental compositions e.g. cristobalite (almost entirely Si and O, with minor Al and Na), plagioclase feldspar (Si, O, Al, Na and Ca) and glass (Si, O and minor Al, K, Na, Ca and Fe), as defined by Horwell et al. [41] as well as compositional variations along 'rim' to 'core' transects (over a distance of 5-10 μm).

Additional file

Additional file 1: Additional methods. 1) Electron microprobe detailed methods; 2) Additional methods for producing sections through ash particles; 3) Method for separation of cristobalite from ash using heavy liquids.

Abbreviations

RCS: Respirable crystalline silica; IARC: International Agency for Research on Cancer; SEM: Scanning electron microscopy; TEM: Transmission electron microscopy; FIB: Focussed ion beam; FEG: Field emission gun; EDS: Energy dispersive X-ray spectroscopy; BSE: Backscattered electron; PDC: Pyroclastic density current; SHV: Soufrière Hills volcano, Montserrat.

Competing interests

There are no financial or non-financial competing interests.

Authors' contributions

CH acquired funding, designed the study, acquired, analysed and interpreted data and wrote the manuscript. BW helped design the study, acquired, analysed and interpreted data and assisted with manuscript preparation. KD assisted with manuscript preparation, contributing specific expertise in toxicological work on RCS. JLB acquired data and assisted with manuscript preparation. DD acquired data and assisted with manuscript preparation. LB developed sample preparation techniques and assisted with manuscript preparation. All authors read and approved the final manuscript.

Authors' information

CH is the founding Director of the International Volcanic Health Hazard Network (www.ivhhn.org) and the UK Natural Dust & Health Network (www.dur.ac.uk/claire.horwell/ukndhn).

Acknowledgements

The work of CH was supported by a NERC Postdoctoral Research Fellowship (Grant No. NE/C518081/2). JLB acknowledges a NERC CASE Studentship while at the University of Cambridge, UK (NER/S/A/2006/14107), and DD acknowledges a Moyes Foundation studentship. We are grateful to Sue Loughlin, Thomas Christopher and Montserrat Volcano Observatory staff for access to MVO collections and guidance in the field. We thank Chris Hayward, formerly of University of Cambridge, now at University of Edinburgh, UK, for assistance and training on the electron microprobe. Thanks to Budhika Mendis, GJ Russell Microscopy Facility, Durham University, for TEM work and Ed Llewellin (Durham University) for statistical expertise. Thanks also to Jeremy Skepper (University of Cambridge) for early development of particle sectioning techniques. We are grateful to Dr Peter Baxter (University of Cambridge) for reading a draft of the manuscript and to the three anonymous reviewers.

Author details

[1]Institute of Hazard, Risk & Resilience, Department of Earth Sciences, Durham University, Science Labs., South Road, Durham DH1 3LE, UK. [2]Camborne School of Mines, College of Engineering, Mathematics and Physical Sciences, University of Exeter, Cornwall Campus, Penryn TR10 9EZ, UK. [3]Department of Earth Sciences, Natural History Museum, Cromwell Road, London SW7 5BD, UK. [4]The Queen's Medical Research Institute, The University of Edinburgh/MRC Centre for Inflammation Research, 47 Little France Crescent, Edinburgh EH16 4TJ, UK. [5]Brighton and Sussex Medical School, University of Sussex, Brighton, East Sussex BN1 9PX, UK. [6]Durham GJ Russell Microscopy Facility, Durham University, Durham DH1 3LE, UK.

Received: 11 July 2012 Accepted: 31 October 2012
Published: 19 November 2012

References

1. International Agency for Research on Cancer: *Silica, some silicates, coal dust and para-aramid fibrils*. Lyon: International Agency for Research on Cancer; 1997.

2. Health and Safety Executive: *Respirable crystalline silica - phase 1. Variability in fibrogenic potency and exposure-response relationships for silicosis*. Sudbury: Health and Safety Executive; 2002.
3. Haklader ACD, Roberts AL: **Transformation of quartz to cristobalite.** *J Am Ceram Soc* 1961, **44:**35–41.
4. Ghiazza M, Gazzano E, Bonelli B, Fenoglio I, Polimeni M, Ghigo D, Garrone E, Fubini B: **Formation of a vitreous phase at the surface of some commercial diatomaceous earth prevents the onset of oxidative stress effects.** *Chem Res Toxicol* 2008, **22:**136–145.
5. Hemenway DR, Absher MP, Trombley L, Vacek PM: **Comparative clearance of quartz and cristobalite from the lung.** *Am Ind Hyg Assoc J* 1990, **51:**363–369.
6. Meldrum M, Howden P: **Crystalline silica: variability in fibrogenic potency.** *Ann Occup Hyg* 2002, **46:**27–30.
7. Driscoll KE: **The toxicology of crystalline silica studies in vitro.** *Appl Occup Environ Hyg* 1995, **10:**1118–1125.
8. Fubini B: **Health effects of silica**. In *The surface properties of silicas*. Edited by Legrand AP. Chichester: John Wiley & Sons Ltd, England; 1998:415–464.
9. Small C, Naumann T: **Holocene volcanism and the global distribution of human population.** *Environ Hazards* 2001, **3:**93–109.
10. Baxter PJ, Bonadonna C, Dupree R, Hards VL, Kohn SC, Murphy MD, Nichols A, Nicholson RA, Norton G, Searl A, *et al*: **Cristobalite in volcanic ash of the Soufriere Hills Volcano, Montserrat, British West Indies.** *Science* 1999, **283:**1142–1145.
11. Dollberg DD, Bolyard ML, Smith DL: **Evaluation of physical health effects due to volcanic hazards: crystalline silica in Mount St. Helens volcanic ash.** *Am J Public Health* 1986, **76:**53–58.
12. Horwell CJ, Williamson BJ, Llewellin EW, Damby DE, Le Blond JS: **Nature and formation of cristobalite at the Soufrière Hills volcano, Montserrat: implications for the petrology and stability of silicic volcanic domes.** *Bull Volcanol* 2013, **75:**696.
13. Horwell CJ, Braña LP, Sparks RSJ, Murphy MD, Hards VL: **A geochemical investigation of fragmentation and physical fractionation in pyroclastic flows from the Soufriere Hills volcano, Montserrat.** *J Volcanol Geotherm Res* 2001, **109:**247–262.
14. Horwell CJ: **Grain size analysis of volcanic ash for the rapid assessment of respiratory health hazard.** *J Environ Monitor* 2007, **9:**1107–1115.
15. Horwell CJ, Hillman SE, Cole PD, Loughlin SC, Llewellin EW, Damby DE, Christopher T: **Controls on variations in cristobalite abundance in ash generated by the Soufrière Hills volcano, Montserrat in the period 1997-2010.** *Geol Soc Lon Mem* 2013, Accepted.
16. Castranova V, Pailes WH, Dalal NS, Miles PR, Bowman L, Vallyathan V, Pack D, Weber KC, Hubbs A, Schwegler-Berry D, *et al*: **Enhanced pulmonary response to the inhalation of freshly fractured silica as compared with aged dust exposure.** *Appl Occup Environ Hyg* 1996, **11:**937–941.
17. Fubini B, Bolis V, Giamello E: **The surface chemistry of crushed quartz dust in relation to its pathogenicity.** *Inorg Chim Acta* 1987, **138:**193–197.
18. Fubini B, Giamello E, Pugliese L, Volante M: **Mechanically induced defects in quartz and their impact on pathogenicity.** *Solid State Ionics* 1989, **32/33:**334–343.
19. Fubini B, Wallace WE: **Modulation of silica pathogenicity by surface processes**. In *Absorption on silica surfaces*. Edited by Papirer E. France: Mulhouse; 1999:645–664.
20. Vallyathan V, Castranova V, Pack D, Leonard S, Shumaker J, Hubbs AF, Shoemaker DA, Ramsay DM, Pretty JR, McLaurin JL, *et al*: **Freshly fractured quartz inhalation leads to enhanced lung injury and inflammation in rats. Potential role of free radicals.** *Am J Respir Crit Care Med* 1995, **152:**1003–1009.
21. Horwell CJ, Fenoglio I, Ragnarsdottir KV, Sparks RSJ, Fubini B: **Surface reactivity of volcanic ash from the eruption of Soufrière Hills volcano, Montserrat, with implications for health hazards.** *Environ Res* 2003, **93:**202–215.
22. Checkoway H, Hughes JM, Weill H, Seixas NS, Demers PA: **Crystalline silica exposure, radiological silicosis and lung cancer mortality in diatomaceous earth industry workers.** *Thorax* 1999, **54:**56–59.
23. Hughes JM, Weill H, Checkoway H, Jones RN, Henry MM, Heyer NJ, Seixas NS, Demers PA: **Radiographic evidence of silicosis risk in the diatomaceous earth industry.** *Am J Respir CritCare Med* 1998, **158:**807–814.
24. Park R, Rice F, Stayner L, Smith R, Gilbert S, Checkoway H: **Exposure to crystalline silica, silicosis, and lung disease other than cancer in diatomaceous earth industry workers: quantitative risk assessment.** *Occup Environ Med* 2002, **59:**36–43.
25. Rice FL, Park R, Stayner L, Smith R, Gilbert S, Checkoway H: **Crystalline silica exposure and lung cancer mortality in diatomaceous earth industry workers: a quantitative risk assessment.** *Occup Environ Med* 2001, **58:**38–45.
26. Horwell CJ, Baxter PJ: **The respiratory health hazards of volcanic ash: a review for volcanic risk mitigation.** *Bull Volcanol* 2006, **69:**1–24.
27. Martin TR, Wehner AP, Butler J: **Evaluation of physical health effects due to volcanic hazards: the use of experimental systems to estimate the pulmonary toxicity of volcanic ash.** *Am J Public Health* 1986, **76:**59–65.
28. Cullen RT, Jones AD, Miller BG, Donaldson K, Davis JMG, Wilson M, Tran CL: *Toxicity of volcanic ash from Montserrat. pp. 55*. Edinburgh: Institute of Occupational Medicine; 2002:55.
29. Wilson MR, Stone V, Cullen RT, Searl A, Maynard RL, Donaldson K: **In vitro toxicology of respirable Montserrat volcanic ash.** *Occup Environ Med* 2000, **57:**727–733.
30. Martin TR, Chi EY, Covert DS, Hodson WA, Kessler DE, Moore WE, Altman LC, Butler J: **Comparative effects of inhaled volcanic ash and quartz in rats.** *Am Rev Resp Dis* 1983, **128:**144–152.
31. Wehner AP, Dagle GE, Clark ML, Buschbom RL: **Lung changes in rats following inhalation exposure to volcanic ash for two years.** *Environ Res* 1986, **40:**499–517.
32. Lee SH, Richards RJ: **Montserrat volcanic ash induces lymph node granuloma and delayed lung inflammation.** *Toxicology* 2004, **195:**155–165.
33. Mannetje A, Steenland K, Attfield M, Boffetta P, Checkoway H, DeKlerk N, Koskela R-S: **Exposure-response analysis and risk assessment for silica and silicosis mortality in a pooled analysis of six cohorts.** *Occup Environ Med* 2002, **59:**723–728.
34. Hincks TK, Aspinall WP, Baxter PJ, Searl A, Sparks RSJ, Woo G: **Long term exposure to respirable volcanic ash on Montserrat: a time series simulation.** *Bull Volcanol* 2006, **68:**266–284.
35. Health and Safety Executive: *A regulatory impact assessment (RIA) on proposals to reduce the UK occupational exposure limit for respirable crystalline silica (RCS)*. London: Health & Safety Executive; 2007.
36. Brown GM, Donaldson K, Brown DM: **Bronchoalveolar leukocyte response in experimental silicosis: Modulation by a soluble aluminium compound.** *Toxicol Appl Pharmacol* 1989, **101:**95–105.
37. Fubini B: **Surface chemistry and quartz hazard.** *Ann Occup Hyg* 1998, **42:**521–530.
38. Begin R, Masse S, Rola-Pleszczynski M, Martel M, Desmarais Y, Geoffroy M, LeBouffant L, Daniel H, Martin J: **Aluminium lactate treatment alters the lung biological activity of quartz.** *Exp Lung Res* 1986, **10:**385–399.
39. Duffin R, Gilmour PS, Schins RPF, Clouter A, Guy K, Brown DM, Macnee W, Borm PJ, Donaldson K, Stone V: **Aluminium lactate treatment of DQ12 quartz inhibits its ability to cause inflammation, chemokine expression, and nuclear factor-κB activation.** *Toxicol Appl Pharmacol* 2001, **176:**10–17.
40. Donaldson K, Stone V, Duffin R, Clouter A, Schins R, Borm P: **The quartz hazard: effects of surface and matrix on inflammogenic activity.** *J Environ Pathol Tox* 2001, **20:**109–118.
41. Horwell CJ, Sparks RSJ, Brewer TS, Llewellin EW, Williamson BJ: **The characterisation of respirable volcanic ash from the Soufriere Hills Volcano, Montserrat, with implications for health hazard.** *Bull Volcanol* 2003, **65:**346–362.
42. Deer WA, Howie RA, Zussman J: *An introduction to the rock forming minerals*. 2nd edition. New York: Longman Scientific and Technical; 1996.
43. Finch GI, Quarrell AG, Roebuck JS: **The Beilby Layer.** *Proc R Soc Lon Ser-A* 1934, **145:**676–681.
44. Williamson BJ, Di Muro A, Horwell CJ, Spieler O, Llewellin EW: **Injection of vesicular magma into an andesitic dome at the effusive–explosive transition.** *Earth Plan Sci Lett* 2010, **295:**83–90.
45. Šolc I: **The optical determination of a surface layer on polished quartz plates.** *Czech J Phys* 1966, **16:**525–528.
46. Talbot JH, Kempis EB: **Finely ground quartz: evidence against a `Disturbed' layer.** *Nature* 1960, **188:**927–929.
47. Quinot E, Cavelier C, Merceron MO: **Surface chemistry and cytotoxic properties of silica.** *Biomedicine* 1979, **30:**155–160.
48. Clouter A, Brown D, Hohr D, Borm P, Donaldson K: **Inflammatory effects of respirable quartz collected in workplaces versus standard DQ12 quartz: particle surface correlates.** *Toxicol Sci* 2001, **63:**90–98.

49. Wallace WE, Harrison JC, Grayson RL, Keane MJ, Bolsaitis P, Kennedy RD, Wearden AQ, Attfield MD: **Aluminosilicate surface contamination of respirable quartz particles from coal mine dusts and from clay work dusts.** *Ann Occup Hyg* 1994, **38:**439–445.
50. Stone V, Jones R, Rollo K, Duffin R, Donaldson K, Brown DM: **Effect of coal mine dust and clay extracts on the biological activity of the quartz surface.** *Toxicol Lett* 2004, **149:**255–259.
51. Jacobsen M, Rae S, Walton WH, Rogan JM: **The relation between pneumoconiosis and dust-exposure in British Coal Mines**. In *Inhaled Particles III. Volume 2*. Edited by Walton WH.: Pergamon Press; 1971:903–917.
52. Walton WH, Dodgson J, Hadden GG, Jacobsen M: **The effect of quartz and other non-coal dusts in coalworkers pneumoconioisis 1) Epidemiological studies**. In *Inhaled Particles IV*. Edited by Walton WH, McGovern B: Oxford Pergamon Press; 1977:669–689.
53. Seaton A, Dick JA, Dodgson J, Jacobsen M: **Quartz and pneumoconiosis in coalminers.** *Lancet* 1981, **318:**1272–1275.
54. Horwell CJ, Fenoglio I, Fubini B: **Iron-induced hydroxyl radical generation from basaltic volcanic ash.** *Earth Plan Sci Lett* 2007, **261:**662–669.
55. Bruch J, Rehn S, Rehn B, Borm PJ, Fubini B: **Variation of biological responses to different respirable quartz flours determined by a vector model.** *Int J Hyg Environ Health* 2004, **207:**203–216.
56. Donaldson K, Borm P: **The quartz hazard: a variable entity.** *Ann Occup Hyg* 1998, **42:**287–294.
57. Bolis V, Fubini B, Marchese L, Martra G, Costa D: **Hydrophilic and hydrophobic sites on dehydrated crystalline and amorphous silicas.** *J Chem Soc Faraday T* 1991, **87:**497–505.
58. Williamson BJ, Pastiroff S, Cressey G: **Piezoelectric properties of quartz and cristobalite airborne particulates as a cause of adverse health effects.** *Atmos Environ* 2001, **35:**3539–3542.
59. Daniel LN, Mao Y, Wang TCL, Markey CJ, Markey SP, Shi XL, Saffiotti U: **DNA strand breakage, thymine glycol production, and hydroxyl radical generation induced by different samples of crystalline silica in vitro.** *Environ Res* 1995, **71:**60–73.
60. Elias Z, Poirot O, Daniere MC, Terzetti F, Marande AM, Dzwigaj S, Pezerat H, Fenoglio I, Fubini B: **Cytotoxic and transforming effects of silica particles with different surface properties in Syrian hamster embryo (SHE) cells.** *Toxicol in Vitro* 2000, **14:**409–422.
61. Porter DW, Barger M, Robinson VA, Leonard SS, Landsittel D, Castranova V: **Comparison of low doses of aged and freshly fractured silica on pulmonary inflammation and damage in the rat.** *Toxicology* 2002, **175:**63–71.
62. Vallyathan V, Shi XL, Dalal NS, Irr W, Castranova V: **Generation of free radicals from freshly fractured silica dust. Potential role in acute silica-induced lung injury.** *Am Rev Resp Dis* 1988, **138:**1213–1219.
63. Fubini B: **Which surface functionalities are implied in dust toxicity?** In *Cellular and molecular effects of mineral and synthetic dusts and fibres Volume H 85*. Edited by Davis JMG, Jaurand MC. Berlin-Heidelberg: Springer-Verlag; 1994:347–358. *NATO ASI Series*.
64. Fubini B, Bolis V, Cavenago A, Volante M: **Physicochemical properties of crystalline silica dusts and their possible implication in various biological responses.** *Scand J Work Environ Health* 1995, **21:**9–14.
65. Lee MR, Brown DJ, Smith CL, Hodson ME, Mackenzie M, Hellmann R: **Characterization of mineral surfaces using FIB and TEM: A case study of naturally weathered alkali feldspars.** *Am Mineral* 2007, **92:**1383–1394.

doi:10.1186/1743-8977-9-44
Cite this article as: Horwell *et al.*: The structure of volcanic cristobalite in relation to its toxicity; relevance for the variable crystalline silica hazard. *Particle and Fibre Toxicology* 2012 **9**:44.

Journal of Volcanology and Geothermal Research (2012)

doi 10.1016/j.jvolgeores.2012.09.001

The respiratory health hazard of tephra from the 2010 Centennial eruption of Merapi with implications for occupational mining of deposits

D.E. Damby, C.J. Horwell, P.J. Baxter, P. Delmelle, K. Donaldson, C. Dunster, B. Fubini, F.A. Murphy, C. Nattrass, S. Sweeney, T.D. Tetley, M. Tomatis

The following paper was published in the Special Issue: 2010 Merapi Eruption facilitated by the Journal of Volcanology and Geothermal Research, which invited contributions from presenters in the associated session at EGU Vienna 2011. It assesses the respiratory hazard posed by the erupted ash through a battery of *in vitro* assays specifically adapted for volcanic ash. In additional to determining the health impact of the 2010 Merapi eruption, it will serve as a crisis-response template for future eruption so that public health hazards can be identified and prioritised. Only the abstract and introduction are included here as the full version is available online.

Contributions from the co-authors to the paper include:

- CJ Horwell: facilitated sample collection during the eruption, compiled grain size results, helped with general editing and proofing of the manuscript prior to and following submission, and presented the information at EGU 2011.
- PJ Baxter: participated in the field mission to Merapi in Nov-Dec 2010, provided expert advice on volcanic health hazards, and helped with general editing and proofing of the manuscript prior to and following submission
- P Delmelle oversaw the leachate work and provided section specific advice on leachate content
- K Donaldson oversaw the haemolysis work
- C Dunster carried out the oxidative capacity work
- B Fubini oversaw the iron release and radical generation work
- FA Murphy carried out the haemolysis assay
- C Nattrass carried out the leachate work
- S Sweeney carried out the TT1 assay and provided section specific results
- TD Tetley oversaw the TT1 work
- M Tomatis carried out the iron release and radical generation work

All authors read the manuscript and approved their analysis-specific results and discussion.

Journal of Volcanology and Geothermal Research xxx (2012) xxx–xxx

Contents lists available at SciVerse ScienceDirect

Journal of Volcanology and Geothermal Research

journal homepage: www.elsevier.com/locate/jvolgeores

The respiratory health hazard of tephra from the 2010 Centennial eruption of Merapi with implications for occupational mining of deposits

D.E. Damby [a,*], C.J. Horwell [a], P.J. Baxter [b], P. Delmelle [c], K. Donaldson [d], C. Dunster [e], B. Fubini [f], F.A. Murphy [d], C. Nattrass [a], S. Sweeney [g], T.D. Tetley [g], M. Tomatis [f]

[a] Institute of Hazard, Risk and Resilience, Department of Earth Sciences, Durham University, Science Labs, South Road, Durham, DH1 3LE, UK
[b] Institute of Public Health, University of Cambridge, Cambridge, CB2 2SR, UK
[c] Earth & Life Institute, SST/ELI/ELIE-Environmental Sciences, Université catholique de Louvain, Croix du Sud 2 bte L7.05.10, B-1348 Louvain-la-Neuve, Belgium
[d] The University of Edinburgh/MRC Centre for Inflammation Research, The Queen's Medical Research Institute, Edinburgh, EH16 4TJ, UK
[e] MRC-HPA Centre for Environment and Health, King's College London, 150 Stamford Street, London, SE1 9NH, UK
[f] Dipartimento di Chimica I.F.M., Interdepartmental Center "G. Scansetti" for Studies on Asbestos and other Toxic Particulates, Università degli studi di Torino, Via P. Giuria 7, 10125, Torino, Italy
[g] Lung Cell Biology, National Heart and Lung Institute, Imperial College London, Dovehouse Street, London SW3 6LY, UK

ARTICLE INFO

Article history:
Received 29 February 2012
Accepted 4 September 2012
Available online xxxx

Keywords:
Merapi
Ash
Health
Hazard
Volcanic deposit
Mining

ABSTRACT

Ashfall into heavily populated areas during the October–November 2010 eruption of Merapi volcano, Indonesia created anxiety regarding the growing impacts to health as the eruption escalated and the hazard zone widened. We made a preliminary assessment of the respiratory hazards to human health of the tephra deposits (ashfall, lahar, and PDC surge) from the eruption using a laboratory protocol specifically developed to study the toxic potential of volcanic ash particles. Twenty samples collected from a range of locations were analysed for health-pertinent mineralogical parameters (grain size, crystalline silica content, morphology, surface area, bulk chemistry, and leachable elements) and bio-reactivity (hydroxyl radical generation, haemolytic potential, oxidative capacity, pro-inflammatory response). The grain size pertinent to respiratory health was variable, ranging from 1.4–15.6 vol.% sub-4 μm and 3.0–28.9 vol.% sub-10 μm diameter material. No fibre-like particles were observed. Cristobalite was present in all samples, ranging from 1.9–9.5 wt.%, but surface reactivity and *in vitro* toxicity assays showed low reactivity for all samples tested. The risk of direct exposure to ash from fallout was in any case low due to seasonal rains limiting its re-suspension and the immediate and effective clean-up of communities by local people who supplied the ash to the Indonesian construction industry for use as aggregate. However, mining of the lahar and thick PDC deposits in the valleys draining the volcano is performed on a vast, industrial scale, which could result in high occupational exposure to thousands of sand miners at Merapi during the dry seasons. Further study of the health hazard of the mined Merapi deposits is warranted.

1. Introduction

Merapi volcano, located in Central Java, Indonesia, is one of the most persistently active volcanoes in the world, and has a history of deadly eruptions in the last century, occurring every 3–5 years. Today, there are 1.1 million people living on its slopes. Merapi has displayed both explosive and effusive activity throughout its eruptive history; however, activity over the last 225 years has been dominated by the viscous extrusion of basaltic-andesite lava domes and subsequent small gravitational, or explosive, dome collapse (Camus et al., 2000), producing pyroclastic density currents (PDCs) with associated plumes. Lava dome eruptions have been interspersed with explosive events every 26–58 years (Camus et al., 2000; Thouret et al., 2000). The most common, potentially lethal hazards are lahars, which result in damage far beyond the more immediate area affected by dome collapse (Thouret et al., 2000).

The October-November 2010 explosive eruption of Merapi was its largest since 1872, when there were reports of up to 30 cm of ashfall, and caused its worst disaster since 1930, when 36 villages were destroyed and 1369 people killed in PDCs. Major explosions on 26 October, 30–31 October, and 4–5 November dispersed large amounts of ash to the west and south, affecting major urban areas of Magelang and Yogyakarta. The total erupted tephra volume was estimated to be 50–100 x 10^6 m^3, approximately 10 times greater than deposits from typical eruptions of the past few decades (Lavigne et al., 2011; Surono et al., 2012). Varying contributions of juvenile dome and older 2006 dome material were incorporated into the discrete eruptive events (Surono et al., 2012). PDCs and associated detached surges extended

Abbreviations: PDC, Pyroclastic density current; BAF, Block-and-ash flow; NGO, Non-governmental organisation; IVHHN, International Volcanic Health Hazard Network; CVGHM, Centre for Volcanology and Geological Hazards Mitigation.

* Corresponding author.
E-mail addresses: david.damby@gmail.com, d.e.damby@dur.ac.uk (D.E. Damby), claire.horwell@durham.ac.uk (C.J. Horwell).

0377-0273/$ – see front matter © 2012 Published by Elsevier B.V.
http://dx.doi.org/10.1016/j.jvolgeores.2012.09.001

beyond the previously delineated hazard zones (Thouret et al., 2000), resulting in the destruction of some villages and 367 official fatalities (Gertisser, 2011; Surono et al., 2012). Nearly a third of a million people were displaced due to the risk of PDC impact to their villages, and many of these individuals would be exposed to re-suspended ash throughout the clean-up and rebuilding phase.

Quarrying of the extensive lahar and PDC deposits for construction began soon after the 2010 eruption and continued on an industrial scale involving thousands of people from local villages and further afield. In response to the immediate and future hazard posed by the erupted material, we embarked on a laboratory assessment of the respiratory health hazard of Merapi ash found in different tephra deposits (ashfall, a detached surge, and a lahar) following a protocol previously developed for eruptions at Rabaul, Papua New Guinea, Chaitén, Chile and Eyjafjallajökull, Iceland (Horwell, in review; Horwell et al., 2010a; Le Blond et al., 2010) (see Fig. 1). Health-pertinent mineralogical data of grain size, bulk composition, particle morphology, surface area, crystalline silica content and leachable elements are combined with toxicological assays (surface hydroxyl radical generation, particle oxidative capacity, haemolysis, pro-inflammatory response) to inform the particle hazard.

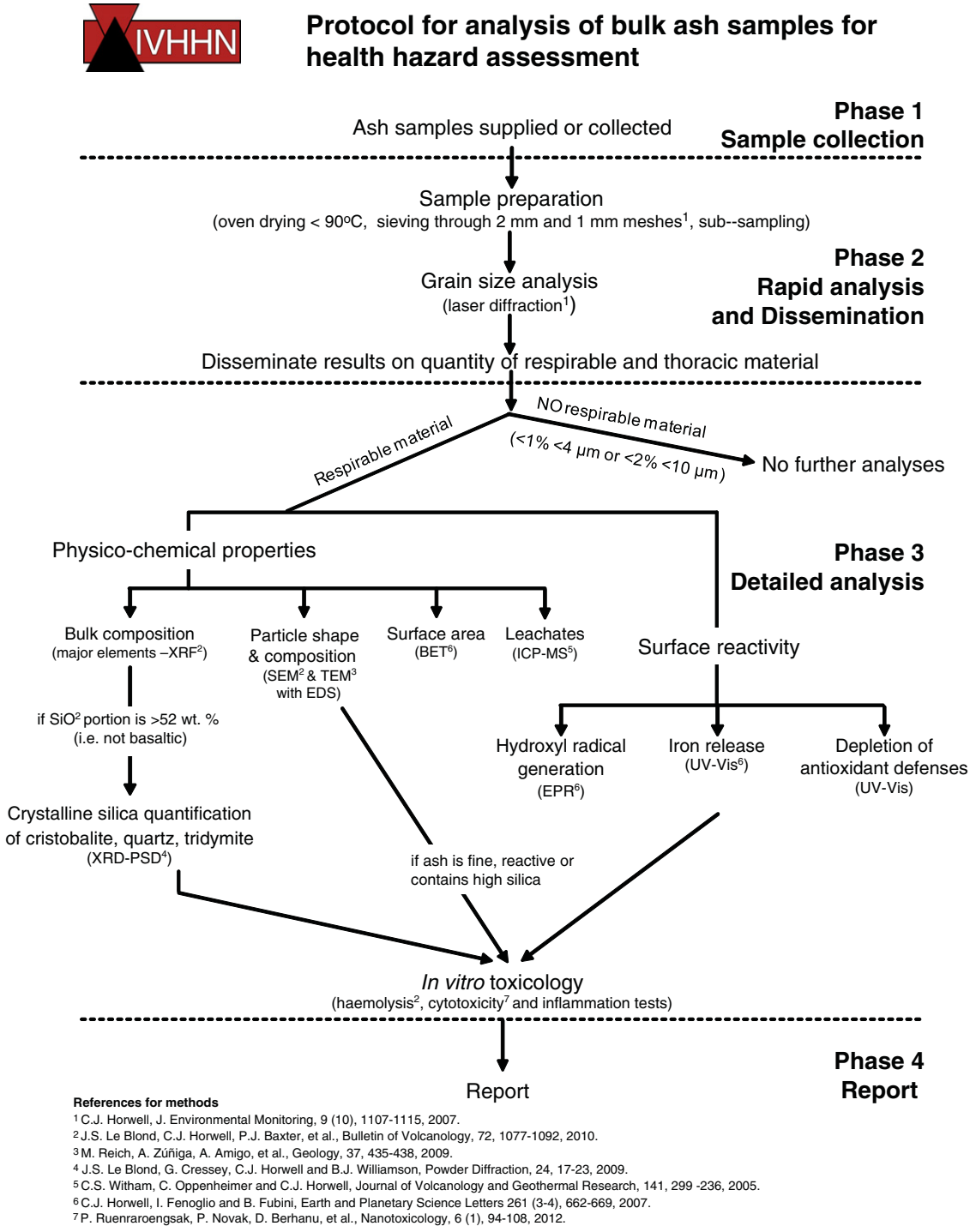

Fig. 1. Protocol for rapid assessment of health hazard after Le Blond et al. (2010).

Please cite this article as: Damby, D.E., et al., The respiratory health hazard of tephra from the 2010 Centennial eruption of Merapi with implications for occupational ..., Journal of Volcanology and Geothermal Research (2012), http://dx.doi.org/10.1016/j.jvolgeores.2012.09.001

1.1. Potential diseases related to the inhalation of volcanic ash

Horwell and Baxter (2006) give a comprehensive review of respiratory diseases associated with inhaling volcanic ash particles <10 μm diameter. Following immediate exposure, susceptible individuals may develop asthma and bronchitis (Baxter et al., 1983); heavy and prolonged exposure to ash containing a high concentration of crystalline silica in the 'respirable' fraction (<4 μm diameter and able to penetrate to the lung alveoli) may lead to the fibrotic lung disease silicosis and possibly lung cancer (International Agency for Research on Cancer, 1997). In addition, pulmonary tuberculosis is common in Indonesia, and its incidence and severity can be promoted by heavy exposure to dusts containing crystalline silica (Hnizdo and Murray, 1998). It is well understood that substantial quantities of crystalline silica can crystallise in volcanic domes as cristobalite through vapour-phase deposition and devitrification of groundmass, e.g., up to ~20 wt.% in ash from both the Soufrière Hillls volcano on Montserrat, West Indies (Baxter et al., 1999; Horwell, in review) and Chaitén, Chile (Horwell et al., 2010a). Eruptions at dome forming volcanoes can generate extremely fine-grained ash (Horwell, 2007), and can further contain cristobalite through incorporation of altered edifice material in an explosive event (Baxter et al., 1999; Horwell et al., 2010a).

1.2. Evidence of crystalline silica generation at Merapi

Cristobalite has previously been identified in volcanic ash near Merapi, with a particular emphasis on its presence in volcanic soils (Hardjosoesastro, 1956). However, no studies have quantified the concentration of cristobalite or addressed it as a respiratory hazard. Archived samples were therefore informative at the onset of the 2010 eruption. Analysis of an ash sample from a 1998 dome collapse event (named MER_arc in this study, see Table 1) raised concerns about the amount of respirable material produced by Merapi, with this sample containing 13 vol.% sub-4 μm particles (Horwell, 2007) but only 3.8 wt.% cristobalite (Table 1). Before this study, we also analysed the cristobalite content of dome rock samples from 1996 and 1998 block-and-ash flows (BAFs) and confirmed the presence of cristobalite (3–5 wt.%). Cristobalite content in dome rock is expected to be substantially lower than that in co-PDC plume deposits due to enrichment of cristobalite in the plume by fractionation (Horwell et al., 2001).

1.3. Initial response to the eruption

When international news agencies began reporting health-related problems attributed to exposure to volcanic ash (27 October) it became clear that rapid dissemination of information on preparedness for ashfall and the health hazards of ash was warranted. The International Volcanic Health Hazard Network (www.ivhhn.org) is a recognised source of such advice, and IVHHN fact sheets were rapidly translated for us into Bahasa Indonesia by a native speaker. High-resolution copies were sent for local printing by NGOs, such as Save the Children, for widespread distribution at the evacuation camps. We sought ash samples for analysis from these contacts and others at Universitas Gadjah Mada, Jogjakarta, with the first batch of samples arriving at Durham University on 18 November 2010, weeks before Indonesia's Centre for Volcanology and Geological Hazards Mitigation (CVGHM) reduced the activity warning from its highest level, level 4. Local scientists and NGOs collected fresh ash fall samples at 10 discrete locations, but it was not possible to co-ordinate a systematic sampling strategy in the emergency period. We undertook a field mission from 29 November to 11 December 2010 to collect further samples and to monitor air quality in populated areas.

2. Materials and methods

2.1. Sample collection and selection

Samples from three different types of tephra deposits were collected, namely ashfall, a detached surge and a lahar, to provide insight into the hazard posed by variably sourced ash at Merapi. Eleven ashfall samples were collected by local scientists and volunteers between 30 October and 13 November 2010. A further 9 samples were collected during our field mission from *in situ* village and field deposits. The village investigated (Bronggang) had been impacted by two detached PDC surges and samples were taken both outside and within affected houses. Although efforts were made to collect samples as fresh as possible, many samples were rained on prior to collection. The eruption took place during the wet season and normal rainfall may have been augmented by the 2010

Table 1
Summary of sample information and analytical techniques carried out on each sample. Further studies include: BET, EPR, iron release, haemolysis, oxidative capacity, inflammatory potential, leachate. Sample MER_10_10 was excluded from the study due to a lack of eruption and collection information. State of ash samples upon collection is reported in Table 2. Samples supplied by [a]Agung Harijoko, Gadjah Mada University; [b]Marie Boichu, Cambridge University, and Noer Cholik, BPPTK; [c]Maharani Hardjoko, Save the Children; [d]Jean-Christophe Komorowski, Institut de Physique du Globe de Paris; [e]Jochen Berger, University of Hohenheim.

Sample	Eruption date	Collection date	Deposit type	Collection location	Distance from vent (km)	Collection coordinates	GSA	XRF	XRD	SEM	Further studies
MER_10_01[a]	30-Oct-10	30-Oct-10	tephra fall	Jogonalan Lor, Bantul (Rumah)	32.0 SSW	07° 49.6850S 110° 21.0817 E	√	√	√	√	
MER_10_02[a]	26-Oct-10	31-Oct-10	tephra fall	Kepuh Harjo	5.5 S	07° 35.4928S 110° 27.0510 E	√	√	√	√	√
MER_10_03[a]	05-Nov-10	05-Nov-10	tephra fall	Jogonalan Lor, Bantul	32.0 SSW	07° 49.6850S 110° 21.0817 E	√	√	√	√	√
MER_10_04[b]	31-Oct-10	31-Oct-10	tephra fall	BPPTK, Yogyakarta	28.0 SSW	07° 47.8743S 110° 23.0713 E	√	√	√	√	√
MER_10_05[c]	05-Nov-10	13-Nov-10	tephra fall	Desa Ngasem, Gulon, Magelang	18.0 SW	07° 36.1527S 110° 17.2003 E	√	√	√		
MER_10_06[c]	05-Nov-10	13-Nov-10	tephra fall	Desa Manquncari, Sawangan, Magelang	16.0 W	07° 32.2773S 110° 18.5593 E	√	√	√		
MER_10_07[c]	05-Nov-10	13-Nov-10	tephra fall	Desa Krogowanan, Sawangan, Magelang	11.0 W	07° 31.7755S 110° 24.6047 E	√	√	√		
MER_10_08[c]	05-Nov-10	13-Nov-10	tephra fall	Desa Mbelan, Sawangan, Magelang	15.0 W	07° 32.6385S 110° 18.6133 E	√	√	√		
MER_10_09[c]	05-Nov-10	13-Nov-10	tephra fall	Desa Ngadipuro, Dukun, Magelang	18.0 W	07° 33.7400S 110° 17.2003 E	√	√	√		
MER_10_11[d]	Unknown	09-Nov-10	tephra fall	Jembatan Kali Juweh	6.0 NW	07° 29.9445S 110° 24.6047 E	√	√	√		
MER_10_12	05-Nov-10	30-Nov-10	surge	Bronggang, Argo Mulyo	17.0 S	07° 39.7307S 110° 27.7743 E	√	√	√	√	√
MER_10_13	05-Nov-10	30-Nov-10	surge	Bronggang, Argo Mulyo	17.0 S	07° 39.7307S 110° 27.7743 E	√		√	√	
MER_10_14	05-Nov-10	30-Nov-10	surge	Bronggang, Argo Mulyo	17.0 S	07° 39.7407S 110° 27.8217 E	√		√		
MER_10_15	05-Nov-10	06-Dec-10	surge	Bronggang, Argo Mulyo	17.0 S	07° 39.7407S 110° 27.8217 E	√		√		
MER_10_16	Unknown	08-Dec-10	lahar	Siderejo (Sinduharjo)	22.0 S	07° 44.9555S 110° 26.9088 E	√		√		
MER_10_17	Unknown	03-Dec-10	tephra fall	SW slope Merbabu, near Selo	4.5 NW	07° 34.7699S 110° 19.4860 E	√		√		
MER_10_18	Unknown	03-Dec-10	tephra fall	SW slope Merbabu, near Selo	8.0 NW	07° 31.0715S 110° 22.7871 E	√		√		
MER_10_19[e]	05-Nov-10	08-Dec-10	surge	N of Gadingan, E of Bronggang	17.0 S	07° 39.7367S 110° 27.9133 E	√		√		
MER_10_20[f]	Unknown	04-Dec-10	tephra fall	S of Dukun, Magelang	12.0 W	07° 33.8713S 110° 20.3336 E	√		√		
MER_arc	11–19-Jul-98	09-Aug-98	tephra fall	Volcano flanks	0.2	Unknown	√	√	√		√

Please cite this article as: Damby, D.E., et al., The respiratory health hazard of tephra from the 2010 Centennial eruption of Merapi with implications for occupational ..., Journal of Volcanology and Geothermal Research (2012), http://dx.doi.org/10.1016/j.jvolgeores.2012.09.001

Bulletin of Volcanology (2012) 74:4, p913-930

Sakurajima volcano: a physico-chemical study of the health consequences of long-term exposure to volcanic ash

S.E. Hillman, C.J. Horwell, A.L. Densmore, D.E. Damby, B. Fubini, Y. Ishimine, M. Tomatis

The following paper was adapted from Sarah Hillman's MSc thesis (2011), whose project was to collate published health-relevant literature on the health effects of ash from Sakurajima volcano, Japan, and to further explicate the hazard posed by her own sample set of ash by using the techniques outlined in the concurrently evolving rapid-response protocol. Only the abstract is included here as the full version is available online.

Contributions to the paper from D E Damby include:

- SEM imaging and EDS analysis of ash samples
- XRD quantitative analysis of ash samples for the crystalline silica polymorphs (cristobalite, tridymite, and quartz) and checking of previous data
- Discussion of raw data and results prior to manuscript construction, including constructive feedback, interpretation and explanation of results
- General editing and proofing of manuscript prior to submission

Bull Volcanol (2012) 74:913–930
DOI 10.1007/s00445-012-0575-3

RESEARCH ARTICLE

Sakurajima volcano: a physico-chemical study of the health consequences of long-term exposure to volcanic ash

S. E. Hillman · C. J. Horwell · A. L. Densmore · D. E. Damby · B. Fubini · Y. Ishimine · M. Tomatis

Received: 15 July 2011 / Accepted: 27 December 2011 / Published online: 27 January 2012

Abstract Regular eruptions from Sakurajima volcano, Japan, repeatedly cover local urban areas with volcanic ash. The frequency of exposure of local populations to the ash led to substantial concerns about possible respiratory health hazards, resulting in many epidemiological and toxicological studies being carried out in the 1980s. However, very few mineralogical data were available for determination of whether the ash was sufficiently fine to present a respiratory hazard. In this study, we review the existing studies and carry out mineralogical, geochemical and toxicological analyses to address whether the ash from Sakurajima has the potential to cause respiratory health problems. The results show that the amount of respirable (<4 μm) material produced by the volcano is highly variable in different eruptions (1.1–18.8 vol.%). The finest samples derive from historical, plinian eruptions but considerable amounts of respirable material were also produced from the most recent vulcanian eruptive phase (since 1955). The amount of cristobalite, a crystalline silica polymorph which has the potential to cause chronic respiratory diseases, is ~3–5 wt.% in the bulk ash. Scanning electron microscope and transmission electron microscope imaging showed no fibrous particles similar to asbestos particles. Surface reactivity tests showed that the ash did not produce significant amounts of highly reactive hydroxyl radicals (0.09–1.35 μmol m^{-2} at 30 min.) in comparison to other volcanic ash types. A basic toxicology assay to assess the ability of ash to rupture the membrane of red blood cells showed low propensity for haemolysis. The findings suggest that the potential health hazard of the ash is low, but exposure and respiratory conditions should still be monitored given the high frequency and durations of exposure.

Keywords Sakurajima · Japan · Volcanic ash · Health · Respiratory · Characterisation

Editorial responsibility: JDL White

S. E. Hillman · C. J. Horwell (✉) · D. E. Damby
Institute of Hazard, Risk and Resilience,
Department of Earth Sciences, Durham University,
Science Labs, South Road,
Durham DH1 3LE, UK
e-mail: Claire.horwell@durham.ac.uk

A. L. Densmore
Institute of Hazard, Risk and Resilience,
Department of Geography, Durham University,
Science Labs, South Road,
Durham DH1 3LE, UK

B. Fubini · M. Tomatis
Dipartimento di Chimica I.F.M., G. Scansetti Interdepartmental Center for Studies on Asbestos and other Toxic Particulates,
Università degli studi di Torino,
Via P. Giuria 7,
10125 Torino, Italy

Y. Ishimine
Organ and Body Scale Team, Integrated Simulation of Living Matter Group, Computational Science Research Program,
RIKEN (The Institute of Physical and Chemical Research),
2-1 Hirosawa,
Wako, Saitama 351-0198, Japan

Introduction

Sakurajima volcano, on Kyushu Island, Southeast Japan, is one of the most active volcanoes in Japan. Frequent, vulcanian-style eruptions have been occurring almost continuously for over half a century, regularly exposing local populations (almost 1 million inhabitants within a 10-km radius of the volcano) to volcanic ash. Since the late 1970s, concerns have been raised about how repeated exposure to volcanic ash over such a long timescale might affect the

Environmental Research, *submitted*

Respiratory health hazard assessment of the ash from the 2010 eruption of the Eyjafjallajökull volcano, Iceland

C.J. Horwell, S.E. Hillman, P.J. Baxter, D.E. Damby, P. Delmelle, K. Donaldson, C. Dunster, J.A. Calkins, B. Fubini, A Hoskuldsson, F. Kelly, G. Larsen, J.S. Le Blond, K.J.T. Livi, B. Mendis, F. Murphy, T. Thordarson, M. Tomatis

The following paper resulted from the effort of an international collaboration on the respiratory health hazard posed by the Eyjafjallajökull ash following the 2010 eruption. It is a bench-mark paper in terms of the application of the rapid-response protocol (figure cross-reference) and the rapidity with which the study was conducted, entirely facilitated by international collaborations. Only the abstract and introduction are included here as a the manuscript has not yet been accepted.

My responsibilities during and in the immediate wake of the eruption were to coordinate experiments and to receive, dry, weigh, split, post and archive samples. Major direct contributions to the paper include:

- SEM imaging and EDS analysis of ash samples
- XRD quantitative analysis of ash samples for the crystalline silica polymorphs (cristobalite, tridymite, and quartz) and checking of previous data
- Extensive editing and proofing of manuscript prior to submission

Elsevier Editorial System(tm) for Environmental Research
Manuscript Draft

Manuscript Number: ER-12-491R1

Title: Physicochemical and toxicological profiling of ash from the 2010 and 2011 eruptions of Eyjafjallajökull and Grímsvötn volcanoes, Iceland using a rapid respiratory hazard assessment protocol

Article Type: Full Length Article

Keywords: Iceland; Eyjafjallajökull; Grímsvötn; Volcano; Respiratory health

Corresponding Author: Dr. Claire J Horwell,

Corresponding Author's Institution: Durham University

First Author: Claire Horwell

Order of Authors: Claire Horwell; Peter J Baxter; Sarah E Hillman; Julie A Calkins; David E Damby; Pierre Delmelle; Ken Donaldson; Christina Dunster; Bice Fubini; Frank Kelly; Jennifer S Le Blond; Ken J Livi; Fiona Murphy; Claire Nattrass; Sinbad Sweeney; Teresa D Tetley; Thor Thordarson; Maura Tomatis

Abstract: The six week eruption of Eyjafjallajökull volcano in 2010 produced heavy ash fall in a sparsely populated area of southern and south eastern Iceland and disrupted European commercial flights for at least 6 days. We adopted a protocol for the rapid analysis of volcanic ash particles, for the purpose of informing respiratory health risk assessments. Ash collected from deposits underwent a multi-laboratory physicochemical and toxicological investigation of their mineralogical parameters associated with bio-reactivity, and selected in vitro toxicology assays related to pulmonary inflammatory responses. Ash from the eruption of Grímsvötn, Iceland, in 2011 was also studied. The results were benchmarked against ash from Soufrière Hills volcano, Montserrat, which has been extensively studied since the onset of eruptive activity in 1995.

For Eyjafjallajökull, the grain size distributions were variable: 2-13 vol. % of the bulk samples were < 4 μm, with the most explosive phases of the eruption generating abundant respirable particulate matter. In contrast, the Grímsvötn ash was almost uniformly coarse (< 3.5 vol. % < 4 μm material). Surface area ranged from 0.3-7.7 m2g-1 for Eyjafjallajökull but was very low for Grímsvötn (< 0.6 m2g-1). There were few fibre-like particles (which were unrelated to asbestos) and the crystalline silica content was negligible in both eruptions, whereas Soufrière Hills ash was cristobalite-rich with a known potential to cause silicosis. All samples displayed a low ability to deplete lung antioxidant defences, showed little haemolysis and low acute cytotoxicity in human alveolar type-1 like epithelial cells (TT1). However, cell-free tests showed substantial hydroxyl radical generation in the presence of hydrogen peroxide for Grímsvötn samples, as expected for basaltic, Fe-rich ash. Cellular mediators MCP-1, IL-6, and IL-8 showed chronic pro-inflammatory responses in Eyjafjallajökull, Grímsvötn and Soufrière Hills samples, despite substantial differences in the sample mineralogy and eruptive styles.

The value of the pro-inflammatory profiles in differentiating the potential respiratory health hazard of volcanic ashes remains uncertain in a protocol designed to inform public health risk assessment, and further research on their role in volcanic crises is warranted.

Physicochemical and toxicological profiling of ash from the 2010 and 2011 eruptions of Eyjafjallajökull and Grímsvötn volcanoes, Iceland using a rapid respiratory hazard assessment protocol

Horwell, C.J.[a], Baxter, P.J.[b], Hillman, S.E.[a], Calkins, J.A.[c], Damby, D.E.[a], Delmelle, P.[c,d], Donaldson, K.[e], Dunster, C.[f], Fubini, B.[g], Kelly, F.J.[f], Le Blond, J.S.[h,i], Livi, K.J.T.[j], Murphy, F.[e], Nattrass, C.[a], Sweeney, S.[k], Tetley, T.D.[k], Thordarson, T.[l], Tomatis, M.[g]

[a] Institute of Hazard, Risk and Resilience, Department of Earth Sciences, Durham University, Science Labs, South Road, Durham, DH1 3LE, UK.
Claire.horwell@durham.ac.uk Tel. ++44(0)191 3342253 Fax. ++44(0)191 3342301

[b] Institute of Public Health, University of Cambridge, Cambridge, CB2 2SR, UK.

[c] Environment Department, University of York, Heslington, York, YO10 5DD, UK.

[d] Earth and Life Institute, Université catholique de Louvain, B-1348 Louvain-la-Neuve, Belgium.

[e] The University of Edinburgh/MRC Centre for Inflammation Research, The Queen's Medical Research Institute, Edinburgh, EH16 4TJ, UK.

[f] MRC-PHE Centre for Environment and Health, King's College London, 150 Stamford Street, London, SE1 9NH, UK.

[g] Dipartimento di Chimica "G. Scansetti" Interdepartmental Center for Studies on Asbestos and other Toxic Particulates, Università degli studi di Torino, Via P. Giuria 7, 10125, Torino, Italy.

[h] Department of Geography, University of Cambridge, Downing Place, Cambridge, CB2 3EN, UK.

[i] Department of Earth Sciences, Natural History Museum, Cromwell Road, London, SW7 5BD, UK.

[j] The High-Resolution Analytical Electron Microbeam Facility of the Integrated Imaging Center, Departments of Earth and Planetary Sciences and Biology, Johns Hopkins University, Maryland 21218, USA.

[k] Lung Cell Biology, National Heart and Lung Institute, Imperial College London, Dovehouse Street, London, SW3 6LY, UK.

[1] Grant Institute, School of Geosciences, The King's Buildings, Edinburgh, EH9 3JW, UK

ABSTRACT

The six week eruption of Eyjafjallajökull volcano in 2010 produced heavy ash fall in a sparsely populated area of southern and south eastern Iceland and disrupted European commercial flights for at least 6 days. We adopted a protocol for the rapid analysis of volcanic ash particles, for the purpose of informing respiratory health risk assessments. Ash collected from deposits underwent a multi-laboratory physicochemical and toxicological investigation of their mineralogical parameters associated with bio-reactivity, and selected *in vitro* toxicology assays related to pulmonary inflammatory responses. Ash from the eruption of Grímsvötn, Iceland, in 2011 was also studied. The results were benchmarked against ash from Soufrière Hills volcano, Montserrat, which has been extensively studied since the onset of eruptive activity in 1995.

For Eyjafjallajökull, the grain size distributions were variable: 2-13 vol. % of the bulk samples were < 4 μm, with the most explosive phases of the eruption generating abundant respirable particulate matter. In contrast, the Grímsvötn ash was almost uniformly coarse (< 3.5 vol. % < 4 μm material). Surface area ranged from 0.3-7.7 m^2g^{-1} for Eyjafjallajökull but was very low for Grímsvötn (< 0.6 m^2g^{-1}). There were few fibre-like particles (which were unrelated to asbestos) and the crystalline silica content was negligible in both eruptions, whereas Soufrière Hills ash was cristobalite-rich with a known potential to cause silicosis. All samples displayed a low ability to deplete lung antioxidant defences, showed little haemolysis and low acute cytotoxicity in human alveolar type-1 like epithelial cells (TT1). However, cell-free tests showed substantial hydroxyl radical generation in the presence of hydrogen peroxide for Grímsvötn samples, as expected for basaltic, Fe-rich ash. Cellular mediators MCP-1, IL-6, and IL-8 showed chronic pro-inflammatory responses in Eyjafjallajökull,

Grímsvötn and Soufrière Hills samples, despite substantial differences in the sample mineralogy and eruptive styles.

The value of the pro-inflammatory profiles in differentiating the potential respiratory health hazard of volcanic ashes remains uncertain in a protocol designed to inform public health risk assessment, and further research on their role in volcanic crises is warranted.

KEYWORDS

Iceland, Eyjafjallajökull, Grímsvötn, Volcano, Respiratory health

FUNDING

This study was funded through two NERC Urgency Grants (NE/I007652/1, Horwell; NE/I00775X/1, Thordarson), a Wolfson Research Institute Early Career Award and Durham University seed-corn funds. S.S. was funded by a Unilever grant.

1. INTRODUCTION

In April 2010, the UK and Europe suffered unprecedented disruption to commercial aviation due to the sudden eruption of Eyjafjallajökull volcano in Iceland. A year later, a second Icelandic volcano, Grímsvötn, erupted and, again, volcanic ash affected northern Europe. Volcanologists believe that the eruptions heralded a predicted period of increased volcanic activity in Iceland, which occurs within a 130-140 year cycle (Larsen et al., 1998). In addition to air traffic disruption and its economic consequences, Iceland and Europe became concerned about the potential impacts of any ashfall on animal health, including chemical contamination of pasture and crops, and were unprepared for assessing and informing the public of the potential human health hazard. Whilst the Grímsvötn eruption only lasted a week, the Eyjafjallajökull eruption was sustained for five and a half weeks and was followed by significant re-suspension of the ash by wind and human activity in the local farmed area, leading to particular concern regarding the respiratory hazard from ash inhalation.

Despite drawing on experience at an increasing number of global eruptions, the small number of medical and epidemiological investigations of human and animal health that have been undertaken means the evidence base on respiratory health effects of ash inhalation remains relatively sparse. Acute clinical manifestations in communities affected by ashfalls have included asthmatic and bronchitic symptoms, with those people suffering from pre-existing chronic lung conditions being the most vulnerable and likely to suffer exacerbations of their conditions (Baxter et al., 1981; Baxter et al., 1983; Forbes et al., 2003). Some volcanic eruptions generate ash with abundant crystalline silica in the form of cristobalite, quartz and tridymite, which may present a chronic hazard of fibrotic lung disease (e.g., silicosis or mixed dust fibrosis) in continuously and heavily exposed groups (Baxter et al., 1999). This is a well-recognised disease process in workers exposed to siliceous dusts in certain industries, but has

not yet been documented in areas of active volcanism (Baxter et al., In press; Buist et al., 1986; Yano et al., 1986).

Information pamphlets on the health effects of volcanic ash and advice on preventive measures are available through the International Volcanic Health Hazard Network (www.ivhhn.org), but are not specific to individual volcanoes, eruption styles or magma types. At the onset of the Eyjafjallajökull eruption, Icelandic agencies rapidly translated the IVHHN pamphlets for public distribution, to provide basic information on the respiratory hazard of volcanic ash.

1.1 IVHHN rapid analysis protocol

To offset the limited number of health studies on volcanic ash, and the time taken to carry out new studies, we developed a laboratory protocol (Figure 1) for rapid ash analysis to determine whether it is possible to identify physicochemical features and inflammatory biomarkers which might provide an early indication of the potential acute and chronic respiratory hazard to populations needing urgent advice following an eruption. The protocol involves physicochemical and toxicological analyses which assess health-pertinent characteristics of the ash and likely biological interactions. It also allows rapid screening of numerous ash samples which may have varying pathogenic properties, depending on eruption style. *In vitro* tests are only general indicators of reactivity *in vivo* but could be useful for rapidly comparing the pro-inflammatory potential of different types of freshly-erupted volcanic ash.

The protocol was first applied during the 2007-8 eruption of Rabaul volcano, Papua New Guinea and has been used since during eruption crises at Kilauea (Hawai'i, 2008), Chaitén (Chile, 2008), Merapi (Indonesia, 2010) and Puyehue Cordón Caulle (Chile, 2011-12)

(Damby et al., 2013; Horwell et al., 2010a; Le Blond et al., 2010) as well as Iceland in 2010 and 2011 (present study). In addition, the methods have been further tested and refined on ash from a number of other volcanoes (e.g. Vesuvius and Etna, Italy, Soufrière Hills, Montserrat, and Sakurajima, Japan) (Hillman et al., 2012; Horwell et al., 2010b). The protocol embodies recent developments in methodologies for ash analysis (e.g., Horwell, 2007; Horwell et al., 2007; Le Blond et al., 2009) and undergoes revision as new techniques become available or are deemed more informative. The protocol is divided into phases, allowing immediate dissemination of data for decisions on the need for respiratory protection, with later dissemination of a report on the full analyses usually within a month of sample receipt. Data on individual analyses such as crystalline silica content may be disseminated prior to the final report if warranted.

For the protocol, we adopt a suite of selected physicochemical analyses and *in vitro* assays. The physicochemical characteristics of the ash may vary widely among volcanoes with different magma composition and eruptive styles; in particular, in the proportion of respiratory-sized particles and their crystalline silica content (Horwell, 2007; Horwell and Baxter, 2006). In addition to particle size, large specific surface area is known to lead to increased biological reactivity (Duffin et al., 2002), as is surface free-radical (hydroxyl) generation and oxidative potential in lung lining fluid, all of which can be tested rapidly, in cell-free *in vitro* analyses (Ayres et al., 2008; Fubini et al., 1995). Iron-catalysed hydroxyl radical generation is a potential lung inflammation factor and a carcinogenic factor (Hardy and Aust, 1995; Kane, 1996). The depletion of antioxidants in the presence of particles may have special significance in triggering airway inflammation in asthma sufferers (Kelly et al., 1999).

The human erythrocyte haemolysis test is a well-tried means of measuring the interaction of the particle surface with a red blood cell membrane, and it may have value as an *in vitro* predictor of *in vivo* pathogenicity of crystalline silica (Clouter et al., 2001).

To establish the cellular reactivity of volcanic ash, the cytotoxic and acute and chronic inflammatory potential responses of human lung epithelial type 1-like (TT1) cells were also assessed as part of the protocol. Type-1 alveolar epithelial cells cover > 95 % of the alveolar surface area and are a major target for respirable material in the lung. The well-characterized (Swain et al., 2010; van den Bogaard et al., 2009) lung epithelial type 1-like cells used in this study are human-derived and recently immortalised (Kemp et al., 2008) to provide a unique model of this important particle deposition site. This model has been used by us previously, for example, to reproducibly confirm the highly-toxic potential of positively-charged polystyrene latex nanoparticles and the comparatively low toxic potential of their neutral and negatively charged counterparts (Ruenraroengsak et al., 2012).

1.2 Soufrière Hills benchmark

To help contextualise the results of our laboratory work we benchmarked our findings by including ash samples from the eruption of Soufrière Hills volcano, Montserrat, which are rich in crystalline silica and therefore may pose a silicosis risk, and have been extensively characterised (e.g. Horwell et al., 2003a; Horwell et al., 2003b). Soufrière Hills volcano began its current eruption in July 1995 and has had several phases of lava dome growth (and collapse), interspersed with periods of explosions and pauses in activity. The ash has been repeatedly studied over time (Baxter et al., In press) to monitor its cristobalite concentration during the different phases of the eruption, which are marked by episodes of growth of a lava dome in its crater. Cristobalite forms within the Soufrière Hills volcano lava domes and,

when these collapse to form pyroclastic density currents, the rock fragments, generating clouds of respirable particles that fall out to form ash deposits (Baxter et al., 1999). The longevity of the eruption and frequency of population exposure to elevated levels of respirable crystalline silica makes the Soufrière Hills volcano eruption unique in recent times (Searl et al., 2002).

In 2002, a group of experts reviewed all the toxicological data on the Soufrière Hills ash which had become available up to that time (Baxter et al., In press). Their judgement was used to inform a probabilistic assessment on the silicosis risk amongst the islanders from continuing exposure to the ash and its high concentration of cristobalite. The main concern was that the volcano showed no sign of decreasing activity, and the risk from the exposure continuing for the foreseeable future needed to be quantified. The principle toxicological studies were:

- Cullen and Searl (1998): *in vitro* testing on human epithelial cells and rat alveolar macrophages
- Wilson et al. (2000): competence of human epithelial cells and the ability of volcanic ash to induce sheep blood haemolysis
- Cullen et al. (2002): inhalation and instillation studies in two groups of rats and further *in vitro* studies
- Housley et al. (2002): instillation study to assess the effects of ash on the lungs of rats
- Lee and Richards (2004): instillation in rats sacrificed at intervals up to 49 weeks

The expert group interpreted the findings of reduced bio-reactivity in these studies to infer that the toxicity of the cristobalite in the Soufrière Hills ash was significantly less than the bio-reactivity expected based on the abundance of cristobalite in the ash alone, perhaps

because the toxicity of pure cristobalite was being masked by the heterogeneous mineral matrix in which it was embedded. A similar conclusion had been reached in the 1980s after comparable laboratory experiments were performed on ash from Mount St. Helens, USA (Baxter et al., In press).

The most comparable example of industrial exposure to cristobalite-laden dust is that of diatomaceous earth workers in California (Hughes et al., 1998). The dose-response model used in the Hughes et al. (1998) study formed the basis for the risk assessment methodology that incorporated modelling of volcanic ash exposure levels and duration, including variable cristobalite concentrations, based on the 1995-1997 volcanic activity and assuming that the eruption could continue for years into the future. The probabilistic model assessed the possible development of silicosis in the island population after a total of 20 years of exposure to ash and found, for example, a 2-4 wt. % risk of developing early detectable radiological evidence of silicosis in gardeners (the highest exposed occupational group) (Hincks et al., 2006). The results formed the basis of applying more stringent measures to reduce future exposure to ash in the population.

Benchmarking toxicological testing between ash from different volcanoes has not been formally undertaken before and we decided to investigate its value in communicating our assay results to health experts with responsibility for advising patients and the general population in Iceland on the health risks from the eruptions.

1.3 Eyjafjallajökull and Grímsvötn volcanoes

Eyjafjallajökull volcano is located in southern Iceland (Figure 2) and last erupted intermittently between 1821-23. After a period of enhanced seismic activity and ground

deformation, particularly during 1994, 1999, and from December 2009, Eyjafjallajökull erupted on 20 March 2010 (Sigmundsson et al., 2010). The initial Fimmvörðuháls eruption was effusive (non-explosive, thereby generating little to no ash) and basaltic (defined as < 52 wt. % bulk SiO_2), and the eruption fissure was located on the north eastern flank of the volcano, just outside of the ice cap. Activity at Fimmvörðuháls stopped on 12 April and two days later a new fissure opened within the summit crater of Eyjafjallajökull volcano, heralding the new phase of explosive activity. The explosive eruption at the summit vent lasted from 14 April to 22 May and can be divided into four phases (Gudmundsson et al., 2012b): Phase I (14-18 April) was characterised by explosive eruption of benmoreite magma (60-61 wt. % SiO_2) that was somewhat enhanced by water - magma interaction, especially during the first day when the vent was partly filled with glacial melt-water. Phase II (18 April – 4 May) was characterised by lower discharge and lava effusion, with some weak but sustained explosive activity, of slightly less silicic magma (58-59 wt. % SiO_2; still classed as benmoreite). Phase III (5-17 May) involved a rejuvenation of more silicic explosive activity, and Phase IV (18-22 May) signalled the decline of the eruption, with reduced explosivity and magma discharge. For detailed information on location of proximal ash fallout, see Supplementary Material.

Ash was reported over Europe between 15-21 April and 6-17 May, but the amount of ash that fell over Europe was negligible (Stevenson et al., 2012), and syndromic surveillance over the UK did not find any unusual increases in presented respiratory ailments (Elliot et al., 2010). In contrast, ashfall was substantial on the small farming community in southern Iceland near the volcano. During the eruption, there was little precipitation in the area and ash deposits continued to be re-suspended by wind and human activity for months after the eruption

ceased. Ambient air monitoring stations were installed by Icelandic scientists in the impacted areas.

Grímsvötn, a basaltic volcano in south-eastern Iceland, is Iceland's most frequently active volcano in historical times and is mostly covered by the Vatnajökull icecap. The recent eruption began on 21 May 2011 and rapidly broke the ice cover, producing an eruption plume up to 20 km high which was sustained as a 50-100 km wide umbrella cloud until 22 May (Gudmundsson et al., 2012a). Heavy ash fall occurred on populations 70-100 km south of the volcano. This explosive eruption was far greater in intensity than the 2010 summit eruption at Eyjafjallajökull, releasing more tephra in the first day than during the earlier five and a half-week eruption (Gudmundsson et al., 2012a; Gudmundsson et al., 2012b). The eruption continued at a lower intensity until 28 May, with tephra mainly falling on Vatnajökull glacier, which surrounds the volcano (Figure 2). There was sporadic air traffic disruption to northern Europe during this time.

The Eyjafjallajökull and Grímsvötn eruptions were examples of the ability of Iceland's volcanoes to produce sustained, as well as sizeable, explosive eruptions, which are likely to produce ash of inhalable size. In particular, Grímsvötn produces explosive basaltic eruptions, in contrast to the more 'stereotypic' effusive basaltic eruptions typical of Hawaii and Etna (Thordarson and Hoskuldsson, 2008). Basaltic eruptions in 'dry' environments are mostly effusive, featuring lava fountains that produce tephra dominated by lapilli sized fragments (2 - 64 mm) and, for that reason, are considered not to pose a respiratory health hazard. Within-glacier eruptions of basaltic magma increases the explosivity significantly. Such events produce fine, iron-rich ash which may present a respiratory hazard through iron-catalysed free radical generation (Horwell et al., 2007).

The different phases of an eruption may produce ash with differing physicochemical profiles of pertinence to health hazard assessment, particularly in terms of grain-size distribution, depending on the explosivity. Therefore, samples were sought which covered the range of eruptive styles during the two eruptions. Samples of ash were collected on Iceland, downwind of the eruption plume, and sent to Durham University, UK where they were distributed to laboratories in the UK and Europe for co-ordinated, rapid analysis.

2. MATERIAL AND METHODS

The protocol methods are described in full elsewhere (Damby et al., 2013; Horwell, 2007; Horwell et al., 2007; Le Blond et al., 2009; Le Blond et al., 2010) so are described briefly here with some further detail in the Supplementary Material, together with information on sample preparation.

2.1 Sample collection

For Eyjafjallajökull, fourteen samples of ground-deposited ash were collected from the ash fallout on Iceland (Figure 2), with twelve of the samples from 14 to 18 April (i.e. Phase I) and the two days following the end of this phase. Two further samples were from ash erupted from 6 to 9 May during Phase III. Details of sample information and collection are given in Table 1.

For Grímsvötn, twelve samples of ground-deposited ash were collected (Figure 2), all from ash deposited between 21-23 May 2011. Samples GRI_11_01-04 were collected during the eruption but samples GRI_11_05-12 were all collected 1-2 weeks after deposition.

The Eruption of Soufrière Hills volcano, Montserrat from 2000-2010, Geological Society of London Memoirs, G. Wadge, R. Robertson and B. Voight (Editors), *submitted*

Cristobalite content of ash generated by 15 years of activity of the Soufrière Hills volcano, Montserrat

C.J. Horwell, P.D. Cole, S.C. Loughlin, D.E. Damby, S.E. Hillman, T. Christopher, P.J. Baxter

The following paper was submitted to *The Eruption of Soufrière Hills Volcano, Montserrat from 2000 to 2010* (Geological Society Memoirs) edited by G. Wadge, R. Robertson and B. Voight. It aims to correlate cristobalite content with dome residence time and degassing in order to further define the potential hazard at any given point during the eruption. Only the abstract and introduction are included here as the manuscript has not yet been accepted for publication.

Contributions to the paper from D E Damby include:

- Proposal of the original idea to correlate cristobalite content with dome residence time
- XRD quantitative analysis of ash samples for the crystalline silica polymorphs (cristobalite, tridymite, and quartz) and checking of previous data
- Discussion of raw data and results prior to manuscript construction
- General editing and proofing of manuscript prior to submission

Horwell CJ[1], Hillman SE[1], Cole PD[2,3,4], Loughlin SC[5], Llewellin EW[1], Damby DE[1], Christopher T[2,3]

Controls on variations in cristobalite abundance in ash generated by the Soufrière Hills volcano, Montserrat in the period 1997-2010

[1] Institute of Hazard, Risk and Resilience, Department of Earth Sciences, Durham University, Science Labs, South Road, Durham, DH1 3LE, UK. Claire.horwell@durham.ac.uk Tel. ++ 44 (0)191 3342253

[2] Montserrat Volcano Observatory, Flemings, Montserrat, West Indies

[3] Seismic Research Centre, University of the West Indies, St Augustine, Trinidad and Tobago

[4] School of Geography, Earth and Environmental Sciences, Plymouth University, PL4 8AA, UK.

[5] British Geological Survey, Murchison House, West Mains Road, Edinburgh EH9 3LA, UK.

Abstract

The Soufrière Hills volcano crystallises cristobalite (crystalline silica) in its lava domes and inhalation of cristobalite-rich ash may pose a chronic respiratory hazard. We investigate the causes of variation in cristobalite abundance (measured by X-ray diffraction) in ash from dome collapses, explosions, and ash venting from 1997-2010.

Cristobalite abundance in bulk dome-collapse ash varies between 4-23 wt.%. During periods of slow lava extrusion (<5 m^3s^{-1}), cristobalite is abundant (7-23 wt.%), which we attribute to extensive devitrification in slow-cooling lava; it can also form rapidly (15 wt.% in 2 months), but we find no correlation between cristobalite abundance and dome residence time. By contrast, during rapid extrusion (>5 m^3s^{-1}), cristobalite abundance is low (4-7 wt.%, similar to that associated with Vulcanian explosions), and correlates strongly with dome residence time. We attribute this correlation to progressive vapour-phase mineralization or devitrification, and the lack of contamination by older lava. Cristobalite abundance is expected to be >7 wt.% for collapse of slowly-extruded lava, for ash venting through a dome, or for incorporation of hydrothermally-altered edifice during explosions; cristobalite abundance is expected to be <7 wt.% for collapse of rapidly-extruded lava, for ash venting without dome incorporation and from Vulcanian explosions.

Introduction

Cristobalite is a high-temperature, low-pressure crystalline silica polymorph which may crystallise as a meta-stable phase in dome lavas, and persists at ambient conditions. In industrial settings, the silica polymorphs of quartz, cristobalite and tridymite are capable of causing silicosis, a fibrotic lung disease. Crystalline silica is also classed as a Group 1 human carcinogen by IARC (International Agency for Research on Cancer, 1997). The discovery of cristobalite in the volcanic ash from the 18 May 1980 eruption of Mount St. Helens, USA prompted intensive research to determine the silicosis risk from inhaling the ash (e.g. Dollberg et al., 1986), but the evidence from a series of toxicological, epidemiological and clinical studies at the time was inconclusive on this point (see Horwell and Baxter, 2006 for a review). In the event, exposure was short-lived and this substantially reduced public concern. Today, the chronic pathogenicity of cristobalite in volcanic ash is still under debate (Horwell et al., 2012).

The Soufrière Hills volcano, Montserrat began its current eruption in July 1995. Lava dome growth started in late 1995 and has continued, intermittently, in a series of five phases (Wadge et al., Accepted, this Memoir). Lava domes are inherently unstable, and are prone to partial or full collapses that generate pyroclastic density currents (PDCs) and associated co-PDC ash plumes. There have also been more than one hundred Vulcanian explosions during the eruption. Baxter et al. (1999) observed that cristobalite is generated within the Soufrière Hills dome and is abundant in the co-PDC ashfall. Horwell et al. (2003) characterised the cristobalite in different grain-size fractions and found that the cristobalite was concentrated in the finest, respirable fractions (< 4 μm diameter).

Over the course of the Soufrière Hills eruption, numerous mineralogical analyses and risk assessments for respiratory health have been carried out, based upon quantification of cristobalite abundance by X-ray diffraction (XRD) and ^{29}Si magic angle spinning nuclear magnetic resonance (MAS NMR) spectroscopy (see review in Baxter et al., Accepted, this Memoir). Initial analyses were carried out on ash from the first major dome-collapse PDC on 3 April 1996 where 25 wt. % cristobalite was found in the sub-10 μm fraction. Similar abundances were found in dome-collapse ash deposited in 1996 and 1997 (10-27 wt. %, 4 samples), in 1999 (30 wt. %, 1 sample) and in Aug./Sept. 2001 (24-29 wt. %, 3 samples) (Baxter et al., 1999; Baxter et al., Accepted, this Memoir). A routine assessment in 2009/10 found that cristobalite abundance had dropped during dome growth in Phase V, to < 5 wt. % in the bulk ash. The current study was devised to quantify cristobalite abundance in samples spanning the entire eruption, using a single XRD technique for consistency, in order to determine if this decrease in cristobalite abundance was real, or an artefact of technique progression over time. Eruption parameters, such as dome residence time, lava extrusion rate, and SO_2 flux were then correlated with the data to investigate the causes of fluctuations in cristobalite abundance.

Assessment of cristobalite abundance in volcanic ash is complicated by the presence of other minerals, in particular, plagioclase feldspar – often the dominant mineral in andesitic ash – which makes rapid quantification by XRD challenging due to a peak overlap with cristobalite. Early studies of Mount St. Helens and Soufrière Hills ash addressed this problem by employing the Talvitie method (Talvitie, 1951) to dissolve all minerals except crystalline silica (Baxter et al., 1999). This method, which involves boiling the ash in phosphoric acid for 8 minutes, is difficult to perform consistently since the final mineral assemblage is very sensitive to small variations in the duration of the heating (Horwell, 2002). Recently, this problem has been overcome with the advent of high-resolution diffractometers, allowing peak separation in bulk ash samples, and the development of a rapid internal attenuation standard (IAS) technique by Le Blond et al. (2009) which allows quantification of a single mineral phase in a heterogeneous dust, without prior knowledge of bulk sample composition. These improvements have facilitated more-rapid and, potentially, more-accurate assessment of cristobalite abundance than previously in ash from Soufrière Hills and other volcanoes (e.g. Merapi, Chaitén, Vesuvius, Rabaul, Eyjafjallajökull, Grímsvötn and Sakurajima) (Damby et al., 2013; Hillman et al., 2012; Horwell et al., Post review; Horwell et al., 2010a; Horwell et al., 2010b; Le Blond et al., 2010). This study systematically quantifies cristobalite abundance in a suite of 24 Soufrière Hills ash samples (1997 to 2010), using the IAS technique of Le Blond et al. (2009).

Horwell et al. (2013) studied the nature and formation of cristobalite in the Soufrière Hills lava domes and consider the likely processes of silica transport. Their observations support the mechanisms for cristobalite crystallization at Soufrière Hills proposed by MacGregor (1938) and Baxter et al. (1999): that cristobalite is formed through vapour-phase crystallization in permeable networks of pores, cracks and vugs, and through devitrification of volcanic glass. Horwell et al. (2013) show that the morphology of vapour-phase cristobalite is variable; crystals are predominantly prismatic but platy, hexagonal crystals are also found in some samples. Devitrification cristobalite appears as ‘feathery’ crystallites in the groundmass with more extensive devitrification leading to ‘fish-scale’ patches (in thin section, characteristic of cristobalite). Where devitrification is complete, Horwell et al. (2013) also found that subhedral quartz may be present instead of cristobalite; they propose that the quartz forms by phase transition from cristobalite, enabled by heat from circulating fluids. Whilst the kinetics of formation of cristobalite through vapour-phase crystallization and of devitrification are not well constrained, Williamson et al. (2010) demonstrate that cristobalite can form in the Soufrière Hills dome within hours to days of magma injection into the upper conduit or dome. Horwell et al. (2013) found up to 11 wt. % cristobalite in Soufrière Hills dome rock.

In K. Ugai, H. Yagi and A. Wakai (Editors), Earthquake-Induced Landslides (2012). *Proceedings of the International Symposium on Earthquake-induced Landslides*, Kiryu, Japan, pp 755-762

Progressive failure cycles and distributions of earthquake-triggered landslides

R.N. Parker, D. Petley, A. Densmore, N. Rosser, D.E. Damby, Matthew Brain

This paper was published in collaboration with researchers at the International Landslide Centre, Institute of Hazard, Risk and Resilience, Department of Geography, Durham University. It is targeted at an engineering geology and landslide hazard community, and was presented by R.N. Parker to the Fourth Session of the ISEL on November 7-9, 2012. Only the abstract and introduction are included here as the topic differs from the primary aims of this thesis.

My contribution to the paper was constructing a conceptual model for the repeating failure of sections of hillslopes through time. This contribution is based in the idea of landscape memory, and introduces a temporal component requiring an understanding of hysteresis on progressive slope failure. From this, a probabilistic cyclicity can be observed which is dependent on landscape topography (i.e., slope) and seismically induced deformation with time, whereby the hillslope surface effectively 'resets' following failure. What results is an evolving temporal stability model and the role of hysteresis on long, multiple earthquake timescales.

The implication of the paper is in redefining the way in which the landslides community models events, understanding that the starting point of slope failure is dependent on hillslope history. Therefore, the relevance is in uprooting the current and pervasive mindset of stochastic hillslope failure, changing the way in which landslide occurrence and resultant hazard are understood.

Specifically, my contributions to the paper are

- Defining the failure cycle occurring in a single hillslope block and probabilistically extrapolating that cycle to a landscape
- Linking observed cyclicity in the failure-cycle model to the root input variables, which were originally thought to be a representative distribution of hillslope parameters

Progressive Failure Cycles and Distributions of Earthquake-Triggered Landslides

82

Robert Parker, David Petley, Alexander Densmore, Nicholas Rosser, David Damby and Matthew Brain

Abstract

Advances in the collection and analysis of landslide inventory data have allowed for greater understanding of spatial distributions of landslides triggered by earthquakes. However, current approaches to analysing and modelling these phenomena do not account for the response of the individual potential landslide masses and their temporally evolving stability. This stems, in part, from the lack of a conceptual model describing the effect of seismic waves on the strength and stability of hillslopes, which can be applied at the regional scale and over long (multiple earthquake) time scales. Here we present such a conceptual model linking weakening via progressive failure, inertial displacements driven by seismic ground accelerations, and the repeating failure of sections of hillslopes through time. We explore the implications of the model for how various characteristics of earthquake-triggered landslide distributions are interpreted and understood. These include the apparently stochastic nature of spatial landslide occurrence, spatial patterns of landsliding, landslide magnitude-frequency distributions, global variability in numbers of landslides triggered by earthquakes, and in particular why in any earthquake smaller areas of hillslope fail than do not, even in regions of apparently high landslide susceptibility. Finally, we also propose means of testing the validity of this model relative to alternative hypotheses.

Keywords

Progressive failure · Newmark · Landslide distributions · Hysteresis

1 Introduction

Newmark analysis forms the basis of most currently available techniques for assessing the effect of seismic accelerations on hillslopes at the regional scale (e.g.: Jibson 2007). Here a potential landslide is modelled as a rigid

R. Parker (✉) · D. Petley · A. Densmore · Nicholas Rosser · D. Damby · M. Brain
Department of Geography, Institute of Hazard, Risk and Resilience, University of Durham, Durham, DH11PY, United Kingdom
e-mail: r.n.parker@durham.ac.uk

K. Ugai et al. (eds.), *Earthquake-Induced Landslides*,
DOI: 10.1007/978-3-642-32238-9_82,

perfectly plastic block sat on an inclined surface. Deformation occurs along the shear plane in response to seismic accelerations that exceed the dynamic shearing resistance, which is assumed to be the same as the static shearing resistance. A key assumption of the Newmark approach is that the shearing resistance does not change in response to seismically-induced deformations. However, movement patterns in failing landslide masses and the results of stress-path triaxial tests have shown that cohesive hillslope materials undergo progressive weakening prior to full failure (Petley et al. 2005a, b). Logic also dictates that a stable section of hillslope must undergo weakening and a reduction in stability in order to reach the point of failure, and that once failed, in simplistic terms, a new more stable section of hillslope is produced. This means that the stability of individual locations in the landscape and therefore their sensitivity to earthquake-triggered landsliding is not temporally constant, but can be understood as evolving cyclically with the occurrence of seismic events.

In this paper, we present a conceptual model linking micro-scale deformation-weakening behaviour in hillslope materials and inertial displacements driven by seismic ground accelerations, in order to provide a physical approach to understanding the temporal evolution of hillslope stability in response to seismic events. We explore the implications of the model for understanding various observed characteristics of landslide distributions and propose means of testing the validity of this model relative to alternative hypotheses.

2 Temporal Model of Hillslope Weakening and Failure

2.1 Background

Failure in cohesive materials generally requires that the material that forms the eventual shear zone undergoes a transition from peak to residual strength (Bjerrum 1967). This requires the material to undergo progressive deformation, resulting in the formation and coalescence of cracks that reduce the strength of the material. Based on observations of pre-failure landslide movement patterns (Petley et al. 2002; Kilburn and Petley 2002) and the results of stress path triaxial tests, Petley et al. (2005b) proposed a conceptual model for the development of progressive first-time failure in hillslopes formed from cohesive materials. The authors proposed that when a temporary reduction in factor of safety (FS) occurs due to elevated pore pressures, local stresses may exceed material strength in parts of the landslide, even though the global FS is still greater than unity. This allows deformation and micro-crack formation to take place in these segments, causing them to transition from peak to residual strength. The stress is then redistributed to other, unsheared, portions of the hillslope. This transfer process eventually reaches the point at which shear stress exceeds shear strength across the whole of the shear zone, such that failure becomes inevitable regardless of pore pressure state. However, it still takes time for the final sections of the shear zone to fail, such that collapse is not instantaneous. Hereafter we refer to this process of deformation, micro-crack formation and weakening by the term "deformation-weakening". Note also that whilst this model was developed for instability associated with hydrologically-triggered landslides, dynamic stresses from the passage of seismic waves may also serve to produce the temporary instabilities required for progressive failure.

2.2 Model Description

The Newmark sliding block model (Newmark 1965) provides a means of analysing the effect of seismic accelerations on hillslope stability in order to predict seismically-induced displacements in landslide masses (for a comprehensive review, see Jibson 2011). In this research we utilise the Newmark sliding block model as the basis for our conceptual model. We supplement the Newmark approach by changing two assumptions. First, we allow Newmark displacement to result in deformation-weakening, which breaks the assumption of perfectly plastic

The Journal of Immunology (2010); 185: 144-156

Slam Haplotypes Modulate the Response to Lipopolysaccharide In Vivo through Control of NKT Cell Number and Function

I. Aktan, A. Chant, Z.D. Borg, D.E. Damby, P.C. Leenstra, G.W.J. Lilley, J. Petty, B.T. Suratt, C. Teuscher, E.K. Wakeland, M.E. Poynter, J.E. Boyson

The following paper resulted from work done prior to commencing my PhD and carried over into the start of my studies. It was published with colleagues in the Division of Transplantation Surgery and Immunology, Department of Surgery, University of Vermont College of Medicine. As it is outside of the realm of this thesis, only the abstract and introduction are included.

Slam Haplotypes Modulate the Response to Lipopolysaccharide In Vivo through Control of NKT Cell Number and Function

Idil Aktan,[*,†,1] Alan Chant,[*,†,1] Zachary D. Borg,[*,†] David E. Damby,[*,†] Paige C. Leenstra,[*,†] Graham W. G. Lilley,[*,†] Joseph Petty,[‡] Benjamin T. Suratt,[‡] Cory Teuscher,[†,‡,§] Edward K. Wakeland,[¶] Matthew E. Poynter,[‡] and Jonathan E. Boyson[*,†]

CD1d-restricted NKT cells make up an innate-like T cell subset that plays a role in amplifying the response of innate immune leukocytes to TLR ligands. The *Slam* locus contains genes that have been implicated in innate and adaptive immune responses. In this study, we demonstrate that divergent *Slam* locus haplotypes modulate the response of macrophages to the TLR4 ligand LPS through their control of NKT cell number and function. In response to LPS challenge in vivo, macrophage TNF production in *Slam* haplotype-2$^+$ 129S1/SvImJ and 129X1/SvJ mice was significantly impaired in comparison with macrophage TNF production in *Slam* haplotype-1$^+$ C57BL/6J mice. Although no cell-intrinsic differences in macrophage responses to LPS were observed between strains, 129 mice were found to be deficient in liver NKT cell number, in NKT cell cytokine production in response to the CD1d ligand α-galactosylceramide, and in NKT cell IFN-γ production after LPS challenge in vivo. Using B6.129c1 congenic mice and adoptive transfer, we found that divergent *Slam* haplotypes controlled the response to LPS in vivo, as well as the diminished NKT cell number and function, and that these phenotypes were associated with differential expression of signaling lymphocytic activation molecule family receptors on NKT cells. These data suggest that the polymorphisms that distinguish two *Slam* haplotypes significantly modulate the innate immune response in vivo through their effect on NKT cells. *The Journal of Immunology*, 2010, 185: 144–156.

CD1d-restricted NKT cells make up an unusual T cell subset that has been implicated in a wide variety of immune responses and in infectious disease (1). Upon recognition of cognate glycolipid ligands presented by CD1d (2–4), NKT cells rapidly produce an assortment of cytokines, such as IFN-γ, TNF, IL-4, and IL-17 (5–7). Activation of NKT cells leads to the activation of a number of leukocyte subsets of the innate and adaptive arms of the immune system (8–11), suggesting that NKT cells may play a role during the early stages of the developing immune response and may represent a link between the innate and adaptive arms of the immune system.

NKT cell activation can occur through two pathways. Activation through the exogenous pathway occurs after uptake of exogenous glycolipids by APCs, followed by their loading onto the CD1d molecule and subsequent presentation on the cell surface (2, 12). NKT cell activation by bacterial glycolipids from *Borrelia*, *Sphingomonas*, and *Ehrlichia* (13–16) and the synthetic glycolipid α-galactosylceramide (αGalCer) occurs through this pathway. NKT cell activation through the endogenous pathway occurs after stimulation of APCs by TLR ligands, such as LPS (17) and CpG oligodeoxynucleotide (ODN) (18, 19). NKT cells, which lack the cognate TLRs, are activated through recognition of autologous CD1d ligands (17, 19, 20) and/or through IL-12 and IL-18 produced by activated APCs (17, 21).

Increasing evidence suggests that NKT cells activated through the endogenous pathway may play an important role in a variety of disease models and that they exert their effects primarily through their ability to modulate the function of other leukocyte subsets (22–24). Indeed, it was recently demonstrated that macrophage TNF production in response to the TLR4 ligand LPS is significantly impaired in NKT cell-deficient mice (21), which is consistent with previous reports that NKT cell-deficient mice are resistant to LPS-induced septic shock (21, 25, 26). These observations suggest that NKT cells activated through the endogenous pathway may play a significant role in modulating the innate immune response.

NKT cell number and function vary, depending on the mouse genetic background (27–32). However, little is known about how naturally occurring variations in NKT cell number and function affect the ability of NKT cells to modulate innate immune function. Recently, the *Slam* locus on chromosome 1 was identified as one of two major loci controlling thymic NKT cell number in NOD mice (33). This is consistent with reports demonstrating that targeted deletion of members of the signaling lymphocytic activation molecule (SLAM) receptor family (34), as well as the intracellular signaling molecule SLAM-associated protein (35), results in impaired NKT cell development. Interestingly, extensive polymorphism at the *Slam* locus distinguishes two major *Slam* haplotypes in commonly used inbred strains of mice (36, 37). *Slam* haplotype-2 is present in NOD, 129X1/SvJ, 129S1/SvImJ,

*Department of Surgery, †Vermont Center for Immunobiology and Infectious Disease, ‡Department of Medicine, and §Department of Pathology, University of Vermont College of Medicine, Burlington, VT 05405; and ¶Department of Immunology, University of Texas Southwestern Medical Center, Dallas, TX 75390

[1]I.A. and A.C. contributed equally to this work.

Received for publication August 12, 2009. Accepted for publication April 27, 2010.

This work was supported by National Institutes of Health Grants AI067897 and RR021905 (to J.E.B.), HL089177 (to M.E.P.), and NS36526, AI41747, AI058052, NS061014, NS060901, and AI45666 (to C.T.).

Address correspondence and reprint requests to Dr. Jonathan E. Boyson, Room E305 Given Building, University of Vermont College of Medicine, 89 Beaumont Avenue, Burlington, VT 05405. E-mail address: jboyson@uvm.edu

Abbreviations used in this paper: αGalCer, α-galactosylceramide; BMDM, bone marrow-derived macrophage; DC, dendritic cell; IHL, intrahepatic leukocyte; MFI, median fluorescence intensity; NIH, National Institutes of Health; ODN, oligodeoxynucleotide; SLAM, signaling lymphocytic activation molecule.

www.jimmunol.org/cgi/doi/10.4049/jimmunol.0902658

BALB/cJ, and SM/J mice, and *Slam* haplotype-1 is present in C57BL/6, C57BR/cdJ, and C57L/J mice, among others (36). In this study, we investigated whether genetic regulation of NKT cell number and function by *Slam* haplotypes would affect the ability of NKT cells to modulate innate immune function.

We identified 129S1/SvImJ and 129X1/SvJ strains as being severely deficient in liver, but not thymus or spleen, NKT cell number and in the response in vivo to the prototypical NKT cell agonist glycolipid, αGalCer. We found that these two 129 strains, as well as other strains with low liver NKT cell numbers, responded poorly to LPS in vivo, as measured by macrophage TNF production. Interestingly, we found no difference between the C57BL/6J and 129 strains in the response in vitro of macrophages and dendritic cells (DCs) to LPS. To investigate whether diminished NKT cell number and function were responsible for the poor response to LPS in vivo, we assessed the response to LPS in B6.129c1 congenic mice, which possess the 129-derived extended *Slam* locus introgressed onto the C57BL/6 background. B6.129c1 mice exhibited a deficiency in liver NKT cell number and an impairment in NKT function. Interestingly, we found that these mice also exhibited impaired in vivo macrophage TNF production in response to LPS and that adoptive transfer of C57BL/6J NKT cells to 129X1/SvJ mice resulted in increased macrophage TNF production after LPS challenge. These data suggest that *Slam* haplotypes significantly modulate the LPS response in vivo and that this phenotype is driven through its control of NKT cell number and function.

Materials and Methods

Mice and reagents

C57BL/6J, 129S1/SvImJ, 129X1/SvJ, LG/J, SM/J, and NOD/ShiLtJ mice were purchased from The Jackson Laboratory (Bar Harbor, ME). B6.129-*JA18*$^{-/-}$ mice were a gift from Dr. Mark Exley (Beth Israel Deaconess Medical Center, Boston, MA). B6.129c1 congenic mice were described previously (36). Single nucleotide polymorphism genotyping indicated that the 129-derived interval extends from rs8245216 to rs30562373 (~6.5 Mbp). All mice were housed in the specific pathogen-free barrier facility at the University of Vermont. All procedures involving animals were approved by the University of Vermont Institutional Animal Care and Use Committee. The α-GalCer (Axxora Pharmaceuticals, San Diego, CA) was prepared as described (30) and was administered i.p. (100 μg/kg) in a 100-μl volume. LPS from *Salmonella enterica* (Sigma-Aldrich, St. Louis, MO) was diluted in sterile PBS. For in vivo experiments, 20 μg LPS was administered i.p. in a 100-μl volume. CpG ODN 1826 (InvivoGen, San Diego, CA) was resuspended in PBS, and 50 μg was administered i.p. in a 100-μl volume.

Serum cytokine analysis

Serum was prepared from blood collected via cardiac puncture at various times after injection. Samples were frozen at −20°C until analysis. Serum cytokines were measured by ELISA (BD Biosciences, San Jose, CA) or Bio-Plex (Bio-Rad, Hercules, CA), according to the manufacturer's instructions.

Cell isolation and culture

Splenocytes and thymocytes were obtained by gentle pressing through nylon mesh. RBCs were lysed using Gey's solution. Intrahepatic leukocyte (IHL) isolation was performed as described (30). Briefly, anesthetized mice were perfused with PBS, after which the liver was removed, minced, and gently pressed through nylon mesh. The resulting cell suspension was washed twice and then resuspended in isotonic 33.8% Percoll (GE Healthcare, Piscataway, NJ). After centrifugation, the IHL cell pellet was resuspended and washed in PBS + 2% FCS.

To obtain neutrophils, bone marrow was flushed with Hanks' buffered saline solution and layered on a three-step Percoll gradient (72, 64, and 52%), which was centrifuged at 1060 × *g* for 30 min. Cytospin samples of the 72:64% interface revealed >95% morphologically mature-appearing neutrophils. These techniques were shown not to cause substantial activation or damage to the isolated cells (38, 39).

Peritoneal macrophages were isolated by injecting mice i.p. with 0.8 ml 3% Brewer's thioglycollate (Sigma-Aldrich). Four days later, peritoneal exudate cells were harvested in RPMI 1640. Cells prepared in this way were ~75% CD11b$^+$F4/80$^+$ (data not shown).

Bone marrow-derived macrophages (BMDMs) were derived by culturing bone marrow preparations in complete RPMI medium (RPMI 1640 supplemented with 10% FCS [Atlanta Biologicals, Lawrenceville, GA], penicillin-streptomycin, L-glutamine, nonessential amino acids, 2-ME, and sodium pyruvate) supplemented with 100 ng/ml M-CSF (eBioscience, San Diego, CA). Cells were used after 6 d and were 95% CD11b$^+$F4/80$^+$ (data not shown). Bone marrow-derived DCs were derived by expanding bone marrow preparations in complete RPMI medium supplemented with 5 ng/ml recombinant mouse GM-CSF (R&D Systems, Minneapolis, MN) for 6–8 d. All incubations were performed at 37°C in a 5% CO_2, humidified incubator.

Flow cytometry

Cells were stained at 4°C in PBS/2% FCS containing 0.1% sodium azide. F_cBlock (BD Biosciences) was used in all samples prior to the addition of Abs to block nonspecific Ab binding. Abs used in these experiments were anti–TCR-β (H57-597), anti–IFN-γ (XMG1.2), anti–IL-4 (11B11), anti-TNF (MP6-XT3), anti-CD3 (145-2C11), anti-CD4 (GK1.5), anti-CD5 (53-7.3), anti-CD8 (53-6.7), anti-CD1d (1B1), anti-CD49b (DX5), and anti-NK1.1 (PK136) all from BD Biosciences. Anti-Gr1, anti-F4/80, anti-CD229 (Ly9ab3), anti-CD48 (HM48-1), and anti-CD84 (mCD84.7) were from BioLegend (San Diego, CA). Anti-CD150 (9D1), anti-CD4 (RM4-5), anti-CD44 (IM7), and anti-Ly108 (13G3-19D) were from eBioscience. CD1d tetramer loaded with PBS57 was obtained from the National Institutes of Health (NIH) tetramer facility (Emory University Vaccine Center, Atlanta, GA).

For intracellular cytokine staining, cells were isolated from liver or spleen as described above and stained with Abs to surface markers. In all experiments, cells were analyzed directly ex vivo with no cell culture or treatment with brefeldin A or monensin. After washing in staining buffer, cells were fixed and permeabilized using fixation/permeabilization buffer (BD Biosciences), according to the manufacturer's instructions, followed by staining with Alexa Fluor 647-conjugated anti-cytokine mAbs or isotype control mAb. Data were collected on an LSRII (BD Biosciences) and analyzed using FlowJo software (Tree Star, Ashland, OR).

Ex vivo cytokine analysis

For ex vivo cytokine analysis by ELISA, splenocytes from αGalCer-injected mice were prepared and incubated in complete RPMI medium for 4 h at 37°C in a humidified 5% CO_2 incubator. Supernatants were harvested, and cytokine levels were assessed by ELISA, according to the manufacturer's instructions (BD Biosciences). Prior to the short-term incubation, the frequency of NKT cells in each preparation was determined by FACS analysis using anti-TCR and CD1dtetramer/PBS57 (data not shown). No significant difference in the percentage of spleen NKT cells between strains was observed, and no difference in the results was observed after normalizing for NKT cell number.

Adoptive transfer

For adoptive transfer, C57BL/6J liver IHLs were purified as described above, and NKT cells were sorted on a FACSAria (BD Biosciences). To avoid activation through TCR cross-linking prior to transfer, NKT cells were sorted using the surrogate markers anti-CD5 and anti-NK1.1 (22). CD8$^+$ T cells from the same samples were sorted as non-NKT controls. Two hundred thousand sorted liver NKT cells were administered to 129X1/SvJ recipients by i.v. injection. Eighteen hours after cell transfer, all mice received 20 μg LPS i.p.; 45 min later, mice were euthanized, and spleen and liver IHL TNF production was assessed by intracellular cytokine staining.

In vitro LPS stimulation

Bone marrow-derived DCs were incubated overnight in 48-well plates in complete RPMI medium and LPS. Supernatants were harvested after 16 h and tested for IL-12p70 by ELISA (BD Biosciences). BMDMs were rested overnight in 48-well plates in complete RPMI medium. Cells were stimulated with 100 ng/ml LPS for 15 h, after which supernatants were collected and tested for TNF by ELISA (BD Biosciences). Thioglycollate-elicited peritoneal macrophages were allowed to adhere to wells in 48-well plates for 2 h at 37°C, after which the nonadherent cells were removed. To prime cells, rIFN-γ (10 ng/ml) was added to some wells overnight. The next day, the medium was changed, and cells were stimulated with LPS in complete RPMI medium for 12 h, after which supernatants were collected. Purified neutrophils were allowed to adhere for 2 h in 24-well plates, after which they were stimulated with 10 ng/ml LPS for 45 min. Supernatants were